

METHODOLOGY AND APPLICATIONS OF HIGH RESOLUTION SOLID-
STATE NMR TO STRUCTURE DETERMINATION OF PROTEINS

by

Józef Romuald Lewandowski

B.A. Chemistry and Theater/Dance
Amherst College (2002)

Submitted to the Department of Chemistry
in Partial Fulfillment of the Requirements for the Degree of
Doctor of Philosophy in Chemistry
at the
Massachusetts Institute of Technology
September 2008

© 2008 Massachusetts Institute of Technology. All rights reserved.

Signature of Author _____

Department of Chemistry
August 25, 2008

Certified by _____

Professor Robert G. Griffin
Thesis Supervisor

Accepted by _____

Professor Robert W. Field
Chairman, Departmental Committee on Graduate Students

This Doctoral thesis has been examined by a Committee of the Department of Chemistry as follows:

Professor Andrei Tokmakoff _____
Chairman

Professor Robert G. Griffin _____
Thesis Supervisor

Professor Troy Van Voorhis _____

Methodology and Applications of High Resolution Solid-State NMR to Structure Determination of Proteins

by

Józef Romuald Lewandowski

Submitted to the Department of Chemistry
on August 25, 2008 in Partial Fulfillment of the
Requirements for the Degree of Doctor of Philosophy in Chemistry

Abstract

A number of methodological developments and applications of solid-state NMR for assignment and high resolution structure determination of microcrystalline proteins and amyloid fibrils are presented. Magic angle spinning spectroscopy on uniformly and selectively ^{13}C and ^{15}N labeled samples is performed at magnetic fields from 11.7 to 21.1 T and spinning frequencies from 9 to 65 kHz.

Dynamic Nuclear Polarization on nanocrystals of amyloidogenic peptide GNNQQNY is presented demonstrating that ^1H - ^1H spin diffusion can efficiently transfer the enhanced polarization across the solute that is not in an intimate contact with the polarizing agent.

An improved theoretical treatment of Rotational Resonance Width (R^2W) experiments and its application to determination of precise ^{13}C - ^{13}C distance is presented.

A general theory of second averaging in modulation frame for designing solid-state NMR experiments is introduced and discussed in the context of two methods: Cosine Modulated Rotary Resonance (CMpRR) for performing a broadband double-quantum ^{13}C - ^{13}C recoupling without the need for additional ^1H decoupling and Cosine Modulated recoupling with Chemical Shift reintroduction (COMICS) that provides a general frequency selective method for measuring precise ^{13}C - ^{13}C distances in uniformly labeled solids. Cosine Modulated Adiabatic Recoupling (CMAR) – an adiabatic extension of the CMpRR, that is particularly robust with respect to rf inhomogeneity, is also introduced. A number of applications CMpRR at 21.1 T to proteins with varying degrees of macroscopic order are presented.

A second order Third Spin Assisted Recoupling (TSAR) mechanism is introduced and discussed in detail. The heteronuclear TSAR – Proton Assisted Insensitive Nuclei Cross-Polarization (PAIN-CP) and homonuclear Proton Assisted Recoupling (PAR) yield long distance ^{13}C - ^{15}N , ^{13}C - ^{13}C and ^{15}N - ^{15}N restraints in uniformly labeled systems with spinning frequencies up to 65 kHz that are used for protein structure calculation.

Structure, dynamics and polymorphism of amyloidogenic peptide GNNQQNY from the yeast protein sup35p are investigated.

Finally, PAIN-CP and ^{13}C - ^{13}C PAR are used for high resolution *de novo* structure determination of 10.4 kDa Crh protein dimer.

Thesis supervisor; Robert Guy Griffin

Title: Professor of Chemistry, Director of Francis Bitter Magnet Laboratory

Table of Contents

Abstract	3
Table of Contents	4
Abbreviations	12
List of Figures	15
List of Tables	37
1. Introduction	41
1.1. Why solid-state NMR?	41
1.2. Roadmap	42
1.3. Spin dynamics essentials	45
1.3.1. Interactions in Nuclear Magnetic Resonance	45
1.3.2. Time evolution of density operator	52
1.3.3. Transformation to the interaction frame	52
1.3.4. Average Hamiltonian Theory	53
1.3.5. Multipole-Multimode Floquet Theory	55
1.4. References	56
2. Dynamic Nuclear Polarization for sensitivity enhancement	59
2.1. Abstract	59
2.2. Introduction	60
2.3. Theory	62
2.4. Experimental	66
2.4.1. Peptide nanocrystal samples	66
2.4.2. DNP experiments	66
2.4.3. Transmission Electron Microscopy	68
2.5. Results and Discussion	68
2.5.1. Enhanced NMR signal intensities of peptide nanocrystals	68
2.5.2. Polarized portions of fibril crystals	71
2.6. Conclusions	74
2.7. Acknowledgements	75
2.8. References	75

3. Accuracy of ^{13}C-^{13}C distance measurements in uniformly labeled solids using rotational resonance width (R^2W) experiments	79
3.1. Abstract	79
3.2. Introduction	80
3.3. Theory	84
3.3.1. Basic theory	84
3.3.2. Spin dynamics using the MMFT approach	87
3.4. Results and Discussion	92
3.5. Conclusion	107
3.6. Acknowledgements	108
3.7. References	108
4. Spin dynamics in the modulation frame: Application to homonuclear recoupling in magic angle spinning solid-state NMR	111
4.1. Abstract	111
4.3 Background	112
4.4 Modulation Frame and second averaging process	116
4.4.1 Cosine modulated phase irradiation: First order effect	116
4.4.2 Reduction to a single frequency problem	119
4.4.3 Spin Hamiltonian in the Interaction Frame	120
4.5 Generalized CM schemes	125
4.5.1 Resonant second audio field averaging: second order effect	125
4.5.2 Generalized cosine modulated recoupling schemes: phase and amplitude rf modulation	127
4.5.2.1 General description	127
4.5.2.2 DQ recoupling conditions I and II	130
4.5.3 Generalized cosine modulated recoupling schemes: frequency, phase and amplitude rf modulation	132
4.5.3.1 General description of CM	132
4.5.3.2 DQ recoupling conditions III-VI	134
4.6 DQ homonuclear recoupling	136
4.6.1 MAS dipolar recoupling sequences	136

4.6.2 Broadband versus selective recoupling	137
4.6.3 DQ rotary resonance recoupling condition in the modulation frame I and II: CMpRR	139
4.6.4 Generalized rotary resonance conditions in the modulation frame: DQ conditions (III) to (IV)	141
4.6.5 Narrowband DQ COMICS recoupling in the modulation frame	142
4.7 Properties of the DQ recoupling with Cosine Modulated Rotary Resonance (CMpRR)	145
4.7.1 Experiments and simulations	145
4.7.1.1 Experimental	145
4.7.1.2 Numerical simulations	146
4.7.2 CMpRR at moderate MAS frequency	146
4.7.3 Effect of the p and p' mismatch on DQ CMpRR efficiency	148
4.7.4 Experimental results and p -dependency of the DQ efficiency	151
4.7.5 Second and third order effects in CMpRR	154
4.7.6 DQ efficiency dependency on the ^1H CW decoupling	157
4.7.7 Low power ^1H irradiation in CMpRR	159
4.7.8 CMpRR: 2D ^{13}C - ^{13}C correlation experiments	162
4.8. Conclusion	165
4.9 Acknowledgments	166
4.10 Supporting Information	167
4.10.1 Appendix A: Cosine and Sine expansion:	167
4.10.2 Appendix B: Irreducible spherical tensor, ZQ and DQ operators:	167
4.10.3 Appendix C: Scaling factor	169
4.10.4 Appendix D: Time dependent expression for the dipolar interaction	169
4.10.5 Appendix E: Euler angles and generalized CM-based interaction frame	170
4.10.6 Appendix F: Generalized CM-based interaction frame: evaluation of the second order cross-terms	173
4.11 References	182
5. Broadband Homonuclear Correlation Spectroscopy at High Magnetic Fields and High Spinning Frequencies	188

5.1 Abstract	188
5.2 Introduction	189
5.3 Results and Discussion	190
5.4 Conclusion	193
5.5 Acknowledgements	193
5.6 Supporting Information	194
5.7 References	194
6. Double-quantum carbon-carbon relayed magnetization transfer for solid-state NMR biomolecular studies at high magnetic fields	199
6.1 Abstract	199
6.2 Introduction	200
6.3 Results and Discussion	203
6.3.1 Chain relayed polarization transfer in biological samples	203
6.3.2 High spinning frequencies recoupling and sample heating	211
6.3.3 Considerations for high field applications	213
6.4 Conclusion	215
6.5 Materials and Methods	216
6.6 Acknowledgements	218
6.7 References	218
7. Proton Assisted Insensitive Nuclei Cross Polarization	223
7.1 Abstract	223
7.2 Introduction	224
7.3 Results and Discussion	226
7.4 Conclusion	228
7.5 Acknowledgements	228
7.6 Supporting Information	228
7.6.1 Model spin system	228
7.6.2 PAIN-CP mechanism	229
7.6.3 Complementary information on the one-bond transfer	231
7.6.4. Transfer to a weakly coupled spin in the presence of a strongly coupled spin	233

7.6.5 DCP versus PAIN-CP – overall polarization transfer (experiment)	235
7.6.6 Comments on the PAIN-CP pulse sequence	236
7.6.7 Elimination of the ^1H - ^{13}C transfer during PAIN-CP mixing	236
7.7 References	237
8. Proton Assisted Homonuclear Recoupling and Protein Structure Determination	239
8.1 Abstract	239
8.2 Introduction	240
8.3 Principles of PAR recoupling	243
8.3.1 PAR pulse sequence	243
8.3.2 Second-order effective Hamiltonian – PAR subspace	244
8.3.3 Second-order effective Hamiltonian – auto-cross terms	249
8.4 Details of the PAR mechanism	250
8.4.1 Numerical versus analytical simulations	250
8.4.2 Local geometry dependency	256
8.4.3 Auto-cross term compensation	263
8.4.4 Experimental results: long distance ^{13}C - ^{13}C contacts in $[\text{U-}^{13}\text{C}, ^{15}\text{N}]$ - <i>f</i> -MLF-OH	265
8.5 Polarization transfer in uniformly labeled systems	266
8.5.1 Dipolar truncation and long distance transfer	266
8.5.2 Multiple spins mechanism: relayed versus direct polarization transfer	269
8.5.3 ^{13}C - ^{13}C Crh distance estimates from ^{13}C - $[\text{}^1\text{H}]$ - ^{13}C PAR data	272
8.5.4 Influence of the ^1H - ^1H couplings on ^{13}C - ^{13}C distance estimates	274
8.6 Concurrent ^{13}C - $[\text{}^1\text{H}]$ - ^{13}C TSAR recoupling during first order ^{13}C - ^{13}C homonuclear recoupling	275
8.6.1 Dual polarization transfer	275
8.6.2 Simultaneous polarization transfer and dipolar truncation	277
8.7 Protein structure calculation	280
8.7.1 Crh monomer structure calculation from PAR spectra using the x-ray structure as a homology model	280
8.7.2 Comparison with alternative techniques	282

8.8 Conclusion	285
8.9 Acknowledgements	286
8.10 Supporting Information	286
8.10.1 PAR subspace, coupled basis, irreducible spherical tensor and ZQ fictitious operators:	286
8.10.2 Materials and methods	287
8.10.2.1 Sample Preparation	287
8.10.3 NMR Spectroscopy	288
8.10.2.2 Simulations, Data Analysis and Structure Calculations	290
8.10.3 Analytical simulations of the TSAR mechanism:	291
8.10.4 Dependence of the TSAR mechanism on local geometry: auto-cross terms compensation	293
8.10.5 Multiple proton effect on TSAR	298
8.10.6 Relayed versus direct transfer mechanism	298
8.10.7 ^{13}C - ^{13}C distance estimates from ^{13}C - ^1H - ^{13}C PAR data	301
8.10.8 Dual polarization transfer: concurrent ^{13}C - ^1H - ^{13}C TSAR recoupling during first order ^{13}C - ^{13}C dipolar recoupling or ^{13}C - ^{13}C J-based polarization transfer experiment	301
8.10.9 ^{13}C - ^{13}C PAR versus CHHC and DARR – a qualitative comparison	309
^{13}C - ^{13}C PAR at low/high spinning frequency	310
8.11 References (manuscript)	311
9. ^{15}N-^{15}N Proton Assisted Homonuclear Recoupling as a Structural Tool in Solid-State NMR	320
9.1 Abstract	320
9.2 Introduction	321
9.3 ^{15}N - ^{15}N correlation spectroscopy:	322
9.4 ^{15}N - ^1H - ^{15}N TSAR – ^{15}N - ^{15}N PAR experiments:	323
9.4.1 TSAR mechanism principles:	323
9.4.2 PAR pulse sequence and effective Hamiltonian:	323
9.5 PAR pulse sequence optimization:	325
9.6 Experimental PAR experiments: application to peptide and protein	327

9.6.1 ^{15}N - ^{15}N PAR on N-[U- ^{13}C , ^{15}N]-f-MLF-OH	327
9.6.2 ^{15}N - ^{15}N PAR on microcrystalline protein GB1	330
9.7 ^{15}N -[^1H]- ^{15}N PAR experiments applied to structure determination	330
9.7.1 Sequential ^{15}N - ^{15}N contacts in an α -helix	332
9.7.2 ^{15}N - ^{15}N contacts in β -sheets	333
9.8 ^{15}N - ^{15}N PAR in the context of other methods	335
9.9 Conclusion	337
9.10 Material and methods	338
9.10.1 Sample preparation:	338
9.10.2 NMR Spectroscopy	339
9.10.3 Numerical simulations and data analysis	340
9.11 Acknowledgement	340
9.12 Supporting Information	341
9.13 References	348
10. ^{13}C-^{13}C PAR at 65 kHz	354
10.1 Abstract	354
10.2 Introduction	355
10.3 Experimental Section	357
10.3.1 Sample preparation	357
10.4 Results and Discussion	359
10.4 Acknowledgement	365
10.5 Supporting Information	366
10.6 References	372
11. Solid state NMR study of amyloid nanocrystals and fibrils formed by the peptide GNNQQNY from yeast prion protein Sup35p	377
11.1 Abstract	377
11.2 Introduction	378
11.3 Experimental Methods	382
11.3.1 Sample Preparation	382
11.3.2 Transmission electron microscopy	382
11.4 NMR methods	384

11.4.1 Nanocrystal and fibril assignments	384
11.4.2 NMR data analysis	385
11.5 Results	385
11.5.1 Peptide aggregate preparation	385
11.5.2 Monoclinic nanocrystal characterization	386
11.5.3 Orthorhombic crystals	392
11.5.4 GNNQQNY peptide fibril characterization	395
11.5.5 Comparison of the GNNQQNY aggregates	400
11.6 Discussion	405
11.6.1 Polymorphism in GNNQQNY aggregation	405
11.6.2 Spectroscopic differences – crystal forms	407
11.6.3 Spectroscopic differences - fibrils	408
11.7 Implications	409
11.8 Conclusion	410
11.9 Acknowledgments	411
11.10 Supporting Information	411
11.10.1 2D assignment data for orthorhombic GNNQQNY nanocrystals	411
11.10.2 Fibril assignment data	413
11.11 References	417
12. Efficient high resolution structure determination of a protein by solid-state	
NMR	423
12.1 Abstract	423
12.2 Conclusion	432
12.3 Acknowledgements	432
12.4 References	432
Curriculum Vitae	439

Abbreviations

1D One-dimensional

2D Two-dimensional

3D Three-dimensional

ADR Ambiguous Distance Restraint

AHT Average Hamiltonian Theory

ARIA Ambiguous Restraints for Iterative Assignment

CE Cross Effect

CF Crystal Frame

CM Cosine Modulation

CMAR Cosine Modulated Adiabatic Recoupling

CMRR Cosine Modulated Rotary Resonance

COMICS COsine Modulated recoupling with Isotropic Chemical Shift reintroduction

CP Cross-Polarization

CPMAS Cross Polarization with Magic Angle Spinning

CS isotropic Chemical Shift

CSA Chemical Shielding Anisotropy

CW Continuous Wave

DARR Dipolar Assisted Rotational Resonance

DNP Dynamic Nuclear Polarization

DQ Double Quantum

DQ-SQ Double Quantum Single Quantum

EPR Electron Paramagnetic Resonance

FID Free Induction Decay

FWHM Full Width at Half Maximum

IF Interaction Frame

MAS Magic Angle Spinning

MDTR Multiple Differential Transverse Relaxation
MF Modulation Frame
MLF Methionyl-Leucyl-Phenylalanine
MMFT Multipole-Multimode Floquet Theory
MQ Multiple Quantum
NMR Nuclear Magnetic Resonance
PAIN-CP Proton Assisted Insensitive Nuclei Cross-Polarization
PAR homonuclear Proton Assisted Recoupling
PAS Principal Axis System
PDSD Proton Driven Spin Diffusion
ppm parts per million
 R^2 Rotational Resonance
 R^2W Rotational Resonance Width
RR Rotary Resonance Recoupling
REDOR Rotational Echo Double Resonance
RF Radio Frequency
RFDR Radio Frequency Driven Recoupling
RMSD Root Mean Square Deviation
SE Solid Effect
SEASHORE Evolution-Assisted Selective HOmonuclear Recoupling
SPC-5 Supercycled Permutationally Offset Stabilized C5
SPECIFIC CP Spectrally Induced Filtering in Combination with CP
SQ-DQ Single Quantum Double Quantum
SQ-SQ Single Quantum Single Quantum
SSNMR Solid State Nuclear Magnetic Resonance
STEM Scanning Transmission Electron Microscopy
TALOS Torsion Angle Likelihood Obtained from Shifts and Sequence Similarity
TEDOR Transferred Echo Double Resonance
TEM Transmission Electron Microscopy
TM Thermal Mixing
TOFU-RADAR Triple Oscillating Field techniqUe - Rotor Assisted DipolAr Refocusing

TPPM Two Pulse Phase Modulation

TSAR Third Spin Assisted Recoupling

ZQ Zero Quantum

List of Figures

Figure 2-1 (a) Illustration of the crystal lattice of the GNNQQNY X-ray structure 24, where the dashed lines delineate two monomers surrounding the largest opening in the lattice, containing a network of hydrogen bonded water molecules. (b) Space filling models of the GNNQQNY monomers, the spacing between them (~0.7 nm maximum width), together with two views of an approximate space filling model of the TOTAPOL biradical showing its size relative to the water opening. The plane of the figure is perpendicular to the longest dimension of the crystallites..... 62

Figure 2-2 (a) Model for an individual peptide crystallite, showing polarization transfer into the core along the narrowest crystal dimension x . (b) Predicted enhanced polarization profile along the dimension x of the nanocrystal. 64

Figure 2-3 The theoretical enhancement ϵ , compared to the homogeneous enhancement ϵ_0 in the glassy matrix, of proton polarization in a nanocrystal of width w . The calculation uses a proton $T_{1n}=17$ s, and the calculated values of the diffusion constant (a) $D=2\times 10^5$ and (b) $1\times 10^5 \text{ \AA}^2/\text{s}$ 66

Figure 2-4 DNP enhanced ^{13}C (a) and ^{15}N (b) CP-MAS spectra of [20% $\text{U-}^{13}\text{C}$, ^{15}N -GNNQ]QNY in d_8 -glycerol/ $\text{D}_2\text{O}/\text{H}_2\text{O}$ (60/30/10) with 10 mM TOTAPOL biradical at 90 K and 5 T, with (top trace) and without (bottom trace) DNP. The microwave power was 1.5 W and irradiation time was 75 s for both spectra. 69

Figure 2-5 DNP-enhanced ^{13}C - ^{13}C R^3 PDS correlation spectrum of [20% $\text{U-}^{13}\text{C}$, ^{15}N -GNNQ]QNY nanocrystals. Indicated assignments are based on previous assignment data, and unmarked cross peaks represent spinning sidebands and experimental artifacts..... 70

Figure 2-6 ^{13}C and ^{15}N cross-polarization spectra of 30% labeled [$\text{U-}^{13}\text{C}$, ^{15}N -GNNQ]QNY nanocrystals without TOTAPOL (a,d) and with 10 mM (b,e) or 50 mM (c,f) TOTAPOL. Data were acquired at 15 kHz MAS and 700 MHz ^1H frequency, using the same sample material. Measured line widths are insensitive to biradical concentration (within their error margins of ~1-3 Hz), showing that the radical is not in close proximity to the bulk of the peptide crystals..... 72

Figure 2-7 Time-dependent growth of the enhancement polarization. (a) Illustration of the 1D ^{13}C spectra as a function of microwave irradiation time, after 5, 10, 20, 30, 45, 60 and 75 s of microwave irradiation. The chemical shift axes are offset for visual clarity. (b) The intensity of the spectral lines normalized to maximum intensity of each signal. Lines indicate calculated fits using growth time constants of 16-17 s for crystal signals (a-d), and 7-8 s for glycerol peaks e and f..... 73

Figure 2-8 Transmission electron micrographs of GNNQQNY nanocrystallites at an approximate magnification of (a) 55,000 and (b) 110,000. The black bars indicate 200 nm. 73

Figure 3-1 Diagram of the di-peptide N-Ac-VL derived from the crystal structure³³. 83

Figure 3-2 Pulse sequence for 3D-R²W experiment. The following phase cycling scheme was employed: $\phi_1=(16\times 1,16\times 3)$; $\phi_2=2$; $\phi_3=1$; $\phi_4=(8\times 2,8\times 4)$; $\phi_5=1$; $\phi_6=(4\times 3,4\times 1)$; $\phi_7=1234$; $\phi_{rec}=(1234,3412,3412,1234,3412,1234,1234,3412)$. The labels 1,2,3,4 correspond to the phases x,y,-x,-y, respectively. The dipolar mixing time (t_{mix}) was fixed at 30 ms. 84

Figure 3-3 One-dimensional ¹³C MAS spectrum of N-Ac-VL recorded at $\omega_r/2\pi=10.5$ kHz. The unlabeled acetyl carbonyl carbon is visible at reduced intensity. 93

Figure 3-4 Representative two-dimensional slices from the ¹³C-¹³C R²W experiment in N-acetyl-[U-¹³C,¹⁵N]L-Val-L-Leu (N-Ac-VL) recorded on a 500 MHz spectrometer at (a) $\omega_r/2\pi=8.791$ kHz and (b) $\omega_r/2\pi=9.116$ kHz, corresponding to the L_C-L_β and L_C-V_β N=2 R² matching conditions, respectively. 94

Figure 3-5 Resonance width profiles (cross-peak intensities) as a function of spinning frequency, polarization transfer from (a) L_C, and (b) V_C carbons to the indicated side-chain carbons. Intensities are scaled relative to the carbonyl CP intensities. 97

Figure 3-6 Illustration of the Euler angles used to define the relative CSA tensor orientations, showing here the CSA tensors for a leucine C_{δ2} methyl group and C' carbonyl. 98

Figure 3-7 The effect of CSA orientations on the R²W polarization transfer profiles. (a) Simulated polarization transfer between a leucine carbonyl and methyl carbon as a function of MAS rate, for two hypothetical CSA orientations using an internuclear distance $r=4.4$ Å and $T_{ZQ}=26$ ms. CSA orientations ($\alpha_{PM}, \beta_{PM}, \gamma_{PM}$) of L_C/L_δ are (0,90,0)/(0,0,0) (solid lines), and (0,0,0)/(0,90,0) (dashed lines), exemplifying two extreme cases. Panels (b) and (c) illustrate the distance-dependence of the maximum and width of the R² matching condition for both orientations, now with $T_{ZQ}=30$ ms (black) and 10 ms (gray). 99

Figure 3-8 Comparison between the x-ray structure and measured SSNMR distances, obtained using effective Hamiltonians with estimated CSA orientations, and free-fit optimization of both the internuclear distance and the zero-quantum relaxation ('model 2'). Open squares indicate distances affected by intermolecular multi-spin effects (see text). 103

Figure 3-9 Simulations and experimental results illustrating the separate contributions of the higher order corrections and the ZQ parameters on the exchange dynamics. The results presented here correspond to the strong coupling, L_C-L_β (2.47 Å X-ray distance). In (a) the experimental data (●●●) is fit using the zero order Hamiltonian both with (solid lines, $T_{ZQ}=63$ ms, $r=2.85$ Å) and without relaxation

((----), $r=2.2\text{\AA}$). In (b) the experimental data is fit using the effective Hamiltonians both with (solid line, $T_{ZQ}=165\text{ms}$, $r=2.55\text{\AA}$) and without relaxation ((----), $r=2.3\text{\AA}$). Panels (c) and (d) show the contour plots for the simulations including relaxation, for the zero order and effective Hamiltonian respectively (contours indicate 95-99% confidence intervals). 105

Figure 3-10 Simulations and experimental results illustrating the separate contributions of the higher order corrections and the ZQ parameters on the exchange dynamics. The results presented here correspond to the weak coupling L_C-V_β (4.98\AA x-ray distance). In (a) the experimental data ($\bullet\bullet\bullet$) is fit using the zero order Hamiltonian both with (solid lines, $T_{ZQ}=12\text{ms}$, $r=4.5\text{\AA}$) and without relaxation ((-- --), $r=3.8\text{\AA}$). In (b) the experimental data is fit using the effective Hamiltonians both with (solid line, $T_{ZQ}=12\text{ms}$, $r=4.6\text{\AA}$) and without relaxation ((----), $r=4.0\text{\AA}$). Panels (c) and (d) show the contour plots for the simulations including relaxation, for the zero order and effective Hamiltonian respectively (contours indicate 95-99% confidence intervals). 105

Figure 4-1 Pulse sequences used in this work for acquisition of (a) ^{13}C DQ coherence buildup, (b) ^{13}C SQ-SQ correlation experiments, and (c) ^{13}C DQ-SQ correlation experiments. In (a) and (c), the phase of the reconversion period ϕ_r is phase cycled to select for DQ coherences. Note that no ^1H decoupling is applied during the recoupling ^{13}C pulses unless specified otherwise. τ_e and τ_r refer to the excitation and reconversion times..... 115

Figure 4-2 Schematic representation of a cosine modulated radio frequency phase modulation. In graphic (a) the rf Hamiltonian is represented as an oscillating field around the axis ϕ_0 in the xy-plane: $\omega_1/2\pi$ stands for the rf field strength, $\omega_c/2\pi$ for the frequency and a the amplitude of the phase modulation. In graphic (b), the mean axis of the irradiation is chosen to be the X-axis. Graphic (c) shows that under some very precise settings, the cosine modulated phase irradiation can be decomposed into two components: a CW component of strength $\omega_c/2\pi$ and a resonant audio field of strength $\omega_{\text{eff}}/2\pi$. In the Modulation Frame (MF), defined as the interaction frame of the first component, the resonant circular audio field appears static aligned with the axis ϕ_0 . Graphic (d) shows the static audio field in the MF (aligned with the Z-axis) for $\phi_0 = 0$ and $\phi_0 = \pi/2$ 117

Figure 4-3 Two-field averaging process first order recoupling conditions for various interactions such as: (a) DQ $m = 1$ (green lines), $m = 2$ (black lines) and ZQ $m = 1$ (brown lines) and $m = 2$ (orange lines) ^{13}C dipolar terms, (b) SQ dipolar ^{13}C dipolar terms $m = 1$ (blue lines) and $m = 2$ (yellow lines), (c) isotropic (magenta line) and anisotropic $m = 1$ (cyan lines) and $m = 2$ (red lines) ^{13}C chemical shift interactions and (d) all previous interactions. For all the recoupling conditions shown in this figure, q and q' represent the successive components of the recoupled interactions during this two steps averaging mechanism. The reduced spin scaling factor of each recoupling branch is defined

by $S_{0,q,q'}^{spin,l} = d_{0q}^l (\pi/2) d_{q',q}^l (\pi/2)$. Note also that if no ^1H irradiation is applied during the ^{13}C recoupling pulses, heteronuclear interactions behave like CSA terms. The dashed lines represent branches with a null reduced spin scaling factor and are not considered in this study..... 123

Figure 4-4 Expansion of the region with $p \leq 2$ and $p' \leq 3$ from Fig. 3(d) illustrating first order recoupling conditions. Black circle at $p = 0.25$, $p' = 0.25$ indicates a recoupling condition named COMICS. COMICS leads to simultaneous recoupling of the DQ dipolar and isotropic chemical shift interaction and results in extremely narrowband behavior. As in Fig. 3 green and black lines represent DQ recoupling conditions, brown and orange ZQ recoupling conditions, yellow and blue lines SQ recoupling conditions, red and cyan lines CSA recoupling and magenta line isotropic chemical shift recoupling condition. 125

Figure 4-5 Relative size of the second order effect (in arbitrary units) induced by the counter rotating component $[3']$ with itself in the Modulation Frame for the six different CM recoupling regimes (Eq. (21-23)). Note that for the regimes I and II (red and green lines respectively) the cross-term contribution is negligible. Regimes other than I and II require compensation for the effect of the counter rotating field, which could be achieved by appropriate frequency modulation (see Sec. III C). 129

Figure 4-6 Fourier series decomposition (ϕ_1, ϕ_2, ϕ_3) of the phase modulation ϕ as a function of the p index for: (a) recoupling regimes I-II (red and green lines respectively), and (b) recoupling conditions III-VI (yellow, blue, magenta and cyan lines respectively) defined in Eq. (18) and (30) respectively. Note that for recoupling conditions I and II the three first Fourier components tend towards zero and that ϕ_5 and ϕ_3 can be neglected for p ranging from 2 to 10. For recoupling conditions III to VI the three first Fourier components tend towards non-zero value as p increases..... 129

Figure 4-7 Contour plots of the periodic time dependent part of the rf field strength as a function of the fraction of the cycle time and the p index for recoupling regime I in (a), and II in (b). The contour levels indicate the rf field deviation in units of spinning frequency..... 132

Figure 4-8 Simulations of the DQ filtered efficiency of a spin system based on a glycine model, with $p=5$ index, for recoupling regimes I to VI: (a) with included ^{13}C - ^{13}C dipolar interaction only (corresponding to 1.54\AA distance), (b) with ^{13}C - ^{13}C dipolar and ^{13}C CSA interactions only ($\sigma_{\text{aniso},1} = 20$ ppm, $\eta_1 = 0.8$, $\sigma_{\text{aniso},2} = 25$ ppm, $\eta_2 = 0.9$), (c) with ^{13}C - ^{13}C dipolar and ^{13}C isotropic CS interactions only ($\sigma_{\text{iso},1} = -10$ ppm, $\sigma_{\text{iso},2} = 10$ ppm), (d) with ^{13}C - ^{13}C dipolar, ^{13}C CS interactions and ^{13}C - ^1H dipolar interactions between carbons and the two alpha protons (directly bonded to C2). Note that regimes I and II ($p' = 0.5$ and $p' = 1$) are the least affected by the ^{13}C chemical shift interactions. The presence of simultaneous first order CSA recoupling conditions for regions III and VI ($p' = 4$ and $p' = 6$)

significantly reduces the DQ efficiency for these branches in a presence of such interactions. In a similar manner regions IV and V ($p' = 4.5$ and $p' = 5.5$) are affected by ^{13}C isotropic chemical shift through a second order effect due to nearby first order isotropic chemical shift recoupling condition (in this particular case for $p' = 5$). The simulation in (d) with all the interactions included clearly shows that region I ($p' = 0.5$) is compensated the best for presence of anisotropic and heteronuclear interactions. This figure confirms that the recoupling map in Fig. 4-3 could be used for qualitative prediction of the performance of CM sequences in presence of various interactions. All the simulations were performed using the full modulation scheme described in Sec. III C. 140

Figure 4-9 COMICS recoupling pulse sequence reintroducing simultaneously DQ dipolar interaction and isotropic chemical shift: (a) amplitude and frequency modulation scheme, (b) phase modulation. (c) COMICS DQ coherence buildup simulation with ^{13}C dipolar interaction only. (d) DQ efficiency for mixing time optimal for 3\AA distance as a function of the ^{13}C mean offset for broadband CM_5RR (at 20 kHz MAS) and narrowband super-cycled COMICS (at 30 kHz MAS). Note the radically different effective bandwidth of > 30 kHz for CM_5RR and $<$ few hundred Hz for COMICS. COMICS simulation in (d) was supercycled according to the scheme described for R sequences in Kristiansen et al.⁵² Both the simulations in (d) were performed at 750 MHz field and included isotropic chemical shift ($\sigma_{\text{iso},\text{C}1} = -10$ ppm, $\sigma_{\text{iso},\text{C}2} = 10$ ppm) and CSA ($\sigma_{\text{aniso},\text{C}1} = -13.86$ ppm, $\eta_{\text{C}1} = 0.93$, $\sigma_{\text{aniso},\text{C}2} = -20.88$ ppm, $\eta_{\text{C}2} = 0.75$). 100 kHz ^1H CW decoupling was used for COMICS. 144

Figure 4-10 DQ coherence buildup simulations of a glycine spin system (4 spins, see Sec. VI A 1) at 12 kHz MAS spinning frequency and 750 MHz field for various pulse sequences. Graphics (a) shows sequences with matching condition of 5 (i.e. ^{13}C rf ~ 60 kHz): SPC5 (black dot-dash line) and CM_5RR , (black solid line); sequences with matching condition of 6 (i.e. ^{13}C rf ~ 72 kHz): $R12_2^5$ (red dash line) and CM_6RR (red solid line). Graphic (b) shows sequences with matching condition of 7 (i.e. ^{13}C rf ~ 84 kHz): POST-C7 (cyan dash line) and CM_7RR (cyan solid line); sequences with matching condition of 10 (i.e. ^{13}C rf ~ 120 kHz): $R20_2^9$, 8.5 (i.e. ^{13}C rf ~ 102 kHz) DRAWS and 0.5: HORROR (^{13}C rf 6 kHz). All the simulations were performed without ^1H irradiation except for HORROR where 200 kHz ^1H rf decoupling was used. 147

Figure 4-11 Simulated maps of the DQ efficiency as function of p and p' mismatch for a glycine spin system. No ^1H irradiation is included in the simulation and the mixing time is chosen to maximize the DQ efficiency transfer. The x-axis represents the deviation δ_{p_0} from the theoretical p_0 value, whereas the y-axis represents the deviation $\delta_{p'_0}$ from the theoretical $p'_0 = 1/2$. The figure shows simulations for three different p -values: (a) $p=3.5$, (b) $p=5$, (c) $p=10$ with only the ^{13}C dipolar coupling

included and (d) $p = 3.5$, (e) $p = 5$, (f) $p = 10$ with all interactions included. Note the systematic shift in p and p' from the theoretical value due to the higher order cross terms in the bottom panel simulations. Simulations were performed for theoretical $\omega_c/2\pi = 100$ kHz and $\omega_c/2\pi$ of 28.571 kHz, 20 kHz and 10 kHz for p equal to 3.5, 5 and 10 respectively. 149

Figure 4-12 Comparison of experimental (a-b) and simulated (c-d) DQ coherence buildups and bandwidth. Experimental CM₅RR DQ coherence buildup (a) and bandwidth (b) obtained on 20% [U-¹³C, ¹⁵N]-glycine at 750 MHz B₀, 20 kHz MAS without any ¹H decoupling during the mixing. Note the efficient and broadband behavior of CM₅RR. (c) Simulated CM_pRR DQ efficiency for glycine spin system as a function of p index for a modulation frequency ω_c of 100 kHz: the solid black line shows simulations when all interactions are included, the dashed red line shows the same simulation with the ¹H-¹H dipolar coupling removed, and finally, the dotted blue line represents DQ efficiency for optimized CM_pRR with all interactions included. Significant gains in DQ efficiency for the optimized CM_pRR indicate that the adjustment of transverse and longitudinal components can compensate for a large part of high order cross terms present. Graphics (d) shows simulated optimized bandwidth for a series of p indexes with ω_c of 100 kHz. Excitation time of 480 μ s was used for (b-d). 151

Figure 4-13 Experimental DQ coherence buildups for 20% [U-¹³C, ¹⁵N]-glycine obtained at 750 MHz ¹H Larmor frequency. The ¹³C rf field strength used was 100 kHz for all the experiments. Both CM₅RR (black solid line) and SPC5 (red dotted line) were obtained at 20 kHz MAS with no ¹H irradiation. CM_{3.5}RR was obtained at 28.571 kHz MAS using no ¹H (blue long-dashed line) and ~5 kHz ¹H irradiation (green short-dashed line). 154

Figure 4-14 Simulated contour plots of DQ efficiency as a function of p index and ¹H rf field strength for (a) glycine and (b) alanine spin systems. Simulations were performed with a constant modulation frequency ω_c of 100 kHz using the theoretical settings of $p' = 0.5$. No isotropic chemical shift was included in the calculations in order to minimize the shift from the theoretical settings and thus focus on the influence of ¹H-¹³C and ¹H-¹H interactions on the DQ recoupling spin dynamics. The plots are divided into three areas: 1 – intermediate decoupling regime, 2 – high power decoupling regime, 3 – low power decoupling regime. See text for the explanations of the fine structure of the plots. 157

Figure 4-15 (a) CM_{3.5}RR DQ efficiency as a function of the ¹H rf power for the glycine spin system. The mixing time was chosen to optimize the transfer efficiency. Graphics (b) and (c) show ¹H-¹H polarization transfer occurring exactly under the same ¹³C/¹H irradiation schemes but with 3 ms mixing time. The magnetization starts on the first proton along the CW irradiation axis / Z-axis and is detected on the second proton spin along the CW irradiation axis/ Z-axis in (b) and (c) respectively. See text for the discussion of the features of the simulations. 160

Figure 4-16 Experimental SQ-SQ 2D ^{13}C - ^{13}C correlation spectra for [U- ^{13}C , ^{15}N]-f-MLF-OH (a) using CM_{3,5}RR, at 900 MHz ^1H Larmor frequency, 23.81 kHz MAS, with 840 μs mixing using \sim 4 kHz ^1H decoupling and 83.3 kHz ^{13}C rf, (b) CM₅RR, at 750 MHz ^1H Larmor frequency, 20 kHz MAS, with 2.1 ms mixing using no ^1H decoupling and 100 kHz ^{13}C rf. The evolution interval t_1 was incremented in steps of 20 μs in (a-b). 100 kHz TPPM ^1H decoupling was used during the acquisition and evolution. The longer mixing time 2D spectrum in (b) features up to 4-bond relayed transfer cross-peaks. 164

Figure 4-17 Experimental SQ-DQ 2D ^{13}C - ^{13}C CM_{3,5}RR correlation spectrum obtained on a 10 % [U- ^{13}C , ^{15}N]-f-MLF-OH at 900 MHz ^1H Larmor frequency, 23.81 kHz MAS, using 420 μs excitation time with 83.3 kHz ^{13}C irradiation and \sim 4 kHz ^1H irradiation. 100 kHz TPPM ^1H decoupling was used during the acquisition and evolution. The t_1 evolution interval was incremented in steps of 10 μs . The overall phase of the conversion was adjusted to correct for the phase acquired by DQ coherence due to not rotor-synchronized evolution period (see text). 164

Figure 5-1 (a) Two-dimensional ^{13}C - ^{13}C correlation pulse sequence used with CMAR recoupling sequence. Note that no ^1H decoupling rf field is applied during the mixing time. (b) ^{13}C rf phase modulation applied during the recoupling period. 190

Figure 5-2 2D correlation spectrum of the tripeptide [U- ^{13}C , ^{15}N] N-f-MLF-OH using CMAR recoupling at 28.6 kHz MAS and approximately 100 kHz of ^{13}C rf field strength using 2 ms (up) and 5 ms (down) mixing time, with no proton decoupling. 192

Figure 5-3 Slices through the C α resonances (a) and C β resonances (b) for each residue in the indirect dimension of the MLF 2D ^{13}C - ^{13}C correlation spectrum with 2ms CMAR mixing time. The MAS spinning frequency was 29.578 kHz, the ^{13}C field strength 100 kHz and the proton frequency 750 MHz. 194

Figure 6-1 CM_pRR pulse sequences for performing two-dimensional (2D) ^{13}C - ^{13}C correlation experiments at high field and spinning frequency with ultralow (less than $0.25\omega_r$) or even without ^1H decoupling: (a) version used for 2D SQ-SQ ^{13}C - ^{13}C correlation experiments, (b) DQ filtered version used for 2D SQ-DQ ^{13}C - ^{13}C correlation experiments. Note, that the pulse sequence in (b) without the t_1 evolution is used for optimizations of polarization transfer. 202

Figure 6-2 CM₅RR data on hydrated [U- ^{13}C , ^{15}N -GNNQ]QNY₇₋₁₃ amyloid-like fibrils obtained at 900 MHz ^1H Larmor frequency (21.1 Tesla) and 20 kHz MAS. Aliphatic 2D ^{13}C - ^{13}C SQ-SQ CM₅RR spectra obtained without additional ^1H decoupling with 0.8 ms mixing (a) and 1.6 ms mixing (b), showing one-bond and two-bond transfer within Asn and Gln side chains (color coding reflects sign of the peaks: blue = positive, red = negative). Note that there are three conformers showing up for each residue (see ref. (23)). (c) Zoomed-in regions reflecting Gln cross peaks at 0.8 ms mixing (favoring

one-bond transfer), and (d) 1.6 ms mixing (favoring 2-bond transfer). The three conformers are indicated. The top panels show C_{β} - C_{γ} cross-peaks, which are close to the diagonal due to their similar frequencies. The bottom panels are overlaid in panel (e), to show how sign alternation avoids confusion between the closely spaced 1-bond and 2-bond cross-peaks. Panel (f) shows Gln C_{β} - C_{γ} cross-peaks from a SQ-DQ experiment with 0.8ms mixing (equivalent to panel (c)). Note that conformer 2 shows up as a recognizable cross-peak, whereas it is overlapped with the diagonal in the SQ-SQ data (black star in panel (c)). For full spectra see Supporting Information..... 205

Figure 6-3 Simulations of polarization transfer along a carbon chain using double-quantum dipolar sequences at 900 MHz ^1H frequency: (a) SPC5 performed at 10 kHz spinning frequency (MAS) using 100 kHz ^1H cw decoupling. (b) SPC5 performed at 20 kHz MAS without additional ^1H decoupling. (c) $\text{CM}_{5\text{RR}}$ performed at 20 kHz MAS without additional ^1H decoupling; The 10-spin simulations at 900 MHz ^1H Larmor frequency (spin system in the inset of panel (c)) were performed using SPINEVOLUTION (32) and included isotropic chemical shift and chemical shift anisotropy modeled on the leucine side chain in N-*f*-MLF-OH (21). The ^{13}C rf was 100 kHz and 50 kHz for 20 kHz and 10 kHz MAS respectively. The ^1H decoupling strength for SPC5 at 10 kHz MAS was optimized beforehand in order to avoid double-quantum efficiency oscillations due to the insufficient decoupling (33). Circles indicate mixing times used in experiments presented in Fig. 6-4. 206

Figure 6-4 Experimental data from two-dimensional ^{13}C - ^{13}C correlation spectra on $[\text{U-}^{13}\text{C},^{15}\text{N}]$ -*f*-MLF-OH obtained using $\text{CM}_{3,5\text{RR}}$ at 900 MHz ^1H frequency and 23.81 kHz MAS, with increasing mixing time from 0.84 ms to 2.52 ms (from left to right). The strips show the transfer of polarization originating on the carbonyl groups being dominated by a one-bond relay process along the amino acid side chains. Positive and negative cross-peaks are indicated respectively in blue and red. The slices are obtained at the Leu C' resonance frequency (dashed line in 2D panels) and show the residual C' peak (*) and the aliphatic side chain signals, at the same absolute vertical scale. Note that in the spectrum using 2.52 ms mixing time we observe up to 4-bond relayed transfer cross-peaks (Leu C δ peaks). Experimental settings are detailed in the NMR spectroscopy section. 208

Figure 6-5 Two-dimensional ^{13}C - ^{13}C correlations spectrum of $[\text{U-}^{13}\text{C},^{15}\text{N}]$ -PI3-SH3 fibrils obtained using $\text{CM}_{4\text{RR}}$ at 900 MHz ^1H frequency and 20.161 kHz MAS without ^1H decoupling. (a) Spectrum obtained with a mixing time of 0.794 ms. (b) Carbonyl-aliphatic strip from a spectrum obtained with a mixing time of 1.488 ms. Positive cross-peaks (diagonal and two-bond cross-peaks) are indicated in blue-green and negative one-bond cross-peaks are indicated in red-yellow. Circles indicate the “appearance” of a positive cross-peak at long mixing time corresponding to a two-bond C'- C_{β} correlation that helps to identify the location of C_{α} site among the one-bond correlations in panel (a). 210

Figure 6-6 Two-dimensional ^{13}C - ^{13}C correlation spectrum of [U- ^{13}C , ^{15}N]-GvpA protein obtained using CM_{3,5}RR at 900 MHz ^1H frequency and 23.81 kHz MAS with ~ 5 kHz ^1H decoupling. The mixing time used was 0.84 ms in (a) and 1.512 ms in (b). Arrows in in panel (a) and (b) highlight regions illustrating relayed cross-peaks along as many as 3-bonds (backbone carbonyl to side chain C γ). Such “relay” peaks tend to be better resolved and therefore are particularly useful for assignment experiments..... 210

Figure 7-1 PAIN-CP ^{15}N - ^{13}C correlation pulse sequence. The proper combination of ^{15}N , ^{13}C and ^1H r.f. power results in enhanced rates and efficiency of ^1H mediated ^{15}N - ^{13}C polarization transfer. 224

Figure 7-2 Comparison of ^{15}N - ^{13}C two-bond polarization transfer for PAIN-CP, DCP, TEDOR, GATE AC sequences at $\omega_r/2\pi=20$ kHz. Note that variants of DCP such as RFDRCP, SPICP, and *i*DCP are not considered here as they mainly improve the recoupling bandwidth, which is not the major concern in this simulation..... 225

Figure 7-3 Aliphatic region of 2D ^{15}N - ^{13}C correlation spectra obtained at 750 MHz with 20 kHz MAS: (a) DCP with 3 ms mixing, (b) PAIN-CP with 4 ms mixing time. The ^1H r.f. field strength was 112 and 62 kHz for (a) and (b) respectively. In (a) the $n=1$ ZQ Hartmann-Hahn condition was matched with 45 kHz ^{13}C r.f. and 25 kHz ^{15}N r.f.. In (b) $\omega_r/2\pi= 50$ kHz for both ^{13}C and ^{15}N . All spectra were acquired and processed in exactly the same manner. The contour levels are set to the same value..... 227

Figure 7-4 PAIN-CP pathways. The simulated curves correspond to N-C β transfer (two-bond transfer) with identical settings as for the PAIN-CP simulations in Fig. 7-2. Note that the simulations with all dipolar couplings included, C-C coupling removed and C-N coupling removed yield essentially the same curve. 230

Figure 7-5 Simulations of ^{15}N - $^{13}\text{C}\beta$ two-bond transfer for PAIN-CP (red), DCP (black) sequences. The solid, dotted red curves correspond to $\delta=0$ and $\delta=1$ PAIN-CP matching respectively. For the DCP simulations, the ^1H decoupling was chosen to be 100 (solid line) and 150 (dotted line) kHz. Except for $\delta=1$ PAIN-CP, the three other simulations are similar to Fig. 7-2. 231

Figure 7-6 N-C α transfer (one-bond transfer) using the same spin system and simulation conditions as in Fig. 7-2 of the text. 232

Figure 7-7 Influence of a nearby carbon (C α) in the polarization transfer from ^{15}N to remote spin (C $_2$). The dashed line represents 0.15 normalized intensity..... 234

Figure 7-8 Experimental comparison of the total magnetization N-C transfer (i.e. sum over all cross peak integrals above the noise level) between DCP and three different $n=1$ PAIN-CP variants. 235

Figure 7-9 N- C_{β} transfer (two-bond transfer) using the same spin system and settings as in Fig. 7-2. The application of a ^1H $\pi/2$ flip pulse before the PAIN-CP mixing period eliminates ^1H - ^{13}C transfer. 236

Figure 8-1 (a) PAR pulse sequence for obtaining 2D homonuclear correlation spectra. The PAR mixing consist of continuous wave (CW) irradiation on ^1H and ^{13}C channel that recouples second order cross term between ^1H - ^{13}C dipolar couplings (term 2 and 3 of Eq. (111)) in order to transfer polarization from $^{13}\text{C}_1$ to $^{13}\text{C}_2$. (b) The PAR subspace can be seen as a coupled basis between a fictitious ZQ operator involving two ^{13}C 's (or ^{15}N 's) and a ^1H spin. The red arrows indicate PAR recoupling axis and longitudinal tilting field resulting from auto-cross terms (see Sect. 3.3). 244

Figure 8-2 PAR optimization map simulated using SPINEVOLUTION78. The initial magnetization is on the C_1 spin ($C_{1,x}$ operator) and is detected after 3 ms PAR mixing on the three spins, C_1 spin in (a), C_2 spin in (b) and H spin in (c) ($C_{1,x}, C_{2,x}, H_x$ operators respectively). The spin system is composed of two directly bonded ^{13}C 's and one ^1H bonded to the $^{13}\text{C}_1$ spin (see the inset of the figure). The distance between the $^{13}\text{C}_2$ spin and the ^1H is 2.15 Å. The angle between the two CH dipolar vectors is 42°. Simulations include typical chemical shift tensor values (see SI for details). The black dashed lines indicate that Hartmann-Hahn matching conditions as well as the n=0 matching condition. 253

Figure 8-3 PAR optimization maps where the polarization transfer between the ^{13}C is monitored as a function of ^{13}C and ^1H irradiation strengths (in units of ω_r). The spin system is identical as in Fig. 8-2. No chemical shift interactions were included in these simulations. The three panels represent: (a) analytical simulations of the ^{13}C polarization transfer from $^{13}\text{C}_1$ to $^{13}\text{C}_2$ arising from only the TSAR term; (b) ^{13}C signal intensity showing the analytical simulation obtained with the TSAR term and the longitudinal auto-cross terms contributions; (c) ^{13}C signal intensity depicting the numerical simulations performed with the SPINEVOLUTION. The two white lines displayed on the contour plots in panels (b) and (c) represent points where $\chi(1, p_C, p_H) = 0$ and $\chi(2, p_C, p_H) = 0$ (i.e. auto-cross terms for spatial components $m=1$ and $m=2$ are equal to 0), described by equations $p_H = \sqrt{p_C^2 - 1}$ and $p_H = \sqrt{p_C^2 - 4}$ respectively. 253

Figure 8-4 Simulations of polarization transfer in the PAR experiment for a HC_1C_2 spin system (same as in Fig. 8-3). No chemical shift is included in the simulations. The PAR ^{13}C and ^1H CW rf fields strengths are defined by $p_C=2.6$ and $p_H=2.35$ respectively (see Fig. 8-3b). The panels show simulations including: (a) all dipolar couplings; (b) all couplings except C_1C_2 ; (c) all couplings except

C₁H; (d) all couplings except C₂H; (e) all couplings except C₂H and C₁C₂; (f) all couplings except C₁H and C₂H..... 256

Figure 8-5 Dependence of PAR polarization transfer on the local geometry of the spin system. (a) The three-spin system geometry used in the simulations: the first ¹³C and the ¹H are fixed in space, whereas the second ¹³C position is defined by θ and ϕ the spherical coordinates with the origin at the ¹H. The distances between the ¹³C's and the ¹H are constant and respectively equal to 1.1 and 2.6 Å. The spherical map represents the ¹³C-¹³C polarization transfer efficiency for a TSAR mixing time of 4.2 ms using $p_C=2.75$ and $p_H=2.5$. Polarization transfer for $\theta=0$ orientation (aligned geometry) as a function of time is presented in panels (b) and (c). The buildup curves noted from (1) to (6) represent analytical simulations with: (1) both $m=1$ and $m=2$ components without auto-cross terms, (2) both $m=1$ and $m=2$ with auto cross terms, (3) and (4) only $m=1$ without and with auto-cross terms, (5) and (6) only $m=2$ without and with auto-cross terms..... 259

Figure 8-6 Analytical contour plots of the TSAR polarization transfer arising from the $m=1$ and $m=2$ components as a function of θ angle for a three spin system described in Fig 8-5a with the mixing time and irradiation settings used in Fig. 8-5 with $\phi=0$. (a) $m=1$ TSAR component, (b) $m=1$ TSAR term plus $m=1$ auto-cross term components, (c) $m=2$ TSAR component included, (d) $m=2$ TSAR term and $m=2$ auto-cross term components, (e) $m=1$ and $m=2$ TSAR components, (f) $m=1$ and $m=2$ TSAR plus $m=1$ and $m=2$ auto-cross term components. 262

Figure 8-7 Analytical contour plots of the TSAR polarization transfer for an aligned symmetrical three spin system with $r_{CC} = 6$ Å (see the inset): (a) $m=1$ component, (b) $m=2$ component, (c) both $m=1$ and $m=2$ components included. Note the constructive interference of the $m=1$ and $m=2$ components that leads to an improved polarization transfer in (c). 264

Figure 8-8 (a) 2D ¹³C-¹³C correlation spectrum of [U-¹³C,¹⁵N]N-*f*-MLF-OH diluted to 10% in a natural abundance lattice. The spectrum was recorded $\tau_{mix}=7.5$ ms on 750 MHz spectrometer (¹H frequency) with $\omega_r/2\pi = 20$ kHz, $\omega_{1C}/2\pi \approx 50$ kHz, $\omega_{1H}/2\pi \approx 47$ kHz, and the offset on the ¹³C channel was set to 101 ppm. The circled cross-peaks in the spectrum are due to attenuated dipolar truncation in the PAR experiment and correspond to ≥ 4 Å ¹³C-¹³C distances. (b) Numerical simulations of PAR polarization transfer between MC _{β} and LC _{α} (corresponding to the highlighted 4.3 Å distance) using rf power levels specified in (a). The spin system includes nearby protons (2xMH _{β} , MC _{α} , LH _{α} , LH) (back solid line), nearby protons plus MC _{α} and MC' (red dash line). The dotted blue line represents simulation on a spin system including nearby protons plus MC _{α} and MC' with the ¹H-¹H couplings removed from the calculation. Simulations include typical chemical shift tensor values (see SI for details). The plot illustrates that the contribution of the polarization relayed through MC _{α} and MC' to

the polarization transfer between MC_β and LC_α is negligible compared to the direct polarization transfer. 265

Figure 8-9 Illustration of dipolar truncation in the CM_5RR and PAR homonuclear recoupling schemes. Spin system 1 is composed of a directly bonded $C_\alpha H_\alpha$ pair and a C_{remote} spin 4.5 Å and 3.56 Å distant from the C_α spin. In the spin system 2, a C_β spin, directly bonded C_α , is added. (a) The black dashed line depicts the polarization transfer (~30%) from C_α to C_{remote} ($r_{C-C} = 4.5$ Å) using the broadband DQ CM_5RR in the three spin system 1. When a directly bonded C_β spin is added to the spin system ($r_{C-C} = 1.5$ Å), the polarization transfer to the C_{remote} (red dash-dot line) is quenched for CM_5RR with most of the polarization being transferred to the directly bonded C_β (blue solid line) thus demonstrating the phenomenon of dipolar truncation. (b) In the PAR simulation the presence of a third strongly coupled spin leads to a partial decrease of polarization transfer to C_{remote} [(b) red dash-dot line] showing that dipolar truncation is attenuated in the TSAR transfer mechanism. Simulations were performed with SPINEVOLUTION⁷⁸ $\omega_r/2\pi = 20$ kHz, $\omega_{0H}/2\pi = 750$ MHz 1H frequency, and do not include chemical shifts. 267

Figure 8-10 2D ^{13}C - ^{13}C correlation spectra of $[U-^{13}C, ^{15}N]$ -Crh protein comparing two advanced recoupling pulse sequences at $\omega_{0H}/2\pi = 750$ MHz 1H Larmor frequency and $\omega_r/2\pi = 20$ kHz MAS spinning frequency: (a) Broadband CM_5RR spectrum corresponding to 800 μs ^{13}C irradiation of ~100 kHz displaying only one-bond dipolar ^{13}C - ^{13}C cross peaks (see the gray monomer of the Crh dimer structure representation in the inset). Note that the spectrum was acquired in ~15h without 1H irradiation during the CMRR mixing time. (b) PAR spectrum corresponding to 14 ms ^{13}C and 1H CW irradiations displaying long short, medium and long distance ^{13}C - ^{13}C cross-peaks. Several illustrative examples are shown on the green monomer of the Crh dimer structure representation. 270

Figure 8-11 PAR polarization transfer as a function of the ^{13}C - ^{13}C distance. (a-d) A sampling of experimental ^{13}C - ^{13}C PAR polarization transfer curves obtained on $[U-^{13}C, ^{15}N]$ -Crh protein with $\omega_r/2\pi = 20$ kHz, $\omega_{0H}/2\pi = 900$ MHz and a carrier frequency set to 38.9 ppm: (a) one-bond distance class; (b) 2.5-3.5 Å distance class; (c) 3.5-5 Å distance class; (d) >5 Å distance class. (e) Spin system used in the PAR polarization transfer simulations (f) and (g). Atom coordinates and chemical shift tensors used in the simulations can be found in the SI Table 8-3). 273

Figure 8-12 Modification of the long distance polarization transfer in uniformly labeled systems when both 1st order ^{13}C - ^{13}C recoupling and second-order TSAR mechanism are simultaneously present. Note the different behavior for the simulations with only ^{13}C - ^{13}C couplings included and the simulations also including 1H 's. The chosen 1H irradiations yield substantial TSAR mechanism contribution to overall polarization transfer (except CM_5RR where no 1H irradiation was used in order

to illustrate a case of pure 1st order ¹³C-¹³C spin dynamics without TSAR contribution). (a) DQ CM₅RR with 100 kHz ¹³C rf and no ¹H rf. (b) DQ HORROR with 15 kHz ¹³C rf and 80 kHz ¹H rf. (c) ZQ PAR with 56 kHz ¹³C rf and 54 kHz ¹H rf. (d) ZQ SR6₂⁶ with 20 kHz ¹³C rf and 82 kHz ¹H rf. (e) ZQ RFDR with 12.5 kHz π pulses and 69 kHz ¹H rf. The simulations were performed at (a, c, d, e) $\omega_r/2\pi = 20$ kHz or (b) $\omega_r/2\pi = 30$ kHz and $\omega_0/2\pi = 700$ MHz and include isotropic chemical shift and CSA typical for the aliphatic sites (see SI). The spin system is based on the leucine sidechain in the structure of N-*f*-MLF-OH.⁹⁸ Note that all the pulse sequences except PAR (in (d)) are designed to reintroduce the ¹³C-¹³C dipolar coupling to the 1st order..... 278

Figure 8-13 (a)-(b) Examples of ¹³C-¹³C correlation spectra of [U-¹³C,¹⁵N]-Crh protein at $\omega_{0H}/2\pi = 900$ MHz and $\omega_r/2\pi = 20$ kHz. Expansion of the aliphatic region for (a) CM₅RR (0.8 ms) and (b) PAR (15 ms). The PAR spectrum contains numerous cross-peaks corresponding to medium to long distances that involve methyl groups. As a comparison, the CM₅RR spectrum displays only one-bond cross-peaks. A detailed description of the PAR optimization protocol can be found in the SI. (c) Ensemble of structures of a Crh monomer (residues 12-85) calculated using a unique 2.5-6 Å distance class for all the unambiguous ¹³C-¹³C cross-peaks identified using the x-ray structure⁵⁴ as a homology model. (e) Numerical simulations of the polarization transfer between CH₃ and CH illustrating the influence of the threefold methyl group hopping on the overall polarization transfer. The coordinates for spin system (d) used in the simulations were taken for A20C α and I47C δ 1 from the x-ray structure⁵⁴ of the Crh protein. Simulations do not include chemical shift..... 281

Figure 8-14 (a) Visualization of PAR spin dynamics subspace. The space can be seen as a coupled basis between a fictitious ZQ operator involving the two carbons (or nitrogens) and a proton spin. The red arrows indicate PAR recoupling axis and longitudinal tilting field resulting from auto-cross terms (see Sect. 3.3). Panel (b) depicts a typical coupled basis encountered for instance in solution NMR 286

Figure 8-15 PAR polarization transfer optimization map (a) versus interference map (b). In PAR optimization map the polarization transfer between the carbons is monitored as a function of carbon (p_C) and proton (p_H) irradiation in units of spinning frequency. In the interference map the decay of the magnetization on the carbons after the PAR mixing is monitored as a function of carbon (p_C) and proton (p_H) irradiation in units of spinning frequency. The initial magnetization is prepared on the x-axis on C₁ in (a) and on both C₁ and C₂ in (b). 289

Figure 8-16 Analytical maps of PAR polarization transfer as a function of carbon (p_C) and proton (p_H) rf field strengths (in units of spinning frequency) for a three spin system described in Section 8.4.1 and Fig. 8-5 of the manuscript. (a) $m=1$ component and (b) $m=2$ component of the TSAR term is used in the simulation, (c) $m=1$ component and (d) $m=2$ component of both the TSAR term and

longitudinal auto-cross terms are used in the simulation. Simulations include only dipolar couplings.
 292

Figure 8-17 Analytical maps of PAR polarization transfer as a function of carbon (p_C) and proton (p_H) irradiation (in units of spinning frequency) for a symmetric, triangular three spin system. The ^1H - ^{13}C dipole couplings are identical and $b_{CH} = 1.119$ kHz. The distance between carbons is 5.9 \AA and the PAR mixing time is $\tau_{mix} = 60$ ms (a) $m=1$ TSAR component only, (b) $m=2$ TSAR component only, (c) $m=1$ and $m=2$ TSAR components together. Note that we do not have to account for the longitudinal auto-cross terms as they are zero for this symmetric spin system. 294

Figure 8-18 Analytical maps of PAR polarization transfer as a function of carbon (p_C) and proton (p_H) rf fields (in units of ω) for an aligned and asymmetric three spin systems. (a) $m=1$ TSAR component only, (b) $m=2$ TSAR component only, (c) $m=1$ and $m=2$ TSAR component only, (d) $m=1$ TSAR and auto-cross term component, (e) $m=2$ TSAR and auto cross-term components, (f) $m=1$ and $m=2$ TSAR and auto-cross term components. Simulations include only dipolar couplings. 297

Figure 8-19 Effect of the partial compensation of the off-resonance auto-cross term contributions on the TSAR polarization transfer. The auto-cross terms are large in (c) for the asymmetric three spin system, minimal in (b) for the asymmetric four spin system, and zero in (a) for the symmetric 4 spin system. Simulations do not include the chemical shifts. The mixing time is set to 20 ms. The geometry of the spin systems are indicated above the contour plots. The CH bond is 1.1 \AA .
 297

Figure 8-20 Simulations of the PAR polarization transfer as a function of the CH distance in several model spin systems (the CCH angle is 180° for the top row and 90° for the bottom row; the ^{13}C - ^{13}C distance r_1 for simulations in each column is specified at the top of the column). Simulations were performed at $\omega_r/2\pi = 20$ kHz, $\omega_{0H}/2\pi = 750$ MHz with $p_C = 2.75$ and $p_H = 2.5$. Isotropic chemical shift and CSA typical for carbon sites are included in the simulation ($\delta_{iso,C1} = -10$ ppm, $\delta_{iso,C2} = 10$ ppm, $\delta_{anis,C1} = -20$ ppm, $\eta_{C1} = 0.43$, $\delta_{anis,C2} = 19$ ppm, $\eta_{C\alpha} = 0.8$). 298

Figure 8-21 Numerical simulations of PAR polarization transfer between (a) LC_α and LC_δ , (b) LC_α and LC_δ with settings similar to the ones used in Fig. 8-10a. The spin system includes nearby protons (the spin system for simulation in (a) and (b) are specified in Table 8-1 and 8-2 respectively). Black line shows the polarization transfer in absence of C_β and C_γ spins, whereas the red dashed line shows the same simulation in presence of C_β and C_γ carbons. Simulations include isotropic chemical shift and CSA for carbon sites ($\delta_{iso,C\alpha} = -20$ ppm, $\delta_{iso,C\delta1} = 20$ ppm, $\delta_{iso,C\delta2} = 20$ ppm, $\delta_{iso,C\beta} = 5$ ppm, $\delta_{iso,C\gamma} = 12$ ppm, $\delta_{anis,C\alpha} = 25.1$ ppm, $\eta_{C\alpha} = 0.0$, $\delta_{anis,C\delta1} = -19.8$ ppm, $\eta_{C\delta1} = 0.0$, $\delta_{anis,C\delta2} = -19.8$ ppm, $\eta_{C\delta2} = 0.0$, $\delta_{anis,C\beta} = 23.8$ ppm, $\eta_{C\delta1} = 0.92$, $\delta_{anis,C\gamma} = -19.8$ ppm, $\eta_{C\gamma} = 0.0$). 299

Figure 8-22 Simulations of the polarization transfer as a function of the ^1H irradiation strength (in units of ω_r) in a spin system composed of two ^{13}C 's separated by the 2.5\AA with directly attached ^1H 's. All the simulations were performed at $\omega_r/2\pi = 20\text{ kHz}$, $\omega_{0\text{H}}/2\pi = 700\text{ MHz}$ and include isotropic chemical shift and CSA for carbon sites ($\delta_{\text{iso,C}\alpha} = -10\text{ ppm}$, $\delta_{\text{iso,C}\beta} = 0\text{ ppm}$, $\delta_{\text{iso,C}\gamma} = 10\text{ ppm}$, $\delta_{\text{anis,C}\alpha} = -20\text{ ppm}$, $\eta_{\text{C}\alpha} = 0.6$, $\delta_{\text{anis,C}\beta} = -19\text{ ppm}$, $\eta_{\text{C}\alpha} = 0.7$, $\delta_{\text{anis,C}\alpha} = -19\text{ ppm}$, $\eta_{\text{C}\alpha} = 0.7$). The simulations in left panels (a, c, e, g, k) include all the dipolar interactions (see Table 8-4). The homonuclear ^{13}C - ^{13}C and ^1H - ^1H dipolar couplings were removed from the system in simulations in right panels (b, d, f, h, l) in order to eliminate all the transfer mechanisms except for the TSAR based mechanism. Simulations in (a-b) are for DQ HORROR pulse sequence with the ^{13}C rf strength of $\omega_r/2$. Simulations in (c-d) are for DQ CM₅RR with ^{13}C irradiation strength of $5\omega_r$ (i.e. 100 kHz). Simulations in (e-f) are for ZQ RFDR with $\omega_{1\text{C}}/2\pi = 12.5\text{ kHz}$ π pulses. Simulations in (g-h) are for ZQ SR6₂⁶ sequence with ^{13}C irradiation strength of ω_r (i.e. 20 kHz). ZQ mechanism results in positive polarization transfer and DQ mechanism results in negative polarization transfer. The polarization transfer in the right hand panels is entirely due to the TSAR-based mechanism..... 302

Figure 8-23 Simulations of the polarization transfer under P9₁₂¹ TOBSY as a function of ^1H irradiation (up to $p_{\text{H}} = 6.66$ i.e. 200 kHz) illustrating the contribution of the TSAR based mechanism to the overall polarization transfer. The initial magnetization was placed on the C α . (a) Spin system for the simulations consisting of 3 carbons and 3 protons. Panels (b-d) show polarization transferred to the C β site. Panels (e-g) show polarization transferred to the C γ site. Panels (b) and (e) include all the interactions. J coupling was removed from the simulations in panel (c) and (f). Panels (d) and (g) show simulations with J coupling, ^{13}C - ^{13}C and ^1H - ^1H dipolar coupling removed and therefore isolated TSAR mechanism contribution. All the simulations were performed at $\omega_r/2\pi = 30\text{ kHz}$, $\omega_{0\text{H}}/2\pi = 700\text{ MHz}$ and include isotropic chemical shift and CSA for ^{13}C 's ($\delta_{\text{iso,C}\alpha} = -10\text{ ppm}$, $\delta_{\text{iso,C}\beta} = 0\text{ ppm}$, $\delta_{\text{iso,C}\gamma} = 10\text{ ppm}$, $\delta_{\text{anis,C}\alpha} = -20\text{ ppm}$, $\eta_{\text{C}\alpha} = 0.6$, $\delta_{\text{anis,C}\beta} = -19\text{ ppm}$, $\eta_{\text{C}\alpha} = 0.7$, $\delta_{\text{anis,C}\alpha} = -19\text{ ppm}$, $\eta_{\text{C}\alpha} = 0.7$). Whenever used, J couplings were set to 35 Hz. Note, that even for $\omega_{1\text{H}}/2\pi = 200\text{ kHz}$ the spin dynamics are strongly influenced by ^1H 's. 307

Figure 8-24 Simulations of the polarization transfer under P9₁₂¹ TOBSY illustrating the contribution of the TSAR based mechanism to the overall polarization transfer. (a) Simulation performed on a spin system consisting only of carbons with J couplings present. Simulations (c-d) are performed on a 6 spin system portrayed in the graphic (b) consisting of 3 carbons and 3 protons. (c) Simulation with J coupling present and ^1H irradiation at $p_{\text{H}} = 4.5$ (135 kHz). (d) Simulation with J coupling present and ^1H irradiation at $p_{\text{H}} = 5.2$ ($\omega_{1\text{H}}/2\pi = 156\text{ kHz}$). (e) Simulation with J coupling absent and ^1H irradiation at $p_{\text{H}} = 4.5$ ($\omega_{1\text{H}}/2\pi = 135\text{ kHz}$). (f) Simulation with J coupling absent and ^1H

irradiation at $p_H=5.2$ ($\omega_{1H}/2\pi =156$ kHz). All the simulations were performed at $\omega_r/2\pi = 30$ kHz, $\omega_{0H}/2\pi =700$ MHz and include isotropic chemical shift and CSA for carbons ($\delta_{iso,C\alpha}=-10$ ppm, $\delta_{iso,C\beta}=0$ ppm, $\delta_{iso,C\gamma}=10$ ppm, $\delta_{anis,C\alpha}=-20$ ppm, $\eta_{C\alpha}=0.6$, $\delta_{anis,C\beta}=-19$ ppm, $\eta_{C\alpha}=0.7$, $\delta_{anis,C\alpha}=-19$ ppm, $\eta_{C\alpha}=0.7$). J couplings were set to 35 Hz. Simulations (e-f) illustrate polarization transfer due to the TSAR mechanism only. Simulations (c-d) show polarization transfer that is a mixture of TSAR mechanism and J coupling based mechanism. Note, that even at $p_H=5.2$, which corresponds to $3.46 p_C$, the TSAR based mechanism is dominating the spin dynamics and almost eliminates the characteristic oscillatory features of the J coupling based transfer present in (a)..... 308

Figure 8-25 Qualitative comparison of different ^{13}C - ^{13}C recoupling techniques on [U- ^{13}C , ^{15}N]-Crh protein: (a) CHHC spectrum with 200 μs mixing time, (b) ^{13}C - ^{13}C PAR spectrum with 9 ms mixing time, (c) DARR spectrum with 200 ms mixing time, (d) ^{13}C - ^{13}C PAR spectrum with 14 ms mixing time spectra. (a,c) were obtained at 11 kHz MAS and 500 MHz 1H Larmor frequency using ~ 20 mg of protein. (b,d) were obtained at $\omega_r/2\pi = 20$ kHz , $\omega_{0H}/2\pi =750$ MHz using ca.6 mg of protein. The total acquisition time of the spectra is detailed above the each spectrum. See main text (Sec 8.6.2) for details on Fig. 8-25..... 309

Figure 8-26 Numerical simulations illustrating applicability of the PAR technique at ultrahigh and moderate spinning frequencies. Graphics (a,b) depict PAR optimization map for the CH-CH₃ spin system in the inset (b) performed at $\omega_r/2\pi = 70$ kHz MAS (a) and $\omega_r/2\pi = 10$ kHz MAS (c) at $\omega_{0H}/2\pi = 750$ MHz. The mixing time in (a-c) was fixed at 10 ms. Spin system includes isotropic chemical shift and CSA for carbon nuclei ($\delta_{iso,C1}=-10$ ppm, $\delta_{iso,C2}=10$ ppm, $\delta_{anis,C1}=20$ ppm, $\eta_{C1}=0.6$, $\delta_{anis,C1}=19$ ppm, $\eta_{C1}=0.8$). Simulation includes methyl group rotation. Graphic (b-d) shows a polarization build-up simulated for the settings highlighted in the map i.e. $p_C=1.07$ ($\omega_{1C}/2\pi = 74.9$ kHz) and $p_H=0.37$ ($\omega_{1H}/2\pi =25.9$ kHz) in (b) and $p_C=7.1$ ($\omega_{1C}/2\pi = 71$ kHz) and $p_H=6.9$ ($\omega_{1H}/2\pi =69$ kHz) in (d)..... 310

Figure 9-1 Pulse sequence for the 2D ^{15}N - ^{15}N PAR correlation experiment. The PAR mixing period consists of C.W. irradiations on 1H and ^{15}N channels with the irradiation strengths chosen to produce an appreciable second order TSAR mechanism. The TSAR term of the form $H_z N_1^\pm N_2^m$ is a result of a cross term between the 1H - $^{15}N_1$ and 1H - $^{15}N_2$ dipolar couplings (terms 2 and 3 in the spin system graphics). 324

Figure 9-2 Visualization of the PAR subspace. The space can be seen as a coupled basis between a fictitious ZQ operator involving the two carbons (or nitrogens) and a proton spin. The red arrows indicate PAR recoupling axis and longitudinal tilting field resulting from auto-cross terms. Panel (b) depicts the coupled basis encountered in solution NMR..... 324

Figure 9-3 Numerical simulation of a ^{15}N - ^{15}N PAR polarization transfer map for backbone nitrogens in an α -helix. (a) Spin system used in the simulation consisting of the two backbone nitrogens with directly bonded amide protons (see Table 9-2). Simulations were performed at $\omega_r/2\pi=20$ kHz and $\omega_{0H}/2\pi=750$ MHz using 20 ms mixing and include typical isotropic and anisotropic chemical shifts (see Table 9-2). (b) Contour plot of the ^{15}N - ^{15}N PAR polarization transfer between neighboring nitrogens in an α -helix as a function of the nitrogen and proton irradiation magnitudes in units of spinning frequency: p_N and p_H . The two main areas used for performing ^{15}N - ^{15}N PAR experiments are indicated with numerals 1 and 2. The dashed magenta lines indicate conditions for which the $m=1$ and $m=2$ components of the auto cross-term arising from the heteronuclear ^{15}N - ^1H dipolar coupling is zero. These lines are defined by the following equations: $p_H = \sqrt{p_N^2 - 1}$ and $p_H = \sqrt{p_N^2 - 4}$ 326

Figure 9-4 (a) Low power 2D ^{15}N - ^{15}N PAR correlation spectrum obtained on [U- ^{13}C , ^{15}N]-f-MLF-OH⁷¹ at $\omega_r/2\pi=20$ kHz and $\omega_{0H}/2\pi=900$ MHz using 20 ms of mixing time. The red cross-peaks correspond to a short LN-FN sequential contact ($r_{\text{NN}}=2.7$ Å) and the blue cross-peaks correspond to the long sequential LN-MN contact ($r_{\text{NN}}=3.6$ Å) (see graphics (b)). (c) Cross-peak intensity build-ups in [U- ^{13}C , ^{15}N]-N-f-MLF-OH as a function of ^{15}N - ^{15}N PAR mixing time. The PAR mixing consisted of ~ 4 kHz ^{15}N and ~ 53 kHz ^1H C.W. irradiations for both (a) and (c)..... 328

Figure 9-5 (a) 2D ^{15}N - ^{15}N PAR correlation spectrum on [1,3- ^{13}C , U- ^{15}N]-GB1. The spectrum was obtained using 18 ms PAR mixing with $\omega_{1N}/2\pi \sim 52$ kHz and $\omega_{1H}/2\pi \sim 49$ at $\omega_r/2\pi=20$ kHz and $\omega_{0H}/2\pi=900$ MHz. The cross-peaks circled in red correspond to sequential contacts in loop regions that are also indicated with red lines in (b)). The cross-peaks circled in blue correspond to contacts between the strands in antiparallel β -sheets (nitrogens for the residues participating in a β -bridge) that are also indicated with blue lines in (b). The unmarked cross-peaks correspond primarily to the sequential contacts in the α -helix that are marked with green lines in (b). 329

Figure 9-6 Numerical simulations of ^{15}N - ^{15}N PAR polarization transfer in an α -helix. The spin system (a) consists of 4 backbone ^{15}N 's and amide ^1H 's only for simulation in (b) and amide protons plus 3 H α 's for simulation in (c). The coordinates were taken from residues 31 to 34 in the x-ray structure of GB1 (PDB ID 2GI9)⁴⁵ – see Table 9-3). Simulations include nitrogen and proton chemical shifts (see Table 9-3). The initial magnetization is placed on Q₃₂N. Simulations were performed at $\omega_r/2\pi=20$ kHz MAS and $\omega_{0H}/2\pi=750$ MHz with $p_N=2.7$ and $p_H=2.5$ 333

Figure 9-7 Numerical simulations of ^{15}N - ^{15}N PAR polarization transfer in an antiparallel β -(a-b) and parallel β -sheet (c-d). In (a) the spin system consists of 5 backbone nitrogens with directly bonded protons from two strands in an antiparallel β -sheet (coordinates for residues 43-45 and 53-55 from x-

ray structure of GB1, PDB ID 2GI9⁴⁵ – see Table 9-4). The spin system consists of 5 backbone nitrogens with directly bonded protons from two strands in an parallel β -sheet (coordinates from SSNMR structure of the HET-s(218-289) prion, PDB ID 2RNM² – see Table 9-5). Simulations include nitrogen and proton chemical shifts (see Table 9-4 and 9-5). The initial magnetization is placed on the $T_{44}N$ in (b) and $I_{231}N$ in (d). Simulations were performed at $\omega_r/2\pi=20$ kHz MAS and $\omega_{0H}/2\pi=750$ MHz with $p_N=2.7$, $p_H=2.5$ 334

Figure 9-8 Numerical simulation of PAR (a) and NHHN (b) polarization transfer between nitrogens from a β -bridge partner residues in an antiparallel β -sheet. The black solid line represents simulations with only amide protons included, and the red dashed line represents simulation with amide protons plus 6 other closest protons. The simulations were performed at $\omega_r/2\pi=20$ kHz and $\omega_{0H}/2\pi=750$ MHz and include all chemical shifts (see Table 9-6). The 1H - ^{15}N CP steps in NHHN are simulated explicitly using 0.15 ms contact time with $\omega_{1H}/2\pi=100$ kHz and $\omega_{1N}/2\pi=80$ kHz. The PAR mixing settings are: $p_N=2.7$ and $p_H=2.5$ 337

Figure 9-9 2D ^{15}N - ^{15}N PAR correlation spectrum on $[1,3-^{13}C,U-^{15}N]$ -protein GB1. The spectrum was obtained using 22 ms PAR mixing with $\omega_{1N}/2\pi \sim 4$ kHz and $\omega_{1H}/2\pi \sim 52$ CW irradiation at $\omega_r/2\pi = 20$ kHz and $\omega_{0H}/2\pi = 900$ MHz. 343

Figure 9-10 Comparison of the ^{15}N - ^{15}N PAR polarization transfer map (a) and the interference map (b). Simulation was performed for the spin system described in Table 9-2 using 20 ms of PAR mixing at $\omega_r/2\pi=20$ kHz and $\omega_{0H}/2\pi = 750$ MHz. In the PAR optimization map the polarization transfer between the nitrogens is monitored as a function of nitrogen (p_N) and proton (p_H) irradiation in units of spinning frequency. In the interference map the decay of the magnetization on the nitrogens after the PAR mixing is monitored as a function of nitrogen (p_N) and proton (p_H) irradiation in units of spinning frequency. The initial magnetization is prepared on the x-axis on one of the nitrogens in (a) and on both nitrogens in (b)..... 345

Figure 9-11 2D ^{15}N - ^{15}N PAR correlation spectrum on $[U-^{13}C,^{15}N]$ - protein GB1. The spectrum was obtained using 20 ms PAR mixing with $\omega_{1N}/2\pi \sim 71$ kHz and $\omega_{1H}/2\pi \sim 69$ CW irradiation at $\omega_r/2\pi = 11.11$ kHz and $\omega_{0H}/2\pi = 500$ MHz. The acquisition time was 46.1 ms in t_1 and 46.1 ms in t_2 . The temperature (as read by thermocouple) was maintained at $-5^\circ C$ using 50 scfh flow of nitrogen.. 347

Figure 10-1 Pulse sequence for 2D ^{13}C - ^{13}C PAR experiments. The PAR mixing consists of simultaneous C.W. irradiation on the 1H and ^{13}C channels with the irradiation strengths chosen to produce an appreciable second order TSAR mechanism.^{35,37} The TSAR term is a result of a cross term between the 1H - ^{13}C dipolar couplings (terms 2 and 3 in the spin system graphics). 356

Figure 10-2 Simulated PAR polarization transfer map obtained on the spin system shown in the inset of the figure (see also Table 10-1). The contour plots represent polarization transfer between the C_α and C_β spins as a function of ^{13}C and ^1H irradiation strengths in units of spinning frequency. Simulations were performed using 5 ms PAR mixing at $\omega_r/2\pi = 65$ kHz MAS and $\omega_{0\text{H}}/2\pi = 500$ MHz and include chemical shifts (see Table 10-1). Similar maps for C_α -C' and C_α - C_β polarization transfer can be found in Fig. 10-5. For the settings indicated by the black dashed lines the CH auto-cross term is zero. The irradiation settings employed in this study are indicated with 'x's (blue for N-*f*-MLF-OH and black for GB1). 360

Figure 10-3 (a) 1D ^{13}C CP-MAS spectrum of microcrystalline [U - ^{13}C , ^{15}N]-GB1 (2.5 mg protein packed in 1.3 mm rotor) obtained at $\omega_r/2\pi = 65$ kHz and $\omega_{0\text{H}}/2\pi = 500$ MHz with low power (~16.25 kHz) TPPM decoupling^{56,57} during acquisition. (b) Expansion of the aromatic region illustrating the excellent resolution. 361

Figure 10-4 2D ^{13}C - ^{13}C PAR correlation spectra of microcrystalline [U - ^{13}C , ^{15}N]-GB1 obtained at $\omega_r/2 = 65$ kHz and $\omega_{0\text{H}}/2 = 500$ MHz with 10 ms PAR mixing. The PAR mixing employed ~73 kHz ^{13}C and 19.5 kHz ^1H irradiation. Low power TPPM^{56,57} ($\omega_{1\text{C}} = \omega_r/4 = 16.25$ kHz) was applied during acquisition and t_1 evolution. The high resolution achievable with this decoupling scheme is illustrated in panels (a) and (b), which depict an expansion of a carbonyl-aliphatic region of the spectrum. The data in panel (a) were processed without linear prediction in the direct dimension ($t_2 = 25$ ms) and the data in panel (b) with linear prediction in the direct dimension. In both panels in the direct dimension we can clearly distinguish splitting due to the J-couplings for most of the cross-peaks. Panel (c) illustrates some of the representative long distance contacts that are observed in an experiment with 10 ms PAR mixing. The cross-peaks corresponding to the contacts in panel (c) are circled and marked with numbers in the spectrum. 363

Figure 10-5 Numerical simulation of the ^{13}C - ^{13}C PAR polarization transfer optimization map performed on the spin system shown in (a). The contour plots represent polarization transfer between the C_α and C' in (b), and C_α and C_γ in (c) as a function of ^{13}C and ^1H irradiation strength in units of spinning frequency. Simulations were performed using 5 ms PAR mixing at $\omega_r/2\pi = 65$ kHz MAS and $\omega_{0\text{H}}/2\pi = 500$ MHz and include chemical shift. The details of the spin system are listed in Table 10-1. 366

Figure 10-6 Numerical simulations of the ^{13}C - ^{13}C PAR optimization maps on the aliphatic region. (a) spin system used in simulation taken from the SSNMR structure of N-*f*-MLF-OH¹ (see Table 10-2). The contour plots represent polarization transfer between the carbons (indicated by black arrow – C_α - C_β in (a) and C_α - C_δ in (b)) as a function of ^{13}C and ^1H irradiation strength in units of

spinning frequency. Simulations were performed using 5 ms PAR mixing at $\omega_r/2\pi=65$ kHz MAS and $\omega_{0H}/2\pi=500$ MHz and include chemical shift. Simulation accounts for the threefold methyl group hop. For the settings indicated by the black dashed lines the CH auto-cross term is zero. 367

Figure 10-7 2D ^{13}C - ^{13}C PAR correlation spectra on [U- ^{13}C , ^{15}N]-GB1 obtained at $\omega_r/2 =65$ kHz and $\omega_{0H}/2 =500$ MHz. The PAR mixing time was 2.5 ms and used ~ 19.5 kHz ^{13}C and ~ 72.8 kHz ^1H irradiation. 16.5 kHz low power TPPM decoupling was employed during the acquisition and t_1 evolution. 369

Figure 10-8 2D ^{13}C - ^{13}C PAR correlation spectra on [U- ^{13}C , ^{15}N]-f-MLF-OH obtained at $\omega_r/2 =65$ kHz and $\omega_{0H}/2 =500$ MHz. The PAR mixing time was (a) 2 ms, (b) 5 ms, (c) 10 ms and used ~ 110 kHz ^{13}C and ~ 85 kHz ^1H irradiation. 230 kHz XiX decoupling (the XiX pulse was 60.2 μs i.e. 3.91 τ_r) was employed during the acquisition and t_1 evolution. 370

Figure 10-9 Numerically simulated “interference” map on the spin system in Table 10-1. In the interference map the decay of the magnetization on the carbons after the PAR mixing is monitored as a function of carbon (p_C) and proton (p_H) irradiation in units of spinning frequency. The initial magnetization is prepared on the x-axis on all the carbons. The settings for the simulation are identical to the settings used in Fig. 10-5. The comparison between the interference maps and the polarization transfer map shown in Fig. 10-2 and Fig. 10-5 allows one to choose the appropriate rf settings for performing PAR experiment. 371

Figure 11-1 Photographs of various GNNQQNY aggregates: (a) fibrils prepared at 25 mg/ml, (b) clusters of monoclinic crystals at 10 mg/ml after filtration, (c) monoclinic crystals imbedded in fibril gel at 10 mg/ml (no filtration), and (d) a suspension of orthorhombic crystals obtained after swirling a 2 mg/ml solution. 386

Figure 11-2 Transmission electron micrograph images of GNNQQNY monoclinic nanocrystals obtained at (a) 10 mg/ml and (b,c) fibrillar aggregates formed at 25 mg/ml. 387

Figure 11-3 ^{13}C 1D spectra of natural abundance (a) monoclinic nanocrystals and (b) isotopically dilute ($\sim 3\%$ segmentally labeled in GNNQ₇₋₁₀) orthorhombic nanocrystals of GNNQQNY. Spectra were acquired at 750 and 700 MHz ^1H frequencies, respectively. Red labels indicate sites displaying the most significant change in chemical shift between the two forms. 387

Figure 11-4 1D ^{13}C and ^{15}N spectra of (a,b) monoclinic and (c,d) orthorhombic GNNQQNY nanocrystals, obtained at 500 MHz and 700MHz ^1H fields, respectively. Rows (a) and (c) are for labeled [U- ^{13}C , ^{15}N -GNNQ]QNY samples M2 and M3, while (b) and (d) are labeled GNN[U- ^{13}C , ^{15}N -QQNY] O1 and O2. 388

Figure 11-5 2D assignment data for monoclinic crystal samples of [U- ¹³ C, ¹⁵ N-GNNQ]QNY (sample M2, panels a-d), and GNN[U- ¹³ C, ¹⁵ N-QQNY] (M3, e-f). The data were obtained at 500 MHz ¹ H frequency and 10 kHz MAS. ¹³ C- ¹³ C correlations (a,e) were obtained via DARR/RAD and SPC5 mixing, respectively. ¹⁵ N- ¹³ C correlations were obtained in N-CO (b,f), NCA (c,g) and NCACX experiments (d,h).....	389
Figure 11-6 Secondary chemical shift for the monoclinic and orthorhombic nanocrystals. Color coding: black = β-sheet, white = α-helical, grey = indeterminate.....	392
Figure 11-7 1D ¹³ C and ¹⁵ N spectra of fibrils formed using [U- ¹³ C, ¹⁵ N-GNNQ]QNY: (a) 100%-labeled sample F1 (20 mg/ml) at 700 MHz, (b) 25%-labeled sample F2 (25 mg/ml) at 700 MHz, (c) sample F3 (12 mg/ml) at 900 MHz (contains monoclinic crystals as well (*)).....	396
Figure 11-8 Secondary chemical shift analysis of GNNQ ₇₋₁₀ in GNNQQNY fibril forms 1-3. Color coding: black = β-sheet, white = α-helical, grey = indeterminate.....	399
Figure 11-9 Tyrosine-13 in fibril samples consisting of (a) diluted [U- ¹³ C, ¹⁵ N-GNNQ]QNY (F2) and (b) diluted GNN[U- ¹³ C, ¹⁵ N-QQNY] (F4).....	399
Figure 11-10 Comparison of the 2D ¹⁵ N- ¹³ CO correlation spectra of [U- ¹³ C, ¹⁵ N-GNNQ]QNY for the two nanocrystalline forms: (a) monoclinic and (b) orthorhombic. Panels (c) and (d) show spectra obtained from the two independent fibril samples F1 and F2. The assignments of the color-coded peaks are indicated in panel (a). Panel (c) includes the fibril form designations for the color-coded peaks. Data were acquired at 500 MHz (a) and 700 MHz ¹ H field (b-d), respectively.	402
Figure 11-11 Comparison of the aliphatic ¹³ C- ¹³ C correlations of monoclinic and orthorhombic crystalline (a,b) and fibril (c,d) forms of [U- ¹³ C, ¹⁵ N-GNNQ]QNY (samples F1,F3). Cross-peaks in panels (a)-(c) are color coded by residue, with the fibril forms marked by number in panel (c).Panel (d) shows the co-existence of monoclinic crystals (dashed lines) and fibrils in a sample prepared at 12 mg/ml.....	403
Figure 11-12 Illustration of chemical shift deviations between aggregate forms, projected onto the monoclinic crystal structure. We show the absolute chemical shift deviation (in ppm) relative to the monoclinic nanocrystals for the orthorhombic crystals (a), or each of the three dominant fibril forms 1-3 (panels b-d). The graphics were generated using UCSF Chimera ⁹¹	404
Figure 11-13 Illustration of the Tyr-Tyr contacts in the monoclinic crystals. Panel (a) contains a view along the fibril axis, highlighting the interactions of stacked Tyr across the ‘wet interface’ between peptide monomers. The side-ways view in panel (b), with space-filling Tyr residues, illustrates the steric interactions limiting the ring dynamics in the monoclinic crystals. The graphics were generated using UCSF Chimera and Pymol ^{91,92}	408

Figure 11-14 2D assignment data for orthorhombic nanocrystals of GNNQQNNY. Spinning side bands are indicated with (*).....	412
Figure 11-15 Correlation traces of fibril form 1 in 100%-labeled [U- ¹³ C, ¹⁵ N-GNNQ]QNY fibrils.....	414
Figure 11-16 Correlation traces of fibril form 2 in 100%-labeled [U- ¹³ C, ¹⁵ N-GNNQ]QNY fibrils.....	415
Figure 11-17 Correlation traces of fibril form 3 in 100%-labeled [U- ¹³ C, ¹⁵ N-GNNQ]QNY fibrils.....	416
Figure 12-1 2D correlation spectra used for the de novo [U- ¹³ C, ¹⁵ N]-Crh protein dimer structure calculation : (a) 2 ms ¹³ C- ¹³ C PAR spectrum, (b) combined 5 ms, 10 ms and 15 ms ¹³ C- ¹³ C PAR spectra (c) 20 ms ¹³ C- ¹³ C PAR spectrum, (d) 15 ms ¹⁵ N- ¹³ C PAIN-CP spectrum. All spectra were obtained at $\omega_r/2\pi = 20$ kHz. Spectra (a)-(c) were obtained at $\omega_{0H}/2\pi = 900$ MHz and spectrum (d) at $\omega_{0H}/2\pi = 750$ MHz.....	427
Figure 12-2 Contact plot of distance restraints unambiguously assigned at the end of Step III. (b) Number of distance restraints as a function of the primary sequence of the protein. The intramonomer restraints in panels (a) and (b) are indicated in black and the intermonomer restraints are indicated in orange. (c) Local rmsd of the 10 lowest energy conformers after Step III. The number of restraints corresponding to distances > 7 Å in x-ray structure is indicated in blue (see right hand axis).....	430
Figure 12-3 Lowest energy Crh structures from ARIA calculations: (a) 20 lowest energy conformers after the end of monomer calculations using PAR data, (b) 10 lowest energy dimer conformers after the calculations with PAR and intermonomer NHHC data, (c) 10 lowest energy dimer conformers after calculation with PAR, PAIN-CP and intermonomer NHHC data, (d) x-ray structure.....	431

List of Tables

Table 1-1 Spatial and spin rank of some typical NMR interactions.....	47
Table 1-2 Multipole-operator basis for two spin system with its equivalent in the standard product basis representation.	48
Table 1-3 Reduced Wigner matrix elements for the tensor of rank 1.....	51
Table 1-4 Reduced Wigner matrix elements for the tensor of rank 2.....	51
Table 3-1 Multipole-operator basis for two spin system with its equivalent in the standard product basis representation.	87
Table 3-2 The G coefficients involved in the Floquet Hamiltonian (Eq. 9). (a) N=1, R ² condition. (b) N=2, R ² condition.....	88
Table 3-3 Coefficients involved in the second order correction terms (Eq. 16). The indices involved have the following values, $m_1 = -4$ to 4 , $m = -2$ to 2 . In the case of N=1 R ² condition $m_1 = -3$ to 3	91
Table 3-4 Estimated ¹³ C- ¹³ C internuclear distances in N-Ac-VL using zero-order Hamiltonians derived from the MMFT and the fictitious spin operator approach. The CSA interactions were neglected in the simulations. The ZQ relaxation rate in model-1 was calculated based on the URF approach while in model-2, it was employed as a free-fit parameter. In all the simulations the internuclear distance r was used as a free-fit parameter.	96
Table 3-5 Estimated range for ¹³ C- ¹³ C internuclear distances with systematic variation of the orientation of the CSA tensors covering both the extremes. These calculations employ the MMFT model, include 2 nd order terms, and use relaxation models 1 and 2 as in Table 3-4...100	100
Table 3-6 CSA parameters used for simulation of the examined ¹³ C- ¹³ C distances. The orientations were estimated using SIMMOL software package and MPACKAGES from Levitt et al. The relationships between the structural elements and CSA tensor orientations for side-chain carbons were obtained from Veeman. ³⁹ The magnitudes of the CSA tensors were approximated by free amino acid ⁴² values from Ye et al ⁴⁰ (* marks missing values, assumed same as V _β).	101

Table 3-7 Calculated ^{13}C - ^{13}C internuclear distances in N-Ac-VL, using the unique set of orientations given in Table 3-6 based on the MMFT-model with 2 nd order terms and a free-fit T_{zQ}	102
Table 4-1 Theoretical phase modulation settings for CMpRR (sine).....	182
Table 8-1 Atom coordinates in the spin system used in the simulation of Fig. 8-21a...300	
Table 8-2 Atom coordinates in the spin system used in the simulation of Fig. 8-21b. .300	
Table 8-3 Atom coordinates of the spin system used in the simulation of Fig. 8-11f-g. Atom coordinates were extracted from the Crh x-ray structure (1MU4) ⁴ . Isotropic chemical shifts were extracted from ssNMR experimental data and anisotropic chemical shift tensors were chosen based on published data. ⁵	301
Table 8-4 Dipolar couplings in the spin system used in simulations in Fig 8-22. Spins 1 and 2 are ^{13}C nuclei, spins 3 and 4 are ^1H nuclei.....	303
Table 9-1 Average N-N and H-N distances in typical elements of secondary structure in proteins. The values were extracted based on 100 randomly chosen protein structures in the program STARS. ⁸⁰	331
Table 9-2 Atom coordinates and chemical shift values of the spin system used in the numerical simulation in the Fig. 2. The coordinates are taken from the x-ray structure of GB1 protein (PDB ID 2GI9). The ^1H 's were added in Chimera ⁸¹ and NH bonds adjusted to 1.04 Å in Accelrys DS Visualizer 2.0.....	341
Table 9-3 Atom coordinates and chemical shift values for the α -helix spin system used in simulation in Fig. 5. The coordinates are taken from the x-ray structure of protein GB1 (PDB ID 2GI9) and NH bonds adjusted to 1.04 Å in Accelrys DS Visualizer 2.0.	341
Table 9-4 Atom coordinates and chemical shift values for the spin system used in the simulation in Fig. 6b. The coordinates are taken from the x-ray structure of protein GB1 (PDB ID 2GI9) and NH bonds adjusted to 1.04 Å in Accelrys DS Visualizer 2.0.	342
Table 9-5 Atom coordinates and chemical shift values for the spin system used in simulation in Fig. 6d. The coordinates are taken from the model 0.1 from the SSNMR structure of HET-s (218-289) prion (PDB ID 2RNM) and NH bonds adjusted to 1.04 Å in Accelrys DS Visualizer 2.0.	342

Table 9-6 Cross-peaks observed in the spectra in Fig. 4. The sequential cross-peaks in the loop regions are highlighted in red, sequential cross-peaks in the α -helix are highlighted in green, and interstrand cross-peaks within the antiparallel β -sheets are highlighted in blue....344

Table 9-7 Atom coordinates and chemical shift values for the spin system used in simulation in Fig. 9-7. The coordinates are taken from the x-ray structure of protein GB1 (PDB ID 2GI9) and NH bonds adjusted to 1.04 Å in Accelrys DS Visualizer 2.0.346

Table 10-1 Spin system used in simulation in the Fig. 10-2 in the main text and Figure 10-5. The coordinates were taken from the SSNMR structure of N-*f*-MLF-OH⁶³ (PDB ID 1Q7O). The CH bond lengths were set to 1.12 Å.367

Table 10-2 Spin system used in simulation in the Fig. 10-6. The coordinates were taken from the SSNMR structure of N-*f*-MLF-OH¹ (PDB ID 1Q7O). The CH bond lengths were set to 1.12 Å.368

Table 11-1 Description of the isotopically enriched samples used in this study. Samples were prepared using segmentally labeled peptides where either the N-terminus (GNNQ) or the C-terminus (QQNY) was U-¹³C, ¹⁵N labeled. The samples are indicated as monoclinic (M), orthorhombic (O), or fibrillar (F), prepared at 4°C starting from an aqueous solution at peptide concentrations as marked.383

Table 11-2 Chemical shifts of the nuclei in monoclinic nanocrystals of GNNQQNY. The listed ¹³C frequencies are based on natural abundance spectra, and have an uncertainty of 0.05-0.1ppm. The ¹⁵N frequencies are based on ¹⁵N enriched samples, and have an uncertainty of ~0.2ppm. ¹³C chemical shifts are referenced relative to DSS and ¹⁵N chemical shifts are referenced relative to liquid NH₃, according to IUPAC^{65,66} using indirect referencing based on adamantane⁶⁴.390

Table 11-3 Torsion angle data for the peptide backbone of crystalline GNNQQNY. The predicted torsion angles are based on analysis of the isotropic chemical shift values using the TALOS program⁸³. The table also lists the equivalent torsion angles found in the x-ray crystal structure of the monoclinic crystals²⁶.393

Table 11-4 Chemical shifts of the nuclei in orthorhombic nanocrystals of GNNQQNY. The resonances are based on a combination of natural abundance and labeled data. * Tyr side chain resonances (in italics) are partially averaged indicating dynamics of the aromatic ring.394

Table 11-5 Assignment of fibril form resonances for the three predominant forms found in 100% [U-¹³C,¹⁵N-GNNQ]QNY fibril sample F1, prepared at 20 mg/ml. The sets of resonance labeled as 1-3 are listed alongside their estimated relative intensities in the spectra.398

Table 11-6 Overall chemical shift deviations between the different aggregate forms. Deviations are shown as the RMSD (in ppm) between any two polymorphs, based on all ¹³C or ¹⁵N assignments common to both forms (but excluding the mobile Tyr positions). The most similar pair in each row is indicated in bold.401

1. Introduction

1.1. Why solid-state NMR?

Solid-state NMR is rapidly developing as a *unique technique* for molecular structure determination due to its ability to provide detailed structural information in a wide variety of samples, whether (nano)crystalline, fibrillar, or immobilized by association with biomembranes. It has been employed in a range of biologically important studies into topics such as protein folding/misfolding, amyloid aggregation, signal transduction and molecular transport across biomembranes¹⁻⁵. The applied structural methods have been developed and demonstrated on a number of microcrystalline soluble proteins⁶⁻⁹. These techniques allow not only whole-molecule structural determinations, but also tackle essential challenges such as *in situ* structure determination of bound ligands^{10,11}, their effect on membrane protein structure and the detection of protein-protein interactions^{12,13}.

The ongoing development of methodology to enable these biomolecular applications of solid state magic angle spinning NMR at high-field require one to consider the following crucial points:

i. Maximizing sensitivity and resolution

For a given sample volume, the increasing size and complexity of studied biomolecular systems raises the requirements for both resolution and sensitivity. An increase in magnetic field strength, as well as magic angle spinning frequency allows one to maximize both parameters. Of course, sample preparation also plays a crucial role when it comes to achieving the highest possible resolution and sensitivity.

Not all proteins are easily expressed in large amounts, making minimization of the required sample volume an important consideration. For instance membrane proteins, obvious targets for SSNMR studies, often tend to suffer from this limitation.

ii. Biologically relevant conditions

Biologically relevant samples often have specific requirements in terms of temperature, hydration, and other sample conditions. Unfortunately, such hydrated samples are sensitive to

excessive heating due to the radio frequency (r.f.) irradiation. As such, the objective is to optimize the SSNMR techniques for the best compromise between performance and sample preservation. A central approach would involve a reduction of the r.f. irradiation in terms of both the time and the overall strength of the irradiation.

iii. Maximizing the information content

Since access to (high-field) spectrometer time is (still) limited, the requirement for maximizing the information content of the obtained spectra is also important. The development of methods applicable to fully labeled proteins rather than selectively labeled systems is one important step in this direction. This can be optimized further by the application of well-chosen recoupling techniques.

As we will see below, these considerations are intricately linked and influence each other. They affect various steps involved in biological SSNMR structure determination, ranging from assignment of the observed resonances to each of the atoms, to the determination of structural parameters such as distances and torsion angles. We will illustrate the current potential in state of the art biological MAS SSNMR by focusing on the specific aspect of the assignment of ^{13}C and ^{15}N sites and structural measurements in biological molecules via the recoupling of dipolar interactions. More specifically, we introduce a number of new methods optimized for application at $B_0 > 14.1 \text{ T}$ ($\omega_{\text{OH}}/2\pi = 600 \text{ MHz}$) and $\omega_r/2\pi > 20 \text{ kHz}$ that provide the high resolution and sensitivity required for structure determination of proteins. Moreover, we will also describe a number of applications of solid-state NMR to dynamics studies and high resolution structure determination of peptides and proteins.

1.2. Roadmap

This thesis is organized in 12 chapters.

Chapter 1 provides a brief outlook of solid-state NMR for biomolecular studies and gives a short introduction including the basic theory necessary for understanding solid-state NMR experiments presented in this work.

In Chapter 2 we demonstrate the efficient transfer of DNP enhanced ^1H polarization from an aqueous, radical-containing solvent matrix into amyloid-forming peptide GNNQQNY₇₋₁₃

peptide crystals via ^1H - ^1H spin diffusion across the matrix-crystal interface. This work provides the basis for application of DNP for sensitivity enhancement on the samples where the polarizing agent is not in an intimate contact with the solute e.g. crystals, large fibrils etc.

In Chapter 3 we present an improved theoretical description of Rotational Resonance Width (R^2W) experiments and subsequently use the derived formalism for fitting accurate ^{13}C - ^{13}C distances on a [U - ^{13}C , ^{15}N]-VL dipeptide.

In Chapter 4 we introduce a family of solid state NMR pulse sequences that generalizes the concept of second averaging in the modulation frame and therefore provides a new approach to perform magic angle spinning dipolar recoupling experiments. We focus on two particular recoupling mechanisms -- cosine modulated rotary resonance (CMpRR) and cosine modulated recoupling with isotropic chemical shift reintroduction (COMICS). The first technique, CMpRR, is based on a cosine modulation of the rf phase and yields broadband double-quantum (DQ) ^{13}C recoupling using > 70 kHz $\omega_{1,C}/2\pi$ rf field for the spinning frequency $\omega_r/2\pi=10$ – 30 kHz and ^1H Larmor frequency $\omega_{0,H}/2\pi$ up to 900 MHz. CMpRR mitigates the heating effects of simultaneous high power ^{13}C recoupling and ^1H decoupling. The second technique, COMICS, involves low power ^{13}C irradiation that induces simultaneous recoupling of the ^{13}C DQ dipolar and isotropic chemical shift terms. In contrast to CMpRR, where the DQ bandwidth (~ 30 kHz at $\omega_{0,H}/2\pi = 750$ MHz) covers the entire ^{13}C spectral width, COMICS recoupling, through the reintroduction of the isotropic chemical shift, is selective with respect to the carrier frequency, having a typical bandwidth of ~ 100 Hz. This approach is intended as a general frequency selective method circumventing dipolar truncation (supplementary to R^2 experiments).

In Chapter 5 we describe an adiabatic extension of the CMpRR sequence called CMAR (Cosine Modulated Adiabatic Recoupling) that is more robust with respect to the rf inhomogeneity.

In Chapter 6 we demonstrate how the CMpRR pulse sequence using ultra-low or even no ^1H decoupling overcomes some practical limitations (including polarization losses due to insufficient ^1H decoupling and prohibitive sample heating) of application of broadband DQ experiments at $\omega_{0,H}/2\pi=900$ MHz on proteins and thus enables SSNMR study of a range of biomolecular systems. We apply CMpRR to samples with varying degrees of macroscopic order without compromising the integrity of the samples. We demonstrate the efficient

polarization transfer along multiple carbon-carbon bonds, as well as the advantages of the cross-peak sign alternation, a signature of double-quantum polarization transfer, and how these features benefit resonance assignment as well as assignment cross-validation (especially for proteins with significant spectral overlap).

In Chapter 7 we present a solid-state NMR ^{15}N - ^{13}C polarization transfer scheme based on the second order Third Spin Assisted Recoupling (TSAR) mechanism that is applicable at high B_0 and high spinning frequencies, requiring moderate rf powers (~ 50 kHz $^{13}\text{C}/^{15}\text{N}$) and mixing time (< 20 ms). The sequence, PAIN-CP, involves the abundant nearby protons in the heteronuclear recoupling dynamics, and provides a new tool for obtaining long distance ^{15}N - ^{13}C contacts.

In Chapter 8 we discuss a homonuclear version of the TSAR mechanism. We provide a second order AHT description of the phenomenon and discuss the method in the context of structure determination of proteins. More specifically we demonstrate that ^{13}C - ^{13}C PAR yields long range/long distance contacts in uniformly ^{13}C and ^{15}N labeled proteins that can be used as distance restraints for structure calculation.

In Chapter 9 we present application of PAR experiment to ^{15}N - ^{15}N correlation spectroscopy. We demonstrate that ^{15}N - ^{15}N PAR provides a sensitive probe of the secondary and tertiary structure of proteins.

In Chapter 10 we demonstrate that ^{13}C - ^{13}C PAR in spite of being a second order technique can be used successfully to provide long distance contacts even at the highest currently achievable spinning frequencies (here $\omega_r/2\pi=65$ kHz). We also demonstrate that at > 50 kHz low power decoupling methods provide a viable alternative for performing high resolution studies of biomolecules.

In Chapter 11 we present structural and dynamics studies of the nanocrystals and, more importantly, amyloid fibrils of the GNNQQNY peptide fragment from the N domain of the yeast prion protein sup35p.

Finally, in Chapter 12 we present a new approach for *de novo* structure determination of proteins based on the experiments relying on the TSAR mechanism (introduced in Chapters 7-10) and use it for high resolution structure determination of the 2×10.4 kDa $[\text{U-}^{13}\text{C}, ^{15}\text{N}]$ -Crh protein dimer.

1.3. Spin dynamics essentials

This section introduces a number of essential concepts helpful for understanding nuclear spin dynamics in the solid state under magic angle spinning. For a more in depth and systematic introduction to theory of solid-state NMR the reader should consult references¹⁴⁻¹⁸.

1.3.1. Interactions in Nuclear Magnetic Resonance

The nuclear spin dynamics can be described by the following Hamiltonian

$$H = H_z + H_{\text{int}} + H_{\text{RF}} \quad (1)$$

where H_z is the Zeeman Hamiltonian describing interaction of the nucleus with the static magnetic field, H_{int} is the internal Hamiltonian describing internal nuclear spin interactions and H_{RF} is the term describing the interaction with the applied radiofrequency (RF) field.

The Zeeman Hamiltonian is given by

$$H_z = -\gamma\hbar B_0 I \quad (2)$$

where γ is the gyromagnetic ratio, B_0 is the magnetic field, and I_z is the z-component of the nuclear angular momentum operator I . Since the interaction of the nucleus with the magnetic field is the largest in the nuclear spin dynamics, the reference frame (which is termed the laboratory frame) is usually chosen so that the z-axis coincides with the magnetic field. Consequently in the laboratory frame the Zeeman Hamiltonian can be written as

$$H_z = \omega_z I_z \quad (3)$$

where ω_z is the Larmor frequency and I_z is the z-component of the nuclear spin angular momentum operator I . The ^1H Larmor frequency, $\omega_{z,\text{H}}/2\pi$, is customarily used to describe the strength of the magnets used in NMR spectroscopy. At the time of writing this thesis the typical NMR spectrometers operate at ^1H Larmor frequencies 0.1-1 GHz, which corresponds to magnetic fields of 2.4-23.5 T.

For the sake of convenience we usually describe NMR spin dynamics in the frame of the Zeeman term, which is called the rotating frame.

In the rotating frame the internal Hamiltonian (H_{int}) for the nuclear interactions (or terms which depend on the direction of the nuclear polarization) can be written as

$$H_{\text{int}} = H_{CS} + H_D + H_Q + H_J \quad (4)$$

where H_{CS} is the chemical shift Hamiltonian, H_D is the dipolar Hamiltonian, H_Q is the quadrupolar Hamiltonian and H_J is scalar coupling Hamiltonian.

The particular terms in Eq. (4) can be written in the laboratory frame as¹⁵

$$H_{CS} = \sum_k \gamma_k I_k \cdot \sigma_k \cdot B_0 \quad (5)$$

$$H_D = \sum_{i < j} I_i \cdot D_{ij} \cdot I_j \quad (6)$$

$$H_J = 2\pi \sum_{i < j} I_i \cdot J_{ij} \cdot I_j \quad (7)$$

$$H_Q = \sum_k \frac{eQ_k}{2I_k(2I_k - 1)\hbar} I_k \cdot V_k \cdot I_k \quad (8)$$

where σ_k , D_{ij} , J_{ij} , V_k , and Q_k are respectively: the chemical shielding, dipolar coupling, indirect spin-spin coupling (J-coupling), electric field gradient tensor, and quadrupole moment of the nucleus. In this work we are not going to be concerned with quadrupolar interactions and will thus not consider them any further.

Usually in magic angle spinning (MAS) experiments in which the sample is spun within a rotor tilted at the “magic angle” ($\sim 54.74^\circ$) we have to perform a series of transformation to express the tensors in the laboratory frame

$$\text{principal frame} \xrightarrow{\Omega_{\text{PM}}} \text{molecular frame} \xrightarrow{\Omega_{\text{MR}}} \text{rotor frame} \xrightarrow{\Omega_{\text{RL}}} \text{lab frame} \quad (9)$$

where $\Omega_{AB} = (\alpha_{AB}, \beta_{AB}, \gamma_{AB})$ is a set of Euler angles. There are several conventions for defining the Euler angles (12 to be precise). Here we follow the convention introduced by Rose¹⁹. In this convention to rotate the (X, Y, Z) coordinate system into (x, y, z) system we perform the following:

- a. rotation 1: rotation about Z axis by the angle α until Y axis coincides with the node line. The node line is defined by the intersection of the XY and the xy planes.
- b. rotation 2: rotation about the node line by the angle β until the Z axis coincides with z axis.
- c. rotation 3: rotation about z axis by the angle γ until Y coincides with the y axis.

Since the effect of the pulses on the Hamiltonian also can be treated in the form of rotations it is often convenient to rewrite the internal Hamiltonian in terms of spherical tensors separating it into the spatial and spin part

$$H = \sum_{k,q,\lambda} (-1)^q R_{\lambda}^{(k)q} T_{\lambda}^{(k)-q} \quad (10)$$

The spatial part $R_{\lambda}^{(k)q}$ can be manipulated by reorientation of the molecules (e.g. sample spinning) and the spin part $T_{\lambda}^{(k)-q}$ can be independently modulated by rf pulses. Here k describes the individual rank of the tensor, q describes the component of the tensor and λ is used to identify the interaction. Note that it is customary to use l and m for the spatial rank and component and k and q for the spin rank and component. The table below lists the spatial and spin ranks for selected interactions.

Table 1-1 Spatial and spin rank of some typical NMR interactions.

Interaction	Spatial rank, l	Spin rank, k
J-coupling	0	0
CSA	2	1
Dipole-dipole	2	2

There are several conventions for constructing an irreducible spherical tensor basis set. One of the general formulations used for an arbitrary number of spins with arbitrary integer and half-integer nuclei introduced by Sanctuary is called multipole basis. The multiple basis set for two spin $\frac{1}{2}$ spins is presented in Table 1-2.

Table 1-2 Multipole-operator basis for a two spin system with its equivalent in the standard product basis representation.

Multipole representation	Standard representation
<i>Single spin operators</i>	<i>Single spin operators</i>
$T^{(1)0}(10)$ ($T^{(1)0}(01)$)	iI_{1z} (iI_{2z})
$T^{(1)\pm 1}(10)$ ($T^{(1)\pm 1}(01)$)	$\mp \frac{1}{\sqrt{2}} iI_1^\pm$ ($\mp \frac{1}{\sqrt{2}} iI_2^\pm$)
<i>Two spin operators</i>	<i>Two spin operators</i>
$T^{(0)0}(11)$	$\frac{2}{\sqrt{3}} I_1 \cdot I_2$
$T^{(1)0}(11)$	$\frac{1}{\sqrt{2}} (I_1^+ I_2^- - I_1^- I_2^+)$
$T^{(1)\pm 1}(11)$	$I_1^\pm I_{2z} - I_{1z} I_2^\pm$
$T^{(2)0}(11)$	$-\frac{2}{\sqrt{6}} (3I_{1z} I_{2z} - I_1 \cdot I_2)$
$T^{(2)\pm 2}(11)$	$-I_1^\pm I_2^\pm$
$T^{(2)\pm 1}(11)$	$\pm (I_1^\pm I_{2z} + I_{1z} I_2^\pm)$

One notable difference between the multiple basis set formulation used in Chapter 3 and another formulation used in this thesis is that in the former for generality reasons all the spins are treated the same way whereas in the latter heteronuclear two spin operators are expressed as a product of single spin operators. More specifically if we consider a ^1H - ^{13}C

dipolar coupling in the multiple basis we would write it as $T^{(2)0}$ (11) but we could also alternatively write it as $T_H^{(1)0}T_C^{(1)0}$.

With the basis specified with irreducible spherical tensors its manipulations can be treated as a series of simple rotations. The rotation of a spherical tensor from one coordinate system to a new coordinate system can be conveniently expressed using Wigner rotation matrices

$$D(\Omega_{AB})T^{(k)q}D^{-1}(\Omega_{AB}) = \sum_{q'=-k}^k T_{\lambda}^{(k)q'} D_{q'q}^{(k)}(\Omega_{AB}) \quad (11)$$

The Wigner rotation matrices may in turn be expressed as

$$D_{q'q}^{(k)}(\Omega_{AB}) = e^{-iq\alpha_{AB}} d_{q'q}^{(k)}(\beta_{AB}) e^{-iq'\gamma_{AB}} \quad (12)$$

where $d_{q'q}^{(\lambda)}(\beta)$ is a reduced Wigner matrix element. The reduced Wigner matrix elements for tensors of the first and second rank are shown in Tables 1-3 and 1-4.

The successive rotations can be described as

$$D_{q'q}^{(k)}(\Omega_{AC}) = \sum_{q''=-k}^k D_{q'q''}^{(k)}(\Omega_{AB}) D_{q''q}^{(k)}(\Omega_{BC}) \quad (13)$$

Using Eq. (13) and relationship (9) the spatial tensor describing each interaction λ in the laboratory frame can be expressed as

$$R_{\lambda,LAB}^{(l)m} = \sum_{m_1, m_2, m_3=-l}^l R_{\lambda,PAS}^{(l)m_1} D_{m_1 m_2}^{(l)}(\Omega_{PM}) D_{m_2 m_3}^{(l)}(\Omega_{MR}) D_{m_3 m}^{(l)}(\Omega_{RL}) \quad (14)$$

where $R_{\lambda,PAS}^{(l)m}$ is the tensor element in the principal axis system. Note that in the PAS the interaction tensors are diagonal. For CSA the only relevant tensor elements in the PAS are

$R_{CSA,PAS}^{(2)\pm 2} = -\frac{1}{2}\eta\delta_{aniso}^j$ and $R_{CSA,PAS}^{(2)0} = \sqrt{\frac{3}{2}}\delta_{aniso}^j$, for isotropic chemical shift $R_{CS,PAS}^{(0)0} = \gamma\sigma_{iso}^j$ and for dipolar coupling $R_{D,PAS}^{(2)0} = \sqrt{6}b^{jk}$, where η is the asymmetry, δ_{aniso}^j is anisotropy, σ_{iso}^j is isotropic chemical shift, and b^{jk} is the dipolar coupling constant ($b_{jk} = \frac{\mu_0\gamma_j\gamma_k\hbar}{4\pi r_{jk}^3}$ (rad/s)).

Note, that in the Zeeman interaction frame based on the high field approximation only the terms commuting with the Zeeman term (i.e. $T_\lambda^{(k)0}$ terms) are retained. Consequently Eq. (14) can be rewritten as

$$R_{\lambda,LAB}^{(l)0} = \sum_{m_1,m_2,m_3=-l}^l R_{\lambda,PAS}^{(l)m_1} D_{m_1m_2}^{(l)}(\Omega_{PM}) D_{m_2m_3}^{(l)}(\Omega_{MR}) D_{m_30}^{(l)}(\Omega_{RL}) \quad (15)$$

As we already mentioned above the effect of the pulses on the Hamiltonian can be treated as rotations of the spin part

$$D(\alpha, \beta, \gamma) T^{(k)0} D^{-1}(\alpha, \beta, \gamma) = \sum_{q=-k}^k T^{(k)q} D_{q0}(\alpha, \beta, \gamma) \quad (16)$$

After we define the Hamiltonian describing the spin system we have to solve the Liouville-von Neuman equation in order to learn about the evolution of the considered spin system.

Table 1-3 Reduced Wigner matrix elements for the tensor of rank 1

$d_{m'm}^{(1)}(\beta)$ - reduced Wigner matrix element for the tensor rank 1			
m'/m	1	0	-1
1	$\frac{1}{2}(1 + \cos \beta)$	$-\frac{1}{\sqrt{2}} \sin \beta$	$\frac{1}{2}(1 - \cos \beta)$
0	$\frac{1}{\sqrt{2}} \sin \beta$	$\cos \beta$	$-\frac{1}{\sqrt{2}} \sin \beta$
-1	$\frac{1}{2}(1 - \cos \beta)$	$\frac{1}{\sqrt{2}} \sin \beta$	$\frac{1}{2}(1 + \cos \beta)$

Table 1-4 Reduced Wigner matrix elements for the tensor of rank 2

$d_{m'm}^{(2)}(\beta)$ - reduced Wigner matrix element for the tensor rank 2					
m'/m	2	1	0	-1	-2
2	$\frac{1}{4}(1 + \cos(\beta)^2)$	$-\frac{1}{2}(1 + \cos(\beta)) \sin(\beta)$	$\frac{1}{2\sqrt{2}} \sqrt{3} \sin^2(\beta)$	$-\frac{1}{2}(1 - \cos(\beta)) \sin(\beta)$	$\frac{1}{4}(1 + \cos(\beta)^2)$
1	$\frac{1}{2}(1 + \cos(\beta)) \sin(\beta)$	$\frac{1}{2}(\cos(\beta) + \cos(2\beta))$	$-\sqrt{\frac{3}{2}} \cos(\beta) \sin(\beta)$	$\frac{1}{2}(\cos(\beta) - \cos(2\beta))$	$\frac{1}{2}(-1 + \cos(\beta)) \sin(\beta)$
0	$\frac{1}{2\sqrt{2}} \sqrt{3} \sin^2(\beta)$	$\sqrt{\frac{3}{2}} \cos(\beta) \sin(\beta)$	$\frac{1}{4}(1 + 3\cos(2\beta))$	$-\sqrt{\frac{3}{2}} \cos(\beta) \sin(\beta)$	$\frac{1}{2\sqrt{2}} \sqrt{3} \sin^2(\beta)$
-1	$-\frac{1}{2}(-1 + \cos(\beta)) \sin(\beta)$	$\frac{1}{2}(\cos(\beta) - \cos(2\beta))$	$-\sqrt{\frac{3}{2}} \cos(\beta) \sin(\beta)$	$\frac{1}{2}(\cos(\beta) + \cos(2\beta))$	$-\frac{1}{2}(1 + \cos(\beta)) \sin(\beta)$
-2	$\frac{1}{4}(1 - \cos(\beta)^2)$	$\frac{1}{2}(1 - \cos(\beta)) \sin(\beta)$	$\frac{1}{2\sqrt{2}} \sqrt{3} \sin^2(\beta)$	$\frac{1}{2}(1 + \cos(\beta)) \sin(\beta)$	$\frac{1}{4}(1 + \cos(\beta)^2)$

1.3.2. Time evolution of density operator

The state of nuclear spins can be described by the density operator $\rho(t)$. In order to know, at any given time, the state of the system we have to solve the Liouville-von Neumann equation

$$\frac{d}{dt}\rho(t) = -i[H(t), \rho(t)] \quad (17)$$

A general solution for Eq. (17) is

$$\rho(t) = U(t)\rho(0)U(t)^{-1} \quad (18)$$

where $U(t)$ is the propagator defined as

$$U(t) = T \exp\left[-i\int_0^t H(t')dt'\right] \quad (19)$$

where T is the Dyson time-ordering operator.

In most NMR experiments the time-dependent Hamiltonian does not commute with itself at different times. In that case the time evolution of the density operator has to be evaluated either numerically or using approximations such as Average Hamiltonian Theory (AHT)^{20,21} or Multipole-Multimode Floquet Theory (MMFT)²²⁻²⁴.

1.3.3. Transformation to the interaction frame

Before we describe AHT and MMFT let us quickly introduce the concept of interaction frame.

In numerous NMR experiments the internal Hamiltonian is manipulated by rf pulses. It is often true that the applied rf fields are substantially larger than the internal interactions (at least in the case of dipolar coupling and chemical shift) i.e.

$$|\omega_1| \gg |H_{\text{int}}| \quad (20)$$

Consequently, for the purpose of describing the spin dynamics in an NMR experiment it is often convenient to transform the internal Hamiltonian in to the interaction frame of the rf irradiation. The propagator in the experiment with time-dependent perturbations from the rf pulses can be expressed as

$$U(t) = T \exp \left\{ -i \int_0^t dt_1 H_{\text{int}} + H_{\text{rf}}(t_1) \right\} \quad (21)$$

We can also rewrite Eq. (19) as

$$U(t) = U_{\text{rf}}(t) U_{\text{int}}(t) \quad (22)$$

where

$$U_{\text{rf}}(t) = T \exp \left\{ -i \int_0^t dt_1 H_{\text{rf}}(t_1) \right\} \quad (23)$$

$$U_{\text{int}}(t) = T \exp \left\{ -i \int_0^t dt_1 \widetilde{H}_{\text{int}}(t_1) \right\} \quad (24)$$

with the internal Hamiltonian in the interaction frame ($\widetilde{H}_{\text{int}} = U_{\text{rf}}^{-1}(t) H_{\text{int}} U_{\text{rf}}(t)$) indicated with tilde. Note that $\widetilde{H}_{\text{int}}$ is now time-dependent.

1.3.4. Average Hamiltonian Theory

Average Hamiltonian theory (AHT)^{20,21} is used to describe the effective evolution of a spin system under time dependent Hamiltonian $H(t)$ over a given time interval τ_c by a time-

independent average Hamiltonian \bar{H} . In that case Eq. (19) can be rewritten over the τ_c period as

$$U(\tau_c) = T \exp \left\{ -i \int_0^{\tau_c} dt H(t) \right\} = \exp \{ -i \bar{H} \tau_c \} \quad (25)$$

In order to calculate the evolution over longer periods of time with AHT we usually require that the $H(t)$ is periodic ($H_1(t + N\tau_c) = H_1(t)$) and cyclic ($U_1(N\tau_c) = 1$) (which can be assumed for many rotor synchronized pulse sequences). In that case we can strictly describe the spin system evolution for stroboscopic observation synchronized with the period of the $H(t)$

$$U(n\tau_c) = U(\tau_c)^n = \exp \{ -i \bar{H} n \tau_c \} \quad (26)$$

Usually the time-independent effective Hamiltonian is evaluated by using Magnus expansion²⁵

$$\bar{H} = \bar{H}^{(0)} + \bar{H}^{(1)} + \bar{H}^{(2)} + \bar{H}^{(3)} + \dots \quad (27)$$

where

$$\begin{aligned} \bar{H}^{(0)} &= C \\ \bar{H}^{(1)} &= \frac{1}{\tau_c} \int_0^{\tau_c} dt_1 \tilde{H}(t_1) \\ \bar{H}^{(2)} &= -\frac{i}{2\tau_c} \int_0^{\tau_c} dt_2 \int_0^{t_2} dt [\tilde{H}(t_2), \tilde{H}(t_1)] \\ \bar{H}^{(3)} &= -\frac{1}{6\tau_c} \int_0^{\tau_c} dt_3 \int_0^{t_3} dt_2 \int_0^{t_2} dt \left\{ [\tilde{H}(t_3), [\tilde{H}(t_2), \tilde{H}(t_1)]] + [[\tilde{H}(t_3), \tilde{H}(t_2)], \tilde{H}(t_1)] \right\} \end{aligned} \quad (28)$$

Note that in the literature there are two different conventions for referring to different orders of the Magnus expansion. Sometimes $\bar{H}^{(1)}$ in Eq. (28) is referred to as a zero order

term. However, in this thesis in order to avoid confusion we follow the convention that the zero order corresponds to the time independent part of the $H(t)$ and the first order is evaluated using $\overline{H}^{(1)}$ expression in Eq. (28).

All of the experiments presented in this dissertation can be adequately described by the AHT expressions up to the second order.

1.3.5. Multipole-Multimode Floquet Theory

In Floquet theory²²⁻²⁴ the time-dependent Hamiltonian is transformed to a time independent Floquet-Hamiltonian expressed in a matrix form using infinite dimensional basis set. The basis set is a direct product of a finite spin basis and Fourier index (which can have infinite values). The coefficients in the transformed Hamiltonian are time-independent and the evolution of the spin system may be studied by solving a set of linear equations. However, in order to know the evolution of the spin system the infinite Floquet-Hamiltonian matrix has to be diagonalized either numerically or, as we do in Chapter 3, using a contact (van Vleck)²⁶ transformation. In the van Vleck transformation the Hamiltonian is diagonalized using a series of unitary transformations

$$\widehat{H} = UHU^{-1} = e^{i\lambda^n S_n} \dots e^{i\lambda^2 S_2} e^{i\lambda S_1} H e^{-i\lambda S_1} e^{-i\lambda^2 S_2} e^{-i\lambda^n S_n} \quad (29)$$

where S_n 's are Hermitian operators and λ is perturbation parameter.

If we write the untransformed Hamiltonian as

$$H = H_0 + \lambda H_1 + \lambda^2 H_2 \dots \quad (30)$$

where H_0 is the zero order (time-independent part) Hamiltonian and H_n are consecutive perturbing Hamiltonians (in an order of decreasing magnitude).

The transformed Hamiltonian $H^{(1)}$ after the first transformation is

$$H^{(1)} = U_1 H U_1^{-1} = e^{i\lambda S_1} H e^{-i\lambda S_1} = H_0^{(1)} + \lambda H_1^{(1)} + \lambda^2 H_2^{(1)} + \dots \quad (31)$$

The operator S_I is chosen such that $H^{(I)}$ is purely diagonal to the λ -th order, which we achieve by

$$\begin{aligned} H^{(1)} &= U_1 H U_1^{-1} = H_0^{(1)} + \lambda H_1^{(1)} + \lambda^2 H_2^{(1)} + \dots \\ &= H_0 + \lambda (H_1 + i[S_1, H_0]) + \lambda^2 (H_2 + i[S_1, H_1] - \frac{1}{2}[S_1, [S_1, H_0]]) \dots \end{aligned} \quad (32)$$

After we equate the powers of λ on both sides of the equation we get

$$\begin{aligned} H_0^{(1)} &= H_0 \\ H_1^{(1)} &= H_1 + i[S_1, H_0] \\ H_2^{(1)} &= H_2 + i[S_1, H_1] - \frac{1}{2}[S_1, [S_1, H_0]] \text{ etc.} \end{aligned} \quad (33)$$

This procedure can be repeated iteratively to include higher order terms.

A rigorous introduction to the Multipole-Multimode Floquet Theory used in Chapter 3 can be found in ref. 27 and the examples of various applications in refs. 28-30

1.4. References

- (1) Jaroniec, C. P.; MacPhee, C. E.; Bajaj, V. S.; McMahon, M. T.; Dobson, C. M.; Griffin, R. G. *Proceedings of the National Academy of Sciences of the United States of America* **2004**, *101*, 711-716.
- (2) Andronesi, O. C.; Becker, S.; Seidel, K.; Heise, H.; Young, H. S.; Baldus, M. *J Am Chem Soc* **2005**, *127*, 12965-12974.
- (3) Frericks, H. L.; Zhou, D. H.; Yap, L. L.; Gennis, R. B.; Rienstra, C. M. *J Biomol NMR* **2006**, *36*, 55-71.
- (4) Tycko, R. *Quarterly Reviews of Biophysics* **2006**, *39*, 1-55.
- (5) Lange, A.; Giller, K.; Hornig, S.; Martin-Eauclaire, M. F.; Pongs, O.; Becker, S.; Baldus, M. *Nature* **2006**, *440*, 959-962.
- (6) Franks, W. T.; Zhou, D. H.; Wylie, B. J.; Money, B. G.; Graesser, D. T.; Frericks, H. L.; Sahota, G.; Rienstra, C. M. *J Am Chem Soc* **2005**, *127*, 12291-305.

- (7) Bockmann, A.; Lange, A.; Galinier, A.; Luca, S.; Giraud, N.; Juy, M.; Heise, H.; Montserret, R.; Penin, F.; Baldus, M. *Journal of Biomolecular Nmr* **2003**, *27*, 323-339.
- (8) Zech, S. G.; Wand, A. J.; McDermott, A. E. *J Am Chem Soc* **2005**, *127*, 8618-8626.
- (9) Castellani, F.; van Rossum, B.; Diehl, A.; Schubert, M.; Rehbein, K.; Oschkinat, H. *Nature* **2002**, *420*, 98-102.
- (10) Jovanovic, T.; McDermott, A. E. *J Am Chem Soc* **2005**, *127*, 13816-13821.
- (11) Williamson, P. T. F.; Watts, J. A.; Addona, G. H.; Miller, K. W.; Watts, A. *Proc Natl Acad Sci U S A* **2001**, *98*, 2346-2351.
- (12) Etzkorn, M.; Bockmann, A.; Lange, A.; Baldus, M. *Journal of the American Chemical Society* **2004**, *126*, 14746-14751.
- (13) Baldus, M. *Current Opinion in Structural Biology* **2006**, *16*, 618-623.
- (14) Abragam, A. *Principles of Nuclear Magnetism*; Oxford University Press, New York, 1961: New York, 1961.
- (15) Ernst, R. R.; Bodenhausen, G.; Wokaun, A. *Principles of Nuclear Magnetic Resonance in One and Two Dimensions*; Clarendon Press: Oxford, 1991.
- (16) Haeberlen, U. *High-Resolution NMR in Solids: Selective Averaging*; Academic Press: New York, 1976.
- (17) Slichter, C. P. *Principles of Magnetic Resonance*; Springer-Verlag: Berlin, 1990.
- (18) Mehring, M.; Wehner, V. A. *Object-Oriented Magnetic Resonance : Classes and Objects, Calculations and Computations*; Academic Press, 2001.
- (19) Rose, M. E. *Elementary Theory of Angular Momentum*; Wiley: New York, 1957.
- (20) Haeberle, U.; Waugh, J. S. *Physical Review* **1968**, *175*, 453-&.
- (21) Haeberle, U. *High-Resolution NMR in Solids: Selective Averaging*; Academic Press: New York, 1976.
- (22) Schmidt, A.; Vega, S. *Journal of Chemical Physics* **1987**, *87*, 6895-6907.
- (23) Schmidt, A.; Vega, S. *Journal of Chemical Physics* **1992**, *96*, 2655-2680.
- (24) Shirley, J. H. *Physical Review* **1965**, *138*, B979-B987.
- (25) Magnus, W. *Commun. Pure and Appl. Math.* **1954**, *7*, 649.
- (26) Ho, T. S.; Laughlin, C.; Chu, S. I. *Physical Review A* **1985**, *32*, 122-133.

(27) Ramachandran, R.; Griffin, R. G. *Journal of Chemical Physics* **2005**, *122*, 164502:1-10.

(28) Ramachandran, R.; Bajaj, V. S.; Griffin, R. G. *Journal of Chemical Physics* **2005**, *122*, 164503:1-14.

(29) Ramachandran, R.; Griffin, R. G. *Journal of Chemical Physics* **2006**, *125*, 044510:1-14.

(30) Ramachandran, R.; Lewandowski, J. R.; van der Wel, P. C. A.; Griffin, R. G. *Journal of Chemical Physics* **2006**, *124*, 214107:1-14.

2. Dynamic Nuclear Polarization for sensitivity enhancement

Reproduced with permission from van der Wel P.C., Hu K.N., Lewandowski J., Griffin R.G. "Dynamic nuclear polarization of amyloidogenic peptide nanocrystals: GNNQQNY, a core segment of the yeast prion protein Sup35p." *J. Am. Chem. Soc.* (2006) 128(33):10840-6. Copyright © 2006 American Chemical Society.

2.1. Abstract

Dynamic nuclear polarization (DNP) permits a $\sim 10^2$ - 10^3 enhancement of the nuclear spin polarization and therefore increased sensitivity in nuclear magnetic resonance (NMR) experiments. Here, we demonstrate the efficient transfer of DNP enhanced ^1H polarization from an aqueous, radical-containing solvent matrix into peptide crystals via ^1H - ^1H spin diffusion across the matrix-crystal interface. The samples consist of nanocrystals of the amyloid-forming peptide GNNQQNY₇₋₁₃, derived from the yeast prion protein Sup35p, dispersed in a glycerol-H₂O matrix containing a biradical polarizing agent, TOTAPOL. These crystals have an average width of 100-200 nm and their known crystal structure suggests that the size of the biradical precludes its penetration into the crystal lattice; therefore, intimate contact of the molecules in the nanocrystal core with the polarizing agent is unlikely. This is supported by the observed differences between the time dependent growth of the enhanced polarization in the solvent as opposed to the nanocrystals. Nevertheless, DNP enhanced MAS spectra recorded at 5 T and 90 K exhibit an average signal enhancement $\epsilon \sim 120$. This is slightly lower than the DNP enhancement of the solvent mixture surrounding the crystals ($\epsilon \sim 160$), and we show that it is consistent with spin diffusion across the solvent-matrix interface. In particular, we correlate the expected DNP enhancement to several properties of the sample, such as crystal size, the nuclear T_1 , and the average ^1H - ^1H spin diffusion constant. The enhanced ^1H polarization was subsequently transferred to ^{13}C and ^{15}N via cross-polarization, and allowed rapid acquisition of 2D ^{13}C - ^{13}C correlation data.

2.2. Introduction

In dynamic nuclear polarization (DNP) experiments, the large polarization of electron spins is transferred to the nuclear spins, enhancing the signal intensities by $\sim 10^2$ - 10^3 for subsequent nuclear magnetic resonance (NMR) spectroscopy¹⁻⁴, an approach that has been demonstrated in several solid state NMR applications⁵⁻¹³. More specifically, the recent development of high-field DNP spectrometers, equipped with gyrotron microwave sources^{14,15} and cryogenic magic angle spinning probes^{10,16}, have demonstrated promising results for studies of membrane proteins and other biological systems^{9,11,16}. In addition, development of biradical polarizing agents^{17,18} has significantly improved the enhancement factors of the nuclear polarization in DNP experiments and concurrently attenuated the residual paramagnetic broadening.

In several previous DNP experiments the nitroxide polarizing agent, 4-amino-TEMPO (4-amino-2,2,6,6-tetramethylpiperidine-1-oxyl) (4AT), was in intimate contact with the solute to be polarized. However, experiments on many macromolecular assemblies require that we consider the possibility that the paramagnet is excluded from close contact with the solute, and thus the question arises if DNP experiments will be applicable to this type of system. In particular, will bulky biradical polarizing agents such as TOTAPOL, consisting of two TEMPO moieties tethered by a three carbon chain (4-oxy-TEMPO-4-amino-TEMPO-2-propanol), be useful in polarizing for example virus particles, membrane proteins, amyloid fibrils, and peptide and protein nanocrystals? In these cases the sample domains are potentially macroscopically separated from solvent domains containing the polarizing agents. This question was initially addressed by Schaefer, et al. when they attempted to transfer enhanced nuclear polarization across a polymer interface^{7,19} with the result that they observed no significant enhancements correlated to internuclear spin diffusion. This may partly be ascribed to the fact that the DNP process was based on the solid effect polarizing mechanism using BDPA radicals, which is known to have an inherently low efficiency. In addition, the spin diffusion process was governed by the short nuclear T_1 of the polymer material observed at room temperature that may have limited the extent of the spin diffusion. Subsequently, Rosay, et. al.⁹ successfully demonstrated the homogeneous distribution of enhanced polarization in experiments that compared the size of the ³¹P and ¹⁵N signal enhancements from the DNA on the inside and the ¹⁵N-labeled coat protein on the outside of bacteriophage,

which is ~6.5 nm in diameter. In these experiments, which were performed at ~20 K and employed the more efficient cross effect DNP polarization mechanism, the ^{31}P and ^{15}N signal enhancements were identical, suggesting that spin diffusion distributed the polarization uniformly throughout the solute – the bacteriophage particle. However, the polarizing agent employed was 4AT and it could have diffused into the phage particles. Further, the phage particles are much smaller than most of the macromolecular assemblies mentioned above (6.5 nm diameter as opposed to >100 nm). We therefore decided to address this question again with studies of another system, nanocrystals of the amyloidogenic peptide GNNQQNY₇₋₁₃ and the improved, but bulky, biradical polarizing agent, TOTAPOL¹⁸.

GNNQQNY is an excellent system to use in the investigations presented here. The peptide corresponds to the residues 7-13 of the prion-forming protein Sup35p^{20,21} found in yeast and the protein is seen as a model system for an important class of amyloid related diseases characterized by a preponderance of Gln and Asn residues in the prion-forming protein domains. Specifically, the GNNQQNY₇₋₁₃ peptide resembles the short Gln- and Asn-rich repeats found throughout the Sup35p N-terminal domain and constitutes one of the shortest segments shown to form prion-like fibril aggregates²². Upon dissolution in water it also forms nanocrystals on a short timescale with a width varying from 20 nm to 1 μm ^{22,23}, and a structure of these species was recently determined with microcrystal X-ray diffraction²⁴. Once formed these crystals, like many amyloid fibrils, resist dissolution and it is therefore easy to disperse them in cryoprotectants and polarizing agents for DNP experiments. Thus, GNNQQNY₇₋₁₃ is an excellent system to test the applicability of the DNP technique to amyloid peptides, proteins and other macromolecular assemblies.

Figure 2-1 is an illustration of the crystal lattice²⁴ and shows the presence of (a) a water channel with a width of ~0.7 nm, together with (b) a space filling models of the lattice and a potential average conformation of TOTAPOL, which has limited flexibility in its short linker. An examination of this figure suggests that it is unlikely that the bulky biradical will diffuse into the channel and that the peptide molecules inside the crystallites are in intimate contact with the paramagnetic center. Nevertheless, we observe a substantial enhancement in the nuclear spin polarization ($\epsilon \sim 120$) as opposed to the full enhancement ($\epsilon \sim 160$) observed from the solvent (*vide infra*). This observation is explained quantitatively by considering the size of the crystals, the nuclear T_1 , the ^1H - ^1H spin diffusion constants, and the initial polarization

enhancement of the solvent. In addition, we demonstrate that the enhanced ^1H polarization can be readily transferred to ^{13}C and ^{15}N in the peptide and multidimensional spectra acquired with reduced acquisition periods. Thus, DNP experiments will likely evolve to an important spectroscopic ingredient in determining structures of amyloid peptides and proteins in the form of macroscopic nanocrystals and fibrils.

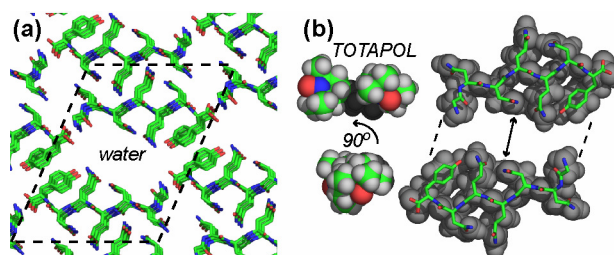


Figure 2-1 (a) Illustration of the crystal lattice of the GNNQQNY X-ray structure 24, where the dashed lines delineate two monomers surrounding the largest opening in the lattice, containing a network of hydrogen bonded water molecules. (b) Space filling models of the GNNQQNY monomers, the spacing between them (~ 0.7 nm maximum width), together with two views of an approximate space filling model of the TOTAPOL biradical showing its size relative to the water opening. The plane of the figure is perpendicular to the longest dimension of the crystallites.

2.3. Theory

We begin with a brief discussion of the processes involved in the application of DNP to insulating solids, involving bulk nuclei doped with dilute concentrations of paramagnets. The DNP process involves transfer of spin polarization from electrons to nuclei, which can occur through at least three different mechanisms, the solid effect (SE)⁴, the cross effect (CE)²⁵⁻³¹ and thermal mixing (TM)^{5,32}. The relative importance of these mechanisms is determined by the relationship between the homogeneous EPR linewidth (δ) and the nuclear Larmor frequency (ω_n). When the EPR linewidth is smaller than the nuclear Larmor frequency ($\delta < \omega_n$) only the SE is possible, while the CE and TM are operative when $\delta > \omega_n$. The spin dynamics associated with the SE, CE and TM involve single, pairwise and multiple electron spins, respectively. While an increase in the applied external magnetic field tends to reduce the

efficiency of the polarization, the extent of this reduction is dependent on the type of polarization mechanism involved. In the case of the CE and TM, the impact of higher magnetic fields on the polarization transfer efficiency can be compensated by optimizing the EPR spectral parameters, e.g. the electron-electron dipole interaction and the EPR frequency separation of the paramagnetic species¹⁷, for the desired field strength.

The resulting locally enhanced nuclear polarization is distributed to the bulk nuclei via ¹H nuclear spin diffusion. In a homogeneous sample, the efficiency of this process depends on the density and possibly orientations of nuclear spins. However, the presence of a diffusion barrier^{33,34}, for instance resulting from the proximity of a paramagnetic center or two domains characterized by large differences in nuclear spin characteristics, can reduce the efficiency of spin diffusion. The nuclear spin diffusion barrier near a paramagnetic species arises from a strong electron-nuclear dipolar field at the nucleus that isolates the surrounding nuclei in terms of resonance frequency. Similarly, a diffusion barrier can be caused by gaps in resonance frequency between two domains that have different magnetic susceptibilities in response to the external magnetic field.³⁵⁻³⁷ This might be a concern for dehydrated nanocrystals embedded in a frozen aqueous solvent matrix. Note that the latter boundary is less intrusive when the domain size is smaller (e.g., in nanometer range).

For simplicity of our discussion, we assume the bulk solvent nuclear spins surrounding the crystals are uniformly polarized with an enhancement factor ϵ_0 . The magnitude of this factor is characteristic of the bulk solvent/radical composition and the experimental and instrumental details^{17,18}. In our analysis we assume that penetration of enhanced nuclear polarization into a nanocrystal is dominated by uniform nuclear spin diffusion along the smallest dimension of the crystal. This pseudo-1D spin diffusion depends on the width of the smallest crystal dimension, the nuclear T_1 , and the nuclear spin diffusion constant, D , of the nanocrystal.

To illustrate our description of the polarization transfer into uniformly sized crystals, we show the model depicted in Figure 2-2a. A steady-state enhanced polarization of the glass matrix results from microwave irradiation and diffuses into the nanocrystals through the crystal surface. Within the crystal, the enhanced polarization, ϵ_0 , diffuses into the core, following a process that is assumed to be dominated by one-dimensional nuclear spin diffusion along crystal x -axis²⁴ and described by Fick's law^{19, 38}:

$$\frac{\partial P}{\partial t} = D \frac{\partial^2 P}{\partial x^2} - \frac{P}{T_{1n}}, \quad (1)$$

where $P(x,t)$ is the polarization, after subtraction of the Boltzmann polarization, at a time t and a distance x from the center of the crystal; D is the diffusion constant, and T_{1n} is nuclear spin-lattice relaxation time. In the steady-state $\partial P / \partial t = 0$, and we obtain

$$D \frac{\partial^2 P}{\partial x^2} = \frac{P}{T_{1n}}. \quad (2)$$

If we assume that the nuclei in the nanocrystal reach a steady-state and that their enhanced polarization is evenly-distributed, then we have the boundary condition for the surfaces of the crystals:

$$P\left(\frac{w}{2}\right) = P\left(-\frac{w}{2}\right) = \varepsilon_0 P_0, \quad (3)$$

where w is the crystal width along the x axis; ε_0 is the steady state enhancement factor for the solvent nuclear polarization and P_0 is the nuclear Boltzmann polarization at thermal equilibrium. As illustrated in Figure 2-2b, the solution to equation (2) in the region $-w/2 \leq x \leq w/2$ with the boundary condition in equation (3) is

$$P(x) = \varepsilon_0 P_0 \cosh^{-1}\left(\frac{w}{2\sqrt{DT_{1n}}}\right) \cosh\left(\frac{x}{\sqrt{DT_{1n}}}\right), \quad (4)$$

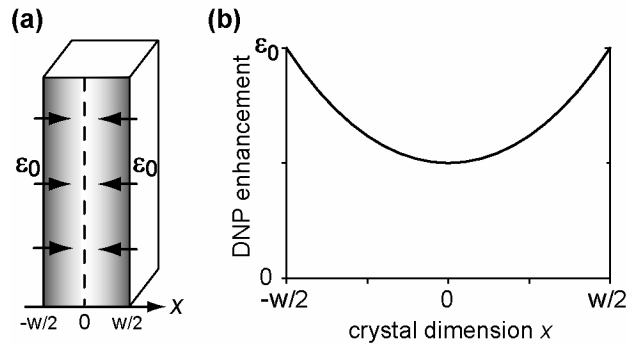


Figure 2-2 (a) Model for an individual peptide crystallite, showing polarization transfer into the core along the narrowest crystal dimension x . (b) Predicted enhanced polarization profile along the dimension x of the nanocrystal.

Experimentally one observes the average polarization across the whole crystal ($-w/2 \leq x \leq w/2$), as given by

$$\frac{1}{w} \int_{-w/2}^{w/2} P(x) dx = \frac{2\sqrt{DT_{1n}}}{w} \varepsilon_0 P_0 \tanh\left(\frac{w}{2\sqrt{DT_{1n}}}\right), \quad (5)$$

which dictates that the measured enhancement factor ε of the crystals is

$$\varepsilon = \varepsilon_0 \frac{2\sqrt{DT_{1n}}}{w} \tanh\left(\frac{w}{2\sqrt{DT_{1n}}}\right). \quad (6)$$

The spin diffusion constant D in a proton rich solid can be estimated as $D = \lambda^2 \pi B_L$, where B_L is the average dipolar interaction at a characteristic ^1H - ^1H distance λ . At room temperature, the average dipolar interaction depends on molecular dynamics affecting the proton coordinates¹⁹. These dynamics are mostly quenched at cryogenic temperatures, except for the threefold hopping of methyl groups. Nonetheless, the application of sample rotation in solid state MAS NMR to the frozen sample can significantly modulate the dipolar interaction. Once the ^1H - ^1H dipolar coupling constant ω_d is smaller than the spinning frequency ω_r , Average Hamiltonian Theory³⁹ suggests $B_L \propto (\omega_d)^2 / \omega_r$. Based on the published crystal structure²⁴ combined with computational modeling, the ^1H - ^1H distances along the two shortest crystal axes range from 2.0 to 3.2 Å for a continuous trajectory throughout the crystal, resulting in $\omega_d / 2\pi$ of 15 to 3.5 kHz. Notice that the magic angle spinning at $\omega_r / 2\pi \sim 5$ kHz has little effect for these magnitudes of the ^1H - ^1H dipolar interaction. In other words, the corresponding spin diffusion constant D should approximate 1×10^5 to 2×10^5 Å²/s. Typical experimental values that were previously obtained for a variety of organic polymers ranged from $2-8 \times 10^4$ Å²/s⁴⁰⁻⁴³, but these are likely to reflect the presence of more molecular dynamics than are present in our system, related to higher temperatures and more mobile moieties including methyl groups. Using the estimated diffusion coefficients D and measured T_{1n} (~ 17 s, *vide infra*) with equation (6), we can predict the theoretical enhancement factor of the ^1H polarization in GNNQQNY₇₋₁₃ as a function of

crystal size, as illustrated in Figure 2-3. These predicted DNP enhancements in nanocrystals will be compared to experimental results from DNP measurements and TEM observations.

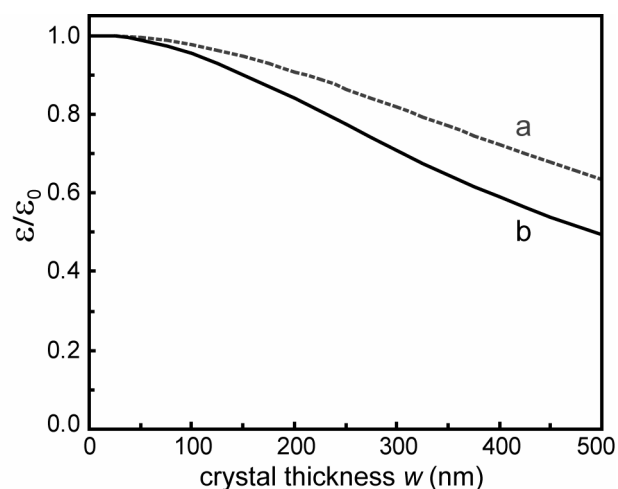


Figure 2-3 The theoretical enhancement ϵ , compared to the homogeneous enhancement ϵ_0 in the glassy matrix, of proton polarization in a nanocrystal of width w . The calculation uses a proton $T_{1n}=17$ s, and the calculated values of the diffusion constant (a) $D=2\times 10^5$ and (b) 1×10^5 $\text{\AA}^2/\text{s}$.

2.4. Experimental

2.4.1. Peptide nanocrystal samples

The peptide GNNQQNY was synthesized using solid phase synthesis methods in both a natural abundance form, and a segmentally, isotopically labeled form [$U\text{-}^{13}\text{C}, ^{15}\text{N}\text{-GNNQ}\text{]QNY}$ by CS Bio Co. (Menlo Park, CA). A mixture of 20% labeled and 80% unlabeled material was mixed and then crystallized as follows. A solution of 10 mg/ml in de-ionized water was filtered through a 0.2 μm filter to remove residual particles and then crystallized for at least 24 hours at 4°C. This protocol yields homogeneous monoclinic nanocrystals.

2.4.2. DNP experiments

The DNP samples were prepared by washing the fully crystallized sample several times with 80/20 $\text{D}_2\text{O}/\text{H}_2\text{O}$, then mixed with 60/30/10 glycerol- $\text{d}_8/\text{D}_2\text{O}/\text{H}_2\text{O}$, containing 10 mM of biradical polarizing agent. The extent of deuteration in the solvent system is optimized for

optimal channeling of the DNP proton-polarization to the sample material of interest, while maintaining the proton-proton spin diffusion necessary for distribution of the polarization throughout the sample. The deuterated solvents were obtained from Cambridge Isotope Laboratories (Andover, MA). The biradical TOTAPOL, composed of two TEMPO moieties tethered by a 5-atom linker, was synthesized as described elsewhere¹⁸. The resulting heterogeneous mixture, containing a total of ~20 mg peptide, was center-packed into a 4 mm sapphire MAS rotor. A similarly-prepared, undiluted sample consisting of 100% [U-¹³C, ¹⁵N-GNNQ]QNY crystals hydrated in de-ionized water was used as a reference sample.

All DNP enhanced CP-MAS experiments were performed in a 5 Tesla superconducting magnet (¹H frequency of 212 MHz) with a superconducting sweep coil capable of changing the magnetic field by ± 750 G. A custom-designed probe was used to perform triple resonance experiments -- two rf frequencies (¹H, ¹³C) and a waveguide provided for irradiation of the 4 mm sample with microwaves -- during MAS (~4-6 kHz) at ~90 K¹⁰. High-power, 139.66 GHz microwaves were obtained from a gyrotron (~10 W output power) delivering ~1.5 W to the sample. Since there is not a resonant microwave structure in the probe, the quality factor is low (Q ~1) for the microwave radiation. The Q of the RF circuit is not perturbed by the microwave waveguide. The pulse sequence¹⁷ begins with saturation of ¹H polarization by a series of 90° pulses and delays (10 ms) followed by a period of polarization recovery (1-75 s). Application of microwaves during the recovery period leads to a buildup of enhanced ¹H polarization that is subsequently transferred to the ¹³C or ¹⁵N spins through ramped cross-polarization (CP) (spin-lock for 1.2 ms with a constant 30 kHz ¹H field and a ramped 26-30 kHz ¹³C field). The resulting ¹³C and ¹⁵N CP-signals were detected using ~70 kHz TPPM ¹H decoupling⁴⁴. The two-dimensional ¹³C-¹³C correlation experiment was performed using DNP enhancement after 5 s microwave irradiation and involved ¹³C-¹³C mixing with 6 ms of ¹H-driven spin diffusion (PDSD) with R³ ¹H irradiation⁴⁵. It was executed in the absence of the saturating proton pulses with the following experimental details: 5 s recycle delay, 56 t₁ points of four scans each, resulting approximately 20 minutes of acquisition time. The data were processed using NMRPipe⁴⁶.

2.4.3. Transmission Electron Microscopy

A Philips EM410 electron microscope was used to examine the peptide crystals by transmission electron microscopy (TEM) before and after the DNP measurements. TEM micrographs were obtained after negative staining with aqueous uranyl acetate. The dimensions of numerous peptide nanocrystals were measured by comparison to calibration micrographs of reference grid samples (Electron Microscope Sciences, Hatfield PA).

2.5. Results and Discussion

2.5.1. Enhanced NMR signal intensities of peptide nanocrystals

One-dimensional CP/MAS NMR data recorded for the 20% labeled peptide nanocrystal sample in the absence of DNP yielded relatively poor signal-to-noise spectra. The measurements were repeated in the presence of microwave irradiation, which resulted in a dramatic increase in the signal intensity, as illustrated in Figure 2-4. The signal-to-noise without microwave irradiation was insufficient to observe well resolved spectral lines for the (20%) isotopically labeled ^{13}C . However, in the presence of microwaves even the natural abundance ^{13}C signals could be seen (from the unlabeled residues in the segmentally labeled peptide and the glycerol in the frozen solvent matrix). The same enhancement effect is observed for the ^{15}N spectrum, where the signals were undetectable in the absence of DNP, but are rather intense with DNP enhancement. The maximum observed enhancement was quantified to be $\epsilon \sim 120 \pm 10$ after 75 s of microwave irradiation, relative to the ^{13}C spectrum without DNP. Note that the NMR signals of the solute (e.g. the glycerol carbons) in the glass matrix are also strongly enhanced, with an estimated enhancement $\epsilon_0 \sim 160$, based on previous measurements. The intensity of the ^{15}N signals without microwave irradiation was too weak to allow an accurate measurement of the enhancement, but its enhancement should be similar to that measured for the peptide ^{13}C 's since both are determined by the polarization enhancement of the ^1H spins.

While the signal intensity in the absence of DNP was too low for a two dimensional NMR experiment to be practical, the observed DNP enhancement stimulated us to perform a 2D experiment to evaluate the applicability of DNP to this and other amyloid samples. This

involves a two-dimensional ^{13}C - ^{13}C homonuclear correlation experiment with 6 ms spin diffusion mixing. The results are shown in Figure 2-5 and the combined acquisition time of the entire experiment required approximately 20 minutes. This of course compares extremely favorably with the anticipated acquisition time in the absence of DNP. Note that one can discern several signals from the natural abundance Tyr side chain further highlighting the high enhancement factor resulting from the microwave irradiation.

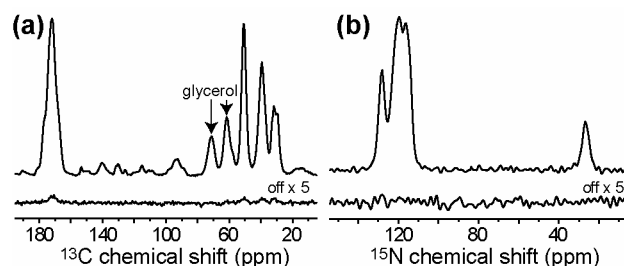


Figure 2-4 DNP enhanced ^{13}C (a) and ^{15}N (b) CP-MAS spectra of [20% U- ^{13}C , ^{15}N -GNNQ]QNY in d_8 -glycerol/ D_2O / H_2O (60/30/10) with 10 mM TOTAPOL biradical at 90 K and 5 T, with (top trace) and without (bottom trace) DNP. The microwave power was 1.5 W and irradiation time was 75 s for both spectra.

The assignments of the cross peaks in the spectrum are indicated in the figure, and were based on experiments performed at higher fields to be described in a separate publication. As mentioned we observe the natural abundance glycerol peaks on the diagonal, which are broadened because of the amorphous nature of the frozen glass matrix and the proximity of the biradical species. The presence of a substantial radical concentration in a solution is known to cause significant broadening in any co-dissolved solute. Especially when using high concentrations of less efficient polarizing agents, this is also seen in DNP experiments on frozen solutions. In contrast, the crystalline nature of the sample shields the molecules on the interior of the crystals from both the glassy solvent and the direct interaction with the radicals (except for narrow regions near the crystal surface), resulting in peptide peaks that are narrower than the glycerol signals. However, the peptide signals are significantly broader than observed in our assignment experiments mentioned above, where the spectra were recorded on a 500 MHz instrument. To evaluate whether any broadening is due to the experimental DNP conditions and examine whether it could be indicative of the radical having direct access to a

significant portion of the peptide, we performed a number of tests. In room temperature spectra comparing the glycerol and TOTAPOL-containing DNP sample to a non-DNP reference sample (lacking glycerol and radicals) we observe the same line width for both samples, which also matches the line widths at low temperature. This fact, plus the observation that the spectra of the reference sample are narrow at high fields, suggest that the additional linewidth is not due to the glass formation or interaction with the radicals, but rather arises from $n = 0$ rotational resonance effects^{39,47}. These effects are important when the shift separation is comparable to the dipolar coupling and the spinning frequency is low as was the case in these experiments. As a more sensitive test for the penetration of TOTAPOL biradicals into the crystals, we performed room temperature measurements at higher field (700 MHz ^1H frequency) and faster spinning (15 kHz MAS) comparing GNNQQNY nanocrystals before and after the addition of biradical (see Fig. 2-6). The line widths in these data are significantly smaller (approximately 100 ± 2 Hz for the various labeled ^{13}C carbons and as low as 35 ± 2 Hz for the N-terminal glycine- ^{15}N) and should be sensitive to broadening by nearby radicals. Even at a concentration of 50 mM TOTAPOL, five times the amount used in the DNP experiments, no broadening of the above carbon and nitrogen line widths was observed, confirming the absence of radicals from the inside of the crystals.

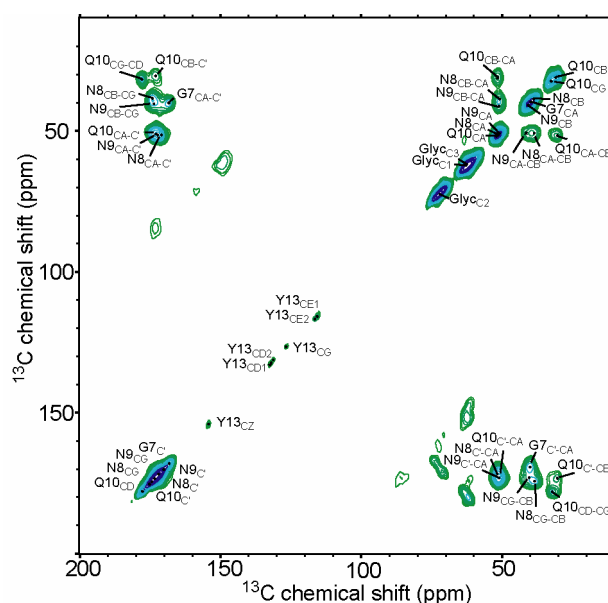


Figure 2-5 DNP-enhanced ^{13}C - ^{13}C R^3 PDS correlation spectrum of [20% U - ^{13}C , ^{15}N -GNNQ]JQNY nanocrystals. Indicated assignments are based on previous assignment data, and unmarked cross peaks represent spinning sidebands and experimental artifacts.

The recycle delay for the acquisition of the 2D spectrum was significantly shorter than required for the development of the full DNP enhanced polarization of the ^1H 's in the crystals, and reflects a compromise between a large signal enhancement and the phase cycling requirements of the experiment. The result of this choice of recycle delay is that the relative intensities of the glass-embedded glycerol solvent relative to the peptide signals are shifted in favor of the solvent signals, reflecting a difference in the polarization rate between the crystals and the solvent molecules. This difference is further illustrated in a series of one-dimensional experiments, examining the buildup of magnetization as a function of the microwave irradiation time. These experiments were performed according to the procedure described previously¹⁷ and the resulting ^{13}C spectra confirm that the polarization buildup for the glycerol is substantially faster than for the peptide crystal signals Fig. 2-7. The time constants for the glycerol signals range from 7 to 8 s, which is shorter than those of the nanocrystal signals which range from 15.5 to 17 s. The presence of the biradicals at 10 mM reduces the ^1H T_{1n} in the glassy solvent, giving a rapid polarization transfer and shorter time constants for polarization. Since the peptide crystals exclude the TOTAPOL, polarization time constants in the crystals reflect the intrinsic ^1H T_{1n} , which is relatively long due to the low temperatures and determines the internuclear spin diffusion within the crystals. Note that, in general, relatively long spin lattice relaxation times are necessary for optimal DNP enhancement. We will now correlate the diffusion constant, T_{1n} and size of nanocrystal with the observed enhancement using the Fick's law treatment discussed above.

2.5.2. Polarized portions of fibril crystals

Based on the TEM micrographs illustrated in Fig. 2-8, we were able to measure the dimensions of the nanocrystals in the samples used to record the DNP enhanced spectra shown in Figures 2-4, 2-5 and 2-6. The average width of the crystals approximates 150 nm, with a typical range between 100 and 200 nm. The distribution of crystal sizes in these samples is not entirely uniform, with a few exceptions of significantly thicker or thinner (down to ~50 nm) width. Narrowing of the crystals tends to occur at their ends. These observations correspond well to previously published TEM data and dimensions of GNNQQNY nanocrystals²³.

We will now compare these experimental observations to the predicted relative enhancements in Figure 2-3, obtained using the Fick's law formula in Eq. (6) together with the

estimates of the D and measured values of T_{1n} . The central assumption in that calculation that the biradical TOTAPOL does not penetrate the crystals, was originally based on the realization that the size of TOTAPOL exceeds the width of the water channel in these crystals (see Figure 2-1) and reinforced by the observed reduction of the enhancement inside the crystals. Further experimental data, including the longer peptide T_{1n} compared to the solvent and the insensitivity of peptide crystal line widths to the presence or absence of TOTAPOL radicals indeed show that there is no significant direct interaction between the radical and the bulk of the peptide nanocrystals.

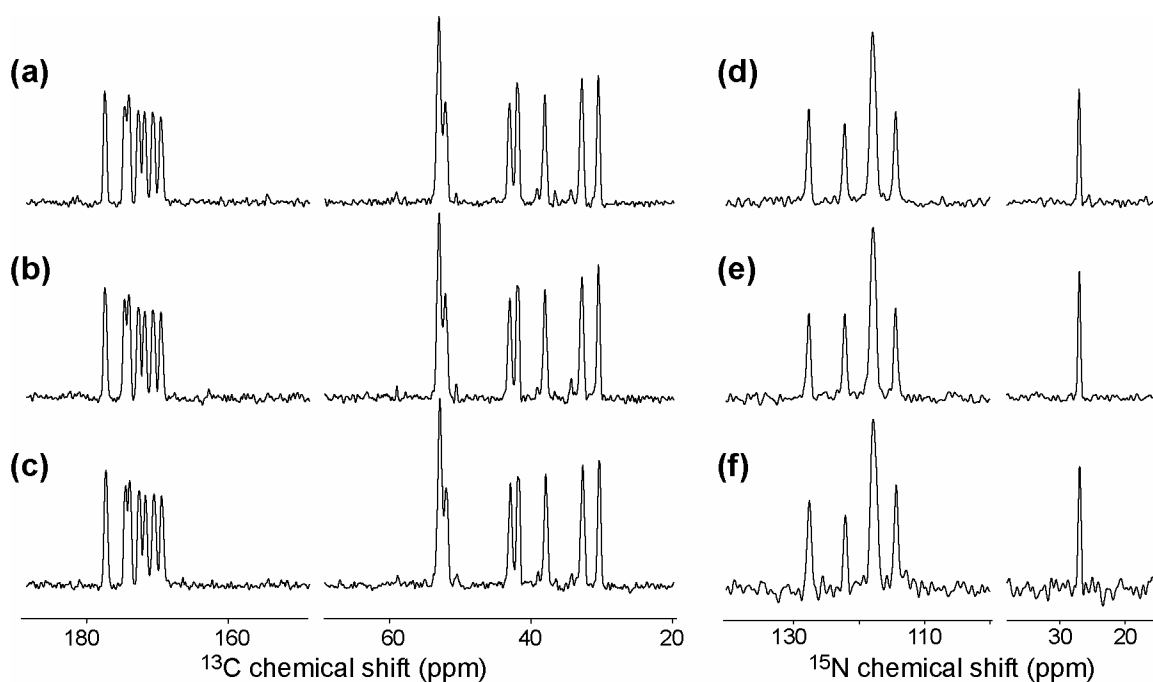


Figure 2-6 ^{13}C and ^{15}N cross-polarization spectra of 30% labeled $[\text{U-}^{13}\text{C},^{15}\text{N-GNNQ}]\text{QNY}$ nanocrystals without TOTAPOL (a,d) and with 10 mM (b,e) or 50 mM (c,f) TOTAPOL. Data were acquired at 15 kHz MAS and 700 MHz ^1H frequency, using the same sample material. Measured line widths are insensitive to biradical concentration (within their error margins of $\sim 1\text{-}3$ Hz), showing that the radical is not in close proximity to the bulk of the peptide crystals.

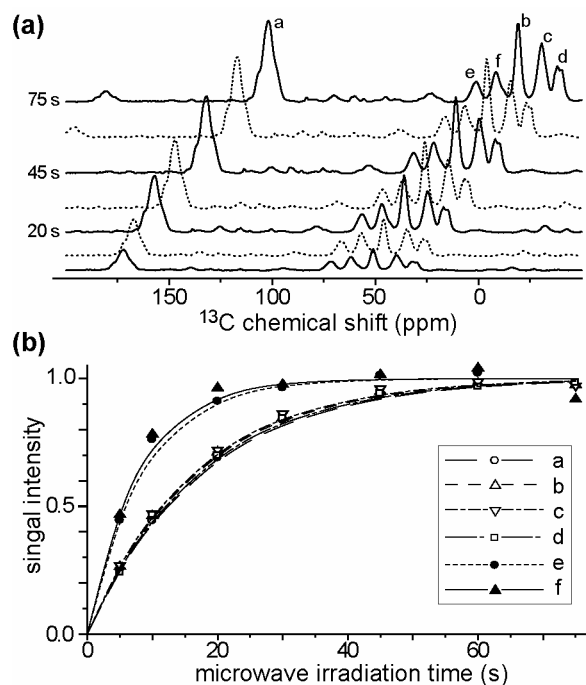


Figure 2-7 Time-dependent growth of the enhancement polarization. (a) Illustration of the 1D ^{13}C spectra as a function of microwave irradiation time, after 5, 10, 20, 30, 45, 60 and 75 s of microwave irradiation. The chemical shift axes are offset for visual clarity. (b) The intensity of the spectral lines normalized to maximum intensity of each signal. Lines indicate calculated fits using growth time constants of 16-17 s for crystal signals (a-d), and 7-8 s for glycerol peaks e and f.

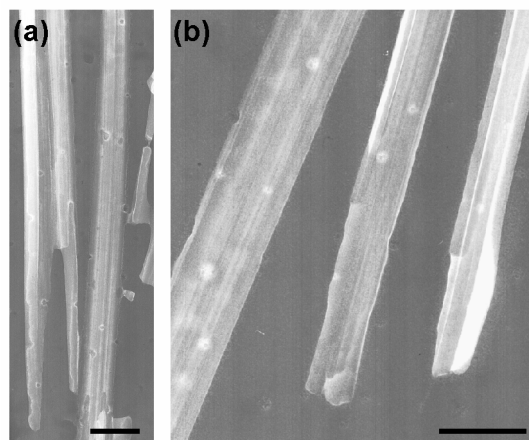


Figure 2-8 Transmission electron micrographs of GNNQQNY nanocrystallites at an approximate magnification of (a) 55,000 and (b) 110,000. The black bars indicate 200 nm.

Considering that the polarizing agent is absent from the crystal core, direct polarization of the crystal surface layer alone is unable to explain the observed large crystal signal enhancement. Rather it is due to diffusion into the crystals of the enhanced nuclear polarization $\epsilon_0 P_0$ uniformly present throughout the solvent matrix, and at the surface of the crystals, as described in Section 2. There, we estimated the ^1H spin diffusion constants as lying in the range 1×10^5 - $2 \times 10^5 \text{ \AA}^2/\text{s}$. On the basis of these assumptions and the measured $T_{1n} \sim 17 \text{ s}$ we predicted the enhancements to be observed in crystals with a various characteristic widths (Figure 2-3). In our case we observed an average crystal enhancement ϵ that is ~ 0.75 ($120/160$) of the enhancement ϵ_0 in the bulk solvent matrix. Combined with the crystal dimensions that were observed in our TEM experiments (100 - 200 nm), this result falls slightly under the curve shown for the lower diffusion constant. Considering the relatively simple nature of the applied model, it is unclear whether very detailed conclusions concerning the exact value of the spin diffusion rate can be drawn on the basis of these results. The lower rate could indicate that the effective diffusion rate is limited by a ‘bottleneck’ across the direction of transfer that is not apparent in the crystal structure, possibly near the crystal-solvent interface. Inhomogeneity and anisotropy in the crystal packing could affect the effective spin diffusion constant. Furthermore, one could also consider other experimental features such as the distribution of crystal sizes and possible factors affecting the uniformity of the surface polarization and the diffusion pattern.

2.6. Conclusions

We have shown that DNP experiments are applicable to enhancing the ^1H polarization of peptide nanocrystals of ~ 100 - 200 nm width, yielding intense NMR signals and significant reductions in acquisition times. The increased signal intensity opens new possibilities for significantly more complex and informative pulse experiments to be performed on relatively dilute samples. Dilution of the isotopically labeled sample is often essential when intermolecular interactions have to be suppressed, as is the case for small molecules like the peptides studied here. DNP enhancement would allow a high level of dilution while maintaining sufficient signal intensity for accurate and sensitive NMR measurements.

One of the limiting aspects of the data shown here is the limited resolution that can be achieved on this relatively low-field prototype equipment. Ongoing experiments on different instrumentation^{14,16} in our group have demonstrated the acquisition of higher resolution DNP spectra^{12,13}. We note that the experiments discussed here show little or no sign of additional broadening due to the cooling to 90 K, or the presence of the radicals (even at five times increased concentration in the high field, high spinning reference experiments). These observations can be attributed to the nature of these crystals, which are very tightly packed and exclude both the TOTAPOL radicals and the amorphously freezing solvent system.

The exclusion of the bulky biradical polarizing agent from the crystal lattice highlights the importance of ^1H - ^1H spin diffusion in DNP experiments on heterogeneous samples. We presented a simple calculation based on 1D spin diffusion that explains the observed extent of polarization and correlates it to the observed crystal size. A more detailed evaluation of the exact role of spin diffusion in these experiments, and further quantification, would benefit from further experiments with particles (or crystals) of a carefully controlled size. The theory discussed here (supported by our data) would suggest that nanocrystals with a size up to 1 μm can be efficiently polarized, opening avenues for further applications of DNP to studies of protein microcrystals. Further experiments with a wider variety of crystalline and fibril compounds should provide further insights into the importance of sample features such as the presence of methyl groups, molecular motion and crystal packing for spectral features such as low-temperature resolution, nuclear spin diffusion, and the achievable DNP enhancement.

2.7. Acknowledgements

This research was supported by the National Institutes of Health through grants EB-002804, EB003151 and EB-002026. Thanks are accorded to Dr. Chan-Gyu Joo for helpful conversations during the course of these experiments.

2.8. References

- (1) Overhauser, A. W. *Phys. Rev.* 1953, 92, 411-415.
- (2) Carver, T. R.; Slichter, C. P. *Phys. Rev.* 1953, 92, 212-213.

- (3) Carver, T. R.; Slichter, C. P. *Phys. Rev.* 1956, 102, 975-980.
- (4) Abragam, A.; Goldman, M. *Nuclear magnetism: order and disorder*; Clarendon Press: Oxford, 1982.
- (5) Wind, R. A.; Duijvestijn, M. J.; Vanderlugt, C.; Manenschijn, A.; Vriend, J. *Prog. Nucl. Mag. Reson. Spectrosc.* 1985, 17, 33-67.
- (6) Singel, D. J.; Seidel, H.; Kendrick, R. D.; Yannoni, C. S. *J. Mag. Res.* 1989, 81, 145-161.
- (7) Afeworki, M.; McKay, R. A.; Schaefer, J. *Macromolecules* 1992, 25, 4084-4091.
- (8) Afeworki, M.; Vega, S.; Schaefer, J. *Macromolecules* 1992, 25, 4100-4105.
- (9) Rosay, M.; Zeri, A.-C.; Astrof, N. S.; Opella, S. J.; Herzfeld, J.; Griffin, R. G. *J. Am. Chem. Soc.* 2001, 123, 1010-1011.
- (10) Rosay, M.; Weiss, V.; Kreisler, K. E.; Temkin, R. J.; Griffin, R. G. *J. Am. Chem. Soc.* 2002, 124, 3214-3215.
- (11) Rosay, M.; Lansing, J. C.; Haddad, K. C.; Bachovchin, W. W.; Herzfeld, J.; Temkin, R. J.; Griffin, R. G. *J. Am. Chem. Soc.* 2003, 125, 13626-13627.
- (12) Bajaj, V. S.; Mak, M.; Hornstein, M. K.; Belenky, M.; Herzfeld, J.; Temkin, R. J.; Griffin, R. G. *Biophys. J.* 2005, 88, 203A-203A.
- (13) Mak, M. L.; Bajaj, V. S.; Hornstein, M. K.; Belenky, M.; Temkin, R. J.; Griffin, R. G.; Herzfeld, J. *Biophys. J.* 2005, 88, 506A-506A.
- (14) Hornstein, M. K.; Bajaj, V. S.; Griffin, R. G.; Kreisler, K. E.; Mastovsky, I.; Shapiro, M. A.; Sirigiri, J. R.; Temkin, R. J. *IEEE Trans. Electron Devices* 2005, 52, 798-807.
- (15) Joye, C. D.; Griffin, R. G.; Hornstein, M. K.; Hu, K.-N.; Kreisler, K. E.; Rosay, M.; Shapiro, M. A.; Sirigiri, J. R.; Temkin, R. J.; Woskov, P. P. *IEEE Trans. Plasma Sci.* 2006, in press.
- (16) Bajaj, V. S.; Farrar, C. T.; Hornstein, M. K.; Mastovsky, I.; Viereg, J.; Bryant, J.; Elena, B.; Kreisler, K. E.; Temkin, R. J.; Griffin, R. G. *J. Mag. Res.* 2003, 160, 85-90.
- (17) Hu, K.-N.; Yu, H.-H.; Swager, T. M.; Griffin, R. G. *J. Am. Chem. Soc.* 2004, 126, 10844-10845.
- (18) Song, C.; Hu, K.-N.; Joo, C.-G.; Swager, T. M.; Griffin, R. G. *J. Am. Chem. Soc.* 2006, in press.
- (19) Afeworki, M.; Schaefer, J. *Macromolecules* 1992, 25, 4092-4096.

- (20) Liebman, S. W.; Derkatch, I. L. *J. Biol. Chem.* 1999, 274, 1181-4.
- (21) Krishnan, R.; Lindquist, S. L. *Nature* 2005, 435, 765-72.
- (22) Balbirnie, M.; Grothe, R.; Eisenberg, D. S. *Proc. Natl. Acad. Sci. USA* 2001, 98, 2375-80.
- (23) Diaz-Avalos, R.; Long, C.; Fontano, E.; Balbirnie, M.; Grothe, R.; Eisenberg, D.; Caspar, D. L.; Eisenberg, D. S. *J Mol Biol.* 2003, 330, 1165-75.
- (24) Nelson, R.; Sawaya, M. R.; Balbirnie, M.; Madsen, A. O.; Riek, C.; Grothe, R.; Eisenberg, D. *Nature.* 2005, 435, 773-8.
- (25) Kessenikh, A. V.; Lushchikov, V. I.; Manenkov, A. A.; Taran, Y. V. *Soviet Physics-Solid State* 1963, 5, 321-329.
- (26) Kessenikh, A. V.; Manenkov, A. A.; Pyatnitskii, G. I. *Soviet Physics-Solid State* 1964, 6, 641-643.
- (27) Hwang, C. F.; Hill, D. A. *Phys. Rev. Lett.* 1967, 18, 110-112.
- (28) Hwang, C. F.; Hill, D. A. *Physical Review Letters* 1967, 19, 1011-1014.
- (29) Wollan, D. S. *Physical Review B* 1976, 13, 3671-3685.
- (30) Wollan, D. S. *Physical Review B* 1976, 13, 3686-3696.
- (31) Atsarkin, V. A. *Sov. Phys. Usp.* 1978, 21, 725-744.
- (32) Goldman, M. *Spin temperature and nuclear magnetic resonance in solids*; Clarendon press: Oxford, 1970.
- (33) Blumberg, W. E. *Physical Review* 1960, 119, 79-84.
- (34) Furman, G. B.; Goren, S. D. *J. Phys.: Cond. Matter* 2002, 14, 873-881.
- (35) Hurlimann, M. D. *J. Mag. Res.* 1998, 131, 232-240.
- (36) Sen, P. N.; Axelrod, S. J. *Appl. Phys.* 1999, 86, 4548-4554.
- (37) Vasenkov, S.; Galvosas, P.; Geier, O.; Nestle, N.; Stallmach, F.; Karger, J. J. *Mag. Res.* 2001, 149, 228-233.
- (38) Lowe, I. J.; Tse, D. *Phys. Rev.* 1968, 166, 279-291.
- (39) Maricq, M. M.; Waugh, J. S. *J. Chem. Phys.* 1979, 70, 3300-3316.
- (40) Chen, Q.; Schmidt-Rohr, K. *Solid State Nucl. Magn. Res.* 2006, 29, 142-152.
- (41) Cheung, T.; Gerstein, B. J. *Appl. Phys.* 1981, 52, 5517.
- (42) Clauss, J.; Schmidt-Rohr, K.; Spiess, H. W. *Acta Polymer.* 1993, 44, 1-17.
- (43) Jia, X.; Wolak, J.; Wang, X.; White, J. L. *Macromolecules* 2003, 36, 712-718.

- (44) Bennett, A. E.; Rienstra, C. M.; Auger, M.; Lakshmi, K. V.; Griffin, R. G. J. *Chem. Phys.* 1995, 103, 6951-6958.
- (45) Takegoshi, K.; Nakamura, S.; Terao, T. *Chem. Phys. Lett.* 2001, 344, 631-637.
- (46) Delaglio, F.; Grzesiek, S.; Vuister, G. W.; Pfeifer, J.; Bax, A. J. *Biomol. NMR* 1995, 6, 277-293.
- (47) Levitt, M. H.; Raleigh, D. P.; Cruzet, F.; Griffin, R. G. J. *Chem. Phys.* 1990, 92, 6347-6364.

3. Accuracy of ^{13}C - ^{13}C distance measurements in uniformly labeled solids using rotational resonance width (R^2W) experiments

Reproduced with permission from Ramachandran R., Lewandowski J.R., van der Wel P.C.A., Griffin R.G. "Multipole-multimode Floquet theory of rotational resonance width experiments: ^{13}C - ^{13}C distance measurements in uniformly labeled solids." J. Chem. Phys. (2006) **124**(21):214107. Copyright © 2006 American Institute of Physics.

3.1. Abstract

A formal description of zero-quantum (ZQ) NMR processes using multipole-multimode Floquet theory (MMFT) is proposed for studying polarization transfer in magic angle spinning (MAS) experiments. Specifically, we investigate the factors affecting the accuracy and precision of ^{13}C - ^{13}C distance measurements that are based on ZQ-magnetization exchange processes in rotational resonance width (R^2W) experiments. With suitable examples drawn from measurements in N-acetyl-[U- ^{13}C , ^{15}N]-L-valine-L-leucine (N-Ac-VL), we substantiate our approach and propose methods for improving the accuracy and reliability of such ^{13}C - ^{13}C distance measurements in uniformly ^{13}C , ^{15}N -labeled solids. In addition, the theoretical model presented in this article provides a more general framework for describing relaxation phenomena involving multiple decay rate constants in zero-quantum processes.

3.2. Introduction

Nuclear magnetic resonance (NMR) is one of the most prominent spectroscopic techniques for probing interactions at the molecular level. In particular, it offers great control and flexibility in the design of experiments since it is possible to individually manipulate spin interactions at the atomic level. With recent advances in the methodology for measuring distances and torsion angles, NMR spectroscopy has become an important tool in the arsenal of techniques for structural characterization of biological as well as a wide variety of other systems. Presently, the majority of structural data that exists in the literature is based on x-ray crystallography and solution-state NMR spectroscopy, but in the recent past solid-state NMR (SSNMR) has emerged as a viable alternative for structural studies of both crystalline and amorphous solids of chemical and biological relevance. Specifically, by combining magic angle spinning (MAS),^{1,2} cross-polarization^{3,4} and multiple pulse experiments⁵ in the form of dipolar recoupling techniques⁶⁻⁸ one of which is discussed herein, it is possible to perform structural studies with low- γ or less abundant nuclei, such as ^{13}C , ^{15}N , even on systems with macroscopic disorder. The purpose of this paper is to provide an analysis of experiments to measure ^{13}C - ^{13}C distances in rotational resonance width (R^2W) experiments based on multipole-multimode Floquet theory (MMFT). The approach provides a considerable improvement in the accuracy and precision compared to previous treatments of R^2W experiments and should be applicable to other experiments involving multiple spin systems and relaxation times.

Among the internal spin interactions present in coupled spin systems, the dipole-dipole couplings have special structural significance owing to their rigorous dependence on internuclear distances and distance geometries. In analogy with scalar (or J) couplings in solution NMR spectra, the dipolar interactions are used to establish spatial proximity and connectivity in the solid state. However, because the dipole coupling and the chemical shift anisotropy are second rank interactions, they are both attenuated by MAS. Thus, while MAS increases the spectral resolution by removing the chemical shift anisotropy, it concurrently attenuates the dipolar couplings, removing the source of the structural data. A special class of experiments⁶⁻⁸ known as dipolar recoupling techniques is required to reintroduce these essential interactions into multi-dimensional MAS spectra in a manner consistent with the goal

of high resolution. In addition to their role in spectral assignments, the dipolar interactions provide local structural information via internuclear distances and molecular torsion angles. In particular, intramolecular ^{13}C - ^{13}C and ^{13}C - ^{15}N distances have been used to constrain polypeptide backbone and side chain conformations and are essential for the overall refinement of the three-dimensional molecular structure.⁹ As a consequence, optimization of the accuracy and precision of distance constraints obtained from such experiments is crucial towards obtaining high quality structures. In this article we examine the factors affecting the accuracy of ^{13}C - ^{13}C distance measurements using rotational resonance (R^2) experiments^{10,11} and methods derived from this approach.¹²⁻¹⁴

In the original version of the R^2 experiments,¹¹ the dipolar interaction between a particular spin pair is selectively reintroduced by matching the isotropic chemical shift difference to an integer multiple of the sample spinning frequency, $\omega_r/2\pi$. The distance information is extracted by monitoring the magnetization exchange as a function of the mixing time and simulating the resulting exchange trajectories to a particular dipolar coupling constant, a phenomenological damping rate constant T_{ZQ}^{-1} , and in some cases, the chemical shift tensors of the individual spins.¹² Using such an approach, internuclear distances were determined in several cases using selectively labeled compounds ranging from simple amino acids to membrane proteins.¹⁵⁻¹⁹ However, in uniformly labeled samples the application of the R^2 method is less straightforward, primarily due to the uncertainties associated with the estimation of the zero-quantum (ZQ) relaxation rate, especially for relatively weak couplings. Since interesting distance constraints of biological relevance are often obtained in the weak-coupling limit, it is of considerable importance to gain insight into the exchange dynamics in the presence of such dissipative processes. To this end constant time experiments in the form of R^2W (Reference 13) were proposed as an alternative to the conventional R^2 approach. In the R^2W approach the magnetization exchange profile is obtained by monitoring the exchange dynamics in a series of experiments with varying sample spinning frequencies ($\omega_r/2\pi$) using a fixed mixing time, τ_m . In combination with multi-dimensional spectroscopy, the R^2W approach (3D- R^2W) was demonstrated to permit measurements of intramolecular ^{13}C - ^{13}C distances in uniformly labeled samples.¹⁴ However, while the constant time approach minimizes the sensitivity of the experiments to relaxation, and reduces the errors in the measured distances, there remain inaccuracies in the data. For example, several of the measured distances were ~ 0.5 Å longer

than the diffraction distances suggesting that the theory for describing the experiments is inadequate. These discrepancies could be attributed either to an inadequate description of the exchange dynamics (usually resulting from the residual ^{13}C - ^{13}C and ^{13}C - ^1H interactions)^{20,21} or inaccuracy in the estimation of the relaxation parameters.

The observed decay of the coherences in recoupling experiments is often attributed to the residual heteronuclear ^{13}C - ^1H dipolar interactions during the recoupling period. Although the application of strong decoupling fields on the proton spins minimizes the residual heteronuclear ^{13}C - ^1H dipolar interactions, the combined effects of sample spinning, decoupling fields and chemical shift dispersion (CSD) conspire to complicate the characterization of the zero quantum relaxation rate. Consequently, a simple exponential model incorporating a phenomenological damping rate constant T_{ZQ}^{-1} has been used to model the dissipation (or relaxation) during the recoupling period.¹²

Recently Levitt and co-workers examined the validity of such an approach in detail under several experimental conditions.²² Under strong ^1H decoupling or no decoupling fields, their simulation results based on a simple relaxation model (involving an orientation independent decay rate constant) are in good agreement with the experiments. However, in the intermediate decoupling regime the authors simulate their experimental data using a set of simulations involving different decay rate constants [also referred to as multiple differential transverse relaxation (MDTR) model].²³ Although this study highlights an interesting feature of the R^2 exchange dynamics, their description, based on a vector model (i.e., the spin Hamiltonian and the density operator are approximated by vector quantities), does not describe higher order effects and zero-quantum processes involving multiple relaxation rates.

In this paper we improve the description of the exchange dynamics, and concurrently address the issue of the accurate estimation of the relaxation rates, and advance the quality of the distance measurements. In particular, by using multipole-multimode Floquet theory²⁴ (MMFT)²⁵ we develop an analytical model for describing zero-quantum recoupling sequences in MAS NMR experiments. In the MMFT approach the spin Hamiltonian and the density operator are expressed in terms of irreducible tensor operators dressed with Fourier labels. By means of the effective Hamiltonians, derived from the contact transformation²⁶ procedure, the spin dynamics in the Floquet-Liouville space are constrained to a reduced subspace of finite dimension corresponding to the ZQ subspace (5x5) in the standard operator space. Compared

to existing theoretical models,^{13,14} the spin dynamics predicted by the MMFT approach accounts explicitly for a large part of the damping of the ZQ coherence, which was previously modeled as a free-fit parameter. Besides highlighting the role of ZQ damping parameters in the exchange dynamics, the model provides a framework for describing relaxation phenomena involving multiple decay rate constants. To experimentally test the validity of the approach, we employed 3D-R²W experiments for measuring multiple distances in the dipeptide N-acetyl-[U-¹³C, ¹⁵N]-L-Val-L-Leu (N-Ac-VL). Relative to previous theoretical descriptions,¹⁴ the MMFT approach improves the accuracy of these ¹³C-¹³C distance measurements and allows a systematic evaluation of the ZQ relaxation parameters employed in the fitting of our experimental data.

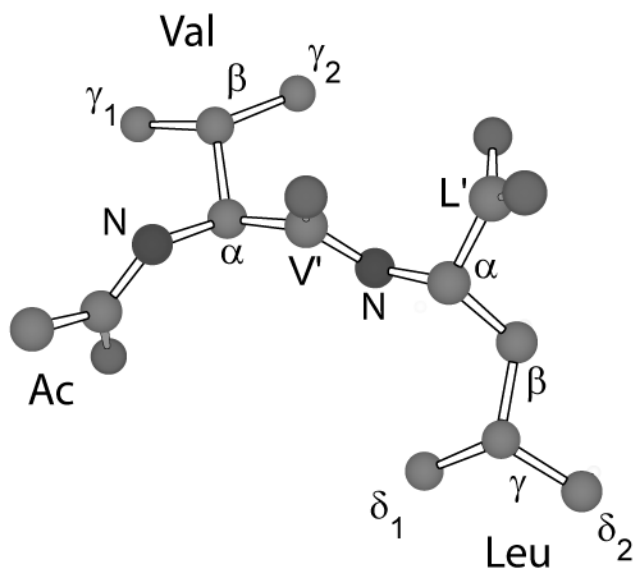


Figure 3-1 Diagram of the di-peptide N-Ac-VL derived from the crystal structure³³.

An outline of the paper is as follows. In Sec. 3.3, we briefly present the basic theory for describing R² experiments followed by a detailed description of the spin dynamics using the MMFT approach. In Sec. 3.4 we describe our results obtained using this approach followed by a brief summary.

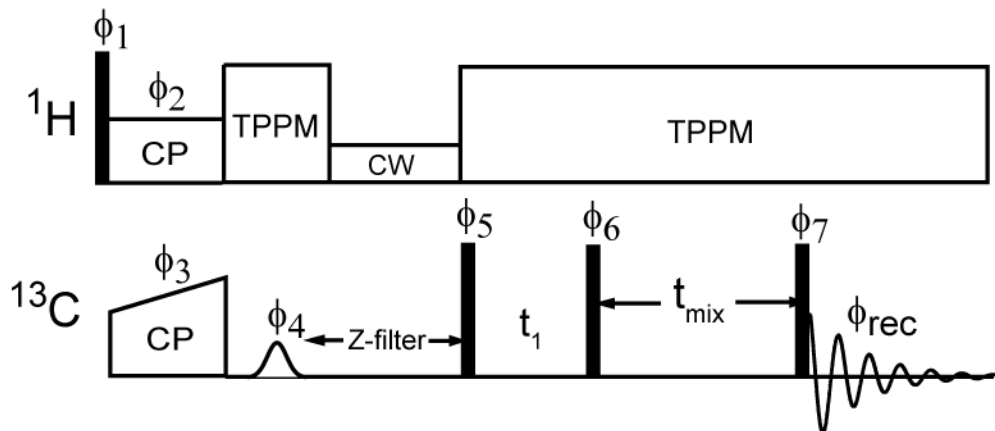


Figure 3-2 Pulse sequence for 3D-R²W experiment. The following phase cycling scheme was employed: $\phi_1=(16\times 1,16\times 3)$; $\phi_2=2$; $\phi_3=1$; $\phi_4=(8\times 2,8\times 4)$; $\phi_5=1$; $\phi_6=(4\times 3,4\times 1)$; $\phi_7=1234$; $\phi_{\text{rec}}=(1234,3412,3412,1234,3412,1234,1234,3412)$. The labels 1,2,3,4 correspond to the phases x,y,-x,-y, respectively. The dipolar mixing time (t_{mix}) was fixed at 30 ms.

3.3. Theory

3.3.1. Basic theory

The Hamiltonian of an isolated two-spin system during MAS is represented by

$$H(t) = (\omega_1(t) + \omega_1) I_{1z} + (\omega_2(t) + \omega_2) I_{2z} + \omega_{12}(t) \left[2I_{1z}I_{2z} - \frac{1}{2}(I_1^+I_2^- + I_1^-I_2^+) \right] \quad (1) \text{ where}$$

ω_1 and ω_2 represents the isotropic chemical shifts of spins 1 and 2 and $\omega_\lambda(t) = \sum_{\substack{m=-2, \\ m \neq 0}}^2 \omega_\lambda^{(m)} e^{im\omega_r t}$

the anisotropic time-dependent interactions characterized by λ . The time-independent components $\omega_\lambda^{(m)}$ are represented by

$$\omega_\lambda^{(m)} = \sum_{m_1} R_{P,\lambda}^{(2)m_1} \sum_{m_2=-2}^2 D_{m_1 m_2}(\Omega_{PM}) \sum_{\substack{m=-2 \\ m \neq 0}}^2 D_{m_2 m}(\Omega_{MR}) \quad (2)$$

where $R_{P,\lambda}^{(2)m_1}$ denotes the component of the irreducible spatial tensor defined in the principal axis system and $D_{m_1 m_2}(\Omega_{AB})$ the Wigner rotation matrix.²⁷ In the case of the chemical shift

anisotropy (CSA), the $R_{P,I(S)}^{(2)0} = \delta_{anis}$, $R_{P,I(S)}^{(2)\pm 2} = -\frac{1}{\sqrt{6}} \delta_{anis} \eta$ (δ_{anis} , η represent the chemical shift anisotropy and asymmetry parameter) components are non-zero in the principal axis frame while in the case of the dipolar interactions only the $R_{P,IS}^{(2)0} = \sqrt{6} b_{jk}$ (where $b_{jk} = \frac{\mu_0 \gamma_I \gamma_S \hbar}{4\pi r_{IS}^3}$ (rad / s) represents the dipolar coupling constant) is non-zero in the dipolar principal axis frame. In order to describe the interference effects under rotational resonance conditions, the rotating frame Hamiltonian [Eq. (1)] is transformed into an interaction frame defined by the transformation operator $U_1 = \exp(in\omega_r t I_{1z}) \exp(-in\omega_r t I_{2z})$,

$$\begin{aligned} \tilde{H}(t) &= U_1 H(t) U_1^{-1} \\ &= (\omega_1 - n\omega_r) I_{1z} + (\omega_2 + n\omega_r) I_{2z} + \omega_1(t) I_{1z} + \omega_2(t) I_{2z} + \\ &\quad \omega_{12}(t) \left[2I_{1z} I_{2z} - \frac{1}{2} (I_1^+ I_2^- e^{i2n\omega_r t} + I_1^- I_2^+ e^{-i2n\omega_r t}) \right] \end{aligned} \quad (3)$$

where the index n=1 represents the standard N=2 condition in R^2 experiments (i.e. $|\omega_1 - \omega_2| = N\omega_r$).

Employing the multipole operator basis^{28,29} (Table 3-1), the Hamiltonian in the interaction frame is re-expressed as,

$$\begin{aligned} \tilde{H}(t) &= (\omega_1 - n\omega_r) iT^{(1)0}(10) + \omega_1(t) iT^{(1)0}(10) + (\omega_2 + n\omega_r) iT^{(1)0}(01) + \omega_2(t) iT^{(1)0}(01) + \\ &\quad \frac{1}{\sqrt{3}} \omega_{12}(t) T^{(0)0}(11) - \sqrt{\frac{2}{3}} \omega_{12}(t) T^{(2)0}(11) - \omega_{12}(t) \left[\frac{1}{2\sqrt{3}} T^{(0)0}(11) + \frac{1}{2\sqrt{2}} T^{(1)0}(11) + \frac{1}{2\sqrt{6}} T^{(2)0}(11) \right] e^{i2n\omega_r t} \quad (4) \\ &\quad - \omega_{12}(t) \left[\frac{1}{2\sqrt{3}} T^{(0)0}(11) - \frac{1}{2\sqrt{2}} T^{(1)0}(11) + \frac{1}{2\sqrt{6}} T^{(2)0}(11) \right] e^{-i2n\omega_r t} \end{aligned}$$

The explicit time-dependence is due both to the MAS Hamiltonian in the interaction frame and the transformation operator U_I . In the conventional R^2 experiments the dipolar interaction between a particular spin pair is selectively introduced by matching the isotropic chemical shift difference to an integer multiple of the sample spinning frequency i.e. $|\omega_1 - \omega_2| = N\omega_r$. Subsequently, the distance information is extracted by monitoring the magnetization trajectory as a function of the dipolar mixing time. In contrast, in the R^2W experiments^{13,14} the

magnetization exchange profile is recorded by monitoring the exchange dynamics as a function of the spinning frequency under constant mixing times.

To zero order the effective Hamiltonian for the N=2 condition in the interaction frame in both cases is represented by

$$\begin{aligned} \tilde{H}_{0,AHT} = & (\omega_1 - n\omega_r) iT^{(1)0}(10) + (\omega_2 + n\omega_r) iT^{(1)0}(01) - \frac{1}{2\sqrt{3}}(G_{12}^{(-2)} + G_{12}^{(2)})T^{(0)0}(11) \\ & - \frac{1}{2\sqrt{2}}(G_{12}^{(-2)} - G_{12}^{(2)})T^{(1)0}(11) - \frac{1}{2\sqrt{6}}(G_{12}^{(-2)} + G_{12}^{(2)})T^{(2)0}(11) \end{aligned} \quad (5)$$

where the G coefficients have the same definitions as illustrated in Eq. 2 i.e. $G_\lambda^{(m)} = \omega_\lambda^{(m)}$.

Expressing the density operator in the multipole basis i.e. $\rho(t) = \Phi_q^{(k)}(k_1 k_2, t) T^{(k)q}(k_1 k_2)$, the spin dynamics in the operator space is described by the following set of differential equations:

$$i\hbar \frac{d}{dt} \begin{bmatrix} \hat{\Phi}_0^{(1)}(10, t) \\ \hat{\Phi}_0^{(1)}(01, t) \\ \hat{\Phi}_0^{(0)}(11, t) \\ \hat{\Phi}_0^{(1)}(11, t) \\ \hat{\Phi}_0^{(2)}(11, t) \end{bmatrix} = \begin{bmatrix} 0 & 0 & -i\sqrt{\frac{2}{3}}G_4 & i\left(\sqrt{\frac{2}{3}}G_3 + \frac{1}{\sqrt{3}}G_5\right) & -i\frac{1}{\sqrt{3}}G_4 \\ 0 & 0 & i\sqrt{\frac{2}{3}}G_4 & -i\left(\sqrt{\frac{2}{3}}G_3 + \frac{1}{\sqrt{3}}G_5\right) & i\frac{1}{\sqrt{3}}G_4 \\ -i\sqrt{\frac{2}{3}}G_4 & i\sqrt{\frac{2}{3}}G_4 & -iT_{zq}^{-1} & -\sqrt{\frac{2}{3}}(G_1 - G_2) & 0 \\ -i\left(\sqrt{\frac{2}{3}}G_3 + \frac{1}{\sqrt{3}}G_5\right) & i\left(\sqrt{\frac{2}{3}}G_3 + \frac{1}{\sqrt{3}}G_5\right) & -\sqrt{\frac{2}{3}}(G_1 - G_2) & -iT_{zq}^{-1} & -\frac{1}{\sqrt{3}}(G_1 - G_2) \\ -i\frac{1}{\sqrt{3}}G_4 & i\frac{1}{\sqrt{3}}G_4 & 0 & -\frac{1}{\sqrt{3}}(G_1 - G_2) & -iT_{zq}^{-1} \end{bmatrix} \begin{bmatrix} \hat{\Phi}_0^{(1)}(10, t) \\ \hat{\Phi}_0^{(1)}(01, t) \\ \hat{\Phi}_0^{(0)}(11, t) \\ \hat{\Phi}_0^{(1)}(11, t) \\ \hat{\Phi}_0^{(2)}(11, t) \end{bmatrix} \quad (6)$$

where the G_i 's represent coefficients corresponding to the operators $T^{(1)0}(10)$, $T^{(1)0}(01)$, $T^{(0)0}(11)$, $T^{(1)0}(11)$ and $T^{(2)0}(11)$ (in that order) respectively. Since polarization transfer experiments involve contributions from coherent and incoherent processes, the incoherent effects are often modeled by a phenomenological damping term T_{ZQ}^{-1} (also referred to as $\frac{1}{T_2^{ZQ}}$ in the literature) along the diagonal corresponding to the two-spin ZQ polarizations $\Phi_0^{(k)}(11, t)$. Subsequently, depending on the initial conditions, the spin polarizations are evaluated by solving the above differential equations and are represented by

$$\Phi_i(t) = \sum_{j,k} \zeta_{ik} e^{i\lambda_k t} \zeta_{kj}^{-1} \Phi_j(0) \quad (7)$$

$$\langle I_z(t) \rangle = \text{Tr}[I_z \rho(t)] = \Phi_0^{(1)}(01, t) \quad (8)$$

where ζ_{ik} and λ_k represent the eigenvectors and eigenvalues, respectively, and the polarization transfer from spin 1 ($\Phi_0^{(1)}(10,t)$) to spin 2 ($\Phi_0^{(1)}(01,t)$) is measured in our experiments. Although we have assumed a uniform relaxation rate corresponding to the ZQ-spin polarizations $\Phi^{(k)0}(11,t)$, the model [Eq. (6)] provides a more general framework for including different relaxation rates corresponding to the rank of the spin polarization. Since quantitative agreement with the experimental data necessitates a complete description inclusive of the CSA and higher order contributions, we employ the MMFT approach for describing the spin dynamics in the zero quantum subspace.

Table 3-1 Multipole-operator basis for two spin system with its equivalent in the standard product basis representation.

Multipole representation	Standard representation
<i>Single spin operators</i>	<i>Single spin operators</i>
$T^{(1)0}(10)$ ($T^{(1)0}(01)$)	iI_{1z} (iI_{2z})
$T^{(1)\pm 1}(10)$ ($T^{(1)\pm 1}(01)$)	$\mp \frac{1}{\sqrt{2}}iI_1^\pm$ ($\mp \frac{1}{\sqrt{2}}iI_2^\pm$)
<i>Two spin operators</i>	<i>Two spin operators</i>
$T^{(0)0}(11)$	$\frac{2}{\sqrt{3}}I_1 \cdot I_2$
$T^{(1)0}(11)$	$\frac{1}{\sqrt{2}}(I_1^+I_2^- - I_1^-I_2^+)$
$T^{(1)\pm 1}(11)$	$I_1^\pm I_{2z} - I_{1z} I_2^\pm$
$T^{(2)0}(11)$	$-\frac{2}{\sqrt{6}}(3I_{1z}I_{2z} - I_1 \cdot I_2)$
$T^{(2)\pm 2}(11)$	$-I_1^\pm I_2^\pm$
$T^{(2)\pm 1}(11)$	$\pm(I_1^\pm I_{2z} + I_{1z} I_2^\pm)$

3.3.2. Spin dynamics using the MMFT approach

Following the MMFT approach,²⁵ the spin Hamiltonian in the interaction frame [Eq. (4)] is transformed into a time-independent Hamiltonian (also referred to as Floquet Hamiltonian) represented below,

$$\begin{aligned}
H_F = & \omega_r N + (\omega_1 - n\omega_r) iT_0^{(1)0}(10) + (\omega_2 + n\omega_r) iT_0^{(1)0}(01) - \frac{1}{2\sqrt{3}}(G_{12}^{(-2)} + G_{12}^{(2)})T_0^{(0)0}(11) \\
& - \frac{1}{2\sqrt{2}}(G_{12}^{(-2)} - G_{12}^{(2)})T_0^{(1)0}(11) - \frac{1}{2\sqrt{6}}(G_{12}^{(-2)} + G_{12}^{(2)})T_0^{(2)0}(11) + \sum_{\substack{m=-2, \\ m \neq 0}}^2 G_1^{(m)} iT_m^{(1)0}(10) + \\
& \sum_{\substack{m=-2, \\ m \neq 0}}^2 G_2^{(m)} iT_m^{(1)0}(01) + \sum_{\substack{m=-4, \\ m \neq 0}}^4 G_{12,m}^{(0)} T_m^{(0)0}(11) + \sum_{\substack{m=-4, \\ m \neq 0}}^4 G_{12,m}^{(1)} T_m^{(1)0}(11) + \sum_{\substack{m=-4, \\ m \neq 0}}^4 G_{12,m}^{(2)} T_m^{(2)0}(11)
\end{aligned} \tag{9}$$

where $T_m^{(k)q}(k_1 k_2)$ represents the irreducible Floquet tensor (IFT) operators (i.e. $T_m^{(k)q}(k_1 k_2) = T^{(k)q}(k_1 k_2) \otimes F_m$). The $G_{12,m}^{(k)}$ coefficients illustrated above have been tabulated in Table 3.2.

Table 3-2 The G coefficients involved in the Floquet Hamiltonian (Eq. 9). (a) N=1, R² condition. (b) N=2, R² condition.

(a) N=1, R² condition

$$\begin{aligned}
G_{12,\pm 1}^{(0)} &= \frac{1}{\sqrt{3}} G_{12}^{(\pm 1)} - \frac{1}{2\sqrt{3}} G_{12}^{(\pm 2)}, \quad G_{12,\pm 2}^{(0)} = \frac{1}{\sqrt{3}} G_{12}^{(\pm 2)} - \frac{1}{2\sqrt{3}} G_{12}^{(\pm 1)}, \\
G_{12,\pm 3}^{(0)} &= -\frac{1}{2\sqrt{3}} G_{12}^{(\pm 2)}, \quad G_{12,\pm 1}^{(1)} = \pm \frac{1}{2\sqrt{2}} G_{12}^{(\pm 2)}, \quad G_{12,\pm 2}^{(1)} = \mp \frac{1}{2\sqrt{2}} G_{12}^{(\pm 1)}, \\
G_{12,\pm 3}^{(1)} &= \mp \frac{1}{2\sqrt{2}} G_{12}^{(\pm 2)}, \quad G_{12,\pm 1}^{(2)} = -\sqrt{\frac{2}{3}} G_{12}^{(\pm 1)} - \frac{1}{2\sqrt{6}} G_{12}^{(\pm 2)}, \\
G_{12,\pm 2}^{(2)} &= -\sqrt{\frac{2}{3}} G_{12}^{(\pm 2)} - \frac{1}{2\sqrt{6}} G_{12}^{(\pm 1)}, \quad G_{12,\pm 3}^{(2)} = -\frac{1}{2\sqrt{6}} G_{12}^{(\pm 2)}
\end{aligned}$$

(b) N=2, R² condition

$$\begin{aligned}
G_1^{(m)} &= \omega_1^{(m)}, \quad G_2^{(m)} = \omega_2^{(m)}, \quad G_{12,\pm 1}^{(0)} = \frac{1}{\sqrt{3}} G_{12}^{(\pm 1)} - \frac{1}{2\sqrt{3}} G_{12}^{(\mp 1)}, \\
G_{12,\pm 2}^{(0)} &= \frac{1}{\sqrt{3}} G_{12}^{(\pm 2)}, \quad G_{12,\pm 3}^{(0)} = -\frac{1}{2\sqrt{3}} G_{12}^{(\pm 1)}, \quad G_{12,\pm 4}^{(0)} = -\frac{1}{2\sqrt{3}} G_{12}^{(\pm 2)}, \\
G_{12,\pm 1}^{(1)} &= \mp \frac{1}{2\sqrt{2}} G_{12}^{(\mp 1)}, \quad G_{12,\pm 3}^{(1)} = \mp \frac{1}{2\sqrt{2}} G_{12}^{(\pm 1)}, \quad G_{12,\pm 4}^{(1)} = \mp \frac{1}{2\sqrt{2}} G_{12}^{(\pm 2)}, \\
G_{12,\pm 1}^{(2)} &= -\sqrt{\frac{2}{3}} G_{12}^{(\pm 1)} - \frac{1}{2\sqrt{6}} G_{12}^{(\mp 1)}, \quad G_{12,\pm 2}^{(2)} = -\sqrt{\frac{2}{3}} G_{12}^{(\pm 2)}, \\
G_{12,\pm 3}^{(2)} &= -\frac{1}{2\sqrt{6}} G_{12}^{(\pm 1)}, \quad G_{12,\pm 4}^{(2)} = -\frac{1}{2\sqrt{6}} G_{12}^{(\pm 2)}
\end{aligned}$$

To reduce the complexity in the Floquet-Liouville space, we employ the effective Hamiltonian approach described in the original articles.³⁰⁻³² In this approach the spin dynamics in the Floquet-Liouville space are reduced to the standard Liouville space description using an effective Hamiltonian derived from the contact transformation procedure. One obvious

advantage of such an approach is the description of the higher order corrections in terms of operators (see ref. 30-32 for a more detailed discussion).

In order to apply the contact transformation procedure the Floquet Hamiltonian [Eq. (9)] is rewritten as a sum involving a zero order and a perturbing Hamiltonian as follows.

$$H_0 = \omega_r N + G_1 iT_0^{(1)0}(10) + G_2 iT_0^{(1)0}(01) + G_3 T_0^{(0)0}(11) + G_4 T_0^{(1)0}(11) + G_5 T_0^{(2)0}(11) \quad (10)$$

$$H_1 = \sum_{\substack{m=-2, \\ m \neq 0}}^2 [G_1^{(m)} iT_m^{(1)0}(10) + G_2^{(m)} iT_m^{(1)0}(01)] + \sum_{\substack{m=-4, \\ m \neq 0}}^4 [G_{12,m}^{(0)} T_m^{(0)0}(11) + G_{12,m}^{(1)} T_m^{(1)0}(11) + G_{12,m}^{(2)} T_m^{(2)0}(11)] \quad (11)$$

Subsequently, the Floquet Hamiltonian [Eq. (9)] is transformed as follows

$$\begin{aligned} H_F^{eff} &= U_1 H_F U_1^{-1} = e^{i\lambda S_1} H_F e^{-i\lambda S_1} \\ &= H_0^{(1)} + H_1^{(1)} + H_2^{(1)} \dots \\ H_0^{(1)} &= H_0 \\ H_1^{(1)} &= H_1 + i[S_1, H_0] \\ H_2^{(1)} &= H_2 + i[S_1, H_1] - \frac{1}{2}[S_1, [S_1, H_0]] \\ H_n^{(1)} &= H_n + \sum_{m=0}^{n-1} \frac{i^{n-m}}{(n-m)!} \underbrace{[S_1, [S_1, \dots [S_1, H_m] \dots]]}_{n-m} \end{aligned} \quad (12)$$

where H_1, H_2, \dots, H_n represent the perturbations and S_1 the transformation function. The transformation function S_1 is expressed by

$$S_1 = i \left[\sum_{\substack{m=-2, \\ m \neq 0}}^2 [C_1^{(m)} iT_m^{(1)0}(10) + C_2^{(m)} iT_m^{(1)0}(01)] + \sum_{\substack{m=-4, \\ m \neq 0}}^4 [C_{12,m}^{(0)} T_m^{(0)0}(11) + C_{12,m}^{(1)} T_m^{(1)0}(11) + C_{12,m}^{(2)} T_m^{(2)0}(11)] \right] \quad (13)$$

where the C coefficients are obtained by solving a set of linear equations corresponding to a particular operator given below:

$$\begin{aligned}
0 &= H_1 + i[S_1, H_0] \\
&= iT_m^{(1)0}(10) \left[G_1^{(m)} - m\omega_r C_1^{(m)} - \frac{1}{\sqrt{3}} G_4 C_{12,m}^{(2)} + \left(\frac{1}{\sqrt{3}} G_5 + \sqrt{\frac{2}{3}} G_3 \right) C_{12,m}^{(1)} - \sqrt{\frac{2}{3}} G_4 C_{12,m}^{(0)} \right] + \\
&\quad iT_m^{(1)0}(01) \left[G_2^{(m)} - m\omega_r C_2^{(m)} + \frac{1}{\sqrt{3}} G_4 C_{12,m}^{(2)} - \left(\frac{1}{\sqrt{3}} G_5 + \sqrt{\frac{2}{3}} G_3 \right) C_{12,m}^{(1)} + \sqrt{\frac{2}{3}} G_4 C_{12,m}^{(0)} \right] + \\
&\quad T_m^{(0)0}(11) \left[G_{12,m}^{(0)} - m\omega_r C_{12,m}^{(0)} + \sqrt{\frac{2}{3}} G_4 C_1^{(m)} - \sqrt{\frac{2}{3}} G_4 C_2^{(m)} - \sqrt{\frac{2}{3}} (G_1 - G_2) C_{12,m}^{(1)} \right] + \\
&\quad T_m^{(1)0}(11) \left[G_{12,m}^{(1)} - m\omega_r C_{12,m}^{(1)} + \left(\frac{1}{\sqrt{3}} G_5 + \sqrt{\frac{2}{3}} G_3 \right) [C_1^{(m)} - C_2^{(m)}] - (G_1 - G_2) \left[\sqrt{\frac{2}{3}} C_{12,m}^{(0)} + \frac{1}{\sqrt{3}} C_{12,m}^{(2)} \right] \right] + \\
&\quad T_m^{(2)0}(11) \left[G_{12,m}^{(2)} - m\omega_r C_{12,m}^{(2)} + \frac{1}{\sqrt{3}} G_4 C_1^{(m)} - \frac{1}{\sqrt{3}} G_4 C_2^{(m)} - \frac{1}{\sqrt{3}} (G_1 - G_2) C_{12,m}^{(1)} \right]
\end{aligned} \tag{14}$$

Employing the following relations between the IFT operators,

$$\text{Tr} \left[T_m^{(k)q}(k_1 k_2) T_m^{(k)q}(k_1 k_2) \right] \approx 1 \tag{15a}$$

$$\left[T_m^{(k)q}(k_1 k_2), N \right] = m T_m^{(k)q}(k_1 k_2) \tag{15b}$$

$$\begin{aligned}
\left[T_m^{(k)q}(k_1 k_2), T_{m'}^{(k')q'}(k'_1 k'_2) \right] &\propto \sum_{k_1'', k_2'', k'', q''} 2\phi_{i=1 \rightarrow 2}(k_i, k'_i, k_i'') T_{m+m'}^{(k'')q''}(k_1'' k_2'') \\
\text{with } \phi_{i=1 \rightarrow 2}(k_i, k'_i, k_i'') &= 1 \text{ if } \sum_{i=1}^2 k_i + k'_i + k_i'' = \text{odd} \\
&= 0 \text{ (Otherwise)}
\end{aligned} \tag{15c}$$

the diagonal corrections to the zero order Hamiltonian are obtained by evaluating $H_2^{(1)}$,

$$\begin{aligned}
H_2^{(1)} &= \frac{i}{2} [S_1, H_1] \\
&= iT_0^{(1)0}(10)A_1 + iT_0^{(1)0}(01)A_2 + T_0^{(0)0}(11)A_3 + T_0^{(1)0}(11)A_4 + T_0^{(2)0}(11)A_5
\end{aligned} \tag{16}$$

where the A_i coefficients are tabulated in Table 3-3.

The commutator relation [Eq. (15c)] between the IFT operators is identical to the multipole operators *without* the Fourier index. Employing Eq. (15c), the second order contributions resulting from the various cross-terms are deduced. The dipolar-dipolar cross-terms result in corrections involving longitudinal single spin operators $T_m^{(1)0}(10)$, $T_m^{(1)0}(01)$ while the cross-terms between the CSA-dipolar interactions result in longitudinal two-spin operators $T_m^{(k)0}(11)$.

Table 3-3 Coefficients involved in the second order correction terms (Eq. 16). The indices involved have the following values, $m_1 = -4$ to 4 , $m = -2$ to 2 . In the case of $N=1$ R² condition $m_1 = -3$ to 3 .

	Expression for the coefficient
A_1	$\frac{1}{2} \left[\underbrace{\sqrt{\frac{2}{3}} \left(C_{12,m_1}^{(1)} G_{12,-m_1}^{(0)} - C_{12,m_1}^{(0)} G_{12,-m_1}^{(1)} \right) + \frac{1}{\sqrt{3}} \left(C_{12,m_1}^{(1)} G_{12,-m_1}^{(2)} - C_{12,m_1}^{(2)} G_{12,-m_1}^{(1)} \right)}_{\text{dipolar-dipolar}} \right]$
A_2	$-\frac{1}{2} \left[\underbrace{\sqrt{\frac{2}{3}} \left(C_{12,m_1}^{(1)} G_{12,-m_1}^{(0)} - C_{12,m_1}^{(0)} G_{12,-m_1}^{(1)} \right) + \frac{1}{\sqrt{3}} \left(C_{12,m_1}^{(1)} G_{12,-m_1}^{(2)} - C_{12,m_1}^{(2)} G_{12,-m_1}^{(1)} \right)}_{\text{dipolar-dipolar}} \right]$
A_3	$\frac{1}{2} \left[\underbrace{\sqrt{\frac{2}{3}} \left\{ \left(C_1^{(m)} - C_2^{(m)} \right) G_{12,-m}^{(1)} - C_{12,m}^{(1)} \left(G_1^{(-m)} - G_2^{(-m)} \right) \right\}}_{\text{csa-dipolar}} \right]$
A_4	$\frac{1}{2} \left[\underbrace{\sqrt{\frac{2}{3}} \left\{ \left(C_1^{(m)} - C_2^{(m)} \right) G_{12,-m}^{(0)} - C_{12,m}^{(0)} \left(G_1^{(-m)} - G_2^{(-m)} \right) \right\} + \frac{1}{\sqrt{3}} \left\{ \left(C_1^{(m)} - C_2^{(m)} \right) G_{12,-m}^{(2)} - C_{12,m}^{(2)} \left(G_1^{(-m)} - G_2^{(-m)} \right) \right\}}_{\text{csa-dipolar}} \right]$
A_5	$\frac{1}{2} \left[\underbrace{\frac{1}{\sqrt{3}} \left\{ \left(C_1^{(m)} - C_2^{(m)} \right) G_{12,-m}^{(1)} - C_{12,m}^{(1)} \left(G_1^{(-m)} - G_2^{(-m)} \right) \right\}}_{\text{csa-dipolar}} \right]$

Using the effective Floquet Hamiltonian ($H_F^{eff} \approx H_0 + H_2^{(1)}$), the spin dynamics in the Floquet-Liouville space are constrained by the following set of differential equations,

$$i\hbar \frac{d}{dt} \begin{bmatrix} \hat{\Phi}_{0,0}^{(1)}(10,t) \\ \hat{\Phi}_{0,0}^{(1)}(01,t) \\ \hat{\Phi}_{0,0}^{(0)}(11,t) \\ \hat{\Phi}_{0,0}^{(1)}(11,t) \\ \hat{\Phi}_{0,0}^{(2)}(11,t) \end{bmatrix} = \begin{bmatrix} 0 & 0 & -i\sqrt{\frac{2}{3}}C'_4 & i\left(\sqrt{\frac{2}{3}}C'_3 + \frac{1}{\sqrt{3}}C'_5\right) & -i\frac{1}{\sqrt{3}}C'_4 \\ 0 & 0 & i\sqrt{\frac{2}{3}}C'_4 & -i\left(\sqrt{\frac{2}{3}}C'_3 + \frac{1}{\sqrt{3}}C'_5\right) & i\frac{1}{\sqrt{3}}C'_4 \\ -i\sqrt{\frac{2}{3}}C'_4 & i\sqrt{\frac{2}{3}}C'_4 & -i(T_{zq}^{(0)})^{-1} & -\sqrt{\frac{2}{3}}(C'_1 - C'_2) & 0 \\ -i\left(\sqrt{\frac{2}{3}}C'_3 + \frac{1}{\sqrt{3}}C'_5\right) & i\left(\sqrt{\frac{2}{3}}C'_3 + \frac{1}{\sqrt{3}}C'_5\right) & -\sqrt{\frac{2}{3}}(C'_1 - C'_2) & -i(T_{zq}^{(1)})^{-1} & -\frac{1}{\sqrt{3}}(C'_1 - C'_2) \\ -i\frac{1}{\sqrt{3}}C'_4 & i\frac{1}{\sqrt{3}}C'_4 & 0 & -\frac{1}{\sqrt{3}}(C'_1 - C'_2) & -i(T_{zq}^{(2)})^{-1} \end{bmatrix} \begin{bmatrix} \hat{\Phi}_{0,0}^{(1)}(10,t) \\ \hat{\Phi}_{0,0}^{(1)}(01,t) \\ \hat{\Phi}_{0,0}^{(0)}(11,t) \\ \hat{\Phi}_{0,0}^{(1)}(11,t) \\ \hat{\Phi}_{0,0}^{(2)}(11,t) \end{bmatrix} \quad (17)$$

where $\hat{\Phi}_{q,0}^{(k)}(k_1 k_2, t)$ represents the spin polarization in the Floquet-Liouville space corresponding to the Fourier index zero and $C'_i = G_i + A_i$. Equation (17) expressed in the

Floquet-Liouville space is exactly identical in form to the one derived in the standard Liouville space using the zero order Average Hamiltonian treatment Eq. (6) *except* for the second order corrections represented by the ‘A’ coefficients. The diagonal terms $(T_{zq}^{(k)})^{-1}$ represent the ZQ relaxation rate corresponding to the two-spin ZQ polarizations $\hat{\Phi}_{0,0}^{(k)}(11,t)$ and provide an apparent validation of the use of multiple decay rate constants. Analogous to Eq. (8), the expectation value of an observable in the Floquet-Liouville space is given by

$$\langle I_z(t) \rangle = \text{Tr} [I_{z,F} \rho_F(t)] = \Phi_{0,0}^{(1)}(01,t) \quad (18)$$

where $I_{z,F}$ is the Floquet-detection operator. In the next section we describe the methods employed for simulating the experimental results.

3.4. Results and Discussion

To substantiate the MMFT model presented in the previous section, we performed 3D-R²W experiments measuring 14 ¹³C-¹³C distances (in the range 2-7 Å) in the dipeptide N-acetyl-[U-¹³C,¹⁵N]-L-valine-L-leucine (the N-terminal acetyl group was not labeled) (Fig. 3-1). The measured distances were compared to the distance constraints previously determined by x-ray crystallography.³³ To minimize intermolecular effects the sample was diluted in natural abundance (91% natural abundance, 9% N-acetyl-[U-¹³C,¹⁵N]L-Val-L-Leu (N-Ac-VL)) prior to crystallization. All of the experiments were performed at 500 MHz (¹H frequency) using the pulse sequence shown in Fig. 3-2. A selective z-filter was used to eliminate all transverse magnetization other than the carbonyls, after which the polarization transfer to the side-chain carbons is monitored. The experimental details are identical to those described previously.¹⁴ Figure 3-3 shows the one dimensional ¹³C spectrum of the sample. The sample spinning frequencies employed in the two-dimensional experiments were chosen to satisfy the $N=2 R^2$ condition between the desired carbonyl and side-chain carbons. This matching condition was chosen for practical reasons; note that the mathematical description would differ slightly for the $N=1$ condition (see Table 3-2).

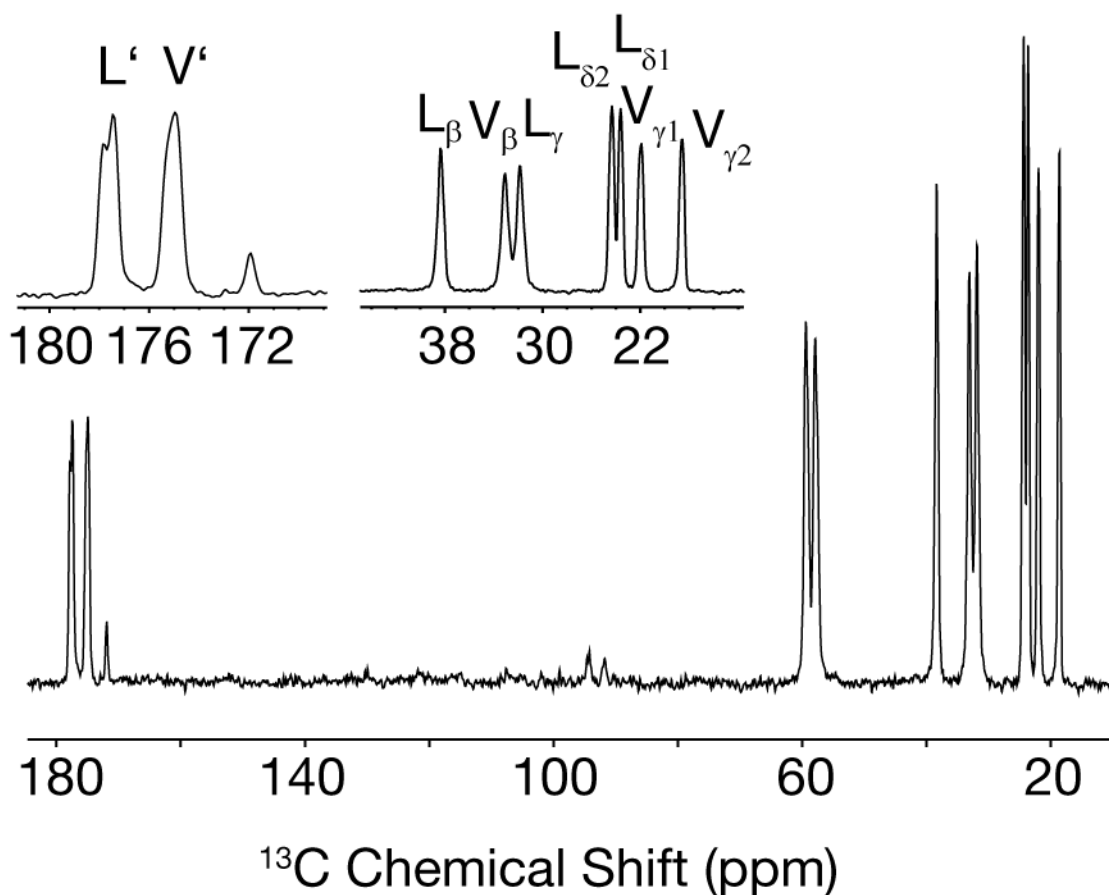


Figure 3-3 One-dimensional ^{13}C MAS spectrum of N-Ac-VL recorded at $\omega_r/2\pi=10.5$ kHz. The unlabeled acetyl carbonyl carbon is visible at reduced intensity.

A series of R^2W experiments were performed as a function of the sample spinning frequency under a constant mixing time of 30 ms, with the spinning frequency ranging from 8.5 to 10.1 kHz, in non-uniform steps of ~ 10 -50 Hz to obtain optimal matching profiles. Figure 3-4 illustrates representative two-dimensional (2D) slices from the 3D- R^2W experiment corresponding to the spinning frequencies 8.791 and 9.116 kHz (two different $N=2$ matching conditions, see figure legend).

The experimental data from the 3D- R^2W experiments were processed using NMRPipe,³⁴ wherein the cross-peak volumes were extracted by automated fitting to two-dimensional Gaussians. To compensate for the dependence of cross-polarization (CP) enhancements on the sample spinning frequency $\omega_r/2\pi$, all the data points in each 2D slice were normalized to the initial carbonyl intensities derived from reference experiments conducted at identical spinning

frequencies with zero mixing time. The extracted cross-peak intensities are illustrated in Fig. 3-5. These plots represent the raw data used in the carbonyl – side chain distance measurements.

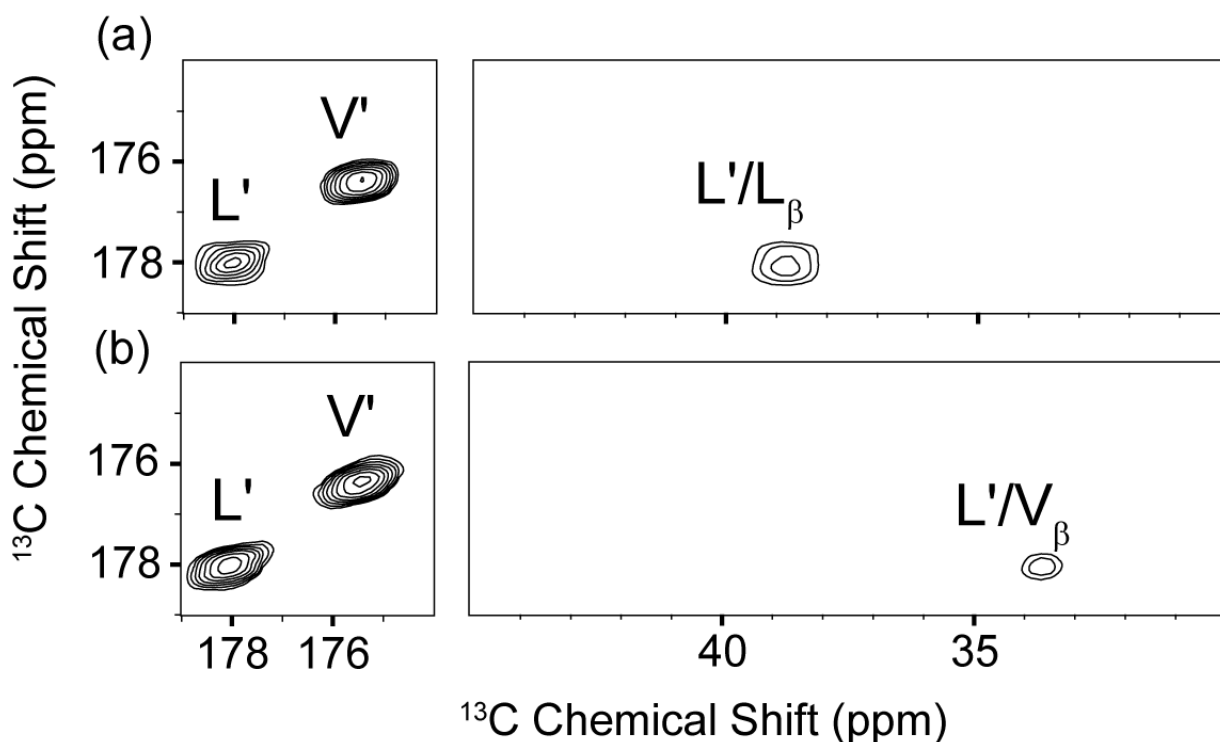


Figure 3-4 Representative two-dimensional slices from the ^{13}C - ^{13}C R^2W experiment in N-acetyl-[U- ^{13}C , ^{15}N]L-Val-L-Leu (N-Ac-VL) recorded on a 500 MHz spectrometer at (a) $\omega_r/2\pi=8.791$ kHz and (b) $\omega_r/2\pi=9.116$ kHz, corresponding to the L_C - L_{β} and L_C - V_{β} $N=2$ R^2 matching conditions, respectively.

In general, several factors, such as the orientation of the chemical shift tensors, residual heteronuclear ^{13}C - ^1H interactions, higher order corrections and ZQ relaxation parameters, affect the accuracy of the distance measurements in uniformly labeled solids. Although residual ^{13}C - ^1H interactions are minimized by strong ^1H RF irradiation, the separation of the ZQ relaxation rate T_{ZQ}^{-1} from the dipolar-coupling constant constitutes a major challenge in measuring distances using R^2 experiments. Previously this issue was partially addressed by invoking the uncorrelated random field (URF) model³⁵⁻³⁷ in which the fluctuations resulting from the random fields at individual spin (^{13}C) sites are estimated with measurements of the single-quantum line-width. In the limit of rapid fluctuations, the random fields between a

particular spin pair are assumed to be uncorrelated and the relaxation mechanism is approximated by an exponential decay of the ZQ coherences. Due to inherent rapid molecular motion, the local fields in the liquid state should be highly uncorrelated (at least in principle) in the strong coupling regime. Nevertheless, such random fields and their correlation properties are difficult to quantify and are highly dependent on the state of the system (i.e. solid or liquid state). To this end, Levitt and co-workers³⁸ measured the ZQ relaxation rates experimentally in both diluted (10%, corresponding to 2.96 Å) and fully labeled samples (98%, corresponding to 1.53 Å). In the diluted sample the measured ZQ relaxation rate was in good agreement with the URF model. However, there were significant deviations in the fully labeled sample, a discrepancy that was attributed primarily to multiple-quantum relaxation arising from intermolecular dipolar interactions. Nevertheless, the results do not clarify the validity or failure of the URF model in the strong and weak-coupling regimes in a single sample (say a diluted sample). In the experiments reported here we can investigate the validity of the URF model in distance measurements by employing a model system (9% labeled N-Ac-VL) involving dipolar-coupling constants ranging from 500 Hz to 28 Hz (i.e. 2.5 – 6.4 Å).

Employing the URF approach, the ZQ relaxation rate Γ_{zq} [(or T_{ZQ}^{-1}) i.e., $\Gamma_{zq} = \Gamma_i + \Gamma_j$ where $\Gamma_{i(j)}$ represents the line-width of spin *i* (or *j*)] in the R²W experiments were calculated by measuring the line widths of the individual resonances from simple CP experiments recorded at spinning frequencies far from any R² matching conditions. To distinguish the contributions of the higher order terms from the ZQ relaxation parameters, the experimental cross peak intensities were simulated using both the zero-order and the effective Hamiltonians derived from the MMFT approach. Additionally, employing two different relaxation models the validity of the URF approach was tested in our simulations. In model-1, the zero-quantum relaxation parameter was calculated based on the URF approach, while in model-2 it was employed as a free-fit parameter. To demonstrate the difference between the current approach and other existing theoretical descriptions, the experimental data was also simulated using the fictitious spin operator approach¹⁴ (**Table 3-4**). In the first set of simulations the ZQ relaxation rate T_{ZQ}^{-1} was calculated based on the URF model and only the internuclear distance *r* was employed as a free-fit parameter (ranging from 2-7Å) to fit the experimental cross-peak intensities.

Table 3-4 Estimated ^{13}C - ^{13}C internuclear distances in N-Ac-VL using zero-order Hamiltonians derived from the MMFT and the fictitious spin operator approach. The CSA interactions were neglected in the simulations. The ZQ relaxation rate in model-1 was calculated based on the URF approach while in model-2, it was employed as a free-fit parameter. In all the simulations the internuclear distance r was used as a free-fit parameter.

Atoms		X-ray [\AA]	Model 1 - URF			Model 2 - free fit			
				Fictitious zeroth order	MMFT zeroth order	Fictitious zeroth order		MMFT zeroth order	
			$1/T_{z0}(\text{Hz})$	$r(\text{\AA})$	$r(\text{\AA})$	$1/T_{z0}(\text{Hz})$	$r(\text{\AA})$	$1/T_{z0}(\text{Hz})$	$r(\text{\AA})$
V'	V β	2.55	46.0	2.7	3.2	5	2.9	5.9	2.6
	V γ 2	2.97	38.7	3.0	3.5	256	3.9	38	3.5
	L β	3.72	42.4	4.1	4.5	476	4.8	81.3	4.3
	V γ 1	3.88	40.4	4.1	4.3	345	4.7	51.8	4.3
	L δ 1	4.29	37.2	4.2	4.5	333	4.9	57.1	4.4
	L γ	4.35	44.6	4.1	4.2	476	4.6	61.3	4.8
	L δ 2	5.90	39.6	4.4	4.9	370	5.4	84.0	4.7
L'	L β	2.47	42.5	2.8	3.2	7	2.9	7.1	2.55
	L γ	3.83	44.8	3.4	4.1	526	4.5	64.5	4.3
	V γ 2	4.36	38.8	4.2	4.6	322	5.0	52.9	4.5
	L δ 1	4.68	37.3	6.8	5.0	357	5.3	55.2	4.8
	L δ 2	4.87	39.7	4.2	4.8	303	5.2	47.8	4.7
	V β	4.98	46.1	4.1	4.5	714	4.7	99	4.3
	V γ 1	6.46	40.5	6.9	5.5	357	5.9	68.0	5.2

Following the URF approximation, the line broadening observed far from the R^2 condition was used to estimate the random fields generated by various spin-spin and spin-lattice interactions. This approach is valid only when the two line-broadening mechanisms observed on R^2 and off- R^2 matching conditions are mutually independent. The distances obtained from the fictitious spin model correlate reasonably well with the X-ray data, but the actual fit quality [e.g., root mean square deviation (RMSD)] is rather poor. Remarkably, while the zeroth order MMFT approach is better able to reproduce the experimental data, its correlation with the X-ray distances is actually worse. The discrepancies noticed in both approaches may be attributed either to an inadequate description of the coherent spin dynamics (i.e. spin Hamiltonian) or due to inaccuracies involved in the estimation of the zero-quantum relaxation rate.

To rule out the latter possibility, the ZQ relaxation rate T_{z0}^{-1} was employed as a free-fit parameter along with the internuclear distance (model-2 in Table 3-4, columns 6-9). Although the MMFT model results in better fits (smaller RMSD), there is no significant improvement in

the agreement between the NMR and X-ray distance (except for an apparent systematic improvement of the two shortest distances $V_{C'}-V_{C\beta}$ and $L_{C'}-L_{C\beta}$). Note that the correlation between the fictitious spin results and the X-ray data is worse than the results obtained from the MMFT approach. In addition, the estimated ZQ relaxation rate T_{ZQ}^{-1} differs significantly in both formalisms. The T_{ZQ}^{-1} values estimated from the fictitious spin operator formalism (typically 300-500 Hz) appear over-damped when compared to the magnitude of the dipolar coupling constants being measured. In contrast, the relaxation rates estimated from the MMFT approach are similar to, or slightly larger than, the relaxation rates calculated based on the URF model, except for a remarkably low T_{ZQ}^{-1} observed for the strong coupling regime ($r \sim 2.5$ Å). The absence of improvement in the distance measurements using both models suggests that the estimation of the relaxation parameter is not the factor limiting the quality of the fits of our data.

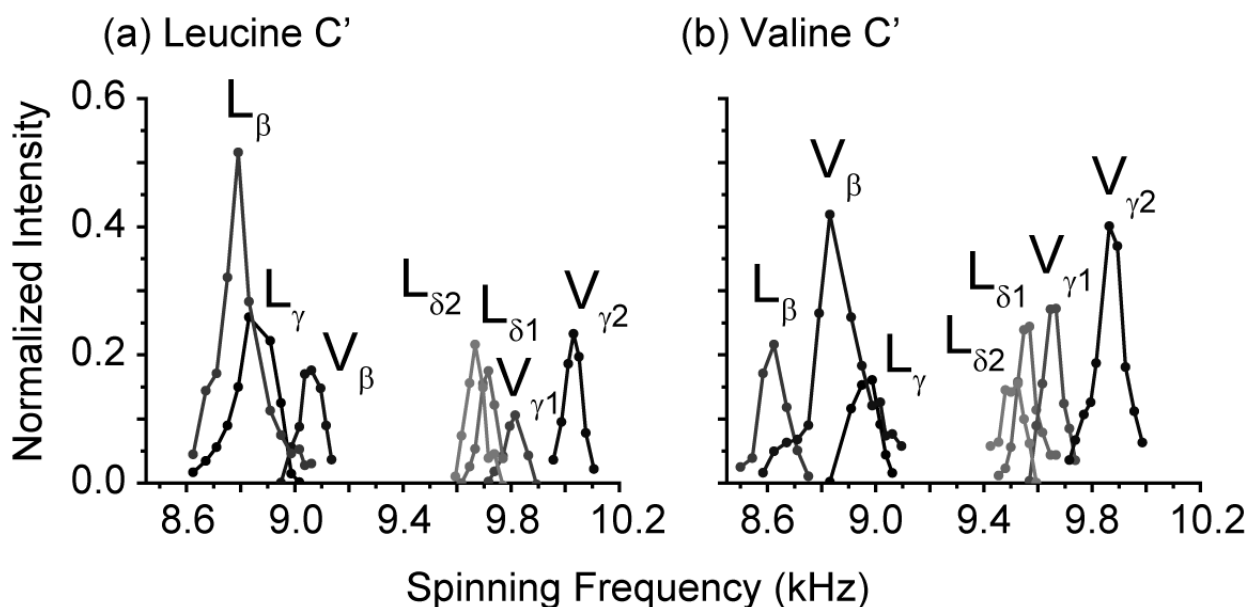


Figure 3-5 Resonance width profiles (cross-peak intensities) as a function of spinning frequency, polarization transfer from (a) $L_{C'}$, and (b) $V_{C'}$ carbons to the indicated side-chain carbons. Intensities are scaled relative to the carbonyl CP intensities.

To improve the accuracy of the coherent description in the MMFT analysis, we incorporated second order corrections including the CSA interactions into the calculations of the distance constraints. The second order corrections in R^2 experiments arise from the cross-terms

between the CSA and the dipolar interactions (i.e. CSA-dipolar and dipolar-dipolar). Our analysis reveals a major contribution from the cross-terms between the CSA and the dipolar interactions in the exchange dynamics. When these corrections involving CSA interactions are included, one has to consider both the magnitudes and orientations of the CSA tensor elements for each nucleus. In typical simulations, where the structure is unknown, the magnitudes can be estimated based on standard values, but the relative orientations are not necessarily known. To explicitly account for the orientation dependence, a series of simulations with different orientations relative to the molecular frame, defined by the internuclear vector, was performed. The conventions employed are depicted schematically in Fig. 3-6.

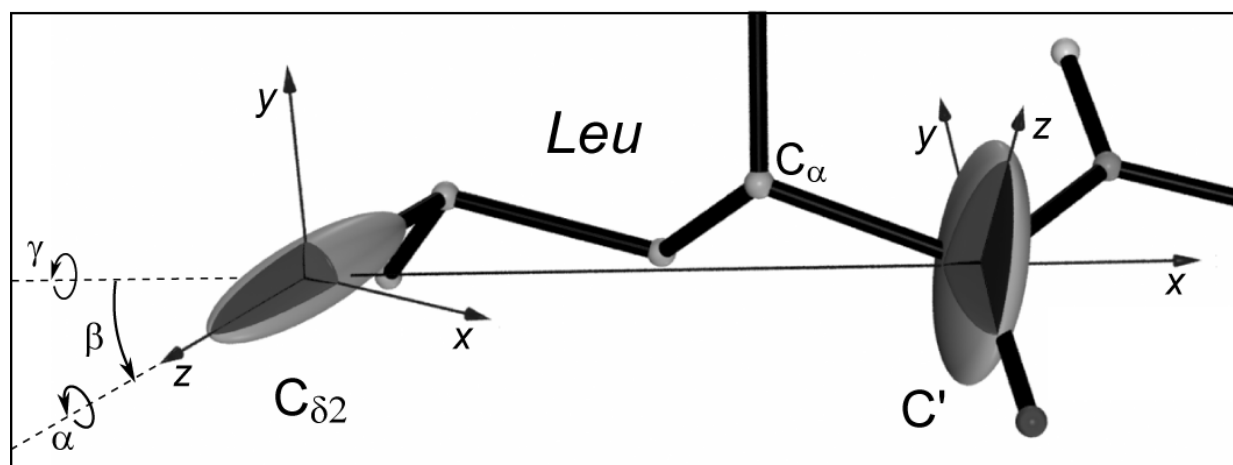


Figure 3-6 Illustration of the Euler angles used to define the relative CSA tensor orientations, showing here the CSA tensors for a leucine $C_{\delta 2}$ methyl group and C' carbonyl.

The simulations reveal that the R^2W matching condition is very sensitive to the CSA orientations. This is schematically illustrated in Fig. 3-7a showing the resonance profiles for two CSA orientations that represent the two extremes. Fig. 3-7b and 3-7c illustrate how these CSA tensor orientations have varying, but generally significant, effects on both the intensity and width of the resonance profile for a wider range of distances and relaxation conditions. Our simulation results predict that these contributions are predominantly governed by the larger CSA (carbonyls) and by the relative orientations of the largest CSA tensor elements, as determined by the β Euler angles (in Ω_{PM}), with a reduced dependence on α and γ . The two

displayed orientations reflect parallel or perpendicular alignments of the shielding tensors with respect to the internuclear vector.

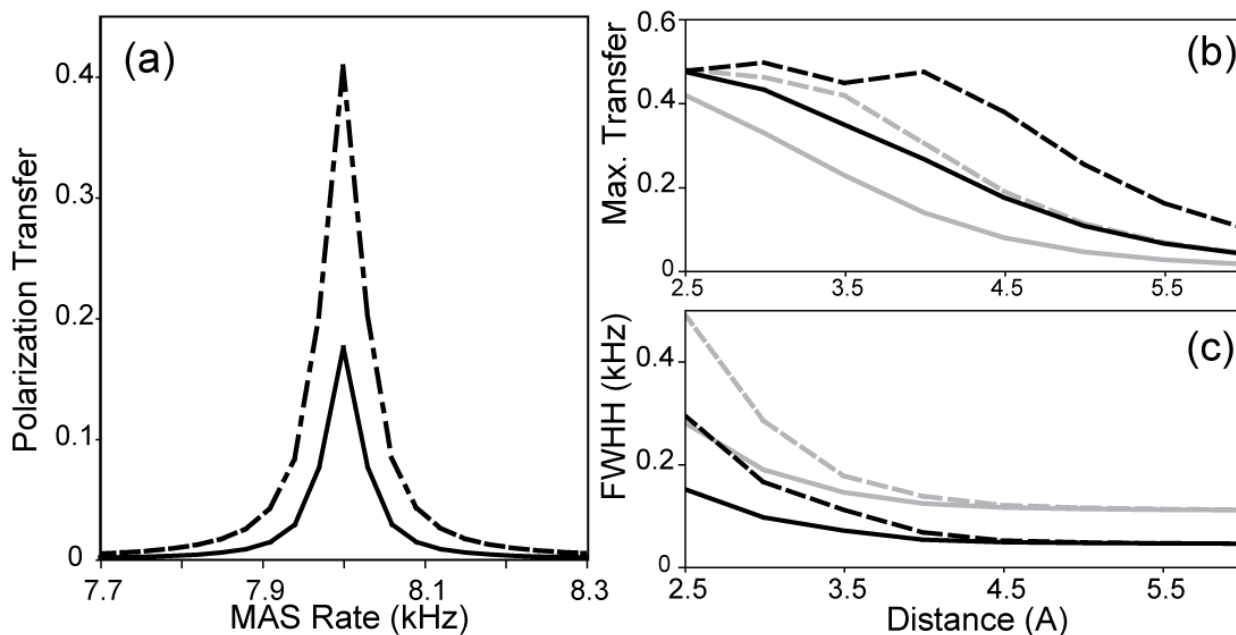


Figure 3-7 The effect of CSA orientations on the R²W polarization transfer profiles. (a) Simulated polarization transfer between a leucine carbonyl and methyl carbon as a function of MAS rate, for two hypothetical CSA orientations using an internuclear distance $r=4.4$ Å and $T_{zQ}=26$ ms. CSA orientations (α_{PM} , β_{PM} , γ_{PM}) of L_C/L_δ are (0,90,0)/(0,0,0) (solid lines), and (0,0,0)/(0,90,0) (dashed lines), exemplifying two extreme cases. Panels (b) and (c) illustrate the distance-dependence of the maximum and width of the R² matching condition for both orientations, now with $T_{zQ}=30$ ms (black) and 10 ms (gray).

When examining an unknown structure where the precise information about the CSA tensor orientation is absent, it is still possible to evaluate the range of possible distances by fitting the data to such theoretical CSA tensor orientation extremes. Later in the structure determination process when a rough structural model is available, the R²W data may be refined with provisional CSA tensor orientations in order to obtain more precise ¹³C-¹³C constraints. The procedure may be repeated in an iterative manner since more precise CSA tensor orientations should lead in principle to more precise distances and *vice versa*. To illustrate this point, we present in Table 3.5 the measured SSNMR distances from a single iteration of simulations in which no assumptions were made regarding the orientations of the CSAs, but using two extreme CSA orientations discussed above. The indicated range of distances reflects the effect of the uncertainty of the CSA orientations. Note that the X-ray distance tends to fall within this

region. The magnitude of this range (typically ~ 1 Å) shows that the orientations of the CSA tensors play a vital role in the accuracy/reliability of the R^2 distance measurements, especially for large B_0 values.

Table 3-5 Estimated range for ^{13}C - ^{13}C internuclear distances with systematic variation of the orientation of the CSA tensors covering both the extremes. These calculations employ the MMFT model, include 2nd order terms, and use relaxation models 1 and 2 as in Table 3-4.

Atoms		X-ray distance (Å)	MMFT Model 1 - URF		MMFT Model 2 - free fit	
			$1/T_{zQ}$ (Hz)	r (Å)	$1/T_{zQ}$ (Hz)	r (Å)
V'	V β	2.55	46.0	3.0-3.8	4.3-40	2.6-2.9
	V γ 2	2.97	38.7	3.0-3.8	13-67	2.6-3.9
	L β	3.72	42.4	4.0-4.9	73-81	3.8-4.8
	V γ 1	3.88	40.4	3.7-4.7	38-55	3.7-4.7
	L δ 1	4.29	37.2	3.9-5.0	44-59	3.9-4.8
	L γ	4.35	44.6	4.3-5.3	61-64	4.2-5.2
	L δ 2	5.90	39.6	4.2-5.3	93-99	4.0-4.9
L'	L β	2.47	42.5	2.8-3.7	3.2-5.6	2.1-2.9
	L γ	3.83	44.8	4.0-4.8	52-70	3.8-4.7
	V γ 2	4.36	38.8	4.0-5.0	41-54	4.0-4.9
	L δ 1	4.68	37.3	4.4-5.4	48-61	4.3-5.0
	L δ 2	4.87	39.7	4.1-5.2	44-57	4.1-5.0
	V β	4.98	41.6	4.2-5.3	71-75	4.1-5.0
	V γ 1	6.46	40.5	4.9-5.9	61-60	4.7-5.7

If a three-dimensional structure is available, either from other sources as is the case here or based on an initial data fit as discussed above, the CSA orientations can be estimated³⁹ and combined with known CSA magnitudes⁴⁰. Here the X-ray structure was used to generate the required CSA orientations with the aid of the SIMMOL software⁴¹, and the MPACKAGES from Levitt's group. The resulting CSA orientations and other relevant parameters employed in our simulations are provided in Table 3-6.

Table 3-6 CSA parameters used for simulation of the examined ^{13}C - ^{13}C distances. The orientations were estimated using SIMMOL software package and MPACKAGES from Levitt et al. The relationships between the structural elements and CSA tensor orientations for side-chain carbons were obtained from Veeman.³⁹ The magnitudes of the CSA tensors were approximated by free amino acid ⁴²values from Ye et al.⁴⁰ (* marks missing values, assumed same as V_β).

Atom-1	CSA parameters			Atom-2	CSA parameters		
	$\delta(\text{ppm})$	η	$\Omega_{\text{PM}}(^{\circ})$		$\delta(\text{ppm})$	η	$\Omega_{\text{PM}}(^{\circ})$
L'	-67.6	0.99	(40,128,122)	L_β	24.0	0.92	(33,160,-149)
			(29,118,157)	L_γ^*	11.3	0.91	(-84,87,-88)
			(118,63,131)	$V_{\gamma 2}$	-15.3	0.0	(-49,102,-84)
			(-138,74,-151)	$L_{\delta 1}$	-20.0	0.0	(173,132,158)
			(-156,47,-126)	$L_{\delta 2}$	-20.0	0.0	(27,138,47)
			(104,50,130)	V_β	11.3	0.91	(148,89,-28)
			(101,53,132)	$V_{\gamma 1}$	-15.3	0.0	(-6,12,7)
V'	68.3	1.00	(160,33,90)	V_β	11.3	0.91	(119,94,-13)
			(156,64,114)	$V_{\gamma 2}$	-15.3	0.0	(-66,64,-60)
			(-100,23,-47)	L_β	24.0	0.92	(-49,48,-170)
			(137,25,105)	$V_{\gamma 1}$	-15.3	0.0	(-41,26,48)
			(-130,55,-50)	$L_{\delta 1}$	-20.0	0.0	(-170,95,-58)
			(-132,35,-4)	L_γ^*	11.3	0.91	(138,88,-75)
			(57,147,20)	$L_{\delta 2}$	-20.0	0.0	(-109,19,120)

Using this information, we performed the final two series of simulations that included the second order terms, the results of which are listed in Table 3-7. Again the reliability of the URF model is compared to a free-fit approach, analogous to the procedure described above. Compared to the zero-order fit results from Table 3-4, there is a general (and significant) improvement of both the determined distance and the quality of fits. This is true in both the strong and weak-coupling regimes, and in particular for the 'free fit' approach, yielding results

that compare well to the X-ray distances, as shown in Fig. 3-8. Further, the improved quality of these simulations permits us to address a few important points.

Table 3-7 Calculated ^{13}C - ^{13}C internuclear distances in N-Ac-VL, using the unique set of orientations given in Table 3-6 based on the MMFT-model with 2nd order terms and a free-fit T_{ZQ} .

Atoms		X-ray distance r (Å)	Model 1 - URF		Model 2 - Free-fit	
			$1/T_{ZQ}$ (Hz)	r (Å)	$1/T_{ZQ}$ (Hz)	r (Å)
Valine	V β	2.55	46.0	3.2	9.5	2.6
	V γ 2	2.97	38.7	3.4	7.4	3
	L β	3.72	42.4	4.1	73.5	4
	V γ 1	3.88	40.4	3.8	44.4	3.9
	L δ 1	4.29	37.2	4.6	49.8	4.6
	L γ	4.35	44.6	4.6	76.3	4.4
	L δ 2	5.90	39.6	4.4	102.0	4.7
Leucine	L β	2.47	42.5	3.4	6.1	2.55
	L γ	3.83	44.8	4.2	58.5	4.2
	V γ 2	4.36	38.8	4.6	50.2	4.6
	L δ 1	4.68	37.3	4.7	51.3	4.6
	L δ 2	4.87	39.7	4.7	51	4.6
	V β	4.98	41.6	4.8	82.0	4.6
	V γ 1	6.46	40.5	5.5	61.3	5.3

One instance where the importance of using the proper CSA orientations is highlighted is in the R^2W profiles describing the polarization transfer from the leucine carbonyl carbon to the δ -carbons [i.e., L_C -L δ 1 (4.67Å) and L_C -L δ 2 (4.87Å)]. Since the L_C -L δ 1 distance is 0.2 Å shorter, one would expect the (maximum) polarization transfer to be larger than for the L_C -L δ 2 pair. However, as can be seen in Fig. 3-5a, the actual profiles show the reverse pattern. Our data fits attribute this to the differences in the relative orientation of the CSA tensors.

As an illustration of typical results in both the strong and weak coupling regimes, we examine the polarization transfer in the cases L_C -L β (2.54Å) and L_C -V β (4.98Å). Figures 3-9 and 3-10 show the data fits obtained in the various MMFT-based analyses, where both the internuclear distance r and T_{ZQ}^{-1} were employed as free-fit parameters ('model 2'). In Fig. 3-9a and 3-10a the experimental cross-peak intensities (represented by ●●●) are compared to results obtained using the zero order Hamiltonian *with* free-fit optimized ZQ relaxation (solid line). In Fig. 3-9b and 3-10b, the same set of simulations is performed with the effective Hamiltonians

instead of the zero order Hamiltonian. As can also be seen in the RMSD plots [panels (c) and (d)], the improvement of the fit is accompanied by a shift of the optimum T_{ZQ} and distances (closer to the x-ray values).

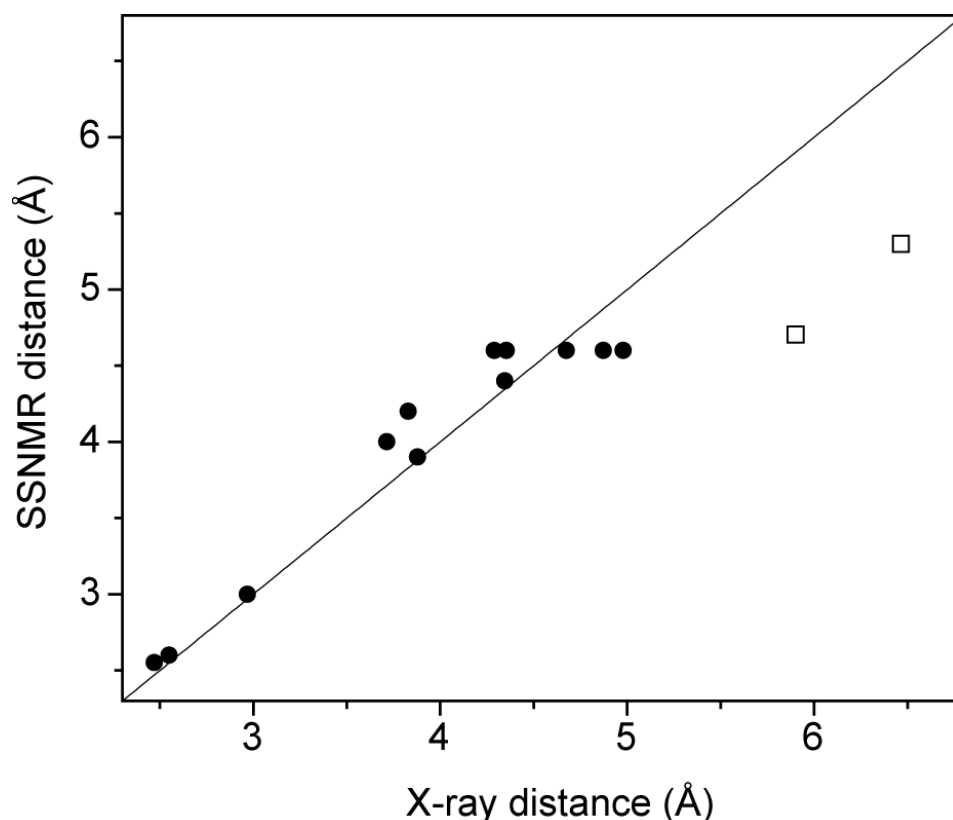


Figure 3-8 Comparison between the x-ray structure and measured SSNMR distances, obtained using effective Hamiltonians with estimated CSA orientations, and free-fit optimization of both the internuclear distance and the zero-quantum relaxation ('model 2'). Open squares indicate distances affected by intermolecular multi-spin effects (see text).

Figures 3-9 and 3-10 also show the same fits in the absence of any relaxation, T_{zq} (represented by grey ----). Remarkably, for shorter distances (2.5-3.0 Å) the data is reproduced quite well without any relaxation, in line with the observation that simulations of these short distances fit best when a ZQ relaxation is used that is significantly *smaller* than suggested by the URF calculation. This apparent disagreement with the shorter distances might be attributed to the breakdown of the URF model in the strong coupling regime, i.e. the random fields at the individual spin sites may be correlated at least in the strong coupling regime (2.5-3.0 Å). In

general, the local fields at any given carbon spin site originates from its interaction with the surrounding protons in addition to its own interaction with the external magnetic field (say the isotropic and anisotropic chemical shift interactions). When the separation between the two carbons decrease, the local fields become correlated, which, for instance, may be associated with efficient spin diffusion among the protons. Consequently, the URF-based ZQ relaxation rate seems to overestimate the damping observed under R^2 conditions in the strong coupling regime. By contrast, in the weak-coupling regime the two line broadening mechanisms (residual ^{13}C - ^1H interactions and homonuclear ^{13}C - ^{13}C recoupling due to R^2 condition) seem to be uncorrelated and independent of one another, thereby resulting in a ZQ relaxation rate similar to the URF estimate.

In the extreme weak-coupling limit (long distances), there is a significant contribution from intermolecular interactions with equivalent spins in surrounding molecules (in addition to the *intramolecular* interaction of interest). This is reflected in all the models, resulting in large discrepancies for distances exceeding 6 Å (indicated as open squares in Fig. 3-8). In spite of the dilution (9% in our case) the residuals from short *intermolecular* contacts make the weaker *intramolecular* couplings (<40Hz) appear substantially stronger. To estimate the magnitude of this effect, appropriate two and three spin systems were simulated numerically using SPINEVOLUTION⁴² and the resulting profiles were combined using a weighted average based on isotopic dilution. For example, in the case of the L_C - $\text{V}_{\gamma 1}$ *intramolecular* dipolar coupling (corresponding to 28Hz, or 6.46Å), the (diluted) presence of two stronger couplings due to *intermolecular* contacts (98 Hz / 4.26 Å and 45 Hz / 5.51 Å) should result in an effective coupling of ~40 Hz (5.7 Å). This apparent ‘shortening’ of the longest distances is clearly seen in Fig. 3-8. Since knowledge of intermolecular contacts corresponding to the *intramolecular* distances of interest are not available *a priori* for an unknown structure, caution should be exercised while fitting such long distances, especially in undiluted samples. These effects are however characteristic only of small molecules and should in principle be minimal in larger (bio) molecules wherein the probability of encountering such short intermolecular contacts is remote.

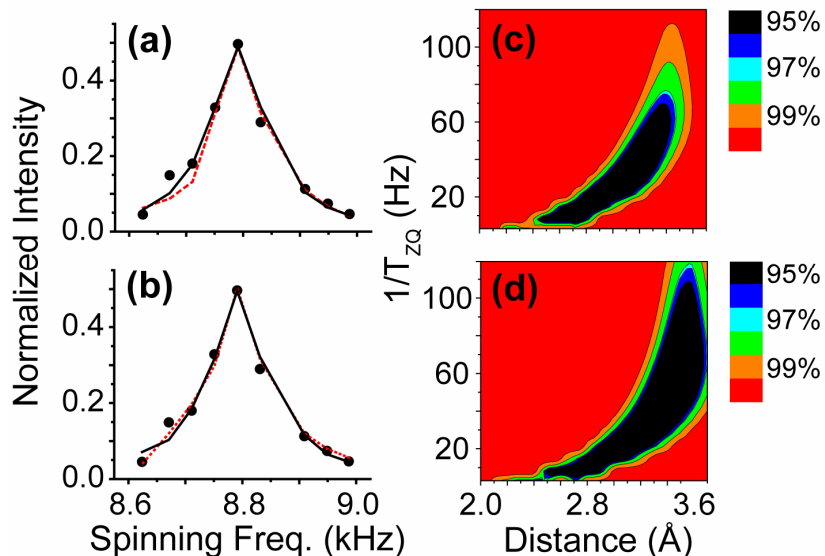


Figure 3-9 Simulations and experimental results illustrating the separate contributions of the higher order corrections and the ZQ parameters on the exchange dynamics. The results presented here correspond to the strong coupling, L_C-L_β (2.47\AA X-ray distance). In (a) the experimental data ($\bullet\bullet\bullet$) is fit using the zero order Hamiltonian both with (solid lines, $T_{ZQ} = 63\text{ms}$, $r = 2.85\text{\AA}$) and without relaxation ((---) , $r = 2.2\text{\AA}$). In (b) the experimental data is fit using the effective Hamiltonians both with (solid line, $T_{ZQ} = 165\text{ms}$, $r = 2.55\text{\AA}$) and without relaxation ((---) , $r = 2.3\text{\AA}$). Panels (c) and (d) show the contour plots for the simulations including relaxation, for the zero order and effective Hamiltonian respectively (contours indicate 95-99% confidence intervals).

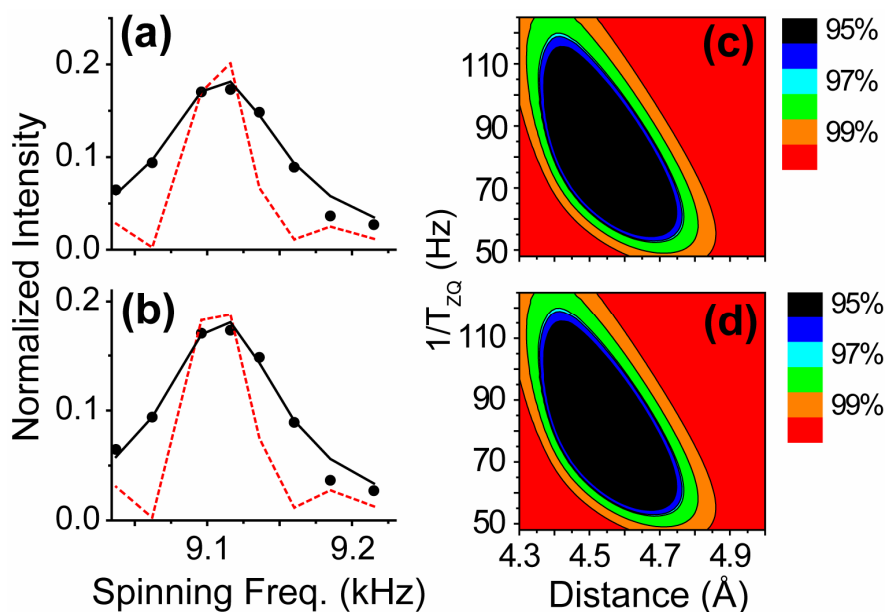


Figure 3-10 Simulations and experimental results illustrating the separate contributions of the higher order corrections and the ZQ parameters on the exchange dynamics. The results presented here

correspond to the weak coupling L_C-V_β (4.98Å x-ray distance). In (a) the experimental data (●●●) is fit using the zero order Hamiltonian both with (solid lines, $T_{ZQ}=12$ ms, $r=4.5$ Å) and without relaxation ((----), $r=3.8$ Å). In (b) the experimental data is fit using the effective Hamiltonians both with (solid line, $T_{ZQ}=12$ ms, $r=4.6$ Å) and without relaxation ((----), $r=4.0$ Å). Panels (c) and (d) show the contour plots for the simulations including relaxation, for the zero order and effective Hamiltonian respectively (contours indicate 95-99% confidence intervals).

Another way that other spins affect a particular distance measurement is when multi-spin effects take place due to non-equivalent spins. This occurs when, at a certain MAS rate, a single carbonyl is transferring magnetization to two different aliphatic carbons. Such a scenario is not addressed in our analysis, but despite the overlap of various resonance profiles (see Fig. 5), the distance measurements seem generally reliable. However, these effects could explain why some of those resonance profiles do not fit well. The small effect on the accuracy of the distance measurement in cases as the one presented above is encouraging for the intended application of the MMFT treatment to larger bio-molecules, where spectral overlap is not uncommon. In this context, it is important to note that multi-spin effects on a particular carbon-carbon (e.g. carbonyl-aliphatic) pair requires not just proximity of the resonances in the spectrum, but also a reasonable proximity of the corresponding nuclei in space. Distant sites in a large bio-molecule having similar resonances would still be independent for the purposes of the presented analysis.

Although the ZQ relaxation rate in model-2 is employed as a free-fit parameter in the simulations, it does in fact correspond to actual spin interactions neglected in the definition of the spin system and should not be mistaken as a random variable employed to fit the experimental data. A formal understanding of the ZQ relaxation (or damping) behavior requires a treatment incorporating at least four spins (two carbons and two protons) and will be discussed elsewhere. In contrast to the existing fictitious spin operator formalism, the MMFT approach does provide a general framework for describing multi-exponential relaxation processes in ZQ experiments. In the ZQ subspace [Eq. (17)], the two-spin ZQ polarizations $\hat{\Phi}_0^{(k)}(11,t)$ could in principle be assigned with three separate decay constants $\left[T_{zq}^{(k)}\right]^{-1}$ corresponding to the rank (represented by k) of the spin polarizations. A formal treatment to explain multi-exponential decay processes should address the various contributions to the

relaxation mechanism. Work along these lines requires a more sophisticated approach for describing relaxation in SSNMR, wherein the radiofrequency irradiation on protons during the recoupling period is included and will be addressed in future publications.

3.5. Conclusion

In summary the MMFT approach improves the accuracy of the ^{13}C - ^{13}C distance measurements in R^2W experiments for a wide range of distances. The analytical two-spin model provides a general framework for describing ZQ relaxation processes involving multiple decay rate constants. The ZQ relaxation rates estimated from the MMFT model are significantly lower than the best-fit values obtained from the fictitious spin operator approach and tend to give a less degenerate solution. The requirement for lower ZQ relaxation rates can be explained by the inclusion of higher order terms, dominated by the CSA-dipolar cross-terms that result in damping of the desired coherence. In the intermediate and weak-coupling regimes, the estimated ZQ relaxation rate from model-2 (free-fit of relaxation) is in good agreement with the URF model. However, in the strong coupling limit (say $< 3 \text{ \AA}$) the ZQ relaxation rates calculated from the URF model overestimate the actual relaxation thereby underlining the breakdown of the basic assumptions of the URF approach. In the strong coupling limit the local fields at the individual spin sites may be correlated through residual heteronuclear ^{13}C - ^1H dipolar interactions and homonuclear dipolar ^1H - ^1H interactions. For the sake of simplicity we have neglected any explicit contributions arising from these interactions in our description of the exchange dynamics. Still, our data fits result in accurate distances, with the few exceptions being in the form of inherent intermolecular and other multi-spin effects resulting in explainable and rather small deviations.

In combination with the effective Hamiltonians and the free-fit of the ZQ relaxation parameter, the MMFT model presented herein provides a convenient and reliable framework for extracting distances in uniformly ^{13}C , ^{15}N labeled solids both in the weak and strong coupling regimes. A formal theory quantifying the ZQ relaxation rate employed in the R^2W experiments will be presented in future publications.

3.6. Acknowledgements

This work was supported by grants from the National Institutes of Health (EB-001960, EB-003151, and EB-002026).

3.7. References

- (1) E. R. Andrew, A. Bradbury, and R. G. Eades, *Nature* **182**, 1659 (1958).
- (2) I. J. Lowe, *Phys. Rev. Lett.* **2**, 285 (1959).
- (3) S. R. Hartmann and E. L. Hahn, *Phys. Rev.* **128**, 2042 (1962).
- (4) A. Pines, M. G. Gibby, and J. S. Waugh, *J. Chem. Phys.* **59**, 569 (1973).
- (5) U. Haeberlen, *High-Resolution NMR in Solids: Selective Averaging*. (Academic Press, New York, 1976).
- (6) M. H. Levitt, in *Encyclopedia of Nuclear Magnetic Resonance*, edited by D. M. Grant, and R. K. Harris (John Wiley & Sons, 2002), Vol. 9, pp. 165.
- (7) A. E. Bennett, R. G. Griffin, and S. Vega, in *Solid State NMR IV: Methods and Applications of Solid-State NMR*, edited by B. Blumich (Springer-Verlag, Berlin, 1994), Vol. 33, pp. 1.
- (8) S. Dusold and A. Sebald, *Ann. R. NMR S.* **41**, 185 (2000).
- (9) R. Tycko, *Annu. Rev. Phys. Chem.* **52**, 575 (2001).
- (10) E. R. Andrew, S. Clough, L. F. Farnell, T. A. Gledhill, and I. Roberts, *Phys. Lett.* **21**, 505 (1966).
- (11) D. P. Raleigh, M. H. Levitt, and R. G. Griffin, *Chem. Phys. Lett.* **146**, 71 (1988).
- (12) M. H. Levitt, D. P. Raleigh, F. Cruzet, and R. G. Griffin, *J. Chem. Phys.* **92**, 6347 (1990).
- (13) P. R. Costa, B. Sun, and R. G. Griffin, *J. Magn. Reson.* **164**, 92 (2003).
- (14) R. Ramachandran, V. Ladizhansky, V. S. Bajaj, and R. G. Griffin, *J. Am. Chem. Soc.* **125**, 15623 (2003).
- (15) P. R. Costa, D. A. Kocisko, B. Q. Sun, P. T. Lansbury, and R. G. Griffin, *J. Am. Chem. Soc.* **119**, 10487 (1997).

- (16) F. Creuzet, A. McDermott, R. Gebhard, K. van der Hoef, M. B. Spijker-Assink, J. Herzfeld, J. Lugtenburg, M. H. Levitt, and R. G. Griffin, *Science* **251**, 783 (1991).
- (17) L. K. Thompson, A. E. McDermott, J. Raap, C. M. van der Wielen, J. Lugtenburg, J. Herzfeld, and R. G. Griffin, *Biochemistry* **31**, 7931 (1992).
- (18) K. V. Lakshmi, M. Auger, J. Raap, J. Lugtenburg, R. G. Griffin, and J. Herzfeld, *J. Am. Chem. Soc.* **115**, 8515 (1993).
- (19) A. E. McDermott, F. Creuzet, R. Gebhard, K. Vanderhoef, M. H. Levitt, J. Herzfeld, J. Lugtenburg, and R. G. Griffin, *Biochemistry* **33** (20), 6129 (1994).
- (20) P. T. F. Williamson, A. Verhoeven, M. Ernst, and B. H. Meier, *J. Am. Chem. Soc.* **125** (9), 2718 (2003).
- (21) L. Sonnenberg, S. Luca, and M. Baldus, *J. Magn. Reson.* **166**, 100 (2004).
- (22) T. Karlsson and M. H. Levitt, *J. Chem. Phys.* **109**, 5493 (1998).
- (23) M. Helmle, Y. K. Lee, P. J. E. Verdegem, X. Feng, T. Karlsson, J. Lugtenburg, H. J. M. de Groot, and M. H. Levitt, *J. Magn. Reson.* **140**, 379 (1999).
- (24) J. H. Shirley, *Phys. Rev. B* **4**, 979 (1965).
- (25) R. Ramachandran and R. G. Griffin, *J. Chem. Phys.* **122**, 164502 (2005).
- (26) J. H. V. Vleck, *Phys. Rev.* **33**, 467 (1929).
- (27) A. R. Edmonds, *Angular momentum in Quantum mechanics*, Third ed. (Princeton University Press, Princeton, New Jersey, 1974).
- (28) B. C. Sanctuary, *J. Chem. Phys.* **64**, 4352 (1976).
- (29) B. C. Sanctuary and T. K. Halstead, *Adv. Magn. Opt. Reson.* **15**, 79 (1990).
- (30) M. R. Aliev and V. T. Aleksanyan, *Optika Spectroscopia* **24**, 520 (1968).
- (31) M. R. Aliev and V. T. Aleksanyan, *Optika Spectroscopia* **24**, 695 (1968).
- (32) R. Ramesh and M. S. Krishnan, *J. Chem. Phys.* **114**, 5967 (2001).
- (33) P. J. Carroll, P. L. Stewart, and S. J. Opella, *Acta Cryst.* **C46**, 243 (1990).
- (34) F. Delaglio, S. Grzesiek, G. W. Vuister, J. Pfeifer, and A. Bax, *J. Biomol. NMR* **6**, 277 (1995).
- (35) A. Kubo and C. A. McDowell, *J. Chem. Soc. Faraday T. I* **84**, 3713 (1988).
- (36) D. Suter and R. R. Ernst, *Phys. Rev. B* **32**, 5608 (1985).
- (37) P. M. Henrichs, M. Linder, and J. M. Hewitt, *J. Chem. Phys.* **85**, 7077 (1986).

- (38) T. Karlsson, A. Brinkmann, P. J. E. Verdegem, J. Lugtenburg, and M. H. Levitt, *Solid State Nucl. Magn.* **14**, 43 (1999).
- (39) W. S. Veeman, *Prog. Nucl. Mag. Res. Sp.* **16**, 193 (1984).
- (40) C. Ye, R. Fu, J. Hu, L. Hou, and S. Ding, *Mag. Reson. Chem.* **31**, 699 (1993).
- (41) M. Bak, R. Schultz, T. Vosegaard, and N. C. Nielsen, *J. Magn. Reson.* **154**, 28 (2002).
- (42) M. Veshtort and R. G. Griffin, *J. Magn. Reson.* **178**, 248 (2006).

4. Spin dynamics in the modulation frame: Application to homonuclear recoupling in magic angle spinning solid-state NMR

Reproduced with permission from de Paëpe G., Lewandowski J.R., Griffin R.G. "Spin dynamics in the modulation frame: Application to homonuclear recoupling in magic angle spinning solid-state NMR" J. Chem. Phys. (2008) 128(12):124503. Copyright © 2008 American Institute of Physics.

4.1. Abstract

We introduce a family of solid state NMR pulse sequences that generalizes the concept of second averaging in the modulation frame and therefore provides a new approach to perform magic angle spinning dipolar recoupling experiments. Here, we focus on two particular recoupling mechanisms -- cosine modulated rotary resonance (CMpRR) and cosine modulated recoupling with isotropic chemical shift reintroduction (COMICS). The first technique, CMpRR, is based on a cosine modulation of the rf phase and yields broadband double-quantum (DQ) ^{13}C recoupling using > 70 kHz $\omega_{1,C}/2\pi$ rf field for the spinning frequency $\omega_r/2=10\text{--}30$ kHz and ^1H Larmor frequency $\omega_{0,H}/2\pi$ up to 900 MHz. Importantly, for $p \geq 5$, CMpRR recouples efficiently in the absence of ^1H decoupling. Extension to lower p values ($3.5 \leq p < 5$) and higher spinning frequencies is possible using low power ^1H irradiation ($< 0.25 \omega_r/2\pi$). This phenomenon is explained through higher order cross terms including a homonuclear third spin assisted recoupling (TSAR) mechanism among protons. CMpRR mitigates the heating effects of simultaneous high power ^{13}C recoupling and ^1H decoupling. The second technique, COMICS, involves low power ^{13}C irradiation that induces simultaneous recoupling of the ^{13}C DQ dipolar and isotropic chemical shift terms. In contrast to CMpRR, where the DQ bandwidth (~ 30 kHz at $\omega_{0,H}/2\pi = 750$ MHz) covers the entire ^{13}C spectral width, COMICS recoupling, through the reintroduction of the isotropic chemical shift, is selective with respect to the carrier frequency, having a typical bandwidth of ~ 100 Hz. This approach is intended as a general frequency selective method circumventing dipolar truncation (supplementary to R^2 experiments). These new γ -encoded sequences with attenuated rf requirements extend the applicability of homonuclear recoupling techniques to new regimes—high spinning and Larmor frequencies—and therefore should be of major interest for high resolution bio-molecular studies.

4.2 Introduction

In recent years, improvements in methodology, instrumentation, and sample preparation have significantly extended the applicability of high resolution solid-state NMR (SSNMR) to structural studies of large biological molecules – notably, to systems not amenable to solution NMR or diffraction studies such as amyloid fibrils and membrane proteins. A prominent part of this successful and expanding effort has been the development of dipolar recoupling techniques that permit the reintroduction of dipolar interactions attenuated by magic angle spinning (MAS). The presence of these couplings enables spectral assignments and subsequently structural studies based on measurement of ^{13}C - ^{13}C and ^{13}C - ^{15}N distances and torsion angles. However, most current structural applications are based on dipolar recoupling methods developed over the last ~20 years and therefore function most effectively at low to moderate MAS frequencies ($\omega_r/2\pi \leq 10$ kHz) and fields of ~12 T or lower ($\omega_{0,\text{H}}/2\pi \leq 500$ MHz, where $\omega_{0,\text{H}}$ is the ^1H Larmor frequency). In contrast, contemporary SSNMR structural experiments are moving rapidly to higher spinning and Larmor frequencies ($\omega_r/2\pi \sim 20$ -70 kHz and $\omega_{0,\text{H}}/2\pi = 700$ -900 MHz), and require an appropriate new methodology. The goal of this paper is to describe a new class of ^{13}C - ^{13}C homonuclear techniques that recouple efficiently the high B_0 field, high spinning frequencies regime. In particular, we introduce a class of techniques that perform ^{13}C - ^{13}C recoupling and ^1H decoupling with the application of the ^{13}C field alone.

4.3 Background

Spectral assignments are a prerequisite for performing quantitative structural measurements such as distances and torsion angles, which in turn constrain the structure of the molecule.¹⁻¹¹ Thus, multidimensional homonuclear (^{13}C - ^{13}C and ^{15}N - ^{15}N) and heteronuclear (primarily ^{13}C - ^{15}N) spectra were used in many cases to either partially or completely assign spectra of small peptides, microcrystalline proteins (up to 15 kDa), amyloid and membrane proteins.^{12,13} Most of these experiments used one of a variety of rotor synchronized techniques that require that the recoupling rf fields be a multiple, $n \geq 5$, of the spinning frequency ($\omega_{l,s} \geq 5\omega_r$) and that the decoupling field be at least three times larger than the recoupling field and therefore $\omega_{l,H} > 15\omega_r$. Clearly at high spinning frequencies ($\omega_r/2\pi \geq 20$ kHz), these requirements place

stringent demands on the integrity of the probe and significant sample heating can occur from both the recoupling and the decoupling.

In addition, several different approaches have been proposed to extract structural parameters during recoupling experiments. Initially, these efforts relied on methods for high precision measurements of ^{13}C - ^{13}C and ^{13}C - ^{15}N distances in spin pair labeled samples,^{3,14} with the goal of addressing specific mechanistic questions. This approach was very successful, continues to be used effectively, and will likely remain important in future experiments. More recently, many studies have exploited the idea of uniform ^{13}C , ^{15}N labeling¹⁵ or alternate ^{13}C labeling¹⁶ as approaches to determine multiple structural constraints from a single sample. Such uniform ^{13}C , ^{15}N labeling circumvents the labor intensive preparation of multiple samples and, in principle, permits multiple distances and torsion angles to be determined from a series of multidimensional experiments.^{17,18} Methods for accurate and precise measurements of both ^{13}C - ^{13}C and ^{13}C - ^{15}N distances in uniformly labeled peptides and proteins are in the literature and have been demonstrated to produce accurate ^{13}C - ^{13}C and ^{13}C - ^{15}N distance and torsion angle measurements.^{6,7,19} Using these methods, Jaroniec *et al.* showed that the structure of amyloidogenic peptides can be resolved at atomic detail at moderate fields ($\omega_{0,H}/2\pi \sim 500$ MHz) and spinning frequencies ($\omega_r/2\pi < 10$ kHz).^{7,8} Such high resolution structures are a direct consequence of the accurate distance measurements (tens of picometer accuracy) available via SSNMR dipolar recoupling.

An alternate approach to structure determination is to rely on spin diffusion and related experiments to estimate simultaneously multiple approximate distance restraints. While these experiments have led to the first structures of model proteins,¹ the available number of unambiguous distance restraints per residue was relatively small and therefore the resulting resolution lower than for systems of comparable size solved by solution NMR. The accurate distance and torsion angle measurement methods in solid-state NMR, successfully used for *de novo* structure determination of small systems, provide a powerful tool for refining these initial biomolecular structures. It is therefore desirable to develop new methods for assignments and accurate distance and torsion angle measurements especially at high fields and spinning frequencies in order to fully exploit the resolution and sensitivity enhancement necessary for proteins studies.

In this paper, we introduce a new family of solid state NMR pulse sequences that we believe are a step towards achieving this goal. The innovative approach presented here is based on a generalization of the concept of second averaging in the modulation frame²⁰⁻²³ (MF), which provides a versatile approach to MAS dipolar recoupling. Among the different recoupling mechanisms, we focus on two particular cases of double-quantum (DQ) homonuclear recoupling mechanisms. The first technique, cosine modulated rotary resonance (CMpRR), is based on a cosine modulation (CM) of the rf phase²⁴ and yields broadband DQ ¹³C recoupling at 10-30 kHz MAS frequencies and ¹H Larmor frequencies up to 900 MHz *without application of additional ¹H irradiation*.^{25,26} The second technique, cosine modulated recoupling with isotropic chemical shift reintroduction (COMICS), involves low power ¹³C irradiation that induces simultaneous recoupling of the ¹³C DQ dipolar and isotropic chemical shift terms. In contrast to CMpRR, where the DQ bandwidth (~30 kHz at 750 MHz) covers the entire ¹³C spectral width, COMICS recoupling, through the reintroduction of the isotropic chemical shift, is selective with respect to the carrier frequency, having a typical bandwidth of ~100 Hz. This approach is intended as a general frequency selective method circumventing dipolar truncation. COMICS supplements R^2 types of sequences,^{27,28} which work for sites with large chemical shift separation. These new γ -encoded sequences extend the applicability of homonuclear recoupling techniques to spinning frequencies $\omega_r/2\pi \geq 20$ kHz and high B_0 fields by decreasing the rf power requirement and allowing studies of biomolecules without compromising the sample integrity.

This manuscript is organized into six main sections. Section 4.4 introduces cosine phase modulation of the rf field (Section 4.4.1) and shows that it leads to a three frequency dependent problem under MAS (Section 4.4.2) which in turn allows us to rewrite the Hamiltonian in the interaction frame defined by the irradiation (Section 4.4.3) and to predict various first order recoupling conditions. Section 4.5 shows that the versatility of the simple CM scheme can be improved by introducing a *generalized CM-based recoupling scheme* involving a simultaneous phase, amplitude, and frequency modulation of the irradiation. As we shall see this leads to a *very versatile pulse sequence* that allows access to any recoupling mechanism outlined in Section 4.5. Section 4.6 discusses ¹³C DQ homonuclear recoupling mechanisms introducing cosine modulated rotary resonance (CMpRR) and cosine modulated recoupling with isotropic chemical shift reintroduction (COMICS). Section 4.7 is devoted to

an analysis of CMpRR recoupling, and the performance of this new pulse sequence is investigated through Average Hamiltonian Theory (AHT) analysis, simulations and experiments. Notably, this study shows that efficient broadband DQ ^{13}C recoupling can be obtained with no or very a weak ($< \omega_r/4$) ^1H CW irradiation.

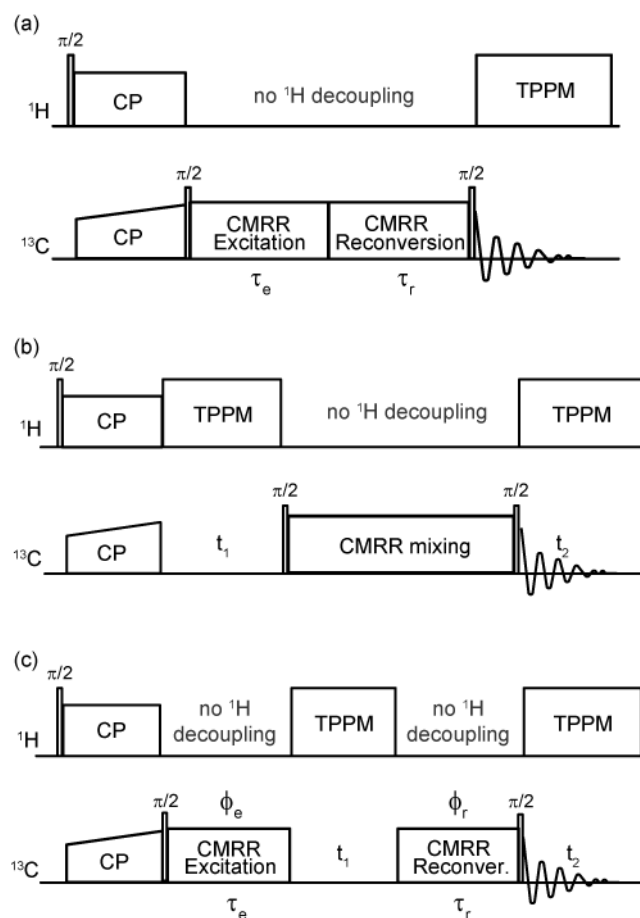


Figure 4-1 Pulse sequences used in this work for acquisition of (a) ^{13}C DQ coherence buildup, (b) ^{13}C SQ-SQ correlation experiments, and (c) ^{13}C DQ-SQ correlation experiments. In (a) and (c), the phase of the reconversion period ϕ_r is phase cycled to select for DQ coherences. Note that no ^1H decoupling is applied during the recoupling ^{13}C pulses unless specified otherwise. τ_e and τ_r refer to the excitation and reconversion times.

4.4 Modulation Frame and second averaging process

The use of phase alternated modulation (two pulse phase modulation - TPPM) in solid state NMR was introduced by Bennett *et al.* in 1995 in the context of heteronuclear decoupling.²⁰ The improved decoupling performance over simple continuous wave (CW) irradiation of this scheme and its variants²¹⁻²³ was mainly explained by a second averaging of the residual heteronuclear couplings. Subsequently, these principles were used to understand the performance of the CM pulse sequences (cosine phase modulated rf irradiation).²¹ The properties of the CM sequences were studied extensively and explained through the induced proton spin dynamics.²⁹ Interestingly, one of the optimal conditions that provides both heteronuclear decoupling (long T_2^* or reduced natural ^{13}C full width at half height) and long transverse dephasing times due to non-refocusable interaction³⁰ (T_2' or ^{13}C time decay during a spin-echo period) was obtained by matching a ^1H - ^1H HORROR recoupling condition in the modulation frame.²⁹

In this manuscript we generalize the concept of second averaging^{20-22,29} in the modulation frame and use the CM scheme to perform efficient DQ ^{13}C recoupling. Note that the theoretical framework presented here can be used to explore different decoupling and recoupling mechanisms and allows one to efficiently design pulse sequences for specific purposes.

For the readers' reference Fig. 4-1 presents the basic pulse sequence schemes used in this work for performing DQ ^{13}C - ^{13}C recoupling experiments using one of the techniques introduced in this manuscript -- CMpRR. Note that this specific sequence does not employ ^1H decoupling during the mixing periods. The approach used in CMpRR in regard to ^1H decoupling allows one to address two of important issues for DQ recoupling techniques applied to biological systems at high magnetic fields and high spinning frequencies: the increased rf heating and increased bandwidth, and thus extends the applicability of such experiments to this regime.

4.4.1 Cosine modulated phase irradiation: First order effect

In this section we review the concept of second averaging in the modulation frame (MF) in the presence of a cosine modulated rf field.²⁹ Such a scheme is depicted in Fig. 4-2 and can be

understood as follows. In Fig. 4-2a the rf field, with magnitude $\omega_1/2\pi$, oscillates around its mean value ϕ_0 , with an amplitude a (radian) and a frequency ω_c (kHz). Note that $\omega_l = -\gamma B_1$, where γ is the gyromagnetic ratio of the nucleus usually ^{13}C . For simplicity, in Fig. 4-2b we assume that $\phi_0 = 0$.

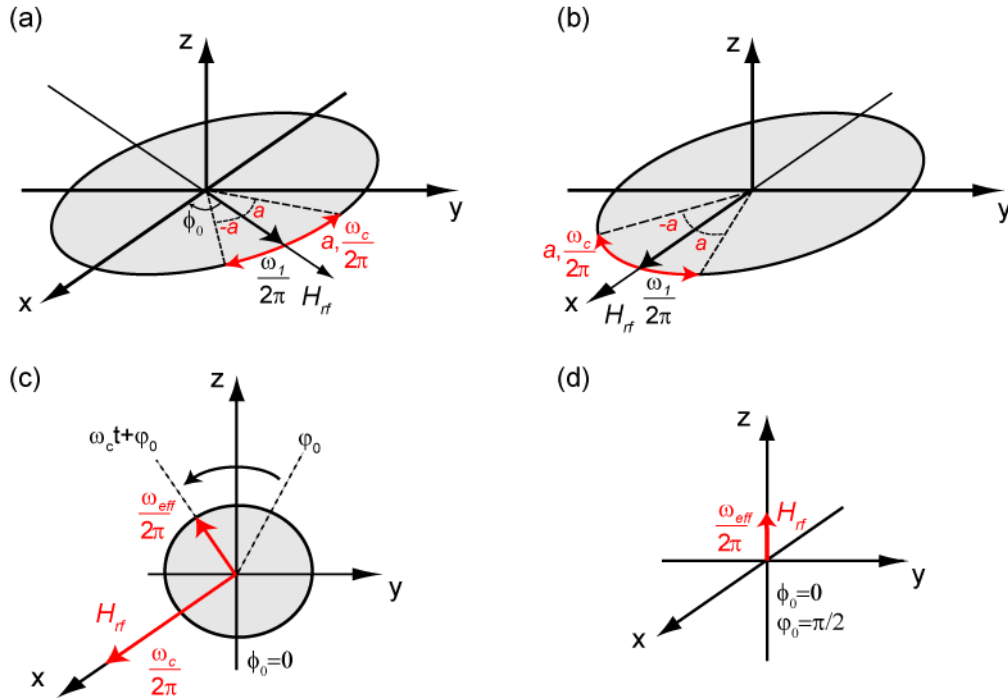


Figure 4-2 Schematic representation of a cosine modulated radio frequency phase modulation. In graphic (a) the rf Hamiltonian is represented as an oscillating field around the axis ϕ_0 in the xy-plane: $\omega_1/2\pi$ stands for the rf field strength, $\omega_c/2\pi$ for the frequency and a the amplitude of the phase modulation. In graphic (b), the mean axis of the irradiation is chosen to be the X-axis. Graphic (c) shows that under some very precise settings, the cosine modulated phase irradiation can be decomposed into two components: a CW component of strength $\omega_c/2\pi$ and a resonant audio field of strength $\omega_{eff}/2\pi$. In the Modulation Frame (MF), defined as the interaction frame of the first component, the resonant circular audio field appears static aligned with the axis ϕ_0 . Graphic (d) shows the static audio field in the MF (aligned with the Z-axis) for $\phi_0 = 0$ and $\phi_0 = \pi/2$.

The Hamiltonian for the radio frequency field can be written:

$$H_{rf} = \omega_1 \left\{ \sum_i S_x^i \cos(\phi(t)) + \sum_i S_y^i \sin(\phi(t)) \right\} \quad (1)$$

where $\phi(t)$ is the phase of the irradiation applied to the spins (S^i) that defines the recoupling scheme.

As previously reported²⁹, the cosine modulation (CM) of the phase can be written: $\phi(t) = a \cos(\omega_c t - \phi_0)$. For $\phi \leq 1.8$ radian, we can expand and truncate the expressions for sine and cosine as follows: $\cos(\phi) \approx 1 - \frac{\phi^2}{2!} + \frac{\phi^4}{4!}$ and $\sin(\phi) \approx \phi - \frac{\phi^3}{3!} + \frac{\phi^5}{5!}$. Following insertion into Eq. (1) we obtain (see Supporting Information Appendix A for details):

$$H_{rf} = \omega_1 \left[\begin{array}{c} 1 - \frac{a^2}{4} + \frac{a^4}{64} \\ - \left(\frac{a^2}{4} - \frac{a^4}{48} \right) \cos(2(\omega_c t - \phi_0)) \\ + \frac{a^4}{192} \cos(4(\omega_c t - \phi_0)) \end{array} \right] \sum_i S_x^i + \omega_1 \left[\begin{array}{c} \left(a - \frac{a^3}{8} + \frac{a^5}{192} \right) \cos(\omega_c t - \phi_0) \\ - \left(\frac{a^3}{24} - \frac{a^5}{384} \right) \cos(3(\omega_c t - \phi_0)) \\ + \left(\frac{a^5}{1920} \right) \cos(5(\omega_c t - \phi_0)) \end{array} \right] \sum_i S_y^i \quad (2)$$

Assuming that $a < 0.5$, Eq. (2) simplifies to:

$$H_{rf} = \omega_1 \left[1 - \frac{a^2}{4} \right] \sum_i S_x^i + \omega_1 \left[a \cos(\omega_c t - \phi_0) \right] \sum_i S_y^i \quad (3)$$

which illustrates that the CM scheme can be decomposed into a continuous wave (CW) field along the mean axis of the irradiation (here the X-axis) of amplitude $\omega_1 \left[1 - a^2/4 \right]$ and a transverse audio field of amplitude $\omega_1 a$ oscillating at the frequency ω_c . Note, that the linearly oscillating field can be viewed [Fig. 4-2c] as a superposition of two counter rotating circular fields rotating at $\omega_c/2\pi$ and $-\omega_c/2\pi$ respectively around the X-axis (the mean axis of the irradiation) and starting in the YZ plane at an angle ϕ_0 with respect to the Y-axis. When the strength of the CW components matches the modulation frequency ω_c , a resonance effect occurs leading to second averaging in the MF [Fig. 4-2c].

The harmonics of the oscillating fields in Eq. 2 (i.e. fields with frequencies $2\omega_c, 3\omega_c, \dots$), as well as the circular rotating component at $-\omega_c$ have a non negligible effect when the phase amplitude a becomes large. However, as we shall see in the Section 4, a *simultaneous phase and amplitude modulation* can circumvent the effect of the components at $2\omega_c, 3\omega_c$, etc.

Moreover, the effect of the circular rotating component at $-\omega_c$ can be suppressed when necessary with an *additional simultaneous frequency modulation* that selects only the positive circular component.

As we shall see in detail below, the generalized CM-based recoupling scheme considered here can always be decomposed into two contributions [Fig. 4-2c]: a CW component of strength $\omega_c/2\pi$ and a resonant circular audio field of strength $\omega_{eff}/2\pi$. As previously introduced, we define the MF,²⁹ as the frame rotating around the mean irradiation axis ϕ_0 at the frequency $\omega_c/2\pi$. In the MF, the rf Hamiltonian can be viewed as a static component of strength $\omega_{eff}/2\pi$ aligned along the ϕ_0 angle. In Fig. 4-2d we have assumed $\phi_0=\pi/2$, and hence the effective field is along the Z-axis.

4.4.2 Reduction to a single frequency problem

As stated above, the use of a *generalized CM-based recoupling scheme* in MAS experiments yields a problem dependent on three frequencies: $\omega_c/2\pi$, the rotor spinning frequency, $\omega_c/2\pi$ the strength of the CW component, and $\omega_{eff}/2\pi$ the strength of the resonant audio field.

Let us assume that we can find integers p_1, p_2, p_1', p_2' such that:

$$\frac{\omega_c}{2\pi} = \frac{p_2}{p_1} \left(\frac{\omega_r}{2\pi} \right) = p \left(\frac{\omega_r}{2\pi} \right) \quad (4)$$

$$\frac{\omega_{eff}}{2\pi} = \frac{p_2'}{p_1'} \left(\frac{\omega_r}{2\pi} \right) = p' \left(\frac{\omega_r}{2\pi} \right) \quad (5)$$

Where p_2/p_1 and p_2'/p_1' are irreducible ratios (coprime integers), and we assume that the three frequencies are commensurate. This permits us to reduce the problem to single frequency dependence and to simplify the description of the recoupling mechanism. In particular, Average Hamiltonian Theory can now be applied for a period $n\tau_r$, where n is the lowest common multiple of p_1 and p_1' , given that n is sufficiently small to ensure rapid convergence, and τ_r is a rotor period. With this assumption, the indices p and p' constrain the amplitudes of the CW and audio fields, respectively.

4.4.3 Spin Hamiltonian in the Interaction Frame

In this section we consider the influence of the generalized CM irradiation on the dynamics of the system governed by the internal spin Hamiltonian. We choose a system of $n_I I$ and $n_S S$ spins, respectively, where S represents the spins that are irradiated (here ^{13}C), and I the surrounding spins (here ^1H). For such systems, the internal Hamiltonian can be expressed in the doubly rotating frame as follows:

$$\begin{aligned} \mathbf{H} = & \sum_{i=1}^{n_S} \omega_{S,i} S_z^i + \sum_{j=1}^{n_I} \omega_{I,j} I_z^j + \sum_{i,j} \omega_{SI,ij} 2S_z^i I_z^j + \sum_{k<l} \omega_{SS,kl} \left[2S_z^k S_z^l - (S_x^k S_x^l + S_y^k S_y^l) \right] \\ & + \sum_{k<l} \omega_{II,kl} \left[2I_z^k I_z^l - (I_x^k I_x^l + I_y^k I_y^l) \right] \\ & + \omega_1 \left\{ \cos(\phi) \sum_{i=1}^{n_S} S_x^i + \sin(\phi) \sum_{i=1}^{n_S} S_y^i \right\} \end{aligned} \quad (6)$$

In Eq. (6) $\omega_{S,i}$ and $\omega_{I,j}$ account for the resonance offsets and chemical shift tensor of the S^i (^{13}C) and I^j (^1H) spins, respectively. $\omega_{SI,ij}/2\pi$ is the magnitude of the heteronuclear dipolar coupling between spin S^i and spin I^j , and $\omega_{SS,kl}/2\pi$ and $\omega_{II,kl}/2\pi$ the magnitudes of the homonuclear $^{13}\text{C}_k$ - $^{13}\text{C}_l$ and $^1\text{H}_k$ - $^1\text{H}_l$ couplings, respectively. Note that unless specified otherwise there is no ^1H decoupling applied. The influence of additional ^1H irradiation will be discussed at the end of this publication.

The spin system Hamiltonian can be rewritten using spherical tensor notation as (see Supporting Information Appendix B for details):

$$\begin{aligned} \mathbf{H} = & \sum_{i=1}^{n_S} \left(\omega_{S,i} + \sum_{j=1}^{n_I} \omega_{SI,ij} 2T_{I,10}^j \right) T_{S,10}^i + \sum_{k<l} \sqrt{6} \omega_{SS,kl} T_{SS,20}^{kl} \\ & + \sum_{j=1}^{n_I} \omega_{I,j} T_{I,10}^j + \sqrt{6} \sum_{k<l} \omega_{II,kl} T_{II,20}^{kl} \\ & + \omega_1 \left\{ \sum_{i=1}^{n_S} \left(\frac{T_{S,1-1}^i - T_{S,11}^i}{\sqrt{2}} \right) \cos(\phi) + \sum_{i=1}^{n_S} \left(\frac{T_{S,11}^i + T_{S,1-1}^i}{-i\sqrt{2}} \right) \sin(\phi) \right\} \end{aligned} \quad (7)$$

The rotation of the sample at the magic angle imposes time dependence (expression of the time dependent interactions can be found in Supporting Information Appendix D):

$$\omega_{\lambda,i(j)}(t) = \sum_{m=-2}^2 \omega_{\lambda,i(j)}^m \exp(-im\omega_r t) \quad (8)$$

Following the arguments in Section III A, we assume that the rf irradiation can be decomposed into a CW component and a resonant audio field, an assumption which we justify in the following section. In order to study the dynamics induced by this modulation scheme, it is convenient to rewrite the Hamiltonian in the rf interaction frame defined by the two field components (see Supporting Information Appendix E for details).³¹

The spherical tensor operator in this frame can be expressed as:

$$\left[T_{lq''}^\lambda \right] = e^{iq''\phi_0} \sum_{q'} \widetilde{T}_{lq'} e^{-iq'(\omega_{eff}t + \phi_0)} e^{-iq(\omega_c t + \phi_0 - \pi/2)} d_{q''q}^l \left(\frac{\pi}{2} \right) d_{q'q}^l \left(\frac{\pi}{2} \right) \quad (9)$$

where \widetilde{T}_{lq_2} is a spherical tensor operator in the tilted frame defined by a rotation around the mean irradiation axis ϕ_0 by an angle $(-\pi/2 + \phi_0)$:

$$\widetilde{T}_{lq'} = \sum_{q''} T_{lq''} e^{-iq''(\frac{\pi}{2} + \phi_0)} d_{q''q'}^l \left(\frac{\pi}{2} - \phi_0 \right) e^{iq'(\frac{\pi}{2} + \phi_0)} \quad (10)$$

Note that if take $\phi_0 = \pi/2$, we obtain:

$$\begin{aligned} \left[T_{lq''}^\lambda \right] &= e^{iq''\phi_0} \sum_{q'} e^{-iq'(\omega_{eff}t + \phi_0)} e^{-iq(\omega_c t)} d_{q''q}^l \left(\frac{\pi}{2} \right) d_{q'q}^l \left(\frac{\pi}{2} \right) T_{lq'}^\lambda \\ &= e^{iq''\phi_0} \sum_{q'} e^{-iq'(\omega_{eff}t + \phi_0)} e^{-iq(\omega_c t)} S_{q'',q,q'}^{spin,l} T_{lq'}^\lambda \end{aligned} \quad (11)$$

with $S_{q'',q,q'}^{spin,l} = d_{q''q}^l \left(\frac{\pi}{2} \right) d_{q'q}^l \left(\frac{\pi}{2} \right)$ representing the reduced spin scaling factor of the sequence when the interaction λ is transformed from the component q'' to the component q' through the component q (see Supporting Information Appendix C for details).

The angle ϕ_0 can be chosen arbitrarily. The choice of $\phi_0 = \pi/2$ has the advantage that the effective recoupling axis is parallel to the Z-axis of the laboratory frame every rf cycle τ_c . Consequently, the polarization transfer is longitudinal if the magnetization is prepared along the Z-axis of the laboratory frame. Using Eq. (11), we obtain:

$$\left[T_{l0}^\lambda \right] = \sum_{q'q} T_{lq'}^\lambda e^{-iq'(\omega_{eff}t + \phi_0)} e^{-iq(\omega_c t)} S_{0,q,q'}^{spin,l} \quad (12)$$

We can write the spin Hamiltonian in the double interaction frame:

$$\begin{aligned}
\tilde{\mathbf{H}} = & \overbrace{\sum_{i=1}^{n_S} \sum_{m,q,q'} \left(\omega_{S,i}^m + \sum_{j=1}^{n_I} \omega_{SI,ij}^m 2T_{I,10}^j \right) e^{-iq'\phi_0} S_{0,q,q'}^{spin,1} e^{-i\omega_r(m+pq+p'q')t} T_{S,1q'}^i}^{\boxed{1}} \\
& + \overbrace{\sqrt{6} \sum_{k<l} \sum_{m,q,q'} \omega_{SS,kl}^m e^{-iq'\phi_0} S_{0,q,q'}^{spin,2} e^{-i\omega_r(m+pq+p'q')t} T_{SS,2q'}^{kl}}^{\boxed{2}} \\
& + \overbrace{\sum_{j=1}^{n_I} \sum_m \omega_{I,j}^m e^{-im\omega_r t} T_{I,10}^j}^{\boxed{3}} + \overbrace{\sqrt{6} \sum_{k<l} \sum_m \omega_{II,kl}^m e^{-im\omega_r t} T_{II,20}^{kl}}^{\boxed{4}}
\end{aligned} \tag{13}$$

The first term $\boxed{1}$ in Eq. (13) accounts for the ^{13}C chemical shift tensor and the heteronuclear dipolar interaction. Note that in the absence of ^1H irradiation the two interactions transform identically under a given ^{13}C irradiation.³² The second term $\boxed{2}$ in Eq. (13) represents the ^{13}C dipolar interaction expressed in the interaction frame, and the two last terms $\boxed{3-4}$ account for the ^1H chemical shift tensor and the ^1H - ^1H dipolar interaction respectively.

The first two terms in Eq. (13) (terms involving ^{13}C spins) have the following type of phase dependency: $(m + pq + p'q')\omega_r$. First order recoupling is achieved when this phase factor is zero leading to either zero-quantum/single-quantum/double-quantum (ZQ/SQ/DQ) homonuclear dipolar recoupling (corresponding to the spherical operators $T_{SS,20}^{kl}$, $T_{SS,2\pm 1}^{kl}$, $T_{SS,2\pm 2}^{kl}$ respectively), or either isotropic chemical shift (CS) or chemical shift anisotropy (CSA) recoupling. The corresponding scaling factor is given by the coefficient $S_{0,q,q'}^{spin,l} = d_{0q}^l(\pi/2) d_{q',q}^l(\pi/2)$.

Figure 4-3a shows the map of (p, p') indices resulting in DQ and ZQ first order dipolar recoupling. The green lines represent DQ recoupling associated with a spatial component $m = 1$ and the black lines with a spatial component $m = 2$. The DQ recoupling conditions can be separated into three different areas. The middle area leads to a null scaling factor (dotted lines) and will not be considered further. To assist the reader we have numbered the different DQ recoupling branches with Roman numerals from I to VI. Recoupling condition I corresponds to $p' = 1/2$, condition II to $p'=1$, condition III to $p' = p-1$, condition IV to $p' = p-1/2$, condition V to $p' = p+1/2$ and condition VI to $p' = p+1$. Note that recoupling conditions I-II have a reduced

spin scaling factor two times larger than branches III-VI. The vertical brown and orange lines correspond to ZQ recoupling conditions $m = 1$ and $m = 2$ respectively.

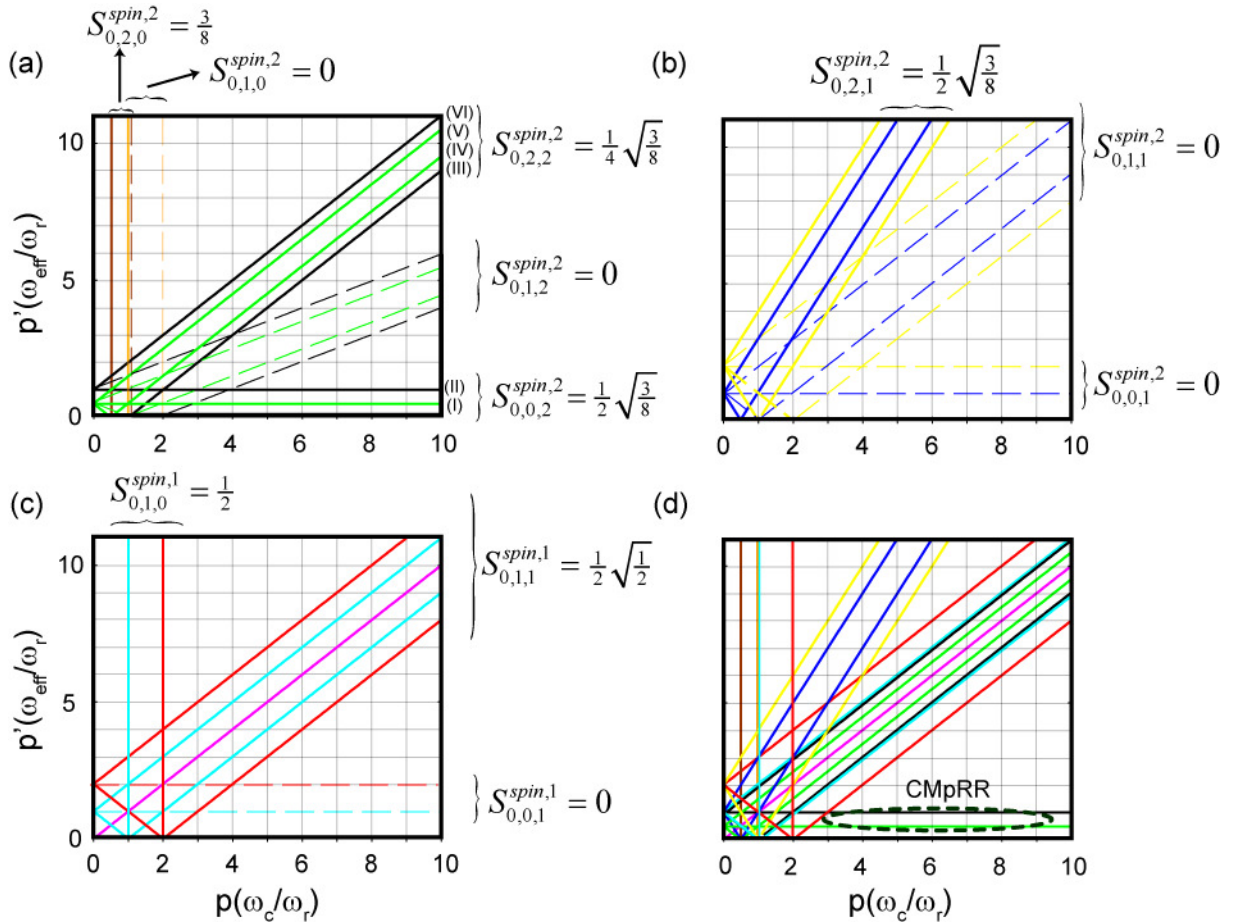


Figure 4-3 Two-field averaging process first order recoupling conditions for various interactions such as: (a) DQ $m = 1$ (green lines), $m = 2$ (black lines) and ZQ $m = 1$ (brown lines) and $m = 2$ (orange lines) ^{13}C dipolar terms, (b) SQ dipolar ^{13}C dipolar terms $m = 1$ (blue lines) and $m = 2$ (yellow lines), (c) isotropic (magenta line) and anisotropic $m = 1$ (cyan lines) and $m = 2$ (red lines) ^{13}C chemical shift interactions and (d) all previous interactions. For all the recoupling conditions shown in this figure, q and q' represent the successive components of the recoupled interactions during this two steps averaging mechanism. The reduced spin scaling factor of each recoupling branch is defined by $S_{0,q,q'}^{\text{spin},l} = d_{0q}^l(\pi/2)d_{q',q}^l(\pi/2)$. Note also that if no ^1H irradiation is applied during the ^{13}C recoupling pulses, heteronuclear interactions behave like CSA terms. The dashed lines represent branches with a null reduced spin scaling factor and are not considered in this study.

Figure 4-3b outlines the SQ homonuclear recoupling conditions. Note that only one set of conditions (blue and yellow solid lines) has a non-zero scaling factor. Figure 4-3c corresponds to CS and CSA recoupling. The dotted lines represent sequences with a zero scaling factor and can be neglected. It is worth noting that DQ recoupling conditions (III) and (VI) lead to the simultaneous recoupling of ^{13}C CSA interactions (see Fig. 4-3b for example). This will have a major impact on the practical applicability of these two conditions. Finally, Fig. 4-3d displays all the non-zero first order recoupling conditions.

Figure 4-3 can be used to predict various first order recoupling mechanisms and their associated scaling factors. However it is worth noting that higher order effects are not described in Figure 4-3 and that they can greatly influence the efficiency of the first order recoupling dynamics. Notably, second order recoupling can be large in the vicinity of first order recoupling.

So far we have outlined the framework for a comprehensive description of decoupling and recoupling mechanisms in solid state NMR using generalized CM schemes. The remainder of this article mainly focuses on DQ recoupling sequences and notably on two different regimes. The first regime corresponds to the area circled in dashed lines [see Fig. 4-3d] and appears isolated from other first order recoupling conditions. We refer to this regime as CMpRR “(where we retain only the p index specifying the cw component since the p' index is constant in this regime and equal to 0.5 or 1). CMpRR leads to a very efficient, broadband, recoupling mechanism without need for additional ^1H decoupling. The second regime, named cosine modulated recoupling with isotropic chemical shift reintroduction (COMICS), is shown in Fig. 4 (circled area), and corresponds to $p = 1/4$ and $p' = 1/4$. These settings produce a simultaneous reintroduction of DQ ^{13}C - ^{13}C interactions and ^{13}C CS interactions. As we shall see in the later part of the manuscript, this will lead to an extremely narrowband recoupling mechanism. COMICS is intended to provide a general alternative to R^2 ^{27,28} based experiments that are restricted to the nuclei with large chemical shift separation and are used to circumvent dipolar truncation problem in uniformly labeled systems.

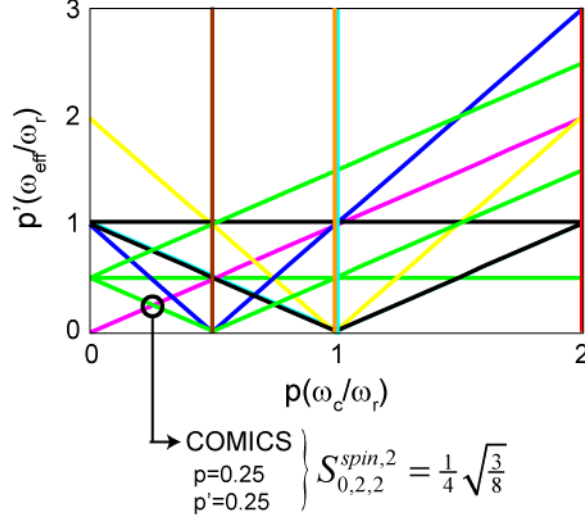


Figure 4-4 Expansion of the region with $p \leq 2$ and $p' \leq 3$ from Fig. 3(d) illustrating first order recoupling conditions. Black circle at $p = 0.25$, $p' = 0.25$ indicates a recoupling condition named COMICS. COMICS leads to simultaneous recoupling of the DQ dipolar and isotropic chemical shift interaction and results in extremely narrowband behavior. As in Fig. 3 green and black lines represent DQ recoupling conditions, brown and orange ZQ recoupling conditions, yellow and blue lines SQ recoupling conditions, red and cyan lines CSA recoupling and magenta line isotropic chemical shift recoupling condition.

4.5 Generalized CM schemes

4.5.1 Resonant second audio field averaging: second order effect

In this section, we investigate the dynamics induced by the resonant audio field component precessing at the frequency ω_c around the mean axis ϕ_0 (i.e. first harmonic). We also evaluate the influence of the other audio field components precessing at $-\omega_c$ (i.e. the counter rotating component), and $\pm 2\omega_c$, $\pm 3\omega_c$, $\pm 4\omega_c \dots$ (i.e. higher order harmonics).

Following the previous paragraph, we define the interaction frame by the two indices p and p' and express the effective rf Hamiltonian in this frame [Eqs. (4) and (5)]:

$$\tilde{\mathbf{H}}_{r.f.} - A = \sum_{i=1,2} \left[\begin{array}{l} \overbrace{\left[\omega_1 \cos(\phi - \phi_0) - \omega_c \right] \left[\frac{-T_{S,11}^i e^{-i(p'\omega_c t + \phi_0)} + T_{S,1-1}^i e^{i(p'\omega_c t + \phi_0)}}{\sqrt{2}} \right]}^{\text{[1]}} \\ + \overbrace{\left[\omega_1 \sin(\phi - \phi_0) \sin(\omega_c t) - \omega_{eff} \right] T_{10}^i}^{\text{[2]}} \\ + \omega_1 \sin(\phi - \phi_0) \cos(\omega_c t) \overbrace{\left[\frac{i(T_{S,11}^i e^{-i(p'\omega_c t + \phi_0)} + T_{S,1-1}^i e^{i(p'\omega_c t + \phi_0)})}{\sqrt{2}} \right]}^{\text{[3]}} \end{array} \right] \quad (14)$$

with $A = \omega_c \left[\frac{-T_{S,11}^i e^{-i(p'\omega_c t + \phi_0)} + T_{S,1-1}^i e^{i(p'\omega_c t + \phi_0)}}{\sqrt{2}} \right] + \omega_{eff} T_{10}^i$.

Assuming $\phi_0 = \pi/2$, we expand the cosine and sine functions for $a \ll 1$ and obtain:

$$\tilde{\mathbf{H}}_{r.f.} - A = \sum_{i=1,2} \left[\begin{array}{l} \overbrace{\left[\omega_1 \left(1 - \frac{a^2}{4} + \frac{a^4}{64} \right) - \omega_c \right] \left[\frac{-T_{S,11}^i e^{-i(p'\omega_c t + \phi_0)} + T_{S,1-1}^i e^{i(p'\omega_c t + \phi_0)}}{\sqrt{2}} \right]}^{\text{[1]}} \\ + \overbrace{\left(\omega_1 \right) \left(a - \frac{a^3}{8} + \frac{a^5}{192} \right) \sin^2(\omega_c t) T_{10}^i - \omega_{eff} T_{10}^i}^{\text{[2]}} \\ + \frac{\omega_1}{2} \overbrace{\left(a - \frac{a^3}{8} + \frac{a^5}{192} \right) \sin(2\omega_c t) \left[\frac{i(T_{S,11}^i e^{-i(p'\omega_c t + \phi_0)} + T_{S,1-1}^i e^{i(p'\omega_c t + \phi_0)})}{\sqrt{2}} \right]}^{\text{[3]}} \\ + \overbrace{\left(\omega_1 \right) \left(\frac{a^2}{4} - \frac{a^4}{48} \right) \cos(2\omega_c t) \left[\frac{(-T_{S,11}^i e^{-i(p'\omega_c t + \phi_0)} + T_{S,1-1}^i e^{i(p'\omega_c t + \phi_0)})}{\sqrt{2}} \right]}^{\text{[4]}} \\ + \overbrace{\left(\omega_1 \right) \left(\frac{a^3}{24} - \frac{a^5}{384} \right) \sin(3\omega_c t) \sin(\omega_c t) T_{10}^i}^{\text{[5]}} \\ - \overbrace{\left(\omega_1 \right) \left(\frac{a^3}{24} - \frac{a^5}{384} \right) \sin(3\omega_c t) \cos(\omega_c t) \left[\frac{i(T_{S,11}^i e^{-i(p'\omega_c t + \phi_0)} + T_{S,1-1}^i e^{i(p'\omega_c t + \phi_0)})}{\sqrt{2}} \right]}^{\text{[6]}} \end{array} \right] \quad (15)$$

Using first order AHT, applied over a period $n\tau_r$, we find that only the two first terms of the Eq. (15) yield a non-zero contribution. The interaction frame is properly defined if:

$$\omega_c = \left(1 - \frac{a^2}{4} + \frac{a^4}{64}\right) \omega_1 = p \omega_r \quad (16)$$

$$\omega_{eff} = \omega_1 \frac{1}{2} \left(a - \frac{a^3}{8} + \frac{a^5}{192} \right) = p' \omega_r \quad (17)$$

The two last equations link the rf amplitude and phase (ω_l , a) to the indices (p , p').

The third term of Eq. (15) has a $2\omega_c$ dependency and represents the counter rotating component of the audio field ($-\omega_c$) expressed in the interaction frame. The fourth term represents a $2\omega_c$ -dependent term arising from the expansion of $\omega_l \cos(\phi)$. The fifth and sixth terms represent the $3\omega_c$ and $5\omega_c$ dependent terms coming from the expansion of $\omega_l \sin(\phi)$.

We can easily verify that if Eq. (16) and Eq.(17) are satisfied, then the rf Hamiltonian vanishes to first order, validating the definition of the interaction frame. In particular, the first order approximation is sufficient (see below) to describe the recoupling regimes I and II, but fails to properly describe the recoupling conditions III, IV, V, VI and COMICS. In the latter regimes, the second order contribution of terms [\[3\]](#) and [\[4\]](#) is non-negligible. In the following sections, we investigate the extension of the previous description to all the recoupling conditions.

4.5.2 Generalized cosine modulated recoupling schemes: phase and amplitude rf modulation

4.5.2.1 General description

The simplest approach to eliminate the contribution of unwanted terms in Eq. (15) is to define the recoupling scheme as follows:

$$\begin{cases} \phi = \phi_0 + \arctan\left(\frac{2p' \cos(p\omega_r t - \phi_0)}{p}\right) \\ \omega_1 = p\omega_r \left[1 + \left(\frac{2p'}{p} \cos(p\omega_r t - \phi_0)\right)^2 \right]^{\frac{1}{2}} \end{cases} \quad (18)$$

With this scheme, the magnitude of the CW field is constant *at all times*, equal to $p\omega_r$, and the magnitude of the oscillating field $\omega_c = 2p'\omega_r$, which yields the following relations:

$$\begin{cases} \omega_1 \cos(\phi - \phi_0) = p\omega_r \\ \omega_1 \sin(\phi - \phi_0) = 2p'\omega_r \cos(p\omega_r t - \phi_0) \end{cases} \quad (19)$$

With the scheme defined in Eq. (18) and assuming $\phi_0 = \pi/2$, we can rewrite Eq. (15) as follows:

$$\tilde{\mathbf{H}}_{r.f.} - A = \sum_{i=1,2} \left[\begin{array}{l} \overbrace{\left[p\omega_r - \omega_c \right]}^{[1]} \left[\frac{-T_{S,11}^i e^{-i(p'\omega_r t + \phi_0)} + T_{S,1-1}^i e^{i(p'\omega_r t + \phi_0)}}{\sqrt{2}} \right] \\ + 2p'\omega_r \sin^2(\omega_c t) T_{10}^i - \omega_{eff} T_{10}^i \\ + p'\omega_r \sin(2\omega_c t) \left[\frac{i(T_{S,11}^i e^{-i(p'\omega_r t + \phi_0)} + T_{S,1-1}^i e^{i(p'\omega_r t + \phi_0)})}{\sqrt{2}} \right] \end{array} \right] \quad (20)$$

The expression for the rf Hamiltonian in the interaction frame is thus simplified -- in particular, terms [4], [5] and [6] disappear. The contribution of these terms disappear to the first order since $\omega_c = p\omega_r$ and $\omega_{eff} = p'\omega_r$.

The contribution of the third term [3'] (counter rotating audio field) to the residual effective field appears to the second order,

$$[3'] \otimes [3'] = \sum_i \frac{\omega_r}{4} \left[\frac{(p')^3}{(p'-2p)(p'+2p)} \right] T_{10}^{(i)} \quad (21)$$

For recoupling conditions I and II, we find:

$$\begin{aligned} [3'] \otimes [3'] &\stackrel{\Downarrow}{=} \sum_{p'=p_0'} \frac{\omega_r}{4} \left[\frac{(p_0')^3}{(p_0'-2p)(p_0'+2p)} \right] T_{10}^{(i)} \\ &\rightarrow - \sum_i \frac{\omega_r}{2^7} \frac{1}{p^2} T_{10}^{(i)} \end{aligned} \quad (22)$$

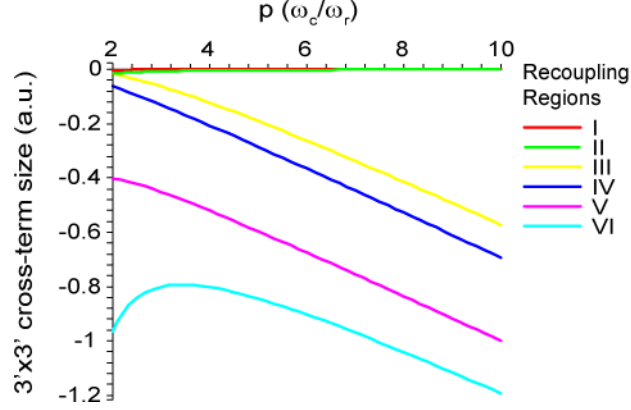


Figure 4-5 Relative size of the second order effect (in arbitrary units) induced by the counter rotating component $\boxed{3'}$ with itself in the Modulation Frame for the six different CM recoupling regimes (Eq. (21-23)). Note that for the regimes I and II (red and green lines respectively) the cross-term contribution is negligible. Regimes other than I and II require compensation for the effect of the counter rotating field, which could be achieved by appropriate frequency modulation (see Sec. III C).

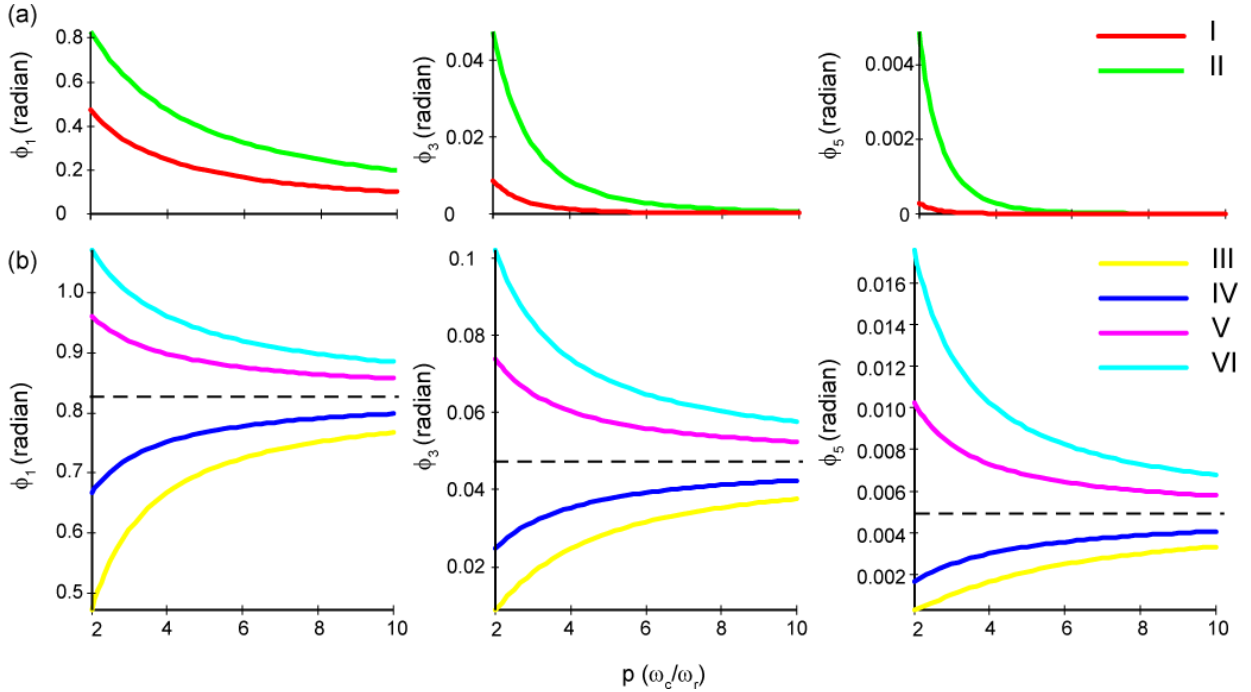


Figure 4-6 Fourier series decomposition (ϕ_1, ϕ_3, ϕ_5) of the phase modulation ϕ as a function of the p index for: (a) recoupling regimes I-II (red and green lines respectively), and (b) recoupling conditions III-VI (yellow, blue, magenta and cyan lines respectively) defined in Eq. (18) and (30) respectively. Note that for recoupling conditions I and II the three first Fourier components tend towards zero and that ϕ_5 and ϕ_3 can be neglected for p ranging from 2 to 10. For recoupling conditions III to VI the three first Fourier components tend towards non-zero value as p increases.

For recoupling conditions III, IV, V and VI, we obtain:

$$\begin{aligned} \boxed{3'} \otimes \boxed{3'} &\stackrel{\text{III-VI}}{\equiv} \sum_{p'=p+p_0'} \frac{\omega_r}{4} \left[\frac{(p+p_0')^3}{(p_0'-p)(p_0'+3p)} \right] T_{10}^{(i)} \\ &\xrightarrow{p \rightarrow \infty} - \sum_i \frac{\omega_r}{12} p T_{10}^{(i)} = - \sum_i \frac{\omega_c}{12} T_{10}^{(i)} \end{aligned} \quad (23)$$

Equation (22) shows that the effect of the counter rotating field can safely be neglected for recoupling conditions I and II, but leads to substantial longitudinal contribution in other cases (see Fig. 4-5). One could try to compensate this effect by redefining an effective p'_{eff} index for recoupling conditions III-VI as follows:

$$p'_{eff} = p' + \frac{1}{4} \left[\frac{(p')^3}{(p'-2p)(p'+2p)} \right] \quad (24)$$

This would allow us to correctly predict the effective field corresponding to a given p and p' set of parameters, but would not avoid the higher order cross terms between term $\boxed{3'}$ and the internal interactions (^{13}C dipolar and ^{13}C CSA interactions) leading to a decrease in the recoupling efficiency.

4.5.2.2 DQ recoupling conditions I and II

The previous section demonstrated that Eq. (18) provides a sufficient description of recoupling conditions I and II. For these recoupling conditions, the phase modulation can easily be expanded in Fourier series as follows:

$$\phi = \phi_0 + \sum_k \phi_k \sin(k\omega_c t) \quad (25)$$

with

$$\phi_k = \frac{2^{k+1} p_0'^k}{kp^k \left(1 + \sqrt{1 + 4 \left(\frac{p_0'}{p} \right)^2} \right)^k} \approx \frac{2}{k} \left(\frac{p_0'}{p} \right)^k \left(1 - k \left(\frac{p_0'}{p} \right)^2 \right) \quad (26)$$

All of the ϕ_k terms tend towards zero when p increases for $p'_0 \in \{1/2; 1\}$. In particular, we find that $\phi_1 \sim \frac{2p'_0}{p}$, which is consistent with Section 3.1.

Figure 4-6a-b shows the three first Fourier components of the phase ϕ as a function of the index p for the recoupling regime I and II. This figure clearly illustrates that all the harmonics except the first can safely be neglected.

The expression of the rf amplitude can also be expanded in a Fourier series. Note that only the two first harmonics are contributing.

$$\omega_1 = \sum_k \omega_1^{(k)} \cos(k\omega_c t) \quad (27)$$

with

$$\begin{aligned} \omega_1^{(0)} &= \omega_r \frac{4p'_0}{\pi\lambda} \text{EllipticE}(\lambda) \\ &\approx p\omega_r \left(1 + \left(\frac{p'_0}{p} \right)^2 \right) \end{aligned} \quad (28)$$

where EllipticE represents an elliptic integral of the second kind and

$$\lambda = 2p'_0 / p \sqrt{1 + \left(\frac{4p'_0}{p} \right)^2}.$$

$$\begin{aligned} \omega_1^{(2)} &= \omega_r \frac{4}{3\pi\lambda p'_0} \left(p^2 \text{EllipticK}(\lambda) \right. \\ &\quad \left. - (p^2 + 2p'^0_0) \text{EllipticE}(\lambda) \right) \quad (29) \\ &\simeq -\omega_r \left(\frac{p'^0_0}{p} \right) \end{aligned}$$

where EllipticK is an elliptic integral of the first kind.

Figure 4-7 shows the deviation of the exact amplitude modulation that should be applied [see Eq. (18)] with respect to its mean value $\omega_1^{(0)}$ as a function of the p index and the fraction of the cycle time τ_c . For the recoupling condition I, Fig. 4-7a shows that the deviation is less than 7% of the spinning frequency for $p > 3.5$, and that it can be correctly approximated by a cosine phase modulation of constant rf amplitude. On the contrary, recoupling condition II shows wider deviations that imply that one must employ the exact scheme defined by Eq. (18).

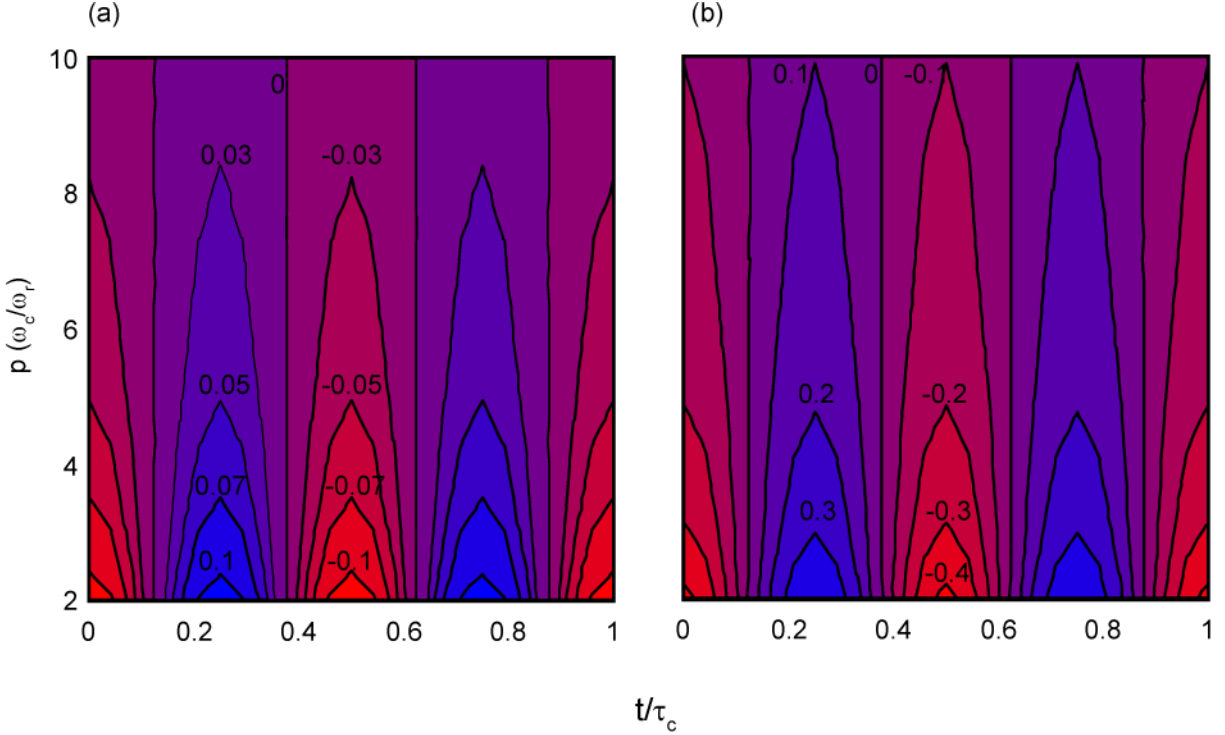


Figure 4-7 Contour plots of the periodic time dependent part of the rf field strength as a function of the fraction of the cycle time and the p index for recoupling regime I in (a), and II in (b). The contour levels indicate the rf field deviation in units of spinning frequency.

In the next section, we introduce a new scheme that suppresses the $\boxed{3'}$ term of the effective rf Hamiltonian [Eq. (20)] and thus extends the previous description to all points (p, p') of the maps in Fig. 4-3 and in particular to the recoupling conditions III to VI.

4.5.3 Generalized cosine modulated recoupling schemes: frequency, phase and amplitude rf modulation

4.5.3.1 General description of CM

In this section, we introduce an additional frequency modulation based on a cosine modulation that is $\pi/2$ out of phase with respect to the phase modulation. If the amplitude of this additional frequency modulation matches the amplitude of the audio field strength induced by the phase modulation only, it cancels out one of the two circular components of the phase

modulation and double the amplitude of the second one. In this case the phase, amplitude and frequency modulation should be rewritten as

$$\left\{ \begin{array}{l} \phi = \phi_0 + \arctan\left(\frac{p' \cos(p\omega_r t - \phi_0)}{p}\right) \\ \omega_1^{(0)} = p\omega_r \left[1 + \left(\frac{p'}{p} \cos(p\omega_r t - \phi_0)\right)^2 \right]^{\frac{1}{2}} \\ \Omega = \underbrace{\Omega_0}_{=p'\omega_r} \cos\left(p\omega_r t - \phi_0 + \frac{\pi}{2}\right) \end{array} \right. \quad (30)$$

The rf Hamiltonian in the laboratory frame can be rewritten as

$$H_{rf} = \omega_1 \left\{ \sum_i S_x^i \cos(\phi(t)) + \sum_i S_y^i \sin(\phi(t)) \right\} + \Omega \sum_i S_z^i \quad (31)$$

With $\phi_0 = \pi/2$, we get

$$\tilde{H}_{r.f.} - A = \sum_{i=1,2} \left[\begin{array}{l} \overbrace{\left[p\omega_r - \omega_c \right]}^{1''} \underbrace{\left[\frac{-T_{S,11}^i e^{-i(p'\omega_r t + \phi_0)} + T_{S,1-1}^i e^{i(p'\omega_r t + \phi_0)}}{\sqrt{2}} \right]}^{2''} + p'\omega_r \sin^2(\omega_c t) T_{10}^i - \omega_{eff} T_{10}^i \\ + \frac{p'\omega_r}{2} \sin(2\omega_c t) \underbrace{\left[\frac{i(T_{S,11}^i e^{-i(p'\omega_r t + \phi_0)} + T_{S,1-1}^i e^{i(p'\omega_r t + \phi_0)})}{\sqrt{2}} \right]}^{3''} \\ + \Omega_0 \cos^2(\omega_c t) \sum_i T_{10}^i \underbrace{- \frac{\Omega_0}{2} \sin(2\omega_c t) \left[\frac{i(T_{S,11}^i e^{-i(p'\omega_r t + \phi_0)} + T_{S,1-1}^i e^{i(p'\omega_r t + \phi_0)})}{\sqrt{2}} \right]}^{4''} \end{array} \right] \quad (32)$$

Given that frequency $\Omega = p'\omega_r$, we get:

$$\tilde{H}_{r.f.} - A = \sum_{i=1,2} \left[\overbrace{\left[p\omega_r - \omega_c \right]}^{1''} \underbrace{\left[\frac{-T_{S,11}^i e^{-i(p'\omega_r t + \phi_0)} + T_{S,1-1}^i e^{i(p'\omega_r t + \phi_0)}}{\sqrt{2}} \right]}^{2'' \& 4''} + p'\omega_r T_{10}^i - \omega_{eff} T_{10}^i \right] = 0 \quad (33)$$

Equation (33) confirms that the strength of the CW (ω_c) and of the audio (ω_{eff}) field components, that define the interaction frame, are at all times equal to $p\omega_r$ and $p'\omega_r$ respectively. Such a pulse sequence [Eq. (30)] allows one to describe any point of the (p, p') maps discussed in Section II C, generalizes the concept of second averaging in the modulation frame, and sets the theoretical framework for various future studies such as CSA recoupling, heteronuclear and homonuclear dipolar decoupling, heteronuclear dipolar recoupling etc. Note that for practical implementations of such experiments the modulation of the amplitude, phase and frequency can be performed using an appropriate combination of phase and amplitude modulation only. We keep the frequency modulation in our theoretical treatment to facilitate the understanding of the spin dynamics.

In the next section, we focus on the modulation schemes for DQ recoupling branches III-VI and COMICS.

4.5.3.2 DQ recoupling conditions III-VI

In order to describe the DQ recoupling regimes III-VI and COMICS, we define:

$$p' = p + p'_0 \quad (34)$$

with $p'_0 \in \{-1, -1/2, 1/2, 1\}$ for recoupling conditions III, IV, V, VI respectively.

The phase modulation (see Eq. (35)) can be easily expanded in Fourier series as follows:

$$\phi = \phi_0 + \sum_k \phi_k \sin(k\omega_c t) \quad (35)$$

with

$$\phi_k = \frac{2(p + p'_0)^k}{kp^k \left(1 + \sqrt{1 + \left(1 + \frac{p'_0}{p} \right)^2} \right)^k} \approx \frac{2}{k(1 + \sqrt{2})^k} + \frac{\sqrt{2}}{(1 + \sqrt{2})^k} \frac{p'_0}{p} \quad (36)$$

To correctly describe recoupling conditions III and VI, the two first harmonics are required. As showed in Fig. 4-6, the amplitude of the first and third harmonics, for $p'_0 \in \{1/2, 1\}$,

approaches $2/(1+\sqrt{2}) \simeq 0.828$ radian and $2/(3(1+\sqrt{2})^3) \simeq 0.047$ radian respectively when p increases.

The expression of the rf amplitude can also be expanded in a Fourier series with only the first two harmonics contributing.

$$\omega_1 = \sum_k \omega_1^k \cos(k\omega_c t) \quad (37)$$

with

$$\omega_1^0 = \omega_r \frac{2p}{\pi} \left[\sqrt{2} \text{EllipticE} \left(\frac{\sqrt{2}}{2} \right) \left(1 + \frac{p'_0}{p} \right) - \frac{\sqrt{2}}{2} \text{EllipticK} \left(\frac{\sqrt{2}}{2} \right) \frac{p'_0}{p} + \mathcal{O} \left(\frac{p'_0}{p} \right)^2 \right] \quad (38)$$

$$\simeq \omega_r (1.216p + 0.381p'_0)$$

$$\omega_1^2 = \omega_r \frac{4p}{3\pi} \frac{1}{\left(1 + \frac{p'_0}{p} \right)^2} \left[\begin{array}{l} 2 \left(1 + \left(1 + \frac{p'_0}{p} \right)^2 \right) \text{EllipticK} \left(i \left(1 + \frac{p'_0}{p} \right) \right) \\ - \left(2 + \left(1 + \frac{p'_0}{p} \right)^2 \right) \text{EllipticE} \left(i \left(1 + \frac{p'_0}{p} \right) \right) \end{array} \right] \quad (39)$$

$$\simeq \omega_r (-0.206p + 0.350p'_0)$$

From the previous equations, it is clear that both the zeroth and the second Fourier harmonics increase with p . These recoupling regimes appear much more demanding in terms of rf field strength than the recoupling regimes I and II. Practically, for a given p index, the rf field strength for the recoupling regimes III, IV, V, VI oscillate approximately between $p\omega_r$ and $\sqrt{2}p\omega_r$.

In the above we have introduced and discussed all the necessary changes to generalize the concept of second averaging. The remainder of the paper focuses on DQ homonuclear recoupling mechanisms and discusses their applicability to real systems at high spinning frequencies and magnetic fields.

4.6 DQ homonuclear recoupling

4.6.1 MAS dipolar recoupling sequences

MAS dipolar recoupling was initially performed in the early 1980's for the case of heteronuclear ^1H - ^{15}N and ^1H - ^{13}C spin pairs³³ followed by the introduction of rotational resonance (R^2) for homonuclear spin pairs and REDOR for heteronuclear recoupling.^{14,28} The concept of recoupling was rapidly extended to the homonuclear case with DRAMA (Refs. 10,34) and RFDR (Refs. 11,35). A different approach to dipolar recoupling was then introduced in 1994 with the homonuclear DQ-HORROR (double-quantum homonuclear rotary resonance) experiment.³⁶ The HORROR method also introduced the concept of γ -encoding, and demonstrated efficient DQ-excitation in a powder sample. The effort in extending the recoupling mechanism to coupled spins with large chemical shifts difference led to non- γ -encoded MELODRAMA (Ref. 9) and then γ -encoded C7 pulse scheme and its variants^{37,38} capable of efficient broadband double-quantum recoupling.

Until recently most reported studies were conducted at low spinning frequencies (< 10 kHz) using high power ^1H decoupling. For instance, the POST-C7 recoupling sequence at 5 kHz MAS frequency requires a ^{13}C irradiation of 35 kHz and is usually performed with a ^1H decoupling field of at least 100 kHz. The ^1H field is chosen to avoid interference with the ^{13}C recoupling mechanism, and a factor 2.5 to 3 mismatched is necessary to avoid any losses.^{35,39,40}

Pulse sequences with lower symmetry number (SPC5 (Ref. 41), $\text{C}14^5_4$ (Ref. 42)) allowed access to higher MAS frequencies (~ 10 kHz). Generalization of the C7 pulse sequence led to multiple C and R symmetry based sequences.^{42,43}

The above sequences have been widely used in the 5 to 15 kHz MAS regime to perform a number of experiments on biomolecules including assignments,¹² two dimensional DQ spectroscopy,^{39,44} high-order multiple-quantum excitation,⁴⁵ inter-nuclear distances⁴⁶ and torsion angles measurements.^{18,47}

However, the incorporation of higher ^1H Larmor frequencies (currently ~ 900 MHz for ^1H) places a stringent demand on developing sequences applicable in the 20-30 kHz MAS

frequency regime. The DREAM scheme introduced by Verel *et al.*, which consists of an adiabatic passage through the HORROR condition, is a good candidate for experiments at high spinning frequencies as it requires only a mean ^{13}C irradiation of $\omega_r/2$ and thus allows the factor 3 mismatch with the ^1H decoupling field to be fulfilled.⁴⁸ However, HORROR/DREAM suffers from a restricted ^{13}C recoupling bandwidth that allows only aliphatic-aliphatic correlation experiments at high B_0 fields. In 2001, Ishii *et al.* showed that fp-RFDR can be applied at 30 kHz MAS frequency and 17.6 T B_0 field with no ^1H decoupling to measure carbonyl-carbonyl distances in spin pair labeled material.⁵ The use of high spinning frequencies hence suggested the investigation of the “no decoupling regime”. For example, Hughes *et al.* notably show that substantial DQ efficiency could be still achieved in the absence of ^1H decoupling using preexisting recoupling sequences.⁴⁹ This work was further investigated by Marin-Montesinos *et al.* in a study of the interference of DQ efficiency with the ^1H decoupling field for the R-symmetry sequences.³² At the same time, De Paëpe *et al.* introduced the cosine modulated adiabatic recoupling (CMAR) pulse sequence (an adiabatic version of the CMpRR sequence discussed in this article) and showed that at 750 MHz ^1H frequencies and $\omega_r/2\pi = 30$ kHz, that ^{13}C - ^{13}C correlation experiments without ^1H decoupling were possible in a uniformly labeled tripeptide.^{25,26,50} CMAR can be understood as an adiabatic passage through the HORROR condition in a modulation frame where the ^{13}C anisotropic and isotropic chemical shift as well as the ^1H - ^{13}C dipolar interactions are averaged out to first order.

Note that in the absence of decoupling, the ^{13}C CSA interaction have the same symmetry as the ^1H - ^{13}C interactions, so it is not surprising that most broadband recoupling sequences developed in the moderate MAS frequencies still function to a certain degree in the high spinning regime. It is also not surprising that one of the most efficient decoupling sequence^{20,21,29} could also be used for the ^{13}C - ^{13}C recoupling problem.

4.6.2 Broadband versus selective recoupling

Solid-state NMR homonuclear DQ/ZQ sequences are usually classified as broadband, band-selective and selective depending on their sensitivity to chemical shift offsets at a given magnetic field. In the range of magnetic fields currently used to perform biological SSNMR

studies, the broadband category includes POST-C7,³⁸ SPC5,⁴¹ etc., the band-selective class includes HORROR,³⁶ C7,³⁷ etc., whereas R^2 (Refs. 27,28) and its derivatives are used to selectively recouple spins with isotropic chemical separation matching the MAS frequency.

Broadband and band-selective methods are used in correlation experiments and torsion angle measurements. Due to the presence of non-commuting terms in the ZQ/DQ recoupled Hamiltonian, the recoupling dynamics is largely dominated by strong ^{13}C - ^{13}C couplings inducing one-bond relayed transfer mechanisms. One of the challenges to implement such experiments at high magnetic fields (>600 MHz) and high spinning frequencies (>15 kHz) concerns the efficient suppression of the heteronuclear couplings (e.g. ^1H - ^{13}C). In this paper, we demonstrate experimentally that the CMpRR family of sequences achieve this goal for $\omega_{0,\text{H}}/2\pi \leq 900$ MHz and $\omega_r/2\pi \leq 30$ kHz, with no or minimal additional ^1H irradiation. In principle there is no reason that the approaches will not function at higher fields and spinning frequencies, but they have yet to be tested under these conditions.

The last category of dipolar recoupling sequences can be used to selectively reintroduce one dipolar interaction present in a complicated network of couplings, and in this way selective sequences circumvent dipolar truncation. The rotational resonance (R^2)^{27,28} recoupling sequence family ($R^2\text{W}$, $R^2\text{TR}$, $R^2\text{TRW}$)^{2,3,19,51} has yielded accurate distance measurement (up to 6Å) between carbonyl and aliphatic ^{13}C resonances in uniformly labeled molecules. Recoupling in R^2 experiments is achieved by matching the chemical shift difference of two spins to the MAS frequency. However, reliable R^2 methods for recoupling spins with small chemical shift separation still need to be developed.

In order to address this problem, we also introduce here a new approach that simultaneously performs DQ dipolar and chemical shift recoupling. As we shall see below, this new pulse sequence (COMICS) is very narrowband and can be used to selectively reintroduce couplings by setting the carrier frequency at the mean offset value of the two sites. This approach should be an attractive solution for distance measurements between closely spaced resonances such as exhibited by amino acid side chains in proteins.

4.6.3 DQ rotary resonance recoupling condition in the modulation frame I and II: CMpRR

In this section we present the recoupling mechanism involved in the CMpRR regime I and II. The corresponding field decomposition in this case is a CW component of strength $p\omega_r$ and a resonant audio field of strength $(0.5, 1)\omega_r$. These two recoupling regimes can be seen as matching the rotary resonance conditions ($n=0.5, 1$) in the MF defined by the first CW field.²⁹

The first recoupling regime (I) corresponds to a DQ recoupling condition with ($m=1, q=0, q'=2$) recoupling indices. If $p=p_2/p_1 \geq 3.5$ and $p'=0.5$ [Fig. 4-3d], *all other interactions are decoupled to first order*. From Eq. (13), we can apply AHT over the period $n\tau_r$ in the interaction frame, with n being the lowest common multiple of the number two and the p_1 index, and obtain the following first order expression,

$$\begin{aligned} \overline{\tilde{H}}_I^{(1)} &= \frac{-1}{2} \sqrt{6} \overbrace{\left\{ \omega_{SS,12}^1 e^{i2\phi_0} d_{-20}^2 \left(\frac{\pi}{2} \right) T_{SS,2-2}^{12} + \omega_{SS,12}^{-1} e^{-i2\phi_0} d_{20}^2 \left(\frac{\pi}{2} \right) T_{SS,22}^{12} \right\}}^{\text{HORROR HAMILTONIAN}} + \sum_{j=1}^n \omega_{I,j}^{(0)} T_{I,10}^j \\ &= S_{1,0,0,2}^2 \omega_{SS,12} \sin(2\beta) \left\{ e^{-i\gamma} e^{i2\phi_0} T_{SS,2-2}^{12} + e^{i\gamma} e^{-i2\phi_0} T_{SS,22}^{12} \right\} + \sum_{j=1}^n \omega_{I,j}^{(0)} T_{I,10}^j \end{aligned} \quad (40)$$

with $S_{m,q'',q,q'}^l = \sqrt{6} S_m^{spatial} \cdot S_{q'',q,q'}^{spin,l}$. The coefficient $S_{1,0,2,2}^2$ represents the scaling factor of the CMpRR DQ recoupling sequence and is equal to 0.27. This number can be compared to the following scaling factor: 0.232 for POST-C7, 0.203 for SPC5 and 0.54 for HORROR.

Figure 4-8 shows simulations of cosine phase modulated recoupling for $p = 5$ on a two carbon spin system including ^{13}C dipolar coupling only in (a), isotropic chemical shift and ^{13}C dipolar coupling only in (b), chemical shift anisotropy (CSA) and ^{13}C dipolar coupling only in (c) (details of the simulation can be found in the figure caption). In the case of region I, the DQ recoupling appears very robust with respect to the presence of both isotropic chemical shift (CS) and chemical shift anisotropy (CSA).

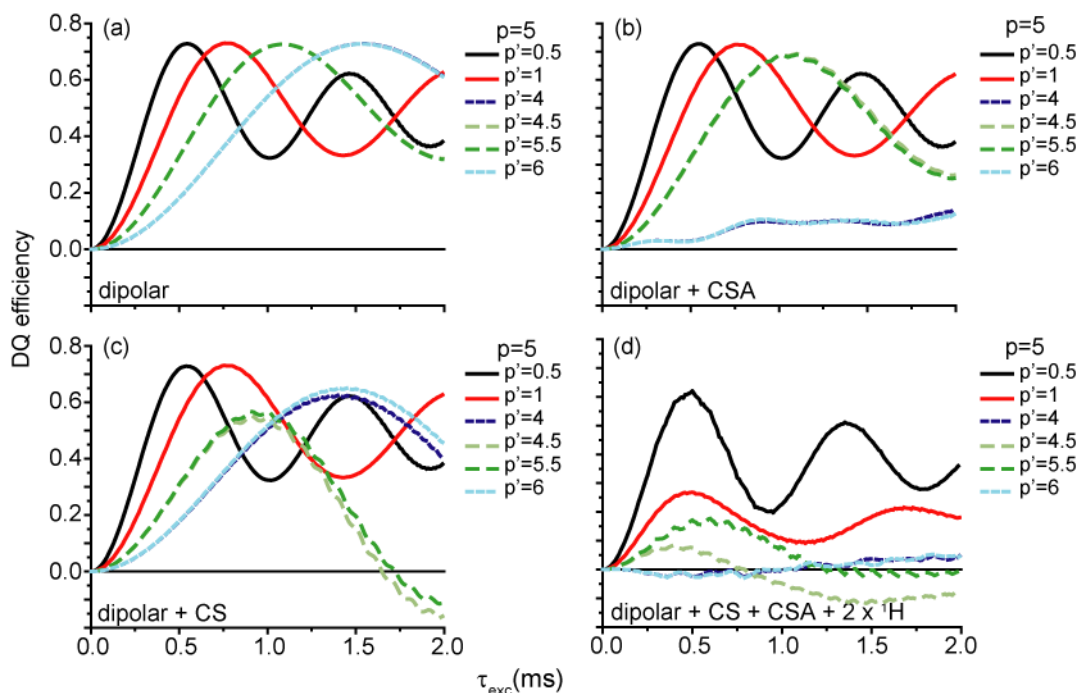


Figure 4-8 Simulations of the DQ filtered efficiency of a spin system based on a glycine model, with $p=5$ index, for recoupling regimes I to VI: (a) with included ^{13}C - ^{13}C dipolar interaction only (corresponding to 1.54Å distance), (b) with ^{13}C - ^{13}C dipolar and ^{13}C CSA interactions only ($\sigma_{\text{aniso},1} = 20$ ppm, $\eta_1 = 0.8$, $\sigma_{\text{aniso},2} = 25$ ppm, $\eta_2 = 0.9$), (c) with ^{13}C - ^{13}C dipolar and ^{13}C isotropic CS interactions only ($\sigma_{\text{iso},1} = -10$ ppm, $\sigma_{\text{iso},2} = 10$ ppm), (d) with ^{13}C - ^{13}C dipolar, ^{13}C CS interactions and ^{13}C - ^1H dipolar interactions between carbons and the two alpha protons (directly bonded to C2). Note that regimes I and II ($p' = 0.5$ and $p' = 1$) are the least affected by the ^{13}C chemical shift interactions. The presence of simultaneous first order CSA recoupling conditions for regions III and VI ($p' = 4$ and $p' = 6$) significantly reduces the DQ efficiency for these branches in a presence of such interactions. In a similar manner regions IV and V ($p' = 4.5$ and $p' = 5.5$) are affected by ^{13}C isotropic chemical shift through a second order effect due to nearby first order isotropic chemical shift recoupling condition (in this particular case for $p' = 5$). The simulation in (d) with all the interactions included clearly shows that region I ($p' = 0.5$) is compensated the best for presence of anisotropic and heteronuclear interactions. This figure confirms that the recoupling map in Fig. 4-3 could be used for qualitative prediction of the performance of CM sequences in presence of various interactions. All the simulations were performed using the full modulation scheme described in Sec. III C.

The study of the recoupling regime II is straightforward and leads to the following first order effective Hamiltonian:

$$\begin{aligned}
\overline{\tilde{\mathbf{H}}}_{II}^{(1)} &= \frac{-1}{2} \sqrt{6} \left\{ \omega_{SS,12}^2 e^{i2\phi_0} d_{-20}^2 \left(\frac{\pi}{2} \right) T_{SS,2-2}^{12} + \omega_{SS,12}^{-2} e^{-i2\phi_0} d_{20}^2 \left(\frac{\pi}{2} \right) T_{SS,22}^{12} \right\} + \sum_{j=1}^n \omega_{I,j}^{(0)} T_{I,10}^j \\
&= S_{2,0,0,2}^2 \omega_{SS,12} \sin^2(\beta) \left\{ e^{-i2\gamma} e^{i2\phi_0} T_{SS,2-2}^{12} + e^{i2\gamma} e^{-i2\phi_0} T_{SS,22}^{12} \right\} + \sum_{j=1}^n \omega_{I,j}^{(0)} T_{I,10}^j
\end{aligned} \tag{41}$$

with $\kappa_{2222}^2 = 0.19$, representing the scaling factor of the CMpRR recoupling sequence.

The scaling for the regime II is smaller than for the regime I, resulting in an about two times longer optimal mixing time (see Fig. 4-8a). The sequence is still quite robust with respect to ^{13}C isotropic [see Fig. 4-8b] and anisotropic [see Fig. 4-8c] chemical shifts. As previously pointed out, the ^{13}C CSA tensor transforms the same way as the ^1H - ^{13}C interaction if no ^1H irradiation is applied. Figure 4-8d shows the influence of the two alpha protons of glycine in the absence of ^1H irradiation. Recoupling condition II appears much more sensitive to protons than condition I.

The recoupling condition I reaches more than 60% DQ efficiency at 750 MHz ^1H frequency, which is more than twice the value obtained with condition II. This can be explained through second order effects discussed below. In the following we refer as CMpRR to the pulse sequence that fulfills recoupling condition (I) only.

4.6.4 Generalized rotary resonance conditions in the modulation frame: DQ conditions (III) to (IV)

In this section we investigate recoupling regimes III to VI in order to determine if they are better candidates for broadband DQ recoupling sequence than region I. To first order, this regimes lead to the same type of DQ recoupled Hamiltonian. More precisely regimes III and VI correspond to the $m = 2$ recoupling condition and have a scaling factor two times smaller than that in the regime II. Similarly, recoupling regimes IV and V corresponding to the $m = 1$ condition have a scaling factor two times smaller than that in I. This is reflected in the optimum buildup times for the different regimes in Fig. 4-8a. In Fig. 4-8b, we observe the collapse of the DQ efficiency of recoupling regime III and VI. This can be explained by a simultaneous first order recoupling of the dipolar and CSA interactions. Finally, Fig. 4-8c shows that recoupling regimes IV and V are more sensitive to isotropic chemical shift

compared to other recoupling conditions. This is consistent with Fig. 4-3, where recoupling regimes IV and V are very close to an isotropic chemical shift reintroduction ($p = p'$).

Recoupling conditions III to VI appear generally more sensitive to isotropic and anisotropic chemical shift interactions. Notably, concurrent CSA recoupling clearly prevents regimes III and VI from being used in usual dipolar recoupling experiments. Recoupling conditions IV and V reach about 10-15 % DQ efficiency in the limit of no decoupling. The heteronuclear decoupling step limits efficiency for regimes II, IV and V (see Fig. 4-8). Recoupling condition IV and V is of interest for performing band-selective recoupling experiments benefiting from the sensitivity to CS interaction. Super-cycle considerations may also be a useful help to improve DQ efficiency in these regimes.

4.6.5 Narrowband DQ COMICS recoupling in the modulation frame

In this section, to demonstrate the flexibility of the generalized CM schemes outlined above, we introduce a new recoupling condition cosine modulated recoupling with isotropic chemical shift reintroduction (COMICS). This recoupling condition corresponds to $p = 0.25$ and $p' = 0.25$ and induces a simultaneous recoupling of the DQ dipolar interaction and the isotropic chemical shift. The corresponding field decomposition in this case is a CW component of strength $0.25\omega_r$ and a resonant audio field of strength $0.25\omega_r$.

The COMICS pulse sequence corresponds to a DQ recoupling condition with ($m = 1, q = 2, q' = 2$) recoupling indices, and at the precise COMICS condition, all other interactions are decoupled to first order. From Eq. (13), we can apply AHT over the period $4\tau_r$ in the interaction frame to derive to first order:

$$\tilde{\mathbf{H}}_{COMICS}^{(1)} = \sum_{i=1}^2 \frac{\omega_{S,i}^{(0)}}{2\sqrt{2}} \left(-e^{-i\phi_0} T_{S,11}^i + e^{i\phi_0} T_{S,1-1}^i \right) - \frac{3\sqrt{2}}{32} \sin(2\beta) \omega_{SS,12} \left(e^{-i\gamma} e^{-i2\phi_0} T_{SS,22}^{12} + e^{i\gamma} e^{i2\phi_0} T_{SS,2-2}^{12} \right) + \sum_{j=1}^n \omega_{I,j}^{(0)} T_{I,10}^j \quad (42)$$

The COMICS irradiation scheme is obtained in a straightforward manner from Eq. (30) with $\phi_0 = \pi/2$:

$$\left\{ \begin{array}{l} \phi = \phi_0 + \arctan \left[\sin \left(\frac{\omega_r t}{4} \right) \right] \\ \omega_1^{(0)} = \frac{\omega_r}{4} \left[1 + \sin^2 \left(\frac{\omega_r t}{4} \right) \right]^{\frac{1}{2}} \\ \Omega = \frac{\omega_r}{4} \cos \left(\frac{\omega_r t}{4} \right) \end{array} \right. \quad (43)$$

Figure 4-9 illustrates simulations of the amplitude, frequency [Fig. 4-9a] and phase [Fig. 4-9b] modulation over the cycle time of $\tau_c = 4\tau_r$ for $\omega_r/2\pi = 30$ kHz. In the simulations the amplitude of the rf field evolves between $(\omega_r/4)$ kHz and $(\omega_r/2\sqrt{2})$ kHz, while the frequency of the rf field oscillates between $\pm\omega_r/4$ kHz. Finally, the phase of the rf fields is shifted by 90° with respect to the frequency between $\pm\arctan(1) = \pm 45^\circ$.

Figure 4-9c depicts an ideal DQ buildup curve obtained with COMICS when only the ^{13}C dipolar coupling is included. Since the sequence is γ -encoded its scaling factor is comparable to recoupling condition IV and V, i.e. about two times smaller than for CMpRR.

As we can see from Eq. (42), the isotropic chemical shift interaction reappears to first order in the experiment. We used the CS interaction to truncate the DQ recoupled Hamiltonian leading to a narrowband pulse sequence. This is illustrated in Fig. 4-9d that compares the DQ bandwidth obtained for CMpRR and COMICS. As expected, CMpRR is very robust versus the mean offset ^{13}C chemical shift and approximately has a bandwidth of ~ 30 kHz. On the other hand, COMICS is very sensitive to the mean offset and behaves like a narrowband gate with no recoupling taking place unless the carrier frequency lies between the two carbons of interest. The bandwidth of this sequence is on the order of magnitude of a ^{13}C linewidth in a uniformly labeled sample.

COMICS can be applied to selectively reintroduce a specific coupling among a complicated network. A detailed investigation of this recoupling scheme to measure aliphatic-aliphatic distances in fully labeled material is currently under investigation.

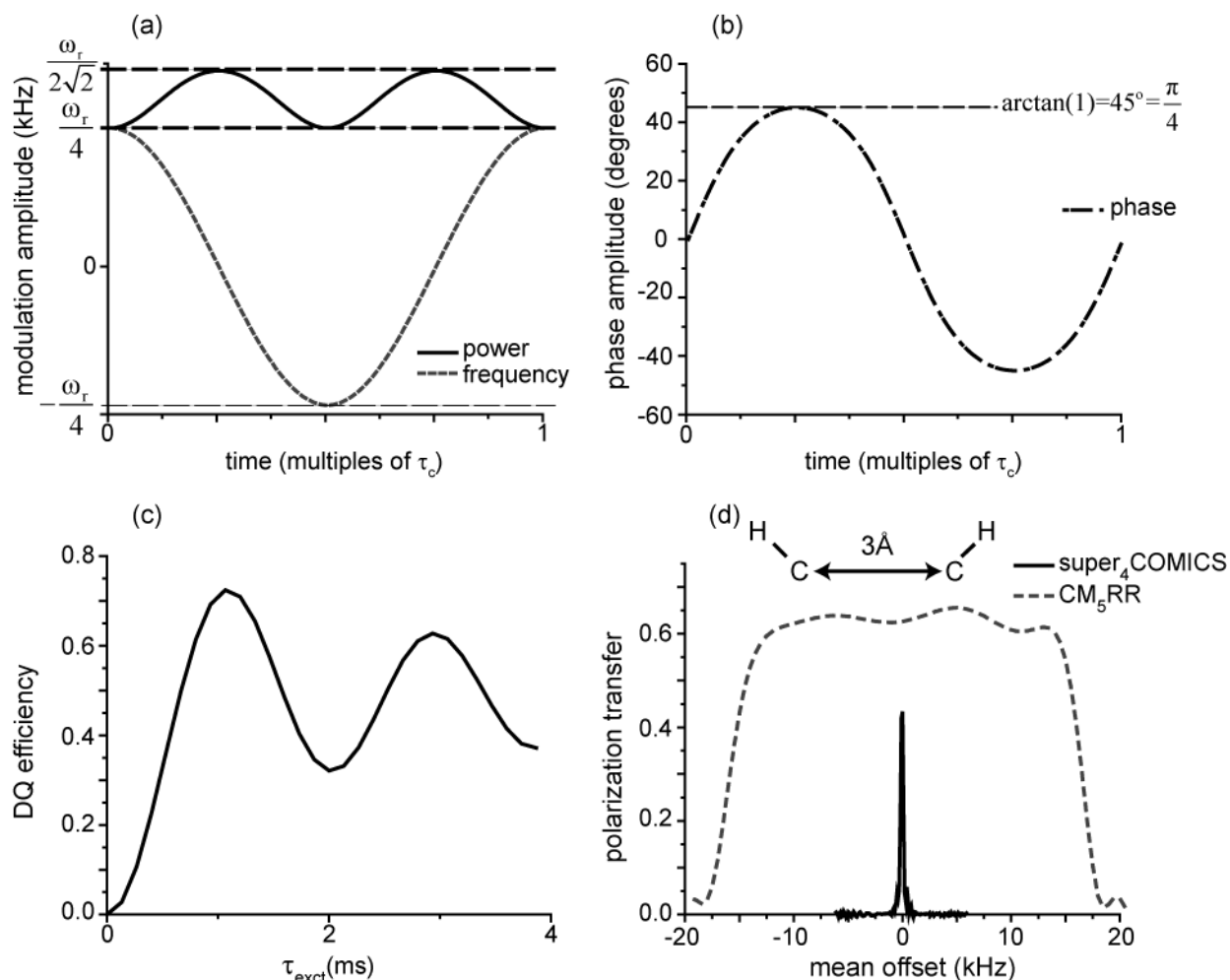


Figure 4-9 COMICS recoupling pulse sequence reintroducing simultaneously DQ dipolar interaction and isotropic chemical shift: (a) amplitude and frequency modulation scheme, (b) phase modulation. (c) COMICS DQ coherence buildup simulation with ^{13}C dipolar interaction only. (d) DQ efficiency for mixing time optimal for 3 Å distance as a function of the ^{13}C mean offset for broadband CM_5RR (at 20 kHz MAS) and narrowband super-cycled COMICS (at 30 kHz MAS). Note the radically different effective bandwidth of > 30 kHz for CM_5RR and < few hundred Hz for COMICS. COMICS simulation in (d) was supercycled according to the scheme described for R sequences in Kristiansen et al.⁵² Both the simulations in (d) were performed at 750 MHz field and included isotropic chemical shift ($\sigma_{\text{iso},\text{C1}} = -10$ ppm, $\sigma_{\text{iso},\text{C2}} = 10$ ppm) and CSA ($\sigma_{\text{aniso},\text{C1}} = -13.86$ ppm, $\eta_{\text{C1}} = 0.93$, $\sigma_{\text{aniso},\text{C2}} = -20.88$ ppm, $\eta_{\text{C2}} = 0.75$). 100 kHz ^1H CW decoupling was used for COMICS.

4.7 Properties of the DQ recoupling with Cosine Modulated Rotary Resonance (CMpRR)

In the remaining part of the manuscript we focus on the CMpRR recoupling (I), assuming that the ^{13}C rf irradiation fulfills Eq. (18). In this section, we show that CMpRR can efficiently be applied at high magnetic field ($\omega_{0,\text{H}}/2\pi \geq 750$ MHz) and MAS frequencies in the range $10 \text{ kHz} \leq \omega_r/2\pi \leq 30$ kHz with no additional ^1H decoupling or very low ^1H irradiation (a few kHz). This study is supported by both theoretical and experimental evidence.

4.7.1 Experiments and simulations

4.7.1.1 Experimental

Uniformly $[1,2-^{13}\text{C}, ^{15}\text{N}]$ -glycine was obtained from Cambridge Isotope Laboratories (Andover, MA) and diluted to 20% with natural abundance materials to attenuate intermolecular ^{13}C - ^{13}C interactions. The sample was center-packed in a 2.5mm zirconium rotor from Bruker (Billerica, MA). N-*f*-MLF-OH peptide was obtained by solid phase peptide synthesis from CS Bio Inc. (Menlo Park, CA). The peptide was prepared both without isotopic enrichment, and with U- ^{13}C , ^{15}N labeled amino acids from Cambridge Isotope Laboratories (Andover, MA). One sample was diluted to 10% with natural abundance material and center-packed in a 2.5mm Bruker rotor. Undiluted $[\text{U-}^{13}\text{C}, ^{15}\text{N}]$ -*f*-MLF-OH was packed into a 2.5mm Bruker rotor without center-packing.

All experiments were carried out using two high field instruments. The first system is a commercial Bruker spectrometer operating at 900.1 MHz ^1H frequency using a Bruker triple resonance probe equipped with 2.5 mm spinner module. The second system is a Cambridge Instruments spectrometer operating at 750 MHz ^1H frequency using a Bruker triple resonance probe equipped with 2.5 mm spinner module. Spinning frequencies of 10-30 kHz were used in all experiments and regulated to ± 2 Hz with a Bruker spinning frequency controller (Bruker BioSpin, Billerica MA).

To compensate for cross term contributions (see Sec. VI E) each CMpRR condition was optimized by varying the mean power and phase excursion on a grid around the theoretical point while conserving the theoretical periodicity. The phase and rf power shift were smaller

than 0.5° and 5 kHz, respectively. Note that the rf field was approximated by a constant field amplitude. The maximum number of slices per sine period used was 32.

4.7.1.2 Numerical simulations

All the simulations were performed using SPINEVOLUTION.⁵³ and the model spin systems used are based on glycine and alanine. Glycine was modeled by a C_α ($\sigma_{\text{iso}} = -65$ ppm, $\sigma_{\text{anis}} = 19.3$ ppm, $\eta = 0.98$) and a C' carbon ($\sigma_{\text{iso}} = 65$ ppm, $\sigma_{\text{anis}} = 74.5$ ppm, $\eta = 0.8$) and two H_α's ($\sigma_{\text{iso}} = 0, 0.5$ ppm, $\sigma_{\text{anis}} = 4$ ppm, $\eta = 0$). Alanine was modeled by two carbons: C_α ($\sigma_{\text{iso}} = -15.5$ ppm, $\sigma_{\text{anis}} = -20$ ppm, $\eta = 0.78$), C_β ($\sigma_{\text{iso}} = -15.5$ ppm, $\sigma_{\text{anis}} = 12$ ppm, $\eta = 1$), and two protons: H_α ($\sigma_{\text{iso}} = 0$ ppm, $\sigma_{\text{anis}} = 4$ ppm, $\eta = 0$), and H_β ($\sigma_{\text{iso}} = 0.5$ ppm, $\sigma_{\text{anis}} = 4$ ppm, $\eta = 0$). In the following, when we refer to glycine or alanine spin system we mean the systems described above including all the dipolar and chemical shift interactions unless specified otherwise. Note that the alanine spin model does not specifically include a CH₃ group nor CH₃ group rotation.

4.7.2 CMpRR at moderate MAS frequency

Let us first look at the performance of CMpRR sequences in the no ¹H decoupling regime at moderate MAS frequency.

Figure 4-10a and 4-10b show simulated DQ filtered buildups for different recoupling sequences (SPC5,⁴¹ CM₅RR, R12₂^{5, 32}, CM₆RR, POST-C7,³⁸ CM₇RR, DRAWS,⁵⁴ R20₂^{9, 32}, HORROR (Ref. 36)) on a glycine system at 750 MHz ¹H frequency and 12 kHz MAS spinning frequency with no additional ¹H decoupling except HORROR where 200 kHz ¹H decoupling was used. The simulations do not include rf inhomogeneity or relaxation. The sequences R12₂⁵ and R20₂⁹ were chosen among the R-sequences family based on a recent study on heteronuclear decoupling interference during symmetry-based homonuclear recoupling in solid-state NMR that shows their superior performance in the no ¹H decoupling regime.³²

Figure 4-10a compares SPC5 to CM₅RR (~60 kHz ¹³C irradiation for both the sequences) and R12₂⁵ to CM₆RR (~72 kHz ¹³C irradiation for both sequences). In both cases under

comparable experimental conditions ($\omega_r/2\pi$, $\omega_1/2\pi$), the CMpRR pulse sequences show improved DQ efficiency (39 and 53% respectively).

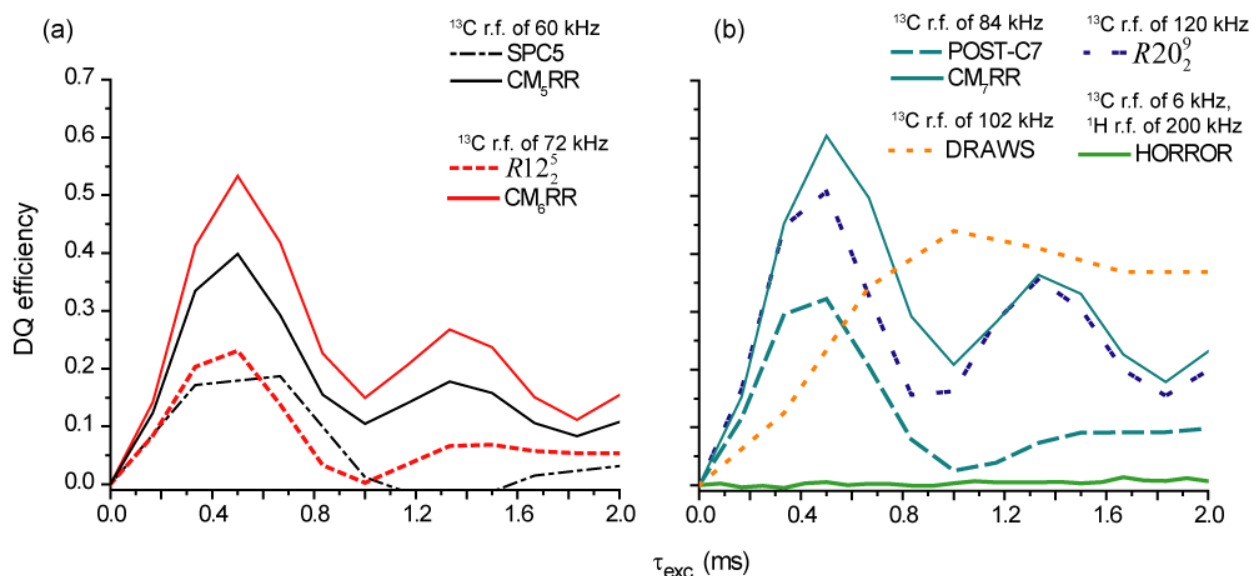


Figure 4-10 DQ coherence buildup simulations of a glycine spin system (4 spins, see Sec. VI A 1) at 12 kHz MAS spinning frequency and 750 MHz field for various pulse sequences. Graphics (a) shows sequences with matching condition of 5 (i.e. ^{13}C rf ~ 60 kHz): SPC5 (black dot-dash line) and CM_5RR , (black solid line); sequences with matching condition of 6 (i.e. ^{13}C rf ~ 72 kHz): $\text{R}12_2^5$ (red dash line) and CM_6RR (red solid line). Graphic (b) shows sequences with matching condition of 7 (i.e. ^{13}C rf ~ 84 kHz): POST-C7 (cyan dash line) and CM_7RR (cyan solid line); sequences with matching condition of 10 (i.e. ^{13}C rf ~ 120 kHz): $\text{R}20_2^9$, 8.5 (i.e. ^{13}C rf ~ 102 kHz) DRAWS and 0.5: HORROR (^{13}C rf 6 kHz). All the simulations were performed without ^1H irradiation except for HORROR where 200 kHz ^1H rf decoupling was used.

Figure 4-10b compares POST-C7 to CM_7RR (~ 84 kHz ^{13}C irradiation for both sequences), DRAWS (102 kHz ^{13}C irradiation), $\text{R}20_2^9$ (120 kHz ^{13}C irradiation), HORROR (6 kHz ^{13}C irradiation, 200 kHz ^1H irradiation). At 750 MHz ^1H frequency, due to large CS and CSA interactions, HORROR is not able to provide any transfer even in presence of large ^1H decoupling. DRAWS reaches more than 40 % DQ efficiency with 102 kHz ^{13}C irradiation in 1 ms. $\text{R}20_2^9$ reaches around 50% in ~ 500 μs under demanding conditions (120 kHz ^{13}C irradiation). Finally, CM_7RR reaches $\sim 60\%$ in 500 μs using (~ 84 kHz).

The maximum DQ efficiency for optimized CMpRR seems to be increasing with the p index at constant MAS frequency. In this particular regime the increase of DQ efficiency can be attributed to the increase of the averaging frequency ω_c . The same holds for all the alternative DQ sequences where increasing matching condition corresponding to increasing rf field strength results in better performance. In addition, the CMpRR simulations suggest that ^{13}C rf field strength > 80 kHz leads to adequate decoupling of the proton bath from the ^{13}C - ^{13}C spin dynamics.

In conclusion, simulations show that CMpRR recoupling sequences provide efficient DQ excitation in the absence of any ^1H irradiation for reasonable ^{13}C rf fields at 12 kHz MAS frequency and $\omega_{0,\text{H}}/2\pi = 750$ MHz. Note that such a MAS frequency is close to the technological and practical upper limit for many of the presented pulse sequences (POST-C7, DRAWS, R20₂⁹). In the following sections we will see that CMpRR can be efficiently applied from 10 kHz up to 30 kHz with a ^{13}C rf field strength ≤ 100 kHz.

4.7.3 Effect of the p and p' mismatch on DQ CMpRR efficiency

As we have already mentioned in Sec. VI A, in order to minimize the detrimental effects of higher order cross terms on the DQ efficiency, the CMpRR sequence has to be optimized by varying the mean power (effective p) and phase excursion (effective p') (see Supporting Information Table 4-1 for theoretical phase excursion values). Before discussing the various cross terms that can be compensated by such a fine optimization (see Sec. VI D), we first concentrate on explaining the underlying fine structure of the optimization maps.

Figure 4-11a-f shows simulations of the DQ efficiency for a modulation frequency $\omega_c/2\pi$ of 100 kHz as function of p and p' mismatch for the glycine spin system. The simulation does not include any ^1H irradiation and the mixing time is chosen to maximize the DQ efficiency transfer. The horizontal axis represents the deviation δ_{p_0} from the theoretical p_0 value, whereas the vertical axis represents the deviation $\delta_{p'_0}$ from the theoretical $p'_0 = 1/2$. Figure 4-11 shows simulations for three different p -values: 3.5, 5, 10 with all interactions included (Fig 4-11d, 4-11e and 4-11f respectively) and only the ^{13}C dipolar coupling included (Fig 4-11a, 4-

11b and 4-11c respectively). Notably, the optimization maps show that in the absence of any interactions other than the ^{13}C dipolar couplings, the DQ maximum is centered on the theoretical point ($\delta p_0 = \delta p'_0 = 0$) and that the shape of the maximum area is not symmetrical with respect to δp_0 and $\delta p'_0$ deviations. The latter observation can be explained by the following argument.

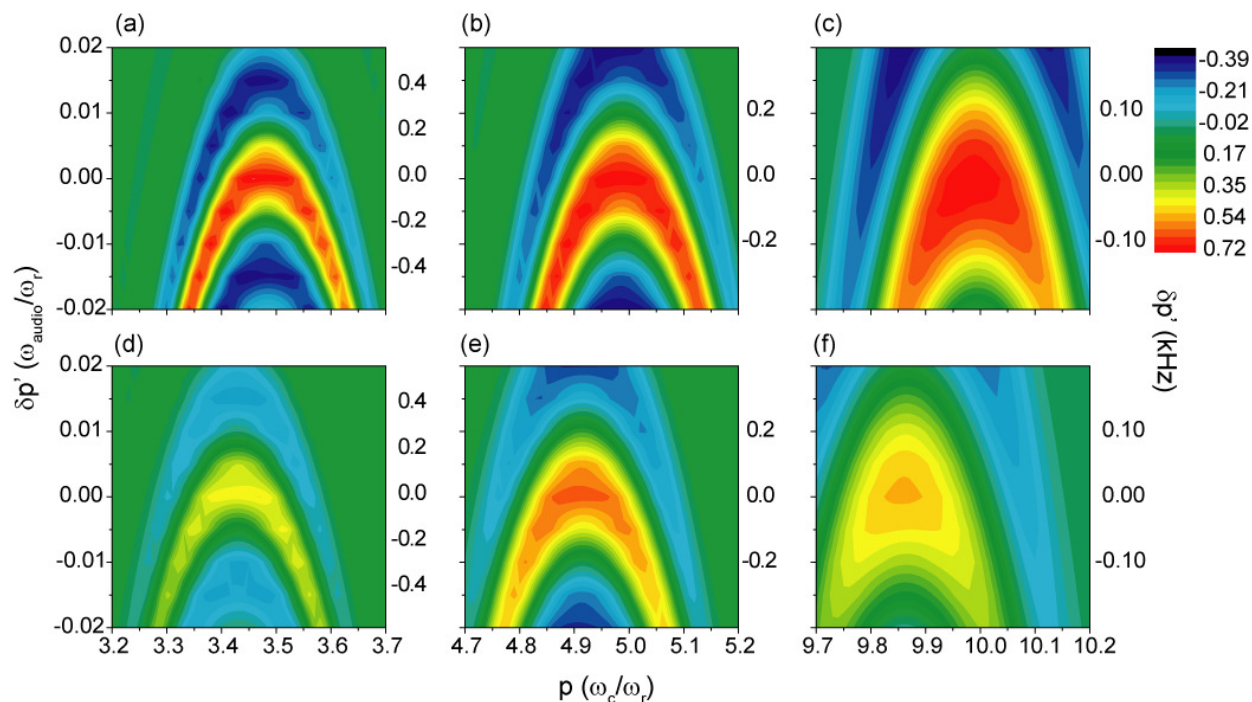


Figure 4-11 Simulated maps of the DQ efficiency as function of p and p' mismatch for a glycine spin system. No ^1H irradiation is included in the simulation and the mixing time is chosen to maximize the DQ efficiency transfer. The x-axis represents the deviation δp_0 from the theoretical p_0 value, whereas the y-axis represents the deviation $\delta p'_0$ from the theoretical $p'_0 = 1/2$. The figure shows simulations for three different p -values: (a) $p=3.5$, (b) $p=5$, (c) $p=10$ with only the ^{13}C dipolar coupling included and (d) $p = 3.5$, (e) $p = 5$, (f) $p = 10$ with all interactions included. Note the systematic shift in p and p' from the theoretical value due to the higher order cross terms in the bottom panel simulations. Simulations were performed for theoretical $\omega_c/2\pi = 100$ kHz and $\omega_r/2\pi$ of 28.571 kHz, 20 kHz and 10 kHz for p equal to 3.5, 5 and 10 respectively.

Deviation from the theoretical p_0 and p'_0 index leads to the following modified equations:

$$\begin{cases} \omega_1^{(0)} \cos(\phi - \phi_0) = (p_0 + \delta_{p_0}) \omega_r \\ \omega_1^{(0)} \sin(\phi - \phi_0) = 2(p_0' + \delta_{p_0'}) \omega_r \sin(p_0 \omega_r t) \end{cases} \quad (44)$$

Equation (46) allows one to rewrite the modified rf phase and power functions:

$$\begin{cases} \phi = \phi_0 + \arctan\left(\frac{2(p_0' + \delta_{p_0'})}{(p_0 + \delta_{p_0})} \sin(p_0 \omega_r t)\right) \\ \omega_1^{(0)} = (p_0 + \delta_{p_0}) \omega_r \left[1 + \left(\frac{2(p_0' + \delta_{p_0'})}{(p_0 + \delta_{p_0})} \sin(p_0 \omega_r t)\right)^2\right]^{\frac{1}{2}} \end{cases} \quad (45)$$

From Eq. (45), we can write the rf Hamiltonian in the modulation frame defined by p_0 and p_0' :

$$\begin{aligned} \tilde{H}_\delta &= \tilde{H}_{\delta_{p_0}} + \tilde{H}_{\delta_{p_0'}} \\ &= \sum_{i=1,2} \left[[(\delta_{p_0}) \omega_r] \left[\frac{-T_{S,11}^i e^{-i(p_0' \omega_r t + \phi_0)} + T_{S,1-1}^i e^{i(p_0' \omega_r t + \phi_0)}}{\sqrt{2}} \right] + [2\delta_{p_0} \omega_r \sin^2(\omega_c t)] T_{10}^i \right] \end{aligned} \quad (46)$$

We apply the AHT and obtain to second order:

$$\overline{\overline{H}}_\delta \equiv_{\substack{\text{first} \\ \& \\ \text{second} \\ \text{order}}} \left(\frac{\delta_{p_0}^2}{2p_0'} + \delta_{p_0'} \right) \omega_r \sum_i T_{10}^i \quad (47)$$

The last equation shows that, in the absence of other interactions than the ^{13}C dipolar couplings, a deviation from the theoretical index p_0 and p_0' leads respectively to a quadratic and linear contribution to the longitudinal term. This polynomial function ($\delta_{p_0'} = -\delta_{p_0}^2$) explains the shape of the maximum DQ area present in Fig. 411a-c in the ^{13}C dipolar only case. Along this line but sufficiently close to the point $(\delta_{p_0}, \delta_{p_0'}) = (0,0)$, the higher order effect of the rf field mismatch with itself are close to zero.

The bottom panels of Fig. 4-11 show that, when all the interactions are considered, the DQ efficiency maximum is shifted. A slight mismatch in p and p' can compensate for a large part of second and third order cross terms contributions. This will be further detailed in the Sec. VI D outlining the cross terms calculations.

At this point, it is important to note that in the limit where $p\omega/p \sim 0$, CMpRR is, to a very good approximation, described by a square phase modulation (scaled by a factor $\pi/4$) with a rf field strength constant and equal to $p\omega$. In this limit, the theory of the CMpRR converges towards the theory of the R-sequence family ($R4p_2^1$) when using series of π pulses. Note however that this regime has not been, to our knowledge, explicitly explored.

4.7.4 Experimental results and p-dependency of the DQ efficiency

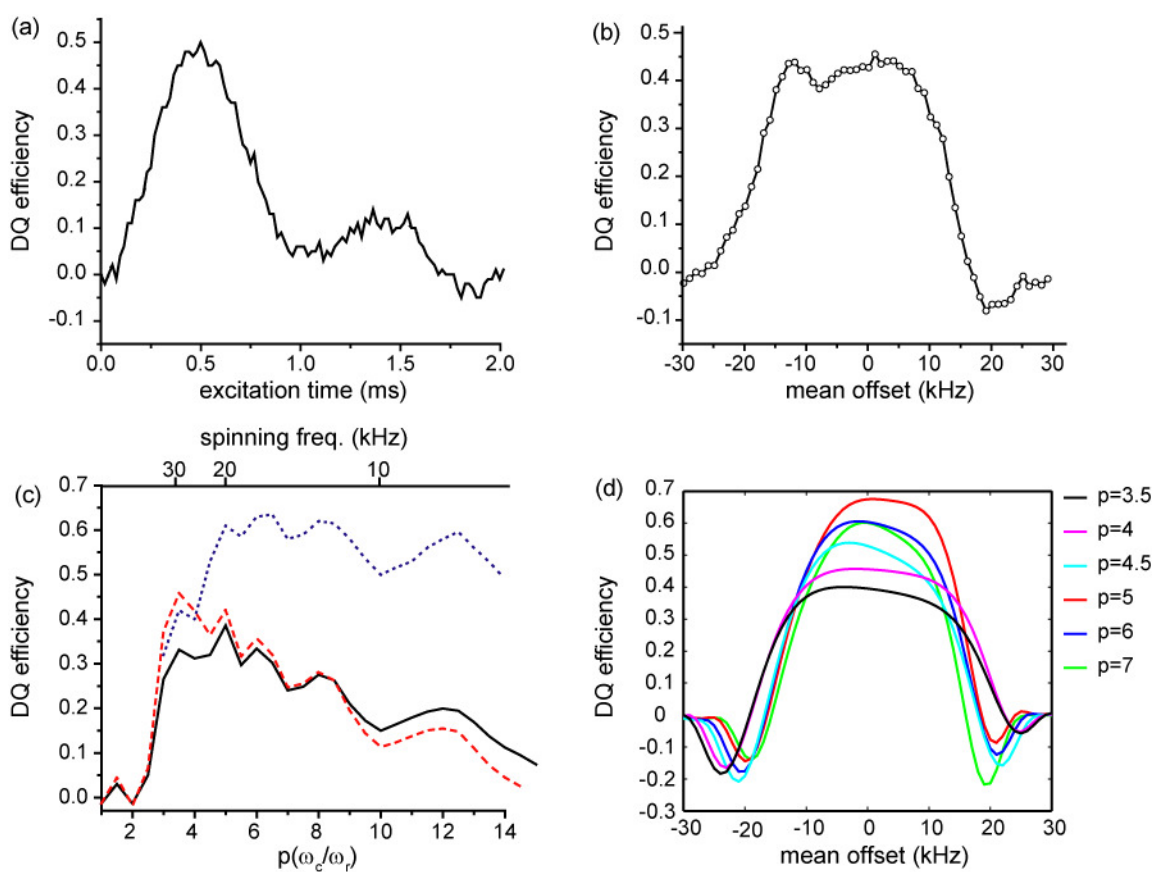


Figure 4-12 Comparison of experimental (a-b) and simulated (c-d) DQ coherence buildups and bandwidth. Experimental CM₅RR DQ coherence buildup (a) and bandwidth (b) obtained on 20% [¹³C,¹⁵N]-glycine at 750 MHz B₀, 20 kHz MAS without any ¹H decoupling during the mixing. Note the efficient and broadband behavior of CM₅RR. (c) Simulated CMpRR DQ efficiency for glycine spin system

as a function of p index for a modulation frequency ω_c of 100 kHz: the solid black line shows simulations when all interactions are included, the dashed red line shows the same simulation with the ^1H - ^1H dipolar coupling removed, and finally, the dotted blue line represents DQ efficiency for optimized CMpRR with all interactions included. Significant gains in DQ efficiency for the optimized CMpRR indicate that the adjustment of transverse and longitudinal components can compensate for a large part of high order cross terms present. Graphics (d) shows simulated optimized bandwidth for a series of p indexes with ω_c of 100 kHz. Excitation time of 480 μs was used for (b-d).

Figure 4-12a-b shows experimental data recorded on $[\text{U-}^{13}\text{C}, ^{15}\text{N}]$ -glycine at $\omega_{0,\text{H}}/2\pi = 750$ MHz for a modulation frequency $\omega_c/2\pi = 100$ kHz and without additional ^1H irradiation. Figure 4-12a depicts the DQ recoupling efficiency as a function of the excitation time for $p = 5$ (i.e. $\omega_c/2\pi = 20$ kHz). In this case, CM₅RR reaches around 50% DQ efficiency, which is consistent with the simulated value (~60%) obtained on a model glycine spin system under identical conditions (no rf inhomogeneity included). Figure 4-12b represents the experimental DQ recoupling efficiency as a function of the ^{13}C mean offset for the optimum excitation time (480 μs): the bandwidth is approximately 30 kHz and covers the entire ^{13}C spectral width at 750 MHz.

Figure 4-12c-d shows simulations on the glycine spin system that do not include any ^1H irradiation. Figure 4-12c shows the DQ efficiency at $\omega_c/2\pi = 100$ kHz as a function of the p value, i.e. as with varying MAS frequency, for an excitation time of 480 μs . The solid line represents the DQ efficiency as a function of the p for the theoretical settings. For $p > 5$ the DQ efficiency appears to decay as a function of the p index. This can largely be explained by the increase of higher order cross terms as the MAS frequency decreases (or the p index increases).

The dotted line in Fig. 4-12c indicates DQ efficiency after p and p' indexes optimizations. *For p_0 ranging from 3 to 14, it is possible to regain more than 50 % DQ efficiency, which suggests that a large part of the cross terms contribution comes as longitudinal and transverse T_{1q}^{C} operators, and thus can be compensated by p and p' mismatch.* Such optimization in practical terms involves a grid search over average rf power and phase excursion around the theoretical value. With a fixed modulation frequency $\omega_c/2\pi = 100$ kHz, CMpRR leads to

efficient DQ recoupling for p ranging from 3.5 to 10 with a maximum around 5 (i.e. for a MAS frequency ranging approximately from 10 to 30 kHz). Further details about the DQ p -dependency can be found in the next section.

Finally, Fig. 4-12d represents the simulated DQ efficiency for glycine as a function of the ^{13}C mean offset for several p indices with fixed modulation frequency $\omega_c/2\pi = 100$ kHz. The bandwidth plotted is slightly asymmetric with respect to the ^{13}C mean offset zero, which is consistent with the fact that the two carbons are not equivalent. The resulting bandwidth ranges from 25 to 30 kHz for MAS from 14 to 29 kHz.

Figure 4-13 compares CM_5RR and SPC5 DQ recoupling efficiency and *highlights the importance of the phase modulation scheme itself* in contrast to the shear rf field strength. Indeed, both pulse sequences require a rf field strength equal to 5 times the MAS frequency and were obtained at $\omega_{0,\text{H}}/2\pi = 750$ MHz and $\omega_r/2\pi = 20$ kHz from a sample of 20% [$^{13}\text{C}, ^{15}\text{N}$]-glycine without any ^1H decoupling. CM_5RR performs about 2.5 times better than SPC5 in terms of DQ efficiency with a better scaling factor- shorter excitation time (~ 0.5 ms versus ~ 1 ms). This clearly shows that even though the recoupling field strength is an important factor for improving polarization transfer, the pulse sequence scheme can be of major importance. Note that this is also consistent with the simulations presented in Fig. 4-10a for a MAS frequency of 12 kHz, where CMpRR always performs better than the other sequences using equivalent $\omega_1/2\pi$ at the $\omega_r/2\pi$. Figure 4-13 also compares the experimental performance of CM_5RR ($\omega_r/2\pi = 20$ kHz) and $\text{CM}_{3,5}\text{RR}$ ($\omega_r/2\pi = 28.57$ kHz) for a fixed modulation frequency equal to 100 kHz. As predicted by the simulations, $\text{CM}_{3,5}\text{RR}$ is less efficient than CM_5RR in exciting DQ coherence when no ^1H irradiation is applied (see also Sect. 6.4 for details on the CMpRR decoupling efficiency as a function of p). Note that even though $\text{CM}_{3,5}\text{RR}$ ($\omega_r/2\pi = 28.57$ kHz) displays decreased performance in absence of ^1H decoupling when compared to CM_5RR , it still performs better than SPC5 ($\omega_r/2\pi = 20$ kHz).

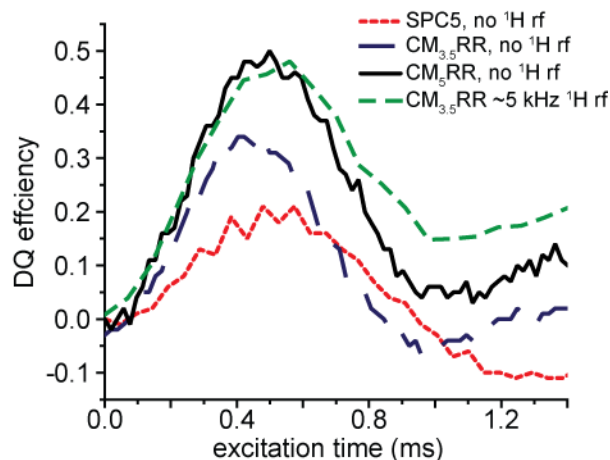


Figure 4-13 Experimental DQ coherence buildups for 20% [U- ^{13}C , ^{15}N]-glycine obtained at 750 MHz ^1H Larmor frequency. The ^{13}C rf field strength used was 100 kHz for all the experiments. Both CM_5RR (black solid line) and SPC5 (red dotted line) were obtained at 20 kHz MAS with no ^1H irradiation. $\text{CM}_{3.5}\text{RR}$ was obtained at 28.571 kHz MAS using no ^1H (blue long-dashed line) and ~ 5 kHz ^1H irradiation (green short-dashed line).

4.7.5 Second and third order effects in CMpRR

The aim of this section is to qualitatively understand the CMpRR DQ efficiency as a function of the p index [Fig. 4-12c] and the fine structure of the maps presented in bottom panel in Fig. 4-11. As previously explained, Average Hamiltonian Theory can be applied over a period equal to $2\tau_r$ for the CMpRR recoupling sequence. Second and third order effects are necessary to explain the CMpRR performance. Calculations are detailed in Supporting Information Appendix F.

First, the absence of DQ transfers for $p < 2.5$ [Fig. 4-12c] can be explained by concurrent first order recoupling of interactions other than DQ dipolar term. This can clearly be seen in Fig. 4-4 that displays all the first order recoupling conditions for the $p < 2.5$.

There are numerous second order contributions but the most important of these involve the chemical shift and heteronuclear dipolar coupling tensors. As already stated above, in absence of ^1H decoupling, the heteronuclear interactions and the chemical shift anisotropy transform in the same manner under ^{13}C rf irradiation. The cross term of the first term of Eq. 13 with itself has the following expression for $p > 2.5$:

$$\begin{aligned} \widetilde{\widetilde{\mathbf{H}}}^{(2)} &= \left[\sum_{m=1}^2 \left(\frac{\left(2m^2 + 2p^2 - \frac{1}{2} \right)}{\left(m + p + \frac{1}{2} \right) \left(m - p + \frac{1}{2} \right) \left(m + p - \frac{1}{2} \right) \left(m - p - \frac{1}{2} \right)} \right) d^m d^{-m} \right] \frac{1}{8\omega_r} \sum_{i=1}^2 T_{S,10}^i \quad (48) \\ &\approx \sum_{p \rightarrow \infty}^2 \sum_{i=1}^2 \frac{1}{4\omega_r} \left(\frac{1}{p^2} \right) d^m d^{-m} T_{S,10}^i \approx \sum_{p \rightarrow \infty}^2 \sum_{i=1}^2 \frac{1}{4\omega_c} \left(\frac{1}{p} \right) d^m d^{-m} T_{S,10}^i \end{aligned}$$

Equation (50) shows that this cross term leads to a *longitudinal contribution* $T_{S,10}^i$ in the effective Hamiltonian and that, at a constant MAS frequency, the size of this cross term decreases as the p increases, i.e. as the rf power is increased. More interestingly, the last part of Eq. (48) also shows that, at a constant modulation frequency $\omega_c/2\pi$, i.e. at approximately constant rf power, the size of the cross terms decrease as the p increases, i.e. as $\omega_r/2\pi$ decreases.

This term alone cannot explain the p -dependency that we observe in Fig. 4-12c. On the contrary, this cross term decreases as p increases (or $\omega_r/2\pi$ decreases) for a given modulation frequency.

If we now consider the cross term involving the first and the second term of Eq. (13), we find after some calculations that there are non-zero contributions only for discrete p -values with $p < 4.5$ (see Supporting Information Appendix F for details). This term can not explain the p -dependency observed in Fig. 4-12c, but is consistent with the fact that CMpRR can efficiently excite DQ efficiency for p ranging from 4 to 14.

The cross terms involving the second term (homonuclear ^{13}C dipolar interaction) of Eq. (13) with itself lead to a wide variety of second order recoupling effects. At constant modulation frequency, it can be shown that they do increase with the p index. However, they are too small to explain the DQ p -dependency of Fig. 4-12c.

Finally, let us consider the ^1H - ^1H dipolar interaction and try to evaluate its influence on the ^{13}C DQ first order recoupling dynamics. This interaction is particularly important in methylene groups. The glycine model system chosen here should thus be an ideal reference system to account for ^1H - ^1H effects on DQ recoupling dynamics. The ^1H - ^1H dipolar interaction does not commute with the ^1H - $^{13}\text{C}_\alpha$ dipolar tensor. In the absence of ^1H irradiation, it is possible to show that this type of second order recoupling occurs, notably for $p= 3.5, 4, 4.5$ (see Supporting Information Appendix F). This is in a perfect agreement with behavior in Fig. 4-

12c which shows that the DQ efficiency is improved for p ranging from 3 to 4.5 when the ^1H - ^1H interaction is removed from the simulation. Note that when we reverse the role of ^{13}C and ^1H we gain some insight into the performance of CM and TPPM decoupling, namely that for $p \leq 4.5$ the decoupling performance of these sequences may decrease due to second order recoupling of ^{13}C - ^{13}C dipolar interaction.

At this point, second order contributions do not explain why the theoretical DQ efficiency decays at high p -values. Let us now consider third order contributions. The main possible third order effect involves the chemical shift tensor with itself ($CS \times CS \times CS$) leading to a transverse contribution to the effective Hamiltonian. For high p values, this term tends towards $|\lambda|/p\omega_r^2$, with λ representing an anisotropic coefficient determined by the spin system interactions only. If we now replace one chemical shift term by the residual rf Hamiltonian ($\tilde{H}_{\delta p_0}$), we keep the same spin operators but modify the magnitude of the third order effect and obtain in the limit of high p -value: $|\lambda'|(\delta p_0\omega_r)/p\omega_r^2 \approx |\lambda'|(\delta p_0)/p\omega_r$, where λ' represents an anisotropic coefficient fixed by the spin system interactions. The sign of this second contribution is given by the sign of δp_0 . A negative shift $\delta p_0\omega_r \approx -|\lambda/\lambda'|$ can thus compensate for third order contributions. This is consistent with the contour plots presented in Fig. 4-11 that show for three different p -values 3.5, 5, 10 an approximately constant negative shift $\delta p_0\omega_r$ of 1.8, 1.5, 1.6 kHz respectively.

The previous paragraph implies a few points. First, the third order contribution of the chemical shift tensor can be rewritten as $|\lambda|p/\omega_c^2$ which implies that at constant modulation frequency, this term contribution increases with p explaining the decay of the dashed and solid lines in Fig. 4-12 (corresponding to the DQ efficiency for unoptimized CMpRR without and with ^1H - ^1H coupling included). Moreover, the previous paragraph also explains why a shift in δp index can compensate for transverse cross terms contributions. A more detailed investigation of all third order contributions is currently under investigation and should enable us to quantify more accurately the δp shift and to explain in more details the dotted line (corresponding to the DQ efficiency for the optimized CMpRR with all interaction included) evolution. From a practical point of view we should mention that for $p < 15$ it appears possible to compensate for most part of such cross term effects by mismatching the p and p' values.

4.7.6 DQ efficiency dependency on the ^1H CW decoupling

Up to this point in the discussion of CMpRR, we have not considered the possible influence of ^1H irradiation. In this section we investigate the effect of an additional ^1H rf field applied during ^{13}C irradiation. In order to simplify the problem of the interference of ^{13}C - ^{13}C DQ homonuclear recoupling with ^1H - ^{13}C heteronuclear decoupling, we first performed simulations with *no ^{13}C isotropic and anisotropic chemical shift interactions* (Fig. 4-14).

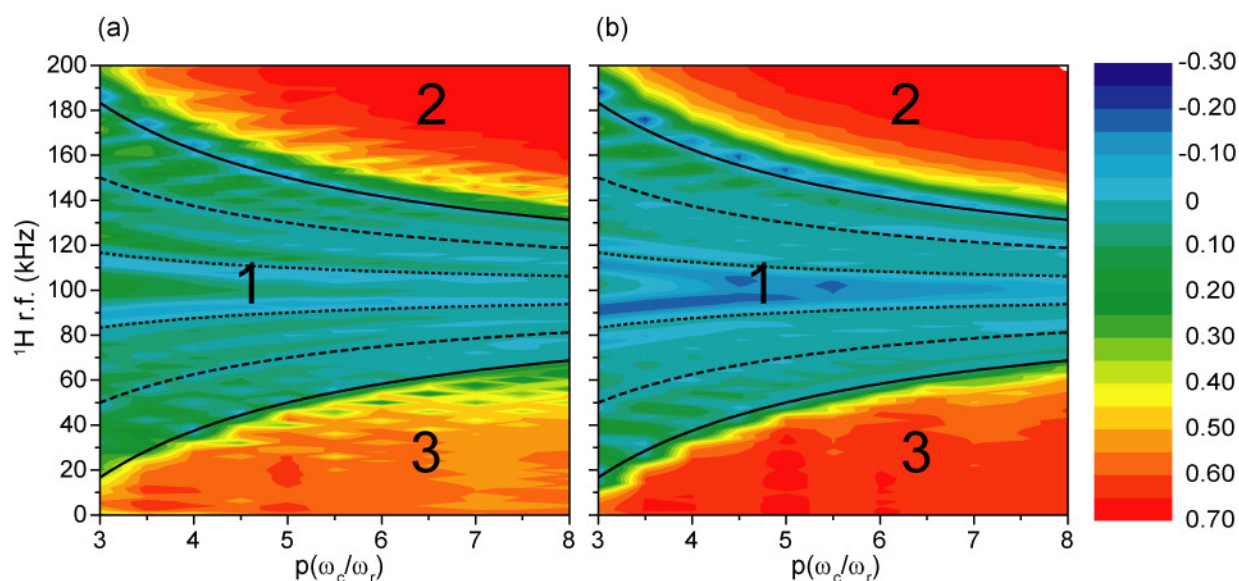


Figure 4-14 Simulated contour plots of DQ efficiency as a function of p index and ^1H rf field strength for (a) glycine and (b) alanine spin systems. Simulations were performed with a constant modulation frequency ω of 100 kHz using the theoretical settings of $p' = 0.5$. No isotropic chemical shift was included in the calculations in order to minimize the shift from the theoretical settings and thus focus on the influence of ^1H - ^{13}C and ^1H - ^1H interactions on the DQ recoupling spin dynamics. The plots are divided into three areas: 1 – intermediate decoupling regime, 2 – high power decoupling regime, 3 – low power decoupling regime. See text for the explanations of the fine structure of the plots.

Figure 4-14 depicts the simulated DQ efficiency on two model spin systems - glycine (Fig 4-14a) and alanine (Fig. 4-14b), as a function of the CMpRR p index and the ^1H CW rf field strength. These two amino acids are good representatives of the ^1H environment in various amino acids present in peptides and proteins and thus are good model systems to understand

DQ recoupling dynamics in large bio-molecular system. In all the simulations, the modulation frequency of the CMpRR $\omega_c/2\pi$ sequence was chosen to be 100 kHz.

The contour plots in Fig. 4-14 can be divided into three main areas: the intermediate decoupling regime (area 1), the high power decoupling regime (area 2), and the low power decoupling regime (area 3).

The fine structure of the intermediate decoupling regime (area 1) can be explained by the presence of Hartmann-Hahn (HH) matching conditions represented by the black lines (solid, dashed and dotted) for which $p_H = p_C \pm \{0.5, 1.5, 2.5\}$. More precisely, pure DQ/ZQ HH conditions are obtained for $p_H = p_C + \{-0.5, 2.5\} / p_H = p_C + \{0.5, -2.5\}$ (note that these conditions may be used as an alternative to CP for systems with large chemical shift anisotropy) and a superposition of DQ and ZQ process for $p_H = p_C + \{-1.5, 1.5\}$. Along these lines ^1H - ^{13}C interactions are reintroduced to first order leading to leakage of the ^{13}C magnetization to the ^1H 's. In the area between the HH lines, some DQ efficiency transfer can be recovered, especially in the glycine case. The precise theoretical description of this effect is beyond the scope of this article so we will only comment briefly on the reasons for this behavior. The spin dynamics in the area 1 off the HH conditions is greatly influenced by cross terms involving heteronuclear ^{13}C - ^1H couplings.

Note that this mechanism has recently been introduced by the same authors as a Third Spin Assisted Recoupling (TSAR) phenomenon and applied to design new recoupling sequences suitable for structure determination studies by SSNMR. More precisely, this new concept has been applied to heteronuclear ^{15}N - ^{13}C transfer with the PAINCP pulse sequence, and homonuclear ^{13}C - ^{13}C and ^{15}N - ^{15}N transfer with the proton assisted homonuclear recoupling (PAR) pulse sequence.⁵⁵ Both of these techniques use protons to assist the polarization transfer.

To understand the structure of the first area of the map, we need to consider contributions of the following forms $T_{1\pm 1}^{H^1} T_{1\mp 1}^{H^2} T_{10}^{C^\alpha}$ and $T_{1\pm 1}^{C^1} T_{1\mp 1}^{C^2} T_{10}^H$ where carbons and protons are the assisting spins respectively. The relative size of these contributions is dependent on the rf pulse sequence applied and the geometry of the spin system considered. In the Alanine case, terms of the form $T_{1\pm 1}^{C^1} T_{1\mp 1}^{C^2} T_{10}^H$ lead to ZQ ^{13}C - ^1H - ^{13}C polarization transfer (negative area in the center of the map) that directly interfere with the CMpRR DQ transfer. In the glycine case,

terms of the form $T_{1\pm 1}^{H_1} T_{1\mp 1}^{H_2} T_{10}^{C_\alpha}$, that yield ZQ ^1H - ^{13}C - ^1H recoupling, have a more important influence. They strongly interfere with the ZQ ^{13}C - $[\text{}^1\text{H}]$ - ^{13}C effective terms leading to a partial recovery of the CMpRR DQ recoupling transfer. This is illustrated at the center of the HH area, where 40% DQ transfer can be recovered in the glycine case, compared to almost no transfer in the alanine case.

The second area of Fig. 4-14 corresponds to a high power ^1H decoupling regime. The second order effects discussed above, although still present, are now weaker and do not substantially modify the DQ spin dynamics. Here it is important to note that we can define the minimal ^1H decoupling field strength enabling the access to efficient high power decoupling regime as $\omega_1^H = p_H \omega_R \geq (p_C + 3.5) \omega_R = \omega_C + 3.5 \omega_R$. This condition is somewhat different from the factor of three mismatch between ^1H and ^{13}C rf field strengths used as a rule of thumb to assure efficient ^{13}C - ^{13}C recoupling.³⁹

The third area of Fig. 4-14 appears very different for the two amino acids. The differences can be attributed to a large extent to the presence of a strong ^1H - ^1H dipolar coupling in the glycine case. A detailed analysis of the DQ maps is complicated and beyond the scope of this article. Nevertheless, it is clear from the map that in the absence of ^1H decoupling efficient DQ transfers comparable to the high power decoupling regime are possible for the alanine spin system. In the glycine spin system, it is worth noting however, that the performance in the absence of decoupling may be improved by applying a weak ^1H field during the CMpRR pulses for $p \leq 5$.

4.7.7 Low power ^1H irradiation in CMpRR

This section focuses on the low power ^1H irradiation regime and provides some insight into this process by considering the $p = 3.5$ case in detail.

Figure 4-13 shows an experimental DQ efficiency curve for 20% $[\text{U-}^{13}\text{C}, ^{15}\text{N}]$ -glycine using CM_{3.5}RR with and without the application of a 5 kHz of ^1H rf field. As expected from Fig. 4-14 we recover an additional 14% efficiency by the application of a weak ^1H field which clearly illustrates the importance of this low ^1H field irradiation using $p = 3.5$. Similar effects occurs for $p = 4$ and 4.5. Above $p = 5$, the low field irradiation does not improve the one-bond DQ transfer efficiency of the glycine spin system compared to the simulation without decoupling.

Thus the application of a weak ^1H field extends the application of CMpRR to $p = 3.5, 4$ and 4.5 .

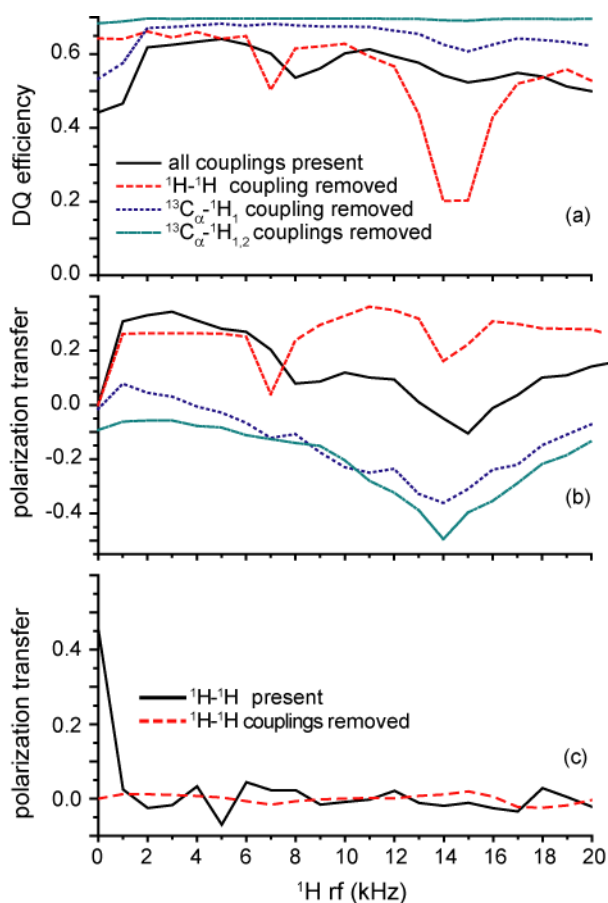


Figure 4-15 (a) CM_{3.5}RR DQ efficiency as a function of the ^1H rf power for the glycine spin system. The mixing time was chosen to optimize the transfer efficiency. Graphics (b) and (c) show ^1H - ^1H polarization transfer occurring exactly under the same $^{13}\text{C}/^1\text{H}$ irradiation schemes but with 3 ms mixing time. The magnetization starts on the first proton along the CW irradiation axis / Z-axis and is detected on the second proton spin along the CW irradiation axis / Z-axis in (b) and (c) respectively. See text for the discussion of the features of the simulations.

Figure 4-15a shows a simulated DQ efficiency curve for a glycine spin system as a function of the ^1H rf power and compares it to the same simulation obtained by removing either the $H_\alpha^1 - H_\alpha^2$, $C_\alpha - H_\alpha^1$ or both $C_\alpha - H_\alpha^1$ and $C_\alpha - H_\alpha^2$ couplings. In these simulations, the mixing time was set to maximize the DQ transfer. To complement the study, Fig. 4-15b-c shows the ^1H - ^1H polarization transfer occurring under the same $^{13}\text{C}/^1\text{H}$ irradiations. In Figure 4-15b, the

magnetization starts on the first proton along the ^1H CW irradiation axis ($I_x^{H^1}$) and is detected on the second proton spin along the same axis ($I_x^{H^2}$). In Figure 4-15c, the magnetization starts on the first proton along the lab frame Z-axis ($I_z^{H^1}$) and is detected on the second proton spin along the Z-axis ($I_z^{H^2}$).

In absence of ^{13}C - ^1H couplings, we can see from Fig. 4-15a that the DQ efficiency is close to the maximum theoretical value ($\sim 70\%$) and independent of the ^1H irradiation strength. This is exactly the expected behavior as the two spin baths are completely decoupled. For the same settings, Fig. 4-15b shows the presence of a ^1H - ^1H transfer over the whole range of ^1H irradiation (0 to 20 kHz) with a maximum around the HORROR condition at $\omega_r/2$.

In absence of ^1H - ^1H couplings, the DQ efficiency [Fig. 4-15a] starts, for small ^1H irradiation, with a flat dependency close to the theoretical maximum. This shows that in the absence of ^1H - ^1H couplings, the $\text{CM}_{3.5}\text{RR}$ recoupling sequence provides high DQ efficiency with no additional ^1H decoupling and confirms the findings for the alanine simulation map in Fig. 4-14.

In the case where all interactions are included, the DQ efficiency rapidly increases from 44 to 62 % in between 0 to 5 kHz ^1H irradiation and then slowly decreases as the ^1H CW irradiation increases up to 20 kHz. When no ^1H irradiation is applied, for $p = 3.5, 4, 4.5$, cross terms involving ^1H - ^1H and ^1H - ^{13}C dipolar interactions result in operators of the form $T_{1\pm 1}^{H^1} T_{1\mp 1}^{H^2} T_{1\{\pm 1, 0\}}^{C_\alpha}$ (see Supporting Information Appendix F). They actively recouple the protons as shown in Fig. 4-15c for $p_H = 0$ and do not commute with the DQ ^{13}C - ^{13}C Hamiltonian leading to a significant decrease the CMpRR efficiency. Figure 4-15c confirms the involvement of the ^1H - ^1H coupling in the polarization transfer from $I_z^{H^1}$ to $I_z^{H^2}$. Indeed the polarization transfer is completely quenched when the ^1H - ^1H coupling is removed. For non-zero ^1H irradiation, the previous term vanishes and is progressively replaced by second order TSAR terms (involving ^1H - ^{13}C dipolar interaction). This type of second order cross terms mainly yields to ^1H - ^{13}C - ^1H recoupling in this regime. This can clearly be seen in Fig. 4-15b. Indeed, even in absence of ^1H - ^1H couplings, the two methylene protons do communicate efficiently over almost the whole range of ^1H fields. This phenomenon is due to a second order effect involving the two $\text{C}_\alpha\text{-H}_1$ and $\text{C}_\alpha\text{-H}_2$ dipolar couplings leading, in the double tilted interaction frame, to terms of the

forms $T_{1\pm 1}^{H^1} T_{1\mp 1}^{H^2} T_{1,0}^{C_\alpha}$ that yield efficient ZQ proton-proton recoupling with carbons as assisting spins. As stated above, this type of terms do not commute with the CMpRR DQ ^{13}C term and lead to a decrease of ^{13}C - ^{13}C transfer efficiency. Note that this effect is smaller than the one induced by the cross term between the ^1H - ^1H and ^{13}C - ^1H dipolar interactions, as almost 60% ^{13}C DQ CMpRR transfer can still be reached.

In the case where only one of the heteronuclear couplings is turned off (i.e. $C_\alpha\text{-H}_\alpha^1$), the arguments listed above are confirmed by the simulations shown in Fig. 4-15a and b. First, the decrease in DQ efficiency at $\omega_1^H = 0$ is still present but to a lesser degree as only the $C_\alpha\text{-H}_\alpha^2$ dipolar interaction can contribute to the cross terms with the ^1H - ^1H coupling. In addition, it is also clear that this efficiency drop is absent in simulation with either ^1H - ^1H or both $C_\alpha\text{-H}_\alpha^{1,2}$ couplings are removed. Second, the ^1H - ^1H transfer curve roughly follows the case where both $C_\alpha\text{-H}_\alpha^1$ and $C_\alpha\text{-H}_\alpha^2$ are absent, as no ZQ ^1H -($^{13}\text{C}_\alpha$)- ^1H TSAR recoupling occurs.

As a conclusion of this section, we have investigated in detail the effect of a low ^1H rf field on the CMpRR DQ efficiency for $p = 3.5, 4, 4.5$. We have notably proved that it allows recovering high ^{13}C DQ efficiency comparable to CMpRR with $p > 5$ and no ^1H decoupling.

4.7.8 CMpRR: 2D ^{13}C - ^{13}C correlation experiments

In this section, we provide experimental demonstrations of the use of the CMpRR pulse sequence for spectral assignment at high magnetic fields. A series of broadband ^{13}C SQ-SQ 2D correlations of 10% [U- ^{13}C , ^{15}N]-*f*-MLF-OH tripeptide are shown in Fig. 4-16. Figure 4-16a shows a 900 MHz (21.1 T) $\text{CM}_{3.5}\text{RR}$ spectrum with a short mixing (840 μs - optimal for directly bonded carbons). As previously explained, a low power (ca. 4 kHz) ^1H irradiation was applied during the ^{13}C CMpRR pulses to increase the DQ efficiency transfer. A 1D slice through from the 2D spectrum in Fig. 4-16c illustrates the efficiency of the CMpRR recoupling. Note that the leucine $C_\alpha\text{-C}_\beta$ cross peak is actually larger than the diagonal peak. Figure 4-16b shows a 2D spectrum obtained at $\omega_{0,H}/2\pi = 750$ MHz, $\omega_1/2\pi = 20$ kHz with no ^1H irradiation and a mixing time of 2.1 ms. The spectrum contains multiple relayed cross

peaks and allows notably to connect the leucine C' to the end of the leucine sidechain through a 4-bond relayed transfer. The relayed transfer mechanism has already been discussed in the literature and is typical for homonuclear DQ recoupling sequences. This mechanism is also a signature of dipolar truncation which means that the spin dynamics is dominated by one-bond couplings. It is worth noting that the sequence appears very efficient in propagating the magnetization through one-bond distances since multiple bond cross peak intensities are oftentimes larger than one bond cross peaks at long mixing times. The optimum CMpRR mixing times are 0.8-0.9, 1.5-1.6 and 2.1-2.3 ms for one, two and three bond relayed contacts respectively (simulations not shown).

Cross peaks arising from relays across multiple bonds should be of major interest for assignment of congested spectra for which one-bond cross peaks are oftentimes not sufficient to reliably establish the connectivity.

Figure 4-17 shows an example of multiple quantum spectroscopy with a 2D DQ-SQ CM_{3,5}RR correlation spectrum of 10% [U-¹³C,¹⁵N]-*f*-MLF-OH obtained at $\omega_{0,H} / 2\pi = 900$ MHz with $\omega_r / 2\pi = 23.81$ kHz using ¹³C CM_{3,5}RR pulses of 83.3 kHz with ~4 kHz ¹H irradiation during the mixing. The mixing time used was 840 μ s (i.e. 420 μ s excitation) corresponding to 70 CM_{3,5}RR cycles or 20 rotor periods. The evolution interval t_1 was incremented in steps of 10 μ s, corresponding to 100 kHz spectral width in the indirect dimension. Because the indirect t_1 increment is not a multiple of the rotor period (here 42 μ s), the excitation and reconversion pulses do not start at the same rotor position inducing a phase-shift between the DQ excitation and reconversion Hamiltonians.^{42,56} Equation (40) can be rewritten for the excitation and reconversion pulses in order to account for this effect:

$$\overline{\tilde{H}}_{Exc}^{(1)} = \kappa_{1,0,0,2}^2 \omega_{SS,12} \sin(2\beta) \left\{ e^{-i\gamma} e^{i2\phi_E} e^{i\omega_r t_0^E} T_{SS,2-2}^{12} + e^{i\gamma} e^{-i2\phi_E} e^{-i\omega_r t_0^E} T_{SS,22}^{12} \right\} \quad (49)$$

$$\overline{\tilde{H}}_{Rec}^{(1)} = \kappa_{1,0,0,2}^2 \omega_{SS,12} \sin(2\beta) \left\{ e^{-i\gamma} e^{i2\phi_R} e^{i\omega_r t_0^R} T_{SS,2-2}^{12} + e^{i\gamma} e^{-i2\phi_R} e^{-i\omega_r t_0^R} T_{SS,22}^{12} \right\} \quad (50)$$

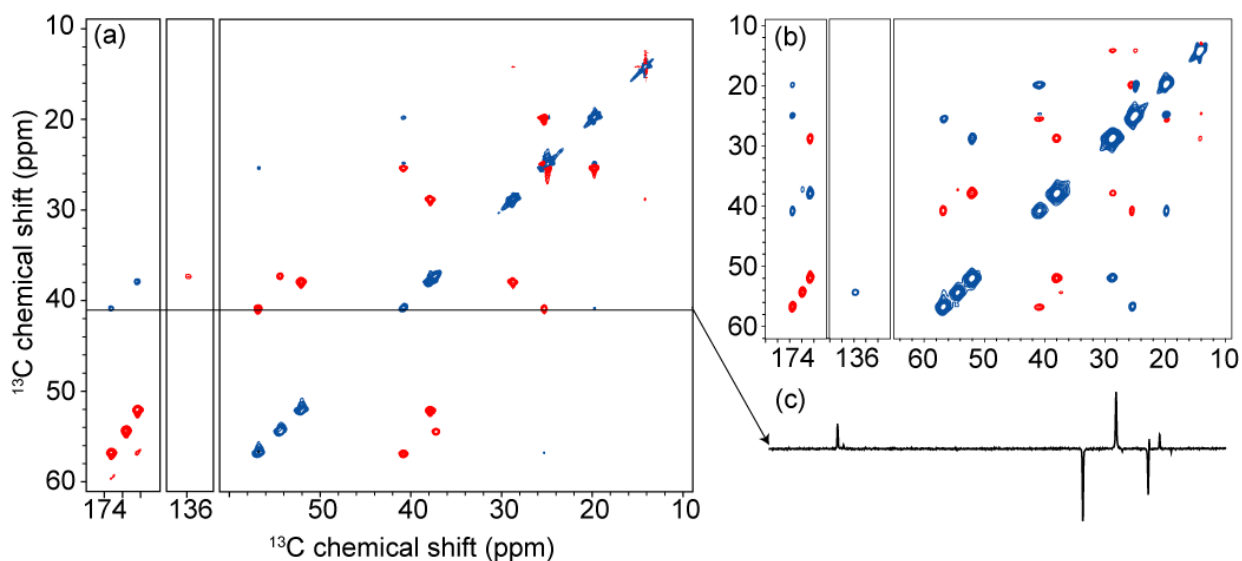


Figure 4-16 Experimental SQ-SQ 2D ^{13}C - ^{13}C correlation spectra for $[\text{U-}^{13}\text{C},^{15}\text{N}]\text{-}\beta\text{-MLF-OH}$ (a) using $\text{CM}_{3,5}\text{RR}$, at 900 MHz ^1H Larmor frequency, 23.81 kHz MAS, with 840 μs mixing using ~ 4 kHz ^1H decoupling and 83.3 kHz ^{13}C rf, (b) $\text{CM}_{3,5}\text{RR}$, at 750 MHz ^1H Larmor frequency, 20 kHz MAS, with 2.1 ms mixing using no ^1H decoupling and 100 kHz ^{13}C rf. The evolution interval t_1 was incremented in steps of 20 μs in (a-b). 100 kHz TPPM ^1H decoupling was used during the acquisition and evolution. The longer mixing time 2D spectrum in (b) features up to 4-bond relayed transfer cross-peaks.

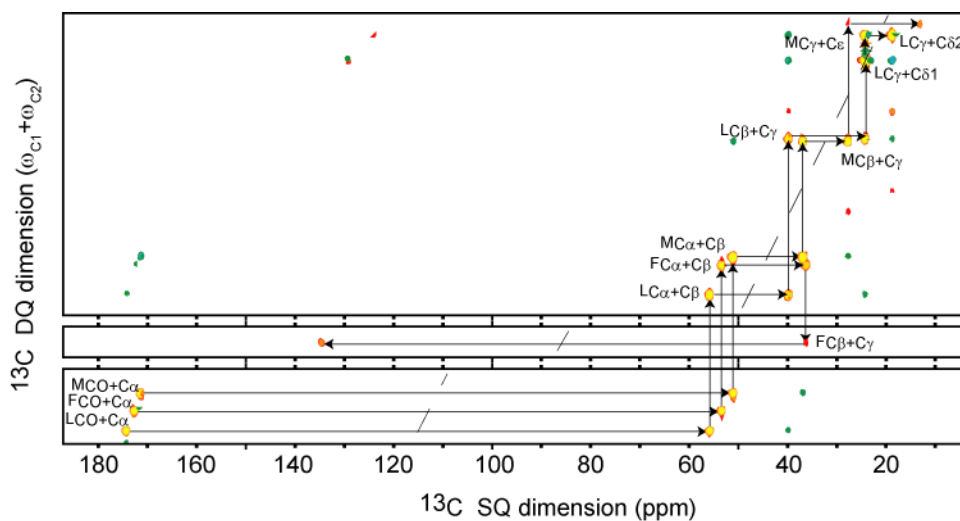


Figure 4-17 Experimental SQ-DQ 2D ^{13}C - ^{13}C $\text{CM}_{3,5}\text{RR}$ correlation spectrum obtained on a 10% $[\text{U-}^{13}\text{C},^{15}\text{N}]\text{-}\beta\text{-MLF-OH}$ at 900 MHz ^1H Larmor frequency, 23.81 kHz MAS, using 420 μs excitation time with 83.3 kHz ^{13}C irradiation and ~ 4 kHz ^1H irradiation. 100 kHz TPPM ^1H decoupling was used during

the acquisition and evolution. The t_1 evolution interval was incremented in steps of 10 μ s. The overall phase of the conversion was adjusted to correct for the phase acquired by DQ coherence due to not rotor-synchronized evolution period (see text).

In order to compensate for this shift the reconversion pulses should be shifted proportionally to the t_1 time increment.^{42,56}

$$\Delta\phi_R(n_1) = \frac{1}{2}\omega_r(t_0^R - t_0^E) = \frac{1}{2}\omega_r\tau_E + \frac{1}{2}\omega_r t_1 = \frac{n_r}{2}(2\pi) + \frac{1}{2}\omega_r n_1 \delta t_1 = \frac{1}{2}\omega_r n_1 \delta t_1 \quad (51)$$

where n_r is 20 here and n_1 stands as the increment number in the indirect dimension. In addition to the $\Delta\phi_R(n_1)$ phase shift, a regular DQ phase cycling was applied to the reconversion pulses to ensure a proper selection of the (± 2)-quantum coherences evolving during the t_1 dimension. Finally for each t_1 point, two spectra were recorded in order to differentiate the (± 2) coherences. In the second set of spectra, the phase of the all the pulses before the t_1 evolution are shifted by $\pi/4$ in order to use a States⁵⁷ procedure for phase sensitive detection.

Following the nomenclature introduced by Brinkmann *et al.*, we observe the presence of direct ($jk \rightarrow j$) and indirect ($jk \rightarrow l$) cross peaks.⁴² For the short mixing time shown here, cross peaks are in absorption phases with a positive/ negative sign for the strong direct/ indirect cross peaks respectively. The assignment of the N-*f*-MLF-OH can be done easily using the spectral walk represented by the black arrows. Direct cross peaks connect directly bonded ¹³C's whereas indirect cross peaks show contacts to the nearest neighbors.

In this final section we have shown that efficient DQ/SQ ¹³C correlation is feasible at high Larmor and spinning frequencies. This can potentially be very useful for assigning larger biomolecular systems especially for cross peaks close to the diagonal in conventional SQ/SQ ¹³C experiments. Moreover, the presence of the indirect cross peaks should provide a convenient way to help assigning crowded spectra.

4.8. Conclusion

In this paper we have introduced a new family of MAS dipolar recoupling sequences that stem from the concept of Modulation Frame and second averaging. We discuss in detail the

properties of the DQ cosine modulated rotary resonance (CMpRR). The salient feature of this recoupling sequence is that it allows efficient, broadband DQ recoupling experiments at high fields and high spinning frequencies without application of ^1H decoupling fields. The performance of this new recoupling scheme has been discussed in the context of Average Hamiltonian Theory up to third order. We show that a slight mismatch with respect to the theoretical settings can compensate for undesirable cross terms and allows one to efficiently apply this approach to recoupling from $\omega_r/2\pi = 10$ to 30 kHz and at $\omega_{0,\text{H}}/2\pi = 700$ -900 MHz. Moreover, we show that in some cases (i.e. for $p \leq 4.5$), the use of a small ^1H irradiation can enhance substantially the DQ recoupling efficiency. Finally, we present examples of SQ/SQ and DQ/SQ correlation experiments at high magnetic fields and high spinning frequencies. Applications of this recoupling technique to biological systems at 900 MHz have already been presented²⁶ and will be reported elsewhere.

Finally we also illustrate the flexibility of the generalized CM schemes by introducing a new concept for performing selective homonuclear recoupling experiments (COMICS) through the simultaneous reintroduction of the ^{13}C DQ dipolar and ^{13}C isotropic chemical shift interactions. This approach is intended as a general frequency selective scheme (in contrast to R^2 experiments that are suitable only for nuclei pairs with large chemical shift separation) circumventing dipolar truncation in uniformly labeled systems. Application of this concept to structural studies is under investigation.

4.9 Acknowledgments

This work was supported by National Institutes of Health Grant EB001960 and EB002026. We would like to thank Drs. P. van der Wel, R. Ramachandran, J. Struppe, M. Veshtort, and D. Ruben for stimulating discussions and Matthew Eddy for a careful reading of the manuscript. We also would like to give special thanks to M. Bayro for active involvement in the initial stages of the work on use of cosine modulation for ^{13}C - ^{13}C recoupling.

4.10 Supporting Information

4.10.1 Appendix A: Cosine and Sine expansion:

A cosine modulated rf phase (CM) can be written as: $\phi(t) = a \cos(\omega_c t - \phi_0)$. With $|\phi| \leq 1.8$ radian, we can use the following approximations: $\cos(\phi) \approx 1 - \frac{\phi^2}{2!} + \frac{\phi^4}{4!}$ and $\sin(\phi) \approx \phi - \frac{\phi^3}{3!} + \frac{\phi^5}{5!}$.

We can rewrite the expression of the rf Hamiltonian in the Lab frame:

$$H_{rf} = \omega_1 \left(1 - \frac{a^2 \cos^2(\omega_c t - \phi_0)}{2!} + \frac{a^4 \cos^4(\omega_c t - \phi_0)}{4!} \right) \sum_i S_x^i + \omega_1 \left[\begin{aligned} & \left(a - \frac{a^3}{8} + \frac{a^5}{192} \right) \cos(\omega_c t - \phi_0) \\ & - \left(\frac{a^3}{24} - \frac{a^5}{384} \right) \cos(3 * (\omega_c t - \phi_0)) \\ & + \left(\frac{a^5}{1920} \right) \cos(5 * (\omega_c t - \phi_0)) \end{aligned} \right] \sum_i S_y^i \quad (52)$$

i.e.

$$H_{rf} = \omega_1 \left[\begin{aligned} & 1 - \frac{a^2}{4} + \frac{a^4}{64} \\ & - \left(\frac{a^2}{4} - \frac{a^4}{48} \right) \cos(2\omega_c t - 2\phi_0) \\ & + \frac{a^4}{192} \cos(4\omega_c t - 4\phi_0) \end{aligned} \right] \sum_i S_x^i + \omega_1 \left[\begin{aligned} & \left(a - \frac{a^3}{8} + \frac{a^5}{192} \right) \cos(\omega_c t - \phi_0) \\ & - \left(\frac{a^3}{24} - \frac{a^5}{384} \right) \cos(3 * (\omega_c t - \phi_0)) \\ & + \left(\frac{a^5}{1920} \right) \cos(5 * (\omega_c t - \phi_0)) \end{aligned} \right] \sum_i S_y^i \quad (53)$$

4.10.2 Appendix B: Irreducible spherical tensor, ZQ and DQ operators:

Irreducible spherical tensor operators:

$$\begin{aligned}
T_{10}^i &= S_{iz} \\
T_{1\pm 1}^i &= \mp \frac{1}{\sqrt{2}} S_i^\pm \\
T_{00}^{jk} &= -\frac{1}{\sqrt{3}} \overrightarrow{S_j} \cdot \overrightarrow{S_k} \\
T_{10}^{jk} &= \frac{-1}{2\sqrt{2}} (S_j^+ S_k^- - S_j^- S_k^+) \\
T_{1\pm 1}^{jk} &= \frac{-1}{2} (S_j^\pm S_{kz} - S_{jz} S_k^\pm) \\
T_{20}^{jk} &= \frac{1}{\sqrt{6}} (3S_{jz} S_{kz} - \overrightarrow{S_j} \cdot \overrightarrow{S_k}) \\
T_{2\pm 1}^{jk} &= \mp \frac{1}{2} (S_j^\pm S_{kz} + S_{jz} S_k^\mp) \\
T_{2\pm 2}^{jk} &= \frac{1}{2} S_j^\pm S_k^\pm
\end{aligned} \tag{54}$$

Two spins ZQ subspace operators for spins k and l:

$$\begin{aligned}
I_x^{(kl),(23)} &= \frac{1}{2} (2I_{kx} I_{lx} + 2I_{ky} I_{ly}) = \frac{1}{2} (I_k^+ I_l^- + I_k^- I_l^+) = -(T_{11}^k T_{1-1}^l + T_{1-1}^k T_{11}^l) \\
I_y^{(kl),(23)} &= \frac{1}{2} (2I_{ky} I_{lx} - 2I_{kx} I_{ly}) = \frac{i}{2} (-I_k^+ I_l^- + I_k^- I_l^+) = i (T_{11}^k T_{1-1}^l - T_{1-1}^k T_{11}^l) \\
I_z^{(kl),(23)} &= \frac{1}{2} (I_{kz} - I_{lz}) = \frac{1}{2} (T_{10}^k - T_{10}^l)
\end{aligned} \tag{55}$$

Two spins DQ subspace operators for spins k and l:

$$\begin{aligned}
I_x^{(kl),(14)} &= \frac{1}{2} (2I_{kx} I_{lx} - 2I_{ky} I_{ly}) = \frac{1}{2} (I_k^+ I_l^+ + I_k^- I_l^-) \\
I_y^{(kl),(14)} &= \frac{1}{2} (2I_{kx} I_{ly} + 2I_{ky} I_{lx}) = \frac{i}{2} (-I_k^+ I_l^+ + I_k^- I_l^-) \\
I_z^{(kl),(14)} &= \frac{1}{2} (I_{kz} + I_{lz})
\end{aligned} \tag{56}$$

4.10.3 Appendix C: Scaling factor

For the sequences described in this manuscript we use the following conventions for scaling factor:

a. Spatial part: $S_m^{spatial}$:

$$\begin{aligned} S_1^{spatial} &= S_{-1}^{spatial} = \frac{1}{2\sqrt{2}} \\ S_2^{spatial} &= S_{-2}^{spatial} = \frac{1}{4} \end{aligned} \quad (57)$$

b. Spin part: $S_{m,q'',q,q'}^{spin}$:

$$S_{q'',q,q'}^{spin,l} = d_{q''q}^2 \left(\frac{\pi}{2} \right) d_{q'q}^2 \left(\frac{\pi}{2} \right) \quad (58)$$

Scaling factor obtained for homonuclear dipolar recoupling experiments is:

$$S_{m,q'',q,q'} = \sqrt{6} S_m^{spatial} S_{q'',q,q'}^{spin,l} \quad (59)$$

Properties:

$$\begin{aligned} S_{m,q'',q,q'} &= S_{-m,q'',q,q'} \\ S_{m,q'',q,q'} &= (-1)^q S_{m,-q'',q,q'} \\ S_{m,q'',q,q'} &= (-1)^{q'+q''} S_{m,q'',-q,q'} \\ S_{m,q'',q,q'} &= (-1)^q S_{m,q'',q,-q'} \end{aligned} \quad (60)$$

4.10.4 Appendix D: Time dependent expression for the dipolar interaction

λ represents the type of dipolar interaction (II/ SS/ IS, for homonuclear ^1H - ^1H , ^{13}C - ^{13}C , and heteronuclear ^1H - ^{13}C respectively).

$$\omega_{\lambda,ij}^{(0)} = 0 \quad (61)$$

and

$$\omega_{\lambda,ij}^{(m)} = -\omega_{\lambda}^{ij} D_{0,-m}^2 \left(\Omega_{PR}^{\lambda,ij} \right) d_{-m,0}^2 \left(\beta_{RL} \right) \quad (62)$$

$\omega_{\lambda}^{ij} = \left(\frac{\mu_0}{4\pi} \right) \frac{\gamma_i \gamma_j \hbar}{r_{ij}^3}$ indicates the dipolar coupling constant in between spin i and spin j. $\Omega_{PR}^{\lambda,ij}$

represents the Euler angles between the Principal Axis Frame and the Rotor Frame.

We then easily obtain:

$$\omega_{\lambda,ij}^{(1)} = -\frac{\omega_{\lambda,ij}}{2\sqrt{2}} \sin(2\beta) e^{-i\gamma} = -\omega_{\lambda,ij} S_1 \sin(2\beta) e^{-i\gamma} = \omega_{\lambda,ij}^{(-1)*} \quad (63)$$

$$\omega_{\lambda,ij}^{(2)} = -\frac{\omega_{\lambda,ij}}{4} \sin^2(\beta) e^{-i2\gamma} = -\omega_{\lambda,ij} S_2 \sin^2(\beta) e^{-i2\gamma} = \omega_{\lambda,ij}^{(-2)*} \quad (64)$$

4.10.5 Appendix E: Euler angles and generalized CM-based interaction frame

Any rotation (transformation in the spin space $U_{MM'}^J(\omega, \theta, \varphi)$) can be expressed as a rotation of angle ω around an axis $\vec{n}(\theta, \varphi)$, where θ stands for the angle between the initial z-axis and the rotation axis, φ for the angle in between the x-axis and the projection of the rotation axis on the xy plane, and finally ω for the nutation angle.⁵⁸ The previous rotation can be decomposed into three successive rotations of coordinate system:

$$\begin{cases} R_1(\alpha_1 = \varphi, \beta_1 = \theta, \gamma_1 = -\varphi) \\ R_2(\alpha_2 = \omega, \beta_2 = 0, \gamma_2 = 0) \\ R_3(\alpha_3 = \varphi, \beta_3 = -\theta, \gamma_3 = -\varphi) \end{cases} \quad (65)$$

The first rotation (R_1) turns the z-axis to the direction $\vec{n}(\theta, \varphi)$; the second rotation (R_2) is performed around $\vec{n}(\theta, \varphi)$ through an angle ω ; the third rotation (R_3) stands as the inverse of R_1 .

The result of these three rotations yields the relation between $U_{MM'}^J(\omega, \theta, \varphi)$ and the Wigner D-functions:¹

$$U_{MM'}^J(\omega, \theta, \varphi) = \exp(-i\omega \vec{n} \cdot \vec{J}) = \sum_{M''} D_{MM''}^J(\varphi, \theta, -\varphi) e^{-iM''\omega} D_{M''M'}^J(\varphi, -\theta, -\varphi) \quad (66)$$

Equation (66) enables one to find an explicit form for $U_{MM'}^J(\omega, \theta, \varphi)$ for particular J, M and M'.

As explained in section 2.1, the generalized CM-based recoupling scheme considered in this paper can always be decomposed into two contributions: a C.W. component of strength $\omega_c/2\pi$ and a resonant circular audio field of strength $\omega_{\text{eff}}/2\pi$. The Interaction Frame (IF), defined by the two steps averaging, can be depicted by the two sets of Euler transformations.

$$\begin{cases} R_1 \left(\alpha_1 = \phi_0, \beta_1 = \frac{\pi}{2}, \gamma_1 = -\phi_0 \right) \\ R_2 \left(\alpha_2 = \omega_c t, \beta_2 = 0, \gamma_2 = 0 \right) \\ R_3 \left(\alpha_3 = \phi_0, \beta_3 = -\frac{\pi}{2}, \gamma_3 = -\phi_0 \right) \end{cases} \quad (67)$$

$$\begin{cases} R_4 \left(\alpha_4 = \pi/2 + \phi_0, \beta_4 = \pi/2 - \phi_0, \gamma_4 = -(\pi/2 + \phi_0) \right) \\ R_5 \left(\alpha_5 = \omega_{\text{eff}} t, \beta_5 = 0, \gamma_5 = 0 \right) \\ R_6 \left(\alpha_6 = \pi/2 + \phi_0, \beta_6 = \phi_0 - \pi/2, \gamma_6 = -(\pi/2 + \phi_0) \right) \end{cases} \quad (68)$$

The first set of Euler Angle defines the first rotation of coordinate system (passive rotation), $S(x, y, z) \rightarrow S'(x', y', z')$: i.e. a rotation of an angle $(\omega_c t)$ around the mean axis of irradiation which defines the transformation to the Modulation Frame. Because we have chosen that the strength of the first C.W. component matches the frequency of the audio field, the second rotation of coordinate system from $S'(x', y', z') \rightarrow S''(x'', y'', z'')$ can easily be seen as a rotation around an axis tilted along the angle ϕ_0 in the initial system coordinate [Fig. 4-2d] and expressed by the three rotations R_4, R_5, R_6 .

Let us assume that the effect of these two successive rotations can be treated as a global rotation defined by $(\omega, \vec{n}(\theta, \varphi))$. Let us write how the spherical tensors T_{lm}^λ are transformed into this double frame:

$$\begin{aligned} \left[T_{lq}^\lambda \right]'' &= \sum_{q'} T_{lq'}^\lambda U_{q'q''}^l(\omega, \theta, \varphi) \\ &= \sum_{q'} T_{lq'}^\lambda \left\{ \sum_{q_1} U_{q'q_1}^l(\omega_2, \theta_2, \varphi_2) U_{q_1q''}^l(\omega_1, \theta_1, \varphi_1) \right\} \\ &= \sum_{q_1, q'} T_{lq'}^\lambda U_{q'q_1}^l(\omega_2, \theta_2, \varphi_2) U_{q_1q''}^l(\omega_1, \theta_1, \varphi_1) \end{aligned} \quad (69)$$

With:

$$U_{q'q_1}^l(\omega_2, \theta_2, \varphi_2) = \sum_{q_2} e^{-i(q'-q_1)\phi_2} d_{q'q_2}^l(\theta_2) d_{q_1q_2}^l(\theta_2) e^{-iq_2\omega_2} \quad (70)$$

and

$$U_{q_1q''}^l(\omega_1, \theta_1, \varphi_1) = \sum_{q''} e^{-i(q_1-q'')\phi_1} d_{q_1q''}^l(\theta_1) d_{q''q''}^l(\theta_1) e^{-iq''\omega_1} \quad (71)$$

Note that the order of appearance of the two successive rotations in Eq. (108) reflects the fact that the second rotation of coordinate system is defined with respect to the initial Laboratory Frame coordinate system.¹ Hence, the order would have been reversed with the second rotation expressed in the second coordinate system (linked to the Modulation Frame).

In our case Eq. (108) can thus be rewritten:

$$U_{q'q_1}^l(\omega_2, \theta_2, \varphi_2) = \sum_{q_2} e^{-i(q'-q_1)\left(\frac{\pi}{2}+\phi_0\right)} d_{q'q_2}^l\left(\frac{\pi}{2}-\varphi_0\right) d_{q_1q_2}^l\left(\frac{\pi}{2}-\varphi_0\right) e^{-iq_2\omega_2} \quad (72)$$

and

$$U_{q_1q''}^l(\omega_1, \theta_1, \varphi_1) = \sum_{q''} e^{-i(q_1-q'')\phi_0} d_{q_1q''}^l\left(\frac{\pi}{2}\right) d_{q''q''}^l\left(\frac{\pi}{2}\right) e^{-iq''\omega_1} \quad (73)$$

By replacing Eqs. (72) and (73) in Eq. (108), we get:

$$\left[T_{lq''}^\lambda\right] = \sum_{q_1q'q_2q''} T_{lq'}^\lambda e^{-iq'\left(\frac{\pi}{2}+\phi_0\right)} e^{iq_1\left(\frac{\pi}{2}\right)} e^{iq''\phi_0} e^{-iq_2\omega_2} e^{-iq''\omega_1} d_{q'q_2}^l\left(\frac{\pi}{2}-\varphi_0\right) d_{q_1q_2}^l\left(\frac{\pi}{2}-\varphi_0\right) d_{q_1q''}^l\left(\frac{\pi}{2}\right) d_{q''q''}^l\left(\frac{\pi}{2}\right) \quad (74)$$

Here we can use the following identity:

$$\sum_{q_1} e^{iq_1\pi/2} d_{q_2q_1}^l\left(\varphi_0 - \frac{\pi}{2}\right) d_{q_1q''}^l\left(\frac{\pi}{2}\right) = e^{iq_2\pi/2} d_{q_2q''}^l\left(\frac{\pi}{2}\right) e^{-iq''(\varphi_0 - \pi/2)} \quad (75)$$

And we get:

$$\begin{aligned}
\left[T_{lq''}^\lambda \right]'' &= \sum_{q' q_2 q''} T_{lq'}^\lambda e^{-iq' \left(\frac{\pi}{2} + \phi_0 \right)} e^{iq'' \phi_0} e^{-iq_2 \omega_{\text{eff}} t} e^{-iq'' \omega_c t} d_{q' q_2}^l \left(\frac{\pi}{2} - \varphi_0 \right) d_{q'' q''}^l \left(\frac{\pi}{2} \right) e^{iq_2 \pi/2} d_{q_2 q''}^l \left(\frac{\pi}{2} \right) e^{-iq'' (\varphi_0 - \pi/2)} \\
&= e^{iq'' \phi_0} \sum_{q' q_2 q''} \left\{ T_{lq'}^\lambda e^{-iq' \left(\frac{\pi}{2} + \phi_0 \right)} d_{q' q_2}^l \left(\frac{\pi}{2} - \varphi_0 \right) \right\} e^{-iq_2 \left(\omega_{\text{eff}} t - \frac{\pi}{2} \right)} e^{-iq'' (\omega_c t + \varphi_0 - \pi/2)} d_{q'' q''}^l \left(\frac{\pi}{2} \right) d_{q_2 q''}^l \left(\frac{\pi}{2} \right)
\end{aligned} \tag{76}$$

Here we can define a tilted final frame by a rotation of $(\varphi_0 - \pi/2)$ around the axis ϕ_0 :

$$\sum_{q'} T_{lq'} e^{-iq' \left(\frac{\pi}{2} + \phi_0 \right)} d_{q' q_2}^l \left(\frac{\pi}{2} - \varphi_0 \right) e^{iq_2 \left(\frac{\pi}{2} + \phi_0 \right)} = \widetilde{T}_{lq_2} \tag{77}$$

We finally obtain:

$$\begin{aligned}
\left[T_{lq''}^\lambda \right]'' &= e^{iq'' \phi_0} \sum_{q_2 q''} \widetilde{T}_{lq_2} e^{-iq_2 (\omega_{\text{eff}} t + \phi_0)} e^{-iq'' (\omega_c t + \varphi_0 - \pi/2)} d_{q'' q''}^l \left(\frac{\pi}{2} \right) d_{q_2 q''}^l \left(\frac{\pi}{2} \right) \\
&= e^{iq'' \phi_0} \sum_{q' q} \widetilde{T}_{lq'} e^{-iq' (\omega_{\text{eff}} t + \phi_0)} e^{-iq'' (\omega_c t + \varphi_0 - \pi/2)} d_{q'' q}^l \left(\frac{\pi}{2} \right) d_{q' q}^l \left(\frac{\pi}{2} \right)
\end{aligned} \tag{78}$$

Note that if $\varphi_0 = \pi/2$, we get:

$$\left[T_{lq''}^\lambda \right]'' = e^{iq'' \phi_0} \sum_{q' q} T_{lq'} e^{-iq' (\omega_{\text{eff}} t + \phi_0)} e^{-iq'' (\omega_c t)} d_{q'' q}^l \left(\frac{\pi}{2} \right) d_{q' q}^l \left(\frac{\pi}{2} \right) \tag{79}$$

4.10.6 Appendix F: Generalized CM-based interaction frame: evaluation of the second order cross-terms

In this section, we aim at expressing the AHT second order cross terms in the IF for the CMpRR pulse sequence. Note that we limit ourselves to $p > 3$ since it represents the settings yielding efficient polarization transfer.

1. From Eq. (13) of the manuscript, we can write the second order Hamiltonian using Average Hamiltonian Theory applied on a nT_R period. As an example, let us detail the calculation of the first term with itself:

$$\widetilde{\widetilde{\mathbf{H}}}^{(1)} = \sum_{i=1}^2 \sum_{m_a, m_b, q_a, q_b, q'_a, q'_b} \left[\frac{1}{2iT} d^{m_a} d^{m_b} e^{-i(q'_a + q'_b)\phi_0} d_{q'_a, q_a}^1 \left(\frac{\pi}{2}\right) d_{q'_b, q_b}^1 \left(\frac{\pi}{2}\right) d_{0q_a}^1 \left(\frac{\pi}{2}\right) d_{0q_b}^1 \left(\frac{\pi}{2}\right) \int_0^{T=nT_r} dt_2 \int_0^{t_2} e^{-ix_b \omega_r t_2} e^{-ix_a \omega_r t_1} dt_1 \left[T_{S,1q_b}^i, T_{S,1q_a}^i \right] \right] \quad (80)$$

We have to evaluate this kind of expression, given that $x_a \neq 0$, $x_b \neq 0$, and nx_a , nx_b are integers:

$$\int_0^T dt_2 \int_0^{t_2} e^{-ix_b \omega_r t_2} e^{-ix_a \omega_r t_1} dt_1 \Big|_{\omega_r = \frac{2\pi n}{T}} = T^2 \frac{(-i2\pi n x_b) \left[e^{-i2\pi n(x_a + x_b)} - 1 \right] - (-i2\pi n(x_a + x_b)) \left[e^{-i2\pi n x_a} - 1 \right]}{(-i2\pi n x_a)(-i2\pi n x_b)(-i2\pi n(x_a + x_b))} \\ = \begin{cases} \frac{2\pi n}{(-i\omega_r^2 x_b)} & \text{if } x_a + x_b = 0 \\ 0 & \text{if } x_a + x_b \neq 0 \end{cases} \quad (81)$$

where $x_a = m_a + p q_a + p' q'_a$ and n stands as the number of rotor periods over which the AHT is applied. From Eq.(81), we know that the cross term is potentially non-zero if $x_a + x_b = 0$. Moreover, the cross term is also null if $q_a = 0$, $q_b = 0$ ($d_{00}^1 \left(\frac{\pi}{2}\right) = 0$) or $q'_a = q'_b$ ($[T_{S,1q'}^i, T_{S,1q'}^i] = 0$). This yields the following simplifications:

$$x_a + x_b = 0 \Rightarrow \begin{cases} \underbrace{m_a + m_b}_{\in\{-4,-3,\dots,3,4\}} + p \underbrace{(q_a + q_b)}_{\in\{-2,0,2\}} + \frac{1}{2} \underbrace{(q'_a + q'_b)}_{\in\{-1,0,1\}} = 0 \end{cases} \quad (82)$$

For $p > 2.5$, the previous equation further simplifies to:

$$x_a + x_b = 0 \Rightarrow \begin{cases} \underbrace{m_a + m_b}_{\in\{-4,-3,\dots,3,4\}} + p \underbrace{(q_a + q_b)}_{=0} + \frac{1}{2} \underbrace{(q'_a + q'_b)}_{\in\{-1,0,1\}} = 0 \end{cases} \quad (83)$$

Since $q_a \neq 0$, $q_b \neq 0$ and $q_a + q_b = 0$ we get $q_a = -q_b = \pm 1$. Eq. (83) only has solutions when $q'_a + q'_b = 0$, i.e. $q'_a = -q'_b = \pm 1$. Eq. (83) can finally be rewritten:

$$x_a + x_b = 0 \Rightarrow \begin{cases} m_a + m_b = 0 \\ q_a + q_b = 0 \\ q'_a + q'_b = 0 \end{cases} \quad (84)$$

Using the following identity,

$$\left[T_{S,1q'_2}^i, T_{S,1q'_1}^i \right] = \begin{cases} \text{sg}(q'_2) T_{S,10}^i & \text{if } q'_2 = -q'_1 \neq 0 \\ 0 & \text{if else} \end{cases} \quad (85)$$

Equation (80) can be rewritten:

$$\begin{aligned} \tilde{\mathbf{H}}^{(1)} &= \sum_{i=1}^2 \sum_{m,q} \left[\frac{1}{2iT} d^m d^{-m} d_{q,q}^1 \left(\frac{\pi}{2}\right) d_{-q,-q}^1 \left(\frac{\pi}{2}\right) \cdot d_{0,q}^1 \left(\frac{\pi}{2}\right) d_{0,-q}^1 \left(\frac{\pi}{2}\right) \frac{-4\pi n}{(i\omega_r^2 x)} T_{S,10}^i \text{sg}(q') \right] \\ &= \sum_{i=1}^2 \sum_{m,q} \left[\frac{1}{2iT} d^m d^{-m} \frac{1}{4} \cdot \frac{-1}{2} \frac{-4\pi n}{i\omega_r^2 (m + pq + 1/2)} T_{S,10}^i \right] \\ &= \sum_{i=1}^2 \sum_{m=0}^2 \left[\frac{-1}{8\omega_r} d^m d^{-m} T_{S,10}^i \right] \left(\frac{1}{m + p + 1/2} + \frac{1}{m - p + 1/2} + \frac{1}{-m + p + 1/2} + \frac{1}{-m - p + 1/2} \right) \end{aligned} \quad (86)$$

The Eq. 50 of the manuscript can be obtained directly form Eq. (86).

2. From Eq. (13) of the manuscript, we can write the second order contribution of the second term with itself. There are non-zero contributions if we can find a p-value such that, for a given set of (q'_1, q'_2) :

$$\begin{aligned} \left[T_{S,2q'_2}^{kl}, T_{S,2q'_1}^{kl} \right] &\neq 0 \\ \exists (x_1, x_2), x_1 + x_2 &= 0 \end{aligned} \quad (87)$$

a- $\{q'_2 = 0, q'_1 = \pm 1\}$:

$$\begin{aligned}
& \bullet [T_{S,20}^{kl}, T_{S,2\pm 1}^{kl}] \neq 0 \\
& \bullet x_1 + x_2 = 0 \Leftrightarrow m_1 + m_2 + p(q_1 + q_2) + \frac{1}{2}(q_1' + q_2') = 0 \\
& \text{with } q_1 \in \{-2, 0, 2\} \text{ and } q_2 \in \left\{ -2, \underbrace{\emptyset}_{d_{0\pm 1}^2(\frac{\pi}{2})=0}, 2 \right\} \\
& \left(m_1 + m_2 + \frac{1}{2}q_1' \right) \in \left\{ \frac{-9}{2}, \frac{-7}{2}, \dots, \frac{7}{2}, \frac{9}{2} \right\} \text{ and } (q_1 + q_2) \in \underbrace{\{-4, -2, 2, 4\}}_{S_1} \cup \underbrace{\{0\}}_{S_2} \\
& \bullet S_1 \Rightarrow |p| \leq \frac{9}{4} \\
& \bullet S_2 \Rightarrow \emptyset
\end{aligned} \tag{88}$$

This means that we can find non-zero contributions only for a discrete series of p-value with $p \leq 9/4$. As we are only concerned with CM_pRR sequences with $p > 3$, we can neglect the influence of this type of cross terms.

$$\text{b- } \{q_2' = 0, q_1' = \pm 2\}:$$

$$\bullet [T_{S,20}^{kl}, T_{S,2\pm 2}^{kl}] = 0 \tag{89}$$

$$\text{c- } \{q_2' = \pm 1, q_1' = \mp 1\}:$$

$$\bullet [T_{S,2\pm 1}^{kl}, T_{S,2\mp 1}^{kl}] = \frac{\mp 1}{4} \left(\frac{T_{10}^k + T_{10}^l}{2} \right)$$

$$\bullet x_1 + x_2 = 0 \Leftrightarrow m_1 + m_2 + p(q_1 + q_2) + \frac{1}{2} \underbrace{(q_1' + q_2')}_{=0} = 0$$

$$\text{with } q_1 \in \left\{ -2, \underbrace{\emptyset}_{d_{0\pm 1}^2(\frac{\pi}{2})=0}, 2 \right\} \text{ and } q_2 \in \left\{ -2, \underbrace{\emptyset}_{d_{0\pm 1}^2(\frac{\pi}{2})=0}, 2 \right\} \tag{90}$$

$$(m_1 + m_2) \in \{-4, -3, \dots, 3, 4\} \text{ and } (q_1 + q_2) \in \underbrace{\{-4, 4\}}_{S_1} \cup \underbrace{\{0\}}_{S_2}$$

$$\bullet \text{ If } (q_1 + q_2) \in S_1 \Rightarrow \text{discrete series of p-value with } |p| \leq 1$$

$$\bullet \text{ If } (q_1 + q_2) \in S_2 \Rightarrow \begin{cases} \forall p, \exists (x_1, x_2), x_1 + x_2 = 0 \\ m_1 = -m_2, q_1' = -q_2', q_1 = -q_2 \end{cases}$$

The discrete series of p -value that lead to non-zero contribution can be discarded as we are concerned with $p > 3$. The other set of solutions lead to contribution for $p > 3$.

$$\tilde{\tilde{\mathbf{H}}}^{(1)} = \frac{-9}{64\omega_r} \sum_{k,l} \sum_{m=1}^2 \omega_{SS,k,l}^m \omega_{SS,k,l}^{-m} \left(\begin{array}{c} \frac{1}{(m+2p+1/2)} + \frac{1}{(m-2p+1/2)} \\ + \frac{1}{(-m+2p+1/2)} + \frac{1}{(-m-2p+1/2)} \end{array} \right) \left(\frac{T_{S,10}^k + T_{S,10}^l}{2} \right) \quad (91)$$

$$d- \{q_2' = \pm 2, q_1' = \mp 2\}:$$

$$\bullet [T_{S,2\pm 2}^{kl}, T_{S,2\mp 2}^{kl}] = \pm \left(\frac{T_{10}^k + T_{10}^l}{4} \right)$$

$$\bullet x_1 + x_2 = 0 \Leftrightarrow m_1 + m_2 + p(q_1 + q_2) + \frac{1}{2} \underbrace{(q_1' + q_2')}_{=0} = 0$$

$$\text{with } q_1 \in \{-2, 0, 2\} \text{ and } q_2 \in \{-2, 0, 2\}$$

$$(m_1 + m_2) \in \{-4, -3, \dots, 3, 4\} \text{ and } (q_1 + q_2) \in \underbrace{\{-4, 4\}}_{S_1} \cup \underbrace{\{0\}}_{S_2} \quad (92)$$

$$\bullet \text{If } (q_1 + q_2) \in S_1 \Rightarrow \text{discrete serie of } p\text{-value with } |p| \leq 1$$

$$\bullet \text{If } (q_1 + q_2) \in S_2 \Rightarrow \begin{cases} \forall p, \exists (x_1, x_2), x_1 + x_2 = 0 \\ m_1 = -m_2, q_1' = -q_2', q_1 = -q_2 \end{cases}$$

The discrete series of p -value that lead to non-zero contribution can be discarded as we are concerned with $p > 3$. The other set of solutions lead to contribution for $p > 3$.

$$\tilde{\tilde{\mathbf{H}}}^{(1)} = \frac{-9}{32\omega_r} \sum_{k,l} \sum_{m=1}^2 [\omega_{SS,k,l}^m \omega_{SS,k,l}^{-m}] \left[\begin{array}{c} \left(\frac{1}{(m+2p+1)} + \frac{1}{(m-2p+1)} \right) \\ + \left(\frac{1}{(-m+2p+1)} + \frac{1}{(-m-2p+1)} \right) \right] \left(\frac{T_{10}^k + T_{10}^l}{2} \right) \\ + \left(\frac{1}{(m+1)} + \frac{1}{(-m+1)} \right) \quad (93)$$

3. From Eq. (13), we can write the second order contribution of the first term with the second term. There are non-zero contributions if we can find a p-value such that, for a given set of (q_1', q_2') :

$$\begin{aligned} i \in \{k, l\}, [T_{S,2q_2'}^{kl}, T_{S,1q_1'}^i] &\neq 0 \\ \exists(x_1, x_2), x_1 + x_2 &= 0 \end{aligned} \quad (94)$$

$$\text{a- } \{q_2' = 0, q_1' = \pm 1\}:$$

$$\begin{aligned} \bullet [T_{S,20}^{kl}, T_{S,1q_1'}^i] &= \frac{sg(q_1')}{\sqrt{6}} (T_{10}^i T_{1q_1'}^{\neq i} + 2T_{1q_1'}^i T_{10}^{\neq i}) \\ \bullet x_1 + x_2 = 0 &\Leftrightarrow m_1 + m_2 + p(q_1 + q_2) + \frac{1}{2}q_1' = 0 \\ \text{with } q_1 &\in \{-1, 1\} \text{ and } q_2 \in \{-2, 0, 2\} \\ \left(m_1 + m_2 + \frac{1}{2}q_1'\right) &\in \{-4.5, -3.5, \dots, 3.5, 4.5\} \text{ and } (q_1 + q_2) \in \underbrace{\{-3, 3\}}_{S_1} \cup \underbrace{\{-1, 1\}}_{S_2} \\ \bullet \text{ If } (q_1 + q_2) \in S_1 &\Rightarrow \text{discrete series of p-values with } |p| \leq 1.5 \\ \bullet \text{ If } (q_1 + q_2) \in S_2 &\Rightarrow \text{discrete series of p-values with } |p| \leq 4.5 \end{aligned} \quad (95)$$

Cross terms occurring for $p=3.5$ and 4.5 are the only one relevant to understand the CMRR spin dynamics for $p > 3$.

$$\text{b- } \{q_2' = \pm 2, q_1' = \mp 1\}:$$

$$\begin{aligned} \bullet [T_{S,2\pm 2}^{kl}, T_{S,1\mp 1}^i] &= \mp 2T_{10}^i T_{1\pm 1}^{\neq i} \\ \bullet x_1 + x_2 = 0 &\Leftrightarrow m_1 + m_2 + p(q_1 + q_2) + \frac{1}{2}(\pm 1) = 0 \\ \text{with } q_1 &\in \{-1, 1\} \text{ and } q_2 \in \{-2, 0, 2\} \\ \left(m_1 + m_2 \pm \frac{1}{2}\right) &\in \{-4.5, -3.5, \dots, 3.5, 4.5\} \text{ and } (q_1 + q_2) \in \underbrace{\{-3, 3\}}_{S_1} \cup \underbrace{\{-1, 1\}}_{S_2} \\ \bullet \text{ If } (q_1 + q_2) \in S_1 &\Rightarrow \text{discrete series of p-value with } |p| \leq 3/2 \\ \bullet \text{ If } (q_1 + q_2) \in S_2 &\Rightarrow \text{discrete series of p-value with } |p| \leq 4.5 \end{aligned} \quad (96)$$

Cross terms occurring for $p=3.5$ and 4.5 are the only one relevant to understand the CMRR spin dynamics for $p > 3$.

4. From Eq. (13), we can write the second order contribution of the first term with the fourth. There are non-zero contributions if we can find p -value such that:

$$\begin{aligned} & \left[T_{I,20}^{ij}, T_{I,10}^i T_{S,1q_1}^k \right] \neq 0 \\ & \exists (x_1, x_2), x_1 + x_2 = 0 \end{aligned} \quad (97)$$

a- $\{q_1' = \pm 1\}$:

$$\bullet \left[T_{I,20}^{ij}, T_{I,10}^i T_{S,1q_1}^k \right] = T_{S,1q_1}^k \left[T_{I,20}^{ij}, T_{I,10}^i \right] = \frac{1}{\sqrt{6}} T_{S,1q_1}^k (T_{1-1}^i T_{11}^j - T_{11}^i T_{1-1}^j) = \frac{i}{\sqrt{6}} T_{S,1q_1}^k I_y^{ij(23)}$$

where $I_y^{ij(23)} = i(T_{11}^i T_{1-1}^j - T_{1-1}^i T_{11}^j)$

$$\bullet x_1 + x_2 = 0 \Leftrightarrow m_1 + pq_1 + \frac{1}{2}q_1' + m_2 = 0 \quad (98)$$

with $q_1 \in \{-1, 1\}$ and $\left(m_1 + m_2 + \frac{1}{2}q_1'\right) \in \{-4.5, -3.5, \dots, 3.5, 4.5\}$

\Rightarrow discrete series of p -value $p \in \{0.5, \dots, 3.5, 4.5\}$

where $I_y^{ij(23)}$ stands as the y component of the (ij) ZQ subspace defined in appendix C.

Cross terms occurring for $p=3.5$ and 4.5 are the only one relevant to understand the CMRR spin dynamics for $p > 3$. Let us explicitly write the set of solutions in these two cases:

For $p=3.5$:

$$\bullet x_1 + x_2 = 0 \Rightarrow \begin{cases} m_1 = 2, m_2 = 2, q_1 = -1, q_1' = -1 \\ m_1 = -2, m_2 = -2, q_1 = 1, q_1' = 1 \\ m_1 = 2, m_2 = 1, q_1 = -1, q_1' = 1 \\ m_1 = 1, m_2 = 2, q_1 = -1, q_1' = 1 \\ m_1 = -2, m_2 = -1, q_1 = 1, q_1' = -1 \\ m_1 = -1, m_2 = -2, q_1 = 1, q_1' = -1 \end{cases} \quad (99)$$

$$\begin{aligned}
\overline{\tilde{\text{H}}}_{p=3,5}^{(1)} &\propto \frac{1}{\omega_r} \sum_k \sum_{i,j} \left[\left(\frac{1}{2} \omega_{II,ij}^2 \omega_{IS,ik}^2 + \frac{1}{2} \omega_{II,ij}^2 \omega_{IS,ik}^1 + \omega_{II,ij}^1 \omega_{IS,ik}^2 \right) T_{S,1-1}^k \right. \\
&\quad \left. + \left(\frac{1}{2} \omega_{II,ij}^{-2} \omega_{IS,ik}^{-2} + \frac{1}{2} \omega_{II,ij}^{-2} \omega_{IS,ik}^{-1} + \omega_{II,ij}^{-1} \omega_{IS,ik}^{-2} \right) T_{S,11}^k \right] I_y^{ij(23)} \\
&\propto \frac{1}{\omega_r} \sum_k \sum_{i,j} \left| \frac{1}{2} \omega_{II,ij}^2 \omega_{IS,ik}^2 + \frac{1}{2} \omega_{II,ij}^2 \omega_{IS,ik}^1 + \omega_{II,ij}^1 \omega_{IS,ik}^2 \right| \left[e^{-i\kappa} T_{S,11}^k + e^{i\kappa} T_{S,1-1}^k \right] I_y^{ij(23)}
\end{aligned} \tag{100}$$

This term represents a coupling between the carbon spin k and a fictitious ZQ proton spin. It can interfere with the ^{13}C DQ polarization transfer. Note that this type of term can also promote proton-proton polarization transfer in closed subspaces spanned by the following operators: $2S_{x/y}^k I_x^{ij(23)}$, $2S_{x/y}^k I_y^{ij(23)}$, $I_z^{ij(23)}$.

For $p=4,5$:

$$\bullet x_1 + x_2 = 0 \Leftrightarrow \begin{cases} m_1 = 2, m_2 = 2, q_1 = -1, q'_1 = 1 \\ m_1 = -2, m_2 = -2, q_1 = 1, q'_1 = -1 \end{cases} \tag{101}$$

$$\begin{aligned}
\overline{\tilde{\text{H}}}_{p=4,5}^{(1)} &\propto \frac{1}{\omega_r} \sum_k \sum_{i,j} \left[\omega_{II,ij}^2 \omega_{IS,ik}^2 T_{S,11}^k + \omega_{II,ij}^{-2} \omega_{IS,ik}^{-2} T_{S,1-1}^k \right] I_y^{ij(23)} \\
&\propto \frac{1}{\omega_r} \sum_k \sum_{i,j} \left| \omega_{II,ij}^2 \omega_{IS,ik}^2 \right| \left[e^{-i\kappa} T_{S,11}^k + e^{i\kappa} T_{S,1-1}^k \right] I_y^{ij(23)}
\end{aligned} \tag{102}$$

This term represents a coupling between the carbon spin k and a fictitious ZQ proton spin. It can interfere with the ^{13}C DQ polarization transfer. Note that this type of term can also promote proton-proton polarization transfer in closed subspaces spanned by the following operators: $2S_{x/y}^k I_x^{ij(23)}$, $2S_{x/y}^k I_y^{ij(23)}$, $I_z^{ij(23)}$.

For $\{q'_1 = 0\}$:

$$\begin{aligned}
\bullet [T_{I,20}^{ij}, T_{I,10}^i T_{S,10}^k] &= T_{S,10}^k [T_{I,20}^{ij}, T_{I,10}^i] = \frac{1}{\sqrt{6}} T_{S,10}^k (T_{1-1}^i T_{11}^j - T_{11}^i T_{1-1}^j) = \frac{i}{\sqrt{6}} T_{S,10}^k I_y^{ij(23)} \\
\text{where } I_y^{ij(23)} &= i(T_{11}^i T_{1-1}^j - T_{1-1}^i T_{11}^j) \\
\bullet x_1 + x_2 = 0 &\Leftrightarrow m_1 + pq_1 + m_2 = 0 \\
\text{with } q_1 \in \{-1, 1\} &\text{ and } (m_1 + m_2) \in \{-4, -3, \dots, 3, 4\} \\
\Rightarrow \text{discrete series of p-value } p &\in \{1, \dots, 3, 4\}
\end{aligned} \tag{103}$$

Cross term occurring for p=4 is the only one relevant to understand the CMRR spin dynamics for $p > 3$. Let us explicitly write the second order cross term in this case:

$$\bullet x_1 + x_2 = 0 \Leftrightarrow \begin{cases} m_1 = 2, m_2 = 2, q_1 = -1 \\ m_1 = -2, m_2 = -2, q_1 = 1 \end{cases} \tag{104}$$

$$\begin{aligned}
\overline{\tilde{H}}_{p=4}^{(1)} &\propto \frac{1}{\omega_r} \sum_k \sum_{i,j} [\omega_{II,ij}^2 \omega_{IS,ik}^2 T_{S,10}^k I_y^{ij(23)} - \omega_{II,ij}^{-2} \omega_{IS,ik}^{-2} T_{S,10}^k I_y^{ij(23)}] \\
&\propto \frac{1}{\omega_r} \sum_k \sum_{i,j} [\omega_{II,ij}^2 \omega_{IS,ik}^2 - \omega_{II,ij}^{-2} \omega_{IS,ik}^{-2}] T_{S,10}^k I_y^{ij(23)} \\
&\propto \frac{1}{\omega_r} \sum_k \sum_{i,j} [\text{Im}(\omega_{II,ij}^2 \omega_{IS,ik}^2)] 2T_{S,10}^k I_y^{ij(23)}
\end{aligned} \tag{105}$$

This term represents a coupling between the carbon spin k and a fictitious ZQ proton spin. It can interfere with the ^{13}C DQ polarization transfer. Note that this type of term can also promote proton-proton polarization transfer in closed subspaces spanned by the following operators: $2S_z^k I_x^{ij(23)}$, $2S_z^k I_y^{ij(23)}$, $I_z^{ij(23)}$.

Table 4-1 Theoretical phase modulation settings for CMpRR (sine)

p index	Phase excursion (in degree)
3.5	16.21
4	14.21
4.5	12.65
5	11.40
6	9.52
7	8.16
8	7.15
9	6.36
10	5.72

4.11 References

(1) F. Castellani, B. van Rossum, A. Diehl, M. Schubert, K. Rehbein, and H. Oschkinat, *Nature* 420 (6911), 98 (2002); S. G. Zech, A. J. Wand, and A. E. McDermott, *J. Am. Chem. Soc.* 127 (24), 8618 (2005).

(2) P. R. Costa, D. A. Kocisko, B. Q. Sun, P. T. Lansbury, and R. G. Griffin, *J. Am. Chem. Soc.* 119 (43), 10487 (1997); P. R. Costa, B. Q. Sun, and R. G. Griffin, *J. Am. Chem. Soc.* 119 (44), 10821 (1997).

(3) F. Creuzet, A. McDermott, R. Gebhard, K. Vanderhoef, M. B. Spijkerassink, J. Herzfeld, J. Lugtenburg, M. H. Levitt, and R. G. Griffin, *Science* 251 (4995), 783 (1991).

(4) M. Hong, J. D. Gross, W. Hu, and R. G. Griffin, *J. Magn. Reson.* 135 (1), 169 (1998); C. P. Jaroniec, C. E. MacPhee, V. S. Bajaj, C. M. Dobson, and R. G. Griffin, *Biophys. J.* 84 (2), 154A (2003); C. P. Jaroniec, B. A. Tounge, J. Herzfeld, and R. G. Griffin, *Biophys. J.* 80 (1), 368A (2001); C. P. Jaroniec, B. A. Tounge, C. M. Rienstra, J. Herzfeld, and R. G. Griffin, *J. Am. Chem. Soc.* 121 (43), 10237 (1999); C. P. Jaroniec, B. A. Tounge, C. M. Rienstra, J. Herzfeld, and R. G. Griffin, *J. Magn. Reson.* 146 (1), 132 (2000); V. Ladizhansky and R. G. Griffin, *J. Am. Chem. Soc.* 126 (3), 948 (2004); D. P. Raleigh, F. Creuzet, S. K. D.

Gupta, M. H. Levitt, and R. G. Griffin, *J. Am. Chem. Soc.* 111 (12), 4502 (1989); K. Takegoshi, S. Nakamura, and T. Terao, *J. Chem. Phys.* 118 (5), 2325 (2003); W. P. Aue, D. J. Ruben, and R. G. Griffin, 80 (5), 1729 (1984); E. T. Olejniczak, S. Vega, and R. G. Griffin, 81 (11), 4804 (1984); A. C. Kolbert, D. P. Raleigh, M. H. Levitt, and R. G. Griffin, *J. Chem. Phys.* 90 (2), 679 (1989); C. W. B. Lee and R. G. Griffin, *Biophys. J.* 55 (2), 355 (1989); J. H. Ok, R. G. S. Spencer, A. E. Bennett, and R. G. Griffin, 197 (4-5), 389 (1992); J. M. Griffiths, K. V. Lakshmi, A. E. Bennett, J. Raap, C. M. Vanderwielen, J. Lugtenburg, J. Herzfeld, and R. G. Griffin, *J. Am. Chem. Soc.* 116 (22), 10178 (1994).

(5) Y. Ishii, *J. Chem. Phys.* 114 (19), 8473 (2001).

(6) C. P. Jaroniec, C. E. MacPhee, N. S. Astrof, C. M. Dobson, and R. G. Griffin, *P. Natl. Acad. Sci. U.S.A.* 99 (26), 16748 (2002).

(7) C. P. Jaroniec, C. E. MacPhee, V. S. Bajaj, M. T. McMahon, C. M. Dobson, and R. G. Griffin, *P. Natl. Acad. Sci. U.S.A.* 101 (3), 711 (2004).

(8) C. M. Rienstra, L. Tucker-Kellogg, C. P. Jaroniec, M. Hohwy, B. Reif, M. T. McMahon, B. Tidor, T. Lozano-Perez, and R. G. Griffin, *P. Natl. Acad. Sci. U.S.A.* 99 (16), 10260 (2002).

(9) B. Q. Sun, P. R. Costa, D. Kocisko, P. T. Lansbury, and R. G. Griffin, *J. Chem. Phys.* 102 (2), 702 (1995).

(10) R. Tycko and G. Dabbagh, *Chem. Phys. Lett.* 173 (5-6), 461 (1990).

(11) A. E. Bennett, J. H. Ok, R. G. Griffin, and S. Vega, *J. Chem. Phys.* 96 (11), 8624 (1992).

(12) H. Heise, K. Seidel, M. Etzkorn, S. Becker, and M. Baldus, *J. Magn. Reson.* 173 (1), 64 (2005); C. M. Rienstra, M. Hohwy, M. Hong, and R. G. Griffin, *J. Am. Chem. Soc.* 122 (44), 10979 (2000); W. T. Franks, D. H. Zhou, B. J. Wylie, B. G. Money, D. T. Graesser, H. L. Frericks, G. Sahota, and C. M. Rienstra, *J. Am. Chem. Soc.* 127 (35), 12291 (2005); A. McDermott, T. Polenova, A. Bockmann, K. W. Zilm, E. K. Paulsen, R. W. Martin, and G. T. Montelione, *J. Biomol. Nmr* 16 (3), 209 (2000); A. Bockmann, A. Lange, A. Galinier, S. Luca, N. Giraud, M. Juy, H. Heise, R. Montserret, F. Penin, and M. Baldus, *J. Biomol. Nmr* 27 (4), 323 (2003).

(13) M. Baldus, *Prog. Nucl. Mag. Res. Sp.* 41 (1-2), 1 (2002); M. Baldus and B. H. Meier, *J. Magn. Reson.* 128 (2), 172 (1997); M. Baldus and B. H. Meier, *J. Magn. Reson. Ser.*

A 121 (1), 65 (1996); H. Heise, W. Hoyer, S. Becker, O. C. Andronesi, D. Riedel, and M. Baldus, *P. Natl. Acad. Sci. U.S.A.* 102 (44), 15871 (2005).

(14) T. Gullion and J. Schaefer, *J. Magn. Reson.* 81 (1), 196 (1989).

(15) T. A. Cross, J. A. Diverdi, and S. J. Opella, *J. Am. Chem. Soc.* 104 (6), 1759 (1982).

(16) D. M. LeMaster and D. M. Kushlan, *J. Am. Chem. Soc.* 118 (39), 9255 (1996); M. Hong and K. Jakes, *J. Biomol. Nmr* 14 (1), 71 (1999); M. Hong, *J. Magn. Reson.* 139 (2), 389 (1999).

(17) B. Q. Sun, C. M. Rienstra, P. R. Costa, J. R. Williamson, and R. G. Griffin, *J. Am. Chem. Soc.* 119 (36), 8540 (1997); B. Reif, M. Hohwy, C. P. Jaroniec, C. M. Rienstra, and R. G. Griffin, *J. Magn. Reson.* 145 (1), 132 (2000); C. M. Rienstra, M. Hohwy, L. J. Mueller, C. P. Jaroniec, B. Reif, and R. G. Griffin, *J. Am. Chem. Soc.* 124 (40), 11908 (2002).

(18) V. Ladizhansky, C. P. Jaroniec, A. Diehl, H. Oschkinat, and R. G. Griffin, *J. Am. Chem. Soc.* 125 (22), 6827 (2003).

(19) R. Ramachandran, V. Ladizhansky, V. S. Bajaj, and R. G. Griffin, *J. Am. Chem. Soc.* 125 (50), 15623 (2003); R. Ramachandran, J. R. Lewandowski, P. C. A. van der Wel, and R. G. Griffin, *J. Chem. Phys.* 124 (21) (2006).

(20) A. E. Bennett, C. M. Rienstra, M. Auger, K. V. Lakshmi, and R. G. Griffin, *J. Chem. Phys.* 103 (16), 6951 (1995).

(21) G. De Paepe, P. Hodgkinson, and L. Emsley, *Chem. Phys. Lett.* 376 (3-4), 259 (2003).

(22) Z. H. Gan and R. R. Ernst, *Solid State Nucl. Mag.* 8 (3), 153 (1997).

(23) K. Takegoshi, J. Mizokami, and T. Terao, *Chem. Phys. Lett.* 341 (5-6), 540 (2001).

(24) G. De Paepe, A. Lesage, and L. Emsley, *J. Chem. Phys.* 119 (9), 4833 (2003).

(25) G. De Paepe, M. J. Bayro, J. R. Lewandowski, and R. G. Griffin, presented at the 46th Experimental Nuclear Magnetic Resonance, Providence, RI, 2005 (unpublished).

(26) G. De Paepe, J. R. Lewandowski, M. J. Bayro, and R. G. Griffin, presented at the 47th Experimental Nuclear Magnetic Resonance, Asilomar, CA, 2006 (unpublished).

(27) E. R. Andrew, S. Clough, L. F. Farnell, T. D. Gledhill, and I. Roberts, *Phys. Lett.* 21 (5), 505 (1966).

- (28) D. P. Raleigh, M. H. Levitt, and R. G. Griffin, *Chem. Phys. Lett.* 146 (1-2), 71 (1988).
- (29) G. De Paepe, B. Elena, and L. Emsley, *J. Chem. Phys.* 121 (7), 3165 (2004).
- (30) G. De Paepe, N. Giraud, A. Lesage, P. Hodgkinson, A. Bockmann, and L. Emsley, *J. Am. Chem. Soc.* 125 (46), 13938 (2003).
- (31) D. A. Varshalovich, A. N. Moskalev, and V. K. Khersonskii, *Quantum theory of angular momentum.* (World Scientific Co Pte Ltd, Singapore, 1988).
- (32) I. Marin-Montesinos, D. H. Brouwer, G. Antonioli, W. C. Lai, A. Brinkmann, and M. H. Levitt, *J. Magn. Reson.* 177 (2), 307 (2005).
- (33) M. Munowitz, W. P. Aue, and R. G. Griffin, *J. Chem. Phys.* 77 (4), 1686 (1982); M. G. Munowitz, R. G. Griffin, G. Bodenhausen, and T. H. Huang, *J. Am. Chem. Soc.* 103 (10), 2529 (1981).
- (34) R. Tycko and G. Dabbagh, *J. Am. Chem. Soc.* 113 (25), 9444 (1991).
- (35) A. E. Bennett, C. M. Rienstra, J. M. Griffiths, W. G. Zhen, P. T. Lansbury, and R. G. Griffin, *J. Chem. Phys.* 108 (22), 9463 (1998).
- (36) N. C. Nielsen, H. Bildsoe, H. J. Jakobsen, and M. H. Levitt, *J. Chem. Phys.* 101 (3), 1805 (1994).
- (37) Y. K. Lee, N. D. Kurur, M. Helmle, O. G. Johannessen, N. C. Nielsen, and M. H. Levitt, *Chem. Phys. Lett.* 242 (3), 304 (1995).
- (38) M. Hohwy, H. J. Jakobsen, M. Eden, M. H. Levitt, and N. C. Nielsen, *J. Chem. Phys.* 108 (7), 2686 (1998).
- (39) Y. Ishii, J. Ashida, and T. Terao, *Chem. Phys. Lett.* 246 (4-5), 439 (1995).
- (40) C. M. Rienstra, M. E. Hatcher, L. J. Mueller, B. Q. Sun, S. W. Fesik, and R. G. Griffin, *J. Am. Chem. Soc.* 120 (41), 10602 (1998).
- (41) M. Hohwy, C. M. Rienstra, C. P. Jaroniec, and R. G. Griffin, *J. Chem. Phys.* 110 (16), 7983 (1999).
- (42) A. Brinkmann, M. Eden, and M. H. Levitt, *J. Chem. Phys.* 112 (19), 8539 (2000).
- (43) M. Carravetta, M. Eden, X. Zhao, A. Brinkmann, and M. H. Levitt, *Chem. Phys. Lett.* 321 (3-4), 205 (2000); A. Brinkmann and M. H. Levitt, *J. Chem. Phys.* 115 (1), 357 (2001).

(44) W. A. Dollase, M. Feike, H. Forster, T. Schaller, I. Schnell, A. Sebald, and S. Steuernagel, *J. Am. Chem. Soc.* 119 (16), 3807 (1997); F. Fayon, C. Bessada, J. P. Coutures, and D. Massiot, *Inorg. Chem.* 38 (23), 5212 (1999); X. Helluy, C. Marichal, and A. Sebald, *J. Phys. Chem. B* 104 (13), 2836 (2000).

(45) M. Eden, *Chem. Phys. Lett.* 366 (5-6), 469 (2002); M. Eden and M. H. Levitt, *Chem. Phys. Lett.* 293 (3-4), 173 (1998); C. E. Hughes, J. Gunne, and M. H. Levitt, *Chemphyschem* 4 (5), 457 (2003); M. Eden and A. Brinkmann, *J. Magn. Reson.* 173 (2), 259 (2005).

(46) M. Carravetta, M. Eden, O. G. Johannessen, H. Luthman, P. J. E. Verdegem, J. Lugtenburg, A. Sebald, and M. H. Levitt, *J. Am. Chem. Soc.* 123 (43), 10628 (2001); M. Carravetta, X. Zhao, O. G. Johannessen, W. C. Lai, M. A. Verhoeven, P. H. M. Bovee-Geurts, P. J. E. Verdegem, S. Kiihne, H. Luthman, H. J. M. de Groot, W. J. deGrip, J. Lugtenburg, and M. H. Levitt, *J. Am. Chem. Soc.* 126 (12), 3948 (2004).

(47) X. Feng, Y. K. Lee, D. Sandstrom, M. Eden, H. Maisel, A. Sebald, and M. H. Levitt, *Chem. Phys. Lett.* 257 (3-4), 314 (1996); X. Feng, P. J. E. Verdegem, M. Eden, D. Sandstrom, Y. K. Lee, P. H. M. Bovee-Geurts, W. J. de Grip, J. Lugtenburg, H. J. M. de Groot, and M. H. Levitt, *J. Biomol. Nmr* 16 (1), 1 (2000); V. Ladizhansky, M. Veshtort, and R. G. Griffin, *J. Magn. Reson.* 154 (2), 317 (2002); X. Feng, M. Eden, A. Brinkmann, H. Luthman, L. Eriksson, A. Graslund, O. N. Antzutkin, and M. H. Levitt, *J. Am. Chem. Soc.* 119 (49), 12006 (1997); X. Feng, P. J. E. Verdegem, Y. K. Lee, D. Sandstrom, M. Eden, P. BoveeGeurts, W. J. deGrip, J. Lugtenburg, H. J. M. deGroot, and M. H. Levitt, *J. Am. Chem. Soc.* 119 (29), 6853 (1997).

(48) R. Verel, M. Baldus, M. Ernst, and B. H. Meier, *Chem. Phys. Lett.* 287 (3-4), 421 (1998); R. Verel, M. Baldus, M. Nijman, J. W. M. van Os, and B. H. Meier, *Chem. Phys. Lett.* 280 (1-2), 31 (1997); R. Verel, M. Ernst, and B. H. Meier, *J. Magn. Reson.* 150 (1), 81 (2001).

(49) C. E. Hughes, S. Luca, and M. Baldus, *Chem. Phys. Lett.* 385 (5-6), 435 (2004).

(50) G. De Paepe, M. J. Bayro, J. Lewandowski, and R. G. Griffin, *J. Am. Chem. Soc.* 128 (6), 1776 (2006).

(51) N. C. Nielsen, F. Cruzet, R. G. Griffin, and M. H. Levitt, *J. Chem. Phys.* 96 (8), 5668 (1992); M. Eden, Y. K. Lee, and M. H. Levitt, *J. Magn. Reson. A* 120 (1), 56 (1996); T. Karlsson, M. Eden, H. Luthman, and M. H. Levitt, *J. Magn. Reson.* 145 (1), 95 (2000).

(52) P. E. Kristiansen, M. Carravetta, J. D. van Beek, W. C. Lai, and M. H. Levitt, *J. Chem. Phys.* 124 (23) (2006).

(53) M. Veshtort and R. G. Griffin, *J. Magn. Reson.* 178 (2), 248 (2006).

(54) M. A. Mehta, D. M. Gregory, S. Kiihne, D. J. Mitchell, M. E. Hatcher, J. C. Shiels, and G. P. Drobny, *Solid State Nucl. Mag.* 7 (3), 211 (1996).

(55) J. R. Lewandowski, G. De Paepe, and R. G. Griffin, *J. Am. Chem. Soc.* 129 (4), 728 (2007); G. De Paëpe, J. R. Lewandowski, A. Loquet, A. Böckmann, and R. G. Griffin, presented at the 48th Experimental NMR Conference, Daytona Beach, FL, 2007 (unpublished); G. De Paëpe, J. R. Lewandowski, A. Loquet, A. Böckmann, and R. G. Griffin, presented at the 5th Alpine NMR Conference, Chamonix, France, 2007 (unpublished).

(56) M. Hong, *Journal of Magnetic Resonance* 136 (1), 86 (1999); T. Karlsson, A. Brinkmann, P. J. E. Verdegem, J. Lugtenburg, and M. H. Levitt, *Solid State Nucl. Mag.* 14 (1), 43 (1999).

(57) D. J. States, R. A. Haberkorn, and D. J. Ruben, *J. Magn. Reson.* 48 (2), 286 (1982).

(58) D. A. Varshalovich, A. N. Moskalev, and V. K. Khersonskii, *Quantum theory of angular momentum*. (World Scientific Co Pte Ltd, Singapore, 1988).

5. Broadband Homonuclear Correlation Spectroscopy at High Magnetic Fields and High Spinning Frequencies

Reproduced with permission from de Paëpe G., Bayro, M., Lewandowski J. R., Griffin R.G. "Broadband Homonuclear Correlation Spectroscopy at High Magnetic Fields and High MAS Frequencies." *J Am Chem Soc.* (2006) **128**(6):1776-7. Copyright © 2006 American Chemical Society.

5.1 Abstract

We present a new homonuclear recoupling sequence, CMAR, that allows observation of 2D ^{13}C - ^{13}C correlation spectra at high magnetic fields and MAS frequencies (10-30 kHz). The main advantages of the sequence are that it provides efficient, broadband dipolar recoupling and concurrently decouples the ^1H spins from the ^{13}C 's. Thus, no additional ^1H decoupling is required during the mixing period, thereby significantly reducing the radio frequency power requirements for the experiment. Thus, CMAR significantly extends the range of applicability of the usual homonuclear recoupling techniques and should be of major interest for structure determinations of biomolecules at high magnetic fields.

5.2 Introduction

Solid State NMR correlation techniques have become invaluable tools for the assignment of backbone and side chain resonances of peptides and proteins in NMR.¹⁻¹⁷ In high resolution solid-state NMR, the reintroduction of dipolar interactions during magic angle spinning (MAS) experiments (dipolar recoupling) is vital in order to obtain internuclear distance measurements,^{14,18-33} as well as chemical shift correlations. In recent years, a large number of broadband homonuclear recoupling techniques have been introduced with success.^{1,5,21,22,34-52}

At high magnetic fields, the use of high spinning rates is crucial to overcome the increase of chemical shift anisotropy interactions, and exploit the improved resolution and sensitivity provided by high fields. However, the application of many recoupling techniques at high spinning frequencies is restricted by large RF field requirements. The carbon nutation frequency is typically 5 to 7 times the MAS frequency, along with a proton nutation frequency which should be at least three times the carbon nutation frequency.^{5,43} Very high rf power can damage the probe, and thus presents a severe limitation to the implementation, at high spinning frequencies, of many sophisticated recoupling sequences that perform efficiently at lower MAS rates.

In order to circumvent these technical limitations, sequences involving a *low ratio* of rf field to spinning frequency have been proposed.^{43,44,51} Furthermore, dipolar recoupling using an *adiabatic sweep* of the Hamiltonian spin system has been demonstrated using a small rf field on the recoupling channel.^{42,48} Although the latter method reduces the rf power necessary at high spinning frequencies, they suffer from high sensitivity to isotropic and anisotropic chemical shift interactions, which worsen at high B_0 fields.^{38,42} Finally, a recent study has shown that some double quantum (DQ) recoupling sequences can remain efficient in the *absence of 1H decoupling irradiation* at moderate MAS rates.⁵³

Here we report the application of a novel dipolar recoupling scheme to obtain *broadband homonuclear chemical shift correlations* at high spinning frequencies (>15 kHz) and high magnetic fields. This new scheme, called CMAR, combines the use of a rapid cosine modulation of the ^{13}C rf phase together with the use of an adiabatic sweep of the cosine modulation amplitude, with no need for 1H decoupling irradiation (Fig. 5-1).

5.3 Results and Discussion

Recently, it was shown that the use of a properly adjusted Cosine Modulation (CM)⁵⁴ of the ¹H decoupling rf irradiation phase could lead to the reintroduction of the proton-proton couplings through a DQ HORROR²⁰ recoupling mechanism.⁵⁵ The recoupling mechanism occurs in a frame dubbed Modulation Frame and defined by the modulation frequency and the mean axis of the irradiation.^{54,55} This suggests that the application of CM irradiation to the ¹³C spin system can be employed to perform homonuclear recoupling of the ¹³C-¹³C interactions in the *Modulation Frame*, and concurrently perform heteronuclear decoupling of the ¹H-¹³C interactions. Furthermore, in this frame, effects of ¹³C chemical shift anisotropies and rf inhomogeneity are strongly reduced, which leads to efficient DQ excitation even at high magnetic fields.

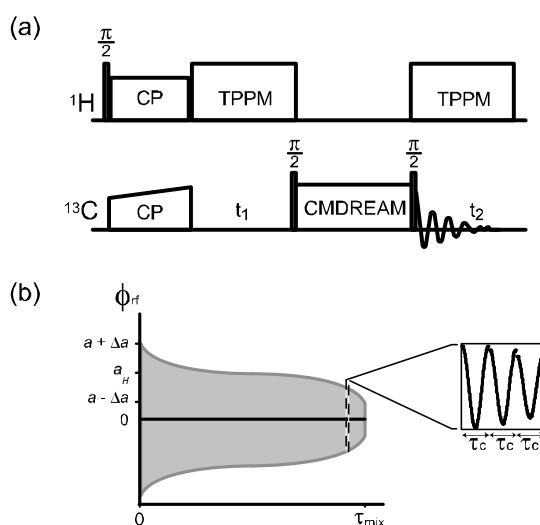


Figure 5-1 (a) Two-dimensional ¹³C-¹³C correlation pulse sequence used with CMAR recoupling sequence. Note that no ¹H decoupling rf field is applied during the mixing time. (b) ¹³C rf phase modulation applied during the recoupling period.

The HORROR condition²⁰ in the Modulation Frame⁵⁵ is defined by the following set of equations:

$$a_H = \frac{\nu_r}{\nu_1}, \quad \frac{\nu_c^H}{\nu_1} = 1 - \frac{1}{4} \left(\frac{\nu_r}{\nu_1} \right)^2$$

where a_H stands for the amplitude (rad), ν_c^H for the frequency (Hz) of the cosine phase modulation, ν_r for the MAS frequency, and ν_1 for the carbon nutation frequency. Under this condition, the rf irradiation can be expressed in the Modulation Frame as a static rf irradiation of amplitude $\nu_{eff} \approx a\nu_1/2$ that matches exactly half the MAS frequency. The Cosine Modulated HORROR (CMHORROR) condition has been recently explored as a part of a homonuclear recoupling technique for ^{13}C spins, and further developments are underway.^{56,57}

The CMAR scheme reported in this Communication is an extension of this new recoupling scheme, in which an adiabatic sweep of the modulation amplitude a through the CMAR matching condition a_H is performed (Fig. 5-1b). The modulation frequency ν_c is kept constant throughout the sweep of the amplitude a . As shown in Fig. 5-1, this irradiation scheme consists of a fast cosine phase modulation enveloped inside an adiabatic function (typically a tangent). The slow variation of the cosine phase modulation amplitude leads to the introduction of a fictitious Zeeman field that allows for an adiabatic passage through the recoupling condition. The spin dynamics induced by this RF phase sweep in the Modulation Frame is analogous to the RF amplitude sweep through the HORROR condition carried out in the rotating frame with the DREAM experiment.^{38,42,48} The adiabatic process involved does not rely on the exact value of the dipolar coupling, and thus constitutes a robust and efficient approach for correlation experiments in multiply labeled samples. Furthermore, recoupling in the Modulation Frame permits the use of CMAR without concurrent proton decoupling irradiation, enabling its application at high spinning rates.

The experimental demonstration of CMAR as a homonuclear correlation technique efficient at high spinning frequencies is presented in Fig. 5-2, which shows ^{13}C - ^{13}C correlation spectra of a sample of the tripeptide [U- ^{13}C , ^{15}N] N-f-MLF-OH,³⁰ at a 28.6 kHz MAS and a magnetic field of 17.6 T. The ^{13}C rf nutation frequency was 100 kHz and no ^1H decoupling irradiation was used. During the evolution and acquisition periods, 83 kHz TPPM decoupling was applied; 512 points were collected in the direct dimension and 128 points in the indirect one, with 8 scans per transient. This data set was collected using a 2.5mm, triple-channel Bruker probe.

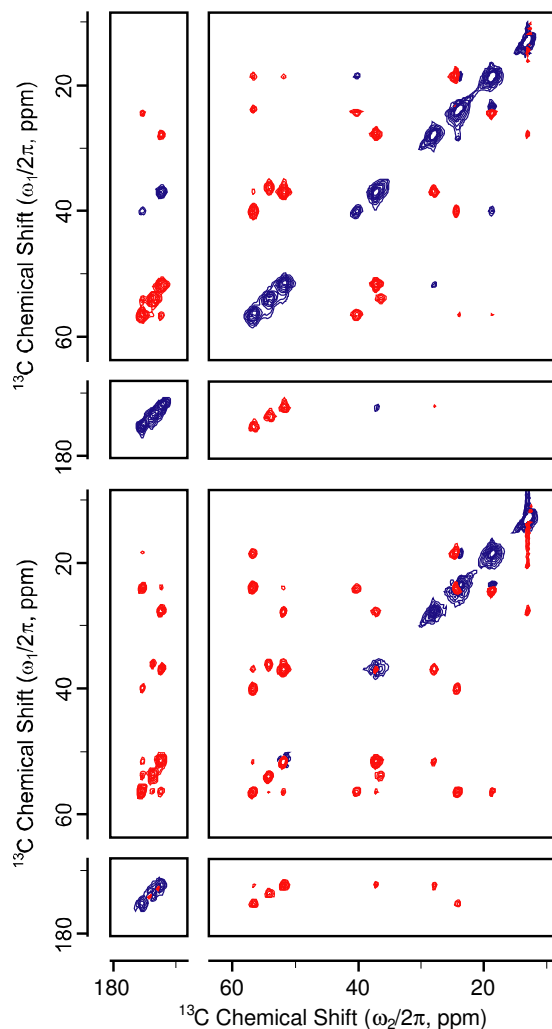


Figure 5-2 2D correlation spectrum of the tripeptide [U- ^{13}C , ^{15}N] N-f-MLF-OH using CMAR recoupling at 28.6 kHz MAS and approximately 100 kHz of ^{13}C rf field strength using 2 ms (up) and 5 ms (down) mixing time, with no proton decoupling.

These high B_0 field, high spinning frequency spectra present correlations for all directly bonded spins, whose isotropic chemical shifts span about 35 kHz, showing the efficient broadband performance of the CMAR recoupling scheme. These correlation spectra also demonstrate one of the remarkable features of this recoupling technique, namely, the fact that high rf recoupling pulses can be safely applied during the mixing time because there is no concurrent proton decoupling irradiation.

5.4 Conclusion

A novel adiabatic DQ recoupling scheme has been introduced. The advantages of this new technique are multiple. First, the experiment can be performed with a ^{13}C rf field sufficiently strong to uniformly recouple the whole carbon spectrum (even at high magnetic fields), and be robust against chemical shift offsets and anisotropies. The result is a very broadband behavior for the CMAR experiment. This characteristic represents an improvement over the original DREAM experiment, in which the mean amplitude of the sweep is only half the MAS frequency. The recently developed DREAM-C7⁵⁸ sequence addresses this issue, but is limited to low MAS frequencies (< 15 kHz) due to high rf power requirements. With CMAR, the ratio (p) of the modulation frequency (approximately the rf field strength) to the MAS frequency can be set to fulfill the experimental requirements. CMAR can thus be applied efficiently at high spinning frequencies using a low p ratio. Furthermore, without ^1H irradiation, a strong rf field strength can be used on the ^{13}C channel (in the limits of probe specification), allowing efficient recoupling at high spinning rates and high magnetic fields. These characteristics extend the range of applicability of homonuclear recoupling techniques to high resolution conditions, and should be of major interest for structure determination of biomolecules. A detailed description of the spin dynamics in the CMAR recoupling mechanism is currently in progress.

5.5 Acknowledgements

This work was supported by National Institutes of Health Grants EB001960 and EB-002026. Thanks are accorded to Drs. P. van der Wel, M. Veshtort, C. Turner, and D. Ruben for stimulating conversations.

5.6 Supporting Information

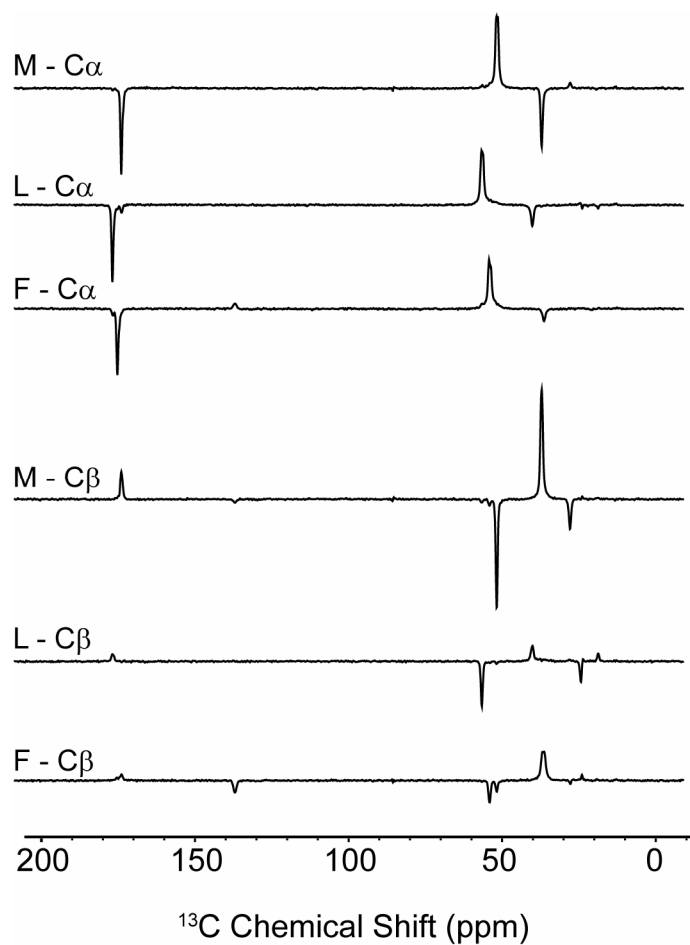


Figure 5-3 Slices through the C α resonances (a) and C β resonances (b) for each residue in the indirect dimension of the MLF 2D ¹³C-¹³C correlation spectrum with 2ms CMAR mixing time. The MAS spinning frequency was 29.578 kHz, the ¹³C field strength 100 kHz and the proton frequency 750 MHz.

5.7 References

- (1) Bennett, A. E.; Ok, J. H.; Griffin, R. G.; Vega, S. J. *Chem. Phys.* **1992**, *96*, 8624-8627.

- (2) Baldus, M.; Meier, B. H. *Journal of Magnetic Resonance Series A* **1996**, *121*, 65-69.
- (3) Baldus, M.; Meier, B. H. *J. Magn. Reson.* **1997**, *128*, 172-193.
- (4) Lesage, A.; Auger, C.; Caldarelli, S.; Emsley, L. *Journal of the American Chemical Society* **1997**, *119*, 7867-7868.
- (5) Bennett, A. E.; Rienstra, C. M.; Griffiths, J. M.; Zhen, W. G.; Lansbury, P. T.; Griffin, R. G. *J. Chem. Phys.* **1998**, *108*, 9463-9479.
- (6) Hong, M.; Griffin, R. G. *Journal of the American Chemical Society* **1998**, *120*, 7113-7114.
- (7) Lesage, A.; Sakellariou, D.; Steuernagel, S.; Emsley, L. *Journal of the American Chemical Society* **1998**, *120*, 13194-13201.
- (8) Griffin, R. G. *Nat. Struct. Biol.* **1998**, *5*, 508-512.
- (9) Lesage, A.; Bardet, M.; Emsley, L. *Journal of the American Chemical Society* **1999**, *121*, 10987-10993.
- (10) Lesage, A.; Charmont, P.; Steuernagel, S.; Emsley, L. *Journal of the American Chemical Society* **2000**, *122*, 9739-9744.
- (11) Rienstra, C. M.; Hohwy, M.; Hong, M.; Griffin, R. G. *Journal of the American Chemical Society* **2000**, *122*, 10979-10990.
- (12) Detken, A.; Hardy, E. H.; Ernst, M.; Kainosho, M.; Kawakami, T.; Aimoto, S.; Meier, B. H. *J. Biomol. NMR* **2001**, *20*, 203-221.
- (13) Baldus, M. *Prog. Nucl. Magn. Reson. Spectrosc.* **2002**, *41*, 1-47.
- (14) Castellani, F.; van Rossum, B.; Diehl, A.; Schubert, M.; Rehbein, K.; Oschkinat, H. *Nature* **2002**, *420*, 98-102.
- (15) Bockmann, A.; Lange, A.; Galinier, A.; Luca, S.; Giraud, N.; Juy, M.; Heise, H.; Montserret, R.; Penin, F.; Baldus, M. *J. Biomol. NMR* **2003**, *27*, 323-339.
- (16) Petkova, A. T.; Baldus, M.; Belenky, M.; Hong, M.; Griffin, R. G.; Herzfeld, J. *J. Magn. Reson.* **2003**, *160*, 1-12.
- (17) Heise, H.; Seidel, K.; Etzkorn, M.; Becker, S.; Baldus, M. *J. Magn. Reson.* **2005**, *173*, 64-74.
- (18) Raleigh, D. P.; Creuzet, F.; Gupta, S. K. D.; Levitt, M. H.; Griffin, R. G. *Journal of the American Chemical Society* **1989**, *111*, 4502-4503.
- (19) Tycko, R.; Dabbagh, G. *Chem. Phys. Lett.* **1990**, *173*, 461-465.

- (20) Nielsen, N. C.; Bildsoe, H.; Jakobsen, H. J.; Levitt, M. H. *J. Chem. Phys.* **1994**, *101*, 1805-1812.
- (21) Sun, B. Q.; Costa, P. R.; Kocisko, D.; Lansbury, P. T.; Griffin, R. G. *J. Chem. Phys.* **1995**, *102*, 702-707.
- (22) Mehta, M. A.; Gregory, D. M.; Kiihne, S.; Mitchell, D. J.; Hatcher, M. E.; Shiels, J. C.; Drobny, G. P. *Solid State Nuclear Magnetic Resonance* **1996**, *7*, 211-228.
- (23) Costa, P. R.; Sun, B. Q.; Griffin, R. G. *J. Am. Chem. Soc.* **1997**, *119*, 10821-10830.
- (24) Hong, M.; Gross, J. D.; Hu, W.; Griffin, R. G. *J. Magn. Reson.* **1998**, *135*, 169-177.
- (25) Jaroniec, C. P.; Tounge, B. A.; Rienstra, C. M.; Herzfeld, J.; Griffin, R. G. *Journal of the American Chemical Society* **1999**, *121*, 10237-10238.
- (26) Jaroniec, C. P.; Tounge, B. A.; Rienstra, C. M.; Herzfeld, J.; Griffin, R. G. *J. Magn. Reson.* **2000**, *146*, 132-139.
- (27) Jaroniec, C. P.; Tounge, B. A.; Herzfeld, J.; Griffin, R. G. *Biophys. J.* **2001**, *80*, 368A-368A.
- (28) Carravetta, M.; Eden, M.; Johannessen, O. G.; Luthman, H.; Verdegem, P. J. E.; Lugtenburg, J.; Sebald, A.; Levitt, M. H. *Journal of the American Chemical Society* **2001**, *123*, 10628-10638.
- (29) Jaroniec, C. P.; Filip, C.; Griffin, R. G. *Journal of the American Chemical Society* **2002**, *124*, 10728-10742.
- (30) Rienstra, C. M.; Tucker-Kellogg, L.; Jaroniec, C. P.; Hohwy, M.; Reif, B.; McMahon, M. T.; Tidor, B.; Lozano-Perez, T.; Griffin, R. G. *Proc. Natl. Acad. Sci. U. S. A.* **2002**, *99*, 10260-10265.
- (31) Ramachandran, R.; Ladizhansky, V.; Bajaj, V. S.; Griffin, R. G. *Journal of the American Chemical Society* **2003**, *125*, 15623-15629.
- (32) Jaroniec, C. P.; MacPhee, C. E.; Bajaj, V. S.; McMahon, M. T.; Dobson, C. M.; Griffin, R. G. *Proc. Natl. Acad. Sci. U. S. A.* **2004**, *101*, 711-716.
- (33) Ladizhansky, V.; Griffin, R. G. *Journal of the American Chemical Society* **2004**, *126*, 948-958.
- (34) Meier, B. H.; Earl, W. L. *J. Chem. Phys.* **1986**, *85*, 4905-4911.
- (35) Tycko, R.; Dabbagh, G. *Journal of the American Chemical Society* **1991**, *113*, 9444-9448.

- (36) Sodickson, D. K.; Levitt, M. H.; Vega, S.; Griffin, R. G. *J. Chem. Phys.* **1993**, *98*, 6742-6748.
- (37) Feike, M.; Demco, D. E.; Graf, R.; Gottwald, J.; Hafner, S.; Spiess, H. W. *Journal of Magnetic Resonance Series A* **1996**, *122*, 214-221.
- (38) Verel, R.; Baldus, M.; Nijman, M.; van Os, J. W. M.; Meier, B. H. *Chem. Phys. Lett.* **1997**, *280*, 31-39.
- (39) Gross, J. D.; Costa, P. R.; Griffin, R. G. *J. Chem. Phys.* **1998**, *108*, 7286-7293.
- (40) Hohwy, M.; Jakobsen, H. J.; Eden, M.; Levitt, M. H.; Nielsen, N. C. *J. Chem. Phys.* **1998**, *108*, 2686-2694.
- (41) Rienstra, C. M.; Hatcher, M. E.; Mueller, L. J.; Sun, B. Q.; Fesik, S. W.; Griffin, R. G. *Journal of the American Chemical Society* **1998**, *120*, 10602-10612.
- (42) Verel, R.; Baldus, M.; Ernst, M.; Meier, B. H. *Chem. Phys. Lett.* **1998**, *287*, 421-428.
- (43) Hohwy, M.; Rienstra, C. M.; Jaroniec, C. P.; Griffin, R. G. *J. Chem. Phys.* **1999**, *110*, 7983-7992.
- (44) Brinkmann, A.; Eden, M.; Levitt, M. H. *J. Chem. Phys.* **2000**, *112*, 8539-8554.
- (45) Carravetta, M.; Eden, M.; Zhao, X.; Brinkmann, A.; Levitt, M. H. *Chem. Phys. Lett.* **2000**, *321*, 205-215.
- (46) Karlsson, T.; Eden, M.; Luthman, H.; Levitt, M. H. *J. Magn. Reson.* **2000**, *145*, 95-107.
- (47) Schnell, I.; Spiess, H. W. *J. Magn. Reson.* **2001**, *151*, 153-227.
- (48) Verel, R.; Ernst, M.; Meier, B. H. *J. Magn. Reson.* **2001**, *150*, 81-99.
- (49) Brinkmann, A.; Gunne, J.; Levitt, M. H. *J. Magn. Reson.* **2002**, *156*, 79-96.
- (50) Hohwy, M.; Rienstra, C. M.; Griffin, R. G. *J. Chem. Phys.* **2002**, *117*, 4973-4987.
- (51) Kristiansen, P. E.; Mitchell, D. J.; Evans, J. N. S. *J. Magn. Reson.* **2002**, *157*, 253-266.
- (52) Karlsson, T.; Popham, J. M.; Long, J. R.; Oyler, N.; Drobny, G. P. *Journal of the American Chemical Society* **2003**, *125*, 7394-7407.
- (53) Hughes, C. E.; Luca, S.; Baldus, M. *Chem. Phys. Lett.* **2004**, *385*, 435-440.
- (54) De Paepe, G.; Hodgkinson, P.; Emsley, L. *Chem. Phys. Lett.* **2003**, *376*, 259-267.
- (55) De Paepe, G.; Elena, B.; Emsley, L. *J. Chem. Phys.* **2004**, *121*, 3165-3180.

- (56) De Paepe, G.; Lewandowski, J.; Bayro, M. J.; Griffin, R. G. *in preparation* **2005**.
- (57) De Paepe, G.; Lewandowski, J.; Bayro, M. J.; Griffin, R. G. In *46th Experimental Nuclear Magnetic Resonance Conference*: Providence (RI), 2005.
- (58) Verel, R.; Meier, B. H. *Chemphyschem* **2004**, 5, 851-862.

6. Double-quantum carbon-carbon relayed magnetization transfer for solid-state NMR biomolecular studies at high magnetic fields

6.1 Abstract

Multidimensional solid-state NMR (SSNMR) at high magnetic fields provides high resolution structural and dynamics information about a variety of biomolecular systems including nanocrystalline and non-crystalline precipitated samples, amyloid fibrils, membrane proteins and protein complexes. Time-efficient and error-free spectral assignment procedures are imperative for making such studies generally applicable and practical. Broadband dipolar double-quantum ^{13}C - ^{13}C recoupling techniques are some of the most powerful assignment tools available in solid-state NMR but are rarely used at high fields for anything other than model systems due to a range of practical limitations including polarization losses due to insufficient ^1H decoupling and prohibitive sample heating. We demonstrate how the Cosine phase Modulated Rotary Resonance (CM_pRR) pulse sequence using ultralow or even no ^1H decoupling overcomes most of these practical limitations and thus enables SSNMR study of a range of biomolecular systems. We apply CM_pRR to samples with varying degrees of macroscopic order without compromising the integrity of the samples. We demonstrate the efficient polarization transfer along multiple carbon-carbon bonds, as well as the advantages of the cross-peak sign alternation, a signature of double-quantum polarization transfer, and how these features benefit resonance assignment as well as assignment cross-validation (especially for proteins with significant spectral overlap). The increased efficiency and reliability of these assignment strategies at high magnetic fields and fast magic angle spinning (MAS) will facilitate the application of advanced SSNMR structural studies on difficult yet important biological systems.

6.2 Introduction

Following a similar trend in biomolecular solution NMR, where 900 MHz magnets have been providing increased resolution for biological structure determination studies, such high-field magnets are becoming increasingly available for solid-state NMR applications (1-4). This implies the promise of improved resolution and sensitivity for studies of biological solids. Solid-state NMR is at a stage where combination of high magnetic fields, appropriate sample preparation (including various labeling schemes (5-8)), modern hardware and cutting-edge pulse sequences allows tackling important structural and dynamical questions in large biomolecules. Thus, solid-state NMR is rapidly developing as a *unique technique* for biomolecular structure determination due to its ability to provide detailed structural information in a wide variety of samples, whether (nano)crystalline, fibrillar, or immobilized by association with biomembranes. It has been employed in a range of biologically important studies into such topics as protein folding/misfolding, amyloid aggregation, signal transduction, and molecular transport across biomembranes (9-13). These studies represent not only whole-molecule structure determinations, but also essential challenges such as *in situ* structure determination of bound ligands (14, 15), their effect on membrane protein structure, and the detection of protein-protein interactions (16-18)

The prerequisite for structural studies by NMR is the identification of specific sites in a molecule as resonances in the spectra. Depending on the sample-specific features such as resolution and sensitivity, this spectral assignment process in solid-state NMR may be time-consuming and arduous. Use of higher magnetic fields for solid state NMR should allow for optimization of both parameters (as far as the inherent sample quality allows). Therefore, design of the most efficient and effective assignment approach for applications in this newly accessible high resolution regime of high magnetic fields and high spinning frequencies is an essential effort.

In contrast to solution NMR, the majority of the assignment methods in solid-state NMR rely on the controlled reintroduction of dipolar interactions between spins. For biomolecular systems this often involves the observation of ^{13}C labeled sites, making ^{13}C - ^{13}C recoupling pulse sequences important building blocks for more complex experiments. Ideally, efficient assignment methods should be able to compensate for chemical shift differences between

recoupled sites and to provide a robust and reliable mechanism that specifically follows the covalent connectivity in uniformly labeled systems. Such requirements are met by recoupling sequences that simultaneously reintroduce all ^{13}C - ^{13}C dipolar couplings. However, the non-commuting nature of the different terms in the effective Hamiltonian favors the strongest couplings (short distances) inducing a so-called dipolar truncation of the smaller terms (longer distances). This can be seen as a drawback for detecting structurally relevant long distances but is of major importance for precise control of the polarization transfer pathways warranting reliable assignment. Since the covalent bonds along the carbon chain also correspond to the strongest ^{13}C - ^{13}C dipolar couplings the presence of dipolar truncation ensures that the ^{13}C - ^{13}C polarization transfer pathways trace out the along-the-chain covalent connectivity of the molecules. This is especially useful in the case of so called double-quantum (DQ) recoupling techniques for which the polarization relayed over each bond changes its sign and thus allows one to distinguish one-bond, two-bond or three-bond connectivity. However, broadband DQ sequences are rarely used on biological samples due to some practical limitations. These limitations include polarization losses due to insufficient decoupling of the ^1H - ^{13}C interaction by the means of ^1H irradiation and prohibitive sample heating (that may compromise the sample integrity). Instead, less informative but also less demanding ^{13}C - ^{13}C recoupling techniques such as PDS and DARR have been used extensively for assignment. However, the increased complexity of the samples studied by solid-state NMR calls for use of practical and efficient assignment procedures provided by DQ methods, especially in the high field and high spinning frequency regime needed to maximize spectral resolution and sensitivity. Therefore we will examine the practical application of our recently introduced ^{13}C - ^{13}C homonuclear recoupling sequence based on Cosine phase Modulated (CM) irradiation, achieving γ -encoded DQ recoupling at high magnetic fields and high spinning frequencies (19, 20). This experiment, Cosine phase Modulated Rotary Resonance (CM_pRR - see Fig. 6-1), is a flexible pulse sequence that possesses excellent homonuclear recoupling and heteronuclear decoupling characteristics. It allows reduction of losses due to surrounding protons and yields efficient and fast ^{13}C - ^{13}C polarization transfer. Moreover, since ^{13}C - ^{13}C CM_pRR polarization transfer is performed with extremely low or even without ^1H decoupling irradiation it minimizes the sample heating detrimental to biological samples (20). In this manuscript we demonstrate how carbon chain-relayed polarization transfer spectroscopy employing the

CM_pRR sequence can be used as a practical tool for efficient assignment and assignment cross-validation of biomolecular systems. In particular we demonstrate the successful application of CM_pRR without or with minimal ¹H decoupling on a number of biological peptide or protein samples at 21.1 T B₀ field (900 MHz ¹H frequency).

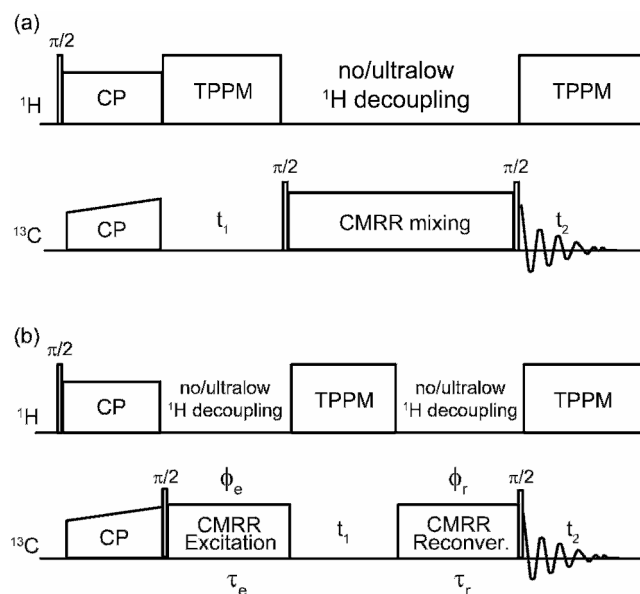


Figure 6-1 CM_pRR pulse sequences for performing two-dimensional (2D) ¹³C-¹³C correlation experiments at high field and spinning frequency with ultralow (less than $0.25\omega_c$) or even without ¹H decoupling: (a) version used for 2D SQ-SQ ¹³C-¹³C correlation experiments, (b) DQ filtered version used for 2D SQ-DQ ¹³C-¹³C correlation experiments. Note, that the pulse sequence in (b) without the t_1 evolution is used for optimizations of polarization transfer.

For this purpose, we examine a variety of biological samples. Dry microcrystals of the chemotactic tripeptide N-*f*-MLF-OH (21) are a standard microcrystalline sample for setting up novel NMR experiments. GNNQQNY is a peptide fragment from the N-domain of the yeast prion protein Sup35p which was demonstrated to form nanocrystals, but also amyloid-like fibrils with characteristics similar to the full length Sup35p fibrils (22-26). It has been used as an amyloid model system, in studies of the crystals and fibrils by X-ray crystallography and solid state NMR (22-26). We include data on the hydrated peptide fibrils, which were found to consist of three co-existing distinct structural forms by solid state NMR (23). The 84-residue SH3 domain of the p85 α subunit of bovine phosphatidylinositol 3-kinase (PI3-SH3) in the native state at neutral pH has a β -barrel structure (27, 28), but also forms amyloid-like fibrils

under acidic conditions (29). The formation of the amyloid fibrils, which we examine in this study, might reflect a common ability for many proteins to adopt a fibrillar (non-native) structure. Finally, gas vesicles are the floatation organelles of aquatic micro-organisms. Their walls are built almost exclusively by repeats of a single, highly hydrophobic 7-8 kDa protein, GvpA (30), which we examine as well. Note that all these samples are studied in hydrated form, except for the (dry) N-*f*-MLF-OH microcrystals.

These samples constitute a representative variety of dry and hydrated samples of both peptides and proteins characterized by a range of structural order and dynamics. We will demonstrate the feasibility of efficient DQ ^{13}C - ^{13}C recoupling at high field and high spinning frequencies without compromising sample integrity and discuss practical issues in the implementation of such experiments as well as interpretation and use of the results. This will include the value of “chain relay” data with DQ sign alternation, made possible by CM_pRR at high magnetic field thus allowing high resolution studies.

6.3 Results and Discussion

6.3.1 Chain relayed polarization transfer in biological samples

The majority of ^{13}C - ^{13}C correlation experiments in solid-state NMR are based on dipolar recoupling techniques that rely on reintroducing (to the first order) either zero- (ZQ) or double-quantum (DQ) dipolar Hamiltonians. In both cases, dipolar truncation favors transfer to the closest nuclei resulting in polarization transfer pathways involving multiple step transfers relayed along the carbon chain via strong one-bond couplings in uniformly labeled systems. In DQ sequences the cross-peaks resulting from consecutive relayed steps have alternating signs, whereas they all have the same sign in the case of the ZQ mixing. Consequently, it is much easier to distinguish multiple-bond (relay) transfers from one-bond transfers when using DQ sequences. An example of spectra utilizing this feature is presented in the CM_5RR ^{13}C - ^{13}C 2D correlation spectra on the aliphatic region of the $[\text{U-}^{13}\text{C}, ^{15}\text{N-GNNQ}]_{\text{QNY}}$ fibrils shown in Fig. 6-2a-e. In these spectra each of the directly bonded carbon pairs results in a negative (red) cross-peak. For a short mixing time (0.8 ms) we only observe one-bond cross-peaks (Fig. 6-2a,c). When the mixing time is increased (1.6 ms), it results in the appearance of positive (blue) cross-peaks which correspond to two-bond transfers relayed over one-bond (Fig. 6-

2b,d). The sign alternation ensures that closely spaced resonances and cross-peaks can be reliably distinguished, as illustrated in Fig. 6-2e where the negative $Q_{10}C_{\alpha}-C_{\beta}$ and positive $Q_{10}C_{\alpha}-C_{\gamma}$ cross peaks from the two different mixing times are overlaid. In the absence of sign alternation, it would be impossible to reliably resolve the combined and overlapping one-bond and two-bond cross peaks.

As an added bonus, DQ sequences allow usage of so-called DQ filters (31) as a convenient way of suppressing the signal from isolated spins, such as those present as natural abundance ^{13}C background. DQ filtering also allows for alternative implementations of the ^{13}C - ^{13}C correlation using so called single-quantum double-quantum (SQ-DQ) versions of the experiments. A SQ-DQ spectrum features an indirect dimension that reflects the frequency of the DQ coherence, which is equal to the sum of the resonance frequencies of the two carbon sites involved. Thus, each directly bonded carbon pair is represented by two cross-peaks with the chemical shift of each particular site in the direct (SQ) dimension and the sum of their chemical shifts in the indirect (DQ) dimension. The SQ-DQ spectrum lacks peaks on a diagonal (typical of 'regular' SQ-SQ spectra) and allows identification of sites with similar or identical chemical shift which are masked by the proximity of strong diagonal peaks in the SQ-SQ spectrum. This is illustrated on the example of the $Q_{10}C_{\beta}-C_{\gamma}$ resonances in GNNQQNY fibrils. In the top half of Fig. 6-2c we can easily identify 4 $Q_{10}C_{\beta}-C_{\gamma}$ cross-peaks (2 on each side of the diagonal) belonging to two out of three fibril forms. It transpires that in the remaining form the chemical shifts of $Q_{10}C_{\beta}$ and $Q_{10}C_{\gamma}$ are almost identical so the resulting cross-peak is masked by the intensive diagonal in Fig. 6-2c (the location where the peak should be observed is marked with a star). However, we can clearly identify the $Q_{10}C_{\beta}-C_{\gamma}$ for the fibril form 2 in the SQ-DQ spectrum in Fig. 6-2f. Note that in this spectrum in contrast to other $Q_{10}C_{\beta}-C_{\gamma}$ sites for which we obtain pairs of cross-peaks the form 2 $Q_{10}C_{\beta}-C_{\gamma}$ appears as a single cross-peak reflecting the almost identical chemical shift for the two sites.

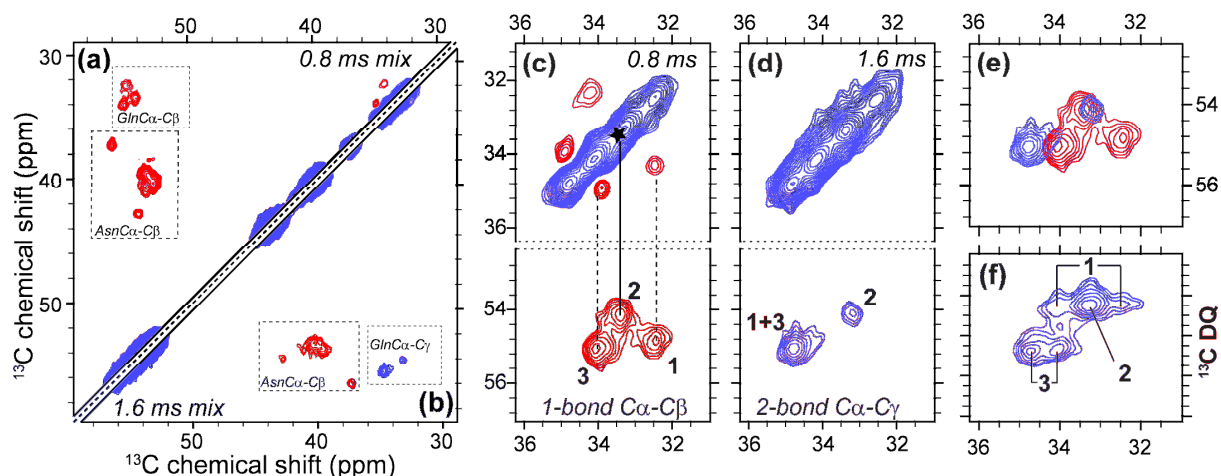


Figure 6-2 CM₃RR data on hydrated [U-¹³C,¹⁵N-GNNQ]QNY₇₋₁₃ amyloid-like fibrils obtained at 900 MHz ¹H Larmor frequency (21.1 Tesla) and 20 kHz MAS. Aliphatic 2D ¹³C-¹³C SQ-SQ CM₃RR spectra obtained without additional ¹H decoupling with 0.8 ms mixing (a) and 1.6 ms mixing (b), showing one-bond and two-bond transfer within Asn and Gln side chains (color coding reflects sign of the peaks: blue = positive, red = negative). Note that there are three conformers showing up for each residue (see ref. (23)). (c) Zoomed-in regions reflecting Gln cross peaks at 0.8 ms mixing (favoring one-bond transfer), and (d) 1.6 ms mixing (favoring 2-bond transfer). The three conformers are indicated. The top panels show C_β-C_γ cross-peaks, which are close to the diagonal due to their similar frequencies. The bottom panels are overlaid in panel (e), to show how sign alternation avoids confusion between the closely spaced 1-bond and 2-bond cross-peaks. Panel (f) shows Gln C_β-C_γ cross-peaks from a SQ-DQ experiment with 0.8ms mixing (equivalent to panel (c)). Note that conformer 2 shows up as a recognizable cross-peak, whereas it is overlapped with the diagonal in the SQ-SQ data (black star in panel (c)). For full spectra see Supporting Information.

In assignment experiments on uniformly labeled systems, DQ ¹³C-¹³C recoupling techniques have typically been used primarily for determining covalent connectivity via cross-peaks due to one-bond polarization transfer. Given the abovementioned DQ sign alternation, cross-peaks resulting from multiple step carbon chain relayed transfers (or so called multi-bond cross-peaks) would be an attractive alternative for increasing the information content of the ¹³C-¹³C correlations. Unfortunately, high magnetic fields (≥ 900 MHz) typically place limitations on the ability to do so. This is due to the field-dependent increase in the chemical shift (isotropic as well as anisotropic), which affects the spin-dynamics as well as the implementation of the

SSNMR experiments. We first examine this through numerical simulations. Fig. 6-3 shows such simulations of the polarization transfer along a leucine sidechain at 900 MHz ^1H Larmor frequency. Panel (a) shows SPC5 polarization transfer with the typical settings that it had originally been designed for: i.e. moderate MAS frequency ($\omega_r/2\pi = 10$ kHz, $\omega_{1\text{C}}/2\pi = 50$ kHz) and high (but realistic) power ^1H decoupling ($\omega_{1\text{H}}/2\pi = 100$ kHz). At 900 MHz ^1H Larmor frequency, the plethora of destructive interferences (cross-terms) involving the chemical shift and ^1H - ^{13}C interactions lead to strong coherent damping of the DQ polarization transfer resulting in only the one-bond cross peaks ($\text{C}' \rightarrow \text{C}\alpha$) having appreciable intensity. The CM_5RR sequence (20), which was designed to efficiently average the chemical shift and decouple the ^1H - ^{13}C interactions through its ^{13}C irradiation, performs much better in relaying magnetization along the carbon chain. As shown in Fig. 6-3 c, simulations suggest that application of CM_5RR without ^1H irradiation should result in up to 4-bond relayed cross-peaks with the optimum for each step clearly separated in time. Moreover, the one-bond transfer is also more efficient and faster than that observed for SPC5. Note that at high spinning frequencies and 900 MHz, even SPC5 itself benefits from application without additional decoupling ^1H irradiation (see Fig 6-3b), but the superior decoupling characteristics of CM_pRR render it the optimal solution for the considered regime (20) (CM_5RR results in several-fold increase in multiple-bond transfers; see also Supporting Information).

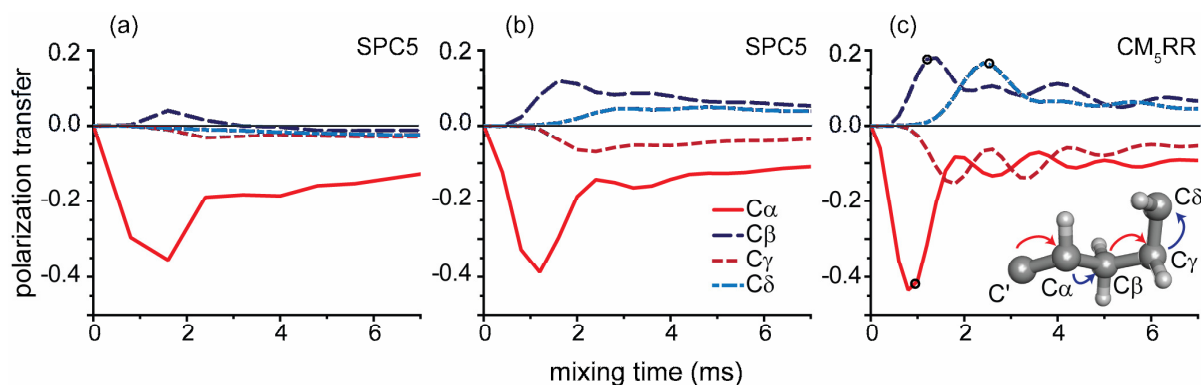


Figure 6-3 Simulations of polarization transfer along a carbon chain using double-quantum dipolar sequences at 900 MHz ^1H frequency: (a) SPC5 performed at 10 kHz spinning frequency (MAS) using 100 kHz ^1H cw decoupling. (b) SPC5 performed at 20 kHz MAS without additional ^1H decoupling. (c) CM_5RR performed at 20 kHz MAS without additional ^1H decoupling; The 10-spin simulations at 900 MHz ^1H Larmor frequency (spin system in the inset of panel (c)) were performed using SPINEVOLUTION (32)

and included isotropic chemical shift and chemical shift anisotropy modeled on the leucine side chain in N-*f*-MLF-OH (21). The ^{13}C rf was 100 kHz and 50 kHz for 20 kHz and 10 kHz MAS respectively. The ^1H decoupling strength for SPC5 at 10 kHz MAS was optimized beforehand in order to avoid double-quantum efficiency oscillations due to the insufficient decoupling (33). Circles indicate mixing times used in experiments presented in Fig. 6-4.

The behavior predicted from numerical simulations is qualitatively reflected in the experimental data in Fig. 6-4 showing $\text{CM}_{3.5}\text{RR}$ spectra on $[\text{U-}^{13}\text{C}, ^{15}\text{N}]$ -*f*-MLF-OH at different mixing times (the mixing times used in the experiments are marked with circles on the CM_5RR simulation in Fig. 6-3). As expected due to the dipolar truncation, the polarization transfer is dominated by one-bond relayed transfers. Note that the sign of magnetization is inverted in each step: the cross-peak is negative for the first step, positive for the second, negative for the third etc. Notably, the optimal polarization buildup times for each of the consecutive steps is clearly separated in time (note, the sign change for the cross-peak near 25 ppm on the vertical axis – the negative three-bond $\text{C}'\text{-C}\gamma$ cross-peak present at 1.2 ms is replaced with a positive four-bond $\text{C}'\text{-C}\delta$ cross-peak at 2.52 ms mixing) and one-bond cross-peaks do not dominate at longer mixing times (which should lead to reduced spectral crowding). Such patterns recorded at several different mixing times greatly simplify the task of establishing covalent connectivity and can lead to unambiguous assignment of multiple-bond transfer cross-peaks. For example, for a short mixing time of 840 μs one-bond cross-peaks can be easily identified by their negative sign and two-bond by their positive sign. Three-bond cross-peaks can be distinguished from the one-bond cross peaks (with the same sign) because they are absent from the short mixing spectra. With 2.5 ms of irradiation we actually observe up to four-bond cross-peaks in this (model) system.

Part of the reason why peptide samples are attractive test samples, is that they can be robust and have favorable relaxation characteristics that reduce the magnetization losses during pulse sequences. Hydrated biological samples consisting of larger proteins can complicate the application of pulse sequences for a variety of reasons and thus reduce their applicability and effectiveness. However, similar results to the ones observed on our model system, are also observed in more challenging systems of non-crystalline proteins. Fig. 6-5 shows the CM_4RR data acquired on $[\text{U-}^{13}\text{C}, ^{15}\text{N}]$ -PI3-SH3 fibrils, where two-bond cross-peaks are observed at

1.488ms mixing (panel b). In Fig. 6-6 we observe up to three-bond cross-peaks with 1.5 ms mixing (panel b) for the non-crystalline $[U-^{13}C,^{15}N]$ -GvpA protein. Obtaining similar information using ZQ recoupling techniques would be less straightforward and would likely require selective experiments and experiments of higher dimensionalities to resolve ambiguities about multiple-bond cross-peak identity (things that could be avoided in DQ experiments). Moreover, some of the most popular assignment techniques such as Proton Driven Spin Diffusion (PDS) (34) and Dipolar Assisted Rotational Resonance (DARR) (35, 36) rely on a ZQ mechanism in which the dipolar truncation is partially alleviated (since the polarization transfer mechanism does not rely on first order ^{13}C - ^{13}C dipolar recoupling but mainly involves second order recoupling of ^{13}C - ^{13}C and 1H - ^{13}C dipolar couplings). The use of such methods substantially lessens our control over the polarization exchange pathways as it leads to a complicated combination of direct and relayed transfer mechanisms. In practice this means that when using PDS/DARR for assignment one has to deal with increased level of ambiguity.

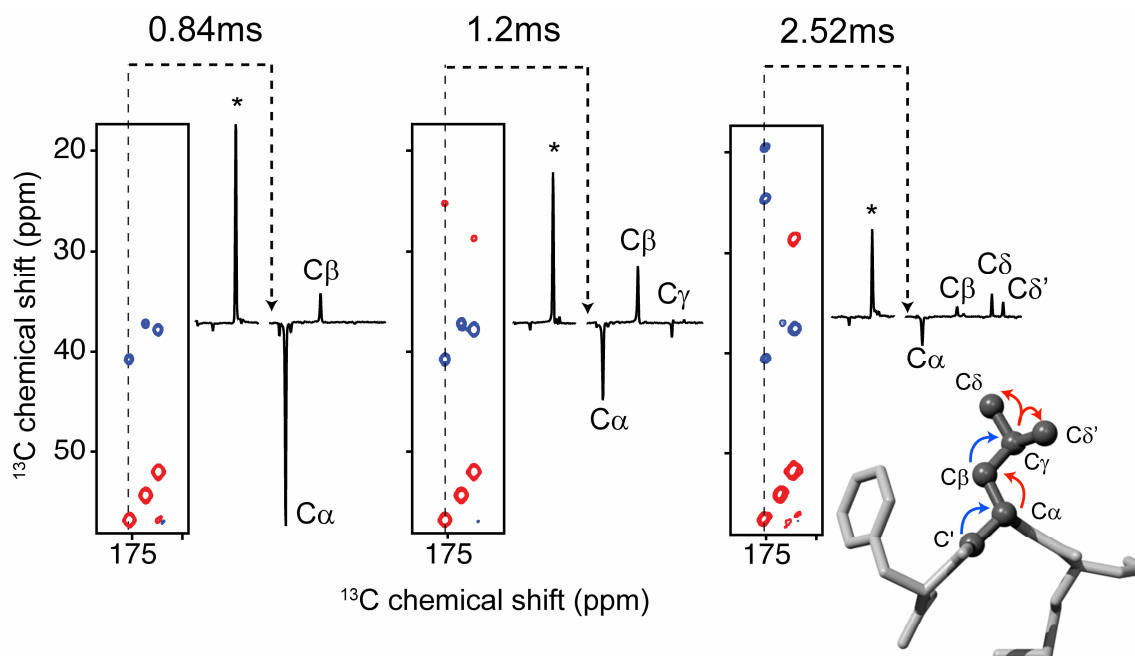


Figure 6-4 Experimental data from two-dimensional ^{13}C - ^{13}C correlation spectra on $[U-^{13}C,^{15}N]$ -*f*-MLF-OH obtained using $CM_{3,5}RR$ at 900 MHz 1H frequency and 23.81 kHz MAS, with increasing mixing time from 0.84 ms to 2.52 ms (from left to right). The strips show the transfer of polarization originating on the carbonyl groups being dominated by a one-bond relay process along the amino acid side chains.

Positive and negative cross-peaks are indicated respectively in blue and red. The slices are obtained at the Leu C' resonance frequency (dashed line in 2D panels) and show the residual C' peak (*) and the aliphatic side chain signals, at the same absolute vertical scale. Note that in the spectrum using 2.52 ms mixing time we observe up to 4-bond relayed transfer cross-peaks (Leu C δ peaks). Experimental settings are detailed in the NMR spectroscopy section.

In these protein spectra the chemical shift dispersion in the C α and C' regions is rather limited and so additional correlations to C β /C γ resonances, which tend to have better chemical shift dispersion, are especially useful and may substantially aid the assignment process. For example, when one compares the C'-C α (red cross-peaks near (x,y) ~ (170 ppm, 50-60 ppm)) and C'-C β regions (green cross-peaks near (170 ppm, 20-40 ppm)) in Fig. 6-5 it becomes immediately apparent that we have substantial gain in the dispersion in the latter region. The blue dashed lines illustrate how a well-resolved C'-C β cross-peak can indicate the location of C'-C α resonance from a very crowded region, a task that would otherwise require additional experiments. Inspection of the CM $_{3,5}$ RR spectrum on [U- ^{13}C , ^{15}N]-GvpA (Fig. 6-6b) also makes one appreciate the much improved chemical shift dispersion of the C'-C β region (blue cross-peaks) compared to the C'-C α region (red-yellow cross-peaks, also present in Fig. 6-6a).

At this point it is important to stress another beneficial aspect of the single channel irradiation employed in CM $_p$ RR. Since it minimizes the influence of the ^{13}C - ^1H couplings in the ^{13}C - ^{13}C spin dynamics it can significantly reduce the level of ambiguity in the assignment process. As we have pointed out elsewhere (37), the contribution of ZQ Third Spin Assisted Recoupling (TSAR) (which is a second order process involving ^{13}C - ^1H cross terms) can significantly perturb the (first order) ^{13}C - ^{13}C recoupling by inducing ZQ ^{13}C - ^{13}C transfer assisted by protons (at ^1H fields that usually would be considered adequate for decoupling the ^{13}C spins from the ^1H bath). This means that if proper care is not taken with optimizing the ^1H decoupling during the DQ ^{13}C recoupling the clear carbon chain relayed pattern may be obfuscated by the presence of the competing ZQ TSAR process resulting in cross-peak attenuation, cross-peak cancellation or even cross-peak sign inversion. In contrast CM $_p$ RR experiments without ^1H irradiation or with ultralow ^1H irradiation reliably result in sign-alternating carbon chain relayed cross-peak patterns (37).

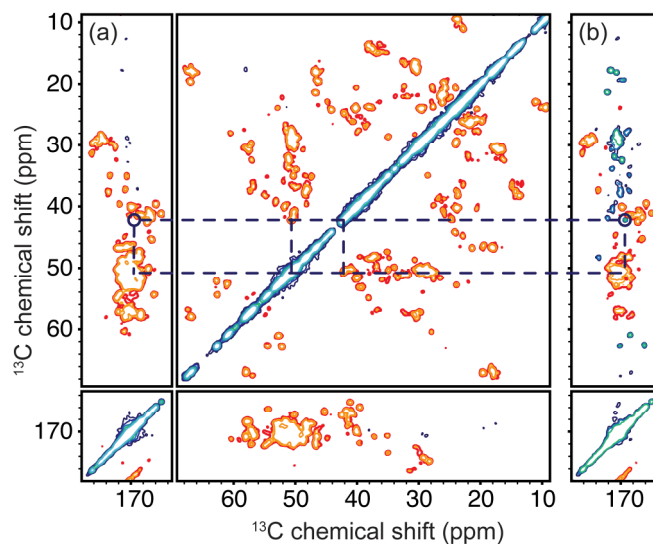


Figure 6-5 Two-dimensional ^{13}C - ^{13}C correlations spectrum of $[\text{U-}^{13}\text{C},^{15}\text{N}]$ -PI3-SH3 fibrils obtained using CM_4RR at 900 MHz ^1H frequency and 20.161 kHz MAS without ^1H decoupling. (a) Spectrum obtained with a mixing time of 0.794 ms. (b) Carbonyl-aliphatic strip from a spectrum obtained with a mixing time of 1.488 ms. Positive cross-peaks (diagonal and two-bond cross-peaks) are indicated in blue-green and negative one-bond cross-peaks are indicated in red-yellow. Circles indicate the “appearance” of a positive cross-peak at long mixing time corresponding to a two-bond $\text{C}'\text{-C}_\beta$ correlation that helps to identify the location of C_α site among the one-bond correlations in panel (a).

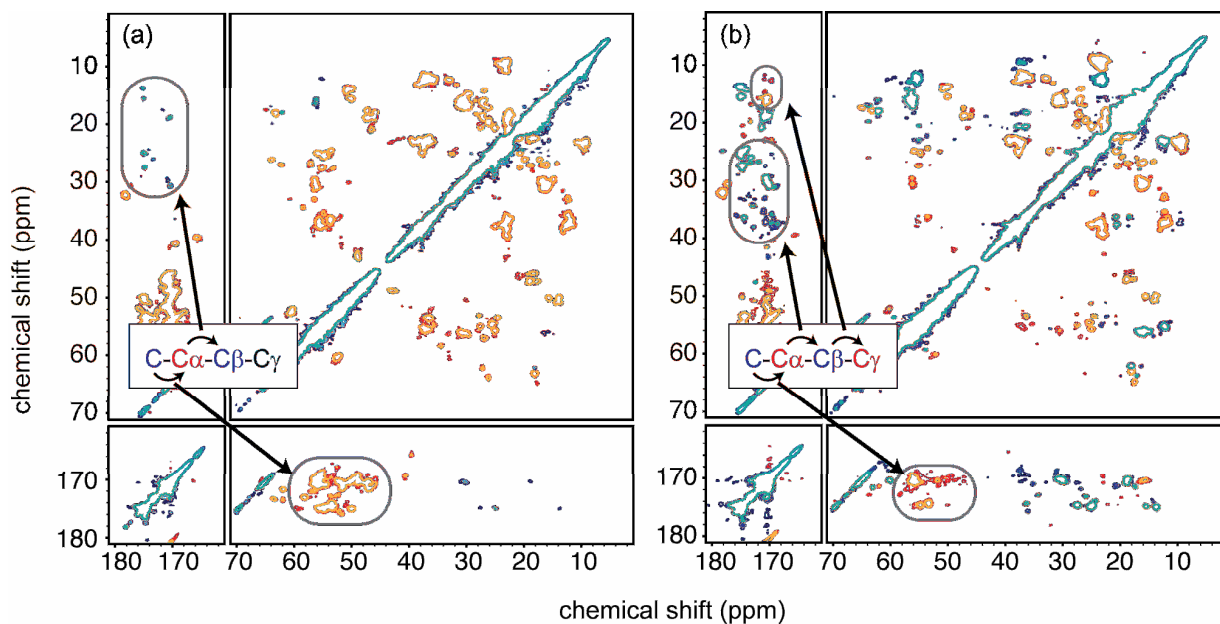


Figure 6-6 Two-dimensional ^{13}C - ^{13}C correlation spectrum of $[\text{U-}^{13}\text{C},^{15}\text{N}]$ -GvpA protein obtained using $\text{CM}_{3.5}\text{RR}$ at 900 MHz ^1H frequency and 23.81 kHz MAS with ~ 5 kHz ^1H decoupling. The mixing time used was 0.84 ms in (a) and 1.512 ms in (b). Arrows in panel (a) and (b) highlight regions illustrating

relayed cross-peaks along as many as 3-bonds (backbone carbonyl to side chain C γ). Such “relay” peaks tend to be better resolved and therefore are particularly useful for assignment experiments.

6.3.2 High spinning frequencies recoupling and sample heating

Part of the reason why DQ techniques have not been used as much at high fields is due to their limitations related to applications to biological samples. A careful control of the sample temperature is required for most biological samples, especially to avoid denaturation at elevated temperatures. In the context of the SSNMR experiments discussed here, there are two main contributions to sample heating: friction due to the (fast) spinning (38) and heating due to the applied radio-frequency (rf) pulses (4, 39-45). The latter is often referred to as rf heating. Most current solid-state MAS probes use solenoid coils to ensure optimum sensitivity at low frequencies and availability of high power ^1H decoupling. Sadly, they also generate considerable electric (E) fields that result in rf sample heating (4, 40, 41, 45). This is particularly problematic for hydrated biological samples, with the dielectric losses originating mostly from water and ionic absorption. The presence of salt, that may be necessary to maintain the protein in a native state, substantially increases the dielectric losses and induces heating in the sub-gigahertz frequency range (45).

It is generally assumed (4, 40, 41, 45) that the rf induced sample heating is linearly proportional to the time of the irradiation (transient regime) and the conductivity of the sample σ , and has a quadratic dependence on both the rf frequency ω_0 and the rf field strength B_1 of the applied pulses ($\sim \sigma \omega_0^2 \cdot B_1^2 \cdot t_{mix}$). This can be rewritten as $\sim \sigma \cdot B_0^2 \cdot \omega_1^2 \cdot t_{mix}$, where B_0 stands for the static magnetic field (in Tesla), and ω_1 is the rf nutation frequency. For typical biological samples the conductivity σ has been shown to increase by only $\sim 10\%$ from 300 to 900 MHz (41), and will therefore be approximated by a constant value over the frequency range considered in this paper. Thus, for a given MAS frequency and recoupling scheme, the rf induced sample heating increases quadratically with the magnitude of the B_0 field, yielding approximately a factor 3.2 increase in sample heating going from 11.7 T (500 MHz ^1H) to 21.1 T (900 MHz ^1H) static B_0 fields.

Moreover in many DQ recoupling experiments, the ^{13}C rf nutation frequency (ω_r) is a (sub)-multiple of the MAS frequency (ω_s). This induces a quadratic dependence of the rf sample heating with respect to the MAS spinning frequency and is of major importance at higher magnetic fields where faster MAS frequencies are required for optimal performance. Hence, the rf sample heating produced by the ^{13}C irradiation of a given pulse sequence increases by a factor 13 if the experiment is performed at 900 MHz and 20 kHz spinning frequency compared to 500 MHz ^1H Larmor frequency and 10 kHz MAS.

Concurrently the ^1H decoupling strength (if needed) applied during recoupling sequences should be sufficiently higher than the carbon's to avoid interference effects and thus contributes significantly to the rf heating at high magnetic field. In the case of CM_pRR , elimination or significant reduction of ^1H irradiation makes it an attractive solution for minimizing sample heating. Table 6-1 in the Supporting Information compares the estimated rf induced sample heating for various established recoupling techniques under some typical conditions. The amount of heating induced by double irradiation at high fields is so large that sometimes the only way to ensure sample safety is to extensively cool or even freeze the sample. However, depending on the specific application, freezing a sample may not be a desirable option, especially when one wants to probe dynamics.

Sample cooling can indeed aid in maintaining the desired temperature in the presence of rf heating. Since cooling occurs by exposure to external cooling gas and rf heating is an internal process, one should also consider the likelihood of the generation of temperature gradients across the sample. Excessive temperature gradients are undesirable since the sample could have sites with temperature dependent chemical shifts thus leading to an effective decrease of the resolution. The rf heating itself is dependent on the sample and coil geometry (rotor size). In a solenoid coil design the ratio of electric field to magnetic field (E/B) is usually assumed to be proportional to the coil radius, and that the maximum temperature rise at the center of the rotor should be proportional to the 4th power of the radius (41). The use of a 2.5 mm rotor (the most common rotor size allowing spinning up to ca. 35 kHz) is thus likely to reduce the sample temperature rise as well as the temperature gradient, compared to larger rotors used for lower MAS rates.

Sample heating considerations are largely responsible for rather sporadic use of DQ sequences on hydrated biological samples, despite their inherent benefits outlined above. Most

biological solid-state NMR studies are currently carried out using 4 mm rotors spinning at 10-12 kHz MAS, at 500-600 MHz ^1H frequency. Although broadband DQ ^{13}C - ^{13}C recoupling techniques have been demonstrated on dry samples under the conditions mentioned above (33, 46-48), they are not widely applied to biological systems. Instead, Proton Driven Spin Diffusion (PDS) is usually employed as it minimizes the rf induced sample heating (no rf pulses applied during the mixing time) and therefore enables the measurement of hydrated systems without sample degradation. However PDS is not a satisfactory solution for higher magnetic field experiments (> 750 MHz), since high spinning frequencies, required to minimize sideband losses, dramatically reduce the polarization transfer as well as increase the required spin diffusion time. Moreover, as we have mentioned earlier, PDS gives us less control over the polarization transfer pathways which greatly complicates the assignment process especially for larger systems.

CM_pRR fills a void by providing an efficient polarization transfer experiment that functions well at high fields and high spinning rates, without excessive rf sample heating. CM_pRR accomplishes this by minimizing the irradiation time (less than 2.6 ms; ca. 0.8 ms for one-bond transfers) and eliminating the need for high power ^1H decoupling (19, 49, 50). Note also that most of the experiments presented here were obtained using less than 85 kHz ^{13}C irradiation.

As the last point concerning sample heating it is important to point out that even though CM_pRR leads to significantly reduced sample heating during the mixing it still requires considerable ^1H decoupling during the t_1 evolution and acquisition. An encouraging step to addressing this issue is the recent introduction of probe designs that aim at minimizing the rf heating due to decoupling while keeping efficient sensitivity for low frequency detection (4, 40, 41). Ongoing progress in pulse program development and such 'low-E field' probe designs should provide complementary advantages and combinations of both techniques should definitely enable powerful biological solid-state NMR studies, even of high-salt ($>1\text{M}$) samples that are problematic for current solenoid probes.

6.3.3 Considerations for high field applications

We have demonstrated that CM_pRR allows for well-controlled and efficient ^{13}C - ^{13}C polarization transfer at high magnetic field (900 MHz) and high spinning frequencies (20-24

kHz) on biological samples without compromising their integrity. However, before we conclude it would be beneficial to comment shortly on the reasons for applications of solid-state NMR at high magnetic fields and high spinning frequencies in the first place.

One of the main attractive features of the use of high magnetic fields in NMR is the increased chemical shift dispersion, resulting in a gain of resolution. This is crucial for the highly degenerate secondary structures found in largely α -helical, hydrophobic membrane proteins and largely β -sheet amyloid aggregates, and even more critical for the highly repetitive primary sequences that often occur in amyloid-forming proteins, such as the Gln-rich sequences involved in Huntington's disease (51) and the Asn- and Gln-rich prion forming domain of yeast prion protein Sup35p (22, 23, 25, 26). Due to the degeneracy in both sequence and structure, there is a large degree of overlap, requiring high resolution and/or higher dimensionality in the experiments. For the GNNQQNY amyloid model system, the benefits of the field-dependent gain of resolution, across a variety of crystalline and fibrillar samples were observed and described (23). The typical linewidth for the GNNQQNY monoclinic crystal sample was around 0.8-1.0 ppm at 500 and 0.5-0.7 ppm at 900 MHz respectively translating to 40-60% improvement in resolution (23). In practice this meant that many peaks for the multiple structural polymorphs present in the amyloid-like fibrils were only distinguishable at 700MHz or above.

It is worth noting that the observed line width is not just determined by the B_0 field-dependent chemical shift dispersion. The homogeneous contribution to the line width is dominated by the residual dipolar ^1H - ^{13}C interactions under optimized (high) ^1H decoupling and should not increase significantly when going to 21.1 T field, provided that the MAS frequency and ^1H rf power can be increased accordingly. Other contributions such as magnetic bulk susceptibility and ^{13}C anisotropic chemical shifts interactions scale up with the strength of the B_0 field, but can be averaged out by the MAS, given higher spinning frequencies (> 20 kHz) at higher magnetic fields (> 750 MHz ^1H frequency). Finally, important contributions to the apparent ^{13}C line width can arise from sample disorder and B_0 inhomogeneity (52-54). These contributions are insensitive to the MAS frequency, but do not get worse at high B_0 fields.

Signal-to-noise (S/N) issues arise for biological samples, not only due to their composition and the frequent scarcity of labeled material, but also due to the small rotors that are required

for the high spinning frequencies (called for by the stronger anisotropic interactions induced by higher magnetic fields). For example, incomplete averaging of the chemical shift anisotropy, due to insufficiently fast MAS, results in a reduction of the isotropic resonance due to the greater intensity in the spinning side bands.¹ In addition, unnecessary side band signals complicate the spectra and can cause increased (cross) peak overlap.

Of course, smaller rotors translate into a decrease of the sample volume. Assuming the availability of sufficient sample material to fill the entire rotor volume (which could actually be a problem in itself), an approximately three-fold decrease in S/N would be predicted between a 4 mm and 2.5 mm rotor. In practice it was reported that S/N ratio per mg of a sample actually increases by 1.82 when going from a 4.0 mm rotor to a 2.5 mm rotor (55), such that using a 2.5 mm rotor translates to about two-fold a decrease in signal (as compared to a 4 mm rotor). In this situation it becomes crucial to employ efficient recoupling techniques such as CM_pRR in order to maximize the size of the cross-peaks in multidimensional spectra (which here we demonstrated to be practical for proteins over 80 residues in size). Note that the information about connectivity, torsion angles and internuclear distances is given by the cross-peaks intensities. Losses in polarization transfer due to using inefficient pulse sequences at low MAS and high field with 4 mm rotors can actually nullify the advantage of larger sample volume (compared to using efficient recoupling experiments at high spinning frequencies with 2.5 mm rotor) and may even result in lower intensity cross-peaks. Furthermore, additional polarization losses may occur because of insufficient 1H decoupling since generation of sufficiently high 1H rf field strengths is much more challenging for larger diameter rotor systems.

6.4 Conclusion

We have demonstrated recent developments in solid-state NMR methodology aimed at structural studies on large biomolecules in the high resolution and high sensitivity regime

¹ At a 900 MHz 1H Larmor frequency, this can lead to a loss of 43% from the isotropic carbonyl resonances for a 4 mm rotor spinning at 10 kHz MAS, whereas a smaller sample spinning at 20 kHz MAS would suffer only a 12% reduction of the isotropic peaks.

provided by high magnetic fields (here 900 MHz ^1H Larmor frequency) and high spinning frequencies. In particular we have illustrated the benefits of multiple-step carbon chain relayed transfer cross-peaks, yielded by the double-quantum CM_pRR technique, in the assignment process. CM_pRR provides unprecedented level of control over DQ ^{13}C recoupling spin dynamics at high spinning frequencies without need to worry about interference from polarization transfer mechanisms involving protons that reduce dipolar truncation. In uniformly ^{13}C labeled systems the CM_pRR experiment with strong dipolar truncation allows for reliable establishment of their covalent connectivity and nicely complements the techniques with reduced dipolar truncation such as PAIN-CP (56) and ^{13}C - ^{13}C PAR (37) that provide long distance contacts in the same samples. With the CM_pRR sequence previous practical limitations for the application of very powerful DQ recoupling sequences at high magnetic fields, including insufficient ^1H decoupling, prohibitive sample heating and bandwidth limitations, can be overcome allowing studies of biological samples without compromising their integrity. Beyond the 2D ^{13}C - ^{13}C applications described here, CM_pRR should prove a flexible and efficient building block in a variety of more complex pulse sequences including higher dimensionality experiments, torsion angle measurements, and spin cluster selection. We have also shown that these solid state MAS NMR methods are applicable to a wide range of biological samples under their biologically relevant conditions. This includes not just dried or lyophilized samples, crystalline or precipitated compounds but also amyloid-like fibrillar samples and the building blocks inside large macroscopic biological assemblies (like the gas vesicles studied here). It is generally hard to obtain high resolution structural information on such systems via other structural methods, despite the substantial biological and medical importance. In these areas in particular we can expect a fruitful future for solid state MAS NMR as a structurally sensitive and versatile technique, given the application of new pulse sequences specifically designed for biological studies at high field along with the ongoing development of numerous technological improvements.

6.5 Materials and Methods

Samples. The peptides *N-formyl*-MLF-OH (MLF) and GNNQQNY were obtained by solid phase peptide synthesis from CS Bio Inc. (Menlo Park, CA). The peptides were prepared both without isotopic enrichment and using Fmoc-protected U-¹³C,¹⁵N labeled amino acids from Cambridge Isotope Laboratories (Andover, MA), yielding *N-for*-[U-¹³C,¹⁵N-MLF-OH] and [U-¹³C,¹⁵N-GNNQ]QNY. The segmentally labeled [U-¹³C,¹⁵N-GNNQ]QNY was used to prepare amyloid-like fibrils as described previously (23). [U-¹³C,¹⁵N]-GvpA was prepared as described (57). [U-¹³C,¹⁵N]-PI3-SH3 was prepared as in (29) and subsequently re-suspended in 60/40 d₅-glycerol/water mixture. All the samples were packed in 2.5 mm zirconia rotors from Bruker BioSpin (Billerica, MA).

NMR spectroscopy. All experiments were carried out on a Bruker spectrometer operating at a frequency of 900.1 MHz for ¹H (20.1T) using a Bruker triple resonance probe equipped with 2.5 mm spinner module and solenoid coil. The spinning frequency was regulated to ± 2 Hz with a Bruker spinning frequency controller (Bruker BioSpin, Billerica MA). The spinning frequencies (of 20-24 kHz) were chosen to avoid the broadening and peak shifting associated with n=1 rotational resonance (R^2) conditions for C'-C $_{\alpha}$ and C'-C $_{\beta}$ occurring typically between 25-31 kHz at 900 MHz field. The temperature was regulated with a Bruker BCU-X unit to provide 0°C cooling gas temperature.

Both power and phase amplitude excursion for the CM_pRR irradiation were optimized using the pulse sequence presented in Fig. 6-1b (without the t₁ evolution) in the vicinity of the theoretical point to compensate for the cross-terms contributions (see (20) for details). Optimizations involved systematic explorations of the phase value in steps of 0.1° up to a deviation of 0.5° from the theoretical optimum, and power values in steps of 0.1dB with a range of a few kHz ($\omega_1/2\pi$) around the theoretical point. Note that such optimization is crucial to maximize DQ efficiency for the transfer and that the precise optimum may vary depending on sample and hardware configuration.

CM_{3,5}RR at 23.81 kHz MAS with 83.3 kHz ¹³C and 5 kHz ¹H irradiation during mixing was used for [U-¹³C,¹⁵N]-*f*-MLF-OH (with phase excursion a=16.8°) and [U-¹³C,¹⁵N]-GvpA (a=16.8°). CM₄RR at 20.161 kHz MAS with 80.6 kHz ¹³C and no ¹H irradiation during mixing was used for [U-¹³C,¹⁵N]-PI3-SH3 (a= 14.65°). CM₅RR at 20 kHz MAS with 100 kHz ¹³C and no ¹H irradiation during mixing was used for [U-¹³C,¹⁵N-GNNQ]QNY (a=11.55°). For a

detailed discussion of the situations when low power ^1H decoupling is or is not needed see ref. (20). The sine was sampled with 30-31 slices per period τ_c . 100 kHz optimized TPPM (58) decoupling was used during t_1 evolution and acquisition. ^{13}C magnetization was prepared by CP ramped on ^1H from 100 kHz to 50 kHz matching the $n=-1$ Hartmann-Hahn condition with ^{13}C and stored on the Z-axis using an 83.3 kHz $\pi/2$ pulse. The indirect dimension was sampled with 384 to 512 points using a 20-24 μs step size. The total acquisition time for each of the experiments were: 1. $[\text{U-}^{13}\text{C},^{15}\text{N}]\text{-f-MLF-OH}$ -- 3.4 hours except for the 2.52 ms spectrum that took 16 hours; 2. $[\text{U-}^{13}\text{C},^{15}\text{N}]\text{-GvpA}$ -- 31 hours for the short mixing and 41 hours for the long mixing data. The total acquisition time for experiment on $[\text{U-}^{13}\text{C},^{15}\text{N}]\text{-PI3-SH3}$ was 61.5 hours for the short mixing and 41 hours for the long mixing. The total acquisition for the experiment on $[\text{U-}^{13}\text{C},^{15}\text{N}]\text{-GNNQIQNY}$ was 43 hours for the short mixing and 25.6 hours for the long mixing. The data were processed using the NMRPipe software package (59) and plotted with Sparky (T. D. Goddard & D. G. Kneller, University of California).

6.6 Acknowledgements

This work was supported by National Institute of Health Grants EB-003151 and EB-002026.

6.7 References

- (1) Brouwer, D. H.; Ripmeester, J. A. *J Magn Reson* **2007**, *185*, 173-8.
- (2) Nevzorov, A. A.; Park, S. H.; Opella, S. J. *Journal of Biomolecular Nmr* **2007**, *37*, 113-116.
- (3) Park, S. H.; De Angelis, A. A.; Nevzorov, A. A.; Wu, C. H.; Opella, S. J. *Biophysical Journal* **2006**, *91*, 3032-3042.
- (4) Gor'kov, P. L.; Chekmenev, E. Y.; Li, C.; Cotten, M.; Buffy, J. J.; Traaseth, N. J.; Veglia, G.; Brey, W. W. *J Magn Reson* **2007**, *185*, 77-93.
- (5) Castellani, F.; van Rossum, B.; Diehl, A.; Schubert, M.; Rehbein, K.; Oschkinat, H. *Nature* **2002**, *420*, 98-102.

- (6) Klammt, C.; Lohr, F.; Schafer, B.; Haase, W.; Dotsch, V.; Ruterjans, H.; Glaubitz, C.; Bernhard, F. *European Journal of Biochemistry* **2004**, *271*, 568-580.
- (7) Chen, C. Y.; Cheng, C. H.; Chen, Y. C.; Lee, J. C.; Chou, S. H.; Huang, W. Y.; Chuang, W. J. *Proteins-Structure Function and Bioinformatics* **2006**, *62*, 279-287.
- (8) Goldbourn, A.; Day, L. A.; McDermott, A. E. *J Magn Reson* **2007**, *189*, 157-65.
- (9) Andronesi, O. C.; Becker, S.; Seidel, K.; Heise, H.; Young, H. S.; Baldus, M. *J Am Chem Soc* **2005**, *127*, 12965-12974.
- (10) Frericks, H. L.; Zhou, D. H.; Yap, L. L.; Gennis, R. B.; Rienstra, C. M. *J Biomol NMR* **2006**, *36*, 55-71.
- (11) Jaroniec, C. P.; MacPhee, C. E.; Bajaj, V. S.; McMahon, M. T.; Dobson, C. M.; Griffin, R. G. *Proceedings of the National Academy of Sciences of the United States of America* **2004**, *101*, 711-716.
- (12) Lange, A.; Giller, K.; Hornig, S.; Martin-Eauclaire, M. F.; Pongs, O.; Becker, S.; Baldus, M. *Nature* **2006**, *440*, 959-962.
- (13) Tycko, R. *Quarterly Reviews of Biophysics* **2006**, *39*, 1-55.
- (14) Jovanovic, T.; McDermott, A. E. *J Am Chem Soc* **2005**, *127*, 13816-13821.
- (15) Williamson, P. T. F.; Watts, J. A.; Addona, G. H.; Miller, K. W.; Watts, A. *Proc Natl Acad Sci U S A* **2001**, *98*, 2346-2351.
- (16) Baldus, M. *Current Opinion in Structural Biology* **2006**, *16*, 618-623.
- (17) Etzkorn, M.; Bockmann, A.; Lange, A.; Baldus, M. *Journal of the American Chemical Society* **2004**, *126*, 14746-14751.
- (18) Lopez, J. J.; Shukla, A. K.; Reinhart, C.; Schwalbe, H.; Michel, H.; Glaubitz, C. *Angew Chem Int Ed Engl* **2008**.
- (19) De Paepe, G.; Bayro, M. J.; Lewandowski, J.; Griffin, R. G. *J Am Chem Soc* **2006**, *128*, 1776-7.
- (20) De Paepe, G.; Lewandowski, J. R.; Griffin, R. G. *J Chem Phys* **2008**, *128*, 124503.
- (21) Rienstra, C. M.; Tucker-Kellogg, L.; Jaroniec, C. P.; Hohwy, M.; Reif, B.; McMahon, M. T.; Tidor, B.; Lozano-Perez, T.; Griffin, R. G. *Proc Natl Acad Sci U S A* **2002**, *99*, 10260-5.

- (22) Diaz-Avalos, R.; Long, C.; Fontano, E.; Balbirnie, M.; Grothe, R.; Eisenberg, D.; Caspar, D. L. *J Mol Biol* **2003**, *330*, 1165-75.
- (23) van der Wel, P. C. A.; Lewandowski, J. R.; Griffin, R. G. *J Am Chem Soc* **2007**, *129*, 5117-30.
- (24) van der Wel, P. C. A.; Hu, K. N.; Lewandowski, J.; Griffin, R. G. *J Am Chem Soc* **2006**, *128*, 10840-6.
- (25) Sawaya, M. R.; Sambashivan, S.; Nelson, R.; Ivanova, M. I.; Sievers, S. A.; Apostol, M. I.; Thompson, M. J.; Balbirnie, M.; Wiltzius, J. J.; McFarlane, H. T.; Madsen, A. O.; Riek, C.; Eisenberg, D. *Nature* **2007**.
- (26) Nelson, R.; Sawaya, M. R.; Balbirnie, M.; Madsen, A. O.; Riek, C.; Grothe, R.; Eisenberg, D. *Nature* **2005**, *435*, 773-778.
- (27) Booker, G. W.; Gout, I.; Downing, A. K.; Driscoll, P. C.; Boyd, J.; Waterfield, M. D.; Campbell, I. D. *Cell* **1993**, *73*, 813-822.
- (28) Koyama, S.; Yu, H. T.; Dalgarno, D. C.; Shin, T. B.; Zydowsky, L. D.; Schreiber, S. L. *Cell* **1993**, *72*, 945-952.
- (29) Gujjarro, J. I.; Sunde, M.; Jones, J. A.; Campbell, I. D.; Dobson, C. M. *Proc Natl Acad Sci U S A* **1998**, *95*, 4224-8.
- (30) Walsby, A. E. *Microbiol Rev* **1994**, *58*, 94-144.
- (31) Wokaun, A.; Ernst, R. R. *Chemical Physics Letters* **1977**, *52*, 407-412.
- (32) Veshtort, M.; Griffin, R. G. *J Magn Reson* **2006**, *178*, 248-82.
- (33) Hohwy, M.; Rienstra, C. M.; Jaroniec, C. P.; Griffin, R. G. *Journal of Chemical Physics* **1999**, *110*, 7983-7992.
- (34) Suter, D.; Ernst, R. R. *Physical Review B* **1985**, *32*, 5608-5627.
- (35) Takegoshi, K.; Nakamura, S.; Terao, T. *Chemical Physics Letters* **2001**, *344*, 631-637.
- (36) Morcombe, C. R.; Gaponenko, V.; Byrd, R. A.; Zilm, K. W. *Journal of the American Chemical Society* **2004**, *126*, 7196-7197.
- (37) De Paepe, G.; Lewandowski, J. R.; Loquet, A.; Bockmann, A.; Griffin, R. G. **2008**, *submitted*.
- (38) Grimmer, A. R.; Kretschmer, A.; Cajipe, V. B. *Magnetic Resonance in Chemistry* **1997**, *35*, 86-90.

- (39) d'Espinose de Lacaillerie, J. B.; Jarry, B.; Pascui, O.; Reichert, D. *Solid State Nucl Magn Reson* **2005**, *28*, 225-32.
- (40) Dillmann, B.; Elbayed, K.; Zeiger, H.; Weingertner, M. C.; Piotta, M.; Engelke, F. *J Magn Reson* **2007**.
- (41) Doty, F. D.; Kulkarni, J.; Turner, C.; Entzminger, G.; Bielecki, A. *J Magn Reson* **2006**, *182*, 239-53.
- (42) Li, C.; Mo, Y.; Hu, J.; Chekmenev, E.; Tian, C.; Gao, F. P.; Fu, R.; Gor'kov, P.; Brey, W.; Cross, T. A. *J Magn Reson* **2006**, *180*, 51-7.
- (43) Lim, H. B.; Cook, G. G.; Barker, A. T.; Coulton, L. A. *Radiat Res* **2005**, *163*, 45-52.
- (44) Petryakov, S.; Samouilov, A.; Roytenberg, M.; Li, H.; Zweier, J. L. *Magn Reson Med* **2006**, *56*, 654-9.
- (45) Stringer, J. A.; Bronnimann, C. E.; Mullen, C. G.; Zhou, D. H.; Stellfox, S. A.; Li, Y.; Williams, E. H.; Rienstra, C. M. *J Magn Reson* **2005**, *173*, 40-8.
- (46) Hohwy, M.; Jakobsen, H. J.; Eden, M.; Levitt, M. H.; Nielsen, N. C. *Journal of Chemical Physics* **1998**, *108*, 2686-2694.
- (47) Carravetta, M.; Eden, M.; Zhao, X.; Brinkmann, A.; Levitt, M. H. *Chemical Physics Letters* **2000**, *321*, 205-215.
- (48) Kristiansen, P. E.; Carravetta, M.; Lai, W. C.; Levitt, M. H. *Chemical Physics Letters* **2004**, *390*, 1-7.
- (49) Hughes, C. E.; Luca, S.; Baldus, M. *Chemical Physics Letters* **2004**, *385*, 435-440.
- (50) Marin-Montesinos, I.; Brouwer, D. H.; Antonioli, G.; Lai, W. C.; Brinkmann, A.; Levitt, M. H. *Journal of Magnetic Resonance* **2005**, *177*, 307-317.
- (51) Yamada, M.; Shimohata, M.; Sato, T.; Tsuji, S.; Takahashi, H. *Neuropathology* **2006**, *26*, 346-351.
- (52) De Paepe, G.; Giraud, N.; Lesage, A.; Hodgkinson, P.; Bockmann, A.; Emsley, L. *Journal of the American Chemical Society* **2003**, *125*, 13938-13939.
- (53) De Paepe, G.; Lesage, A.; Emsley, L. *Journal of Chemical Physics* **2003**, *119*, 4833-4841.

- (54) De Paepe, G.; Lesage, A.; Steuernagel, S.; Emsley, L. *Chemphyschem* **2004**, *5*, 869-875.
- (55) Sakellariou, D.; Le Goff, G.; Jacquinet, J. F. *Nature* **2007**, *447*, 694-+.
- (56) Lewandowski, J. R.; De Paepe, G.; Griffin, R. G. *J Am Chem Soc* **2007**, *129*, 728-9.
- (57) Belenky, M.; Meyers, R.; Herzfeld, J. *Biophys J* **2004**, *86*, 499-505.
- (58) Bennett, A. E.; Rienstra, C. M.; Auger, M.; Lakshmi, K. V.; Griffin, R. G. *Journal of Chemical Physics* **1995**, *103*, 6951-6958.
- (59) Delaglio, F.; Grzesiek, S.; Vuister, G. W.; Zhu, G.; Pfeifer, J.; Bax, A. *Journal of Biomolecular Nmr* **1995**, *6*, 277-293.

7. Proton Assisted Insensitive Nuclei Cross Polarization

Reproduced with permission from Lewandowski J. R., de Paëpe G., Griffin R.G. "Proton Assisted Insensitive Nuclei Cross Polarization" *J Am Chem Soc.* (2007) **129**(4):728-9. Copyright © 2007 American Chemical Society.

7.1 Abstract

This communication presents a solid-state NMR ^{15}N - ^{13}C polarization transfer scheme applicable at high B_0 and high spinning frequencies, requiring moderate r.f. powers (~ 50 kHz $^{13}\text{C}/^{15}\text{N}$) and mixing time (1-6 ms). The sequence, PAIN-CP, involves the abundant nearby protons in the heteronuclear recoupling dynamics, and provides a new tool for obtaining long distance ^{15}N - ^{13}C contacts. It should be of major interest for biomolecular structural studies.

7.2 Introduction

Polarization transfer between different nuclear spin species that relies mainly on heteronuclear J-couplings¹ or dipolar couplings transfers,²⁻¹⁶ is extensively used in magic angle spinning (MAS)¹⁷ solid-state NMR structural studies to provide chemical shifts, distances^{6-8,12,18-22} and torsion angles.²³⁻²⁶

Heteronuclear dipolar recoupling sequences can be classified into two categories depending on their behavior with respect to dipolar truncation. The first group includes the double CP sequence (DCP²⁷) and its variants (SPICP²⁸, RFDRCP⁵, *i*DCP¹⁰) which lead to non-commuting terms in the effective Hamiltonian, and thus are mainly used to perform one-bond transfers (NCO, NCA) sometimes followed by a homonuclear ¹³C-¹³C recoupling period for obtaining ¹⁵N-¹³C multiple-bond contacts.^{29,30} The second group of sequences (REDOR⁶, TEDOR²/REPT²⁰, GATE¹⁸) yields a longitudinal effective Hamiltonian and enables measurement of long distances (< 4 Å).^{21,22}

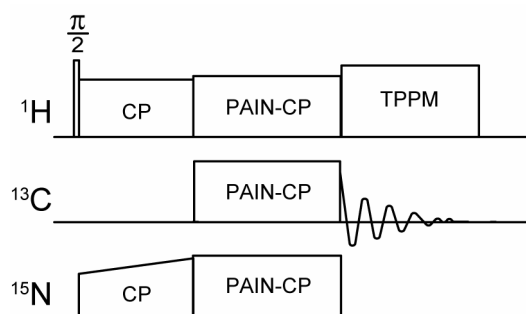


Figure 7-1 PAIN-CP ¹⁵N-¹³C correlation pulse sequence. The proper combination of ¹⁵N, ¹³C and ¹H r.f. power results in enhanced rates and efficiency of ¹H mediated ¹⁵N-¹³C polarization transfer.

High magnetic fields (>600 MHz) are an important experimental constituent for improving sensitivity and resolution in biomolecular MAS experiments involving ¹⁵N-¹³C magnetization transfer, provided that experiments can be performed at high spinning frequencies (>15 kHz) to compensate for increases in chemical shift anisotropies (CSA). Unfortunately, the application of the sequences mentioned above becomes problematic in this regime as the

applied high r.f. powers lead to increased sample heating, jeopardize the integrity of the probe, but concurrently often do not provide sufficient ^1H decoupling.

Here we present an efficient ^{15}N - ^{13}C heteronuclear recoupling technique that involves nearby protons in the transfer and is applicable at high spinning frequency ($\omega_r/2\pi > 20$ kHz). This new scheme, Proton Assisted Insensitive Nuclei Cross Polarization (PAIN-CP), reduces dipolar truncation and therefore is particularly well suited for obtaining long distance contacts. PAIN-CP demonstrates that *the involvement of protons in the polarization transfer between low- γ nuclei does not have to be deleterious in nature; on the contrary ^1H 's can be used to enhance the rate and efficiency of the transfer.* The PAIN-CP experiment utilizes a mechanism which we refer to as Third Spin Assisted Recoupling (TSAR). Its extension to the homonuclear case is straightforward and will be discussed elsewhere. Note that ^1H irradiation has previously been part of ^{13}C - ^{13}C recoupling experiments,³¹⁻³³ but that the underlying mechanism is different.

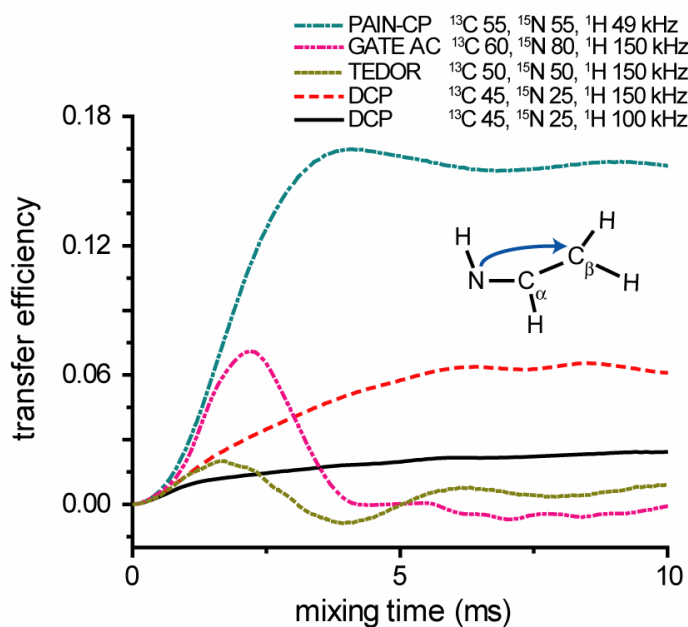


Figure 7-2 Comparison of ^{15}N - ^{13}C two-bond polarization transfer for PAIN-CP, DCP, TEDOR, GATE AC sequences at $\omega_r/2\pi = 20$ kHz. Note that variants of DCP such as RFDRCPP, SPICP, and *i*DCP are not considered here as they mainly improve the recoupling bandwidth, which is not the major concern in this simulation.

7.3 Results and Discussion

Even though PAIN-CP and DCP²⁷ have similar pulse sequences (see Fig. 7-1), they rely on very different mechanisms. The PAIN-CP mechanism corresponds to a second order recoupling in an interaction frame defined by the three C.W. r.f. fields involving cross terms between heteronuclear N-H and C-H dipolar couplings (see 7.6.2). In this process, nearby ¹H's are used to create trilinear (N, C, H) terms in the effective Hamiltonian that can lead to ZQ and DQ ¹⁵N-¹³C polarization transfer. In this publication we explore only the ZQ transfer.

Figure 7-2 shows simulations comparing ¹⁵N-¹³C polarization transfer for the PAIN-CP, DCP, TEDOR and GATE sequences at 750 MHz and $\omega_r/2\pi=20$ kHz. The model spin system consists of seven spins (¹⁵N, ¹³C_α, ¹³C_β, 4 ¹H's). Simulations were performed with SPINEVOLUTION³⁴ (see S.I.-1 for details).

DCP simulations utilized typical r.f. field strengths -- ($\omega_{1C}/2\pi$)=45 kHz, ($\omega_{1N}/2\pi$)=25 kHz, ($\omega_{1H}/2\pi$)=100 and 150 kHz of ¹H C.W. decoupling respectively, illustrating that r.f. power levels should satisfy the condition (ω_{1H}/ω_{1C}) \geq 3 to ensure correct ¹H decoupling.³⁵ However, even for 150 kHz of ¹H decoupling, a challenge for most triple resonance probes, the two-bond transfer from ¹⁵N to C_β reaches only about 6.5% efficiency in 6.5 ms, a result of the dipolar truncation effect (see S.I.-4). Longitudinal recoupling sequences such as TEDOR or GATE, where there is no dipolar truncation, do not provide efficient two-bond transfer in the presence of strong one-bond coupling. For example, GATE reaches about 7% transfer in 2.3 ms for extremely demanding experimental settings. On the other hand, the PAIN-CP buildup obtained with a ¹³C and ¹⁵N fields set to the same value (n=0 Hartmann-Hahn)^{36,37} reaches 16.5% transfer efficiency in 4 ms, an improvement of 3 to 8 times when compared to DCP with high power ¹H decoupling. In addition, contrary to TEDOR and GATE results, the transferred magnetization achieves an equilibrium value simplifying the choice of the mixing time in a correlation experiment.

In practice, it is possible to utilize the PAIN-CP mechanism provided that ¹H-¹⁵N and ¹H-¹³C Hartmann-Hahn (H.H.) as well as rotary resonance⁴ (R.R.) conditions are avoided. The ¹⁵N and ¹³C r.f. fields do not necessarily have to match n=0 H.H. condition (see S.I.-2, 6). Optimal PAIN-CP settings are a compromise between avoiding destructive H.H. or R.R. recoupling conditions and retaining significant second order scaling to ensure efficient polarization

transfer. Accordingly, there are usually a few different ^1H r.f. levels that lead to an appreciable PAIN-CP effect (see S.I.-6).

Figure 7-3 is an experimental demonstration that PAIN-CP is an efficient technique for heteronuclear ^{15}N - ^{13}C correlation experiments. The spectra were obtained with $[\text{U-}^{13}\text{C}, ^{15}\text{N}]$ N-*f*-MLF-OH using $\omega_r/2\pi=20$ kHz, $\omega_{1\text{H}}/2\pi=750$ MHz, and a 2.5 mm, triple-channel Bruker probe. Figure 7-3 (a) shows a NCA DCP spectrum with 3 ms mixing (optimum for one-bond transfer) and 112 kHz ^1H decoupling. Long range cross peaks (more than 2 bonds) are completely absent from the spectrum at this mixing time and do not appear at longer mixing times (data not shown). Figure 7-3 (b) depicts an $n=0$ H.H. PAIN-CP spectrum with 4 ms mixing, using r.f. fields of ~ 50 kHz for ^{13}C , ^{15}N and (a) 112 kHz and (b) 62 kHz respectively for ^1H . We observe cross peaks for ^{15}N - ^{13}C pairs separated by up to 6 Å in a uniformly ^{13}C , ^{15}N labeled compound. Note that part of the long range transfer also involves a homonuclear TSAR effect (see S.I.-2). In addition, in spite of distributing the initial ^{15}N magnetization over a larger number of ^{13}C sites, the one-bond cross peaks are much more intense than in the DCP case. This fact indicates that for this system a ~ 2.5 ratio for $(\omega_{1\text{H}}/\omega_{13\text{C},15\text{N}})$ is not sufficient to provide efficient ^1H decoupling in the DCP case.

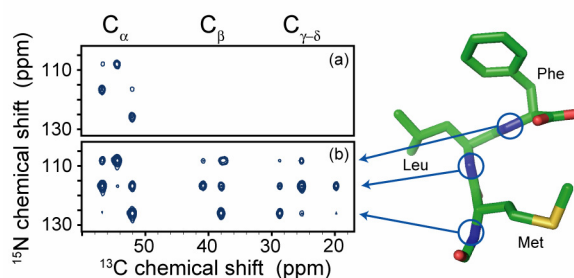


Figure 7-3 Aliphatic region of 2D ^{15}N - ^{13}C correlation spectra obtained at 750 MHz with 20 kHz MAS: (a) DCP with 3 ms mixing, (b) PAIN-CP with 4 ms mixing time. The ^1H r.f. field strength was 112 and 62 kHz for (a) and (b) respectively. In (a) the $n=1$ ZQ Hartmann-Hahn condition was matched with 45 kHz ^{13}C r.f. and 25 kHz ^{15}N r.f.. In (b) $\omega_r/2\pi=50$ kHz for both ^{13}C and ^{15}N . All spectra were acquired and processed in exactly the same manner. The contour levels are set to the same value.

7.4 Conclusion

In summary, we present a new heteronuclear ^{15}N - ^{13}C correlation mechanism, applicable at high $\omega_r/2\pi$, leading, in this regime, to superior recoupling performance compared to alternative techniques. PAIN-CP can provide long ^{15}N - ^{13}C contacts, circumventing the usual dipolar truncation encountered with DCP-type sequences. The method provides a highly efficient alternative to NCX and NCXCY experiments, extends the range of applicability of heteronuclear recoupling techniques to high B_0 and $\omega_r/2\pi$, and should thus be of major interest for structure determination of biomolecules.

7.5 Acknowledgements

This work was supported by National Institutes of Health Grants EB-001960 and EB-002026. We would like to thank Dr Patrick van der Wel for stimulating discussions and criticism.

7.6 Supporting Information

7.6.1 Model spin system

All of the simulations shown in the manuscript and in this section of Supporting Information (with the exception of those in Section 6) utilized a model seven spin system composed of $^{15}\text{NH}^{13}\text{C}_\alpha\text{H}^{13}\text{C}_\beta\text{H}_2$. The spatial coordinates, isotropic and anisotropic shifts, asymmetry parameter and orientation of the CSA for each shift tensor for each spin are included in Table 7-1 below. The same parameters were used for the simulations in Fig. 7-2 of the text.

Table 7-1 Spin system used in the simulations reported in Fig. 7-2 of the text. *Homonuclear* and *heteronuclear* indirect J couplings are not included in the simulations. Their effects are small (as suggested by a simulation using 60 Hz J_{C-C} and 10 Hz J_{N-C} ; not shown here), but could be included in quantitative studies.

Index	Nuc.	X (Å)	Y (Å)	Z (Å)	σ_{iso} (ppm)	σ_{aniso} (ppm)	η	CSA orientation
1	^{13}C	1.246	-0.783	-0.894	-16.3	25.3	0.0	(0, 45, 0)
2	^{13}C	0.718	0.033	0.320	0	23.99	0.92	(-80, 15, 3)
3	^{15}N	0.678	-2.128	-0.894	0	100	0.8	(0, 30, 0)
4	1H	1.267	-2.967	-0.894	0	0	0	-
5	1H	0.953	-0.280	-1.833	0	0	0	-
6	1H	1.188	1.036	0.300	0	0	0	-
7	1H	1.097	-0.432	1.252	0	0	0	-

7.6.2 PAIN-CP mechanism

Figure 7-4 shows the dependence of the $n=0$ PAIN-CP ($\omega_{IC}/2\pi$)=($\omega_{IN}/2\pi$)=55 kHz and ($\omega_{IH}/2\pi$)= 49 kHz magnetization transfer from ^{15}N to $^{13}C_{\beta}$ on the various interactions present in the seven spin system.

^{13}C - ^{15}N or $^{13}C_{\alpha}$ - $^{13}C_{\beta}$ couplings absent: When the ^{13}C - ^{15}N or $^{13}C_{\alpha}$ - $^{13}C_{\beta}$ couplings are separately removed, we observe approximately the same buildup curve as with all the couplings present. This indicates that the transfer does not involve a DCP type mechanism, and illustrates that the ^{13}C - ^{13}C couplings are not involved in the long distance transfer observed in PAIN-CP.

1H - 1H couplings off: When the 1H - 1H couplings are removed the transfer is even slightly more efficient and faster. This indicates that PAIN-CP mechanism does not rely on 1H - 1H couplings.

1H - $^{13}C_{\alpha}$ couplings off: When all the couplings from the 1H to the $^{13}C_{\alpha}$ are quenched, we observe a decrease in the efficiency and rate of the transfer. This clearly shows that a part of the ^{15}N to ^{13}C long range transfer also involves a homonuclear ^{13}C TSAR effect.

This figure illustrates that the complex mechanism involved in PAIN-CP is completely different from DCP in spite of the similarity of the two pulse sequences. A detailed quantitative analysis of the process is currently under progress.

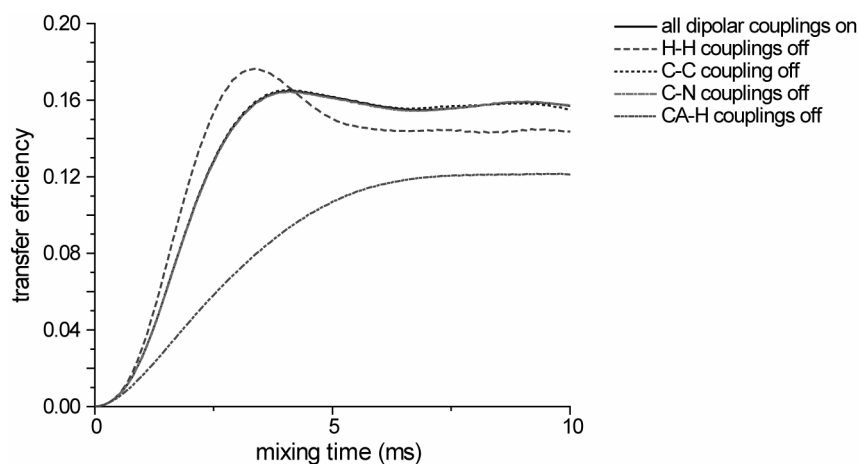


Figure 7-4 PAIN-CP pathways. The simulated curves correspond to N- C_{β} transfer (two-bond transfer) with identical settings as for the PAIN-CP simulations in Fig. 7-2. Note that the simulations with all dipolar couplings included, C-C coupling removed and C-N coupling removed yield essentially the same curve.

The PAIN-CP effect presented in this communication corresponds to the $n=0$ matching condition, meaning that the ^{15}N and ^{13}C r.f. fields are identical. It is worth noting that a substantial PAIN-CP transfer can be achieved even when the ^{13}C and ^{15}N irradiation are mismatched by a multiple of MAS frequency.

For example, in the $n=1$ case, the choice of ^1H irradiation power determines the relative importance of the DCP and PAIN-CP mechanisms during the transfer. Under high ^1H power irradiation (i.e. >100 kHz r.f.), the ^{15}N - ^{13}C polarization transfer is mediated primarily by DCP (see Fig. 7-5) because the scaling factor of PAIN-CP term becomes too small. With a reduced ^1H irradiation (39 kHz) that avoids ^1H -X recoupling, we recover a substantial PAIN-CP effect, though smaller than in the $n=0$ case. Note that when we vary the ^1H power from 0-100 kHz in

the $n=1$ case, we found several optima, with a global maximum at 39 kHz. Each of these optima leads to a polarization transfer that is 2-6 times larger than polarization transfer for DCP with same ^{15}N , ^{13}C powers (25 kHz, 45 kHz respectively) and 100 kHz ^1H CW decoupling.

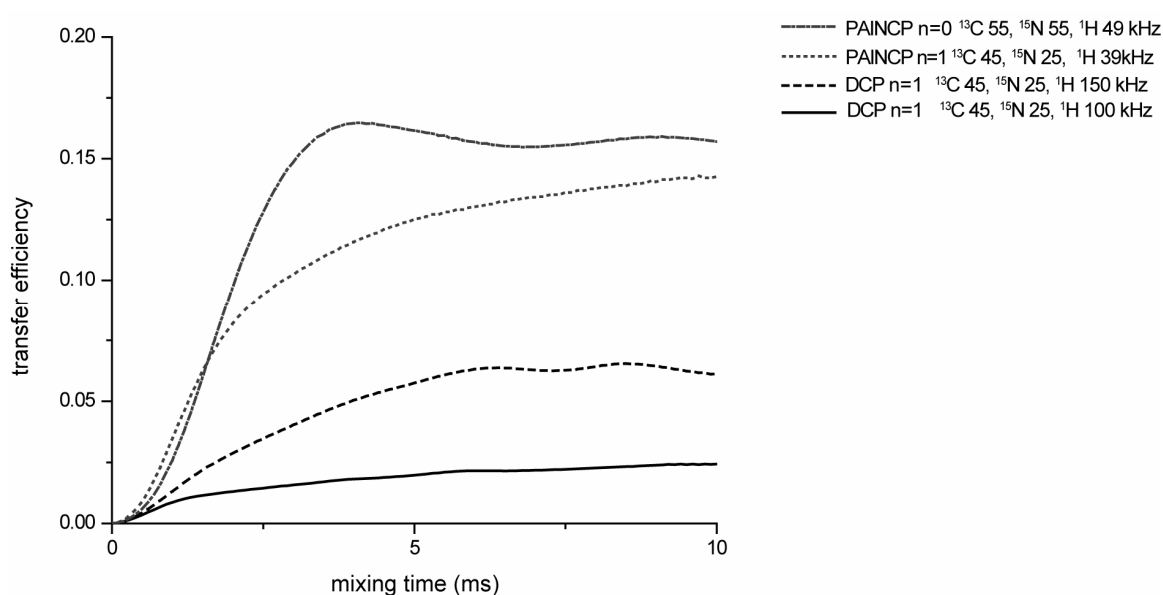


Figure 7-5 Simulations of ^{15}N - $^{13}\text{C}_\beta$ two-bond transfer for PAIN-CP (red), DCP (black) sequences. The solid, dotted red curves correspond to $\delta=0$ and $\delta=1$ PAIN-CP matching respectively. For the DCP simulations, the ^1H decoupling was chosen to be 100 (solid line) and 150 (dotted line) kHz. Except for $\delta=1$ PAIN-CP, the three other simulations are similar to Fig. 7-2.

7.6.3 Complementary information on the one-bond transfer

Figure 7-2 shows simulations of a *two-bond* ^{15}N to C_β magnetization transfer at $\omega_r/2\pi=20$ kHz (using the model seven spin system described above), and illustrates the superior performance of the PAIN-CP sequence in this regime.

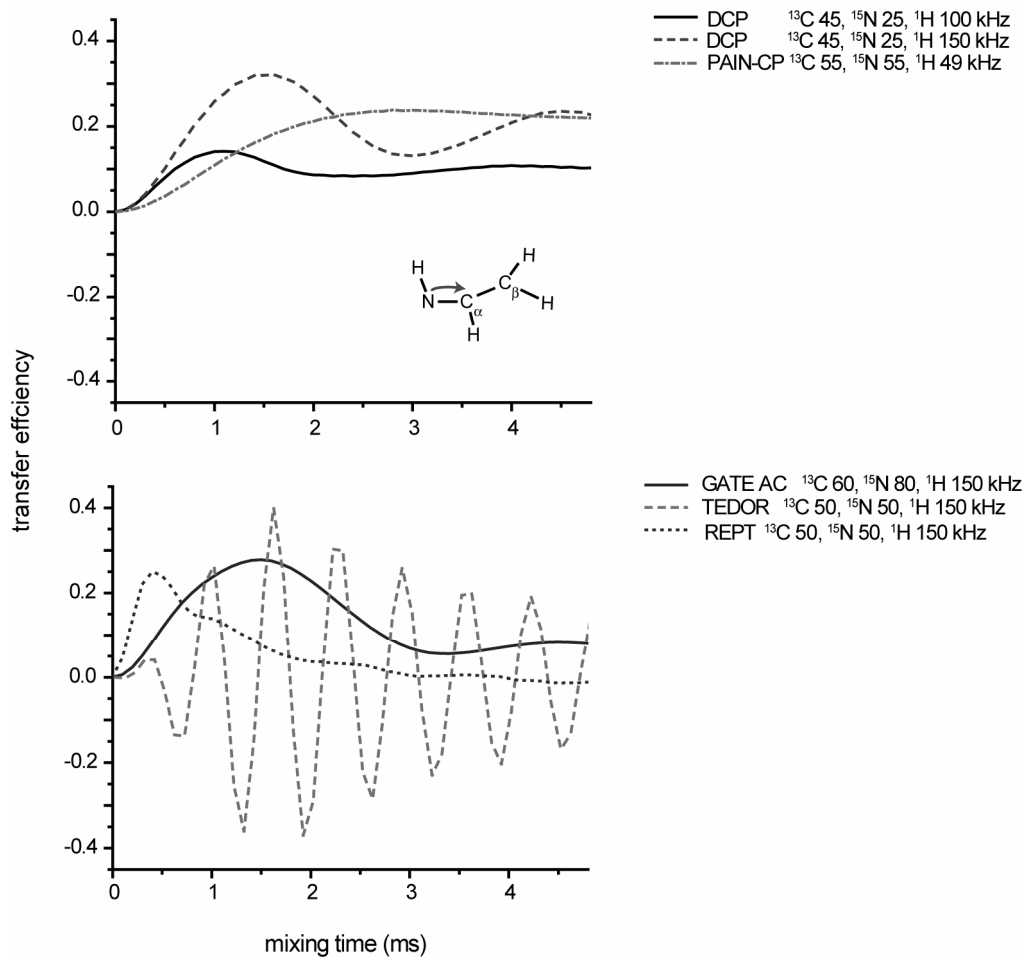


Figure 7-6 N- C_α transfer (one-bond transfer) using the same spin system and simulation conditions as in Fig. 7-2 of the text.

Figure 7-6 shows the *one-bond* ^{15}N to C_α transfer efficiency (using the same spin system and simulation parameters as in Fig. 7-2) and highlights the differences between PAIN-CP, DCP, TEDOR, REPT and GATE with respect to their performance at high spinning and Larmor frequencies. The figure illustrates the following important points.

DCP transfer efficiency dependence on the ^1H r.f. field: DCP is an efficient technique for one-bond transfer, provided that the ^1H r.f. field is at least 3 times higher than ^{13}C and ^{15}N r.f. fields, a condition that is difficult to fulfill at $\omega_r/2\pi \geq 20$ kHz either due to hardware or r.f. heating leading to imperfect ^1H decoupling. Under such constraint PAIN-CP provides comparable or better transfer efficiency compared to DCP.

PAIN-CP one-bond transfer efficiencies: PAIN-CP can be used efficiently for one-bond transfer experiments at high spinning frequencies – and is often the best compromise in between performance and experimental requirements. This method is especially well suited for biological samples which may be sensitive to excessive r.f. heating. Moreover, PAIN-CP buildups reach an equilibrium plateau, which relaxes the constraint on the precise optimal mixing time, making the experimental setup much more straightforward.

TEDOR/REPT: The classical version of TEDOR displays oscillations due to the isotropic chemical shift, which greatly complicates the choice of the mixing time for a real sample with a distribution of chemical shifts. The chemical shift evolution can be refocused by applying a strong π pulse in between the REDOR periods (a sequence referred to as REPT or dipolar INEPT). However, the compensating pulse has a side effect of interfering with the ^1H decoupling. The stronger the pulse the greater is the requirement for the ^1H decoupling field. Therefore a compromise between efficient refocusing and decoupling is required. In the simulations the ^1H decoupling field is 150 kHz except during the 100 kHz $^{13}\text{C}/^{15}\text{N}$ refocusing pulses where no decoupling is applied (these settings yield the best result for 50-100 kHz refocusing and 0-150 kHz decoupling powers).

GATE: The longitudinal recoupling sequence, GATE, has a large scaling factor but requires very demanding conditions at MAS frequencies > 15 kHz.

These simulations show that PAIN-CP should be considered as an alternative to the usual one bond polarization schemes (DCP, TEDOR/REPT) in the high $\omega_r/2\pi$ regime. Moreover, our experiments show that for DCP a decoupling mismatch of 2.5 is not sufficient. As a result PAIN-CP performed better for one-bond transfers than DCP, given our experimental constraints. The PAIN-CP sequence should be widely used since it is a reasonable option for performing efficient heteronuclear ^{15}N - ^{13}C transfer at high Larmor and spinning frequencies.

7.6.4. Transfer to a weakly coupled spin in the presence of a strongly coupled spin

Figure 7-7 below illustrates the influence of a directly bonded ^{13}C on the polarization transfer from ^{15}N to a remote ^{13}C spin for DCP, TEDOR and PAIN-CP. In order to focus on

the effect of the C_α spin, the spin system for the DCP and TEDOR simulations do not contain protons. On the other hand, we include 3 protons in the PAIN-CP spin system, as its mechanism relies on surrounding protons. Isotropic chemical shifts and CSAs were neglected in all the simulations.

The simulation shows a transfer over 3 Å distance in the presence ($N-C_2$, in red) and in the absence ($N-C_2$, in blue) of the C_α spin directly bonded to the nitrogen. Although DCP yields the most efficient transfer in the absence of the C_α spin, almost no magnetization can be transferred when C_α is added. In the TEDOR case, although there is no dipolar truncation due to the longitudinal form of the recoupled Hamiltonian, the transfer to the remote spin C_2 in the presence of a strongly coupled C_α is almost absent. In contrast, PAIN-CP appears to be the only mechanism able to provide significant long distance transfer in both situations. In fact, the transferred magnetization is even larger in the presence of a strongly coupled C_α spin and can be attributed to an additional transfer pathway relying on homonuclear TSAR mechanism. Details of the mechanism are currently under investigation. Note, that the vertical axis is reduced for the simulations in the second row of the figure.

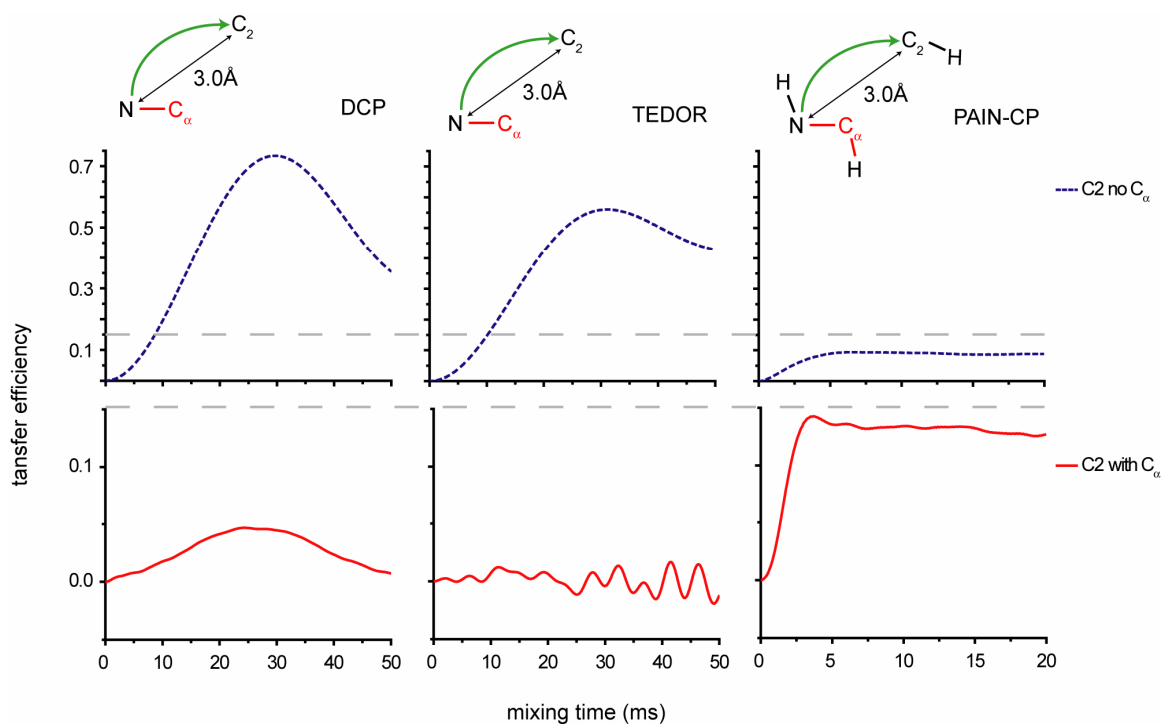


Figure 7-7 Influence of a nearby carbon (C_α) in the polarization transfer from ^{15}N to remote spin (C_2). The dashed line represents 0.15 normalized intensity.

7.6.5 DCP versus PAIN-CP – overall polarization transfer (experiment)

Figure 7-8 shows an experimental comparison of the total ^{15}N - ^{13}C transfer (i.e. sum over all cross peak integrals above the noise level) between PAIN-CP and DCP with high power decoupling (set to 112 kHz, i.e. 2.5 times ^{13}C r.f. field). The r.f. field strengths were respectively 45, 25 kHz on the ^{13}C , ^{15}N channel. 1D data were recorded on a 750 MHz spectrometer with $\omega_r/2\pi=20$ kHz using [U- ^{13}C , ^{15}N]-N- f -MLF-OH.

Direct ^1H - ^{13}C transfer was eliminated by flipping the remaining locked ^1H magnetization (after the first to ^1H - ^{15}N CP pulses) to the Z axis before the PAIN-CP mixing period.

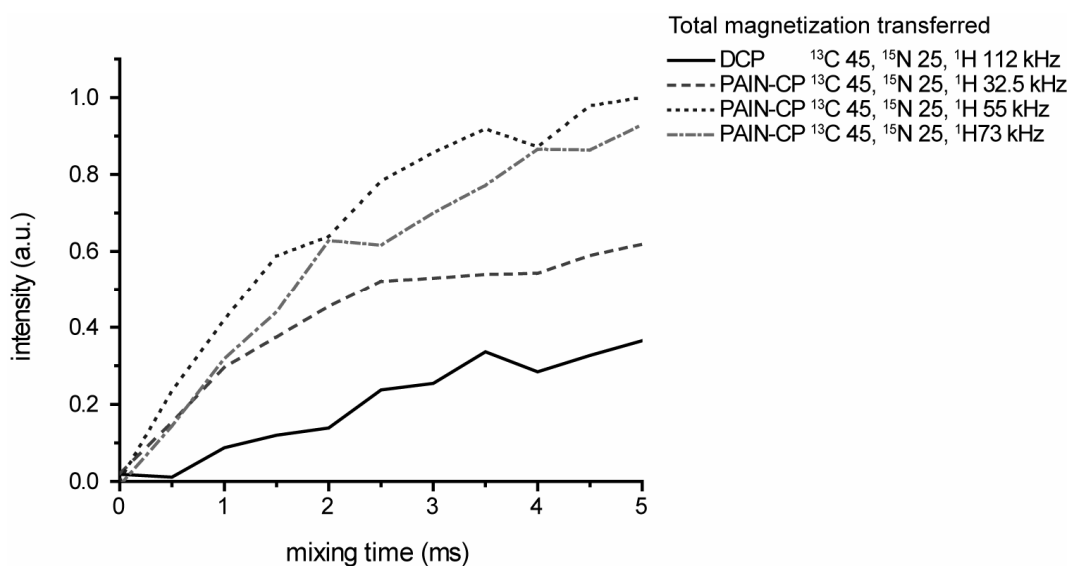


Figure 7-8 Experimental comparison of the total magnetization N-C transfer (i.e. sum over all cross peak integrals above the noise level) between DCP and three different $n=1$ PAIN-CP variants.

At a mixing time of 3 ms, the transferred magnetization is approximately four times larger for PAIN-CP (^{13}C 45/ ^{15}N 25/ ^1H 55 kHz) than for DCP, an observation that is in good agreement with simulations and cross peaks volume ratios extracted from 2Ds obtained under identical conditions (data not shown).

7.6.6 Comments on the PAIN-CP pulse sequence

The pulse sequence used in the simulations and experiments included in this section on supporting information is depicted in Fig. 7-1. While we employed constant amplitude r.f. fields on each channel, extensions involving adiabatic passages can be considered.

7.6.7 Elimination of the ^1H - ^{13}C transfer during PAIN-CP mixing

This section addresses the problem of ^1H - ^{13}C transfer during the ^{15}N - ^{13}C PAIN-CP step. This is not a concern for the simulations as the initial ^1H magnetization was always set to 0. However, during the experiments there may remain some ^1H magnetization along the locking axis after the first ^1H - ^{15}N CP pulses. The application of a ^1H pulse that stores the magnetization along the Z-axis prior to the PAIN-CP mixing is a convenient way to avoid any ^1H - ^{13}C transfer since the residual ^1H magnetization along the Z axis commutes with the effective PAIN-CP Hamiltonian.

This is illustrated in Fig. 7-9 where the black/red curves correspond to C_α/C_β buildups depending on the state of the initial density matrix: the squares correspond to initial polarizations on both ^1H and ^{15}N , the solid lines on ^{15}N only.

Another way to eliminate the ^1H - ^{13}C transfer is to phase shift the ^1H r.f. by π halfway through the PAIN-CP mixing (data not shown).

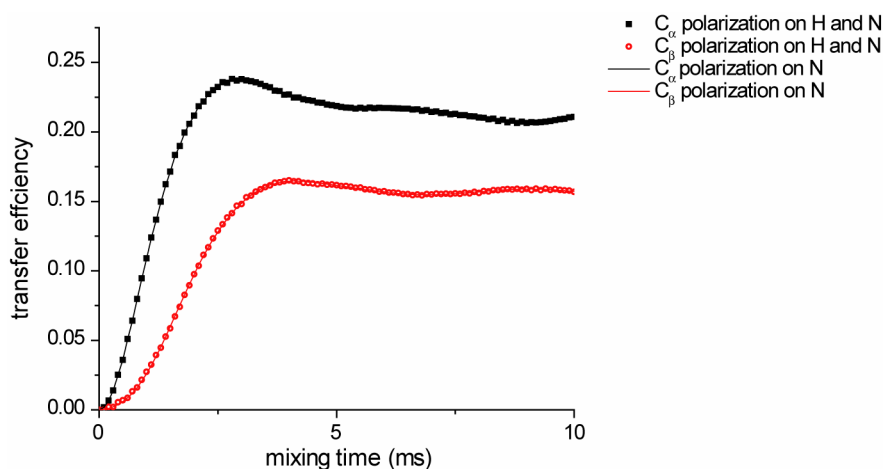


Figure 7-9 N- C_β transfer (two-bond transfer) using the same spin system and settings as in Fig. 7-2. The application of a ^1H $\pi/2$ flip pulse before the PAIN-CP mixing period eliminates ^1H - ^{13}C transfer.

7.7 References

- (1) Lesage, A.; Sakellariou, D.; Steuernagel, S.; Emsley, L. J. *Am. Chem. Soc.* 1998, 120, 13194-13201.
- (2) Hing, A. W.; Vega, S.; Schaefer, J. J. *Magn. Reson.* 1992, 96, 205-209.
- (3) Baldus, M.; Petkova, A. T.; Herzfeld, J.; Griffin, R. G. *Mol. Phys.* 1998, 95, 1197-1207.
- (4) Oas, T. G.; Griffin, R. G.; Levitt, M. H. *J. Chem. Phys.* 1988, 89, 692-695.
- (5) Sun, B. Q.; Costa, P. R.; Griffin, R. G. *J. Magn. Reson. A* 1995, 112, 191-198.
- (6) Gullion, T.; Schaefer, J. J. *Magn. Reson.* 1989, 81, 196-200.
- (7) Zhao, X.; Hoffbauer, W.; auf der Gunne, J. S.; Levitt, M. H. *Solid State Nucl. Magn. Reson.* 2004, 26, 57-64.
- (8) van Rossum, B. J.; de Groot, C. P.; Ladizhansky, V.; Vega, S.; de Groot, H. J. M. *J. Am. Chem. Soc.* 2000, 122, 3465-3472.
- (9) Ladizhansky, V.; Vinogradov, E.; van Rossum, B. J.; de Groot, H. J. M.; Vega, S. *J. Chem. Phys.* 2003, 118, 5547-5557.
- (10) Bjerring, M.; Nielsen, N. C. *Chem. Phys. Lett.* 2003, 382, 671-678.
- (11) Dvinskikh, S.; Chizhik, V. J. *Exp. Theor. Phys.* 2006, 102, 91-101.
- (12) Bertani, P.; Raya, K.; Hirschinger, K. *Comptes Rendus Chimie* 2004, 7, 363-369.
- (13) Ray, S.; Ladizhansky, V.; Vega, S. *J. Magn. Reson.* 1998, 135, 427-434.
- (14) Chan, J. C. C. *Chem. Phys. Lett.* 2001, 335, 289-297.
- (15) Pines, A.; Gibby, M. G.; Waugh, J. S. *J. Chem. Phys.* 1973, 59, 569-590.
- (16) Baldus, M.; Geurts, D. G.; Hediger, S.; Meier, B. H. *J. Magn. Reson. A* 1996, 118, 140-144.
- (17) Lowe, I. J. *Phys. Rev. Lett.* 1959, 2, 285.
- (18) Bjerring, M.; Rasmussen, J. T.; Krogshave, R. S.; Nielsen, N. C. *J. Chem. Phys.* 2003, 119, 8916-8926.
- (19) Hing, A. W.; Vega, S.; Schaefer, J. J. *Magn. Reson. A* 1993, 103, 151-162.
- (20) Saalwachter, K.; Graf, R.; Spiess, H. W. 2001, 148, 398-418.
- (21) Jaroniec, C. P.; Filip, C.; Griffin, R. G. *J. Am. Chem. Soc.* 2002, 124, 10728-10742.

- (22) Jaroniec, C. P.; Tounge, B. A.; Rienstra, C. M.; Herzfeld, J.; Griffin, R. G. *J. Am. Chem. Soc.* 1999, 121, 10237-10238.
- (23) Hong, M.; Gross, J. D.; Hu, W.; Griffin, R. G. *J. Magn. Reson.* 1998, 135, 169-177.
- (24) Hong, M.; Gross, J. D.; Rienstra, C. M.; Griffin, R. G.; Kumashiro, K. K.; Schmidt-Rohr, K. *J. Magn. Reson.* 1997, 129, 85-92.
- (25) Hong, M.; Gross, J. D.; Griffin, R. G. *J. Phys. Chem. B* 1997, 101, 5869-5874.
- (26) Sack, I.; Balazs, Y. S.; Rahimipour, S.; Vega, S. J. *Am. Chem. Soc.* 2000, 122, 12263-12269.
- (27) Schaefer, J.; McKay, R. A.; Stejskal, E. O. *J. Magn. Reson.* 1979, 34, 443-447.
- (28) Wu, X. L.; Zilm, K. W. *J. Magn. Reson. A* 1993, 104, 154-165.
- (29) Pauli, J.; Baldus, M.; van Rossum, B.; de Groot, H.; Oschkinat, H. *ChemBiochem* 2001, 2, 272-281.
- (30) Egorova-Zachernyuk, T. A.; Hollander, J.; Fraser, N.; Gast, P.; Hoff, A. J.; Cogdell, R.; de Groot, H. J. M.; Baldus, M. *J. Biomol. Nmr* 2001, 19, 243-253.
- (31) Morcombe, C. R.; Gaponenko, V.; Byrd, R. A.; Zilm, K. W. *Journal of the American Chemical Society* 2004, 126, 7196-7197.
- (32) Takegoshi, K.; Nakamura, S.; Terao, T. 2001, 344, 631-637.
- (33) Takegoshi, K.; Nakamura, S.; Terao, T. *J. Chem. Phys.* 2003, 118, 2325-2341.
- (34) Veshtort, M.; Griffin, R. G. *J. Magn. Reson.* 2006, 178, 248-282.
- (35) Ishii, Y.; Ashida, J.; Terao, T. *Chem. Phys. Lett.* 1995, 246, 439-445.
- (36) Hartmann, S. R.; Hahn, E. L. *Phys. Rev.* 1962, 128, 2042-2053.
- (37) Stejskal, E. O.; Schaefer, J.; Waugh, J. S. *J. Magn. Reson.* 1977, 28, 105-112.

8. Proton Assisted Homonuclear Recoupling and Protein Structure Determination

Reproduced with permission from Gaël De Paëpe, Józef R. Lewandowski, Antoine Loquet, Anja Böckmann, Robert G. Griffin “Proton Assisted Homonuclear Recoupling and Protein Structure Determination”

8.1 Abstract

We introduce a homonuclear version of Third Spin Assisted Recoupling (TSAR), a second-order mechanism that can be used for polarization transfer between ^{13}C or ^{15}N spins in biomolecular magic angle spinning (MAS) experiments. The resulting sequence, which we refer to as homonuclear Proton Assisted Recoupling (PAR), relies on a cross-term between ^1H - ^{13}C (or ^1H - ^{15}N) couplings to mediate zero quantum ^{13}C - ^{13}C or ^{15}N - ^{15}N recoupling. Using Average Hamiltonian Theory (AHT) we derive a PAR effective Hamiltonian and show that the PAR transfer is mediated by trilinear terms of the form $C_1^\pm C_2^\mp H_Z$ (or $N_1^\pm N_2^\mp H_Z$). We use analytical and numerical simulations to explain the structure of the PAR optimization maps. We also detail the PAR polarization transfer dependence with respect to the local molecular geometry and explain the observed reduction of dipolar truncation. In addition, we demonstrate the utility of PAR in structural studies of proteins with ^{13}C - ^{13}C spectra of uniformly ^{13}C , ^{15}N labeled microcrystalline Crh, a 85 amino acid domain swapped dimer (MW =2x10.4 kDa). The spectra, which were acquired at high spinning frequencies ($\omega_r/2\pi > 20$ kHz) and magnetic fields (750-900 MHz ^1H frequency) using moderate rf fields, yield numerous long distance ^{13}C - ^{13}C contacts (up to 6-7 Å). We use the x-ray structure as a homology model for assigning the ambiguous cross peaks of the PAR spectra. All the restraints obtained with this protocol were used as a unique distance class to perform a back-calculation of the monomer subunit of the Crh protein.

8.2 Introduction

Solid-state NMR (SSNMR) structural studies of proteins are generally performed under high resolution conditions obtained via magic angle spinning (MAS), an approach which averages second rank tensor interactions such as the chemical shift anisotropy and the homonuclear dipolar interaction.^{1, 2} Thus, while MAS introduces high resolution by attenuating the shift anisotropy, it also suppresses the distance information that is the source of structural data in the spectra. This structural information can be reintroduced selectively in a manner consistent with the goal of high resolution by the application of a carefully chosen sequence of rotor synchronized rf pulses³⁻¹⁷, an approach that was introduced approximately 20 years ago and is referred to as dipolar recoupling. Since the original experiments, homonuclear and heteronuclear recoupling sequences have been refined in many ways and now allow accurate measurement^{5, 18-27} of distances and torsion angles²⁸⁻³³ as well as distance estimates using spin diffusion based techniques.³⁴⁻³⁸

Among the various approaches to dipolar recoupling, the homonuclear experiments, which recouple ^{13}C - ^{13}C and ^{15}N - ^{15}N spins, play an especially important role in biomolecular studies. In particular, the favorable dispersion of ^{13}C chemical shifts and the development of efficient methods for ^1H - ^{13}C decoupling³⁹⁻⁴⁶ ensures high spectral resolution and is essential for spectral assignments. Moreover, ^{13}C - ^{13}C spectra also provide structurally valuable restraints and they are potentially more numerous than either ^{15}N - ^{15}N or ^{15}N - ^{13}C distance restraints. Thus, homonuclear ^{13}C - ^{13}C recoupling sequences have been extensively used in solid-state NMR structural studies.^{36, 38, 47-50}

However, in general the measurement of long ^{13}C - ^{13}C distances with non-selective techniques in uniformly labeled samples is hindered by a phenomenon known as dipolar truncation. In particular, the magnetization transfer due to weak dipolar couplings characteristic of long distances is strongly attenuated by the presence of larger non-commuting dipolar interactions characteristic of short distances. While this effect is much maligned, and is usually discussed as the major bottleneck for structure determination, it is actually very important for performing efficient, error free resonance assignments. In fact, efficient truncation of medium and long range transfers in for

example γ -encoded sequences by strong one bond couplings induces a one-bond relayed transfer along the ^{13}C - ^{13}C chains. This is illustrated in Fig. 8-10a, where broadband DQ $\text{CM}_5\text{RR}^{14, 51}$ spectra of $[\text{U-}^{13}\text{C}, ^{15}\text{N}]\text{-Crh}$ protein⁵² (recorded with a short 0.8 ms mixing time) contain exclusively one-bond cross-peaks. At longer mixing times (data not shown), additional cross peaks appear with alternating signs which is a signature of a DQ process that depends on the number of one-bond couplings involved in the transfer. While this spectral behavior is obviously a very attractive feature of the technique for performing resonance assignments, it, nevertheless, does not provide distance information that could be directly related to the fold of the protein (except for what is available through statistical analyses of secondary chemical shifts⁵³).

In order to utilize ^{13}C - ^{13}C recoupling for three-dimensional (3D) structure determination of proteins, we require methods that either attenuate or quench dipolar truncation. A number of different groups of techniques have been proposed to circumvent the problem^{54, 24, 25, 55, 26, 56, 57, 58, 14, 59, 60} (see Sec. 4.1) and three of them have lead to 3D structures of model proteins: (1) second-order techniques including PDS⁶¹ and DARR/RAD^{34, 35, 62}; (2) techniques combining ^1H - ^1H spin diffusion with indirect detection such as CHHC/NHHC^{48, 63-65}; and (3) rotational resonance (R^2) based selective first order techniques⁶⁶.

Both PDS and DARR/RAD rely on the ^1H - ^{13}C \times ^{13}C - ^{13}C and ^{13}C - ^{13}C \times ^{13}C - ^{13}C second order cross-terms to promote ^{13}C - ^{13}C polarization transfer on a time scale of milliseconds to seconds.⁶⁷ To date, high-resolution 3D structure determination using PDS and DARR has been demonstrated primarily on selectively labeled spin systems^{36, 37} and very recently on uniformly labeled systems.³⁸

An alternative approach employs ^1H - ^1H contacts that are detected indirectly via rare spins, as in the case of CHHC and NHHC, or in favorable cases the contacts are dispersed in a ^{13}C and ^{15}N dimension and detected on ^1H .^{63, 64, 68, 69, 70} ^1H - ^1H contacts are probed in the initial rate regime ($\sim 10^2$ μs mixing time). CHHC/NHHC based approaches were successfully used for structural studies of uniformly ^{13}C and ^{15}N labeled peptides/proteins^{65, 71} including the 3D structure determination of Crh dimer.⁷⁰

Finally, R^2 -based frequency selective techniques are well established as methods for measuring accurate ^{13}C - ^{13}C distances and were used extensively in the context of small

peptide structure determination. Recently, it was demonstrated that combined restraints from homogeneously broadened R²W and PDSO are sufficient to constrain the structure of a uniformly ¹³C and ¹⁵N model protein GB1.⁶⁶

In this manuscript we introduce a homonuclear recoupling technique that exhibits substantially reduced dipolar truncation. This sequence, homonuclear **Proton Assisted Recoupling (PAR)**, is based on the more general **Third Spin Assisted Recoupling (TSAR)** mechanism, that was used recently to design experiments for ¹⁵N to ¹³C cross polarization⁷² and to understand the spin dynamics underlying the beneficial effect of a weak ($< 0.25 \omega_r$) ¹H irradiation on the DQ CMpRR ¹³C-¹³C transfer efficiency.¹⁴ More generally, the B-[A]-C TSAR mechanism serves to connect two spins B and C via a cross term involving dipolar couplings with a third spin A (B-A and C-A dipolar couplings, respectively). *The TSAR effective Hamiltonian contains trilinear terms of the forms $B^{\pm}C^{\mp}A_z$ which induce ZQ polarization transfer between spin B and C.*

In proteins and nuclei acids, protons are ideal candidates to mediate second-order TSAR transfers. Thus, the homonuclear PAR experiment is used for ¹³C-[¹H]-¹³C and ¹⁵N-[¹H]-¹⁵N polarization transfer (see Fig.8-1). In contrast to most recoupling sequences that require decoupling of ¹H from the ¹⁵N-¹³C, ¹³C-¹³C and ¹⁵N-¹⁵N spin dynamics, the TSAR effect described here uses the intrinsic properties of protons (high abundance, high γ -ratio) to facilitate the transfer process. As a consequence, and in spite of relying on second order recoupling, TSAR significantly accelerates the polarization transfer between the remote B and C spins (with B/C being either ¹⁵N or ¹³C) as compared to mechanisms based on B-C dipolar coupling. *Note that the homonuclear dipolar B-C coupling is not involved in the TSAR recoupling, a fact that intrinsically differentiates it from the spin diffusion methods that involve homonuclear couplings in their mechanism. Moreover, even though the ¹H's are involved in the PAR mechanism, the polarization is not transferred through the proton network using ¹H-¹H couplings. This is an essential difference with respect to CHHC-type experiments where the polarization is transferred between ¹H's and indirectly detected on ¹³C. The TSAR mechanism also leads to attenuated dipolar truncation as we demonstrate below both theoretically and experimentally, allowing the detection of cross peaks*

corresponding to distances up to ~ 6-7 Å in the spectra of uniformly [^{13}C , ^{15}N]-Crh protein (see Fig. 8-10b).

The manuscript is organized as follows. Section 2 presents the PAR pulse sequence, the PAR effective Hamiltonian (AHT) and the associated ZQ-TSAR subspace. Section 3 compares analytical and numerical PAR simulations and describes in detail the spin dynamics including the local geometry dependency. Section 4 highlights various aspects of the PAR polarization transfer in uniformly labeled proteins with a focus on dipolar truncation, the issue of relayed versus direct polarization transfer as well as the effect of multiple protons. Section 5 revisits the dipolar truncation question and notably shows that additional ZQ ^{13}C - ^1H - ^{13}C TSAR transfer may be present during most of the contemporary first order recoupling sequences. Section 6 demonstrates that the PAR technique is a suitable approach for structure determination and compares its features to other alternative methods such as PDS/DARR and CHHC/NHHC. *Note that a detailed description of the materials and methods (including the PAR optimization protocol) can be found in the SI.*

8.3 Principles of PAR recoupling

8.3.1 PAR pulse sequence

Figure 8-1a illustrates the pulse sequence used throughout this work to record homonuclear 2D correlation spectra (except the spectrum in Fig. 8-10a and 13a for which the pulses sequence can be found in ref. 14). Following the initial CP step (that transfers proton magnetization to $^{13}\text{C}/^{15}\text{N}$ spins) and the $^{13}\text{C}/^{15}\text{N}$ indirect t_1 evolution, CW irradiation, which constitutes the PAR recoupling block, is applied to both the $^{13}\text{C}/^{15}\text{N}$ and ^1H channels, followed by direct $^{13}\text{C}/^{15}\text{N}$ detection in the presence of TPPM³⁹ decoupling. As we shall see in the following, the PAR recoupling mechanism relies on second order recoupling involving $^{13}\text{C}_1\text{-}^1\text{H}$ (or $^{15}\text{N}_1\text{-}^1\text{H}$) and $^1\text{H}\text{-}^{13}\text{C}_2$ ($^1\text{H}\text{-}^{15}\text{N}_2$) dipolar interactions, or in other words $^{13}\text{C}\text{-}^1\text{H}\text{-}^{13}\text{C}$ TSAR (or $^{15}\text{N}\text{-}^1\text{H}\text{-}^{15}\text{N}$ TSAR) mechanism.

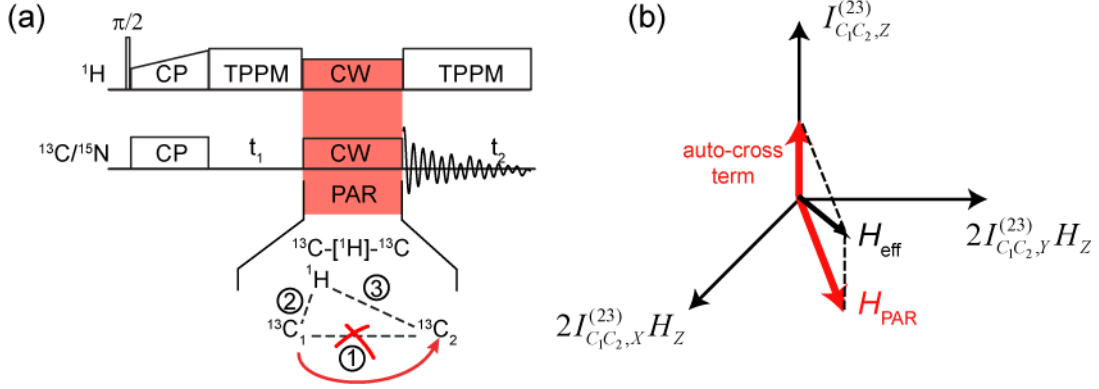


Figure 8-1 (a) PAR pulse sequence for obtaining 2D homonuclear correlation spectra. The PAR mixing consist of continuous wave (CW) irradiation on ^1H and ^{13}C channel that recouples second order cross term between ^1H - ^{13}C dipolar couplings (term 2 and 3 of Eq. (111)) in order to transfer polarization from $^{13}\text{C}_1$ to $^{13}\text{C}_2$. (b) The PAR subspace can be seen as a coupled basis between a fictitious ZQ operator involving two ^{13}C 's (or ^{15}N 's) and a ^1H spin. The red arrows indicate PAR recoupling axis and longitudinal tilting field resulting from auto-cross terms (see Sect. 3.3).

8.3.2 Second-order effective Hamiltonian – PAR subspace

The PAR experiment can be analyzed with Average Hamiltonian Theory (AHT)⁷³ that permits visualization and understanding of the spin dynamics in the PAR subspace. Accordingly, we consider a three spin system consisting of two homonuclear spins $^{13}\text{C}_1$, $^{13}\text{C}_2$ (or $^{15}\text{N}_1$, $^{15}\text{N}_2$) and an assisting ^1H spin subject to two CW rf fields of strength $\omega_{^{13}\text{C}}^{\text{rf}}/2\pi$ (or $\omega_{^{15}\text{N}}^{\text{rf}}/2\pi$) and $\omega_{^1\text{H}}^{\text{rf}}/2\pi$ for the ^{13}C (or ^{15}N) and ^1H channels respectively. The internal Hamiltonian can therefore be written as:

$$\begin{aligned}
 H = & +\omega_{C_1} C_{1z} + \omega_{C_2} C_{2z} + \omega_H H_z \\
 & \omega_{C_1 C_2} \left[2C_{1z} C_{2z} - (C_{1x} C_{2x} + C_{1y} C_{2y}) \right] + \omega_{C_1 H} 2C_{1z} H_z + \omega_{H C_2} 2H_z C_{2z} \quad (106) \\
 & +\omega_{^{13}\text{C}}^{\text{rf}} C_{1x} + \omega_{^{13}\text{C}}^{\text{rf}} C_{2x} + \omega_{^1\text{H}}^{\text{rf}} H_x
 \end{aligned}$$

where ω_{C_1} , ω_{C_2} and ω_H denote the shift tensors and resonant offsets of the ^{13}C (or ^{15}N) and ^1H nuclei respectively, and $\omega_{C_1 C_2}$, $\omega_{C_1 H}$, and $\omega_{H C_2}$ the homonuclear and heteronuclear dipolar couplings. Note that rotation at the magic angle induces a time dependence of the spatial anisotropy of the interactions.

For computational convenience, the spin system Hamiltonian can be rewritten using spherical tensor notation:

$$\begin{aligned}
\mathbf{H} = & \omega_{C_1H} 2T_{10}^{C_1} T_{10}^H + \omega_{HC_2} 2T_{10}^H T_{10}^{C_2} + \sqrt{6} \omega_{C_1C_2} T_{20}^{C_1C_2} \\
& + \omega_{C_1} T_{10}^{C_1} + \omega_{C_2} T_{10}^{C_2} + \omega_H T_{10}^H \\
& + \omega_{1C}^{\text{rf}} \left\{ \frac{-T_{11}^{C_1} + T_{1-1}^{C_1}}{\sqrt{2}} \right\} + \omega_{1C}^{\text{rf}} \left\{ \frac{-T_{11}^{C_2} + T_{1-1}^{C_2}}{\sqrt{2}} \right\} + \omega_{1H}^{\text{rf}} \left\{ \frac{-T_{11}^H + T_{1-1}^H}{\sqrt{2}} \right\}
\end{aligned} \quad (107)$$

In order to see the effect of the CW irradiations, it is convenient to rewrite the Hamiltonian in the interaction frame that they define. Such a change of frame can be decomposed into two rotations: the first rotates the z-axis to the x-axis, and the second rotates the spin system around the new z axis by an angle $\omega_{1C}^{\text{rf}} t$ and $\omega_{1H}^{\text{rf}} t$. Each of the operators transforms as follows:

$$[T_{10}^{\lambda}]^{\text{r}} = \sum_q T_{1q}^{\lambda} d_{q0}^l \left(-\pi/2 \right) e^{-iq\omega_{1C}^{\text{rf}} t} \quad (108)$$

where $d_{q0}^l(\beta)$ is a reduced Wigner matrix element. We reduce the dependence on three different averaging frequencies ($\omega_r/2\pi$ the frequency of the spinning rotor, $\omega_{1C}^{\text{rf}}/2\pi$ (or $\omega_{1N}^{\text{rf}}/2\pi$), $\omega_{1H}^{\text{rf}}/2\pi$ the strength of the carbon (or nitrogen) and proton CW fields respectively) to a single frequency dependence by assuming that these frequencies are commensurate, implying that we can find indices p_C and p_H , and integers $p_C^1, p_C^2, p_H^1, p_H^2$ such that:

$$\omega_{1C}^{\text{rf}}/2\pi = p_C \left(\omega_r/2\pi \right) = \frac{p_C^1}{p_C^2} \left(\omega_r/2\pi \right) \quad (109)$$

$$\omega_{1H}^{\text{rf}}/2\pi = p_H \left(\omega_r/2\pi \right) = \frac{p_H^1}{p_H^2} \left(\omega_r/2\pi \right) \quad (110)$$

where $\frac{p_C^1}{p_C^2}, \frac{p_H^1}{p_H^2}$ denote irreducible ratios. Assuming that the frequencies are

commensurate is not a demanding constraint and allows us to apply Average Hamiltonian Theory on a period $n\tau_r$, where $n = \text{lcm}\{p_C^2, p_H^2\}$, given that n is sufficiently small to ensure rapid convergence and τ_r is a rotor period. The expression of the Hamiltonian in the interaction frame can thus be obtained using Eq. (2)-(5):

$$\begin{aligned}
\tilde{H} = & \overbrace{\sum_{m_1=-2}^2 \sum_{\substack{q_{1C}=-1 \\ q_{1C} \neq 0}}^1 \sum_{\substack{q_{1H}=-1 \\ q_{1H} \neq 0}}^1 \omega_{C_1H}^{m_1} \operatorname{sgn}(q_{1C}) \operatorname{sgn}(q_{1H}) T_{1q_{1C}}^{C_1} T_{1q_{1H}}^H \exp\left\{-i(nX_1) \frac{\omega_r t}{n}\right\}}^1 \\
& + \overbrace{\sum_{m_2=-2}^2 \sum_{\substack{q_{2C}=-1 \\ q_{2C} \neq 0}}^1 \sum_{\substack{q_{2H}=-1 \\ q_{2H} \neq 0}}^1 \omega_{HC_2}^{m_2} \operatorname{sgn}(q_{2H}) \operatorname{sgn}(q_{2C}) T_{1q_{2H}}^H T_{1q_{2C}}^{C_2} \exp\left\{-i(nX_2) \frac{\omega_r t}{n}\right\}}^2 \\
& + \overbrace{\sum_{m_3=-2}^2 \sum_{q_{3C}=-2}^2 \omega_{C_1C_2}^{m_3} d_{q_{3C}0}^2 \left(-\pi/2\right) T_{2q_{3C}}^{C_1C_2} \exp\left\{-i(nX_3) \frac{\omega_r t}{n}\right\}}^3 \\
& + \overbrace{\sum_{i=1}^2 \sum_{m_i=-2}^2 \sum_{\substack{q_{Ci}=-1 \\ q_{Ci} \neq 0}}^1 \omega_{C_i}^{m_i} \left(\operatorname{sgn}(q_{C_i})/\sqrt{2}\right) T_{1q_{Ci}}^{C_i} \exp\left\{-i(nX_{C_i}) \frac{\omega_r t}{n}\right\}}^4 \\
& + \overbrace{\sum_{m=-2}^2 \sum_{\substack{q_H=-1 \\ q_H \neq 0}}^1 \omega_H^m \left(\operatorname{sgn}(q_H)/\sqrt{2}\right) T_{1q_H}^H \exp\left\{-i(nX_H) \frac{\omega_r t}{n}\right\}}^5
\end{aligned} \tag{111}$$

where we use the following expressions

$$\begin{aligned}
X_1 &= m_1 + p_C q_{1C} + p_H q_{1H} \\
X_2 &= m_2 + p_H q_{2H} + p_C q_{2C} \\
X_3 &= m_3 + p_C q_{3C} \\
X_{C_i} &= m_{C_i} + p_C q_{C_i} \\
X_H &= m + p_H q_H
\end{aligned} \tag{112}$$

and $\operatorname{sgn}(q)$ is the sign function of q .

We assume that the rf fields are chosen so that neither Hartmann-Hahn (H-H)⁷⁴ nor rotary resonance (R³)^{75, 76} conditions are matched, i.e. $X_1 \neq 0, X_2 \neq 0, X_{C_i} \neq 0, X_H \neq 0$ and that the ¹³C-¹³C dipolar coupling is not recoupled to first order ($X_3 \neq 0$). Under these conditions, the first order average Hamiltonian vanishes.

In order to describe the TSAR recoupling mechanism, we calculate the cross-term between terms 1 and 2 in Eq. (9):

$$\begin{aligned}
\tilde{H}_{1 \times 2}^{(2)} = & \sum_{\substack{m_1, q_{1C}, q_{1H}, \\ m_2, q_{2C}, q_{2H}}} \left[\frac{1}{2iT} \omega_{C_1H}^{m_1} \operatorname{sgn}(q_{1C}) \operatorname{sgn}(q_{1H}) \omega_{HC_2}^{m_2} \operatorname{sgn}(q_{2H}) \operatorname{sg}(q_{2C}) T_{1q_{1C}}^{C_1} T_{1q_{2C}}^{C_2} \left[T_{1q_{1H}}^H, T_{1q_{2H}}^H \right] \right. \\
& \left. \int_0^T dt_2 \int_0^{t_2} dt_1 \left(\exp\{-i\omega_r (X_1 t_2 + X_2 t_1)\} - \exp\{-i\omega_r (X_2 t_2 + X_1 t_1)\} \right) \right]
\end{aligned} \tag{113}$$

The above expression is non-zero if and only if:

$$1. \quad q_{1H} = -q_{2H} \Rightarrow \left[T_{1q_{1H}}^H, T_{1q_{2H}}^H \right] = -\text{sgn}(q_{1H}) T_{10}^H \quad (114)$$

$$2. \quad X_1 = -X_2 \neq 0 \quad (115)$$

which implies that:

$$(m_1 + m_2) + p_C (q_{1C} + q_{2C}) = 0 \quad (116)$$

Equation (11) has two solutions:

Solution 1: for $q_{1C} = q_{2C} = \pm 1$ and $p_C \in \pm\{0, 0.5, 1, 1.5, 2\}$ with no restriction on p_H , which results in DQ terms of the form $T_{1\pm 1}^{C_1} T_{1\pm 1}^{C_2} T_{10}^H$.

Solution 2: for $q_{1C} = -q_{2C}$ and $m_1 = -m_2$ with no restriction on p_C and p_H , which results in ZQ terms of the form $T_{1\pm 1}^{C_1} T_{1\mp 1}^{C_2} T_{10}^H$.

Thus, it appears that ZQ solution is much easier to fulfill than the DQ solution, and ZQ TSAR recoupling occurs when the following conditions are satisfied:

$$q_{1H} = -q_{2H} = q_H, \quad q_{1C} = -q_{2C} = q_C, \quad m_1 = -m_2 = m \quad (117)$$

and providing that we concurrently avoid the DQ conditions associated with $p_C = \{0, \pm 0.5, \pm 1, \pm 1.5, \pm 2\}$, H-H conditions with $p_C = \pm p_H \pm \{1, 2\}$ and R^3 conditions with $p_C = \{1, 2\}$.

Using the identity $(\omega_{C_1H}^m \omega_{HC_2}^{-m})^* = \omega_{C_1H}^{-m} \omega_{HC_2}^m$, we obtain the following expression for the effective TSAR term:

$$\begin{aligned} \widetilde{H}_{1x2}^{(2)} &= 2\omega_{TSAR} (T_{11}^{C_1} T_{11}^{C_2}) T_{10}^H + 2\omega_{TSAR}^* (T_{11}^{C_1} T_{11}^{C_2}) T_{10}^H \\ &= 2\omega_{TSAR} C_1^+ C_2^- H_Z + 2\omega_{TSAR}^* C_1^- C_2^+ H_Z \quad (118) \\ &= \text{Re}(\omega_{TSAR}) 2I_X^{C_1 C_2, (23)} H_Z + \text{Im}(\omega_{TSAR}) 2I_Y^{C_1 C_2, (23)} H_Z \end{aligned}$$

and the TSAR coupling:

$$\begin{aligned} \omega_{TSAR} &= \left(\frac{\text{Re}(\omega_{C_1H}^1 \omega_{HC_2}^{-1})}{\omega_r} \lambda(1, p_C, p_H) + \frac{\text{Re}(\omega_{C_1H}^2 \omega_{HC_2}^{-2})}{\omega_r} \lambda(2, p_C, p_H) \right) \\ &+ i \left(\frac{\text{Im}(\omega_{C_1H}^1 \omega_{HC_2}^{-1})}{\omega_r} \sigma(1, p_C, p_H) + \frac{\text{Im}(\omega_{C_1H}^2 \omega_{HC_2}^{-2})}{\omega_r} \sigma(2, p_C, p_H) \right) \quad (119) \end{aligned}$$

with

$$\lambda(m, p_C, p_H) = \left(\frac{-(p_C + p_H)}{m^2 - (p_C + p_H)^2} + \frac{-(p_H - p_C)}{m^2 - (p_H - p_C)^2} \right) \quad (120)$$

$$\sigma(m, p_C, p_H) = \left(\frac{m}{m^2 - (p_H + p_C)^2} - \frac{m}{m^2 - (p_H - p_C)^2} \right)$$

The above expressions permit us to visualize the subspace in which the TSAR spin dynamics evolve. The TSAR subspace (Fig. 8-1b) can be seen as a coupled basis (see Fig. 8-14 for an example of coupled basis described extensively in the context of solution NMR⁷⁷) between a fictitious ZQ operator (see SI Sec. 1) involving the two ¹³C's (or ¹⁵N's) and a proton spin. The proton spin plays the role of a bystander spin i.e. no magnetization is sent to this proton in the spin dynamics described by Eq. (118). ***In this process, the dipolar couplings to the proton are used to create an effective transverse PAR component composed of trilinear terms of the forms $C_1^\pm C_2^\mp H_z$ which can invert the z-component in the TSAR subspace ($(C_{1z} - C_{2z})/2$) and thus induce polarization transfer between the two ¹³C's (¹⁵N's).***

The TSAR recoupling term (Eq. (118)) can be decomposed into two terms referred to as the $m=1$ and $m=2$ contributions, where m stands for the spatial component index of the dipolar tensor during MAS. The implicit dependence of the TSAR term on the local geometry and the powder Euler angle is detailed in Sec. 3.2. Note, that the TSAR mechanism usually uses multiple protons: any proton is potentially a candidate to participate in such process but only the closest ones will significantly contribute to the polarization transfer. This issue is discussed further in Sec. 4.3.

The TSAR term derived above drives the polarization transfer under PAR. However, the TSAR term is not the only possible cross-term during double CW irradiation. To have a complete picture of the spin dynamics in the PAR experiment, we need to evaluate the other second-order cross-terms. For example, an important contribution that we have to consider is a cross-term of term 1 in Eq. (9) with itself (i.e. ¹H-¹³C₁ term crossed with ¹H-¹³C₁), which we refer to as an auto-cross term.

8.3.3 Second-order effective Hamiltonian – auto-cross terms

In this section, we evaluate second order cross-terms other than the TSAR terms. An important class of cross-terms, referred to as auto-cross terms, yields non-zero contributions that can be expressed as a function of p_C and p_H rf field strengths (in units of the MAS frequency).

The auto-cross term of term 1 in Eq. (9) (i.e. the term involving the $^1\text{H}-^{13}\text{C}_1$ dipolar coupling crossed with the $^1\text{H}-^{13}\text{C}_1$ dipolar coupling) can be written as follows:

$$\begin{aligned} \bar{H}_{1x1}^{(2)} = & \frac{1}{\omega_r} \left[\omega_{C_1H}^1 \omega_{HC_1}^1 \chi(1, p_C, p_H) + \omega_{C_1H}^2 \omega_{HC_1}^2 \chi(2, p_C, p_H) \right] T_{10}^{C_1} \\ & + \frac{1}{\omega_r} \left[\omega_{C_1H}^1 \omega_{HC_1}^1 \kappa(1, p_C, p_H) + \omega_{C_1H}^2 \omega_{HC_1}^2 \kappa(2, p_C, p_H) \right] T_{10}^H \end{aligned} \quad (121)$$

with

$$\begin{aligned} \chi(m, p_C, p_H) = & -\frac{1}{2} \left(\frac{(p_H + p_C)}{m^2 - (p_H + p_C)^2} - \frac{(p_H - p_C)}{m^2 - (p_H - p_C)^2} \right) \\ \kappa(m, p_C, p_H) = & -\frac{1}{2} \left(\frac{(p_H + p_C)}{m^2 - (p_H + p_C)^2} + \frac{(p_H - p_C)}{m^2 - (p_H - p_C)^2} \right) \end{aligned} \quad (122)$$

Similarly, one can derive $\bar{H}_{2x2}^{(2)}$ -- the second order contribution of term 2 in Eq. (9) with itself (i.e. term involving $^1\text{H}-^{13}\text{C}_2$ dipolar coupling cross $^1\text{H}-^{13}\text{C}_2$ dipolar coupling).

In order to obtain a more complete expression of the longitudinal contribution, one should also evaluate the cross-term of the chemical shift tensors of the ^{13}C 's and ^1H 's with themselves:

$$\begin{aligned} \bar{H}_{4x4}^{(2)} + \bar{H}_{5x5}^{(2)} = & \frac{1}{\omega_r} \left[\frac{(\omega_{C_1}^0)^2}{2p_C} + \xi(1, p_C) \omega_{C_1}^1 \omega_{C_1}^1 + \zeta(2, p_C) \omega_{C_1}^2 \omega_{C_1}^2 \right] T_{10}^{C_1} \\ & + \frac{1}{\omega_r} \left[\frac{(\omega_{C_2}^0)^2}{2p_C} + \zeta(1, p_C) \omega_{C_2}^1 \omega_{C_2}^1 + \zeta(2, p_C) \omega_{C_2}^2 \omega_{C_2}^2 \right] T_{10}^{C_2} \\ & + \frac{1}{\omega_r} \left[\frac{(\omega_H^0)^2}{2p_H} + \zeta(1, p_H) \omega_H^1 \omega_H^1 + \zeta(2, p_H) \omega_H^2 \omega_H^2 \right] T_{10}^H \end{aligned} \quad (123)$$

where

$$\zeta(m, p) = \frac{p}{(p^2 - m^2)} \quad (124)$$

The auto-cross term arising from J coupling may also be present, but is generally negligible compared to the $\bar{H}_{\text{JX}}^{(2)}$ type terms considered above. Finally, the $\bar{H}_{\text{JX}}^{(2)}$ cross-terms yield longitudinal T_{10} operators (along the irradiation axis, see Fig. 8-1b) that directly interfere with the ZQ TSAR polarization transfer described in Eq. (118). The relevant Hamiltonian in the ZQ- ^{13}C subspace can hence be described by the following equation:

$$\bar{H}_{\text{ZQ}}^{(2)} = \text{Re}(\omega_{\text{TSAR}}) 2I_X^{C_1 C_2, (23)} I_Z^H + \text{Im}(\omega_{\text{TSAR}}) 2I_Y^{C_1 C_2, (23)} I_Z^H + \omega_{\text{AUTO}} I_Z^{C_1 C_2, (23)} \quad (125)$$

where

$$\omega_{\text{AUTO}} = \frac{1}{\omega_r} \left[\begin{array}{l} \left(\omega_{C_1 H}^1 \omega_{HC_1}^{-1} - \omega_{C_2 H}^1 \omega_{HC_2}^{-1} \right) \chi(1, p_C, p_H) + \left(\omega_{C_1 H}^2 \omega_{HC_1}^{-2} - \omega_{C_2 H}^2 \omega_{HC_2}^{-2} \right) \chi(2, p_C, p_H) \\ \left[\frac{\left(\omega_{C_1}^0 \right)^2 - \left(\omega_{C_2}^0 \right)^2}{2p_C} + \zeta(1, p_C) \left(\omega_{C_1}^1 \omega_{C_1}^{-1} - \omega_{C_2}^1 \omega_{C_2}^{-1} \right) + \zeta(2, p_C) \left(\omega_{C_1}^2 \omega_{C_1}^{-2} - \omega_{C_2}^2 \omega_{C_2}^{-2} \right) \right] \end{array} \right] \quad (126)$$

To summarize, we have learned that the ZQ-TSAR mechanism can potentially be active for all (p_C, p_H) combinations except when $p_H = \pm p_C \pm \{0, 1, 2, 3, 4\}$ or $p_C = \{0.5, 1, 1.5, 2\}$. Moreover, auto-cross terms from both the heteronuclear dipolar interactions and the chemical shift tensors yield contributions that are depicted in the TSAR-subspace introduced above as longitudinal contributions (see Fig. 8-1b). The importance of these longitudinal terms is discussed in Sec. 3.

8.4 Details of the PAR mechanism

8.4.1 Numerical versus analytical simulations

Even though the expressions derived in Sec. 2 provide considerable insight into the spin dynamics in the PAR subspace, we find it instructive to examine numerical simulations that account for the influence of other interactions and higher order terms on the TSAR spin dynamics. As we will see the salient features of the numerical simulations are in excellent agreement with the analytical expressions derived above.

Figure 8-2 shows simulations illustrating the PAR recoupling mechanism for a simple spin system consisting of two directly bonded ^{13}C 's (C_1 and C_2) and a single ^1H directly bonded to the C_1 carbon, with the magnetization initially present on C_1 . The three contour plots in Fig. 8-2a-c represent the C_1 , C_2 and ^1H magnetization after 3 ms of simultaneous $^{13}\text{C}/^1\text{H}$ PAR irradiation respectively. The x-axis and y-axis of the contour plots indicate the rf field strengths applied in units of spinning frequency, ω_r , for the ^{13}C ($p_C = \omega_{1C}/\omega_r$) and ^1H ($p_H = \omega_{1H}/\omega_r$) channels, respectively. The black dashed lines indicate the ^1H - ^{13}C H-H matching conditions (i.e. $p_H = p_C \pm \{1, 2\}$) and the $p_H = p_C$ condition referred later in the text as the $n = 0$ matching condition.

As expected, we observe magnetization transfer from $^{13}\text{C}_1$ to the ^1H at the H-H conditions. However, more we transfer a substantial amount of magnetization to the C_2 for rf fields that depart from the H-H conditions and match the PAR conditions (see Fig. 8-2b). Such favorable areas lie between first order recoupling conditions of H-H and R^3 . The first noticeable area is located just under the $n = 0$ matching condition (^1H power slightly smaller than ^{13}C power) with $p_C > 2$ whereas the second one corresponds to $p_C < 1$ and $p_H > 3$ (Examples of these locations are denoted by X's in Fig. 8-2b). For practical purposes it is important to keep in mind that the first area that uses high power CW irradiations leads to more broadband recoupling mechanism compared to the second area that employs lower power CW ^{13}C irradiation and thus results in more selective recoupling.

As we will see the TSAR term alone [Equation (13)-(15)] is not sufficient to fully explain the features of the PAR optimization map. Thus, in order to obtain a more complete understanding of the underlying spin dynamics, we performed analytical simulations of the magnetization exchange. The spin dynamics in the TSAR subspace are described by Eq. (125) (and depicted in Fig. 8-1b). After averaging over the Euler Angles, we obtain for the polarization transfer efficiency as a function of the irradiation time:

$$\left\{ \begin{array}{l} E = \frac{1}{8\pi^2} \int_{\alpha=0}^{2\pi} \int_{\beta=0}^{\pi} \int_{\gamma=0}^{2\pi} \cos^2(\theta_{\text{eff}}) \sin^2(|\omega_{\text{eff}}|t/2) \sin(\beta) d\alpha d\beta d\gamma \\ \tan(\theta_{\text{eff}}) = \omega_{\text{AUTO}} / \omega_{\text{TSAR}} \\ \omega_{\text{eff}}^2 = \omega_{\text{TSAR}}^2 + \omega_{\text{AUTO}}^2 \end{array} \right. \quad (127)$$

where ω_{eff} , ω_{TSAR} , ω_{AUTO} and θ_{eff} represent the recoupling frequency along the effective tilted axis, the TSAR recoupling frequency, the auto-cross terms contribution and the angle between the transverse TSAR component and the effective tilted component when longitudinal cross terms are considered, for a given crystallite orientation.

Figure 8-3 compares analytical and numerical simulations performed on the same spin system as in Fig. 8-2 (two carbons and one proton, see figure caption for details). Note that these simulations do not include chemical shifts tensors in order to isolate the effect of the ^1H - ^{13}C auto-cross terms on the TSAR spin dynamics. Chemical shift tensors effects can also be accounted using Eq. (126). The resulting analytical simulations are in excellent agreement with numerical simulations shown in Fig. 8-2 (data not shown).

Figure 8-3a shows the polarization transfer from the $^{13}\text{C}_1$ to $^{13}\text{C}_2$ after 1.5 ms of simultaneous CW $^{13}\text{C}/^1\text{H}$ irradiation when only the TSAR term is included. As expected from Eq. (118), we observe an efficient polarization transfer for a wide range of p_C and p_H values. The influence of the inclusion of the auto-cross term (see Eq. (125)) on the overall spin dynamics is illustrated in the analytical simulation in Fig. 8-3b. The structure of the resulting optimization map is very different than in Fig. 8-3a, but very similar to the numerical SPINEVOLUTION simulation in Fig. 8-3c.

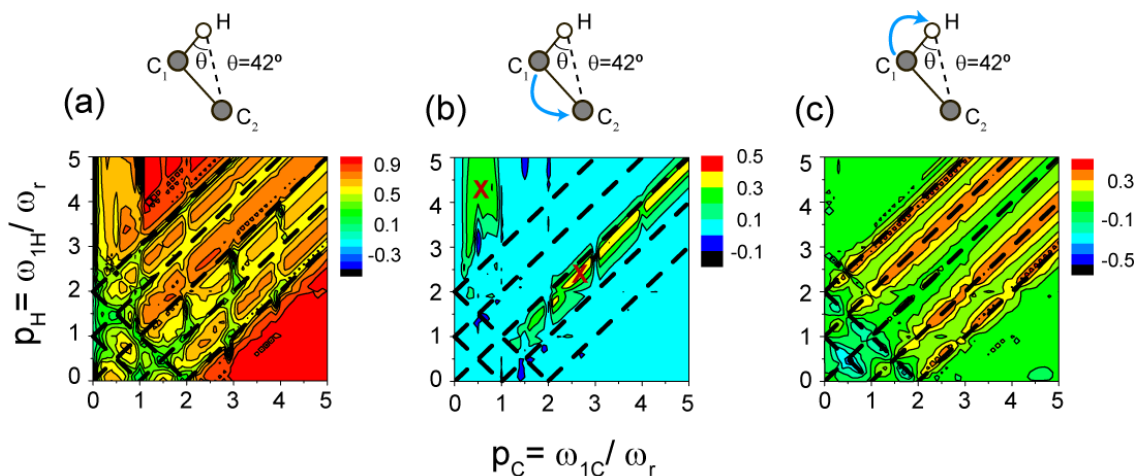


Figure 8-2 PAR optimization map simulated using SPINEVOLUTION⁷⁸. The initial magnetization is on the C_1 spin ($C_{1,x}$ operator) and is detected after 3 ms PAR mixing on the three spins, C_1 spin in (a), C_2 spin in (b) and H spin in (c) ($C_{1,x}, C_{2,x}, H_x$ operators respectively). The spin system is composed of two directly bonded ^{13}C 's and one ^1H bonded to the $^{13}\text{C}_1$ spin (see the inset of the figure). The distance between the $^{13}\text{C}_2$ spin and the ^1H is 2.15 Å. The angle between the two CH dipolar vectors is 42°. Simulations include typical chemical shift tensor values (see SI for details). The black dashed lines indicate that Hartmann-Hahn matching conditions as well as the $n=0$ matching condition.

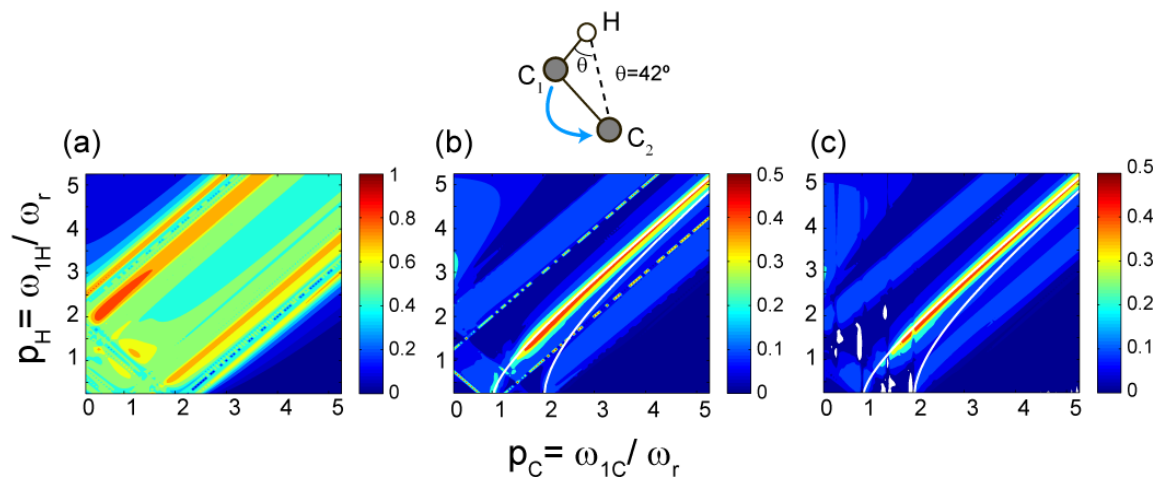


Figure 8-3 PAR optimization maps where the polarization transfer between the ^{13}C is monitored as a function of ^{13}C and ^1H irradiation strengths (in units of ω). The spin system is identical as in Fig. 8-2. No chemical shift interactions were included in these simulations. The three panels represent: (a) analytical simulations of the ^{13}C polarization transfer from $^{13}\text{C}_1$ to $^{13}\text{C}_2$ arising from only the TSAR term; (b) ^{13}C signal intensity showing the analytical simulation obtained with

the TSAR term and the longitudinal auto-cross terms contributions; (c) ^{13}C signal intensity depicting the numerical simulations performed with the SPINEVOLUTION. The two white lines displayed on the contour plots in panels (b) and (c) represent points where $\chi(1, p_C, p_H) = 0$ and $\chi(2, p_C, p_H) = 0$ (i.e. auto-cross terms for spatial components $m=1$ and $m=2$ are equal to 0), described by equations $p_H = \sqrt{p_C^2 - 1}$ and $p_H = \sqrt{p_C^2 - 4}$ respectively.

Note that the TSAR transfer is maximized for points close to the diagonal of the map ($p_C = p_H$, $p_C > 2.25$) and for points where $p_C < 1$ and $p_H > 3$. The optimal rf settings yield a minimal tilt angle θ_{eff} . (i.e. corresponding to points where the TSAR recoupling term dominates the longitudinal T_{10} component). This can easily be seen for the central recoupling condition (near the $n = 0$ matching condition). The two white lines displayed on the contour plots in Fig. 8-3b and 8-3c represent points where $\chi(1, p_C, p_H) = 0$ and $\chi(2, p_C, p_H) = 0$ (i.e. auto-cross terms for spatial components $m=1$ and $m=2$ are equal to 0), described by equations $p_H = \sqrt{p_C^2 - 1}$ and $p_H = \sqrt{p_C^2 - 4}$ respectively. If only one of the two spatial components is taken into account, we clearly observe that either the first or the second conditions maximizes the polarization transfer (see Supporting Information Figure SI 3). In the case where both $m=1$ and $m=2$ components are used, the maximized polarization transfer appears closer to the $m=1$ matching condition, which is consistent with the fact that the TSAR scaling factor is higher for the $m=1$ component. Practically, this means that the optimal transfer will utilize a ^1H rf field slightly smaller than the ^{13}C rf field (with ^{13}C rf $> 2.25 \omega_r$).

The remarkable agreement between Fig. 8-3b and 8-3c demonstrates that second order AHT provides considerable insight into the TSAR process. The TSAR transfer is active as long as the longitudinal off-resonance contribution (auto-cross terms) is sufficiently small, and first order recoupling (H-H, R^3) are avoided. The agreement between the numerical and analytical plots could be further improved by including higher order corrections to the AHT expansion. This does not however appear necessary to understand the fundamentals of the TSAR mechanism.

From the discussion and results above it is clear that the knowledge of longitudinal cross-terms is of primary importance for practical implementations of the TSAR mechanism, and that the maximum TSAR polarization transfer occurs when this

longitudinal component is minimized. The next step is to understand the influence of the various other interactions present in the spin system Hamiltonian during a TSAR polarization transfer. Figure 8-4 illustrates polarization build-up curves corresponding to $p_C=2.6$ and $p_H=2.35$ (indicated with a red cross on the C_2 optimization map in Fig. 8-2). The Fig. 8-4a shows that there is a substantial polarization transfer from C_1 to C_2 with all couplings included in the simulation. Fig. 8-4b depicts the same simulation as in (a) except that the C_1C_2 coupling is absent from the spin system. We note that identical transfer curves are observed Fig. 8-4a and 8-4b illustrating that the polarization transfer does not rely on the C_1C_2 coupling. Since the TSAR mechanism is based on the cross term involving the C_1H and C_2H couplings, we would therefore predict, based on Eqs. (13-15), that removing one or both of the CH couplings would either attenuate or quench polarization transfer from $^{13}C_1$ to $^{13}C_2$. This point is illustrated in Fig. 8-4d and Figs 8-4c and 8-4f, respectively. The small polarization transfer to the H can be mainly explained by cross terms involving the C_1H interactions and through higher order AHT analysis. The proton polarization build-up is indeed almost unchanged when the C_2H couplings and both the C_2H/C_1C_2 couplings are removed (Figs 8-4d and 8-4e). On the contrary, the 1H build-up collapses when the C_1H coupling is removed (Fig. 8-4c). The same explanation should also hold for the C_2H interactions via symmetry arguments, however its effect is not appreciable since the C_2H interaction is much smaller than the C_1H for the particular spin geometry. Thus, only the cross term involving the C_1H dipolar interaction is able to induce polarization transfer from C_1 to 1H on a timescale under 20 ms. Finally, a comparison of Fig. 8-4d and 8-4e shows that the residual slowly-rising C_2 polarization transfer present in Fig. 8-4d does rely on the ^{13}C - ^{13}C couplings. In this case the C_2 polarization is driven by the cross terms involving terms 1 and 3 from Eq. (111). Note, however, that simulation Fig. 8-4b indicates that this contribution is negligible compared to the TSAR term.

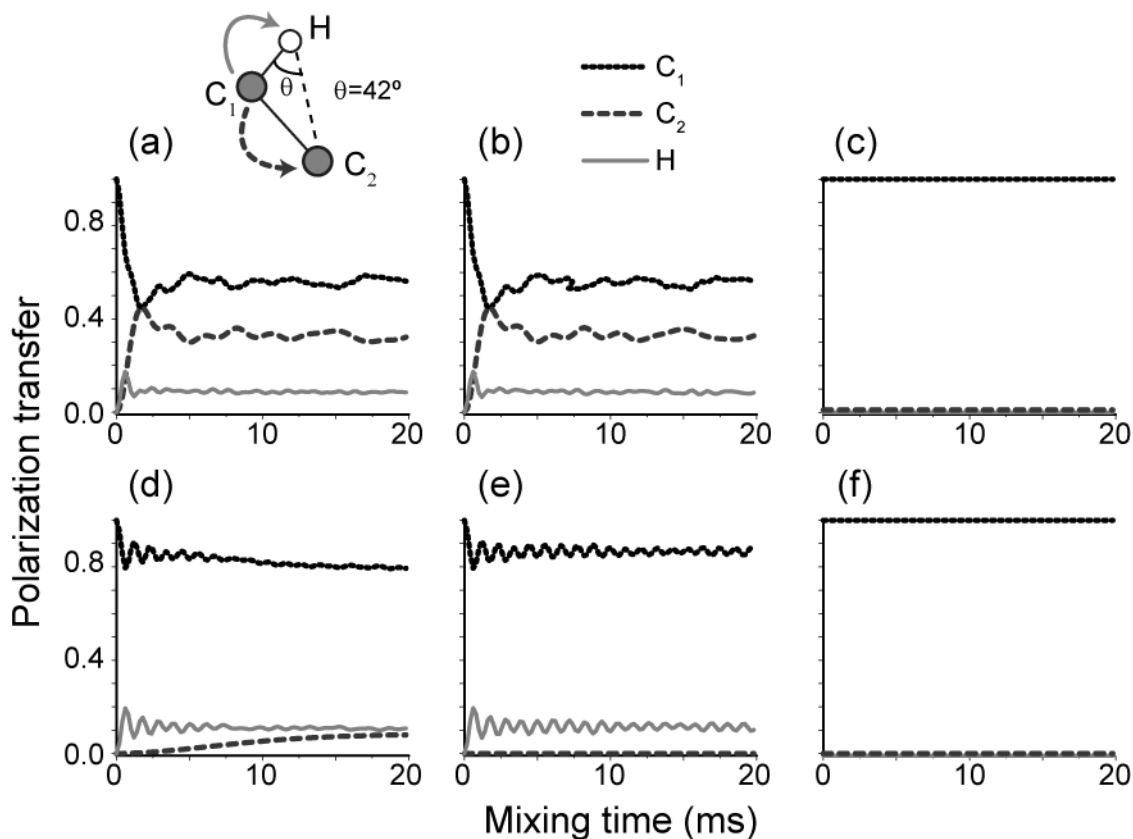


Figure 8-4 Simulations of polarization transfer in the PAR experiment for a HC_1C_2 spin system (same as in Fig. 8-3). No chemical shift is included in the simulations. The PAR ^{13}C and 1H CW rf fields strengths are defined by $p_C=2.6$ and $p_H=2.35$ respectively (see Fig. 8-3b). The panels show simulations including: (a) all dipolar couplings; (b) all couplings except C_1C_2 ; (c) all couplings except C_1H ; (d) all couplings except C_2H ; (e) all couplings except C_2H and C_1C_2 ; (f) all couplings except C_1H and C_2H .

8.4.2 Local geometry dependency

In the discussion above we assumed a model spin system with a particular geometry to analyze the TSAR transfer mechanism. Although this is a useful point of departure, it is clear that the details of the spin system geometry and the averages over the powder Euler angles will influence the TSAR polarization transfer process. We now discuss these two factors in more detail.

As demonstrated above, the TSAR recoupling term is described by Eq. (118). The effective TSAR recoupling frequency contains terms of the form $\omega_{C,H}^m \omega_{H,C_j}^{-m}$

representing the product of the dipolar coupling components. The m -component of the $^{13}\text{C}_i$ - ^1H dipolar coupling interaction can be expressed by the following equation:

$$\begin{aligned}\omega_{C_iH}^m &= \frac{1}{\sqrt{6}} d_{m0}^2(\theta_M) e^{-im\gamma} \sum_{m'} d_{0m'}^2(b_{C_iH}) d_{m'm}^2(\beta) e^{-im'(\alpha+c_{C_iH})} \rho_{20}^{C_iH} \\ &= d_{m0}^2(\theta_M) e^{-im\gamma} \sum_{m'} d_{0m'}^2(b_{C_iH}) d_{m'm}^2(\beta) e^{-im'(\alpha+c_{C_iH})} d_{C_iH}\end{aligned}\quad (128)$$

where $(0, b_{C_iH}, c_{C_iH})$ represents the Euler angles in between the principal axis system (PAS) of the dipolar $^{13}\text{C}_i$ - ^1H interaction and the crystal frame (CF), and (α, β, χ) represent the Euler angles between the crystal frame and the rotor frame (RF). Here the angle between the rotor axis and the B_0 magnetic field is set to the magic angle, i.e. $\theta_M = 54.7^\circ$. Moreover, d_{C_iH} represents the dipolar coupling constant between the $^{13}\text{C}_i$ and ^1H spins, and is related to the inter-nuclear distance by the following identity:

$$d_{C_iH} = -\frac{\mu_0 \gamma_{C_i} \gamma_H \hbar}{4\pi r_{C_iH}^3} \quad (129)$$

where γ is the gyromagnetic ratio of the spin and r_{CH} the distance between the two spins.

In order to simplify the derivation of the expression for $\omega_{C_iH}^m$ $\omega_{HC_j}^{-m}$, one can arbitrarily choose the CF to match the PAS of the $^{13}\text{C}_i$ - ^1H dipolar interaction which implies $(0, b_{C_iH}, c_{C_iH}) = (0, 0, 0)$. We can also rewrite $(0, b_{HC_j}, c_{HC_j}) = (0, \theta, \phi)$, where θ and ϕ represent the spherical coordinates of a system centered on the ^1H spin with the C_iH vector aligned with the z -axis (see Fig. 8-5a).

With the previous simplification,

$$\omega_{C_iH}^m = d_{C_iH} e^{-im\gamma} d_{m0}^2(\theta_M) d_{0m}^2(\beta) \quad (130)$$

and

$$\omega_{HC_j}^m = d_{HC_j} e^{-im\gamma} d_{m0}^2(\theta_M) \sum_{m'} d_{0m'}^2(b_{HC_j}) d_{m'm}^2(\beta) e^{-im'(\alpha+c_{HC_j})} \quad (131)$$

we finally obtain the following two equations for the $m=1$ and $m=2$ components respectively:

$$\omega_{C_{\alpha H}}^1 \omega_{HC_{\beta}}^{-1} = -d_{C_{\alpha H}} d_{HC_{\beta}} \frac{(\sin(2\beta))}{3} \sqrt{\frac{3}{8}} \left(\begin{array}{l} \sqrt{\frac{3}{8}} \sin^2(\theta) \left(\frac{1+\cos(\beta)}{2} \sin(\beta) \right) e^{+2i(\alpha+\phi)} \\ -\sqrt{\frac{3}{8}} \sin(2\theta) \left(\cos^2(\beta) - \frac{1-\cos(\beta)}{2} \right) e^{i(\alpha+\phi)} \\ -\frac{3\cos^2(\theta)-1}{2} \sqrt{\frac{3}{8}} \sin(2\beta) \\ +\sqrt{\frac{3}{8}} \sin(2\theta) \left(\frac{1+\cos(\beta)}{2} - \cos^2(\beta) \right) e^{-i(\alpha+\phi)} \\ -\sqrt{\frac{3}{8}} \sin^2(\theta) \left(\frac{1-\cos(\beta)}{2} \sin(\beta) \right) e^{-2i(\alpha+\phi)} \end{array} \right) \quad (132)$$

$$\omega_{C_{\alpha H}}^2 \omega_{HC_{\beta}}^{-2} = d_{C_{\alpha H}} d_{HC_{\beta}} \frac{\sin^2(\beta)}{6} \sqrt{\frac{3}{8}} \left(\begin{array}{l} \sqrt{\frac{3}{8}} \sin^2(\theta) \left(\frac{1+\cos(\beta)}{2} \right)^2 e^{+2i(\alpha+\phi)} \\ +\sqrt{\frac{3}{8}} \sin(2\theta) \left(\frac{1+\cos(\beta)}{2} \right) \sin(\beta) e^{i(\alpha+\phi)} \\ +\frac{3\cos^2(\theta)-1}{2} \sqrt{\frac{3}{8}} \sin^2(\beta) \\ -\sqrt{\frac{3}{8}} \sin(2\theta) \left(\frac{1-\cos(\beta)}{2} \right) \sin(\beta) e^{-i(\alpha+\phi)} \\ +\sqrt{\frac{3}{8}} \sin^2(\theta) \left(\frac{1-\cos(\beta)}{2} \right)^2 e^{-2i(\alpha+\phi)} \end{array} \right) \quad (133)$$

Equations (132) and (133) show the angular dependence of the TSAR process with respect to the two powder Euler angles α , β and the two polar angles θ , ϕ . Note that the Euler angle γ is absent from the recoupling frequency, and thus the TSAR mechanism appears as a γ -compensated recoupling mechanism.

Figure 8-5a shows the TSAR polarization transfer for a three spin system similar to the one in Fig. 8-2. More specifically, the system is composed of a directly bonded $^{13}\text{C}_1$ -H spin pair and a $^{13}\text{C}_2$ located on a sphere of constant radius centered on the proton spin (see Fig 8-5a). The polarization transfer from C_1 to C_2 after 4.2 ms is illustrated on the spherical map shown in Fig. 8-5a. A substantial polarization transfer is present over the entire sphere with maxima occurring around the poles and the equator. The polarization

transfer efficiency does not depend on the ϕ -angle because of the α -averaging over a period and has a very interesting dependence on the θ -angle.

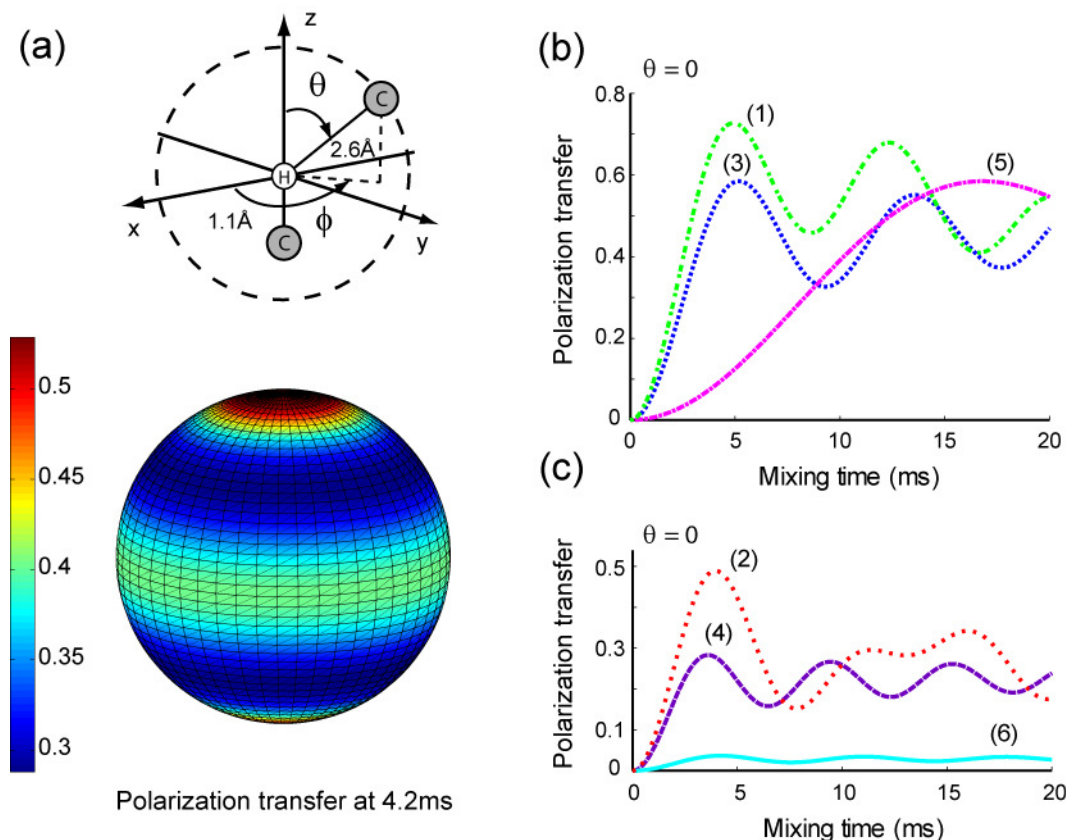


Figure 8-5 Dependence of PAR polarization transfer on the local geometry of the spin system. (a) The three-spin system geometry used in the simulations: the first ^{13}C and the ^1H are fixed in space, whereas the second ^{13}C position is defined by θ and ϕ the spherical coordinates with the origin at the ^1H . The distances between the ^{13}C 's and the ^1H are constant and respectively equal to 1.1 and 2.6 Å. The spherical map represents the ^{13}C - ^{13}C polarization transfer efficiency for a TSAR mixing time of 4.2 ms using $p_C=2.75$ and $p_H=2.5$. Polarization transfer for $\theta = 0$ orientation (aligned geometry) as a function of time is presented in panels (b) and (c). The buildup curves noted from (1) to (6) represent analytical simulations with: (1) both $m=1$ and $m=2$ components without auto-cross terms, (2) both $m=1$ and $m=2$ with auto cross terms, (3) and (4) only $m=1$ without and with auto-cross terms, (5) and (6) only $m=2$ without and with auto-cross terms.

The angular dependence of the TSAR mechanism is given in Eq. (119), and the recoupling frequency is composed of four terms that can be rewritten as:

$$\omega_{TSAR} = \frac{1}{\omega_r} \left[\underbrace{\text{Re}(\omega_{C_1H}^1 \omega_{HC_2}^1) \lambda(1, p_C, p_H) + i \text{Im}(\omega_{C_1H}^1 \omega_{HC_2}^1) \sigma(1, p_C, p_H)}_{\omega_{TSAR}^1} + \underbrace{\text{Re}(\omega_{C_1H}^2 \omega_{HC_2}^2) \lambda(2, p_C, p_H) + i \text{Im}(\omega_{C_1H}^2 \omega_{HC_2}^2) \sigma(2, p_C, p_H)}_{\omega_{TSAR}^2} \right] \quad (134)$$

The first and second terms of Eq. (31) correspond to the $m=1$ and $m=2$ components, respectively. We note that all of the analytical simulations shown in Fig. 8-5 were performed assuming $p_C=2.75$ and $p_H=2.5$, and that these values were chosen based on numerical simulations of the same system. In particular, they maximize the polarization transfer after 4.2 ms, but maintain the rf strengths within experimentally reasonable limits (≤ 55 kHz in this case). The rf field strengths (in units of the MAS frequency) almost fulfill the matching condition $p_H = \sqrt{p_C^2 - 1}$ that corresponds to points when the $m=1$ component of the auto-cross term is cancelled. This reduction of the longitudinal contribution results, for example, in about 50% maximum polarization transfer in 4.2 ms for geometry corresponding to the spins close to the poles of the sphere (see Fig. 8-5).

In order to gain additional insight in the TSAR process (or more specifically to comment on maximum theoretical efficiency of the TSAR process), we can choose $\theta=0$ and simulate the TSAR polarization transfer when all three spins are aligned. In this case, Eq. (132) and (133) simplify yielding a $\sin^2(2\beta)$ and $\sin^4(\beta)$ dependence for the $m=1$ and $m=2$ component, respectively. Figure 8-5b shows the corresponding analytical magnetization buildup curves (1) to (6) where, in the case without inclusion of the auto-cross terms, both the $m=1$ and $m=2$ contribution reaches a theoretical maximum of $\sim 58\%$ (3) and (4). The difference in buildup times, i.e. slower for the $m=2$ component, is also consistent with the $\sin^2(2\beta)$ and $\sin^4(\beta)$ dependence. Interestingly, when both components simultaneously contribute to the transfer, the maximum polarization is enhanced by constructive interference of the two-component process. Note that in the case of first order γ -encoded recoupling sequences, the Euler angle dependence is $\sin(2\beta)$ and $\sin^2(\beta)$, yielding a theoretical maximum of $\sim 73\%$.^{12, 14, 79} Including longitudinal auto-cross terms (see Eq. (126)) leads to an attenuation of the

magnetization transfer in the three spin case mentioned above. The attenuation is more significant for the $m=2$ component due largely to the choice of rf power levels, and consequently scaling factor of the spin part. Indeed, as mentioned above, p_C and p_H were chosen (in this simulation) in order to minimize the $m=1$ component of the auto cross terms. When both the $m=1$ and $m=2$ components are included, the maximum efficiency can still reach around 50% transfer.

The TSAR transfer should thus be seen as a superposition of two simultaneous recoupling pathways involving the $m=1$ and $m=2$ components, and we can decompose the contributions of the different components arising from the two cross-terms and the auto-cross terms. Figure 8-6 shows maps of polarization transfer efficiency as a function of the θ -angle and the mixing time (with $\phi=0$ since as we have shown above ϕ does not influence the transfer). The $m=1$ pathway (Fig. 8-6a-b) has a better scaling factor than the $m=2$ component (Fig. 8-6c-d). This can easily be understood by examining Eqs. (132) and (133). The comparison between Fig. 8-6a and Fig. 8-6b shows the influence of the auto-cross terms for the $m=1$ component. The overall features of Fig. 8-6a are preserved with some attenuation, except around $\theta=0^\circ$ and $\theta=180^\circ$, where the auto-cross terms quench the TSAR polarization transfer. This effect can be explained by noting that the orientation dependence of the $m=1$ TSAR frequency and the $m=1$ auto-cross terms are identical for $\theta=0^\circ$ or 180° , and limited to the β -angle. Even if the choice of p_C and p_H terms are identical for $\theta=0^\circ$ or 180° , and limited to the β -angle. Even if the choice of p_C and p_H minimizes the importance of this longitudinal contribution, its effect is further enhanced when the orientation dependence is identical: i.e. both the $m=1$ TSAR and auto-cross term are minimized for $\beta=0, \pi/2$ and maximized for $\beta=\pi/4, 3\pi/4$. For the $m=2$ component (Fig. 8-6c-d), the effect of the auto-cross terms is larger. This once again is related to the choice of p_C and p_H that strongly attenuates the $m=1$ auto-cross terms compared to the $m=2$ condition. For similar reasons as with $m=1$, the area around $\theta=0^\circ$ and $\theta=180^\circ$ is the most affected. The last two panels -- Fig. 8-6e-f -- show similar simulations as the previous panels but with both the $m=1$ and $m=2$ components included. In this case, the two components constructively interfere yielding 50-70% transfer with and without inclusion of the auto-cross terms.

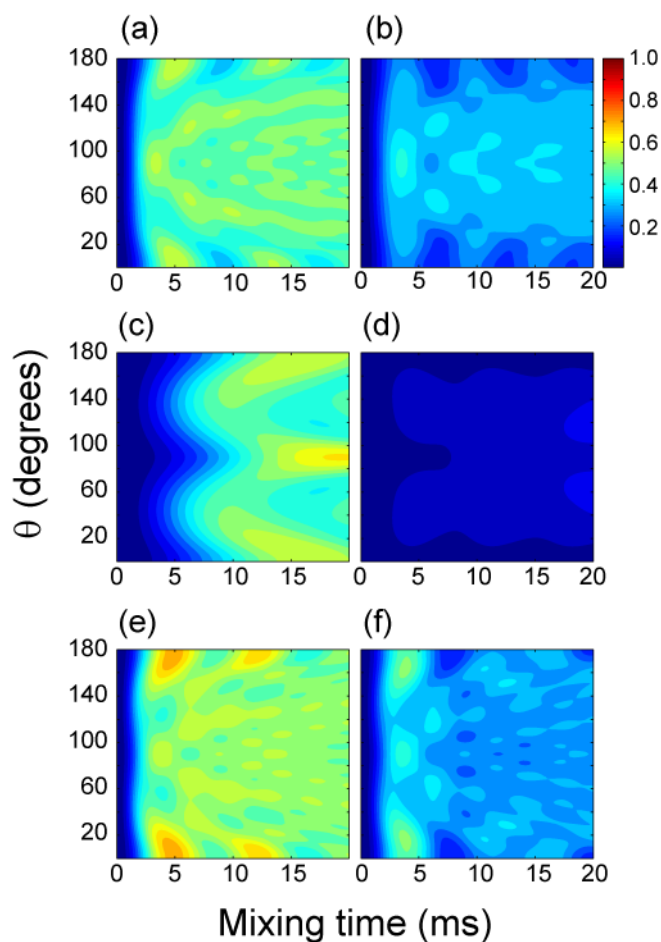


Figure 8-6 Analytical contour plots of the TSAR polarization transfer arising from the $m=1$ and $m=2$ components as a function of θ angle for a three spin system described in Fig 8-5a with the mixing time and irradiation settings used in Fig. 8-5 with $\phi=0$. (a) $m=1$ TSAR component, (b) $m=1$ TSAR term plus $m=1$ auto-cross term components, (c) $m=2$ TSAR component included, (d) $m=2$ TSAR term and $m=2$ auto-cross term components, (e) $m=1$ and $m=2$ TSAR components, (f) $m=1$ and $m=2$ TSAR plus $m=1$ and $m=2$ auto-cross term components.

Note that the rf settings that maximize the transfer for a spin system can be understood as a compromise between minimizing the auto-cross terms and maximizing the constructive interference of the two TSAR pathways ($m=1$ and $m=2$), given that they do have a different dependence on θ and the Euler angles, and thus different scaling factors.

8.4.3 Auto-cross term compensation

The spin system that we have studied thus far is composed of a directly bonded $^{13}\text{C}_1$ - ^1H spin pair and a third $^{13}\text{C}_2$. As we have seen, the optimal rf fields correspond to points that minimize the size of the auto-cross terms. From Eq. (126), we also surmise that the TSAR auto-cross terms disappear when the assisting spin is equidistant from $^{13}\text{C}_1$ and $^{13}\text{C}_2$. This situation is encountered for the spin system in Fig. 8-7 where the three spin are aligned and the ^1H is at 3 Å from each of the ^{13}C 's ($r_{\text{CC}}= 6$ Å). The analytical simulation in Fig. 8-7 shows that efficient polarization transfers can be achieved over a wider range of rf levels. Since the heteronuclear auto-cross term is absent in Fig. 8-7a, the optimal rf fields correspond only to the maximum interference between the $m=1$ and $m=2$ components of the TSAR recoupling frequency. Note that in this case over 85% of the polarization is transferred for a 6 Å distance in 60 ms.

Other examples illustrating various levels of auto-cross term compensation with different spin system geometries can be found in the Supporting Information. Figure SI4 shows the PAR polarization transfer map in the case of a non-aligned three spin system where the ^1H spin is equidistant from the two ^{13}C 's. In such a situation, the off-resonance contribution from the auto-cross terms is null in the ZQ TSAR subspace. Figure SI5 illustrates that in the case of a non symmetric spin system (i.e. two different couplings corresponding to a case where the proton is directly bonded to C_1 and at 4.9 Å from C_2), the polarization transfer occurs only along the white line corresponding to the cancellation of the $m=1$ off-resonance auto-cross terms. In this case the influence of the auto-cross terms is significant because of the very different ^1H - ^{13}C interactions involved.

The auto-cross terms compensation can be generalized as soon as each of the two ^{13}C 's are coupled equally to the ^1H . This is illustrated in Fig. SI6 with the example of 4 spin system consisting of 2 carbons with one directly bonded proton each. In Fig. SI6a the symmetry of the spin system ensures that the ZQ-TSAR off resonant contributions vanishes (see Eq. 24). The effect of the geometrical auto-cross term compensation can be seen in the map shown in Fig. SI6a since the TSAR mechanism is active over a large part of the map and does not need to be close to the two lines defined by $\chi(1, p_C, p_H) = 0$ and $\chi(2, p_C, p_H) = 0$. If the spin system symmetry is broken (as in Fig

SI6b), the ZQ off-resonance contribution is no longer zero, but still sufficiently small so that Fig SI6b looks closer to Fig SI6a compared to the case where only one proton is considered (Fig SI6c).

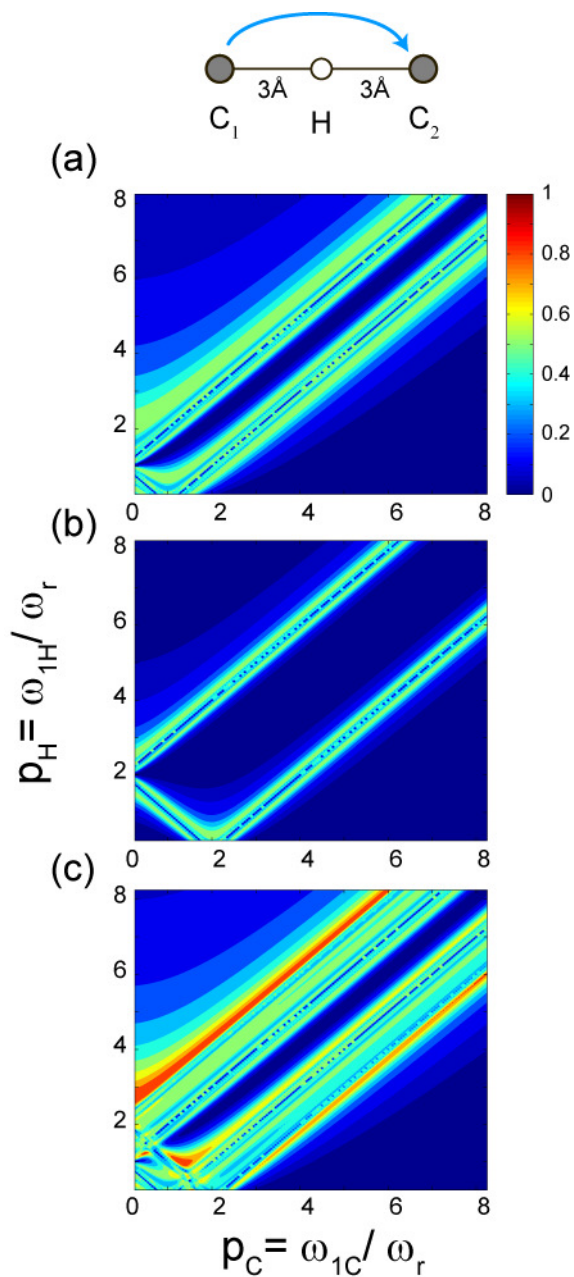


Figure 8-7 Analytical contour plots of the TSAR polarization transfer for an aligned symmetrical three spin system with $r_{CC} = 6 \text{ \AA}$ (see the inset): (a) $m=1$ component, (b) $m=2$ component, (c) both $m=1$ and $m=2$ components included. Note the constructive interference of the $m=1$ and $m=2$ components that leads to an improved polarization transfer in (c).

In practice, this means that the ZQ off-resonant auto-cross term is intrinsically reduced when considering a TSAR transfer between same types of groups (e.g. CH and CH, CH₂ and CH₂, CH₃ and CH₃) and that the TSAR effect is much easier to fulfill in this case (which is manifest as broader rf powers leading to appreciable TSAR effect).

8.4.4 Experimental results: long distance ¹³C-¹³C contacts in [U-¹³C,¹⁵N]-f-MLF-OH

The simulations in Sec. 3.1 and 3.2 demonstrate and explain the PAR mechanism for ¹³C-¹³C polarization transfer. To confirm these predictions with experimental data we show in Fig. 8-8a 2D PAR ¹³C-¹³C correlation spectrum obtained from a tripeptide [U-¹³C,¹⁵N]N-f-MLF-OH diluted to 10% in a natural abundance lattice which insures that the observed contacts are due to the intra-molecular interactions. PAR clearly allows polarization transfer between ¹³C's separated by medium to long distances. For example, the circled cross-peaks correspond to ¹³C-¹³C distances ≥ 4 Å.

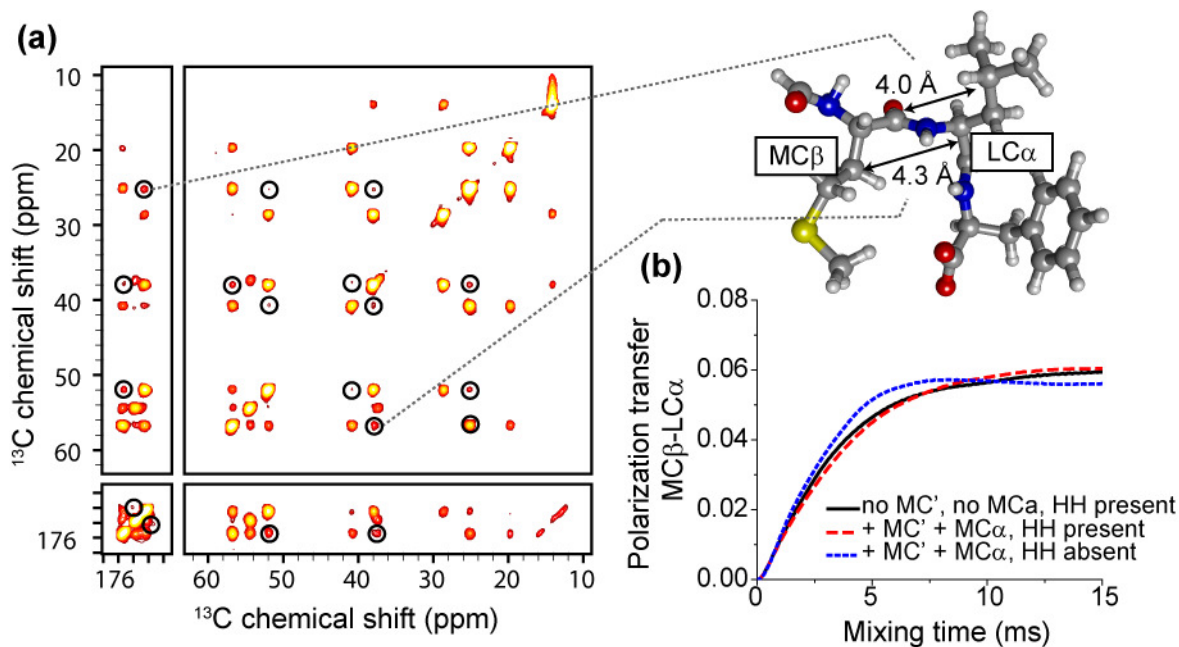


Figure 8-8 (a) 2D ¹³C-¹³C correlation spectrum of [U-¹³C,¹⁵N]N-f-MLF-OH diluted to 10% in a natural abundance lattice. The spectrum was recorded $\tau_{\text{mix}}=7.5$ ms on 750 MHz spectrometer

(^1H frequency) with $\omega_r/2\pi = 20$ kHz, $\omega_{1\text{C}}/2\pi \approx 50$ kHz, $\omega_{1\text{H}}/2\pi \approx 47$ kHz, and the offset on the ^{13}C channel was set to 101 ppm. The circled cross-peaks in the spectrum are due to attenuated dipolar truncation in the PAR experiment and correspond to ≥ 4 Å ^{13}C - ^{13}C distances. (b) Numerical simulations of PAR polarization transfer between MC_β and LC_α (corresponding to the highlighted 4.3 Å distance) using rf power levels specified in (a). The spin system includes nearby protons ($2x\text{MH}_\beta$, MC_α , LH_α , LH) (back solid line), nearby protons plus MC_α and MC' (red dash line). The dotted blue line represents simulation on a spin system including nearby protons plus MC_α and MC' with the ^1H - ^1H couplings removed from the calculation. Simulations include typical chemical shift tensor values (see SI for details). The plot illustrates that the contribution of the polarization relayed through MC_α and MC' to the polarization transfer between MC_β and LC_α is negligible compared to the direct polarization transfer.

8.5 Polarization transfer in uniformly labeled systems

The presence of cross peaks corresponding to long ^{13}C - ^{13}C distances in the 2D spectrum of $[\text{U-}^{13}\text{C}, ^{15}\text{N}] \text{N-f-MLF-OH}$ shown in Fig. 8-8 raises important questions about the mechanism of the polarization transfer. Specifically, to what extent is the dipolar truncation reduced in the PAR experiment? What is the contribution of ^{13}C - $[\text{H}]$ - ^{13}C relayed polarization to the cross peak intensities? And, how can we extend the description of the PAR mechanism from a model three spin process involving a single ^1H to a real lattice where multiple assisting ^1H 's spins can contribute?

8.5.1 Dipolar truncation and long distance transfer

The first question raised above concerns dipolar truncation, which alludes to the difficulty of detecting cross peaks corresponding to long distances arising from weak couplings in the presence of strong dipolar couplings.⁸⁰⁻⁸² This phenomenon is illustrated in Fig. 8-9a with the example of a first order broadband CM_5RR where, in the absence of a directly bonded C_β spin, we achieve significant polarization transfer from the C_α spin to the C_{remote} spin (dashed black line) with a ~ 25 ms buildup time for a 4.5 Å distance. However, in the presence of C_β spin, the polarization transferred from C_α to the C_{remote} (dash-dot red line) is severely attenuated. Note that in the latter case

most magnetization is sent to the directly bonded C_β spin. Thus, for example γ -encoded dipolar recoupling sequences^{12-14, 79, 83} exhibit spectra that are dominated by one-bond relayed transfer mechanism and thus provide excellent tools for assigning ^{13}C - ^{13}C spectra of proteins.⁸⁴

However, in order to determine 3D structures it is necessary to measure weak couplings corresponding to structurally important long distances in the presence of the strong couplings from directly bonded neighbors. Thus, the design of new polarization transfer methods that suppress ^{13}C - ^{13}C dipolar truncation in uniformly ^{13}C labeled compounds is an area of active research. The initial solutions proposed for this problem were approaches based on frequency selective ^{13}C - ^{13}C recoupling methods such as rotational resonance (R^2) and its variants -- R^2 Tickling⁵⁴, R^2 Width^{24, 25, 55} and R^2 in the tilted rotating frame ($R^2\text{TR}$)^{26, 56, 57}. More recently, additional experimental approaches, other than spin diffusion, were introduced and tested on model compounds with the aim of circumventing truncation and providing more accurate ^{13}C - ^{13}C distance restraints.

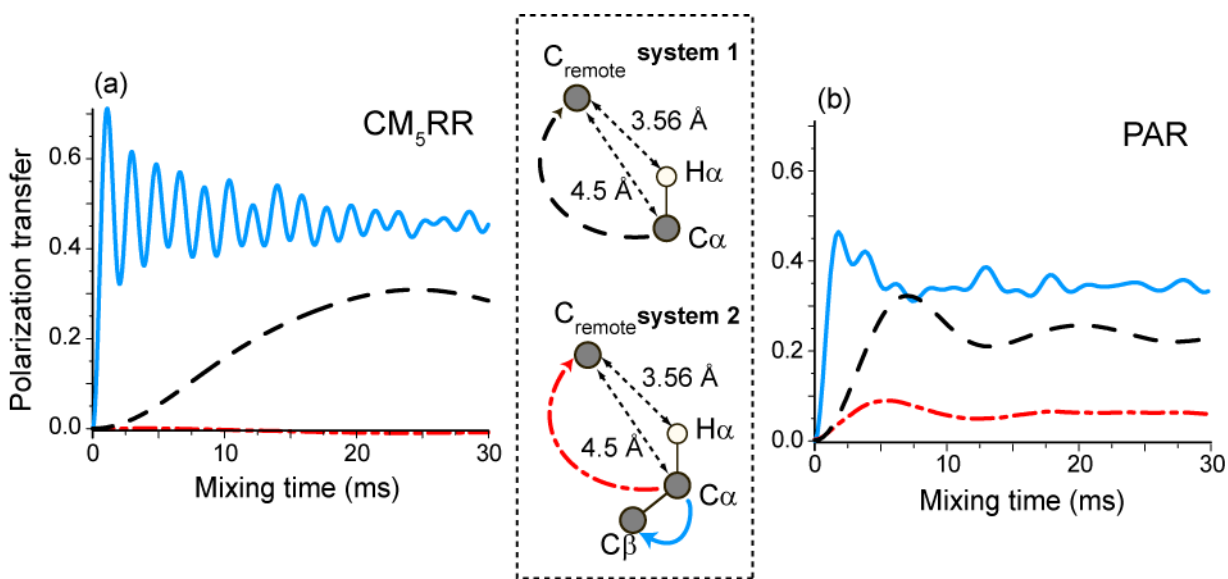


Figure 8-9 Illustration of dipolar truncation in the CM_5RR and PAR homonuclear recoupling schemes. Spin system 1 is composed of a directly bonded $C_\alpha\text{H}_\alpha$ pair and a C_{remote} spin 4.5 Å and 3.56 Å distant from the C_α spin. In the spin system 2, a C_β spin, directly bonded C_α , is added. (a) The black dashed line depicts the polarization transfer ($\sim 30\%$) from C_α to C_{remote} ($r_{C:C} = 4.5$ Å) using the broadband DQ CM_5RR in the three spin system 1. When a directly bonded C_β spin is added to the spin system ($r_{C:C} = 1.5$ Å), the polarization transfer to the C_{remote} (red dash-dot line) is quenched for CM_5RR with most of the polarization being transferred to the directly bonded

C_β (blue solid line) thus demonstrating the phenomenon of dipolar truncation. (b) In the PAR simulation the presence of a third strongly coupled spin leads to a partial decrease of polarization transfer to C_{remote} [(b) red dash-dot line] showing that dipolar truncation is attenuated in the TSAR transfer mechanism. Simulations were performed with SPINEVOLUTION⁷⁸ $\omega_r/2\pi = 20$ kHz, $\omega_{0H}/2\pi = 750$ MHz ^1H frequency, and do not include chemical shifts.

The first category includes the SEASHORE (Shift-Evolution-Assisted Selective HOmonuclear Recoupling) and COMICS (COsine Modulated recoupling with Isotropic Chemical Shift reintroduction) experiments, which rely on the use of chemical shift interactions to dephase unwanted DQ coherences. In the SEASHORE approach DQ excitation periods are alternated with delay windows where DQ coherences are dephased except if the carrier frequency matches the mean offset of the two carbons.⁵⁸ COMICS is based on the generalization of the second averaging principle and consists of the application of two successive averaging fields equal to $0.25 \omega_r$ that simultaneously reintroduce the isotropic chemical shift interaction and the DQ dipolar terms leading to an extremely narrowband sequence.¹⁴

The second category relies on the active truncation of a ZQ dipolar Hamiltonian by chemical shift tensors,⁵⁹ an approach recently introduced by Marin-Montesinos and employed in the TOFU-RADAR (Triple Oscillating Field techniqUe - Rotor Assisted DipolAr Refocusing) experiment.⁶⁰ Whereas COMICS relies on a two step averaging at $0.25 \omega_r$, TOFU-RADAR adds a third averaging step that produces the recoupling of the ZQ dipolar interaction and the chemical shift tensor. To date these sequences have been demonstrated on uniformly labeled model systems and allow measurement of ^{13}C - ^{13}C distances from sites selected using a Gaussian inversion pulse.

The PAR approach differs significantly from the methods presented above since the spin dynamics does not depend on the ^{13}C - ^{13}C couplings and involves couplings to the surrounding protons. One of the important consequences of such original mechanism is the reduction of dipolar truncation compared to first order ^{13}C - ^{13}C recoupling sequences. *This is illustrated in Fig. 8-9b where in the presence of the C_β spin, and in contrast to broadband DQ CM_5RR recoupling, we can still transfer a significant amount of polarization between C_α and C_{remote} spins.*

Such findings are further reinforced by the experimental data presented in Fig. 8-10, which shows 2D ^{13}C - ^{13}C correlations spectra obtained on the [U- ^{13}C , ^{15}N]-Crh protein with (a) CM₅RR and (b) PAR. The CMRR mixing is 800 μs in order to detect only one-bond ^{13}C - ^{13}C dipolar transfer (negative cross peaks in blue). In contrast 14 ms PAR mixing time yields many more ^{13}C - ^{13}C contacts corresponding to ^{13}C - ^{13}C distances of up to 6 Å.

Examples of medium and long distance contacts are marked on the PAR spectrum and on the green part of the Crh structure representation in the inset of the Fig. 8-10. Most of them correspond to contacts between different secondary structure elements and should be very important to constrain the fold of the protein. The next two paragraphs investigate in details the nature of the PAR polarization transfer, i.e. relayed versus direct, as well as the possibility to extract distance estimates from PAR data on uniformly ^{13}C labeled spin systems.

8.5.2 Multiple spins mechanism: relayed versus direct polarization transfer

The second issue relates to the mechanism of the polarization transfer between distant spins, i.e. is the polarization transfer directly through space or is it relayed via a chain of ^{13}C 's and which are the ^1H 's involved in the TSAR mechanism. As shown in this section the answer strongly depends on the topology of the spin system with the considered ^{13}C - ^{13}C distance. Nevertheless, it is possible to predict some qualitative general trends that are useful for evaluating the reliability of the distance estimates for various cases.

As we have already mentioned only the ^1H 's closest to the considered ^{13}C 's contribute significantly to overall polarization transfer. Figure SI7 considers PAR polarization transfer as a function of a ^1H - ^{13}C distance for several different three spin topologies. From these simulations it is apparent that the main contribution to the PAR polarization transfer involves directly bonded ^1H - ^{13}C spin pairs (since they result in the stronger TSAR couplings). At the same time, it is also clear that, in order to accurately simulate the polarization transfer, ^1H 's other than those that are directly bonded to ^{13}C 's

also have to be considered. Indeed the simulations from Fig. SI7 suggest that in general the inclusion of the ^1H 's within 2.5\AA of the ^{13}C 's should lead to an adequate description of the spin dynamics. The contributions from more remote protons have TSAR couplings that are small and do not significantly alter the spin dynamics on the timescale of $\sim 20\text{-}30$ ms. For example, even in the very favorable case described in Fig. 8-8 where the remote proton is at an equal distance of 3\AA from the ^{13}C 's, the PAR polarization transfer requires more than 100 ms to achieve a maximum.

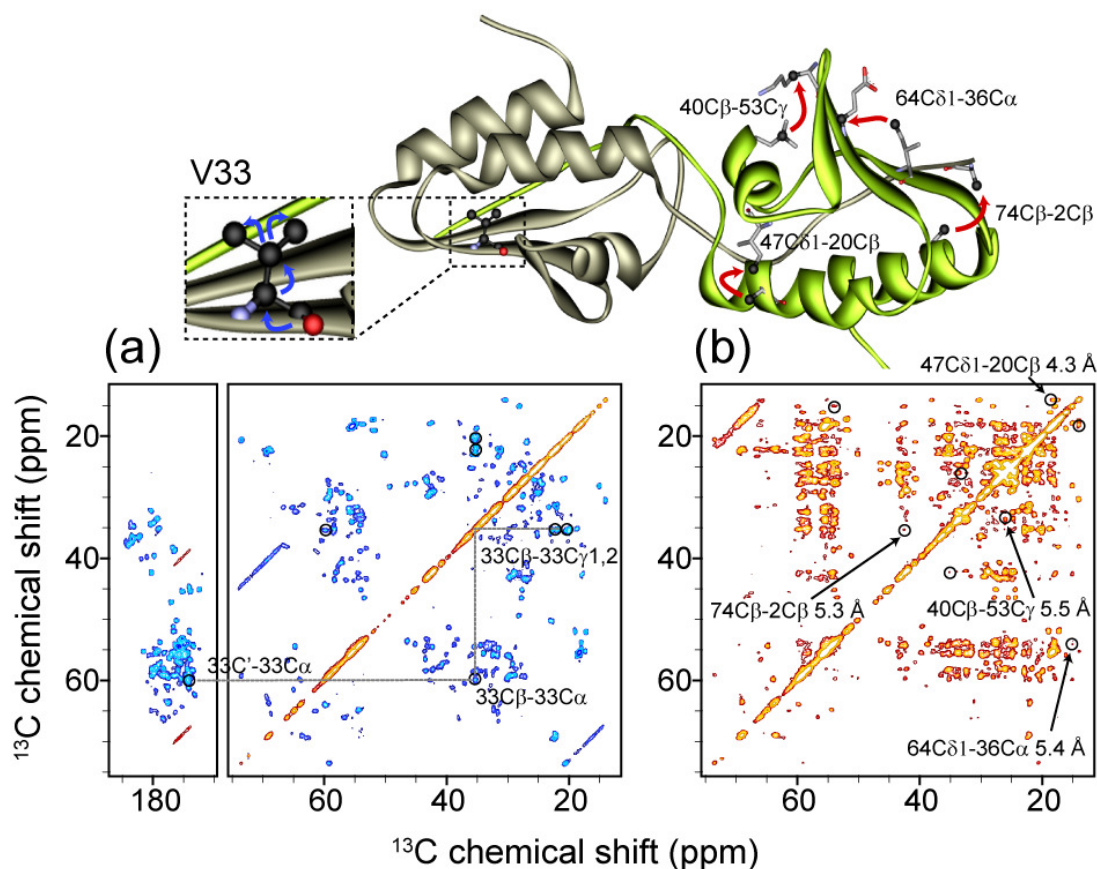


Figure 8-10 2D ^{13}C - ^{13}C correlation spectra of $[\text{U-}^{13}\text{C},^{15}\text{N}]$ -Crh protein comparing two advanced recoupling pulse sequences at $\omega_{0\text{H}}/2\pi = 750$ MHz ^1H Larmor frequency and $\omega_r/2\pi = 20$ kHz MAS spinning frequency: (a) Broadband CM_5RRC spectrum corresponding to $800\ \mu\text{s}$ ^{13}C irradiation of ~ 100 kHz displaying only one-bond dipolar ^{13}C - ^{13}C cross peaks (see the gray monomer of the Crh dimer structure representation in the inset). Note that the spectrum was acquired in ~ 15 h without ^1H irradiation during the CM_5RRC mixing time. (b) PAR spectrum corresponding to 14 ms ^{13}C and ^1H CW irradiations displaying long short, medium and long

distance ^{13}C - ^{13}C cross-peaks. Several illustrative examples are shown on the green monomer of the Crh dimer structure representation.

The relative contribution of ^{13}C relayed versus direct polarization transfer is illustrated below for three typical spin systems encountered in proteins. In all cases, the PAR polarization transfers correspond to structurally valuable ^{13}C - ^{13}C distances ($> 4 \text{ \AA}$). Let us first examine the case of a sequential *inter-residue polarization transfer* between Met- C_β and Leu- C_α ($r_{\text{C-C}} = 4.3 \text{ \AA}$) in N-*f*-MLF-OH (one of the cross-peaks highlighted in Fig. 8-9a). The SPINEVOLUTION simulations of the polarization transfer are displayed in Fig. 8-8b and highlight the influence of other nearby spins. The black solid line corresponds to the case with only neighboring ^1H 's included in the simulation, the red dashed line includes adjacent ^1H 's, Met- C_α and Met- C' . The fact that the simulations from these three cases overlap indicate that the Met- C_α and Met- C' (i.e. ^{13}C 's in between Met- C_β and Leu- C_α) do not really alter the polarization transfer between Met- C_β and Leu- C_α . The polarization transfer is dominated by the Met- C_β - ^1H -Leu- C_α TSAR coupling, and thus the ^{13}C relayed magnetization is a negligible fraction of the overall magnetization transferred.

It is, however, possible to find spin systems where the situation is more complicated and where nearby ^{13}C 's do influence a particular magnetization transfer. This is illustrated in Fig. SI8 for an *intra-residue polarization transfer* along the leucine sidechain. Here we consider two cases: from Leu C_α to Leu C_δ and to Leu $\text{C}_{\delta'}$ in [^{13}C , ^{15}N]-N-*f*-MLF-OH. These very interesting cases illustrate that the nearby carbons (here C_β and C_γ) can influence the polarization transfer in different ways. In the case of the Leu C_α to Leu C_δ transfer, the polarization transfer maximum is significantly decreased but the buildup time is very similar with C_β and C_γ included and without C_β and C_γ . In this case, the decrease of overall efficiency is explained by the fact that the initial magnetization present on the Leu C_α is now distributed over three spins. However, because the buildup time is essentially constant, the polarization transfer is mainly direct. In the case the Leu C_α to Leu $\text{C}_{\delta'}$ transfer, the buildup time is changed when we include C_β and C_γ in the simulation, accounting for the fact that a substantial

part of the polarization transfer in this case is relayed by the C_β and C_γ carbons. This is consistent with the fact that, as shown on Fig. SI8, the C_β and C_γ carbons are located in the path between the C_α and C_{δ_2} spins.

Note that the three-bond PAR polarization transfers from LC_α to LC_δ and $LC_{\delta'}$ with C_β and C_γ included in the simulation are almost identical even though the ^{13}C - ^{13}C distance differ by almost 1 Å. This means that *intra-residue* contacts may generally lead to inaccurate ^{13}C - ^{13}C distance estimates that are not useful restraints for structure determination.

The ^{13}C relayed TSAR mechanism between two distant ^{13}C spins is likely to be non-negligible for spin topologies where additional carbons are located in between them. Cases, with larger TSAR relayed couplings than direct TSAR coupling, will be mainly encountered for medium distance (more than two-bond) intra-residue transfers, sequential contacts (except for $^i\text{C}_\alpha$ $^{i+1}\text{C}_\alpha$ $^i\text{C}_\alpha$ $^{i+1}\text{C}_\beta$). For the rest of the inter-residue transfer, as demonstrated in the next section, it is possible to relate the PAR experimental data to ^{13}C - ^{13}C distance estimates and to use them for protein structure determination in an approach analogous to NOE-based methods in solution NMR.

8.5.3 ^{13}C - ^{13}C Crh distance estimates from ^{13}C - ^1H - ^{13}C PAR data

In Sections 3 and 4 we described the TSAR mechanism in the case of three spins, where only one proton is involved. As we have seen in Sec. 3.2 the PAR polarization transfer depends on the local geometry in the three spin case. It is important to determine how this translates to situations where multiple ^1H 's are involved in the mechanism, and if the polarization transfer can be used to estimate ^1H - ^{13}C or ^{13}C - ^{13}C distances in spin topologies where the contribution of relayed transfers are negligible.

Fig. 8-11a-d shows experimental polarization build-up curves for a number of unambiguously assigned ^{13}C - ^{13}C pairs obtained using the PAR technique on a [^{13}C , ^{15}N]-Crh protein dimer at $\omega_0/2\pi = 900$ MHz ^1H frequency and $\omega_r/2\pi = 20$ kHz MAS. The polarization transfer curves are sorted into different classes depending on the corresponding ^{13}C - ^{13}C distance extracted from the x-ray structure (1MU4⁸⁵). Fig. 8-11a corresponds to one-bond distances, (b) to two-bond distances, (c) to medium and (d) to

long distance classes. The first two panels (a)-(b) represent intra-residue contacts whereas the last two panels (c)-(d) show inter-residue distance ranging from 4 to 7 Å.

Buildup curves corresponding to one-bond distances are easily distinguishable from other polarization transfers: the maximum signal occurs at around 2 ms and the intensity is larger than any other distance transfer. In this case, directly bonded ^1H 's are primarily contributing to the transfer since their TSAR couplings are dominant. Figure 8-11b shows PAR polarization transfer corresponding to two-bond distances and the optimal buildup time is about 5 ms. Figure 8-10c shows *medium distance inter-residue transfer* corresponding to the 4 - 5.5 Å distances, and the buildup time is around 5 to 10 ms with the maximum efficiency is comparable to the two-bond distance case. Note that it does not seem possible to differentiate between the distance classes in Fig. 8-11b and 8-11c based on the polarization profiles alone. For longer *non-sequential inter-residue* distance (>5.5 Å), the PAR buildups are quite distinguishable with the optimal polarization transfer occurring around $\tau_{\text{mix}}=15$ ms. Note that in this case, the polarization transfer efficiency is set to zero for PAR mixing time equal to 2 and 5 ms because the cross peaks intensities were below the noise level.

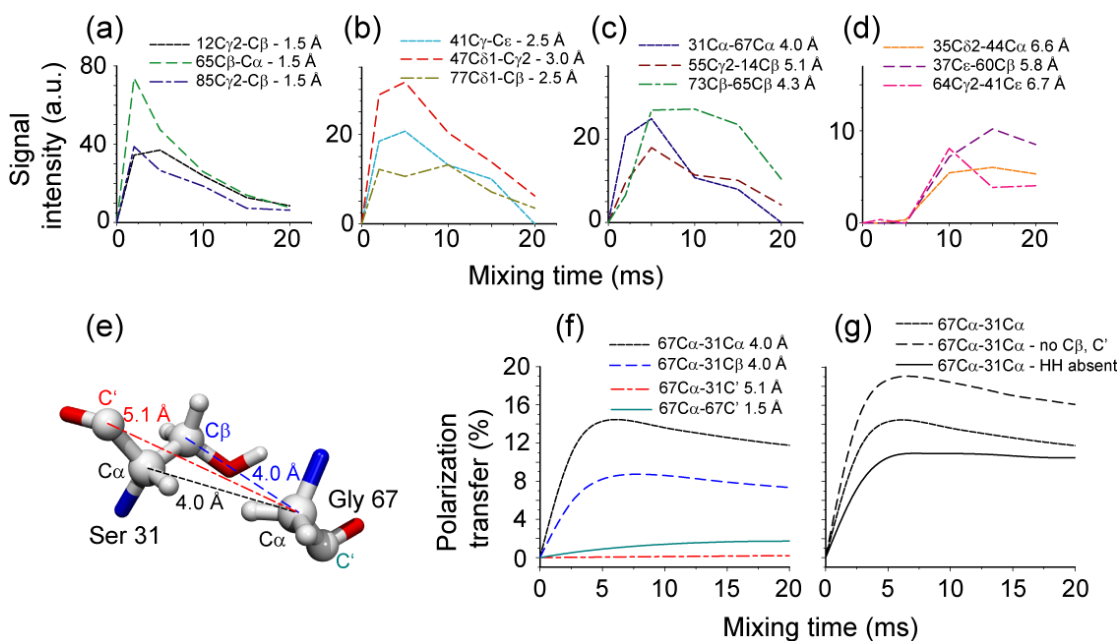


Figure 8-11 PAR polarization transfer as a function of the ^{13}C - ^{13}C distance. (a-d) A sampling of experimental ^{13}C - ^{13}C PAR polarization transfer curves obtained on $[\text{U-}^{13}\text{C},^{15}\text{N}]$ -Crh protein with

$\omega_r/2\pi = 20$ kHz, $\omega_{\text{OH}}/2\pi = 900$ MHz and a carrier frequency set to 38.9 ppm: (a) one-bond distance class; (b) 2.5-3.5 Å distance class; (c) 3.5-5 Å distance class; (d) >5 Å distance class. (e) Spin system used in the PAR polarization transfer simulations (f) and (g). Atom coordinates and chemical shift tensors used in the simulations can be found in the SI Table 8-3).

As the last case, we present in Fig. 8-11e-g detailed data for the case of polarization transfer between $G67C_\alpha$ - $S31C_\alpha$. The spin system is composed of 10 spins [see Fig. 8-11e and Table 8-3] and does not involve relaxation. The magnetization is initially on the $G67C_\alpha$ spin and uses similar settings as for the experimental data shown in Fig 8-13b. The first striking observation is that the buildup curves corresponding to the $G67C_\alpha$ - $S31C_\alpha$ and $G67C_\alpha$ - $S31C_\beta$ cross-peaks have similar characteristic times. This is a very satisfying result since the two distances are close to 4Å. Moreover, the transfer to the carbonyls is small (even for the directly bonded $G67C'$). This behavior is expected since the carrier frequency was set in the middle of the aliphatic ^{13}C region. The PAR ^{13}C CW rf field is not large enough to compensate for the carbonyl chemical shift auto cross-term which induces a significant off-resonance component in the corresponding TSAR subspace. Fig. 8-11g shows the $G67C_\alpha$ - $S31C_\alpha$ transfer in presence or in absence of the $S31C_\beta$ and $S31C'$ spins. The maximum polarization transfer is higher in the latter case but the overall buildup time is preserved ensuring that the TSAR transfer is direct in this case.

In summary, Fig. 8-11a-d indicates that the homonuclear TSAR mechanism yields buildup profiles that can be used to estimate ^{13}C - ^{13}C distances in fully protonated protein (with the exception of intra-residue > 2-bond and sequential contacts different from $^i\text{C}_\alpha$ - $^{i+1}\text{C}_\alpha$ $^i\text{C}_\alpha$ - $^{i+1}\text{C}_\beta$).

8.5.4 Influence of the ^1H - ^1H couplings on ^{13}C - ^{13}C distance estimates

The influence of the ^1H - ^1H couplings network on the TSAR mechanism is a complex question. As shown in Fig. 8-8b and 8-11f-g, the presence of ^1H - ^1H couplings in the PAR simulations can have different effects on the ^{13}C - ^1H - ^{13}C PAR polarization transfer. In the case of the sequential transfer from LC_α to MC_β simulated in Fig. 8-8b,

the polarization transfer is only slightly affected by the removal of the ^1H - ^1H couplings. Concurrently, the long-range PAR transfer between S31C_α and G67C_α spins simulated in Fig. 8-11g is more affected by the presence and absence of ^1H - ^1H couplings. The influence of ^1H - ^1H couplings on the ^{13}C - ^1H - ^{13}C TSAR spin dynamics depends on the spin system topology and the rf settings chosen. Moreover, the influence of the ^1H - ^1H couplings appears through second order effects (i.e. $p_{\text{H}} \neq 0.5, 1$). However, in examples highlighted here, the presence or absence of ^1H - ^1H couplings does not significantly change the ^{13}C - ^1H - ^{13}C build-up profiles, i.e. the maximum buildup time is preserved and the optimal polarization transfer is similar within 30 %. *As a consequence, the effect of the ^1H - ^1H couplings does not appear as a limiting factor for using the PAR experiments to estimate ^{13}C - ^{13}C distances. Further investigations of the influence of ^1H - ^1H couplings on the TSAR spin dynamics are currently under progress.*

8.6 Concurrent ^{13}C - ^1H - ^{13}C TSAR recoupling during first order ^{13}C - ^{13}C homonuclear recoupling

8.6.1 Dual polarization transfer

Thus far we have demonstrated that ^{13}C - ^1H - ^{13}C TSAR transfers can be efficiently achieved by using two CW rf fields (see Fig. 8-1a), and that one of the matching conditions implies similar rf fields on the ^1H and ^{13}C channels. In other words, appreciable PAR transfer is achieved for dual irradiation settings where the mismatch between ^1H and ^{13}C rf field strengths is not sufficient to decouple the ^1H and ^{13}C baths. This in turn suggests the possibility of concurrent ^{13}C - ^1H - ^{13}C TSAR transfer during other homonuclear recoupling experiments, particularly those where the ^1H decoupling is non-ideal. Potentially, this situation arises in first order ^{13}C - ^{13}C dipolar recoupling experiments, where insufficient ^1H decoupling is known to interfere with the ^{13}C - ^{13}C recoupling spin dynamics and produces intensity losses in DQ filtered experiments,^{11, 86, 87} or ^{13}C - ^{13}C J-based transfer experiments.⁸⁷ This interference becomes acute at high $\omega_{\text{r}}/2\pi$, and has stimulated the design of DQ recoupling sequences where no additional ^1H irradiation is required.^{13, 81}

In Figure SI9, SI10 and SI11 we investigate the influence of the ZQ ^{13}C - ^1H - ^{13}C TSAR mechanism during the application of established ^{13}C - ^{13}C dipolar recoupling sequences such as HORROR,¹² CM_pRR ,¹⁴ RFDR,^{10, 88} SR6₂,^{6, 89} and ^{13}C - ^{13}C through bond polarization transfer experiment with P9₁₂¹ TOBSY⁹⁰ experiment. We show that the *TSAR mechanism may become significant or even the dominant homonuclear polarization transfer mechanism* for certain ^1H irradiations, which are considered as adequate ^1H decoupling fields (especially in applications on proteins). Note that this is in stark contrast to previous studies that have only considered interferences with ^1H decoupling fields in the context of ^{13}C - ^{13}C polarization transfer losses and not in terms of potential additional polarization transfer.

This is an important result as it shows that we should exercise caution when interpreting experimental data obtained on protonated samples solely on the basis of the intended ^{13}C - ^{13}C recoupling mechanism. For instance, if the goal is to assign the spectrum of an unknown molecule, it is crucial to be able to distinguish cross-peaks due to covalently bonded nuclei from the cross-peaks due to non-covalently bonded nuclei that are in close spatial proximity. In theory this can be achieved either using broadband dipolar recoupling technique, in which dipolar truncation ensures one-bond relayed transfer, or using J coupling based through-bond methods.^{42, 90-95} In practice, the presence of additional efficient through-space TSAR transfer is likely to jeopardize, or at least greatly complicate, the correct interpretation of the assignment data by producing additional cross-peaks that are not distinguishable from the cross-peaks resulting from the intended dipolar or J-based mechanism. Note that in the case of dipolar methods a solution to this problem has been proposed with the CM_pRR ^{14, 84} pulse sequence (or its adiabatic variant CMAR ¹³ for superior robustness to rf inhomogeneity) that only relies on a single ^{13}C irradiation and thus does not allow the presence of any TSAR transfer, thus ensuring a clean relayed transfer mechanism. Note that this will be also true for any ^{13}C - ^{13}C first order recoupling sequence that can be run without simultaneous ^1H irradiation.^{15, 96, 97}

Finally, since the contribution of the TSAR mechanism can substantially modify the overall polarization transfer curve for long distance ^{13}C - ^{13}C contacts, it is also important

to understand that the TSAR phenomenon could induce errors in inter-nuclear distance fitting in spin pair labeled samples (if no protons are included in the analysis).

8.6.2 Simultaneous polarization transfer and dipolar truncation

To complete the discussion on dipolar truncation it is important to consider the situation where both ^{13}C - ^{13}C and ^{13}C - $[^1\text{H}]$ - ^{13}C TSAR recoupling are simultaneously present. As outlined in the previous section, this can be the case for various first order ^{13}C - ^{13}C recoupling sequences (e.g. HORROR, SR6₂⁶, RFDR, etc.) when the ^1H rf irradiation is not sufficiently strong to properly decouple the ^{13}C spins from the ^1H bath. Figure 8-12 shows 5 spin simulations (for a system composed of 3 ^{13}C 's and 2 ^1H 's) that illustrate the effect of a directly bonded spin (C3) on a long distance transfer from C1 to C2 (3.85 Å). *As we will see the presence of additional ^{13}C - $[^1\text{H}]$ - ^{13}C TSAR mechanism during first order ^{13}C - ^{13}C recoupling pulse sequences may lead to an overall increase of long distance polarization transfer (C1→C2) which may be wrongly interpreted as a reduction of dipolar truncation in ^{13}C - ^{13}C recoupling mechanism.*

If we consider the first set (dashed black lines) of the simulations in Fig. 8-12 where only the ^{13}C spins are included, we confirm the general observation that most first order ^{13}C - ^{13}C recoupling sequences lead to efficient dipolar truncation. The two other sets of curves (dashed red and blue lines) in Fig. 8-12 represent the same simulations with a larger spin system that includes three additional protons. More specifically, the second set of lines (dashed red) represent simulations where all the couplings are present whereas the third set of lines (blue) account only for the TSAR transfer as the ^{13}C - ^{13}C and ^1H - ^1H couplings are removed.

In the case of CMpRR, no ^1H irradiation is applied since the sequence has been introduced and demonstrated to efficiently recouple ^{13}C - ^{13}C couplings using only a ^{13}C irradiation field.^{13, 14} In this case the spin dynamics induced is free from any TSAR contribution and dominated by first order ^{13}C - ^{13}C recoupling yielding a small polarization transfer to the remote spins (about 3% when all couplings are included). On the other hand, for PAR recoupling, the polarization transfer does not rely on ^{13}C - ^{13}C

couplings and long range polarization transfer can reach about 25% efficiency (all couplings included) solely based on ^{13}C - $[^1\text{H}]$ - ^{13}C TSAR mechanism. Note that the polarization transfer is only slightly affected by the ^1H - ^1H couplings.

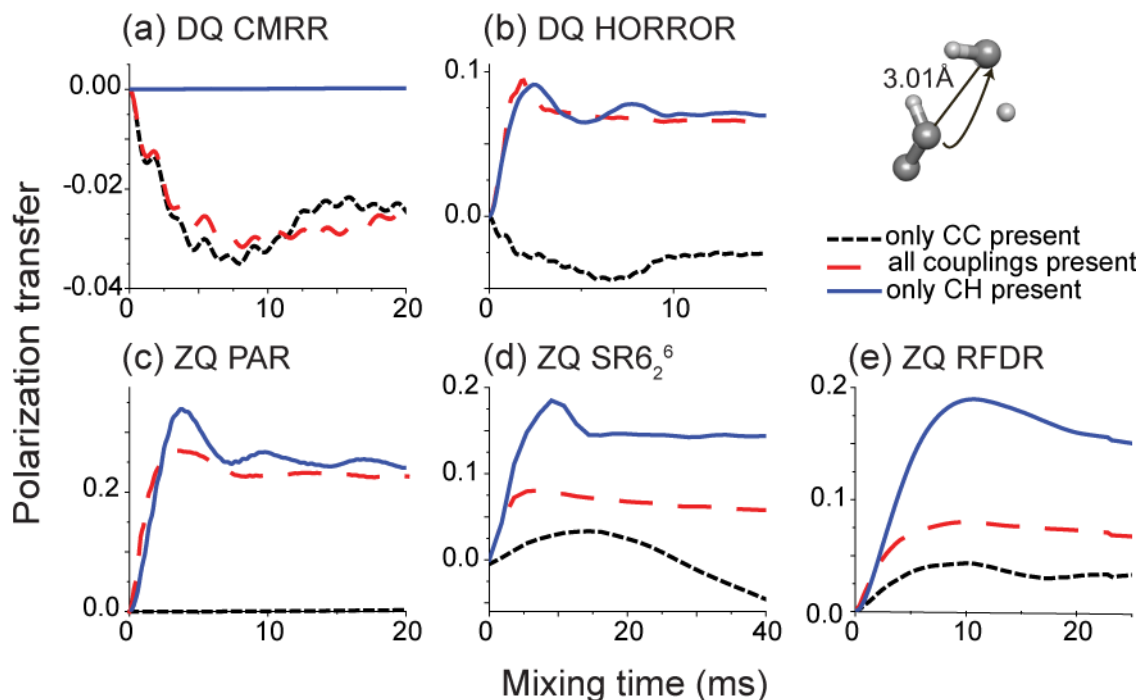


Figure 8-12 Modification of the long distance polarization transfer in uniformly labeled systems when both 1st order ^{13}C - ^{13}C recoupling and second-order TSAR mechanism are simultaneously present. Note the different behavior for the simulations with only ^{13}C - ^{13}C couplings included and the simulations also including ^1H 's. The chosen ^1H irradiations yield substantial TSAR mechanism contribution to overall polarization transfer (except CM₅RR where no ^1H irradiation was used in order to illustrate a case of pure 1st order ^{13}C - ^{13}C spin dynamics without TSAR contribution). (a) DQ CM₅RR with 100 kHz ^{13}C rf and no ^1H rf. (b) DQ HORROR with 15 kHz ^{13}C rf and 80 kHz ^1H rf. (c) ZQ PAR with 56 kHz ^{13}C rf and 54 kHz ^1H rf. (d) ZQ SR6₂⁶ with 20 kHz ^{13}C rf and 82 kHz ^1H rf. (e) ZQ RFDR with 12.5 kHz π pulses and 69 kHz ^1H rf. The simulations were performed at (a, c, d, e) $\omega_r/2\pi = 20$ kHz or (b) $\omega_r/2\pi = 30$ kHz and $\omega_0/2\pi = 700$ MHz and include isotropic chemical shift and CSA typical for the aliphatic sites (see SI). The spin system is based on the leucine sidechain in the structure of N-*f*-MLF-OH.⁹⁸ Note that all the pulse sequences except PAR (in (d)) are designed to reintroduce the ^{13}C - ^{13}C dipolar coupling to the 1st order.

For the other examples, the long distance polarization transfers are substantially different between simulation performed with ^{13}C 's only (first set) and simulations in presence of protons under ^1H decoupling (second set) and can even be larger in the latter case. This can be explained by the presence of a concurrent ^{13}C - $[^1\text{H}]$ - ^{13}C TSAR mechanism and is clearly demonstrated by comparing simulations without ^{13}C - ^{13}C and ^1H - ^1H couplings and simulations with all couplings included. The ^1H “decoupling” field in each case was chosen to obtain an appreciable (though not necessarily optimal) TSAR effect (see Fig SI9). The ^1H field strengths are 80, 82, 69 kHz for HORROR, SR6₂⁶ and RFDR respectively. Note that these ^1H fields correspond to values often used in SSNMR protein studies. This is a very interesting observation as it explains why some first order recoupling sequences under some conditions are able to provide medium to long range contacts. In all the cases studied here, the reason behind involves a second order ^{13}C - $[^1\text{H}]$ - ^{13}C TSAR effect. This is a very satisfying observation as the dipolar truncation efficiency should not vary much between first order recoupling sequences (either DQ or ZQ). Indeed the truncation efficiency primarily relies on the ratio between weak versus strong couplings and is thus independent of the pulse sequence scaling factor. For a given spin system geometry, the powder Euler angle dependency of the recoupling pulse sequence should be able to mainly account for the small variation in dipolar truncation efficiency.

Finally, it is important to highlight that the simultaneous reintroduction of first order ^{13}C - ^{13}C terms and second order ^{13}C - $[^1\text{H}]$ - ^{13}C TSAR terms reduce the polarization transfer to the remote spin compared to the PAR case. As a consequence, if the objective is to record medium to long distances contacts in uniformly or extensively labeled systems, the obvious choice is to use a pulse sequence inducing a pure TSAR spin dynamics and not a mixture of 1st order ^{13}C - ^{13}C and TSAR spin dynamics.

To summarize, it is possible to observe apparent reduction of first order ^{13}C - ^{13}C truncation when sufficiently large second-order ^{13}C - $[^1\text{H}]$ - ^{13}C TSAR effect can be induced at the same time. This can lead, especially for first order ZQ sequences, to an apparent increase of polarization transfer for the long distance contacts compared to the situation where only ^{13}C - ^{13}C couplings are included. This significant effect should

be taken into account when interpreting experimental data both for assignment and structure studies.

8.7 Protein structure calculation

8.7.1 Crh monomer structure calculation from PAR spectra using the x-ray structure as a homology model

Finally, we illustrate the potential of the TSAR based techniques for 3D structure determination of proteins. More precisely, we show that the PAR data presented here contain information on a sufficient number of distances, including medium-range (from the contacts between sites that are between 3 to 4 residues apart) and long-range restraints (from the contacts between the sites that are equal or more than 5 residues apart) to successfully calculate the structure of a Crh monomer.

The ^{13}C - ^{13}C PAR spectra presented in Fig. 8-13b were recorded at 900 MHz and $\omega_r/2\pi = 20$ kHz from a sample of microcrystalline [^{13}C , ^{15}N]-Crh protein with mixing times of (a) 0.8 ms (CM_5RR) and (b) 15 ms (PAR). To reduce the experimental acquisition period, compared to the N- f -MLF-OH PAR spectra presented above, we focused on the aliphatic-aliphatic correlations in which case we need to sample only a ~ 14 kHz spectral width in the indirect dimension rather than ~ 40 kHz for the full bandwidth at 900 MHz ^1H frequency. Moreover, this approach allows us to work with rf fields of ~ 50 kHz without having to address bandwidth issues and concentrates the magnetization on the aliphatic sites, without distributing polarization to the carbonyl and aromatic nuclei.

The ^{13}C - ^{13}C PAR data shown in Fig. 8-13b contains ~ 800 cross-peaks and assigning these unambiguously is a non-trivial task. Thus, we used the x-ray structure⁵⁴ as a homology model to facilitate in the assignment of ambiguous cross peaks present in the PAR data set. More precisely, we combined the chemical shift assignment data²³ and ^{13}C - ^{13}C distances extracted from the x-ray structure to simulate a ^{13}C - ^{13}C spectrum with a ^{13}C - ^{13}C distance cut-off of 7\AA . By allowing the chemical shifts to vary within ± 0.25 ppm and comparing this simulated spectrum with the experimental data, we were able

to unambiguously assign 163 structurally meaningful ^{13}C - ^{13}C cross peaks. 92 of these correspond to long range ^{13}C - ^{13}C contacts (between sites separated by more than 5 residues in the sequence).

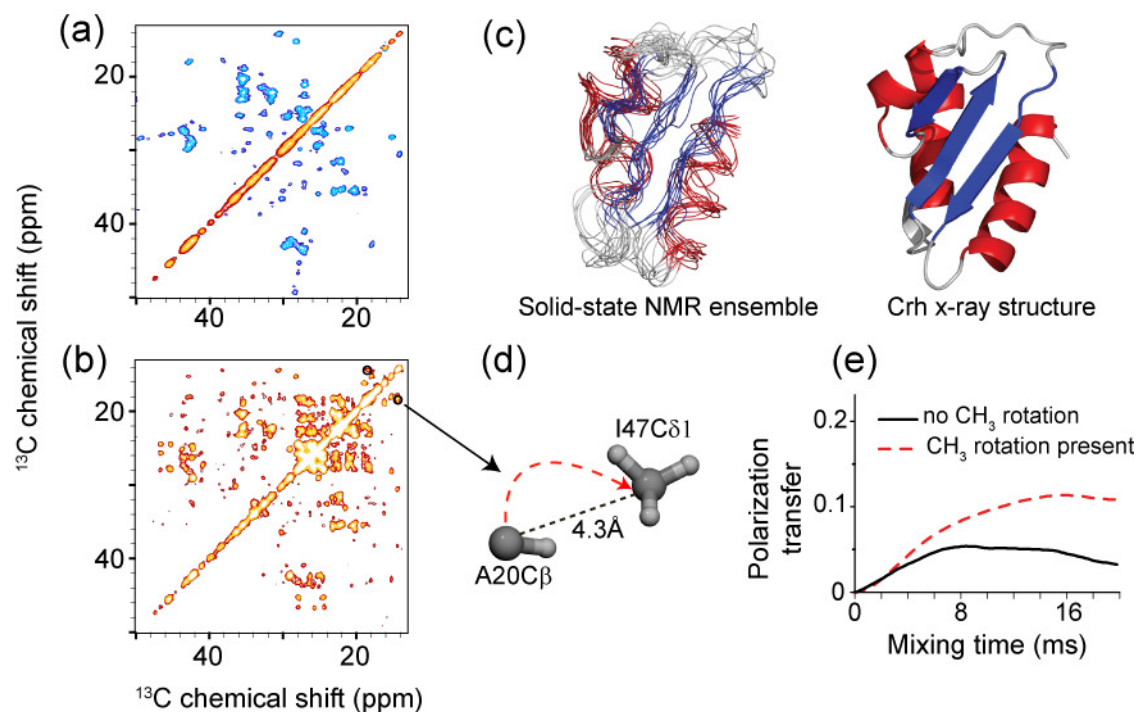


Figure 8-13 (a)-(b) Examples of ^{13}C - ^{13}C correlation spectra of $[\text{U-}^{13}\text{C},^{15}\text{N}]$ -Crh protein at $\omega_{\text{OH}}/2\pi = 900$ MHz and $\omega_r/2\pi = 20$ kHz. Expansion of the aliphatic region for (a) CM_3RR (0.8 ms) and (b) PAR (15 ms). The PAR spectrum contains numerous cross-peaks corresponding to medium to long distances that involve methyl groups. As a comparison, the CM_3RR spectrum displays only one-bond cross-peaks. A detailed description of the PAR optimization protocol can be found in the SI. (c) Ensemble of structures of a Crh monomer (residues 12-85) calculated using a unique 2.5-6 Å distance class for all the unambiguous ^{13}C - ^{13}C cross-peaks identified using the x-ray structure⁵⁴ as a homology model. (e) Numerical simulations of the polarization transfer between CH_3 and CH illustrating the influence of the threefold methyl group hopping on the overall polarization transfer. The coordinates for spin system (d) used in the simulations were taken for $\text{A20C}\alpha$ and $\text{I47C}\delta 1$ from the x-ray structure⁵⁴ of the Crh protein. Simulations do not include chemical shift.

Using the unambiguously assigned cross peaks with a unique distance class of 2.2-6Å, we then performed molecular dynamics simulated annealing in torsion angle space

(CNS⁶³). The backbone precision for the 10 best structures from the 100 calculated conformers was found to be 2.06Å, and the accuracy (defined here as the backbone rmsd of the 10 best conformers with respect to the x-ray structure) 2.31Å. The calculated structure resulting from this simple procedure is presented in Fig. 8-13c. Using only one ¹³C-¹³C PAR data set and one distance class for all the contacts, we obtain the correct general fold of the Crh monomer. Thus, this demonstrates that the PAR data presented here contains information on a sufficient number of distances to calculate a protein structure. It is worth mentioning that we did not use dihedral angles predictions from chemical shifts²⁴.

Note, that we have used only a single class of distances in the above calculation. However, as we have demonstrated in Sec. 7 with polarization transfer curves, we can establish several distance classes that should enhance the precision and accuracy of the structure calculations using data from the TSAR based techniques. A *de novo* structure calculation utilizing ¹³C-¹³C PAR and ¹⁵N-¹³C PAIN-CP⁴² (i.e. ¹⁵N-[¹H]-¹³C TSAR) restraints, that we have performed in a separate study will be reported elsewhere.

8.7.2 Comparison with alternative techniques

In order to complete our discussion of the PAR experiment, we briefly contrast it with other techniques used for solid-state NMR 3D structure determination of proteins.

PDS⁶¹ and DARR^{34, 35, 62} protein structure determination was primarily demonstrated on alternately labeled spin systems, except recently on a uniformly labeled sample of Ubiquitin.³⁸ One of the reasons reported in the literature^{100, 101} is the excessive spectral crowding obtained at long mixing times on uniformly labeled systems, which complicates assignments of the interesting cross-peaks. The extent of crowding in DARR spectra is dependent on multiple variables, such as the protein size, the magnetic field and the MAS frequency. However, because the DARR mechanism relies on ¹³C-¹³C couplings, it is efficient in relaying magnetization through the carbon chain and thus leads to efficient polarization transfer for intra-residue (and also sequential) contacts which compromise the observation of the medium and long range cross peaks.¹⁰¹

The same is not true for PAR, since the TSAR mechanism does not involve ^{13}C - ^{13}C couplings. Indeed, if we compare cross-peak intensities at a 20 ms mixing time, the ratio of long distance cross-peaks ($> 5 \text{ \AA}$) to the other shorter distance transfer, we obtain roughly a 1 to 1 or 1 to 2 ratio.

In contrast to PDS and DARR and similarly to the PAR method, CHHC/NHHC⁶³⁻⁶⁵ yield spectra with reduced spectral crowding. These experiments are used to extract structurally valuable cross-peaks and therefore appear more suitable for application to uniformly labeled systems. This was recently illustrated by a *de novo* structure determination of the [U- ^{13}C , ^{15}N]-Crh dimer based on CHHC/NHHC data,⁷⁰ and similar work is currently under progress using the PAR data.

Even though CHHC/NHHC and TSAR-based techniques appear as complementary techniques to extract relevant structural restraints, it is worth pointing out that they differ in terms of sensitivity. One of the drawbacks of the CHHC/NHHC techniques is their low sensitivity that is a direct consequence of the three polarization transfer steps involved. The PAR method, on the other hand, uses a single efficient polarization transfer step and thus yields improved signal-to-noise. As an illustration, Fig 8.25 in Supporting Information shows a comparison of a CHHC spectrum obtained with ~20 mg of sample at $\omega_{0\text{H}}/2\pi = 500 \text{ MHz}$ in ~46 hours and a ^{13}C - ^{13}C PAR spectrum obtained with ~6 mg of sample at $\omega_{0\text{H}}/2\pi = 750 \text{ MHz}$ in ~21.4 hours. In both spectra, an intermediate mixing time was chosen and the lowest contour level was set at 5 times the noise level as estimated by Sparky 3.1 (T. D. Goddard and D. G. Kneller, University of California)). These spectra illustrate notably the good signal to noise of the PAR data obtained at high magnetic fields on small amount of sample.

Another interesting observation is the significant attenuation or even absence of cross-peaks involving methyl groups in the CHHC spectra. This effect can be explained by the intrinsically inefficient polarization step from the ^{13}C spin to methyl ^1H 's and a reduction in ^1H - ^1H polarization transfer efficiency due to threefold methyl group hopping.⁶⁸ In contrast, cross-peaks involving methyl groups are prominent in the PAR spectra. Fig. 8-13a-b illustrates this point with an expansion of the aliphatic region of the spectrum focusing on the cross-peaks involving methyl groups.

The data suggest that the motion of the $-\text{CH}_3$'s has a positive effect on the polarization transfer in the PAR experiment providing a sensitive tool to probe long range contacts between methyl groups. This point is corroborated by the simulations shown in Fig. 8-13d that compare the 4.3 Å distance transfer between Ala20C $_{\alpha}$ and I47C $_{\delta 1}$ sites of Crh protein with and without methyl group rotation. The polarization transfer is greatly enhanced when the methyl protons are simulated under fast exchange conditions. It is worth noting that methyl groups have already been recognized as very valuable structural and dynamics probes in wide range of biomolecular systems including membrane proteins and were recently used to probe protein-ligand interaction in solid-state NMR.¹⁰²

Even though the ^{13}C - ^{13}C PAR method offers higher sensitivity compared to CHHC and is especially efficient for polarization transfers involving methyl groups, they should be considered as complementary approaches. Indeed they yield different sets of restraints and a combination of both types of restraints should be beneficial for structural studies of larger biomolecular systems.

The last feature of PAR that should be pointed out, especially in contrast to PDS and DARR sequences, is its flexibility with respect to the MAS regime. The PAR sequence has been used in this work at $\omega_r/2\pi = 20$ kHz, but its application at higher, as well as lower frequencies is also possible. This is depicted in Fig. 8-26 in the Supporting Information with a numerical simulation of a ^{13}C - ^{13}C PAR experiment at $\omega_r/2\pi = 10$ and 70 kHz respectively. In PDS the optimal build-up time for a fixed distance increases with $\omega_r/2\pi$, which limits the applicability of the technique to low and moderate spinning frequencies (<15 kHz). The DARR experiment, which relies on the same type of mechanism as PDS with an improved scaling factor, enables access to higher MAS frequencies. However, it is not practical to use DARR for obtaining long distance contacts ≥ 30 kHz MAS for two reasons. First, as in the case of PDS, the spin part of the DARR scaling factor is fixed, so the mixing time required to observe long distance contacts increases with $\omega_r/2\pi$; and second, the application of DARR for $\sim 10^2$ ms to observe long distances at > 30 kHz MAS frequencies may induce a considerable amount of rf heating, which is not desirable for biological samples.

8.8 Conclusion

We have introduced and characterized the homonuclear version of the TSAR mechanism applicable to ^{13}C - ^{13}C and ^{15}N - ^{15}N polarization transfer in biomolecules at moderate to ultrahigh spinning frequencies and high magnetic fields with moderate power requirements. The PAR sequence relies on a three spin process involving second order cross-terms between ^1H - $^{13}\text{C}_1$ (^1H - $^{15}\text{N}_1$) and ^1H - $^{13}\text{C}_2$ (^1H - $^{15}\text{N}_2$) that promotes polarization transfer between $^{13}\text{C}_1$ ($^{15}\text{N}_1$) and $^{13}\text{C}_2$ ($^{15}\text{N}_2$). The analytical expressions derived from Average Hamiltonian Theory permit visualization of the subspace in which the TSAR spin dynamics occurs and indicates that the processes are strongly influenced by the presence of an auto-cross term with major contributions from cross-terms of the ^1H - ^{13}C coupling with itself. Moreover, in the context of analytical and numerical simulations, we discussed the dependence of PAR polarization transfer with respect to the local geometry of the spin system. We show that the auto-cross term may be compensated to a large extent for specific combinations of ^{13}C and ^1H rf fields, as well as for some particular spin topologies. Moreover, we demonstrate that dipolar truncation is significantly reduced in the TSAR mechanism, and that we can use the ^{13}C - ^{13}C PAR experiment to estimate ^{13}C - ^{13}C distances. With this concept in mind, we applied ^{13}C - ^{13}C PAR to the uniformly labeled Crh protein, which allowed us to obtain high quality spectra used to derive the structure of a Crh monomeric subunit. Moreover, we have discussed the possibility of inducing significant ^{13}C - ^1H - ^{13}C TSAR polarization transfer during the application of other ^{13}C - ^{13}C dipolar recoupling and J-based experiments that should be taken into account when interpreting the data. Interestingly, ^{13}C - ^1H - ^{13}C TSAR contributions during the 1st order ^{13}C - ^{13}C recoupling experiments and may lead to the apparent reduction of dipolar truncation.

TSAR based techniques including ^{13}C - ^{13}C PAR, ^{15}N - ^{15}N PAR and the previously introduced ^{15}N - ^{13}C PAIN-CP open a new range of possibilities for high resolution structural studies of large biomolecules at high magnetic fields and high spinning frequencies.

8.9 Acknowledgements

We would like to thank Dr. Patrick van der Wel for his active support and useful discussions and Dr. Carole Gardiennet for recording the CHHC Crh data. We are very grateful to Dr. Mikhail Veshtort for providing the SPINEVOLUTION software that has been used throughout the course of this work. We also would like to thank Dr. David Ruben, Dr. Christopher Turner, Ajay Thakkar and Dr. Anthony Bielecki for technical support, Galia Debelouchina, Matt Eddy, Alexander Barnes, Marvin Bayro, Dr. Thorsten Maly, Marc Caporini, Andrew Casey and Prof. Anne-Frances Miller for helpful discussions. This work was supported by the National Institute of Health Grants EB-001960 and EB-002026 and the French ANR (JC05_44957).

8.10 Supporting Information

8.10.1 PAR subspace, coupled basis, irreducible spherical tensor and ZQ fictitious operators:

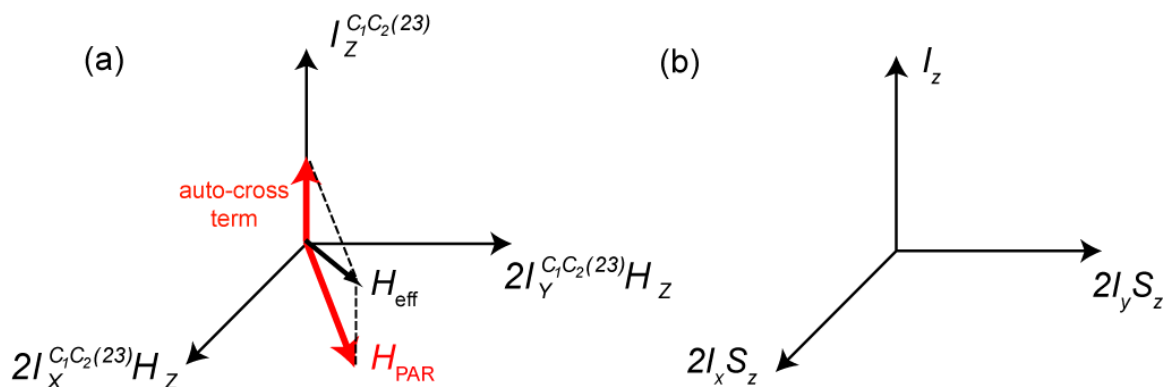


Figure 8-14 (a) Visualization of PAR spin dynamics subspace. The space can be seen as a coupled basis between a fictitious ZQ operator involving the two carbons (or nitrogens) and a proton spin. The red arrows indicate PAR recoupling axis and longitudinal tilting field resulting from auto-cross terms (see Sect. 3.3). Panel (b) depicts a typical coupled basis encountered for instance in solution NMR

Irreducible spherical tensor operators:

$$\begin{aligned}
T_{10}^i &= S_{iz} \\
T_{1\pm 1}^i &= \mp \frac{1}{\sqrt{2}} S_i^\pm \\
T_{00}^{jk} &= -\frac{1}{\sqrt{3}} \overline{S_j \cdot S_k} \\
T_{10}^{jk} &= \frac{-1}{2\sqrt{2}} (S_j^+ S_k^- - S_j^- S_k^+) \\
T_{1\pm 1}^{jk} &= \frac{-1}{2} (S_j^\pm S_{kz} - S_{jz} S_k^\pm) \\
T_{20}^{jk} &= \frac{1}{\sqrt{6}} (3S_{jz} S_{kz} - \overline{S_j \cdot S_k}) \\
T_{2\pm 1}^{jk} &= \mp \frac{1}{2} (S_j^\pm S_{kz} + S_{jz} S_k^\mp) \\
T_{2\pm 2}^{jk} &= \frac{1}{2} S_j^\pm S_k^\pm
\end{aligned} \tag{135}$$

Two spins ZQ subspace operators for spins k and l:

$$\begin{aligned}
I_x^{(kl),(23)} &= \frac{1}{2} (2I_{kx} I_{lx} + 2I_{ky} I_{ly}) = \frac{1}{2} (I_k^+ I_l^- + I_k^- I_l^+) = -(T_{11}^k T_{1-1}^l + T_{1-1}^k T_{11}^l) \\
I_y^{(kl),(23)} &= \frac{1}{2} (2I_{ky} I_{lx} - 2I_{kx} I_{ly}) = \frac{i}{2} (-I_k^+ I_l^- + I_k^- I_l^+) = i(T_{11}^k T_{1-1}^l - T_{1-1}^k T_{11}^l) \\
I_z^{(kl),(23)} &= \frac{1}{2} (I_{kz} - I_{lz}) = \frac{1}{2} (T_{10}^k - T_{10}^l)
\end{aligned} \tag{136}$$

8.10.2 Materials and methods

8.10.2.1 Sample Preparation

N-*f*-MLF-OH peptide was obtained by solid phase peptide synthesis from CS Bio Inc. (Menlo Park, CA). The peptide was prepared both without isotopic enrichment, and with uniformly ^{13}C and ^{15}N labeled amino acids from Cambridge Isotope Laboratories

(Andover, MA), and was diluted to 10% in natural abundance material and center-packed in a 2.5mm Bruker rotor.

Crh was overexpressed with a C-terminal LQ(6xHis) extension as described previously. ^{13}C and ^{15}N -enriched Crh was prepared by growing bacteria in $> 98\%$ ^{13}C , ^{15}N labeled medium (Silantes). The protein was purified on Ni-NTA agarose (QUIAGEN) columns followed by anion exchange chromatography on a Resource Q column.⁶ Crh-containing fractions were dialyzed against 20 mM NH_4HCO_3 . The protein was crystallized as described previously⁷ in the presence of 20 % PEG 6000 in a crystallization plate over a 2M NaCl solution. The microcrystals resulting from about 6 mg of protein were centrifuged directly into a 2.5 mm Bruker rotor, and the rotor cap was sealed.

8.10.3 NMR Spectroscopy

All MAS NMR experiments were performed on one of two high field instruments, the first being a commercial Bruker spectrometer operating at a 900.1 MHz ^1H frequency using a Bruker triple resonance probe equipped with a 2.5 mm stator. The second instrument is a custom designed Cambridge Instruments spectrometer (courtesy of D. J. Ruben, MIT) operating at 750 MHz ^1H frequency using a Bruker triple resonance probe equipped with a 2.5 mm stator. Spinning frequencies of 20 kHz were used in all experiments and regulated to ± 2 Hz with a Bruker spinning frequency controller (Bruker BioSpin, Billerica MA). ^{13}C chemical shifts were referenced to aqueous DSS using external referencing via the published ^{13}C chemical shifts of adamantane.⁸

Optimizing the ZQ TSAR polarization transfer using 1D experiments is not completely straightforward. One can for instance employ selective pulses on the carbonyl's and observe PAR magnetization transfer to the aliphatic carbons. However such a procedure is more difficult for aliphatic-aliphatic correlations as it implies the use of longer selective pulses. In such cases a more convenient way to optimize the ZQ TSAR polarization transfer is to compare an experimental interference map with the corresponding simulation (Fig. SI6(b)) and the simulated polarization transfer map (Fig. SI6a). Such a procedure allows one to reliably optimize the TSAR settings.

Figure 8-15a shows a simulated PAR optimization map in which a polarization transfer in between two carbons is monitored as a function of the irradiation strength on the ^{13}C and ^1H channels (here in units of spinning frequency). Fig. 8-15b shows an “interference” map simulation (1D experiment using pulse sequence in Fig. 8-2 of the manuscript without the t_1 evolution) where we start with one unit of magnetization on both carbons and display the sum of the magnetization after 1.5 ms PAR mixing as a function of the irradiation strength on ^{13}C and ^1H channels (here in units of spinning frequency). Note that the settings that lead to substantial TSAR polarization transfer [Fig. 8-15a] also lead to appreciable intensities in the interference map [Fig. 8-15b] since the TSAR mechanism is a ZQ process that conserve the sum of the carbon magnetization. However the reverse is not true.

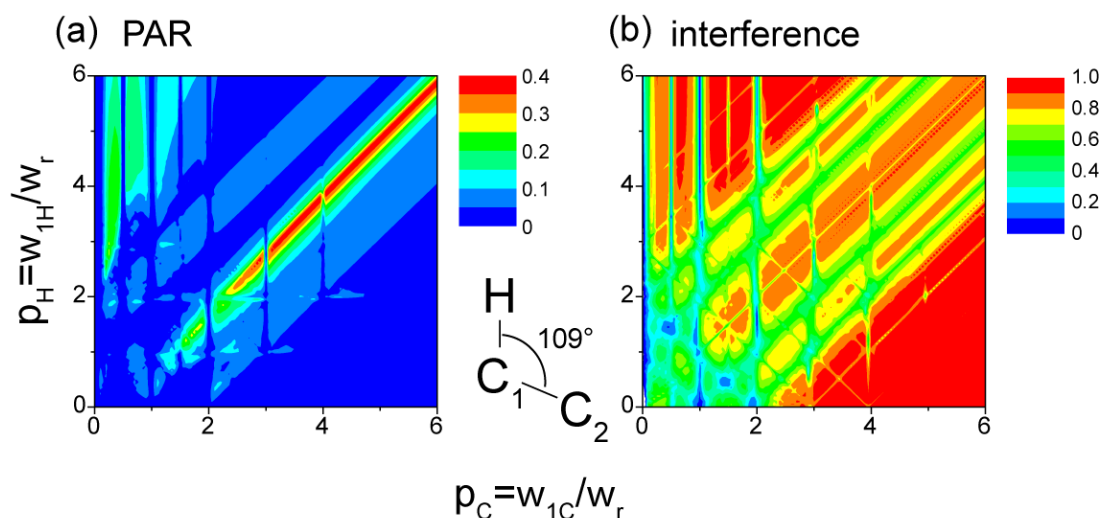


Figure 8-15 PAR polarization transfer optimization map (a) versus interference map (b). In PAR optimization map the polarization transfer between the carbons is monitored as a function of carbon (p_{C}) and proton (p_{H}) irradiation in units of spinning frequency. In the interference map the decay of the magnetization on the carbons after the PAR mixing is monitored as a function of carbon (p_{C}) and proton (p_{H}) irradiation in units of spinning frequency. The initial magnetization is prepared on the x-axis on C_1 in (a) and on both C_1 and C_2 in (b).

The ^{13}C power was set to ~ 53 kHz (i.e. $p_{\text{C}}=2.65$ – the value that leads to appreciable TSAR in simulations) and ^1H rf was scanned to identify Hartmann-Hahn conditions. ^1H

rf power leading to minimal interference just under the $n = 0$ matching condition was used (i.e. ~ 50 kHz).

The ^1H decoupling during t_1 evolution and acquisition was implemented through optimized 100 and 83.3 kHz TPPM⁹. The recycle delay was 3 s. For the 2D ^{13}C - ^{13}C PAR correlation spectrum of $[\text{U-}^{13}\text{C},^{15}\text{N}]$ -*f*-MLF-OH was recorded with acquisition times were 20.4 ms in t_2 and 8.32 ms in t_1 ($320 \times 26 \mu\text{s}$; spectral width 204.5 ppm) and 16 scans per t_1 point. For the 2D ^{13}C - ^{13}C PAR correlation spectrum on $[\text{U-}^{13}\text{C},^{15}\text{N}]$ -Crh at $\omega_{0\text{H}}/2\pi = 900$ MHz, acquisition times were 14 ms in t_2 and 9.95 ms in t_1 ($158 \times 63 \mu\text{s}$; spectral width 70.1 ppm) and 256 scans per t_1 point and the mixing of 15 ms. For the 2D ^{13}C - ^{13}C PAR correlation spectrum on $[\text{U-}^{13}\text{C},^{15}\text{N}]$ -Crh at $\omega_{0\text{H}}/2\pi = 750$ MHz, acquisition times were 17.9 ms in t_2 and 10 ms in t_1 ($150 \times 67 \mu\text{s}$; spectral width ~ 80 ppm) and 320 scans per t_1 point and the mixing of 14 ms with $\omega_{1\text{C}}/2\pi \sim 53$ kHz and $\omega_{1\text{H}}/2\pi \sim 50$ kHz.

For the 2D ^{13}C - ^{13}C CM₅RR correlation spectrum on $[\text{U-}^{13}\text{C},^{15}\text{N}]$ -Crh at $\omega_{0\text{H}}/2\pi = 750$ MHz, acquisition times were 20.5 ms in t_2 and 8.25 ms in t_1 ($375 \times 22 \mu\text{s}$; spectral width ~ 242 ppm) and 24 scans per t_1 point and the mixing of 0.8 ms with $\omega_{1\text{C}}/2\pi \sim 100$ kHz and $\omega_{1\text{H}}/2\pi = 0$ kHz with offset on ^{13}C at 110 ppm. For the 2D ^{13}C - ^{13}C CM₅RR correlation spectrum on $[\text{U-}^{13}\text{C},^{15}\text{N}]$ -Crh at $\omega_{0\text{H}}/2\pi = 900$ MHz, acquisition times were 14 ms in t_2 and 10.2 ms in t_1 ($174 \times 58.8 \mu\text{s}$; spectral width ~ 75 ppm) and 48 scans per t_1 point and the mixing of 0.8 ms with $\omega_{1\text{C}}/2\pi \sim 100$ kHz and $\omega_{1\text{H}}/2\pi = 0$ kHz with offset on ^{13}C at 39 ppm (only aliphatic region).

For the Crh study, at 900 MHz temperature was regulated using Bruker BCU-X (target temperature -18°C , flow 1400L/h, resulting in a sample temperature between 0 to 5°C as indicated by the water ^1H chemical shift referenced to PEG (3.74 ppm, referenced externally to DSS).¹⁰ At 750 MHz temperature was regulated using FTS chiller with target temperature of -15°C .

8.10.2.2 Simulations, Data Analysis and Structure Calculations

All the numerical simulations were performed with SPINEVOLUTION 3.2¹¹. Figure 8-4 uses $\delta_{\text{iso,C1}} = -10$ ppm, $\delta_{\text{iso,C2}} = 10$ ppm, $\delta_{\text{anis,C1}} = -20$ ppm, $\eta_{\text{C1}}=0.43$, $\delta_{\text{anis,C2}} = -20$

ppm, $\eta_{C2}= 0.5$ for the isotropic and anisotropic chemical shift tensors values of the C_1 and C_2 carbons. Figure 8-10 uses $\delta_{iso,MC'} = -67.2$ ppm, $\delta_{iso,MC\alpha} = 53$ ppm, $\delta_{iso,MC\beta} = 58$ ppm, $\delta_{iso,LC\alpha} = 50$, $\delta_{anis,MC'} = -76$ ppm, $\eta_{C'} = 0.9$, $\delta_{anis,MC\alpha} = 11.9$ ppm, $\eta_{LC\alpha} = 1$, $\delta_{anis,MC\beta} = 25.1$ ppm, $\eta_{C\beta}=0$, $\delta_{anis,LC\alpha} = -13.9$ ppm, $\eta_{LC\alpha}=0.93$ for the isotropic and anisotropic chemical shift tensors values. Figure 8-11 uses ($\delta_{iso,C1}=-10$ ppm, $\delta_{iso,C2}=0$ ppm, $\delta_{iso,C1} = 10$ ppm, $\delta_{anis,C1} = -20$ ppm, $\eta_{C1}=0.6$, $\delta_{anis,C2} = -19$ ppm, $\eta_{C2}=0.7$, $\delta_{anis,C3} = -19$ ppm, $\eta_{C3}=0.7$ for the isotropic and anisotropic chemical shift tensors values. Analytical simulations were performed in Matlab. Note that we use 1.1 Å and 1.5 Å for a one bond CH and CC distances, respectively. Data was processed using NMRPipe.¹² Spectral assignments were performed with Sparky 3.1 (T. D. Goddard & D. G. Kneller, University of California). ¹³C-¹³C distance restraints were identified using the X-ray crystallographic structure of Crh as homology model.¹³ ¹³C-¹³C distance restraints were defined by a unique distance class of 2.2-6Å. Calculations of the monomer structure were performed using the program CNS.¹⁴ A molecular dynamics simulated annealing protocol was used with torsion angles as internal degrees of freedom.^{15 16} The structure calculation of 100 conformers of the Crh monomer consists of three stages: (i) 3000 steps of high-temperature torsion angle molecular dynamics at 50000 Kelvin; (ii) 5000 steps of slow-cooling annealing stage in torsion angle space from 50000 Kelvin to 0 Kelvin and (iii) 10 cycles of final conjugate gradient minimization, each cycle comprising 200 steps. The 10 selected conformers were aligned on the backbone atoms and the rmsd values were calculated using MOLMOL 2K.2.¹⁷

8.10.3 Analytical simulations of the TSAR mechanism:

Figure 8-16 complements Sec. 3.1 of the manuscript and illustrates the contribution from the different spatial components to the TSAR polarization transfer. The spin system is the same as for Fig. 8-2 (also at the top of the Fig. 8-16).

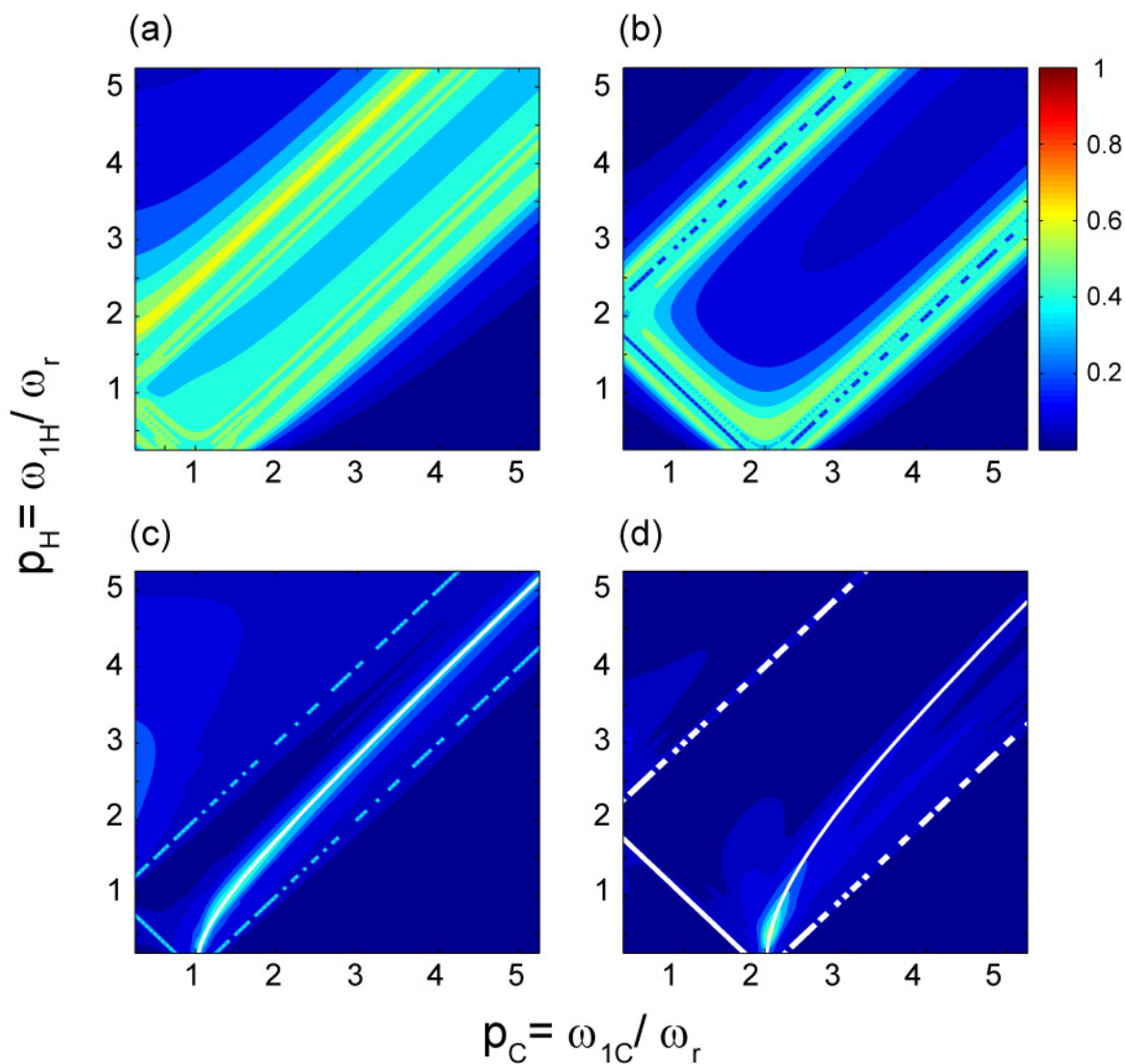
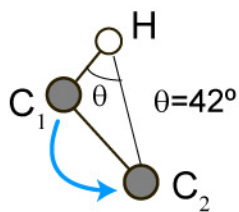


Figure 8-16 Analytical maps of PAR polarization transfer as a function of carbon (p_C) and proton (p_H) rf field strengths (in units of spinning frequency) for a three spin system described in Section 8.4.1 and Fig. 8-5 of the manuscript. (a) $m=1$ component and (b) $m=2$ component of the TSAR term is used in the simulation, (c) $m=1$ component and (d) $m=2$ component of both the TSAR term and longitudinal auto-cross terms are used in the simulation. Simulations include only dipolar couplings.

8.10.4 Dependence of the TSAR mechanism on local geometry: auto-cross terms compensation

Section 3.2 of the manuscript discusses the dependence of the TSAR mechanism on the local geometry of the three spin system involved. Notably Sec. 3.2 highlights the importance of the internuclear angle θ between the two heteronuclear dipolar interactions (C_1H and HC_2).

Figure 8-17 shows the PAR polarization transfer map for the case of a symmetric, triangular three spin configuration where the 1H spin is equidistant from the two ^{13}C 's. In such a situation, the off-resonance contribution from the auto-cross terms vanishes in the ZQ TSAR subspace. The panels (a) and (b) illustrate the PAR transfer for the $m=1$ and $m=2$ components, respectively, and (c) illustrates contributions from both $m=1$ and $m=2$.

Note that the p_C and p_H values that maximize the polarization transfer are not the same as in Fig. 8-2. The TSAR effect is present over almost the entire map except when first order recoupling conditions are matched (H.H. for $^1H-^{13}C$). The scaling factor of the TSAR recoupling is maximized around the H.H. conditions. A proper description of the TSAR efficiency in the vicinity of the H.H. conditions requires the calculation of higher order contributions in the AHT. However, the numerical simulations (data not shown) of the same spin system performed with SPINEVOLUTION match exactly the plot in panel (c).

In addition, the maximum polarization transfer at a given time is higher in (c) than in (a) or (b) illustrating that the $m=1$ and $m=2$ components interfere constructively. Note that for some values of p_C and p_H and with $\tau_{mix} = 60$ ms, the PAR polarization transfer is over 80% efficient for $r_{C1-C2} = 5.9$ Å.

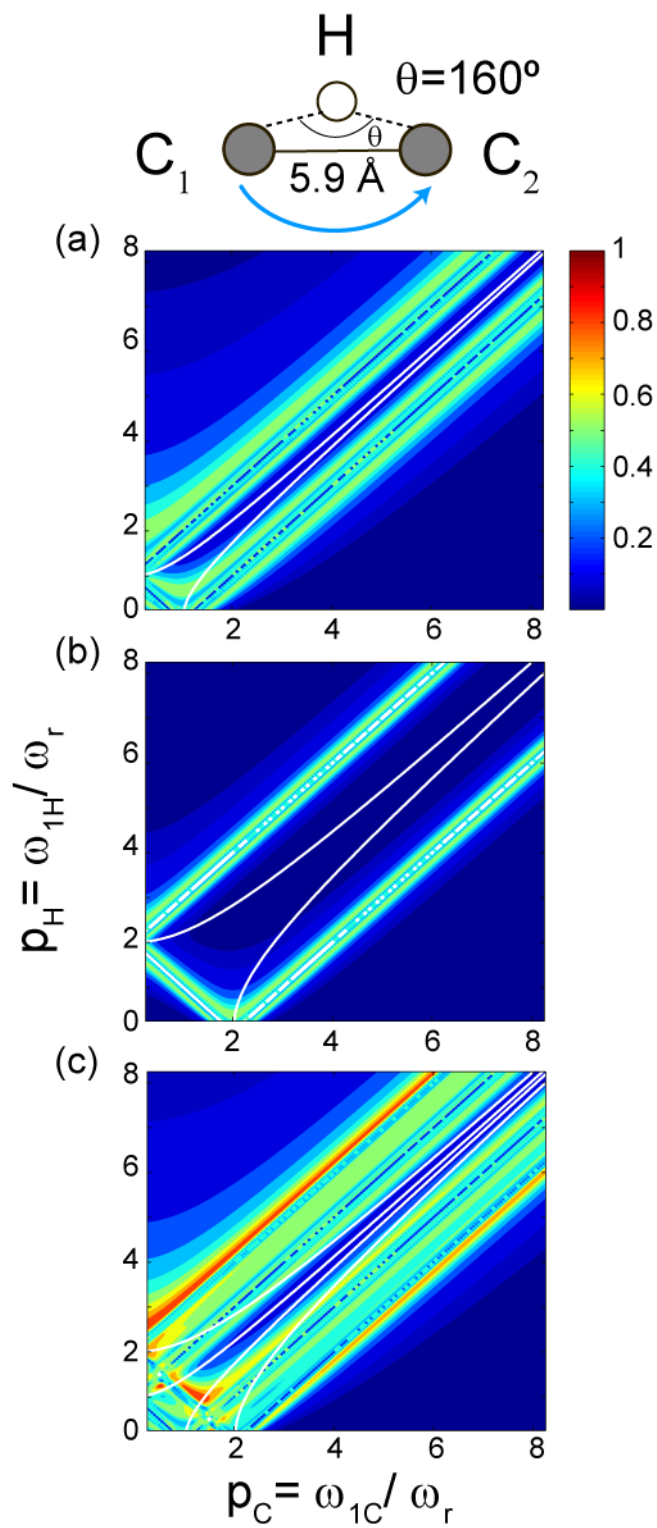


Figure 8-17 Analytical maps of PAR polarization transfer as a function of carbon (p_C) and proton (p_H) irradiation (in units of spinning frequency) for a symmetric, triangular three spin system. The ^1H - ^{13}C dipole couplings are identical and $b_{CH} = 1.119$ kHz. The distance between

carbons is 5.9 Å and the PAR mixing time is $\tau_{mix} = 60$ ms (a) $m=1$ TSAR component only, (b) $m=2$ TSAR component only, (c) $m=1$ and $m=2$ TSAR components together. Note that we do not have to account for the longitudinal auto-cross terms as they are zero for this symmetric spin system.

Figure 8-18 illustrates PAR polarization transfer maps for the case of a linear, asymmetric spin system. The proton is directly bonded to the C_1 carbon ($r_{C_1-H} = 1.1$ Å) and 4.9 Å distant from the C_2 carbon. In this case the two ^1H - ^{13}C couplings are very different and the spatial part of the off-resonance longitudinal terms is significant (see Eq. (16) of the manuscript). As a consequence the TSAR transfer is quenched when auto-cross terms are included except for the p_C and p_H rf settings that minimize the spin part of the auto-cross terms. This can be clearly seen by comparing Fig. 8-18a, b and c with d, e and f respectively. The TSAR polarization transfer is only present along the two parabolic white lines for which the auto-cross terms are zero for the $m=1$ and $m=2$ components respectively and in the area defined by $p_C < 1$ and $p_H > 3$, which also minimizes the auto-cross terms.

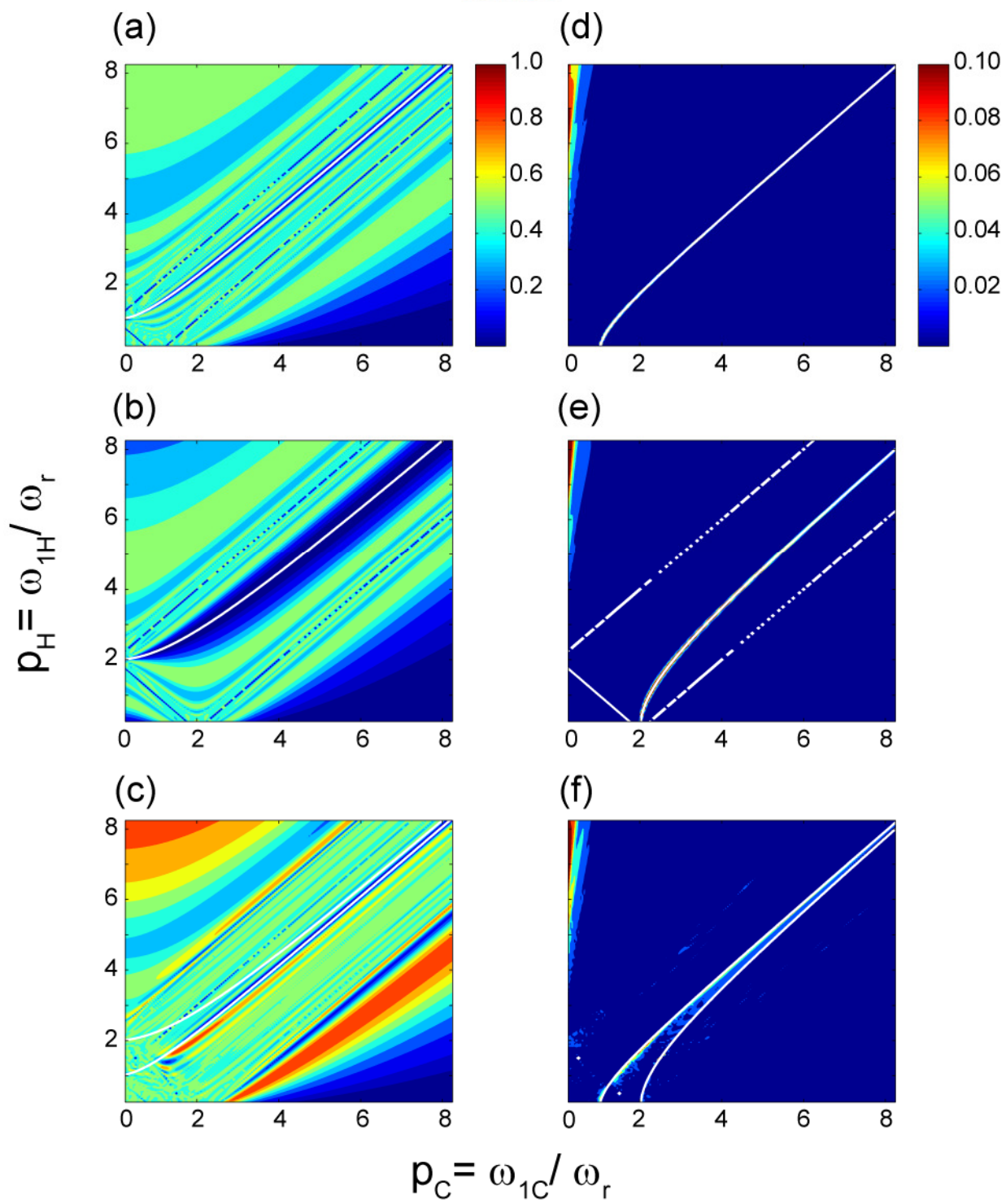
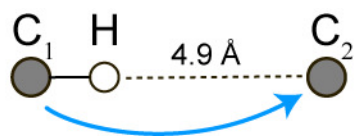


Figure 8-18 Analytical maps of PAR polarization transfer as a function of carbon (p_C) and proton (p_H) rf fields (in units of ω_r) for an aligned and asymmetric three spin systems. (a) $m=1$ TSAR component only, (b) $m=2$ TSAR component only, (c) $m=1$ and $m=2$ TSAR component only, (d) $m=1$ TSAR and auto-cross term component, (e) $m=2$ TSAR and auto cross-term components, (f) $m=1$ and $m=2$ TSAR and auto-cross term components. Simulations include only dipolar couplings.

Figure 8-19 illustrates that the PAR polarization transfer between identical types of ^{13}C spins (i.e. two CH's, CH_2 's, etc.) is a favorable situation since the off-resonance term in the TSAR subspace is likely to be small (see Eq. (16) of the manuscript). In panel (a), the off-resonance term is zero because the two pairs of proton-carbon couplings are the same. As a consequence, the TSAR polarization transfer is efficient over a broad range of rf settings and can reach higher polarization transfer. In panel (b), the couplings between the protons and their remote carbons are slightly different leading to a small off-resonance contribution. In the panel (c), the couplings from the single proton (directly bonded to one of the carbon) to the two carbons is very different leading to a significant off-resonance contribution (see Eq. (16) of the manuscript). As a consequence, the TSAR polarization transfer in panel (c) is only present for rf settings that minimize the spin part of the off-resonance term with a reduced efficiency.

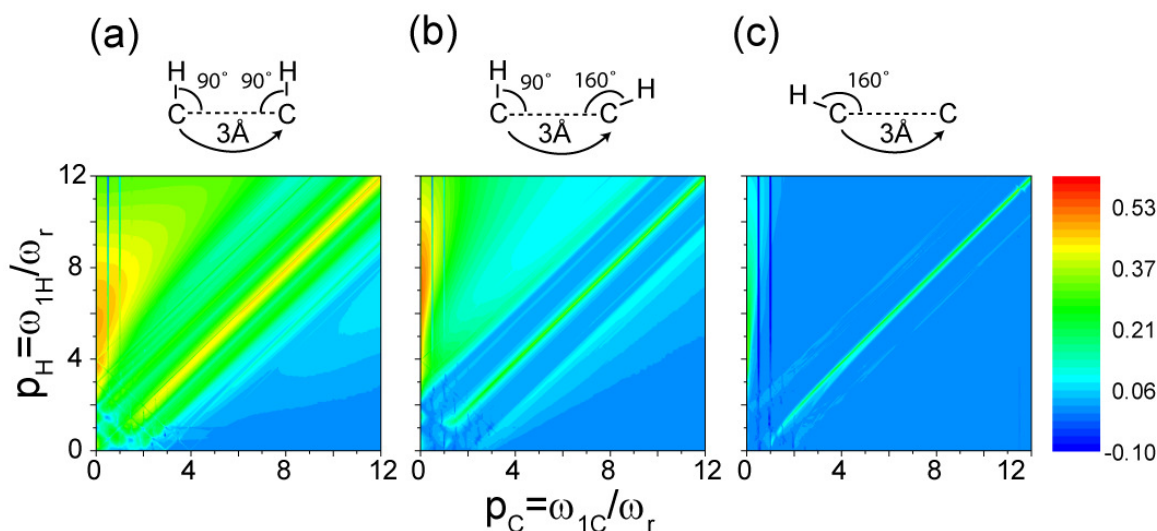


Figure 8-19 Effect of the partial compensation of the off-resonance auto-cross term contributions on the TSAR polarization transfer. The auto-cross terms are large in (c) for the asymmetric three spin system, minimal in (b) for the asymmetric four spin system, and zero in (a)

for the symmetric 4 spin system. Simulations do not include the chemical shifts. The mixing time is set to 20 ms. The geometry of the spin systems are indicated above the contour plots. The CH bond is 1.1 Å.

8.10.5 Multiple proton effect on TSAR

Figure 8-20 is discussed in Section 8.4.2 of the main text.

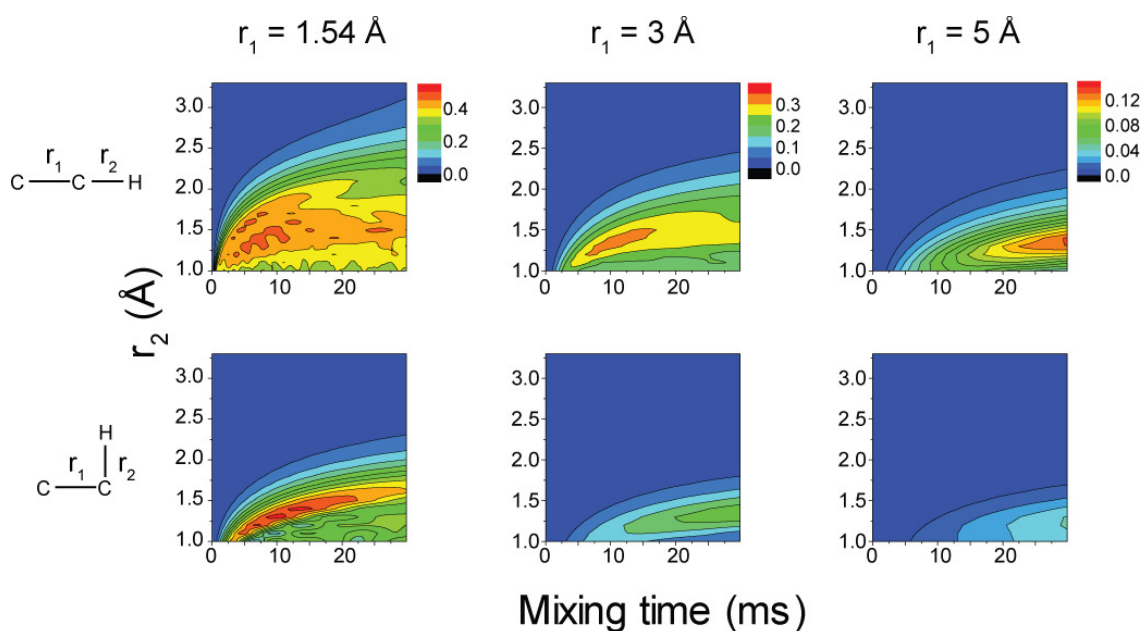


Figure 8-20 Simulations of the PAR polarization transfer as a function of the CH distance in several model spin systems (the CCH angle is 180° for the top row and 90° for the bottom row; the ^{13}C - ^{13}C distance r_1 for simulations in each column is specified at the top of the column). Simulations were performed at $\omega_c/2\pi = 20$ kHz, $\omega_{\text{OH}}/2\pi = 750$ MHz with $p_{\text{C}}=2.75$ and $p_{\text{H}}=2.5$. Isotropic chemical shift and CSA typical for carbon sites are included in the simulation ($\delta_{\text{iso,C1}}=-10$ ppm, $\delta_{\text{iso,C2}}=10$ ppm, $\delta_{\text{anis,C1}}=-20$ ppm, $\eta_{\text{C1}}=0.43$, $\delta_{\text{anis,C2}}=19$ ppm, $\eta_{\text{C}\alpha}=0.8$).

8.10.6 Relayed versus direct transfer mechanism

Figure 8-21 is discussed in Section 8.4.2 of the main text.

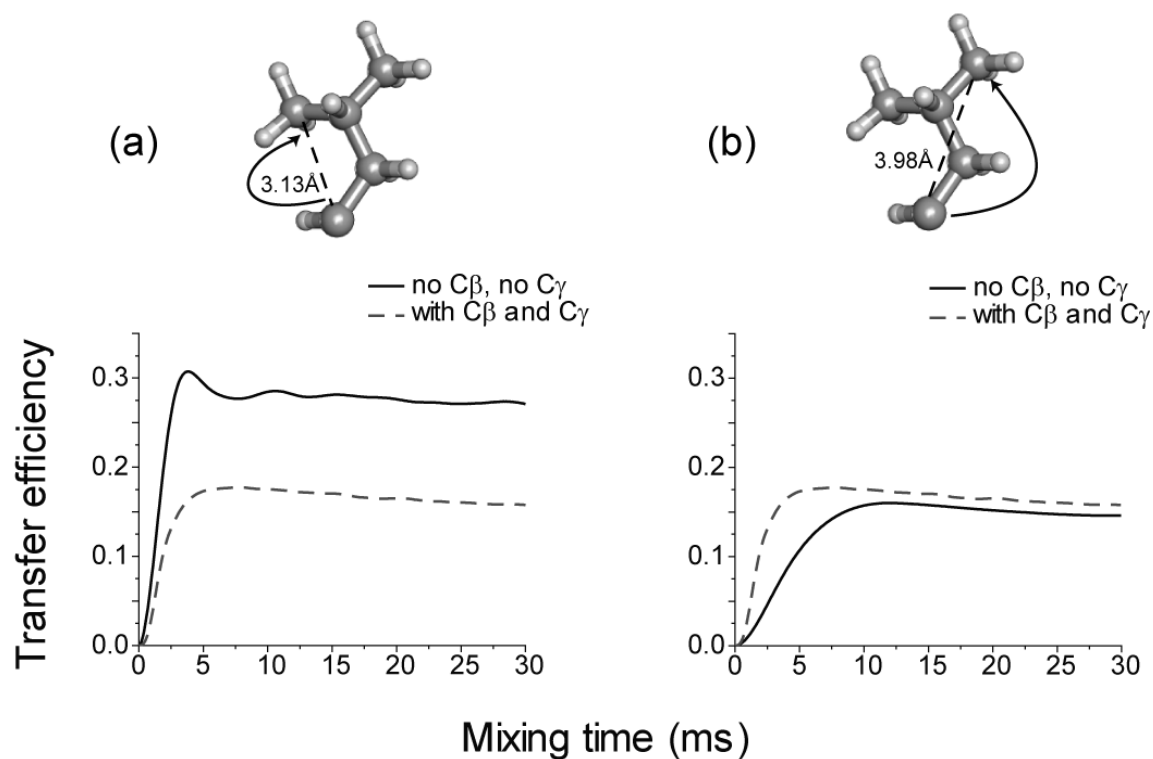


Figure 8-21 Numerical simulations of PAR polarization transfer between (a) LC_{α} and LC_{δ} , (b) LC_{α} and $LC_{\delta'}$ with settings similar to the ones used in Fig. 8-10a. The spin system includes nearby protons (the spin system for simulation in (a) and (b) are specified in Table 8-1 and 8-2 respectively). Black line shows the polarization transfer in absence of C_{β} and C_{γ} spins, whereas the red dashed line shows the same simulation in presence of C_{β} and C_{γ} carbons. Simulations include isotropic chemical shift and CSA for carbon sites ($\delta_{iso,C\alpha}=-20$ ppm, $\delta_{iso,C\delta1}=20$ ppm, $\delta_{iso,C\delta2}=20$ ppm, $\delta_{iso,C\beta}=5$ ppm, $\delta_{iso,C\gamma}=12$ ppm, $\delta_{anis,C\alpha}=25.1$ ppm, $\eta_{C\alpha}=0.0$, $\delta_{anis,C\delta1}=-19.8$ ppm, $\eta_{C\delta1}=0.0$, $\delta_{anis,C\delta2}=-19.8$ ppm, $\eta_{C\delta2}=0.0$, $\delta_{anis,C\beta}=23.8$ ppm, $\eta_{C\delta1}=0.92$, $\delta_{anis,C\gamma}=-19.8$ ppm, $\eta_{C\gamma}=0.0$).

Table 8-1 Atom coordinates in the spin system used in the simulation of Fig. 8-21a.

Atom	x	y	z
LC α	0.288	0.451	0.987
LC δ 2	2.038	-0.912	3.016
LC β	1.822	0.465	0.933
LC γ	2.505	-0.741	1.575
LH α	-0.042	0.456	2.016
L1H δ 2	2.132	0.031	3.534
L2H δ 2	2.65	-1.654	3.506
L3H δ 2	1.007	-1.229	3.026
L2H δ	2.171	1.36	1.431
LH δ	2.235	-1.635	1.024

Table 8-2 Atom coordinates in the spin system used in the simulation of Fig. 8-21b.

Atom	x	y	z
LC α	0.288	0.451	0.987
LC δ 1	4.024	-0.595	1.53
LC β	1.822	0.465	0.933
LC γ	2.505	-0.741	1.575
LH α	-0.042	0.456	2.016
L1H δ 1	4.397	-0.431	2.53
L2H δ 1	4.293	0.244	0.901
L3H δ 1	4.462	-1.498	1.13
L2H β	2.171	1.36	1.431
LH γ	2.235	-1.635	1.024

8.10.7 ^{13}C - ^{13}C distance estimates from ^{13}C - ^1H - ^{13}C PAR data

Table 8-3 Atom coordinates of the spin system used in the simulation of Fig. 8-11f-g. Atom coordinates were extracted from the Crh x-ray structure (1MU4)⁴. Isotropic chemical shifts were extracted from ssNMR experimental data and anisotropic chemical shift tensors were chosen based on published data.⁵

Atom	x (Å)	Y (Å)	Z (Å)	δ_{iso} (ppm)	δ_{anis} (ppm)	η
S31C α	27.151	-21.664	73.956	22.7	-17.3	0.59
S31C	26.179	-20.509	73.835	134.8	63.3	0.98
S31C β	28.298	-21.155	74.859	26	-28	0.75
G67C α	27.273	-24.411	76.908	6.3	20	0.75
G67C	28.556	-25.193	76.866	136	-71.3	0.94
S31H α	26.631	-22.524	74.378	0	5	0.65
S31H β 1	28.942	-20.495	74.278	0	5	0.65
S31H β 2	27.872	-20.603	75.697	0	5	0.65
G67H α 1	26.435	-25.087	77.079	0	5	0.65
G67H α 2	27.130	-23.887	75.963	0	5	0.65

8.10.8 Dual polarization transfer: concurrent ^{13}C - ^1H - ^{13}C TSAR recoupling during first order ^{13}C - ^{13}C dipolar recoupling or ^{13}C - ^{13}C J-based polarization transfer experiment

Figure 8.22 shows contour plots of the polarization transfer between two protonated ^{13}C 's separated by 2.5 Å distance during the application of various first order dipolar recoupling techniques at $\omega_r/2\pi \geq 20$ kHz and $\omega_{0\text{H}}/2\pi = 700$ MHz. In the simulations on the left column we include all of the dipolar interactions, whereas in the simulations on

the right the ^{13}C - ^{13}C and ^1H - ^1H dipolar couplings are absent allowing only the ZQ-TSAR contribution.

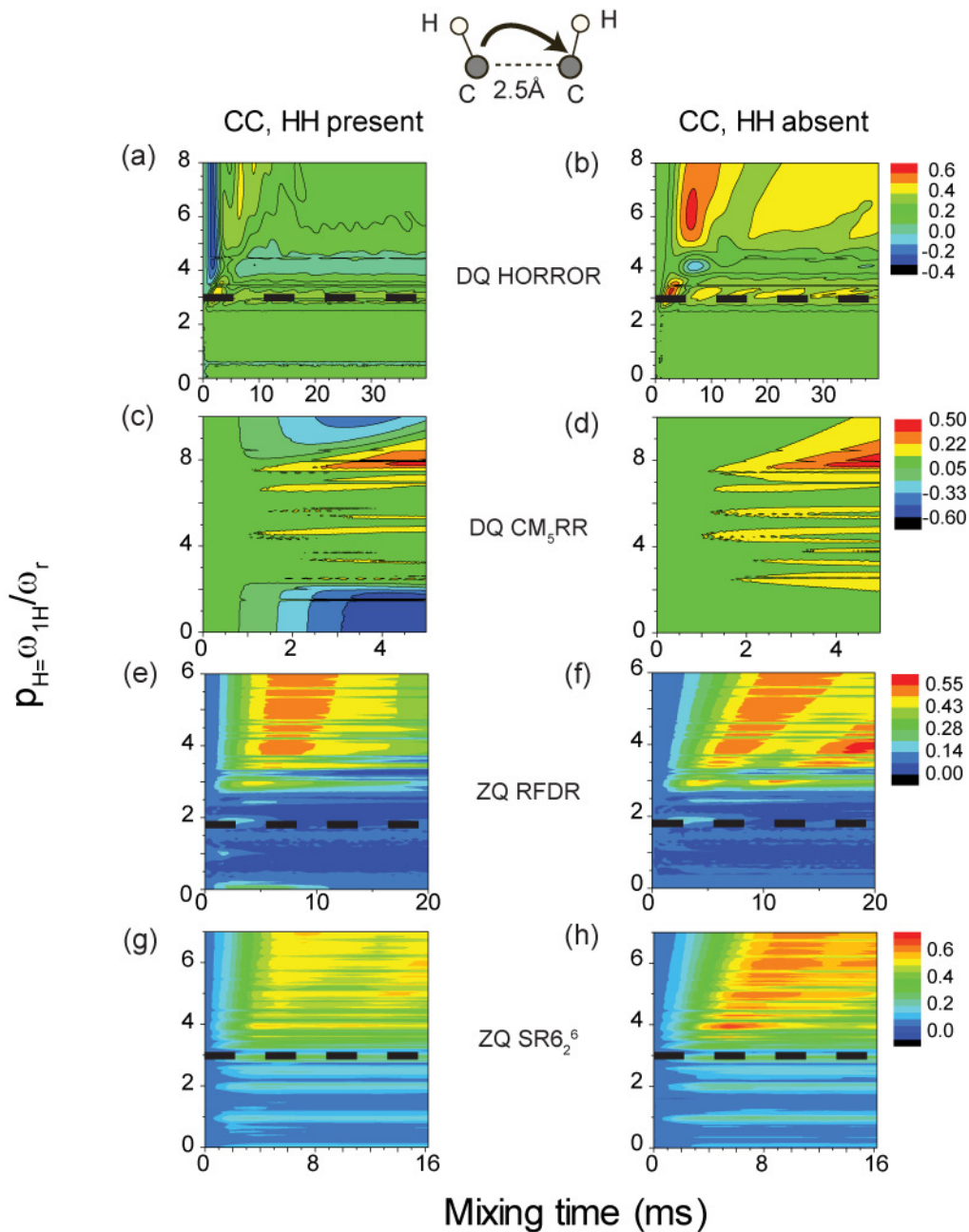


Figure 8-22 Simulations of the polarization transfer as a function of the ^1H irradiation strength (in units of ω_{r}) in a spin system composed of two ^{13}C 's separated by the 2.5\AA with directly attached ^1H 's. All the simulations were performed at $\omega_{\text{r}}/2\pi = 20$ kHz, $\omega_{\text{0H}}/2\pi = 700$ MHz and include isotropic chemical shift and CSA for carbon sites ($\delta_{\text{iso,C}\alpha} = -10$ ppm, $\delta_{\text{iso,C}\beta} = 0$ ppm, $\delta_{\text{iso,C}\gamma} = 10$ ppm, $\delta_{\text{anis,C}\alpha} = -20$ ppm, $\eta_{\text{C}\alpha} = 0.6$, $\delta_{\text{anis,C}\beta} = -19$ ppm, $\eta_{\text{C}\alpha} = 0.7$, $\delta_{\text{anis,C}\alpha} = -19$ ppm, $\eta_{\text{C}\alpha} = 0.7$). The simulations in left panels (a, c, e, g, k) include all the dipolar interactions (see Table 8-4). The

homonuclear ^{13}C - ^{13}C and ^1H - ^1H dipolar couplings were removed from the system in simulations in right panels (b, d, f, h, l) in order to eliminate all the transfer mechanisms except for the TSAR based mechanism. Simulations in (a-b) are for DQ HORROR pulse sequence with the ^{13}C rf strength of $\omega_r/2$. Simulations in (c-d) are for DQ CM₅RR with ^{13}C irradiation strength of $5\omega_r$ (i.e. 100 kHz). Simulations in (e-f) are for ZQ RFDR with $\omega_{1\text{C}}/2\pi = 12.5$ kHz π pulses. Simulations in (g-h) are for ZQ SR6₂⁶ sequence with ^{13}C irradiation strength of ω_r (i.e. 20 kHz). ZQ mechanism results in positive polarization transfer and DQ mechanism results in negative polarization transfer. The polarization transfer in the right hand panels is entirely due to the TSAR-based mechanism.

Table 8-4 Dipolar couplings in the spin system used in simulations in Fig 8-22. Spins 1 and 2 are ^{13}C nuclei, spins 3 and 4 are ^1H nuclei.

Spin i	Spin j	kHz
2	1	-0.486
3	1	-23.329
3	2	-1.085
4	1	-3.015
4	2	-23.328
4	3	-9.626

In the case of first order DQ sequences such as HORROR,¹ CMpRR^{2, 3}, the ZQ-TSAR process (positive sign) directly interferes and competes with the DQ 1st order ^{13}C - ^{13}C recoupling process (negative sign) as the two mechanisms lead to magnetization transfer of opposite signs. For all the DQ sequences studied here, we can find areas where the TSAR mechanism contributes significantly to the overall spin dynamics. This is for instance the case in the HORROR simulation [see Fig. 822b] for ^1H rf fields ranging from $p_H = 3$ to 8 (corresponding to 60 to 160 kHz). For short mixing times, the positive DQ HORROR transfer can be clearly seen (Fig 8-22a), however for mixing

times larger than 3 ms, the concurrent ZQ TSAR process becomes the dominant mechanism and explains the change of sign of the transfer.

At this point it is important to highlight another interesting feature of Fig. 8-22b. The change of sign in the TSAR polarization transfer in panel (b) can be explained by the fact that since the ^{13}C rf field is half of the MAS spinning frequency, a DQ-TSAR process is also present and thus competes with the standard ZQ-TSAR mechanism. The relative contribution of the two mechanisms is strongly dependent on the off-resonant longitudinal terms originating from auto-cross terms and thus varies as a function of the ^1H irradiation. From Fig. 8-22b, it appears that the ZQ TSAR process dominates the DQ process for a large range of ^1H irradiation fields. This can easily be understood from the expression of the off-resonant longitudinal terms in the DQ subspace:

$$\omega_{AUTO} = \frac{1}{2\omega_r} \left[\frac{1}{\omega_r} \left[\frac{(\omega_{C_1}^0)^2 + (\omega_{C_2}^0)^2}{2p_C} + \zeta_C(1, p_C)(\omega_{C_1}^1 \omega_{C_1}^{-1} + \omega_{C_2}^1 \omega_{C_2}^{-1}) + \zeta_C(2, p_C)(\omega_{C_1}^2 \omega_{C_1}^{-2} + \omega_{C_2}^2 \omega_{C_2}^{-2}) \right] + (\omega_{C_1H}^1 \omega_{HC_1}^{-1} + \omega_{C_2H}^1 \omega_{HC_2}^{-1})\chi(1, p_C, p_H) + (\omega_{C_1H}^2 \omega_{HC_1}^{-2} + \omega_{C_2H}^2 \omega_{HC_2}^{-2})\chi(2, p_C, p_H) \right] \quad (137)$$

Contrary to the ZQ TSAR off-resonance expression, the second order contributions of the various cross terms involving the chemical shift tensors, heteronuclear dipolar couplings appears as a sum and are intrinsically more important than in the ZQ subspace.

Note that TSAR recoupling involved in HORROR corresponds to *the low power TSAR area present in Fig. 8-2 and also discussed in Sec. 8.4*. This is an interesting phenomenon since it occurs in the range of ^1H fields typically available experimentally to perform the high power ^1H “decoupling”. It explains why DREAM (that uses long mixing times ~7-10 ms) has been reported to recouple efficiently multiple-bond distant spins in protonated proteins under high power ^1H conditions. Most of the DREAM one bond cross peaks mainly rely on the intended first order adiabatic ^{13}C - ^{13}C recoupling. However, the presence of “extra” peaks can potentially be explained by this concurrent second order low ^{13}C power TSAR recoupling (which is partially responsible for variations of the sign of the multiple-bond cross-peaks). Similarly, the presence of a

substantial concurrent TSAR phenomenon can be found for CM₅RR at $p_H = 7.8$ (i.e. $1.56 p_C = 156$ kHz).

In the case of ZQ techniques (RFDR panels g-h, SR6₂⁶ panel k-l), the relative contribution of the two mechanisms is more complicated to discern from the maps since both processes are ZQ and lead to the same sign of polarization transfer. However, from the maps (h) and (l), it appears clearly that the TSAR mechanism is significant over a large range of ¹H rf fields (except the no decoupling regime). Both mechanisms interfere in a complicated manner but lead for some settings to an overall increase of the polarization transfer. This is especially true for long distance transfer where the TSAR mechanism can easily become predominant.

The contribution of the ZQ ¹³C-[¹H]-¹³C TSAR mechanism is even more striking in the case of P9₁₂¹ TOBSY where the intended transfer should only rely on J-couplings. Figures 8-22 and 8-23 show simulations of the polarization transfer for P9₁₂¹ TOBSY at $\omega_r/2\pi = 30$ kHz, $\omega_{0H}/2\pi = 700$ MHz on a six spin system consisting of three ¹³C's and three ¹H's (see Figure 8-23a).

The desired spin dynamics, governed by J couplings, is illustrated in Fig. 8-23a where the simulation is performed without ¹H's. In this simulation we can observe efficient polarization from the C α spin to the C β and C γ spins mediated through the 35 Hz J couplings included in the calculation.

Figure 8-23 shows simulations of the polarization transfer for P9₁₂¹ TOBSY as a function of the ¹H irradiation applied during the mixing period on the Y-axis and the mixing time along the X-axis. The first observation is that the TOBSY transfer is strongly dependent on the ¹H power applied. This observation is true for the simulations in panels (b) and (e) which include all the interactions and show polarization transfer to C β and C γ respectively. This is also obviously true for the simulations in panels (c) (C β) and (f) (C γ), where J couplings are absent, and simulations in panels (d) (C β) and (g) (C γ), where J couplings, ¹³C-¹³C and ¹H-¹H dipolar couplings have been removed. Note, that the simulations in panels (d) and (g) isolate the TSAR contribution to the overall polarization transfer. The remarkable similarity between panels (d) and (g) ("TSAR only") and the panels (b) and (e) (all interactions present) demonstrates that the

TSAR polarization transfer contributes significantly over the entire range of the ^1H rf fields considered here.

This phenomenon is also clearly illustrated in Fig 8-24c-f, which shows polarization buildups for two ^1H rf field strengths, in presence or in absence of ^{13}C - ^{13}C J couplings. Fig. 8-24c (with J coupling present) and SI10e (with J coupling absent) show that the polarization transfer under 135 kHz of ^1H irradiation ($p_{\text{H}}=4.5=3p_{\text{C}}$) is largely dominated by the TSAR mechanism. Fig. 8-24d (J couplings present) and Fig. 8-24e (J couplings absent) show that the polarization transfer under 156 kHz of ^1H irradiation ($p_{\text{H}}=5.2=3.47p_{\text{C}}$) is still dominated by the TSAR mechanism, although the presence of J couplings does perturb the polarization transfer. As a reference, Fig. 8-24a shows the theoretical TOBSY transfer in absence of protons (i.e. in absence of concurrent TSAR mechanism).

This is a very interesting result since it shows that even when using ^1H irradiations usually considered sufficiently strong to decouple the ^{13}C 's from the ^1H bath ($p_{\text{H}}>3$), the TSAR effect can still be the dominant mechanism. One should thus be cautious when applying this type of experiment to perform assignments of unknown protonated systems based on the assumption that the mechanism proceeds mainly through bond. Assuming a "clean" through-bond mechanism when extra peaks are present in the spectra due to the TSAR mechanism could lead to erroneous assignment.

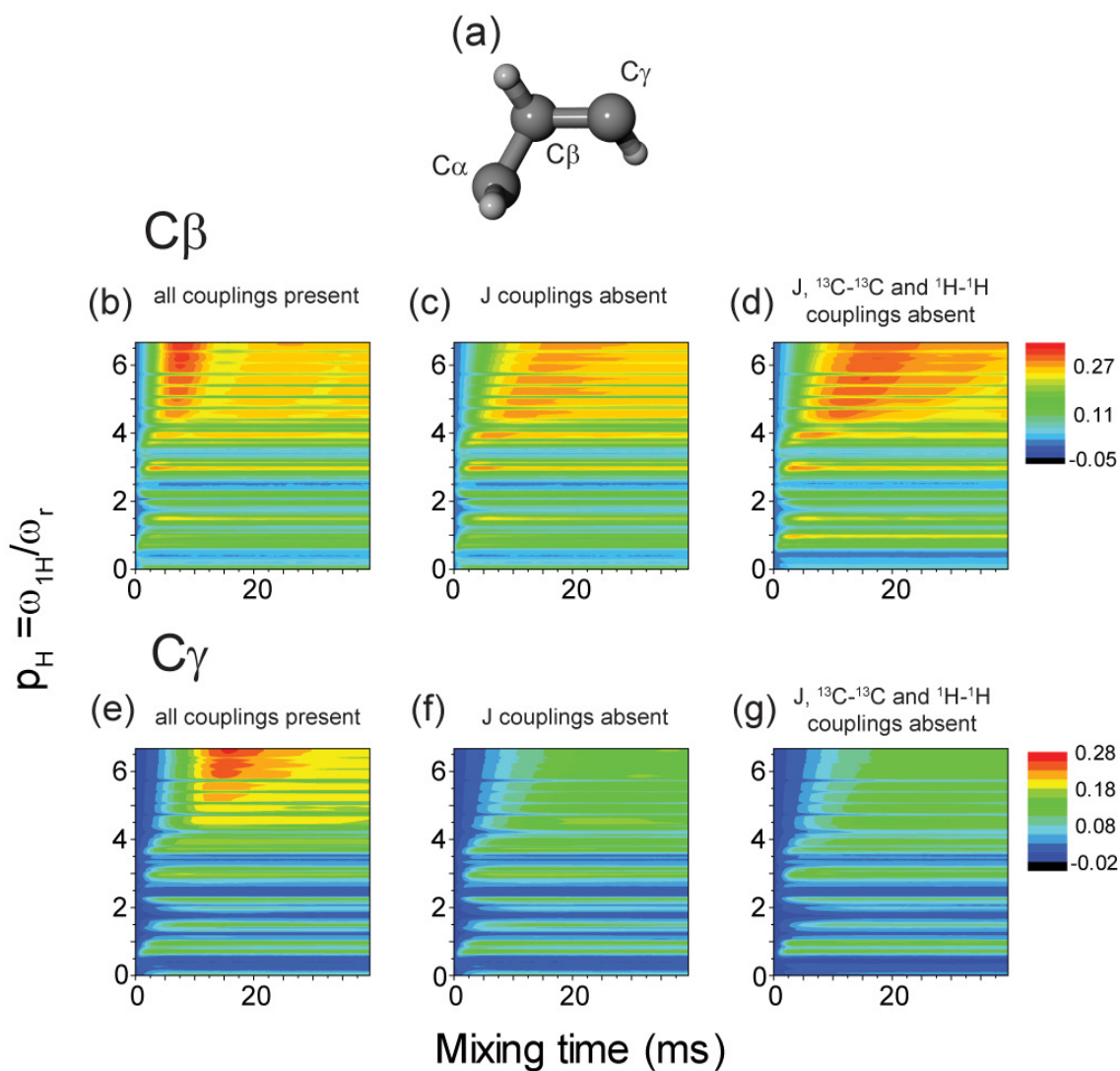


Figure 8-23 Simulations of the polarization transfer under $P9_{12}^1$ TOBSY as a function of ^1H irradiation (up to $p_{\text{H}}=6.66$ i.e. 200 kHz) illustrating the contribution of the TSAR based mechanism to the overall polarization transfer. The initial magnetization was placed on the $\text{C}\alpha$. (a) Spin system for the simulations consisting of 3 carbons and 3 protons. Panels (b-d) show polarization transferred to the $\text{C}\beta$ site. Panels (e-g) show polarization transferred to the $\text{C}\gamma$ site. Panels (b) and (e) include all the interactions. J coupling was removed from the simulations in panel (c) and (f). Panels (d) and (g) show simulations with J coupling, ^{13}C - ^{13}C and ^1H - ^1H dipolar coupling removed and therefore isolated TSAR mechanism contribution. All the simulations were performed at $\omega_r/2\pi = 30$ kHz, $\omega_{\text{H}}/2\pi = 700$ MHz and include isotropic chemical shift and CSA for ^{13}C 's ($\delta_{\text{iso},\text{C}\alpha}=-10$ ppm, $\delta_{\text{iso},\text{C}\beta}=0$ ppm, $\delta_{\text{iso},\text{C}\gamma}=10$ ppm, $\delta_{\text{anis},\text{C}\alpha}=-20$ ppm, $\eta_{\text{C}\alpha}=0.6$, $\delta_{\text{anis},\text{C}\beta}=-19$ ppm, $\eta_{\text{C}\alpha}=0.7$, $\delta_{\text{anis},\text{C}\alpha}=-19$ ppm, $\eta_{\text{C}\alpha}=0.7$). Whenever used, J couplings were set to 35 Hz. Note, that even for $\omega_{\text{H}}/2\pi = 200$ kHz the spin dynamics are strongly influenced by ^1H 's.

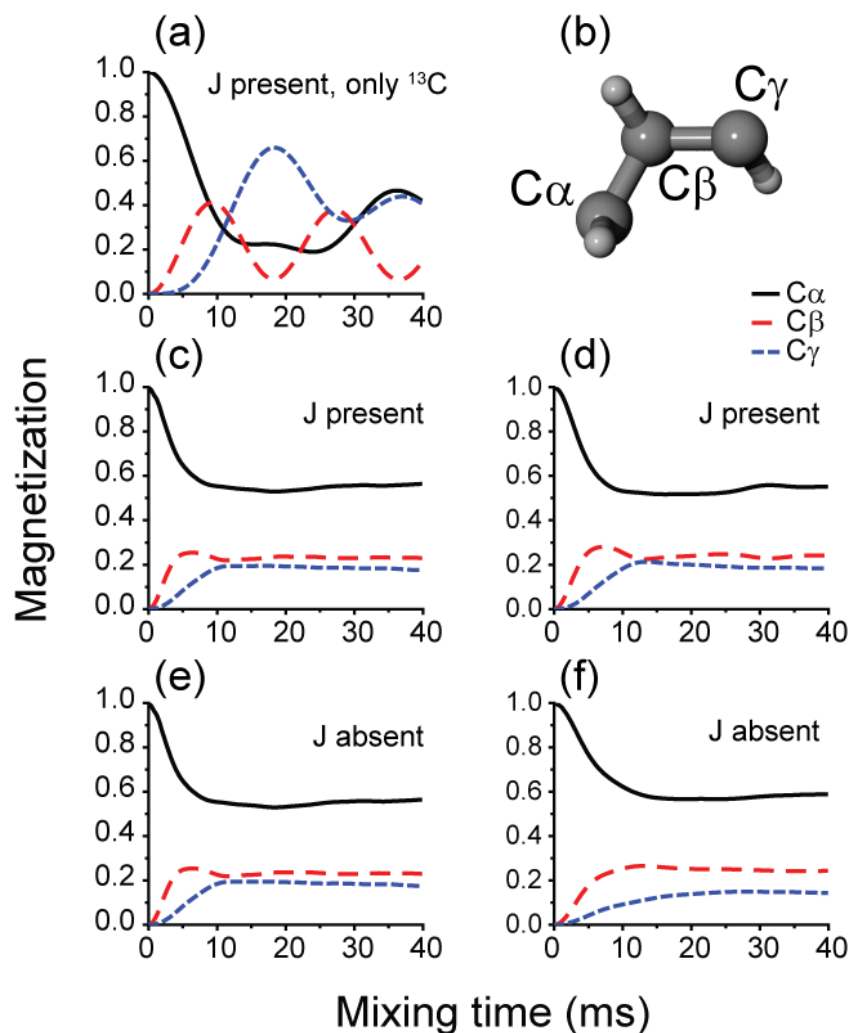


Figure 8-24 Simulations of the polarization transfer under P912¹ TOBSY illustrating the contribution of the TSAR based mechanism to the overall polarization transfer. (a) Simulation performed on a spin system consisting only of carbons with J couplings present. Simulations (c-d) are performed on a 6 spin system portrayed in the graphic (b) consisting of 3 carbons and 3 protons. (c) Simulation with J coupling present and ^1H irradiation at $p_{\text{H}}=4.5$ (135 kHz). (d) Simulation with J coupling present and ^1H irradiation at $p_{\text{H}}=5.2$ ($\omega_{\text{H}}/2\pi = 156$ kHz). (e) Simulation with J coupling absent and ^1H irradiation at $p_{\text{H}}=4.5$ ($\omega_{\text{H}}/2\pi = 135$ kHz). (f) Simulation with J coupling absent and ^1H irradiation at $p_{\text{H}}=5.2$ ($\omega_{\text{H}}/2\pi = 156$ kHz). All the simulations were performed at $\omega_{\text{r}}/2\pi = 30$ kHz, $\omega_{\text{0H}}/2\pi = 700$ MHz and include isotropic chemical shift and CSA for carbons ($\delta_{\text{iso,C}\alpha} = -10$ ppm, $\delta_{\text{iso,C}\beta} = 0$ ppm, $\delta_{\text{iso,C}\gamma} = 10$ ppm, $\delta_{\text{anis,C}\alpha} = -20$ ppm, $\eta_{\text{C}\alpha} = 0.6$, $\delta_{\text{anis,C}\beta} = -19$ ppm, $\eta_{\text{C}\alpha} = 0.7$, $\delta_{\text{anis,C}\alpha} = -19$ ppm, $\eta_{\text{C}\alpha} = 0.7$). J couplings were set to 35 Hz. Simulations (e-f) illustrate polarization transfer due to the TSAR mechanism only. Simulations (c-d) show polarization transfer that is a mixture of TSAR mechanism and J coupling based mechanism. Note, that even at

$p_H=5.2$, which corresponds to $3.46p_C$, the TSAR based mechanism is dominating the spin dynamics and almost eliminates the characteristic oscillatory features of the J coupling based transfer present in (a).

8.10.9 ^{13}C - ^{13}C PAR versus CHHC and DARR – a qualitative comparison

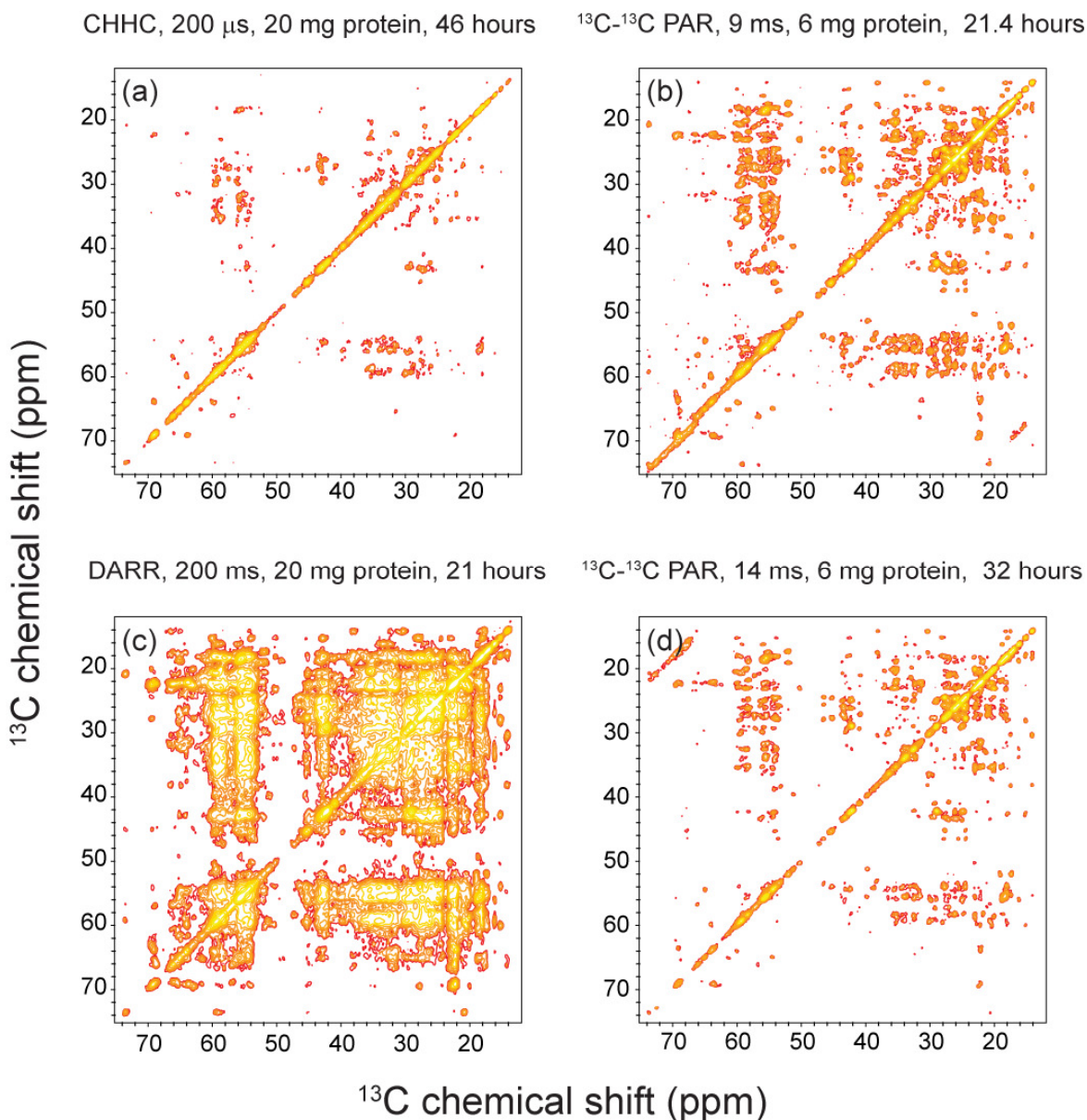


Figure 8-25 Qualitative comparison of different ^{13}C - ^{13}C recoupling techniques on [U- ^{13}C , ^{15}N]-Crh protein: (a) CHHC spectrum with 200 μs mixing time, (b) ^{13}C - ^{13}C PAR spectrum with 9 ms mixing time, (c) DARR spectrum with 200 ms mixing time, (d) ^{13}C - ^{13}C PAR spectrum with 14

ms mixing time spectra. (a,c) were obtained at 11 kHz MAS and 500 MHz ^1H Larmor frequency using ~ 20 mg of protein. (b,d) were obtained at $\omega_r/2\pi = 20$ kHz, $\omega_{\text{OH}}/2\pi = 750$ MHz using ca.6 mg of protein. The total acquisition time of the spectra is detailed above the each spectrum. See main text (Sec 8.6.2) for details on Fig. 8-25.

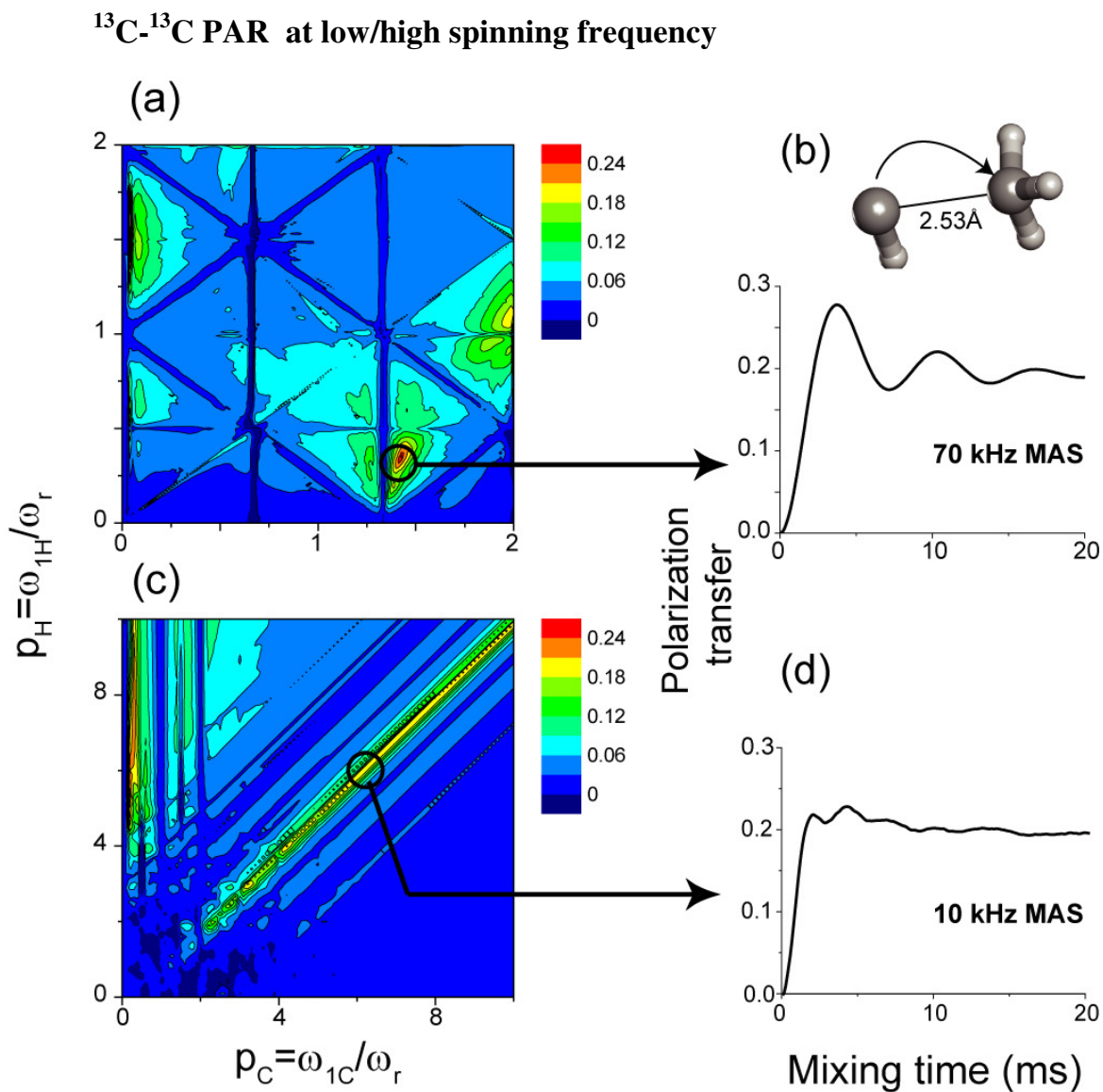


Figure 8-26 Numerical simulations illustrating applicability of the PAR technique at ultrahigh and moderate spinning frequencies. Graphics (a,b) depict PAR optimization map for the $\text{CH}-\text{CH}_3$ spin system in the inset (b) performed at $\omega_r/2\pi = 70$ kHz MAS (a) and $\omega_r/2\pi = 10$ kHz MAS (c) at $\omega_{\text{OH}}/2\pi = 750$ MHz. The mixing time in (a-c) was fixed at 10 ms. Spin system includes

isotropic chemical shift and CSA for carbon nuclei ($\delta_{\text{iso,C1}}=-10$ ppm, $\delta_{\text{iso,C2}}=10$ ppm, $\delta_{\text{anis,C1}}=20$ ppm, $\eta_{\text{C1}}=0.6$, $\delta_{\text{anis,C1}}=19$ ppm, $\eta_{\text{C1}}=0.8$). Simulation includes methyl group rotation. Graphic (b-d) shows a polarization build-up simulated for the settings highlighted in the map i.e. $p_{\text{C}}=1.07$ ($\omega_{\text{1C}}/2\pi = 74.9$ kHz) and $p_{\text{H}}=0.37$ ($\omega_{\text{1H}}/2\pi = 25.9$ kHz) in (b) and $p_{\text{C}}=7.1$ ($\omega_{\text{1C}}/2\pi = 71$ kHz) and $p_{\text{H}}=6.9$ ($\omega_{\text{1H}}/2\pi = 69$ kHz) in (d).

8.11 References (manuscript)

- (1) Andrew, E. R.; Bradbury, A.; Eades, R. G. *Nature* **1958**, *182*, 1659-1659.
- (2) Andrew, E. R.; Bradbury, A.; Eades, R. G. *Nature* **1959**, *183*, 1802-1803.
- (3) Munowitz, M. G.; Griffin, R. G.; Bodenhausen, G.; Huang, T. H. *Journal of the American Chemical Society* **1981**, *103*, 2529-2533.
- (4) Munowitz, M. G.; Griffin, R. G. *Journal of Chemical Physics* **1982**, *76*, 2848-2858.
- (5) Gullion, T.; Schaefer, J. *Journal of Magnetic Resonance* **1989**, *81*, 196-200.
- (6) Raleigh, D. P.; Levitt, M. H.; Griffin, R. G. *Chemical Physics Letters* **1988**, *146*, 71-76.
- (7) Raleigh, D. P.; Creuzet, F.; Gupta, S. K. D.; Levitt, M. H.; Griffin, R. G. *Journal of the American Chemical Society* **1989**, *111*, 4502-4503.
- (8) Tycko, R.; Dabbagh, G. *Chemical Physics Letters* **1990**, *173*, 461-465.
- (9) Tycko, R.; Dabbagh, G. *J. Am. Chem. Soc.* **1991**, *113*, 9444-9448.
- (10) Bennett, A. E.; Ok, J. H.; Griffin, R. G.; Vega, S. *Journal of Chemical Physics* **1992**, *96*, 8624-8627.
- (11) Bennett, A. E.; Rienstra, C. M.; Griffiths, J. M.; Zhen, W. G.; Lansbury, P. T.; Griffin, R. G. *Journal of Chemical Physics* **1998**, *108*, 9463-9479.
- (12) Nielsen, N. C.; Bildsoe, H.; Jakobsen, H. J.; Levitt, M. H. *Journal of Chemical Physics* **1994**, *101*, 1805-1812.
- (13) De Paepe, G.; Bayro, M. J.; Lewandowski, J.; Griffin, R. G. *Journal of the American Chemical Society* **2006**, *128*, 1776-1777.
- (14) De Paepe, G.; Lewandowski, J. R.; Griffin, R. G. *Journal of Chemical Physics* **2008**, *128*, 124503-124526.

- (15) Bayro, M. J.; Ramachandran, R.; Caporini, M. A.; Eddy, M. T.; Griffin, R. G. *Journal of Chemical Physics* **2008**, *128*.
- (16) Brinkmann, A.; Eden, M.; Levitt, M. H. *Journal of Chemical Physics* **2000**, *112*, 8539-8554.
- (17) Brinkmann, A.; Levitt, M. H. *Journal of Chemical Physics* **2001**, *115*, 357-384.
- (18) Creuzet, F.; McDermott, A.; Gebhard, R.; Vanderhoef, K.; Spijkerassink, M. B.; Herzfeld, J.; Lugtenburg, J.; Levitt, M. H.; Griffin, R. G. *Science* **1991**, *251*, 783-786.
- (19) Carravetta, M.; Eden, M.; Johannessen, O. G.; Luthman, H.; Verdegem, P. J. E.; Lugtenburg, J.; Sebald, A.; Levitt, M. H. *Journal of the American Chemical Society* **2001**, *123*, 10628-10638.
- (20) Jaroniec, C. P.; Filip, C.; Griffin, R. G. *J. Am. Chem. Soc.* **2002**, *124*, 10728-10742.
- (21) Jaroniec, C. P.; Tounge, B. A.; Herzfeld, J.; Griffin, R. G. *Journal of the American Chemical Society* **2001**, *123*, 3507-3519.
- (22) Jaroniec, C. P.; Tounge, B. A.; Herzfeld, J.; Griffin, R. G. *Biophysical Journal* **2001**, *80*, 368A-368A.
- (23) Jaroniec, C. P.; Tounge, B. A.; Rienstra, C. M.; Herzfeld, J.; Griffin, R. G. *J. Am. Chem. Soc.* **1999**, *121*, 10237-10238.
- (24) Ramachandran, R.; Ladizhansky, V.; Bajaj, V. S.; Griffin, R. G. *Journal of the American Chemical Society* **2003**, *125*, 15623-15629.
- (25) Ramachandran, R.; Lewandowski, J. R.; van der Wel, P. C. A.; Griffin, R. G. *Journal of Chemical Physics* **2006**, *124*, 214107-214113.
- (26) Ladizhansky, V.; Griffin, R. G. *Journal of the American Chemical Society* **2004**, *126*, 948-958.
- (27) Carravetta, M.; Zhao, X.; Johannessen, O. G.; Lai, W. C.; Verhoeven, M. A.; Bovee-Geurts, P. H. M.; Verdegem, P. J. E.; Kiihne, S.; Luthman, H.; de Groot, H. J. M.; deGrip, W. J.; Lugtenburg, J.; Levitt, M. H. *Journal of the American Chemical Society* **2004**, *126*, 3948-3953.

- (28) Ladizhansky, V.; Jaroniec, C. P.; Diehl, A.; Oschkinat, H.; Griffin, R. G. *Journal of the American Chemical Society* **2003**, *125*, 6827-6833.
- (29) Feng, X.; Lee, Y. K.; Sandstrom, D.; Eden, M.; Maisel, H.; Sebald, A.; Levitt, M. H. *Chemical Physics Letters* **1996**, *257*, 314-320.
- (30) Feng, X.; Verdegem, P. J. E.; Eden, M.; Sandstrom, D.; Lee, Y. K.; Bovee-Geurts, P. H. M.; de Grip, W. J.; Lugtenburg, J.; de Groot, H. J. M.; Levitt, M. H. *Journal of Biomolecular Nmr* **2000**, *16*, 1-8.
- (31) Ladizhansky, V.; Veshtort, M.; Griffin, R. G. *Journal of Magnetic Resonance* **2002**, *154*, 317-324.
- (32) Feng, X.; Eden, M.; Brinkmann, A.; Luthman, H.; Eriksson, L.; Graslund, A.; Antzutkin, O. N.; Levitt, M. H. *Journal of the American Chemical Society* **1997**, *119*, 12006-12007.
- (33) Feng, X.; Verdegem, P. J. E.; Lee, Y. K.; Sandstrom, D.; Eden, M.; BoveeGeurts, P.; deGrip, W. J.; Lugtenburg, J.; deGroot, H. J. M.; Levitt, M. H. *Journal of the American Chemical Society* **1997**, *119*, 6853-6857.
- (34) Takegoshi, K.; Nakamura, S.; Terao, T. *Chemical Physics Letters* **2001**, *344*, 631-637.
- (35) Takegoshi, K.; Nakamura, S.; Terao, T. *Journal of Chemical Physics* **2003**, *118*, 2325-2341.
- (36) Castellani, F.; van Rossum, B.; Diehl, A.; Schubert, M.; Rehbein, K.; Oschkinat, H. *Nature* **2002**, *420*, 98-102.
- (37) Zech, S. G.; Wand, A. J.; McDermott, A. E. *Journal of the American Chemical Society* **2005**, *127*, 8618-8626.
- (38) Manolikas, T.; Herrmann, T.; Meier, B. H. *Journal of the American Chemical Society* **2008**, *130*, 3959-3966.
- (39) Bennett, A. E.; Rienstra, C. M.; Auger, M.; Lakshmi, K. V.; Griffin, R. G. *Journal of Chemical Physics* **1995**, *103*, 6951-6958.
- (40) Detken, A.; Hardy, E. H.; Ernst, M.; Meier, B. H. *Chemical Physics Letters* **2002**, *356*, 298-304.
- (41) De Paepe, G.; Elena, B.; Emsley, L. *Journal of Chemical Physics* **2004**, *121*, 3165-3180.

- (42) De Paepe, G.; Giraud, N.; Lesage, A.; Hodgkinson, P.; Bockmann, A.; Emsley, L. *Journal of the American Chemical Society* **2003**, *125*, 13938-13939.
- (43) De Paepe, G.; Hodgkinson, P.; Emsley, L. *Chemical Physics Letters* **2003**, *376*, 259-267.
- (44) De Paepe, G.; Lesage, A.; Emsley, L. *Journal of Chemical Physics* **2003**, *119*, 4833-4841.
- (45) Ernst, M. *Journal of Magnetic Resonance* **2003**, *162*, 1-34.
- (46) Hodgkinson, P. *Progress in Nuclear Magnetic Resonance Spectroscopy* **2005**, *46*, 197-222.
- (47) van der Wel, P. C. A.; Lewandowski, J. R.; Griffin, R. G. *Journal of the American Chemical Society* **2007**, *129*, 5117-5130.
- (48) Tycko, R.; Ishii, Y. *Journal of the American Chemical Society* **2003**, *125*, 6606-6607.
- (49) Wasmer, C.; Lange, A.; Van Melckebeke, H.; Siemer, A. B.; Riek, R.; Meier, B. H. *Science* **2008**, *319*, 1523-1526.
- (50) Jaroniec, C. P.; MacPhee, C. E.; Astrof, N. S.; Dobson, C. M.; Griffin, R. G. *Proceedings of the National Academy of Sciences of the United States of America* **2002**, *99*, 16748-16753.
- (51) De Paepe, G.; Lewandowski, J.; Bayro, M. J.; Griffin, R. G. In *47th Experimental Nuclear Magnetic Resonance Conference Asilomar (SF)*, 2006.
- (52) Bockmann, A.; Lange, A.; Galinier, A.; Luca, S.; Giraud, N.; Juy, M.; Heise, H.; Montserret, R.; Penin, F.; Baldus, M. *J Biomol NMR* **2003**, *27*, 323-339.
- (53) Cornilescu, G.; Delaglio, F.; Bax, A. *Journal of Biomolecular Nmr* **1999**, *13*, 289-302.
- (54) Costa, P. R.; Sun, B. Q.; Griffin, R. G. *Journal of the American Chemical Society* **1997**, *119*, 10821-10830.
- (55) Costa, P. R.; Sun, B. Q.; Griffin, R. G. *Journal of Magnetic Resonance* **2003**, *164*, 92-103.
- (56) Takegoshi, K.; Nomura, K.; Terao, T. *Chemical Physics Letters* **1995**, *232*, 424-428.

- (57) Takegoshi, K.; Nomura, K.; Terao, T. *Journal of Magnetic Resonance* **1997**, *127*, 206-216.
- (58) Paravastu, A. K.; Tycko, R. *Journal of Chemical Physics* **2006**, *124*.
- (59) Marin-Montesinos, I.; Mollica, G.; Carravetta, M.; Gansmuller, A.; Pilelo, G.; Bechmann, M.; Sebald, A.; Levitt, M. H. *Chemical Physics Letters* **2006**, *432*, 572-578.
- (60) Khaneja, N.; Niels Chr, N. *The Journal of Chemical Physics* **2008**, *128*, 015103.
- (61) Szeverenyi, N. M.; Sullivan, M. J.; Maciel, G. E. *Journal of Magnetic Resonance* **1982**, *47*, 462-475.
- (62) Morcombe, C. R.; Gaponenko, V.; Byrd, R. A.; Zilm, K. W. *Journal of the American Chemical Society* **2004**, *126*, 7196-7197.
- (63) Lange, A.; Seidel, K.; Verdier, L.; Luca, S.; Baldus, M. *Journal of the American Chemical Society* **2003**, *125*, 12640-12648.
- (64) Lange, A.; Luca, S.; Baldus, M. *Journal of the American Chemical Society* **2002**, *124*, 9704-9705.
- (65) Heise, H.; Seidel, K.; Etzkorn, M.; Becker, S.; Baldus, M. *Journal of Magnetic Resonance* **2005**, *173*, 64-74.
- (66) Peng, X.; Libich, D.; Janik, R.; Harauz, G.; Ladizhansky, V. *J. Am. Chem. Soc.* **2008**, *130*, 359-369.
- (67) Grommek, A.; Meier, B. H.; Ernst, M. *Chemical Physics Letters* **2006**, *427*, 404-409.
- (68) Seidel, K.; Etzkorn, M.; Sonnenberg, L.; Griesinger, C.; Sebald, A.; Baldus, M. *Journal of Physical Chemistry A* **2005**, *109*, 2436-2442.
- (69) Zhou, D. H.; Shea, J. J.; Nieuwkoop, A. J.; Franks, W. T.; Wylie, B. J.; Mullen, C.; Sandoz, D.; Rienstra, C. M. *Angew Chem Int Ed Engl* **2007**, *46*, 8380-3.
- (70) Loquet, A.; Bardiaux, B.; Gardiennet, C.; Blanchet, C.; Baldus, M.; Nilges, M.; Malliavin, T.; Boeckmann, A. *Journal of the American Chemical Society* **2008**, *130*, 3579-3589.
- (71) Lange, A.; Becker, S.; Seidel, K.; Giller, K.; Pongs, O.; Baldus, M. *Angewandte Chemie-International Edition* **2005**, *44*, 2089-2092.

- (72) Lewandowski, J. R.; De Paepe, G.; Griffin, R. G. *Journal of the American Chemical Society* **2007**, *129*, 728-729.
- (73) Haeberlen, U.; Waugh, J. S. *Physical Review* **1968**, *175*, 453.
- (74) Hartmann, S. R.; Hahn, E. L. *Phys. Rev.* **1962**, *128*, 2042-2053.
- (75) Levitt, M. H.; Oas, T. G.; Griffin, R. G. *Israel Journal of Chemistry* **1988**, *28*, 271-282.
- (76) Oas, T. G.; Griffin, R. G.; Levitt, M. H. *Journal of Chemical Physics* **1988**, *89*, 692-695.
- (77) Sorensen, O. W.; Eich, G. W.; Levitt, M. H.; Bodenhausen, G.; Ernst, R. R. *Progress in Nuclear Magnetic Resonance Spectroscopy* **1983**, *16*, 163-192.
- (78) Veshtort, M.; Griffin, R. G. *J. Magn. Reson.* **2006**, *178*, 248-82.
- (79) Lee, Y. K.; Kurur, N. D.; Helmle, M.; Johannessen, O. G.; Nielsen, N. C.; Levitt, M. H. *Chemical Physics Letters* **1995**, *242*, 304-309.
- (80) Costa, P. R. Ph.D., MIT, 1996.
- (81) Hohwy, M.; Rienstra, C. M.; Griffin, R. G. *Journal of Chemical Physics* **2002**, *117*, 4973-4987.
- (82) Verel, R.; Ernst, M.; Meier, B. H. *Journal of Magnetic Resonance* **2001**, *150*, 81-99.
- (83) Hohwy, M.; Rienstra, C. M.; Jaroniec, C. P.; Griffin, R. G. *Journal of Chemical Physics* **1999**, *110*, 7983-7992.
- (84) Lewandowski, J. R.; De Paepe, G.; van der Wel, P. C. A.; Birkett, N. R.; Belenky, M.; Maly, T.; Bayro, M. J.; Sivertsen, A. C.; Dobson, C. M.; Herzfeld, J.; Griffin, R. G. **2008**, *submitted*.
- (85) Juy, M.; Penin, F.; Favier, A.; Galinier, A.; Montserret, R.; Haser, R.; Deutscher, J.; Bockmann, A. *Journal of Molecular Biology* **2003**, *332*, 767-776.
- (86) Ishii, Y.; Ashida, J.; Terao, T. *Chemical Physics Letters* **1995**, *246*, 439-445.
- (87) Rienstra, C. M.; Hatcher, M. E.; Mueller, L. J.; Sun, B. Q.; Fesik, S. W.; Griffin, R. G. *Journal of the American Chemical Society* **1998**, *120*, 10602-10612.
- (88) Ishii, Y. *Journal of Chemical Physics* **2001**, *114*, 8473-8483.

- (89) Brinkmann, A.; Gunne, J. S. A. D.; Levitt, M. H. *Journal of Magnetic Resonance* **2002**, *156*, 79-96.
- (90) Hardy, E. H.; Verel, R.; Meier, B. H. *Journal of Magnetic Resonance* **2001**, *148*, 459-464.
- (91) Lesage, A.; Auger, C.; Caldarelli, S.; Emsley, L. *Journal of the American Chemical Society* **1997**, *119*, 7867-7868.
- (92) Lesage, A.; Bardet, M.; Emsley, L. *Journal of the American Chemical Society* **1999**, *121*, 10987-10993.
- (93) Lesage, A.; Sakellariou, D.; Steuernagel, S.; Emsley, L. *Journal of the American Chemical Society* **1998**, *120*, 13194-13201.
- (94) De Paepe, G.; Lesage, A.; Steuernagel, S.; Emsley, L. *Chemphyschem* **2004**, *5*, 869-875.
- (95) Mueller, L. J.; Elliott, D. W.; Leskowitz, G. M.; Struppe, J.; Olsen, R. A.; Kim, K. C.; Reed, C. A. *Journal of Magnetic Resonance* **2004**, *168*, 327-335.
- (96) Hughes, C. E.; Luca, S.; Baldus, M. *Chemical Physics Letters* **2004**, *385*, 435-440.
- (97) Marin-Montesinos, I.; Brouwer, D. H.; Antonioli, G.; Lai, W. C.; Brinkmann, A.; Levitt, M. H. *J. Magn. Reson.* **2005**, *177*, 307-317.
- (98) Rienstra, C. M.; Tucker-Kellogg, L.; Jaroniec, C. P.; Hohwy, M.; Reif, B.; McMahan, M. T.; Tidor, B.; Lozano-Perez, T.; Griffin, R. G. *Proceedings of the National Academy of Sciences of the United States of America* **2002**, *99*, 10260-10265.
- (99) Brunger, A. T.; Adams, P. D.; Clore, G. M.; DeLano, W. L.; Gros, P.; Grosse-Kunstleve, R. W.; Jiang, J. S.; Kuszewski, J.; Nilges, M.; Pannu, N. S.; Read, R. J.; Rice, L. M.; Simonson, T.; Warren, G. L. *Acta Crystallographica Section D-Biological Crystallography* **1998**, *54*, 905-921.
- (100) Franks, W. T.; Kloepper, K. D.; Wylie, B. J.; Rienstra, C. M. *J Biomol NMR* **2007**, *39*, 107-131.
- (101) Marulanda, D.; Tasayco, M. L.; Cataldi, M.; Arriaran, V.; Polenova, T. *Journal of Physical Chemistry B* **2005**, *109*, 18135-18145.
- (102) Zech, S. G.; Olejniczak, E.; Hajduk, P.; Mack, J.; McDermot, A. E. *Journal of the American Chemical Society* **2004**, *126*, 13948-13953.

8.12 References (Supporting Information)

- (1) Penin, F.; Favier, A.; Montserret, R.; Brutscher, B.; Deutscher, J.; Marion, D.; Galinier, A. *Journal of Molecular Microbiology and Biotechnology* **2001**, *3*, 429-432.
- (2) Bockmann, A.; Lange, A.; Galinier, A.; Luca, S.; Giraud, N.; Juy, M.; Heise, H.; Montserret, R.; Penin, F.; Baldus, M. *J Biomol NMR* **2003**, *27*, 323-339.
- (3) Morcombe, C. R.; Zilm, K. W. *Journal of Magnetic Resonance* **2003**, *162*, 479-486.
- (4) Bennett, A. E.; Rienstra, C. M.; Auger, M.; Lakshmi, K. V.; Griffin, R. G. *Journal of Chemical Physics* **1995**, *103*, 6951-6958.
- (5) Cavanagh, J.; Fairbrother, W. J.; Palmer, A. G.; Skelton, N. J.; Rance, M. *Protein NMR Spectroscopy: Principles and Practice*; Academic Press, 2006.
- (6) Veshtort, M.; Griffin, R. G. *J. Magn. Reson.* **2006**, *178*, 248-82.
- (7) Delaglio, F.; Grzesiek, S.; Vuister, G. W.; Zhu, G.; Pfeifer, J.; Bax, A. *J Biomol NMR* **1995**, *6*, 277-93.
- (8) Gardiennet, C.; Loquet, A.; Bockmann, A.; Etzkorn, M.; Heise, H.; Baldus, M. *Journal of Biomolecular Nmr* **2008**, *40*, 239-250.
- (9) Brunger, A. T.; Adams, P. D.; Clore, G. M.; DeLano, W. L.; Gros, P.; Grosse-Kunstleve, R. W.; Jiang, J. S.; Kuszewski, J.; Nilges, M.; Pannu, N. S.; Read, R. J.; Rice, L. M.; Simonson, T.; Warren, G. L. *Acta Crystallographica Section D-Biological Crystallography* **1998**, *54*, 905-921.
- (10) Rice, L. M.; Brunger, A. T. *Proteins-Structure Function and Genetics* **1994**, *19*, 277-290.
- (11) Stein, E. G.; Rice, L. M.; Brunger, A. T. *Journal of Magnetic Resonance* **1997**, *124*, 154-164.
- (12) Koradi, R.; Billeter, M.; Wuthrich, K. *Journal of Molecular Graphics* **1996**, *14*, 51-55.
- (13) Juy, M.; Penin, F.; Favier, A.; Galinier, A.; Montserret, R.; Haser, R.; Deutscher, J.; Bockmann, A. *Journal of Molecular Biology* **2003**, *332*, 767-776.
- (14) Ye, C. H.; Fu, R. Q.; Hu, J. Z.; Hou, L.; Ding, S. W. *Magnetic Resonance in Chemistry* **1993**, *31*, 699-704.

- (15) Nielsen, N. C.; Bildsoe, H.; Jakobsen, H. J.; Levitt, M. H. *Journal of Chemical Physics* **1994**, *101*, 1805-1812.
- (16) De Paepe, G.; Bayro, M. J.; Lewandowski, J.; Griffin, R. G. *Journal of the American Chemical Society* **2006**, *128*, 1776-1777.
- (17) De Paepe, G.; Lewandowski, J. R.; Griffin, R. G. *Journal of Physical Chemistry* **2008**, *In Press*.

9. ^{15}N - ^{15}N Proton Assisted Homonuclear Recoupling as a Structural Tool in Solid-State NMR

9.1 Abstract

We describe a new experiment for obtaining ^{15}N - ^{15}N correlation spectra that yields direct information about the secondary and tertiary structure of proteins, including identification of α -helical stretches and inter-strand connectivity in antiparallel β -sheets, which should be of major interest for structural studies on biological systems including membrane proteins and fibrils. The method, ^{15}N - ^{15}N Proton Assisted homonuclear Recoupling (PAR), relies on a second order Third Spin Assisted Recoupling (TSAR) mechanism used previously in the context of ^{15}N - ^{13}C and ^{13}C - ^{13}C polarization transfer schemes. This new technique accelerates polarization transfer between nitrogen spins up to three orders of magnitude compared to ^{15}N - ^{15}N proton driven spin diffusion (PDSD) experiments, and furthermore it should be applicable over the entire range of currently available magic angle spinning frequencies (10-70 kHz).

9.2 Introduction

Magic angle spinning (MAS)¹ NMR has emerged as the preferred approach for performing detailed studies of the structure and dynamics of insoluble biological systems and systems lacking long range order that are currently not accessible by x-ray diffraction or solution NMR. Specifically, MAS experiments are used to investigate protein folding and misfolding, amyloid aggregation, signal transduction, and molecular transport across biomembranes to name a few of the areas of current research.^{2-12,13}

A number of developments have contributed to the evolving methodology to determine protein structures via MAS NMR. These include access to high field magnets (>15T), improved sample preparation protocols,¹⁴ selective isotopic labeling schemes,¹⁵⁻¹⁸ adaptation of computational protocols for structure calculations^{11,19-22} and new methods for assigning spectra and for measuring distances and torsion angles²³⁻⁴². At present, resonance assignments and structural studies in the solid state rely mainly on multidimensional ¹³C-¹³C and ¹⁵N-¹³C-(¹³C) correlation experiments. In addition, ¹⁵N-¹⁵N correlation spectra, which were first reported by Reif, et al. almost a decade ago,⁴³ are a valuable tool for estimating ¹⁵N-¹⁵N distances⁴⁴ and for measuring the NH_i-NH_{i+1} projection angle $\theta_{i,i+1}$,^{43,45} To date, however, these experiments have been limited to B₀ < 11-13 T and $\omega_r/2\pi$ < 12 kHz and therefore have not achieved their full potential.

In this paper, we show that ¹⁵N-¹⁵N correlation spectroscopy can be extended to MAS frequencies >15 kHz and to magnetic fields >20 T using the ¹⁵N-¹⁵N proton assisted recoupling (PAR) technique²⁹ that was recently introduced in the context of ¹³C-¹³C and ¹³C-¹⁵N recoupling and which relies on a more general third spin assisted recoupling (TSAR) mechanism.^{29,30,41}

We apply the ¹⁵N-¹⁵N PAR pulse sequence (see Fig. 1) to a model tripeptide N-*f*-MLF-OH and to the 56-residue microcrystalline β 1 immunoglobulin binding domain of protein G (GB1). The mixing time required for observing structurally relevant ¹⁵N-¹⁵N contacts (~2.8-4.5 Å) in the PAR experiment corresponds to tens of milliseconds, improving on spin-diffusion based techniques (PDS⁴⁶, DARR³⁹) by two to three orders of magnitude. In addition, the observed cross peak intensities can be related to

the topology of the ^{15}N - ^{15}N network in a straightforward manner, thus allowing protein secondary and tertiary structure to be clearly established.

9.3 ^{15}N - ^{15}N correlation spectroscopy:

Despite its low gyromagnetic ratio, ^{15}N has been a valuable nucleus for biomolecular MAS SSNMR studies. Metabolic sources of ^{15}N are relatively inexpensive, allowing one, for example, to prepare uniformly ^{15}N labeled proteins to screen sample preparation conditions.¹⁴ In addition, an ^{15}N dimension is often incorporated into advanced multidimensional NMR experiments. ^{15}N and ^{13}C labeled samples are routinely used for sequential resonance assignments,^{25,41,47-60} for measuring torsion angles,⁶¹⁻⁶⁴ extracting accurate ^{15}N - ^{13}C distances,^{31,32,45,65-71} and finally for locally probing protein backbone dynamics.⁷²⁻⁷⁵

The two main challenges for ^{15}N - ^{15}N correlation spectroscopy in the solid state have been (1) the poor sensitivity of ^{15}N observed experiments and (2) the relatively restricted range of available methods for transferring magnetization among ^{15}N nuclei. The first issue is currently being addressed by the development of high field dynamic nuclear polarization (DNP)^{76,77}, and the combination of spinning frequencies up to ~70 kHz together with ^1H detected experiments.⁷⁸ The second issue mentioned above is directly related to the small magnitude of ^{15}N - ^{15}N couplings, which currently prevents the wide use of advanced first order recoupling techniques developed for ^{13}C - ^{13}C polarization transfer and restricts acquisition of ^{15}N - ^{15}N correlation experiments primarily to proton driven spin diffusion (PDS) based experiments.^{17,43-46,79}

Although ^{15}N - ^{15}N PDS experiments are relatively straightforward to perform, they are far from ideal for biomolecular systems requiring high resolution conditions available at high magnetic field strengths ($B_0 > 16$ T) and MAS frequencies ($\omega_r/2\pi > 20$ kHz). Such operating conditions require long mixing times which reduces the polarization transfer efficiency (due to the competition with the relaxation), and, more importantly, complicates the interpretation of the ^{15}N - ^{15}N polarization transfer buildups in terms of distance restraints.⁴⁴

9.4 ^{15}N - ^1H - ^{15}N TSAR – ^{15}N - ^{15}N PAR experiments:

9.4.1 TSAR mechanism principles:

The PAR pulse sequence was recently introduced in the context of ^{13}C - ^{13}C recoupling.²⁹ Its underlying mechanism relies on a second-order recoupling process referred to as third spin assisted recoupling (TSAR) that was used to develop the heteronuclear PAINCP⁴¹ (proton assisted insensitive nuclei cross polarization) experiment and has led to an understanding of the beneficial effect of applying a small ($< 0.25 \omega_r$) ^1H irradiation field to improve the double quantum transfer efficiency of CM_pRR (where p ranges from 3.5 to 5).³⁰ The TSAR mechanism, denoted as B-[A]-C, relies on three spin operators that connect spins B and C via a cross term involving dipolar couplings with a third assisting spin A (B-A and C-A dipolar couplings, respectively). In the experiment described here, the ^{15}N - ^{15}N PAR pulse sequence relies on a ^{15}N - ^1H - ^{15}N TSAR mechanism based on cross terms involving heteronuclear ^1H - $^{15}\text{N}_1$ and ^1H - $^{15}\text{N}_2$ dipolar couplings (see inset of Fig. 1) to induce polarization transfer between the nitrogen nuclei. As pointed out in our previous work,^{29,41} the polarization transfer does not rely on the BC coupling (^{15}N - ^{15}N in the experiments described here).

9.4.2 PAR pulse sequence and effective Hamiltonian:

The ^{15}N - ^{15}N PAR pulse sequence is illustrated in Fig. 1 and consists of simultaneous C.W. irradiation on the ^1H and ^{15}N channels.

The spin dynamics during TSAR mixing can be described by the following Hamiltonian:

$$\begin{aligned} H = & \Delta\omega_{N_1} N_{1z} + \Delta\omega_{N_2} N_{2z} + \Delta\omega_H H_z \\ & \underbrace{\omega_{N_1N_2} \left[2N_{1z}N_{2z} - (N_{1x}N_{2x} + N_{1y}N_{2y}) \right]}_{\text{[1]}} + \underbrace{\omega_{N_1H} 2N_{1z}H_z}_{\text{[2]}} + \underbrace{\omega_{N_2H} 2H_zN_{2z}}_{\text{[3]}} \\ & + \omega_{1N} (N_{1x} + N_{2x}) + \omega_{1H} H_x \end{aligned} \quad (138)$$

where $\Delta\omega_{N_1}, \Delta\omega_{N_2}, \Delta\omega_H$ denote the shift tensors and resonant offsets of the ^{15}N and ^1H nuclei respectively, and $\omega_{N_1N_2}, \omega_{N_1H}, \omega_{N_2H}$ the homonuclear and heteronuclear

dipolar couplings. Note that MAS induces a time dependence of the spatial anisotropy of the interactions. The last two terms in (1) denote the rf fields applied at the ^{15}N and ^1H frequencies, respectively.

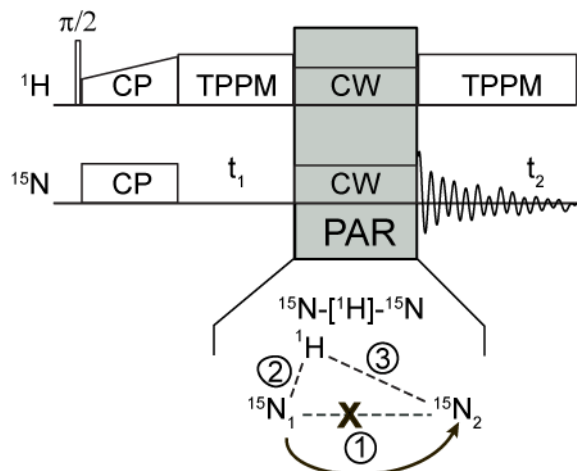


Figure 9-1 Pulse sequence for the 2D ^{15}N - ^{15}N PAR correlation experiment. The PAR mixing period consists of C.W. irradiations on ^1H and ^{15}N channels with the irradiation strengths chosen to produce an appreciable second order TSAR mechanism. The TSAR term of the form $H_z N_1^\pm N_2^m$ is a result of a cross term between the ^1H - $^{15}\text{N}_1$ and ^1H - $^{15}\text{N}_2$ dipolar couplings (terms 2 and 3 in the spin system graphics).

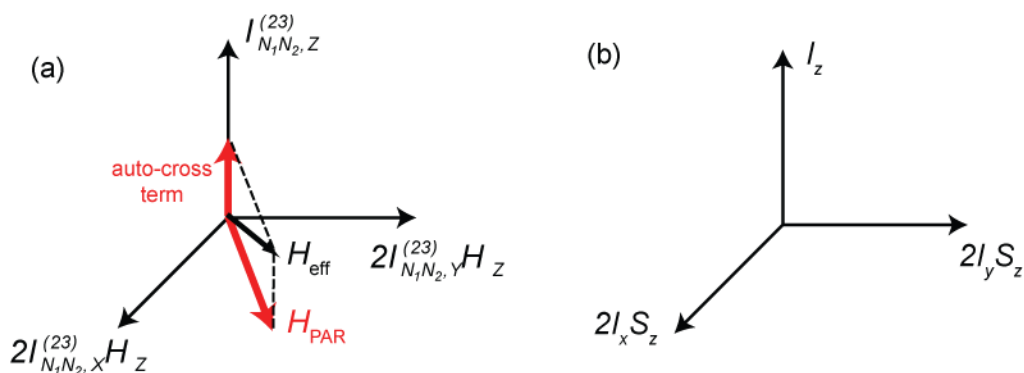


Figure 9-2 Visualization of the PAR subspace. The space can be seen as a coupled basis between a fictitious ZQ operator involving the two carbons (or nitrogens) and a proton spin. The red arrows indicate PAR recoupling axis and longitudinal tilting field resulting from auto-cross terms. Panel (b) depicts the coupled basis encountered in solution NMR.

As described in detail in De Paepe, et al.,²⁹ an effective TSAR Hamiltonian can be derived in the interaction frame described by the two C.W. rf fields of strength $\omega_{1N}/2\pi$ and $\omega_{1H}/2\pi$ for the ^{15}N and ^1H channels. The TSAR subspace (see Fig. 2) associated with the polarization transfer is defined by the following operators: $2I_{N_1N_2,X}^{(23)}I_{H,Z}$, $2I_{N_1N_2,Y}^{(23)}I_{H,Z}$, $I_{N_1N_2,Z}^{(23)}$, which represent a coupled basis between a fictitious ZQ spin (associated with spins N_1 and N_2) and a proton spin H. The TSAR cross term resulting from terms 2 and 3 ($^1\text{H}-^{15}\text{N}_1$ and $^1\text{H}-^{15}\text{N}_2$) in Eq. (1) can be written in the transverse plane defined by the operators $2I_{N_1N_2,X}^{(23)}I_{H,Z}$ and $2I_{N_1N_2,Y}^{(23)}I_{H,Z}$, and leads to polarization transfer between N_1 and N_2 . The other important contribution to the spin dynamics comes from auto-cross terms created by term 2 with itself (i.e. $^1\text{H}-^{15}\text{N}_1$ cross $^1\text{H}-^{15}\text{N}_1$) and term 3 with itself (i.e. $^1\text{H}-^{15}\text{N}_1$ cross $^1\text{H}-^{15}\text{N}_1$) respectively. These auto-cross terms produce an off-resonance contribution along the $I_{N_1N_2,Z}^{(23)}$ operator in the TSAR subspace which leads to a tilting of the effective recoupling axis and reduces the TSAR polarization transfer efficiency. Note that similar longitudinal terms also arise from auto-cross terms involving the chemical shift tensor with itself.²⁹

9.5 PAR pulse sequence optimization:

Figure 3b represents a contour plot of the $^{15}\text{N}-^{15}\text{N}$ PAR polarization transfer efficiency as a function of the $^{15}\text{N}/^1\text{H}$ rf field strength in units of the spinning frequency (p_N or p_H) for a fixed mixing time of 20 ms. The numerical simulations were performed at $\omega_{0H}/2\pi=750$ MHz and $\omega_r/2\pi=20$ kHz with the spin system shown in Fig. 3a (corresponding to backbone nitrogens from neighboring residues in an α -helix with the directly attached protons) and include chemical shifts (the atomic coordinates and chemical shift tensors used in the simulations may be found in Table 9-1).

The optimization map in Fig. 3b displays typical features of PAR polarization transfer.²⁹ $^{15}\text{N}-[^1\text{H}]-^{15}\text{N}$ TSAR polarization transfer is appreciable for settings that avoid first order recoupling conditions such as ^{15}N rotary resonance (i.e. $p_N = 1, 2$) and $^1\text{H}-^{15}\text{N}$ Hartmann-Hahn conditions (black dotted lines). Indeed, in these cases the ^{15}N -

$[^1\text{H}]-^{15}\text{N}$ TSAR polarization transfer is absent either because of ^{15}N CSA recoupling or because the ^{15}N magnetization is transferred to ^1H 's.

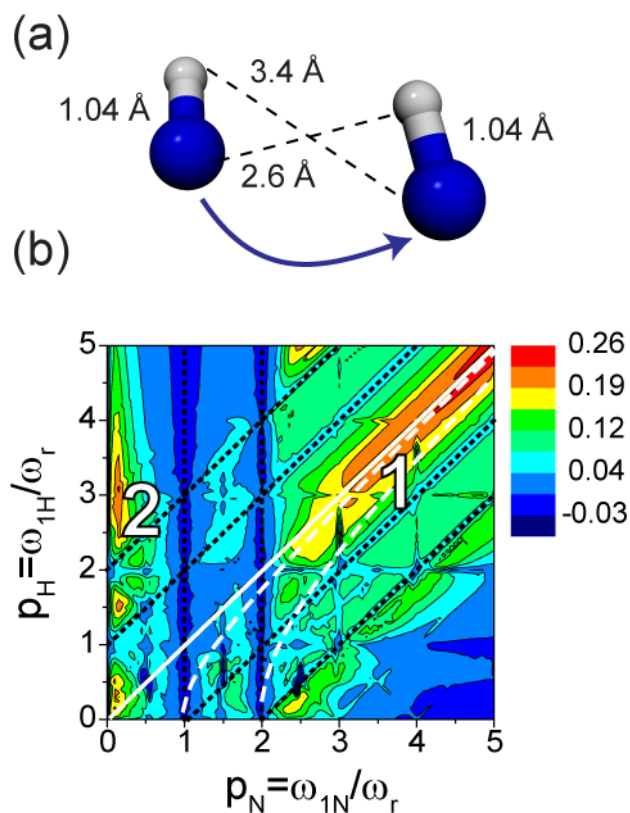


Figure 9-3 Numerical simulation of a ^{15}N - ^{15}N PAR polarization transfer map for backbone nitrogens in an α -helix. (a) Spin system used in the simulation consisting of the two backbone nitrogens with directly bonded amide protons (see Table 9-2). Simulations were performed at $\omega_r/2\pi=20$ kHz and $\omega_{0\text{H}}/2\pi=750$ MHz using 20 ms mixing and include typical isotropic and anisotropic chemical shifts (see Table 9-2). (b) Contour plot of the ^{15}N - ^{15}N PAR polarization transfer between neighboring nitrogens in an α -helix as a function of the nitrogen and proton irradiation magnitudes in units of spinning frequency: p_N and p_H . The two main areas used for performing ^{15}N - ^{15}N PAR experiments are indicated with numerals 1 and 2. The dashed magenta lines indicate conditions for which the $m=1$ and $m=2$ components of the auto cross-term arising from the heteronuclear ^{15}N - ^1H dipolar coupling is zero. These lines are defined by the following equations: $p_H = \sqrt{p_N^2 - 1}$ and $p_H = \sqrt{p_N^2 - 4}$.

The two main regions that lead to appreciable ^{15}N - ^{15}N polarization transfer are marked on the map with numbers. Area **1** is located under the $p_H=p_N$ condition (white solid line) for $p_N > 2$ and area **2** corresponds to settings where $p_N < 1$ and $p_H > 2$. Note that the first of the above conditions leads to more broadband recoupling than the second area as it employs a higher ^{15}N rf field strength. These favorable settings correspond to conditions where the transverse TSAR term dominates the off-resonance longitudinal term originating from auto-cross terms. More precisely each auto-cross terms is the sum of two contributions involving the $m=1$ and the $m=2$ components of the heteronuclear ^{15}N - ^1H dipolar interactions associated with the frequencies ω_r and $2\omega_r$, respectively. The two white dashed lines displayed in Fig. 3 represent rf settings where each of these contributions is zero.²⁹ These lines are defined by the following equations: $p_H = \sqrt{p_N^2 - 1}$ and $p_H = \sqrt{p_N^2 - 4}$. The contribution to the auto-cross terms arising from the $m=1$ component has a higher scaling factor which explains why one set of the optimal rf settings for the TSAR transfer are found along the $p_H = \sqrt{p_N^2 - 1}$ lines.

9.6 Experimental PAR experiments: application to peptide and protein

9.6.1 ^{15}N - ^{15}N PAR on N-[U- ^{13}C , ^{15}N]-*f*-MLF-OH

Figure 4a shows a 2D ^{15}N - ^{15}N PAR correlation spectra obtained at $\omega_{0\text{H}}/2\pi=900$ MHz on the tripeptide N-[U- ^{13}C , ^{15}N]-*f*-MLF-OH using the rf power levels corresponding to area 2 -- $\omega_{1\text{N}}/2\pi \sim 4$ kHz and $\omega_{1\text{H}}/2\pi \sim 53$ kHz -- with $\omega_r/2\pi = 20$ kHz and $\tau_{\text{mix}} = 20$ ms. Note that the low ^{15}N rf power is sufficient to cover the backbone nitrogen bandwidth (~ 2.7 kHz at $\omega_{0\text{H}}/2\pi=900$ MHz). Such low power rf settings minimize the rf sample heating, reducing the danger of compromising the sample integrity during the experiment because of rf heating.

At 20 ms mixing time, the spectrum displays two sequential contacts in the tripeptide N-*f*-MLF-OH corresponding to the ^{15}N - ^{15}N distances of 2.7 Å and 3.6 Å respectively.⁷¹ Although the involved ^{15}N -[^1H]- ^{15}N TSAR recoupling mechanism does not rely on the

^{15}N - ^{15}N couplings, and thus does not directly rely on the ^{15}N - ^{15}N distances,²⁹ the strongest cross-peak corresponds to the shortest ^{15}N - ^{15}N distance. The polarization transfer under the TSAR settings mentioned above is shown in Fig. 4c as a function of the mixing time and clearly appears “indirectly” sensitive to the ^{15}N - ^{15}N distance in this case.

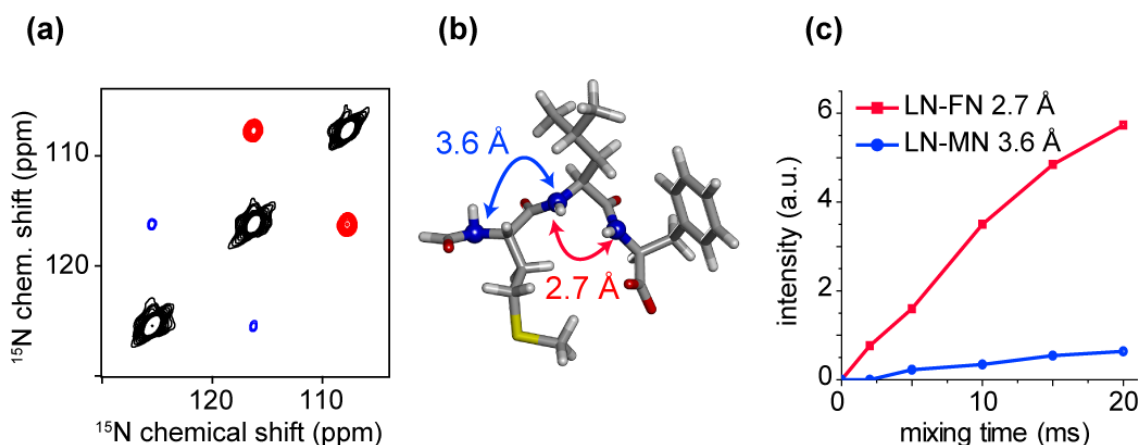


Figure 9-4 (a) Low power 2D ^{15}N - ^{15}N PAR correlation spectrum obtained on [U- ^{13}C , ^{15}N]-*N*-f-MLF-OH⁷¹ at $\omega_r/2\pi=20$ kHz and $\omega_{\text{OH}}/2\pi=900$ MHz using 20 ms of mixing time. The red cross-peaks correspond to a short LN-FN sequential contact ($r_{\text{NN}}=2.7$ Å) and the blue cross-peaks correspond to the long sequential LN-MN contact ($r_{\text{NN}}=3.6$ Å) (see graphics (b)). (c) Cross-peak intensity build-ups in [U- ^{13}C , ^{15}N]-*N*-f-MLF-OH as a function of ^{15}N - ^{15}N PAR mixing time. The PAR mixing consisted of ~ 4 kHz ^{15}N and ~ 53 kHz ^1H C.W. irradiations for both (a) and (c).

N-f-MLF-OH is a well suited model system for testing typical ^{15}N - ^{15}N sequential spin topologies present in proteins. The LN-FN distance falls into the range of distances typical for most nitrogens in neighboring residues in α -helices (~ 2.8 Å). On the other hand, the MN-LN distance falls into the range of ^{15}N - ^{15}N distances typically found for neighboring residues in β -sheets (~ 3.5 Å). In Fig. 4 we can clearly distinguish between these two sets of distances simply on the basis of the cross-peak intensity.

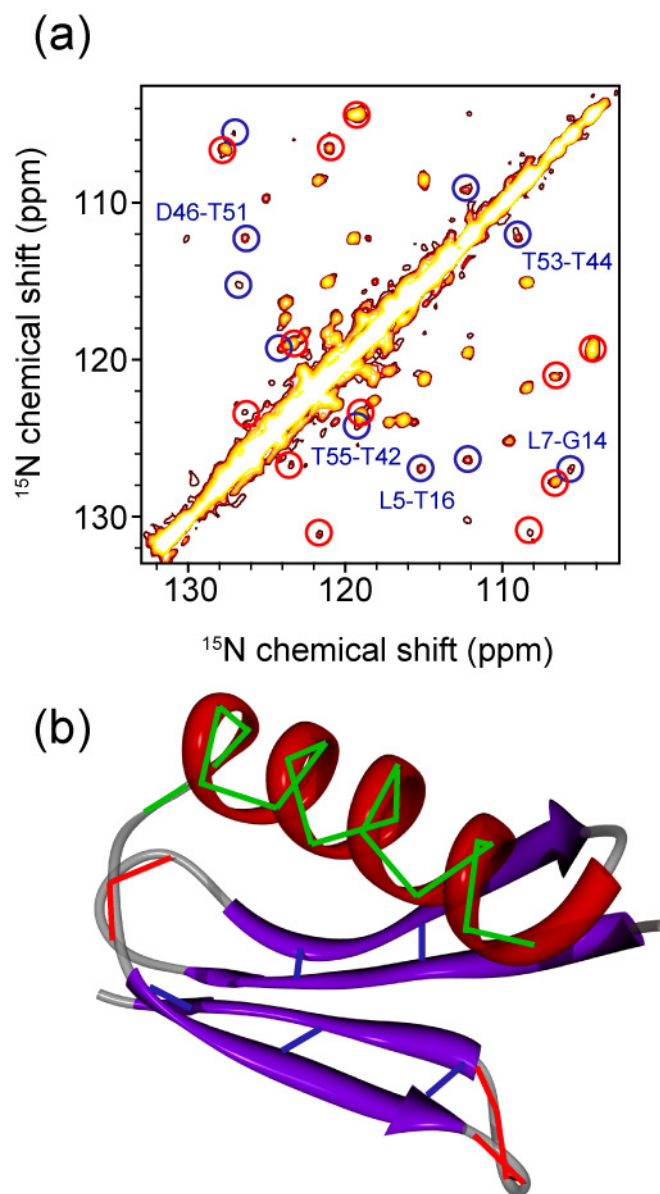


Figure 9-5 (a) 2D ^{15}N - ^{15}N PAR correlation spectrum on $[1,3\text{-}^{13}\text{C},\text{U}\text{-}^{15}\text{N}]$ -GB1. The spectrum was obtained using 18 ms PAR mixing with $\omega_{1\text{N}}/2\pi \sim 52$ kHz and $\omega_{1\text{H}}/2\pi \sim 49$ at $\omega_{\text{r}}/2\pi = 20$ kHz and $\omega_{0\text{H}}/2\pi = 900$ MHz. The cross-peaks circled in red correspond to sequential contacts in loop regions that are also indicated with red lines in (b)). The cross-peaks circled in blue correspond to contacts between the strands in antiparallel β -sheets (nitrogens for the residues participating in a β -bridge) that are also indicated with blue lines in (b). The unmarked cross-peaks correspond primarily to the sequential contacts in the α -helix that are marked with green lines in (b).

These experimental observations can be fully explained by numerical simulations. In the next section we study the relationship between PAR buildups, ^{15}N - ^{15}N distances and the type of contacts involved.

9.6.2 ^{15}N - ^{15}N PAR on microcrystalline protein GB1

Figure 5 shows a 2D ^{15}N - ^{15}N PAR correlation spectrum on $[\text{U-}^{15}\text{N}, 1, 3\text{-}^{13}\text{C}]$ protein GB1 obtained at $\omega_{0\text{H}}/2\pi=900$ MHz and $\omega_r/2\pi=20$ kHz using 18 ms mixing with $\omega_{1\text{H}}/2\pi \sim 49$ kHz and $\omega_{1\text{N}}/2\pi \sim 52$ kHz (see Fig. S11 for the spectrum obtained using 22 ms mixing with $\omega_{1\text{N}}/2\pi \sim 4$ kHz ^{15}N and $\omega_{1\text{H}}/2\pi \sim 55$ kHz $\omega_{0\text{H}}/2\pi=900$ MHz and $\omega_r/2\pi=20$ kHz and Fig. S13 for spectrum obtained using 20 ms mixing with $\omega_{1\text{N}}/2\pi \sim 71$ kHz and $\omega_{1\text{H}}/2\pi \sim 69$ at $\omega_{0\text{H}}/2\pi=500$ MHz and $\omega_r/2\pi=11$ kHz). With this mixing time the spectrum contains two important categories of cross peaks that are well above the noise level (see the cross-peak list in Table 9-5). The first contains sequential ^{15}N - ^{15}N contacts ≤ 3.2 Å which are primarily observed in α -helical regions and occasionally in loops and turns. The second category consists of ^{15}N - ^{15}N contacts corresponding to distances ≥ 4.2 Å, which involve residues participating in β -bridges between antiparallel β -sheets. Note that for these particular settings the sequential cross-peaks in the β -sheets are generally weak or below the noise level. These cross peaks can be recovered by using longer mixing times and longer signal averaging (see Fig. 4).

9.7 ^{15}N - $[\text{H}]$ - ^{15}N PAR experiments applied to structure determination

The relationship between the TSAR buildups and the inter-nuclear distances is discussed in detail for the case of the ^{13}C - $[\text{H}]$ - ^{13}C TSAR mechanism by De Paepe, et. al.²⁹ If only three spins are considered, i.e. two carbons/nitrogens and a single proton, it was shown that the TSAR coupling was proportional to the product of ^{13}C - $^1\text{H}/^{15}\text{N}$ - ^1H couplings, independent from the ^{13}C - $^{13}\text{C}/^{15}\text{N}$ - ^{15}N distance and strongly dependent on the angle between the heteronuclear interactions involved.²⁹

In the case where multiple protons are involved, e.g. fully protonated systems, the TSAR buildup analysis is more complicated, at least analytically. Indeed, the TSAR polarization transfer in this case is the result of the superposition of multiple contributions involving nearby protons (typically protons which are closer than 2.5 Å for the ^{13}C -[^1H]- ^{13}C case). However, it was found experimentally that the ^{13}C -[^1H]- ^{13}C buildups recorded on fully protonated [U - ^{13}C , ^{15}N]-Crh can, to a large extent, be classified in different distance classes and used to perform a 3D structure calculation.²⁹

Table 9-1 Average N-N and H-N distances in typical elements of secondary structure in proteins. The values were extracted based on 100 randomly chosen protein structures in the program STARS.⁸⁰

Type of contact	$\text{N}_1\text{-N}_2$ (Å)	$\text{N}_1\text{-H}_2$ (Å)	$\text{N}_2\text{-H}_1$ (Å)
Sequential $\text{N}_i\text{-N}_{i+1}$ in β -sheet	3.5 ± 0.2	3.9 ± 0.3	3.7 ± 0.7
Sequential - $\text{N}_i\text{-N}_{i+1}$ in α -helix	2.8 ± 0.1	3.3 ± 0.1	2.5 ± 0.1
Sequential - $\text{N}_i\text{-N}_{i+2}$ in α -helix	4.3 ± 0.1	3.6 ± 0.2	5.0 ± 0.1
Sequential - $\text{N}_i\text{-N}_{i+3}$ in α -helix	4.8 ± 0.2	6.8 ± 2.4	7.6 ± 1.8
β -bridge partners in antiparallel β -sheet	4.5 ± 0.4	3.8 ± 0.7	3.8 ± 0.7
β -bridge partners in parallel β -sheet	4.8 ± 0.2	4.0 ± 0.4	5.7 ± 0.5

As we have already mentioned above, the spatial distribution of backbone ^{15}N 's and amide ^1H 's is intimately linked to the secondary, tertiary and often quaternary structure of proteins and nucleic acids through the pattern of hydrogen bonds. Table 9-1 lists ^{15}N - ^{15}N and important ^1H - ^{15}N distances in some typical motifs encountered in proteins. Because PAR polarization transfer is proportional to the product of the ^1H - ^{15}N couplings, it is ideally suited for probing geometries imposed by hydrogen bonding patterns. We illustrate this in the next sections where we consider ^{15}N - ^{15}N PAR

polarization transfer in three different typical secondary and tertiary structural motifs encountered in proteins: α -helix, antiparallel β -sheet and parallel β -sheet.

9.7.1 Sequential ^{15}N - ^{15}N contacts in an α -helix

Figure 6 shows numerical simulations of the ^{15}N - ^{15}N polarization transfer in a typical α -helical spin system taken from the x-ray structure of protein GB1 (PDB 2GI9). The spin system is depicted in Fig. 6a and consists of four backbone ^{15}N 's and amide ^1H 's from four consecutive residues in an α -helix. The initial magnetization is placed on Q_{32}N and the polarization transfer to the other ^{15}N 's is monitored as a function of time. Note that the distances between amide protons ($^1\text{H}_n$) to sequential nitrogens ($^{15}\text{N}_{n\pm 1}$) in α -helices are the shortest ^1H - ^{15}N distances (excluding directly bonded spins) of all the spin topologies presented in Table 9-1. Consequently the corresponding ^{15}N - ^1H - ^{15}N polarization transfer, simulated in Fig. 6b, displays the most rapid (10-20 ms) buildup time and is consistent with the experimental data.

The spin system used in the simulations in Fig. 6b includes only the amide protons, so strictly speaking it corresponds to a perdeuterated sample with back-exchanged amide protons. We have shown that in the case of ^{13}C - ^1H - ^{13}C TSAR usually multiple protons participate and influence polarization transfer between any two given ^{13}C sites. In order to evaluate the influence of protons other than amide protons we have performed a series of multispin simulations on the α -helix spin system. Figure 6c shows simulations for an α -helix with amide protons and alpha protons (which are, besides the amide ^1H 's, consistently the most strongly coupled to the backbone ^{15}N 's). The addition of H_α 's only slightly affects the overall polarization transfer with the change more pronounced for N_i - N_{i+2} polarization transfer. This suggests that in order to predict the general trends of ^{15}N - ^{15}N PAR polarization in proteins we can restrict our analysis to nitrogens and the amide protons (though for a precise analysis requires complex multiple spin simulations).

The simulations in Fig. 6 suggest that for mixing times longer than we employed in the experiment in Fig. 5 we should also observe cross-peaks to $\text{N}_{n\pm 2}$. In fact many

$N_i - N_{i\pm 2}$ contacts in the helix are also detectable in the data presented in Fig. 5 but are much weaker and closer to the noise level.

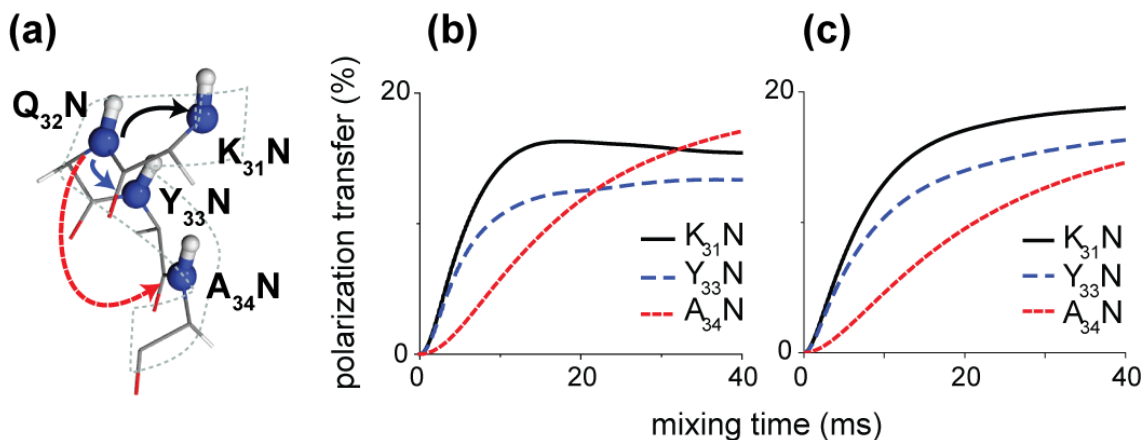


Figure 9-6 Numerical simulations of ^{15}N - ^{15}N PAR polarization transfer in an α -helix. The spin system (a) consists of 4 backbone ^{15}N 's and amide ^1H 's only for simulation in (b) and amide protons plus 3 $\text{H}\alpha$'s for simulation in (c). The coordinates were taken from residues 31 to 34 in the x-ray structure of GB1 (PDB ID 2GI9)⁴⁵ – see Table 9-3). Simulations include nitrogen and proton chemical shifts (see Table 9-3). The initial magnetization is placed on Q_{32}N . Simulations were performed at $\omega_r/2\pi=20$ kHz MAS and $\omega_{\text{OH}}/2\pi=750$ MHz with $p_{\text{N}}=2.7$ and $p_{\text{H}}=2.5$.

9.7.2 ^{15}N - ^{15}N contacts in β -sheets

Figure 7 illustrates numerical simulations of ^{15}N - ^{15}N polarization transfer in two typical β -sheets geometries: the antiparallel β -sheet arrangement shown in Fig. 7a (coordinates from PDB 2GI9)⁴⁵ and the parallel β -sheet arrangement shown in Fig. 7c (with coordinates taken from the SSNMR structure of the Het-s prion²).

The spin system (Fig 7a) used in the simulation in Fig. 7b consists of five backbone ^{15}N 's in an antiparallel β -sheet with their amide ^1H 's. In the case of the antiparallel β -sheet arrangement, the inter-strand polarization transfer between the β -bridge partners (T_{44}N and T_{53}N) is clearly preferred over the transfer to the sequential nitrogens within the strands. Such a situation is a direct consequence of the topology imposed by the

hydrogen bonding pattern: the amide protons from the β -bridge partners are pointing towards the nitrogens in the other strand, leading to strong TSAR couplings. Moreover, the N_1 - H_2 and N_2 - H_1 couplings are identical (see Table 9-1) or very close to each other which results in ideal or close to ideal compensation of the heteronuclear auto-cross term and consequently no effective tilting of the PAR recoupling axis.

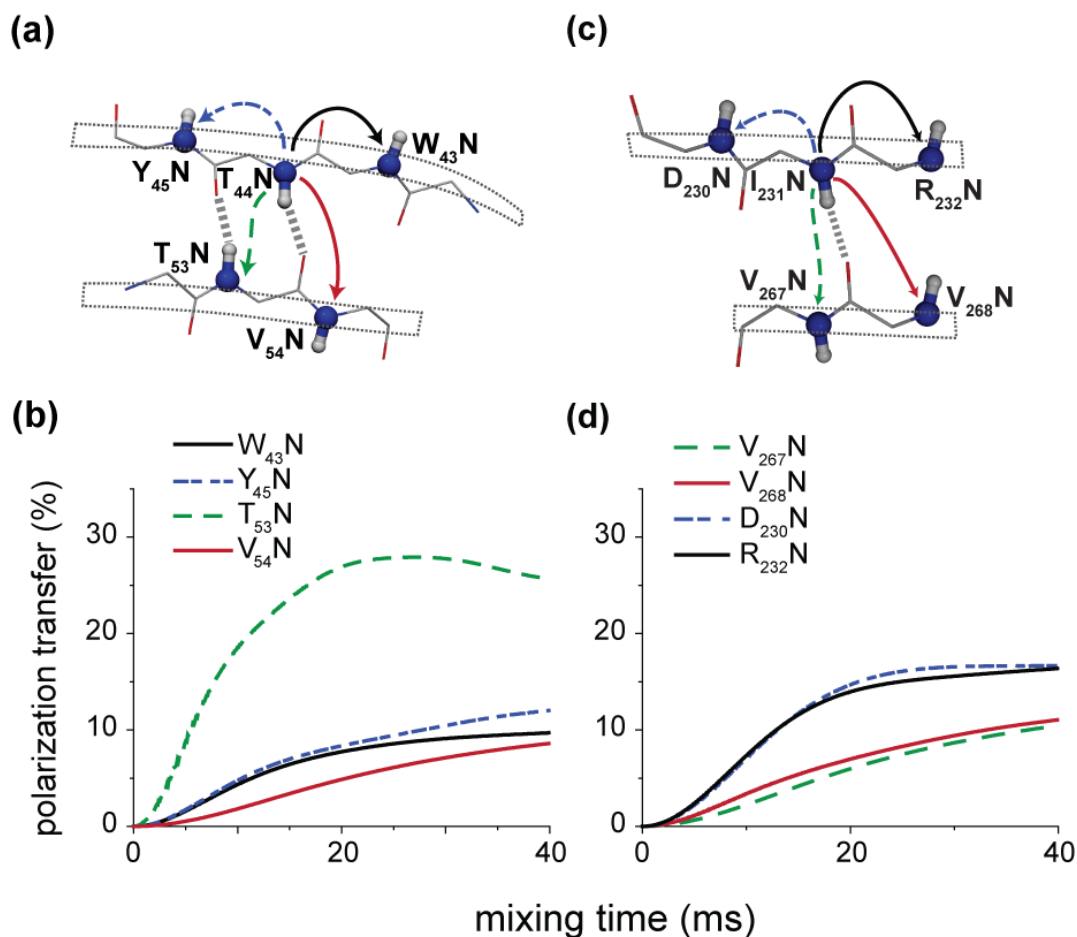


Figure 9-7 Numerical simulations of ^{15}N - ^{15}N PAR polarization transfer in an antiparallel β -sheet (a-b) and parallel β -sheet (c-d). In (a) the spin system consists of 5 backbone nitrogens with directly bonded protons from two strands in an antiparallel β -sheet (coordinates for residues 43-45 and 53-55 from x-ray structure of GB1, PDB ID 2GI9⁴⁵ – see Table 9-4). The spin system consists of 5 backbone nitrogens with directly bonded protons from two strands in a parallel β -sheet (coordinates from SSNMR structure of the HET-s(218-289) prion, PDB ID 2RNM² – see Table 9-5). Simulations include nitrogen and proton chemical shifts (see Table 9-4 and 9-5). The initial

magnetization is placed on the $T_{44}N$ in (b) and $I_{231}N$ in (d). Simulations were performed at $\omega_r/2\pi=20$ kHz MAS and $\omega_{0H}/2\pi=750$ MHz with $p_N=2.7$, $p_H=2.5$.

The spin system of Fig. 7c consists of five backbone ^{15}N 's in a parallel β -sheet and their amide 1H 's. The geometry imposed by the hydrogen bonding pattern is not as favorable as in the case of an antiparallel β -sheet for observing inter-strand contacts (see also Table 9-1). In this case the sequential polarization transfer between the neighboring ^{15}N 's is preferred over the polarization transfer between the ^{15}N 's in the neighboring strands (which is also consistent with the distribution of NH dipolar couplings in Table 9-1).

Naturally, the $N_i-N_{i\pm 1}$ polarization transfer in both parallel and antiparallel β -sheets have similar characteristics (since the NH couplings for sequential sites are similar –see Table 9-1), even though overall efficiency of such transfers in the antiparallel β -sheet are lower due to the presence of more favorable transfer between strands.

The simulations suggest $\tau_{mix}\geq 30$ ms for PAR is required for optimal polarization transfer between sequential contacts in β -sheets. This is consistent with our observation of only a few of such cross peaks in the data presented in Fig. 5, which uses $\tau_{mix} = 18$ ms.

9.8 ^{15}N - ^{15}N PAR in the context of other methods

To complete our discussion, we briefly contrast the ^{15}N - ^{15}N PAR experiment to PDSD and NHHN – two other popular methods used for ^{15}N - ^{15}N polarization transfer.

As we have already mentioned above, the ^{15}N - ^{15}N PAR experiment accelerates polarization transfer between nitrogens by two to three orders of magnitude compared to PDSD (milliseconds in PAR versus seconds in PDSD). Optimal PDSD mixing times increase with increasing spinning frequency, rendering it practical for ^{15}N - ^{15}N correlation experiments employing no more than $\omega_r/2\pi\leq 12$ -14 kHz. In contrast, according to simulations, ^{15}N - ^{15}N PAR should be applicable at all spinning frequencies

presently accessible in solid-state magic angle spinning NMR (up to 70 kHz) requiring reasonable mixing times (on the order of tens milliseconds).

Even though the relationship between PDS polarization buildups and ^{15}N - ^{15}N distances is far from straightforward, it has been shown that one could differentiate between short and long ^{15}N - ^{15}N distances and subsequently probe the secondary structure of the proteins at low magnetic fields.^{43,44} However, at higher magnetic fields one has to take into account the chemical shift difference between the recoupled spins and correct the intensity using the overlap integral between the lines in order to differentiate between longer and shorter ^{15}N - ^{15}N distances.⁴⁴ In practice, this translates to difficulty in correlating cross-peak intensities to secondary structure.⁸¹ Moreover, it suggests that the ^{15}N - ^{15}N spin diffusion experiment will be less efficient with increasing magnetic field strength. The long mixing times (up to 10 s – depending on the studied system^{17,73,79,81}) necessary for obtaining appreciable ^{15}N - ^{15}N polarization transfer using spin diffusion, combined with the low sensitivity of the experiment, places significant constraints on signal averaging time. All of these factors make the ^{15}N - ^{15}N spin diffusion experiment at high magnetic fields challenging, even in the case when the recycle delay may be reduced under favorable conditions.⁴⁵

The NHHN experiment was demonstrated to provide valuable structural information on perdeuterated back-exchanged samples.⁸² For example, similarly to the PAR experiment presented here, NHHN yields contacts between strands in antiparallel β -sheets (though the crowding should be reduced in PAR spectra with sequential cross-peaks in β -sheets significantly attenuated at mixing times favoring the inter-strand polarization transfer). However, it was also noted that the performance of the NHHN experiment deteriorates significantly in fully protonated samples, where mostly sequential cross-peaks are retained.⁸² It transpires that ^{15}N - ^{15}N PAR experiment should be more sensitive than the NHHN experiments for probing ^{15}N - ^{15}N contacts in a fully protonated sample and yield comparable structural information. This is illustrated in Fig. 8 which shows a comparison of the polarization transfer between the β -bridge nitrogen partners in an antiparallel β -sheet in NHHN and ^{15}N - ^{15}N PAR experiments. It turns out that the addition of 6 closest protons (see Table 9-6 for the details on the spin system) leads to substantial reduction of polarization transfer efficiency in the NHHN

experiment, but only a few percent reduction of polarization transfer efficiency in the PAR experiment. Note, that in general the number of neighboring protons is much larger than the number of protons that we have included in these simulations, which means that the experimental performance of NHHN may actually deteriorate even further.

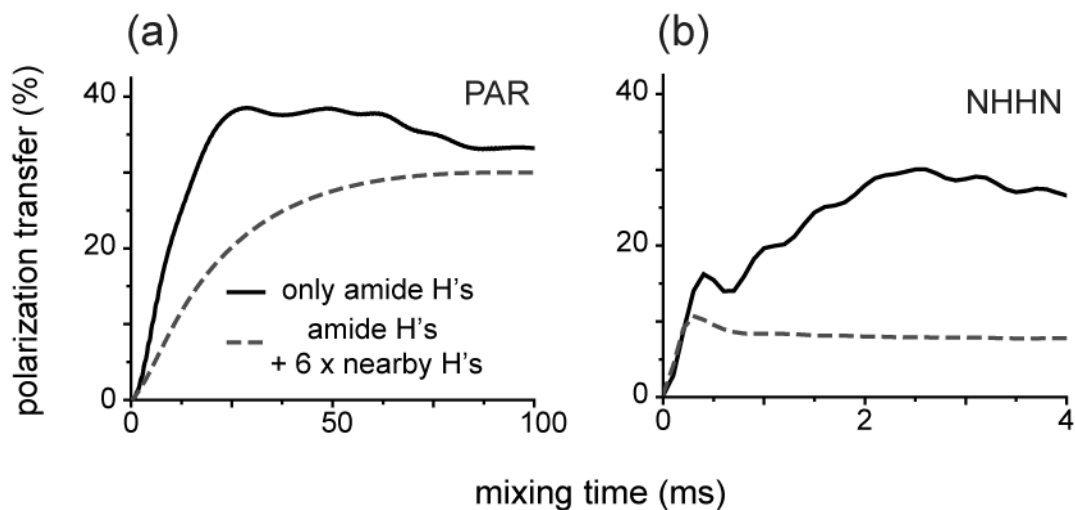


Figure 9-8 Numerical simulation of PAR (a) and NHHN (b) polarization transfer between nitrogens from a β -bridge partner residues in an antiparallel β -sheet. The black solid line represents simulations with only amide protons included, and the red dashed line represents simulation with amide protons plus 6 other closest protons. The simulations were performed at $\omega_t/2\pi=20$ kHz and $\omega_{0H}/2\pi=750$ MHz and include all chemical shifts (see Table 9-6). The ^1H - ^{15}N CP steps in NHHN are simulated explicitly using 0.15 ms contact time with $\omega_{1H}/2\pi=100$ kHz and $\omega_{1N}/2\pi=80$ kHz. The PAR mixing settings are: $p_N=2.7$ and $p_H=2.5$.

9.9 Conclusion

We have described a new experiment for performing ^{15}N - ^{15}N MAS correlation spectroscopy that provides direct access to secondary and tertiary structural information of proteins. ^{15}N - ^{15}N PAR accelerates the ^{15}N - ^{15}N polarization transfer up to three orders of magnitude compared to spin diffusion experiments. Moreover, in fully protonated

samples, ^{15}N - ^{15}N PAR yields interstrand cross-peaks in antiparallel β -sheets as well as the sequential contacts in helices. Most transmembrane proteins consist of either β -barrel or α -helical structural motifs. Provided that sufficient sensitivity is available, our results suggests that the ^{15}N - ^{15}N PAR method should allow straightforward identification of α -helical segments and should permit one to establish connectivities between β -strands in β -barrels, which typically consist of antiparallel β -sheets, and thus provide valuable structural information about membrane proteins. Moreover, the fact that the interstrand ^{15}N - ^{15}N contacts for the β -bridge partners in antiparallel β -sheets are substantially larger than sequential ^{15}N - ^{15}N contacts within the strands should lead to significant simplification of the spectra without need for deuteration or other specific labeling – a feature that should be greatly appreciated in larger systems with significant spectral overlap.

^{15}N - ^{15}N PAR is applicable over almost the entire range of MAS frequencies currently available (10-70 kHz) and could be used as a building block for more sophisticated SSNMR experiments. More importantly, ^{15}N - ^{15}N spectroscopy should benefit strongly from the development of sensitivity enhanced techniques like DNP, and become an integral part of the SSNMR toolkit for structural characterization of proteins.

9.10 Material and methods

9.10.1 Sample preparation:

Preparation of N-[U- ^{13}C , ^{15}N]-*f*-MLF-OH: N-*f*-MLF-OH peptide was obtained by solid phase peptide synthesis from CS Bio Inc. (Menlo Park, CA). The peptide was prepared with uniformly ^{13}C and ^{15}N labeled amino acids from Cambridge Isotope Laboratories (Andover, MA). The peptide was crystallized from isopropanol and packed in a 2.5mm Bruker rotor.

Preparation of GB1 Samples: Two labeled samples were prepared for ^{15}N - ^{15}N TSAR studies: one [1,3 ^{13}C , U- ^{15}N] and one [^{12}C , U- ^{15}N]. Samples were prepared according to previously published protocol.⁸³ E. coli BL21 (DE3) cells (Invitrogen) were transformed with the T2Q mutant of GB1. The [1,3 ^{13}C , U- ^{15}N] sample was

grown in M9 minimal media containing 2.0 grams of [1,3-¹³C] glycerol and 2.0 grams ¹²C NaHCO₃ as the sole carbon sources and 1.0 gram ¹⁵N ammonium chloride as the sole nitrogen source; the U-¹⁵N sample was prepared in M9 minimal media containing 1.0 gram ¹⁵N ammonium chloride and 8.0 g ¹²C glucose. Protein expression, extractions, and purification were done according to previous studies. Microcrystalline samples were prepared according to ref. ⁸³ by dialysis in 50 mM phosphate buffer (pH 5.7) and precipitated with 3 aliquots of 2:1 MPD:IPA at a protein concentration of 25 mg/mL. One sample containing ~9-10 mg of [1,3 ¹³C, U-¹⁵N] labeled protein was centrifuged into a 2.5 mm Bruker rotor, while ~ 20 mg of [¹²C, U-¹⁵N] protein was centrifuged into a 4.0 mm Varian rotor. Both rotors were sealed with epoxy to maintain sample hydration levels throughout the studies.

9.10.2 NMR Spectroscopy

The experiments were carried out using a commercial Bruker spectrometer operating at 900.1 MHz ¹H frequency using a Bruker triple resonance (HCN) probe equipped with a 2.5 mm spinner module. Spinning frequencies of 20 kHz were used in all experiments and regulated to ±2 Hz with a Bruker spinning frequency controller (Bruker BioSpin, Billerica MA).

The PAR experiment was optimized by matching the interference pattern with the simulated PAR optimum (a comparison of the polarization transfer map and the interference map can be found in the Fig. SI2). With an optimization of this kind we take advantage of the fact that the conditions leading to destructive interference of nitrogen polarization (i.e. rotary resonance and ¹H-¹⁵N Hartmann-Hahn conditions) are also outlined as features in the PAR optimization map. The ¹⁵N power was set to ~52 kHz or ~4 kHz (i.e. p_N=2.6 or 0.2 – the value that leads to appreciable TSAR mechanism in simulations) and ¹H rf was scanned through to identify Hartmann-Hahn conditions. ¹H rf power leading to minimal interference just under the n=0 condition was used for the first case and just under the n=3 Hartmann-Hahn condition for the second case.

The ^1H decoupling during t_1 evolution and acquisition was implemented through optimized 100 kHz TPPM²⁴. The recycle delay was 3 s. For the 2D ^{15}N - ^{15}N PAR correlation spectrum on [U- ^{13}C , ^{15}N]-*f*-MLF-OH, acquisition times were 20 ms in t_2 and 12.8 ms in t_1 (64 x 200 μs ; spectral width 54.8 ppm) with 4-16 scans per t_1 point. One of the 2D ^{15}N - ^{15}N PAR correlation spectrum on [1,3- ^{13}C , ^{15}N]-GB1 was obtained with 18 ms mixing time using ca. 52 kHz ^{15}N and 49 kHz ^1H irradiation; acquisition times were 25.6 ms in t_2 and 16 ms in t_1 (80 x 200 μs spectral width 54.8 ppm) with 224 scans per t_1 point. Second of the 2D ^{15}N - ^{15}N PAR correlation spectrum on [1,3- ^{13}C , ^{15}N]-GB1 was obtained with 22 ms mixing time using ~ 4 kHz ^{15}N and ~ 55 kHz ^1H irradiation; acquisition times were 25.6 ms in t_2 and 16 ms in t_1 (64 x 250 μs spectral width 43.8 ppm) with 96 scans per t_1 point. The temperature was regulated using Bruker BCU-X (target temperature -18°C , flow 1400L/h, resulting in a sample temperature between 0 to 5°C as indicated by the water ^1H chemical shift referenced to PEG (3.74 ppm, referenced externally to DSS)).⁸⁴

9.10.3 Numerical simulations and data analysis

Numerical simulations were performed using SPINEVOLUTION 3.3. The NH bonds were set to 1.04 Å for the simulations. For viewing and processing PDB files we used Chimera⁸⁵ and DS Visualizer 2.0 (Accelrys). Chimera was also used for producing some of the graphics used in figures. Data was processed using NMRPipe⁸⁶ and analyzed in Sparky (T. D. Goddard and D. G. Kneller, University of California).

9.11 Acknowledgement

The work in this chapter was done in collaboration with Dr. G. De Paëpe and Matthew Eddy. We would like thank Dr. Patrick van der Wel for insightful discussions. We are very grateful to Dr. Mikhail Veshtort for providing the SPINEVOLUTION software that has been used throughout the course of this work. This work was supported by the National Institute of Health Grants EB-001960, EB-003151, and EB-002026.

9.12 Supporting Information

Table 9-2 Atom coordinates and chemical shift values of the spin system used in the numerical simulation in the Fig. 2. The coordinates are taken from the x-ray structure of GB1 protein (PDB ID 2GI9). The ^1H 's were added in Chimera⁸¹ and NH bonds adjusted to 1.04 Å in Accelrys DS Visualizer 2.0.

Atom	X	Y	Z	δ_{iso} (ppm)	δ_{aniso} (ppm)	η
N ₃₅ N	6.433	0.681	21.962	-5	-106	0.2
N ₃₅ H	5.718	1.142	21.364	5	-110	0.2
D ₃₆ N	5.419	-1.641	23.313	0	5.7	0.65
D ₃₆ H	4.904	-1.32	22.468	0	5.7	0.65

Table 9-3 Atom coordinates and chemical shift values for the α -helix spin system used in simulation in Fig. 5. The coordinates are taken from the x-ray structure of protein GB1 (PDB ID 2GI9) and NH bonds adjusted to 1.04 Å in Accelrys DS Visualizer 2.0.

Atom	X	Y	Z	δ_{iso} (ppm)	δ_{aniso} (ppm)	η
K ₃₁ N	3.707	3.18	17.231	-5	-106	0.2
Q ₃₂ N	2.57	1.986	19.467	5	-110	0.2
Y ₃₃ N	3.579	-0.659	18.994	1	-106	0.2
A ₃₄ N	6.33	-0.189	19.299	3	-110	0.2
K ₃₁ H	2.982	3.7	16.696	5	5.7	0.65
Q ₃₂ H	1.892	2.273	18.733	0	5.7	0.65
Y ₃₃ H	3.186	-0.156	18.173	0	5.7	0.65
A ₃₄ H	5.812	0.508	18.727	0	5.7	0.65

Table 9-4 Atom coordinates and chemical shift values for the spin system used in the simulation in Fig. 6b. The coordinates are taken from the x-ray structure of protein GB1 (PDB ID 2GI9) and NH bonds adjusted to 1.04 Å in Accelrys DS Visualizer 2.0.

Atom	X	Y	Z	δ_{iso} (ppm)	δ_{aniso} (ppm)	η
T ₄₃ N	11.226	9.874	16.505	-5	-106	0.2
T ₄₄ N	10.639	9.569	12.975	5	-106	0.2
T ₄₅ N	8.75	10.166	9.967	2	-106	0.2
T ₅₃ N	10.547	5.747	11.227	-3	-106	0.2
V ₅₄ N	12.114	4.79	14.309	1	-106	0.2
T ₄₃ H	10.945	10.753	16.916	0	5.7	0.65
T ₄₄ H	10.777	8.569	12.993	0	5.7	0.65
T ₄₅ H	8.907	11.164	9.947	0	5.7	0.65
T ₅₃ H	10.255	6.709	11.323	0	5.7	0.65
V ₅₄ H	12.455	3.893	13.995	0	5.7	0.65

Table 9-5 Atom coordinates and chemical shift values for the spin system used in simulation in Fig. 6d. The coordinates are taken from the model 0.1 from the SSNMR structure of HET-s (218-289) prion (PDB ID 2RNM) and NH bonds adjusted to 1.04 Å in Accelrys DS Visualizer 2.0.

Atom	X	Y	Z	δ_{iso} (ppm)	δ_{aniso} (ppm)	η
D ₂₃₀ N	-38.088	27.067	-13.66	-3	-106	0.2
I ₂₃₁ N	-34.794	26.728	-12.382	-5	-106	0.2
R ₂₃₂ N	-31.47	27.642	-12.164	1	-106	0.2
V ₂₆₇ N	-34.544	21.857	-11.351	5	-106	0.2
V ₂₆₈ N	-31.194	22.88	-11.52	2	-106	0.2
D ₂₃₀ H	-38.252	27.981	-13.191	0	5.7	0.65
I ₂₃₁ H	-34.757	25.695	-12.496	0	5.7	0.65
R ₂₃₂ H	-31.714	28.643	-12.306	0	5.7	0.65
V ₂₆₇ H	-34.665	20.829	-11.247	0	5.7	0.65
V ₂₆₈ H	-31.439	23.889	-11.464	0	5.7	0.65

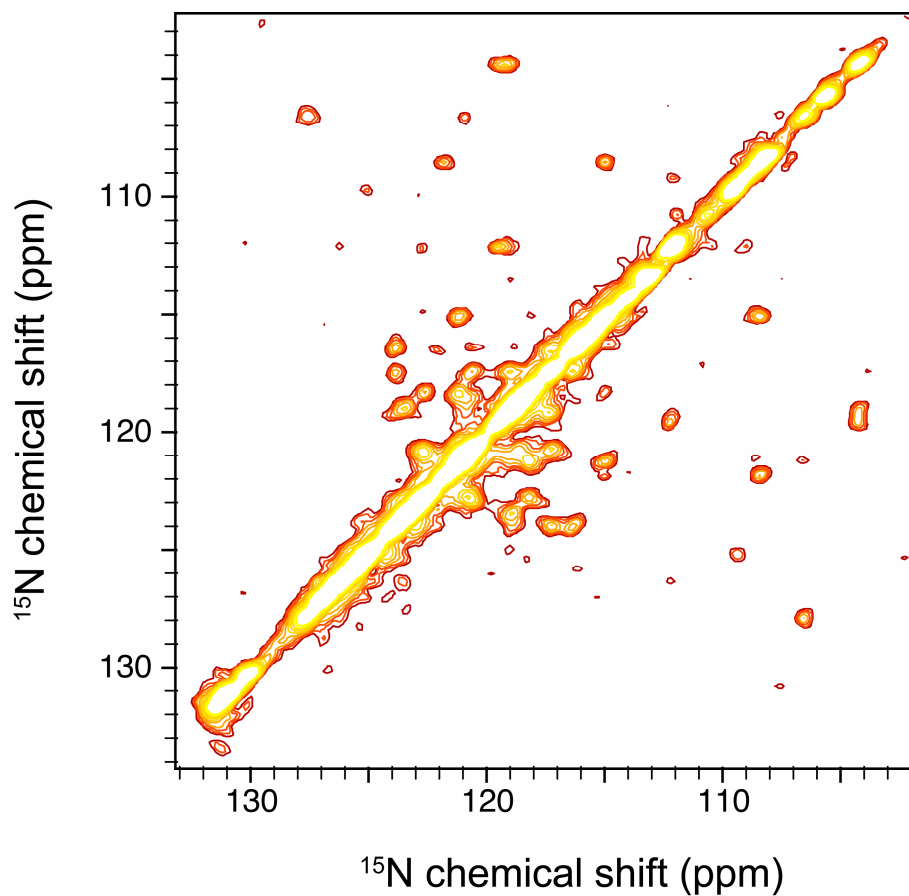


Figure 9-9 2D ^{15}N - ^{15}N PAR correlation spectrum on $[1,3\text{-}^{13}\text{C},\text{U}\text{-}^{15}\text{N}]$ -protein GB1. The spectrum was obtained using 22 ms PAR mixing with $\omega_{1\text{N}}/2\pi \sim 4$ kHz and $\omega_{1\text{H}}/2\pi \sim 52$ CW irradiation at $\omega_r/2\pi = 20$ kHz and $\omega_{0\text{H}}/2\pi = 900$ MHz.

Table 9-6 Cross-peaks observed in the spectra in Fig. 4. The sequential cross-peaks in the loop regions are highlighted in red, sequential cross-peaks in the α -helix are highlighted in green, and interstrand cross-peaks within the antiparallel β -sheets are highlighted in blue.

Assignment	ω_1	ω_2	Assignment	ω_1	ω_2	Assignment	ω_1	ω_2
M1N-Q2N	40.1	125.3	V29N-F30N	119.0	118.3	D46N-D47N	126.8	123.4
L5N-T16N	126.9	115.2	F30N-V29N	118.2	119.0	D46N-T51N	126.4	112.2
L7N-G14N	127.0	105.6	F30N-K31N	118.7	120.6	D47N-D46N	123.3	126.4
N8N-G9N	125.2	109.5	K31N-F30N	120.7	118.6	D47N-A48N	123.5	119.0
G9N-N8N	109.7	125.0	Q32N-K31N	121.2	119.9	A48N-D47N	119.0	123.3
K10N-T11N	121.1	106.6	Y33N-A34N	121.0	122.6	A48N-T49N	118.9	104.1
T11N-K10N	106.5	121.0	A34N-Y33N	122.5	121.0	T49N-A48N	104.4	119.1
T11N-L12N	106.6	127.6	A34N-N35N	122.5	118.1	T49N-K50N	104.4	119.5
L12N-T11N	127.8	106.6	N35N-A34N	118.5	122.7	K50N-T49N	119.4	104.3
G14N-L7N	105.6	127.1	N35N-D36N	118.3	121.2	K50N-T51N	119.5	112.2
T16N-L5N	115.3	126.8	N35N-N37N	118.3	115.0	T51N-D46N	112.3	126.4
A23N-A24N	122.8	120.6	D36N-A34N	121.3	122.5	T51N-K50N	112.3	119.5
A24N-A23N	120.6	122.8	D36N-N35N	121.2	118.2	T51N-F52N	112.3	130.1
A24N-T25N	120.7	117.2	D36N-N37N	121.2	115.0	F52N-T51N	130.3	112.2
A24N-A26N	120.8	123.8	N37N-N35N	115.0	118.1	T53N-T44N	112.2	109.0
T25N-A24N	117.4	120.5	N37N-D36N	115.1	121.1	T53N-V54N	112.3	118.5
T25N-A26N	117.4	123.8	N37N-G38N	115.1	108.4	V54N-T53N	118.5	112.1
A26N-A24N	124.0	120.6	G38N-N37N	108.5	115.0	T55N-E42N	124.1	119.1
A26N-T25N	124.0	117.2	G38N-V39N	108.6	121.7			
A26N-E27N	123.9	116.4	V39N-G38N	121.8	108.4			
E27N-A26N	116.5	123.9	D40N-V39N	131.2	121.6			
E27N-K28N	116.5	117.2	D40N-G41N	131.0	108.2			
K28N-E27N	117.5	116.3	G41N-D40N	108.4	131.2			
K28N-V29N	117.4	118.8	E42N-T55N	119.3	124.0			
V29N-K28N	119.1	117.3	T44N-T53N	109.1	112.1			

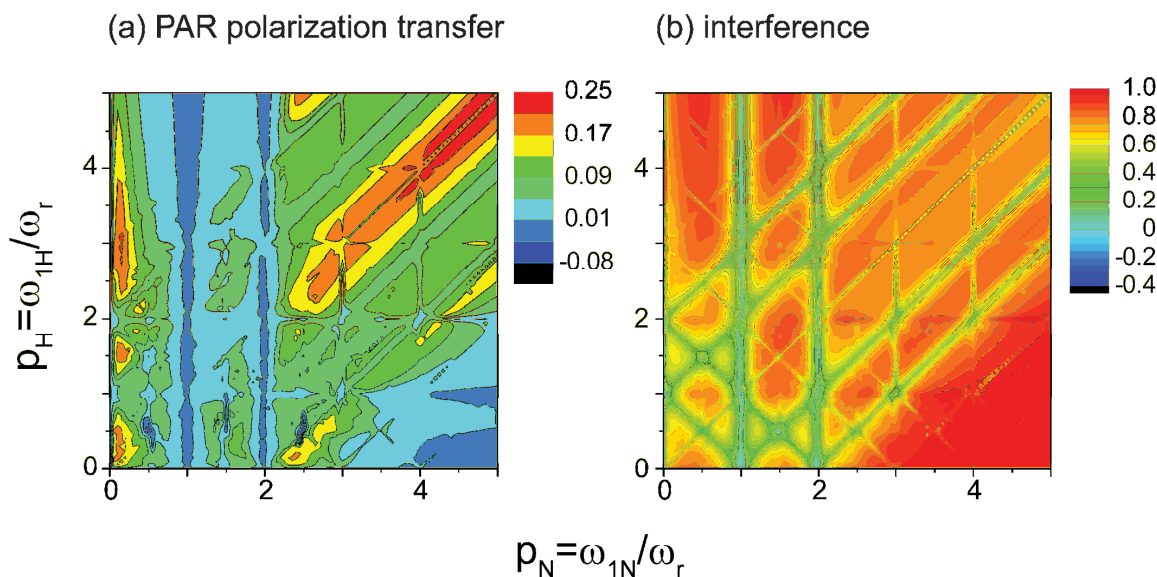


Figure 9-10 Comparison of the ^{15}N - ^{15}N PAR polarization transfer map (a) and the interference map (b). Simulation was performed for the spin system described in Table 9-2 using 20 ms of PAR mixing at $\omega_r/2\pi=20$ kHz and $\omega_{0H}/2\pi = 750$ MHz. In the PAR optimization map the polarization transfer between the nitrogens is monitored as a function of nitrogen (p_N) and proton (p_H) irradiation in units of spinning frequency. In the interference map the decay of the magnetization on the nitrogens after the PAR mixing is monitored as a function of nitrogen (p_N) and proton (p_H) irradiation in units of spinning frequency. The initial magnetization is prepared on the x-axis on one of the nitrogens in (a) and on both nitrogens in (b).

Table 9-7 Atom coordinates and chemical shift values for the spin system used in simulation in Fig. 9-7. The coordinates are taken from the x-ray structure of protein GB1 (PDB ID 2GI9) and NH bonds adjusted to 1.04 Å in Accelrys DS Visualizer 2.0.

Atom	X	Y	Z	δ_{iso} (ppm)	δ_{aniso} (ppm)	η
T ₄₄ N	10.639	9.569	12.975	-5	-106	0.2
T ₅₃ N	10.547	5.747	11.227	5	-106	0.2
W ₄₃ H _{α}	10.835	8.369	15.129	0	5.7	0.65
W ₄ H _{β3}	8.402	9.135	14.812	0	5.7	0.65
W ₄₃ H _{ϵ3}	7.851	6.796	14.29	0	5.7	0.65
T ₄₄ H	10.781	8.539	12.994	0	5.7	0.65
T ₄₄ H _{α}	10.044	11.236	11.893	0	5.7	0.65
T ₄₄ H _{γ2}	13.117	10.317	12.407	0	5.7	0.65
T ₅₃ H	10.246	6.738	11.326	0	5.7	0.65
T ₅₃ H _{γ1}	14.093	7.513	11.659	0	5.7	0.65

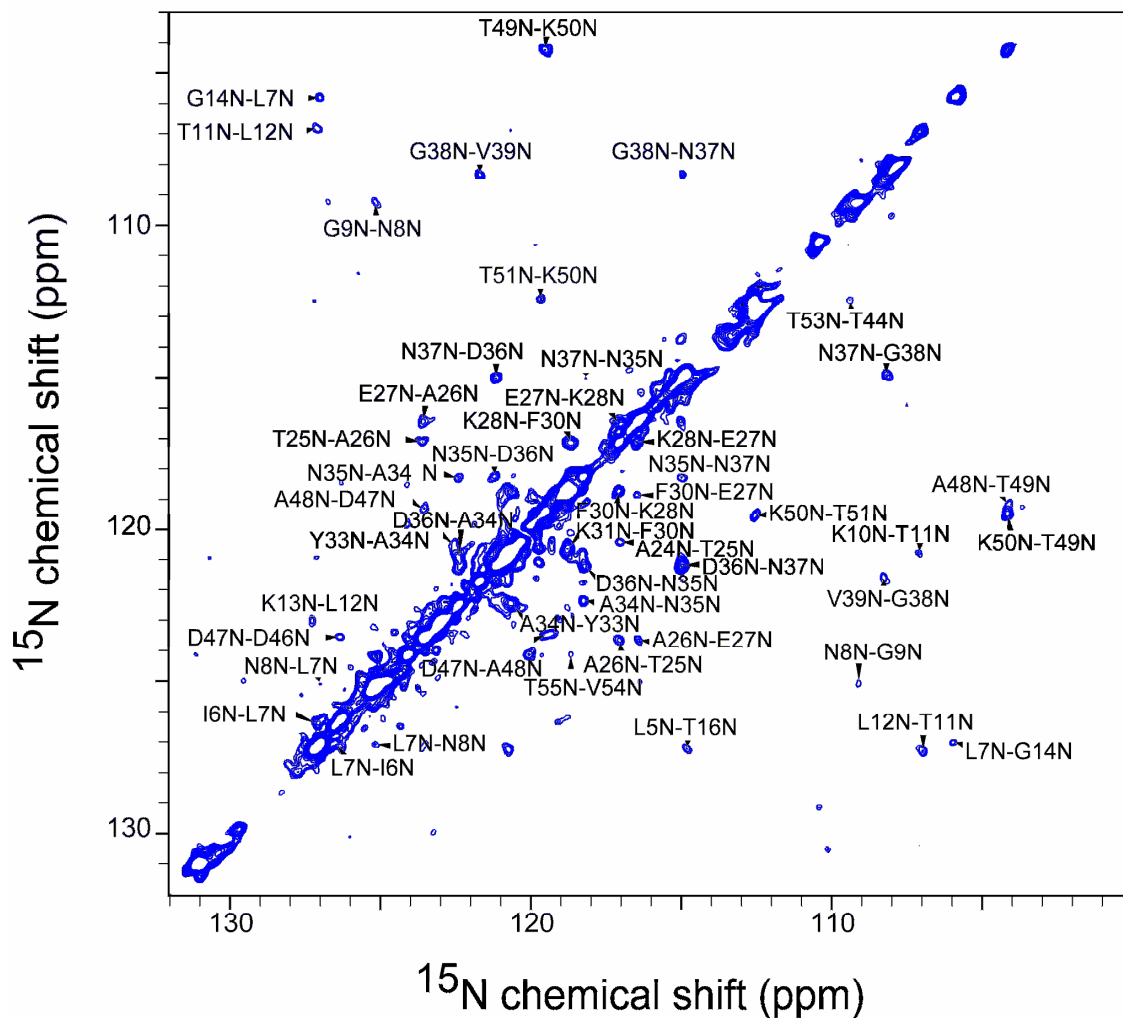


Figure 9-11 2D ^{15}N - ^{15}N PAR correlation spectrum on $[\text{U-}^{13}\text{C}, ^{15}\text{N}]$ - protein GB1. The spectrum was obtained using 20 ms PAR mixing with $\omega_{1\text{N}}/2\pi \sim 71$ kHz and $\omega_{1\text{H}}/2\pi \sim 69$ CW irradiation at $\omega_r/2\pi = 11.11$ kHz and $\omega_{0\text{H}}/2\pi = 500$ MHz. The acquisition time was 46.1 ms in t_1 and 46.1 ms in t_2 . The temperature (as read by thermocouple) was maintained at -5°C using 50 scfh flow of nitrogen.

9.13 References

- (1) Andrew, E. R.; Bradbury, A.; Eades, R. G. *Nature* **1958**, *182*, 1659-1659.
- (2) Wasmer, C.; Lange, A.; Van Melckebeke, H.; Siemer, A. B.; Riek, R.; Meier, B. H. *Science* **2008**, *319*, 1523-1526.
- (3) Andronesi, O. C.; Becker, S.; Seidel, K.; Heise, H.; Young, H. S.; Baldus, M. *Journal of the American Chemical Society* **2005**, *127*, 12965-12974.
- (4) Franks, W. T.; Wylie, B. J.; Schmidt, H. L. F.; Nieuwkoop, A. J.; Mayrhofer, R. M.; Shah, G. J.; Graesser, D. T.; Rienstra, C. M. *Proceedings of the National Academy of Sciences of the United States of America* **2008**, *105*, 4621-4626.
- (5) Frericks, H. L.; Zhou, D. H.; Yap, L. L.; Gennis, R. B.; Rienstra, C. M. *Journal of Biomolecular Nmr* **2006**, *36*, 55-71.
- (6) Hellmus, J. J.; Surewicz, K.; Nadaud, P. S.; Surewicz, W. K.; Jaroniec, C. P. *Proceedings of the National Academy of Sciences of the United States of America* **2008**, *105*, 6284-6289.
- (7) Lange, A.; Giller, K.; Hornig, S.; Martin-Eauclaire, M. F.; Pongs, O.; Becker, S.; Baldus, M. *Nature* **2006**, *440*, 959-962.
- (8) Petkova, A. T.; Ishii, Y.; Balbach, J. J.; Antzutkin, O. N.; Leapman, R. D.; Delaglio, F.; Tycko, R. *Proceedings of the National Academy of Sciences of the United States of America* **2002**, *99*, 16742-16747.
- (9) Thompson, L. K.; McDermott, A. E.; Raap, J.; Vanderwielen, C. M.; Lugtenburg, J.; Herzfeld, J.; Griffin, R. G. *Biochemistry* **1992**, *31*, 7931-7938.
- (10) Yang, J.; Paramasivan, S.; Marulanda, D.; Cataidi, M.; Tasayco, M. L.; Polenova, T. *Magnetic Resonance in Chemistry* **2007**, *45*, S73-S83.
- (11) Loquet, A.; Bardiaux, B.; Gardiennet, C.; Blanchet, C.; Baldus, M.; Nilges, M.; Malliavin, T.; Boeckmann, A. *Journal of the American Chemical Society* **2008**, *130*, 3579-3589.
- (12) Creuzet, F.; McDermott, A.; Gebhard, R.; Vanderhoef, K.; Spijkerassink, M. B.; Herzfeld, J.; Lugtenburg, J.; Levitt, M. H.; Griffin, R. G. *Science* **1991**, *251*, 783-786.

- (13) Hong, M.; deAzevedo, E.; Kennedy, S. B.; Russell, T. P.; Tirrell, D. *Abstracts of Papers of the American Chemical Society* **2000**, *219*, U317-U317.
- (14) Martin, R. W.; Zilm, K. W. *Journal of Magnetic Resonance* **2003**, *165*, 162-174.
- (15) Lemaster, D. M. *Progress in Nuclear Magnetic Resonance Spectroscopy* **1994**, *26*, 371-419.
- (16) LeMaster, D. M.; Kushlan, D. M. *Journal of the American Chemical Society* **1996**, *118*, 9255-9264.
- (17) Goldbourt, A.; Day, L. A.; McDermott, A. E. *Journal of Magnetic Resonance* **2007**, *189*, 157-165.
- (18) Hong, M.; Jakes, K. *Journal of Biomolecular Nmr* **1999**, *14*, 71-74.
- (19) Bennett, A. E.; Ok, J. H.; Griffin, R. G.; Vega, S. *Journal of Chemical Physics* **1992**, *96*, 8624-8627.
- (20) Bennett, A. E.; Rienstra, C. M.; Auger, M.; Lakshmi, K. V.; Griffin, R. G. *Journal of Chemical Physics* **1995**, *103*, 6951-6958.
- (21) Caravatti, P.; Braunschweiler, L.; Ernst, R. R. *Chemical Physics Letters* **1983**, *100*, 305-310.
- (22) De Paepe, G.; Bayro, M. J.; Lewandowski, J.; Griffin, R. G. *Journal of the American Chemical Society* **2006**, *128*, 1776-1777.
- (23) De Paepe, G.; Elena, B.; Emsley, L. *Journal of Chemical Physics* **2004**, *121*, 3165-3180.
- (24) De Paepe, G.; Hodgkinson, P.; Emsley, L. *Chemical Physics Letters* **2003**, *376*, 259-267.
- (25) De Paepe, G.; Lewandowski, J.; Locquet, A.; Bockmann, A.; Griffin, R. G. *Submitted* **2008**.
- (26) De Paepe, G.; Lewandowski, J. R.; Griffin, R. G. *Journal of Chemical Physics* **2008**, *128*, 124503-124526.
- (27) Jaroniec, C. P.; Filip, C.; Griffin, R. G. *J. Am. Chem. Soc.* **2002**, *124*, 10728-10742.
- (28) Jaroniec, C. P.; Tounge, B. A.; Herzfeld, J.; Griffin, R. G. *Journal of the American Chemical Society* **2001**, *123*, 3507-3519.

- (29) Maricq, M. M.; Waugh, J. S. *Journal of Chemical Physics* **1979**, *70*, 3300-3316.
- (30) Nielsen, N. C.; Bildsoe, H.; Jakobsen, H. J.; Levitt, M. H. *Journal of Chemical Physics* **1994**, *101*, 1805-1812.
- (31) Oas, T. G.; Griffin, R. G.; Levitt, M. H. *Journal of Chemical Physics* **1988**, *89*, 692-695.
- (32) Raleigh, D. P.; Levitt, M. H.; Griffin, R. G. *Chemical Physics Letters* **1988**, *146*, 71-76.
- (33) Schaefer, J.; McKay, R. A.; Stejskal, E. O. *J. Magn. Reson.* **1979**, *34*, 443-447.
- (34) Stejskal, E. O.; Schaefer, J.; Waugh, J. S. *J. Magn. Reson.* **1977**, *28*, 105-112.
- (35) Takegoshi, K.; Nakamura, S.; Terao, T. *Chemical Physics Letters* **2001**, *344*, 631-637.
- (36) Bayro, M. J.; Ramachandran, R.; Caporini, M. A.; Eddy, M. T.; Griffin, R. G. *Journal of Chemical Physics* **2008**, *128*.
- (37) Lewandowski, J. R.; De Paepe, G.; Griffin, R. G. *Journal of the American Chemical Society* **2007**, *129*, 728-729.
- (38) Lewandowski, J. R.; De Paepe, G.; van der Wel, P. C. A.; Birkett, N. R.; Belenky, M.; Maly, T.; Bayro, M. J.; Sivertsen, A. C.; Dobson, C. M.; Herzfeld, J.; Griffin, R. G. **2008**, *in preparation*.
- (39) Linge, J. P.; Habeck, M.; Rieping, W.; Nilges, M. *Bioinformatics* **2003**, *19*, 315-316.
- (40) Castellani, F.; van Rossum, B.; Diehl, A.; Schubert, M.; Rehbein, K.; Oschkinat, H. *Nature* **2002**, *420*, 98-102.
- (41) Manolikas, T.; Herrmann, T.; Meier, B. H. *Journal of the American Chemical Society* **2008**, *130*, 3959-3966.
- (42) Zech, S. G.; Wand, A. J.; McDermott, A. E. *Journal of the American Chemical Society* **2005**, *127*, 8618-8626.
- (43) Castellani, F., Freien Universität Berlin, 2003.

- (44) Reif, B.; Hohwy, M.; Jaroniec, C. P.; Rienstra, C. M.; Griffin, R. G. *Journal of Magnetic Resonance* **2000**, *145*, 132-141.
- (45) Franks, W. T.; Wylie, B. J.; Stellfox, S. A.; Rienstra, C. M. *Journal of the American Chemical Society* **2006**, *128*, 3154-3155.
- (46) Szeverenyi, N. M.; Sullivan, M. J.; Maciel, G. E. *Journal of Magnetic Resonance* **1982**, *47*, 462-475.
- (47) Baldus, M. *Progress in Nuclear Magnetic Resonance Spectroscopy* **2002**, *41*, 1-47.
- (48) Baldus, M.; Geurts, D. G.; Hediger, S.; Meier, B. H. *J. Magn. Reson. A* **1996**, *118*, 140-144.
- (49) Castellani, F.; van Rossum, B. J.; Diehl, A.; Rehbein, K.; Oschkinat, H. *Biochemistry* **2003**, *42*, 11476-11483.
- (50) Detken, A.; Hardy, E. H.; Ernst, M.; Kainosho, M.; Kawakami, T.; Aimoto, S.; Meier, B. H. *Journal of Biomolecular Nmr* **2001**, *20*, 203-221.
- (51) Heise, H.; Seidel, K.; Etzkorn, M.; Becker, S.; Baldus, M. *Journal of Magnetic Resonance* **2005**, *173*, 64-74.
- (52) Marulanda, D.; Tasayco, M. L.; Cataldi, M.; Arriaran, V.; Polenova, T. *Journal of Physical Chemistry B* **2005**, *109*, 18135-18145.
- (53) Pauli, J.; Baldus, M.; van Rossum, B.; de Groot, H.; Oschkinat, H. *ChemBiochem* **2001**, *2*, 272-281.
- (54) Rienstra, C. M.; Hohwy, M.; Hong, M.; Griffin, R. G. *Journal of the American Chemical Society* **2000**, *122*, 10979-10990.
- (55) Sun, B. Q.; Rienstra, C. M.; Costa, P. R.; Williamson, J. R.; Griffin, R. G. *Journal of the American Chemical Society* **1997**, *119*, 8540-8546.
- (56) Baldus, M.; Petkova, A. T.; Herzfeld, J.; Griffin, R. G. *Mol. Phys.* **1998**, *95*, 1197-1207.
- (57) Caravatti, P.; Bodenhausen, G.; Ernst, R. R. *Chemical Physics Letters* **1982**, *89*, 363-367.
- (58) Egorova-Zachernyuk, T. A.; Hollander, J.; Fraser, N.; Gast, P.; Hoff, A. J.; Cogdell, R.; de Groot, H. J. M.; Baldus, M. *J. Biomol. Nmr* **2001**, *19*, 243-253.

- (59) Hong, M.; Griffin, R. G. *Journal of the American Chemical Society* **1998**, *120*, 7113-7114.
- (60) van der Wel, P. C. A.; Lewandowski, J. R.; Griffin, R. G. *Journal of the American Chemical Society* **2007**, *129*, 5117-5130.
- (61) Hong, M.; Gross, J. D.; Griffin, R. G. *J. Phys. Chem. B* **1997**, *101*, 5869-5874.
- (62) Hong, M.; Gross, J. D.; Hu, W.; Griffin, R. G. *J. Magn. Reson.* **1998**, *135*, 169-177.
- (63) Ladizhansky, V.; Jaroniec, C. P.; Diehl, A.; Oschkinat, H.; Griffin, R. G. *Journal of the American Chemical Society* **2003**, *125*, 6827-6833.
- (64) Ladizhansky, V.; Veshtort, M.; Griffin, R. G. *Journal of Magnetic Resonance* **2002**, *154*, 317-324.
- (65) Jaroniec, C. P.; MacPhee, C. E.; Astrof, N. S.; Dobson, C. M.; Griffin, R. G. *Proceedings of the National Academy of Sciences of the United States of America* **2002**, *99*, 16748-16753.
- (66) Jaroniec, C. P.; MacPhee, C. E.; Bajaj, V. S.; Dobson, C. M.; Griffin, R. G. *Biophysical Journal* **2003**, *84*, 154A-154A.
- (67) Jaroniec, C. P.; MacPhee, C. E.; Bajaj, V. S.; McMahon, M. T.; Dobson, C. M.; Griffin, R. G. *Proceedings of the National Academy of Sciences of the United States of America* **2004**, *101*, 711-716.
- (68) Jaroniec, C. P.; Tounge, B. A.; Herzfeld, J.; Griffin, R. G. *Biophysical Journal* **2001**, *80*, 368A-368A.
- (69) Jaroniec, C. P.; Tounge, B. A.; Rienstra, C. M.; Herzfeld, J.; Griffin, R. G. *J. Am. Chem. Soc.* **1999**, *121*, 10237-10238.
- (70) Jaroniec, C. P.; Tounge, B. A.; Rienstra, C. M.; Herzfeld, J.; Griffin, R. G. *Journal of Magnetic Resonance* **2000**, *146*, 132-139.
- (71) Rienstra, C. M.; Tucker-Kellogg, L.; Jaroniec, C. P.; Hohwy, M.; Reif, B.; McMahon, M. T.; Tidor, B.; Lozano-Perez, T.; Griffin, R. G. *Proceedings of the National Academy of Sciences of the United States of America* **2002**, *99*, 10260-10265.
- (72) Sein, J.; Giraud, N.; Blackledge, M.; Emsley, L. *Journal of Magnetic Resonance* **2007**, *186*, 26-33.

- (73) Giraud, N.; Blackledge, M.; Bockmann, A.; Emsley, L. *J Magn Reson* **2007**, *184*, 51-61.
- (74) Giraud, N.; Blackledge, M.; Goldman, M.; Bockmann, A.; Lesage, A.; Penin, F.; Emsley, L. *J Am Chem Soc* **2005**, *127*, 18190-201.
- (75) Chevelkov, V.; Zhuravleva, A. V.; Xue, Y.; Reif, B.; Skrynnikov, N. R. *Journal of the American Chemical Society* **2007**, *129*, 12594-+.
- (76) Barnes, A. B.; De Paepe, G.; van der Wel, P. C. A.; Hu, K.; Joo, C.; Bajaj, V. S.; Mak-Jurkauskas, M. L.; Sirigiri, J. R.; Herzfeld, J.; Temkin, R. J.; Griffin, R. G. *Applied Magnetic Resonance* **2008**.
- (77) Zhou, D. H.; Shea, J. J.; Nieuwkoop, A. J.; Franks, W. T.; Wylie, B. J.; Mullen, C.; Sandoz, D.; Rienstra, C. M. *Angewandte Chemie-International Edition* **2007**, *46*, 8380-8383.
- (78) Seidel, K.; Etzkorn, M.; Heise, H.; Becker, S.; Baldus, M. *Chembiochem* **2005**, *6*, 1638-47.
- (79) Franks, W. T.; Zhou, D. H.; Wylie, B. J.; Money, B. G.; Graesser, D. T.; Frericks, H. L.; Sahota, G.; Rienstra, C. M. *Journal of the American Chemical Society* **2005**, *127*, 12291-12305.
- (80) Cavanagh, J.; Fairbrother, W. J.; Palmer, A. G.; Skelton, N. J.; Rance, M. *Protein NMR Spectroscopy: Principles and Practice*; Academic Press, 2006.
- (81) Pettersen, E. F.; Goddard, T. D.; Huang, C. C.; Couch, G. S.; Greenblatt, D. M.; Meng, E. C.; Ferrin, T. E. *Journal of Computational Chemistry* **2004**, *25*, 1605-1612.
- (82) Delaglio, F.; Grzesiek, S.; Vuister, G. W.; Zhu, G.; Pfeifer, J.; Bax, A. *J Biomol NMR* **1995**, *6*, 277-293.
- (83) Zheng, Y.; Yang, D. W. *Bioinformatics* **2005**, *21*, 2925-2926.
- (84) Marulanda, D.; Tasayco, M. L.; McDermott, A.; Cataldi, M.; Arriaran, V.; Polenova, T. *J Am Chem Soc* **2004**, *126*, 16608-20.
- (85) Reif, B.; van Rossum, B. J.; Castellani, F.; Rehbein, K.; Diehl, A.; Oschkinat, H. *Journal of the American Chemical Society* **2003**, *125*, 1488-1489.

10. ^{13}C - ^{13}C PAR at 65 kHz

10.1 Abstract

We demonstrate a successful application of ^{13}C - ^{13}C proton assisted recoupling (PAR) on $[\text{U-}^{13}\text{C}, ^{15}\text{N}]$ MLF and $[\text{U-}^{13}\text{C}, ^{15}\text{N}]$ protein GB1 at 65 kHz magic angle spinning (MAS) frequency. Combining low power Two Pulses Phase Modulation (TPPM) heteronuclear decoupling ($\omega_{1\text{H}} \sim 16$ kHz) and PAR mixing, we obtain high resolution 2D spectra showing long range ^{13}C - ^{13}C contacts. This work demonstrates the possibility of performing high resolution protein structural studies in the highest MAS frequency regime currently available.

10.2 Introduction

Methodological advances¹⁻³⁷ in magic angle spinning^{38,39} (MAS) solid-state NMR (SSNMR) have laid down the foundation for *de novo* protein structure determination of previously inaccessible biologically and medically relevant systems, whether (nano)crystalline, fibrillar, immobilized by association with biomembranes^{20,40-42}, or otherwise insoluble. Advances in NMR probe designs have opened up new experimental venues that substantially expand the capabilities of SSNMR as a structural tool. One such venue, pioneered by Samoson and coworkers, is the extension of magic angle spinning NMR to very high spinning frequencies, in the range of 50-70 kHz.⁴³⁻⁴⁵ Access to spinning frequencies larger than the size of ¹H-¹H dipolar couplings has triggered hopes for the possibility of using the proton dimension in multidimensional SSNMR experiments, and notably in direct detection experiments.^{43,46,47} Historically each extension of the maximum spinning frequency achievable in SSNMR has brought a new set of opportunities for structural studies, but, at the same time, has introduced new methodological challenges. Each new regime has required the development of adequate methodology in order to optimize the resolution and sensitivity of NMR experiments. For example, the capability of performing experiments at $\omega_r/2\pi = 20-35$ kHz led to the development of a number of new tools at high magnetic fields ($B_0 > 15$ T), that promise to be valuable for protein assignments and structural studies.^{34-37,48} One such development has been the introduction of double quantum (DQ) Cosine Modulated Rotary Resonance (CMRR) for ¹³C resonance assignments in proteins. CMRR enables DQ recoupling without the need for any ¹H decoupling during mixing, yielding sign alternation of cross peak data for unambiguous assignments.^{36,48} In another advancement long range distance constraints (up to 5-7 Å) have been measured in uniformly ¹³C and ¹⁵N labeled systems using new techniques based on a Third Spin Assisted Recoupling (TSAR) mechanism such as Proton Assisted Insensitive Cross Polarization (PAINCP)³⁵ and Proton Assisted Recoupling (PAR)³⁷ which were subsequently used to calculate a *de novo* 3D protein structure.⁴⁹

At even higher MAS frequencies, some progress has already been made, but many opportunities remain. Notably, Ernst and coworkers have introduced the concept of low

power ^1H decoupling (i.e. the ^1H rf field strength applied is smaller than the MAS spinning frequency),⁵⁰ and first performed ^{13}C - ^{13}C correlation experiments on proteins in the >40 kHz MAS spinning frequency regime.^{51,52} However, the set of SSNMR methods available at $\omega_r/2\pi H_z C_1^\pm C_2^\mp > 40$ kHz so far^{53,54} is still limited, especially concerning techniques for recording long distance correlation experiments.

In this manuscript we demonstrate that the Proton Assisted homonuclear Recoupling (PAR)³⁷ pulse sequence can be successfully applied at 65 kHz MAS frequency to uniformly ^{13}C and ^{15}N labeled proteins. The PAR technique, which relies on a Third Spin Assisted recoupling mechanism (TSAR),³⁷ was already explained in detail for MAS spinning frequencies $\omega_r/2\pi < 30$ kHz. Here we show that despite the fact that the technique relies on a second order recoupling mechanism, it can still be used to observe long distance ^{13}C - ^{13}C contacts with mixing times on the order of tens of milliseconds at 65 kHz MAS frequency.

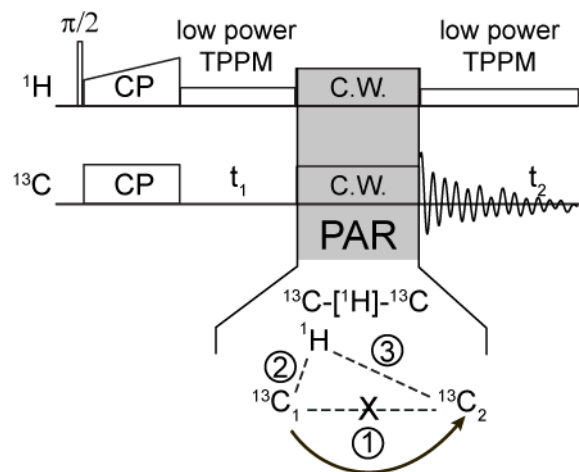


Figure 10-1 Pulse sequence for 2D ^{13}C - ^{13}C PAR experiments. The PAR mixing consists of simultaneous C.W. irradiation on the ^1H and ^{13}C channels with the irradiation strengths chosen to produce an appreciable second order TSAR mechanism.^{35,37} The TSAR term is a result of a cross term between the ^1H - ^{13}C dipolar couplings (terms 2 and 3 in the spin system graphics).

10.3 Experimental Section

10.3.1 Sample preparation

Preparation of N-[U-¹³C,¹⁵N]-*f*-MLF-OH: N-*f*-MLF-OH peptide was obtained by solid phase peptide synthesis from CS Bio Inc. (Menlo Park, CA). The peptide was prepared with uniformly ¹³C and ¹⁵N labeled amino acids from Cambridge Isotope Laboratories (Andover, MA). The peptide was crystallized from isopropanol and packed (~0.5 mg of peptide) in a 1.3mm Bruker rotor together with crystalline KBr.

Preparation of [U-¹³C,U-¹⁵N]-GB1: E. coli BL21 (DE3) cells (Invitrogen) were transformed with the T2Q mutant of GB1. Cells were grown in M9 minimal media with 3.0 grams of [U-¹³C] glucose (Cambridge Isotope Laboratories, Andover, MA) as the sole carbon source, and 1.0 gram ¹⁵N ammonium chloride (Cambridge Isotope Laboratories, Andover, MA) as the sole nitrogen source. Protein expression was induced with 500 M IPTG for 4 h. The cell pellet was homogenized with a tip sonicator in phosphate buffered saline (150 mM NaCl, 50 mM KH₂PO₄/K₂HPO₄, pH 7), and the supernatant purified by heating to 80 °C for 5 minutes followed by gel exclusion chromatography (Sephadex 16/60 Hi Prep). Peak purified fractions were pooled and concentrated using Amicon Ultra-3,500 MWCO devices. Microcrystalline samples were prepared according to ref. 47 by extensive dialysis in a total of 12L of 50 mM sodium phosphate buffer (pH 5.6) and precipitated with 3 aliquots of 2:1 MPD:IPA at a protein concentration of 25 mg/mL. The sample containing ~2.5 mg of protein was centrifuged into a 1.3 mm Bruker rotor.

10.3.2 NMR Spectroscopy: Experiments were performed on a commercial Bruker spectrometer operating at 500 MHz using a two channel ¹H-¹³C probe equipped with a 1.3 mm stator. Spinning frequency was regulated with a Bruker MAS controller to ± 10 Hz.

a. crystalline [U-¹³C,¹⁵N]-MLF: A 1.2 ms ¹H-¹³C CP contact time was used with 98 kHz ¹³C irradiation and ¹H power ramped down through the n=1 Hartmann-Hahn condition (i.e. 163 kHz).

230 kHz XiX decoupling was employed during the t_1 and t_2 evolution periods. The optimal length of the XiX pulse was 60.2 μs ($3.91 \tau_r$). The sweep width in the direct and indirect dimension was 25.2 kHz. Acquisition times were 27.7 ms in t_2 and 12.7 ms in t_1 with 64 scans per t_1 point (resulting in 17 h per 2D experiment). The recycle delay was 1.5 s.

The temperature was maintained at 284 K (at the thermocouple) using a BCU-X with 1400 L/h nitrogen flow rate.

b. microcrystalline [U- ^{13}C , ^{15}N]-GB1: The ^1H - ^{13}C CP contact time was 2.2 ms with 98 kHz ^{13}C irradiation and ^1H power ramped down through $n=1$ Hartmann-Hahn condition (i.e. 163 kHz). During the acquisition and t_1 evolution low power TPPM was used. The pulse length was set to 30.77 μs (π pulse for the $\omega_r/4$ rf power) and the decoupling was optimized by varying the ^1H irradiation strength (near $\omega_r/4$) and phase excursion. The optimal phase excursion was $\pm 24^\circ$. The sweep width in the direct and indirect dimension was 25.2 kHz. Acquisition times were 25 ms in t_2 and 10.1 ms in t_1 with 96 scans per t_1 point for the 2.5 ms spectrum (total acquisition time ~ 48 h) and 192 scan per t_1 point for the 10.1 ms spectrum (total acquisition time ~ 95.6 h). The recycle delay was 3.5 s.

PAR mixing was optimized by matching the experimental interference pattern to the simulated polarization transfer map. The ^{13}C irradiation strength was $p_C \sim 1.12$ (i.e. 72.8 kHz) and ^1H irradiation strength was $p_H \sim 0.3$ (i.e. 19.5 kHz). Mixing times were 2.5 ms and 10 ms.

The temperature was maintained at 255 K, measured at the thermocouple, using a BCU-X with 2000 L/h nitrogen flow rate; from previous calibrations it was ascertained that this corresponded to a sample temperature of approximately 30°C.

10.4 Results and Discussion

Figure 10-1 depicts the pulse sequence used for obtaining 2D ^{13}C - ^{13}C correlation spectra with the PAR method. PAR mixing consists of two C.W. fields. The irradiation strengths on the ^1H and ^{13}C channels are adjusted appropriately to induce polarization transfer between ^{13}C sites due to the second order ^{13}C - ^1H - ^{13}C TSAR mechanism.^{35,37} The TSAR cross term involving terms 2 and 3 (see the inset of Fig. 10-1) can be written as a function of the transverse operators $2C_X^{C_1C_2,(23)}H_Z$ and $2C_Y^{C_1C_2,(23)}H_Z$, and leads to polarization transfer between C_1 and C_2 . Another important contribution to the spin dynamics necessary for understanding the TSAR mechanism comes from auto-cross terms created by term 2 with itself and term 3 with itself respectively. These auto-cross terms lead to an off-resonance contribution in the TSAR subspace represented by $C_Z^{C_1C_2,(23)}$. Note that similar longitudinal terms also arise from the chemical shift tensor with itself. Such contributions lead to a tilting of the effective recoupling axis and reduction of the PAR polarization transfer. The detailed description of the spin dynamics in the PAR experiment can be found in ref. 37.

Figure 10-2 shows a numerical SPINEVOLUTION⁵⁵ simulation of the ^{13}C - ^{13}C PAR polarization transfer at $\omega_r/2\pi = 65$ kHz on a 7 spin system including 4 carbons and 3 protons (see inset of the Fig. 10-2 and Table 10-1 for details). The contour plot depicts polarization transfer from C_α to C_β (see Fig. 10-5 for C_α - C' and C_α - C_β optimization maps) after 5 ms of PAR mixing as a function of ^{13}C and ^1H C.W. irradiation magnitudes in units of spinning frequency (p_C and p_H respectively). The carrier frequency in the simulation was set between the carbonyl and aliphatic resonances, similar to the actual experiments (see Fig. 10-6 for an optimization map with the ^{13}C carrier frequency set in the middle of the aliphatic region only). There are several areas in the map for which the settings lead to appreciable PAR polarization transfer. The settings employed in this study are indicated with an 'x', including the higher power settings used for the ^{13}C - ^{13}C correlation spectra of N-f-MLF-OH⁴⁰ (see Fig. 10-8) and lower power settings used for the correlation spectra of GB1.

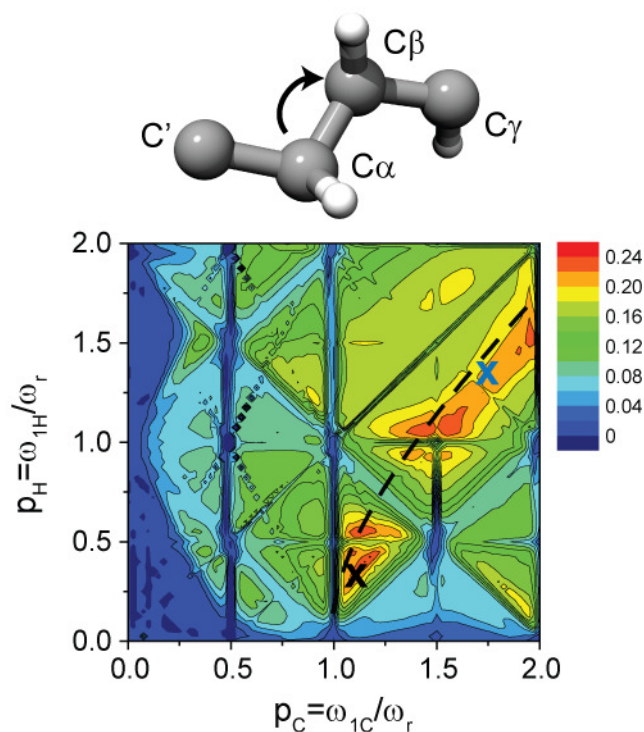


Figure 10-2 Simulated PAR polarization transfer map obtained on the spin system shown in the inset of the figure (see also Table 10-1). The contour plots represent polarization transfer between the C_α and C_β spins as a function of ^{13}C and ^1H irradiation strengths in units of spinning frequency. Simulations were performed using 5 ms PAR mixing at $\omega_r/2\pi = 65$ kHz MAS and $\omega_{0\text{H}}/2\pi = 500$ MHz and include chemical shifts (see Table 10-1). Similar maps for C_α - C' and C_α - C_β polarization transfer can be found in Fig. 10-5. For the settings indicated by the black dashed lines the CH auto-cross term is zero. The irradiation settings employed in this study are indicated with 'x's (blue for N- f -MLF-OH and black for GB1).

The PAR optimization map layout results from a compromise between maximizing the TSAR term and minimizing the longitudinal contribution from the auto-cross terms. The experimental irradiation settings were chosen as described in ref. 37. More specifically, we have simulated a map where we monitor magnetization on carbons as a function of ^1H and ^{13}C irradiation in a 1D experiment with 5 ms PAR mixing. Such an “interference” map (also simulated numerically in Fig. 10-9) allows one to identify irradiation settings leading to destructive interference that also outline the features of

the PAR polarization transfer map. Comparing the interference maps (both simulation and experiment) and the polarization transfer map shown in Fig. 10-2 allows one to choose the appropriate rf settings. Note, that for both the MLF-OH and GB1 spectra presented below we have chosen settings that favor polarization transfer between protonated carbons but also allow transfer between carbonyls and aliphatic carbons (with slightly lower efficiency). If the goal of the experiment is to maximize the magnetization transfer between carbonyls and protonated carbons, the reader should refer to Fig. 10-5b to choose the appropriate rf power levels. The shift in rf settings can be explained by the variation in magnitude of the auto-cross terms involved in a PAR carbonyl to aliphatic versus PAR aliphatic to aliphatic transfer.

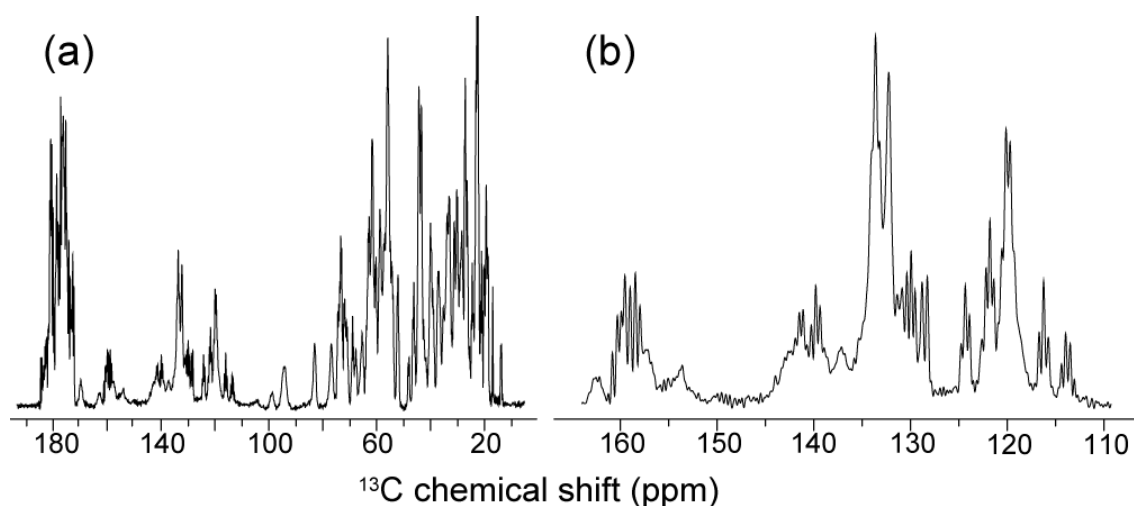


Figure 10-3 (a) 1D ¹³C CP-MAS spectrum of microcrystalline [U-¹³C,¹⁵N]-GB1 (2.5 mg protein packed in 1.3 mm rotor) obtained at $\omega_r/2\pi = 65$ kHz and $\omega_{0H}/2\pi = 500$ MHz with low power (~ 16.25 kHz) TPPM decoupling^{56,57} during acquisition. (b) Expansion of the aromatic region illustrating the excellent resolution.

Combining >50 kHz spinning frequencies and low power ¹H decoupling has already been shown to yield very well resolved spectra in uniformly labeled proteins.⁵² The concept of low power decoupling (introduced by Ernst *et al.*) was also investigated at $\omega_r/2\pi \sim 30$ kHz by De Paëpe *et al.* in the context of the Cosine Modulation^{56,58} and Two Pulse Phase Modulation²³ irradiation scheme where an rf field strength close to the

quarter of the MAS spinning frequency and a phase angle ~ 20 degrees was shown to yield efficient decoupling settings.⁵⁶ This sequence was recently described in greater detail by Kotecha *et al.* at ~ 40 kHz MAS spinning frequency and dubbed low power TPPM.⁵⁷ Figure 10-3 shows CP-MAS spectra obtained on microcrystalline $[U\text{-}^{13}\text{C}, ^{15}\text{N}]$ protein GB1 obtained at $\omega_{\text{H0}}=500$ MHz, $\omega_r/2\pi=65$ kHz with low power TPPM^{56,57} ($\sim \omega_{1\text{C}}=\omega_r/4=16.25$ kHz, $\phi=\pm 24^\circ$) during the acquisition. Although this system has already been demonstrated to yield well resolved spectra in previous publications, it is worthwhile to point out the excellent resolution achieved in this experiment. Notably we observe well resolved aromatic carbon resonances which appear more intense than in any SSNMR study on GB1 reported so far.^{59,60} Moreover we also observe splittings do to J-coupling for most of the sites in the protein.

Several factors could contribute to the excellent resolution of the 65 kHz MAS spinning frequency spectra reported here, including very effective heteronuclear decoupling, efficient averaging of the residual anisotropic contributions (i.e. magnetic bulk susceptibility etc.), and reduction of thermal gradients across the sample compared to a larger rotor.

This result clearly indicates that low power decoupling methods at $\omega_r/2\pi > 50$ kHz provide a viable method for carrying out high resolution protein studies.

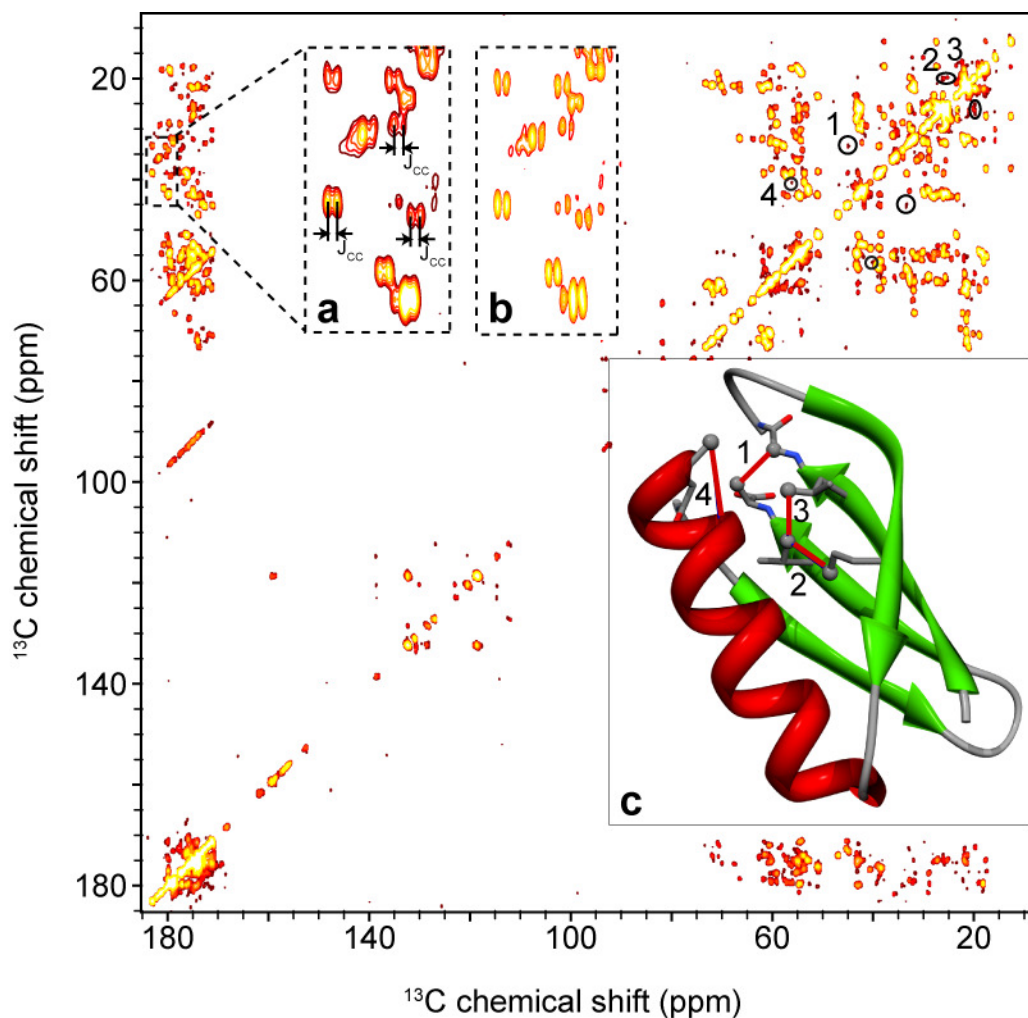


Figure 10-4 2D ^{13}C - ^{13}C PAR correlation spectra of microcrystalline $[\text{U-}^{13}\text{C},^{15}\text{N}]$ -GB1 obtained at $\omega_c/2 = 65$ kHz and $\omega_{\text{OH}}/2 = 500$ MHz with 10 ms PAR mixing. The PAR mixing employed ~ 73 kHz ^{13}C and 19.5 kHz ^1H irradiation. Low power TPPM^{56,57} ($\omega_{1\text{C}} = \omega_c/4 = 16.25$ kHz) was applied during acquisition and t_1 evolution. The high resolution achievable with this decoupling scheme is illustrated in panels (a) and (b), which depict an expansion of a carbonyl-aliphatic region of the spectrum. The data in panel (a) were processed without linear prediction in the direct dimension ($t_2 = 25$ ms) and the data in panel (b) with linear prediction in the direct dimension. In both panels in the direct dimension we can clearly distinguish splitting due to the J-couplings for most of the cross-peaks. Panel (c) illustrates some of the representative long distance contacts that are observed in an experiment with 10 ms PAR mixing. The cross-peaks corresponding to the contacts in panel (c) are circled and marked with numbers in the spectrum.

Figure 10-4 shows a 2D ^{13}C - ^{13}C PAR spectrum of microcrystalline [U- ^{13}C , ^{15}N] protein GB1 at $\omega_r/2\pi = 65$ kHz, $\omega_{\text{OH}}/2\pi = 500$ MHz where low power TPPM^{56,57} ^1H decoupling ($\omega_{1\text{H}}/2\pi \sim 0.25 \omega_r/2\pi = 16.25$ kHz) was applied during both direct and indirect evolution. 10 ms PAR mixing was applied with the irradiation settings corresponding to the black cross noted 'x' on Fig. 10-2. The spectrum shows cross peaks corresponding to both intra-residue and inter-residue medium to long distance contacts. Some representative long distance cross-peaks are marked on the PAR spectrum (Fig. 10-4) and the corresponding contacts are shown on the rendering of the x-ray structure⁶¹ with the distances indicated in Fig. 10-4c.

This result demonstrates that long distance transfers can be observed at 65 kHz spinning frequency with only 10 ms PAR mixing. This mixing time falls approximately in the same range as those used at 20 kHz MAS spinning frequency to perform the *de novo* structure determination of the protein Crh and thus implies that similar work is feasible at > 50 kHz spinning frequencies.^{37,49} To complement Fig. 10-4, a shorter PAR mixing time (2.5 ms) containing primarily one-bond and two-bond cross-peaks can be found in Fig. 10-7.

Since the TSAR mechanism is based on a second order process it is not completely intuitive that the PAR mixing time required for observing a given distance transfer does not increase as the MAS frequency increases. However, as already pointed out in ref. 37, higher MAS frequencies allow one to choose rf settings with an improved scaling factor that can compensate for the increase of MAS frequency. This feature is essential to allow practical implementations of PAR experiments at high spinning frequencies (> 30 kHz) and contrasts with PDS¹⁵ and DARR^{29,32} which would require 2 to 4 orders of magnitude longer mixing times.

The excellent resolution achieved with low power TPPM decoupling at 65 kHz MAS frequency is already obvious from the 1D spectrum displayed in Fig. 10-3, but is further illustrated in the PAR 2D spectrum. The inset in Fig. 10-4 shows expansions of selected carbonyl-aliphatic cross peaks from the spectra processed without (Fig. 10-4a) and with linear prediction in the direct dimension (Fig. 10-4b). We can clearly distinguish J-splitting for most of the resonances in the spectrum processed with linear prediction.

The mixing period and decoupling settings used for the PAR experiment on protein GB1 were chosen to optimize resolution and sensitivity while minimizing rf power requirements and thus rf induced sample heating. However, for samples where rf induced heating is less of a concern, higher power settings for both the PAR mixing and the ^1H decoupling periods can be used. As an illustration Fig. 10-7 shows ^{13}C - ^{13}C PAR spectra obtained on the dry, crystalline tripeptide $[\text{U-}^{13}\text{C},^{15}\text{N}]\text{-f-MLF-OH}$ with high power PAR mixing (the settings are indicated with a blue cross noted "x" in Fig. 10-2) and with ~ 230 kHz XiX^{30,62} decoupling during both direct and indirect evolution periods. Note that in these data we observe clear cross-peaks between the carbons in the phenylalanine ring, which undergoes two-fold flipping motion in the temperature regimes employed for most MAS experiments.

In summary we demonstrate that the ^{13}C - ^{13}C PAR method can be applied for obtaining long distance ^{13}C - ^{13}C contacts in uniformly ^{13}C labeled proteins at $\omega_r/2\pi = 65$ kHz with mixing times on the order of tens of milliseconds or less. Moreover, the PAR irradiation settings can be chosen to minimize rf induced heating even at such high spinning frequencies. This application opens up a venue for *de novo* structure determination of proteins at $\omega_r/2\pi > 50$ kHz in a manner analogous to the study performed at lower spinning frequencies. Notably, PAR provides a flexible tool for structural characterization of biomolecules over the entire range of currently available MAS frequencies and can be used alone or as a building block in more sophisticated pulse sequences.

We also demonstrate that combination of >50 kHz MAS and low power decoupling provides an attractive method for carrying out high resolution protein studies by solid-state NMR. The resolution of the spectra obtained at $\omega_r/2\pi=65$ kHz with low power TPPM rivals the resolution obtainable at $\omega_r/2\pi < 30$ kHz with high power decoupling but with significantly reduced rf strength requirements.

10.4 Acknowledgement

The work in this chapter was done in collaboration with Dr. G. De Paëpe, Matthew Eddy and Jochem Struppe from Bruker BioSpin.

We are very grateful to Dr. Mikhail Veshtort for providing the SPINEVOLUTION software that has been used in this work. We also would like to thank Dr. David Ruben, Dr. Christopher Turner, Ajay Thakkar, Dr. Anthony Bielecki and Dr. Shane Pawsey for technical support, Dr. Patrick van der Wel, Galia Debelouchina, Alexander Barnes, Marvin Bayro, Dr. Thorsten Maly, Marc Caporini, Andrew Casey and Prof. Anne-Frances Miller for helpful discussions. This was supported by the National Institute of Health Grants EB-001960 and EB-002026.

10.5 Supporting Information

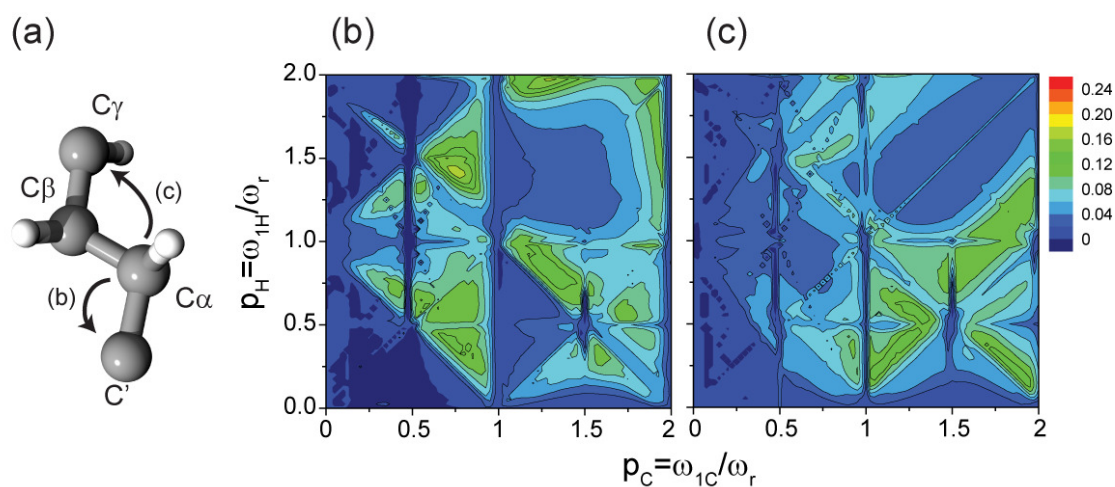


Figure 10-5 Numerical simulation of the ^{13}C - ^{13}C PAR polarization transfer optimization map performed on the spin system shown in (a). The contour plots represent polarization transfer between the C_α and C' in (b), and C_α and C_γ in (c) as a function of ^{13}C and ^1H irradiation strength in units of spinning frequency. Simulations were performed using 5 ms PAR mixing at $\omega_r/2\pi=65$ kHz MAS and $\omega_{0H}/2\pi=500$ MHz and include chemical shift. The details of the spin system are listed in Table 10-1.

Table 10-1 Spin system used in simulation in the Fig. 10-2 in the main text and Figure 10-5. The coordinates were taken from the SSNMR structure of N-*f*-MLF-OH⁶³ (PDB ID 1Q7O). The CH bond lengths were set to 1.12 Å.

Atom	X	Y	Z	δ_{iso} (ppm)	δ_{anis} (ppm)	η
LC α	0.297	0.449	0.95	41.2	25.1	0
LC'	-0.263	1.661	0.227	-77.2	-76	0.99
LC β	1.831	0.463	0.896	57.3	23.8	0.92
LC γ	2.514	-0.743	1.538	73	-19.8	0
LH α	-0.045	0.454	2.017	0	5	0.6
LH β 2	2.192	1.389	1.412	0	5	0.6
LH γ	2.235	-1.667	0.969	0	5	0.6

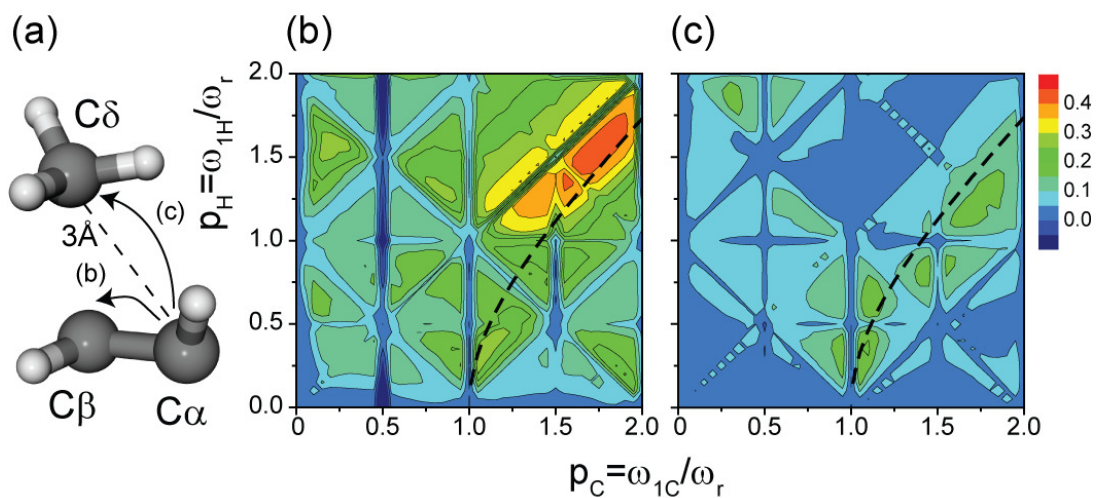


Figure 10-6 Numerical simulations of the ¹³C-¹³C PAR optimization maps on the aliphatic region. (a) spin system used in simulation taken from the SSNMR structure of N-*f*-MLF-OH¹ (see Table 10-2). The contour plots represent polarization transfer between the carbons (indicated by black arrow – C α -C β in (a) and C α -C δ in (b)) as a function of ¹³C and ¹H irradiation strength in units of spinning frequency. Simulations were performed using 5 ms PAR mixing at $\omega_r/2\pi=65$ kHz

MAS and $\omega_{0H}/2\pi=500$ MHz and include chemical shift. Simulation accounts for the threefold methyl group hop. For the settings indicated by the black dashed lines the CH auto-cross term is zero.

Table 10-2 Spin system used in simulation in the Fig. 10-6. The coordinates were taken from the SSNMR structure of N-*f*-MLF-OH¹ (PDB ID 1Q7O). The CH bond lengths were set to 1.12 Å.

Atom	X	Y	Z	δ_{iso} (ppm)	δ_{anis} (ppm)	η
LC α	0.288	0.419	0.932	-15	25.1	0
LC β	1.822	0.433	0.878	10	23.8	0.92
LC δ 2	2.051	-0.907	2.978	17	-19.8	0
LH α	-0.054	0.425	1.999	0	5	0.6
H β 2	2.183	1.36	1.394	0	5	0.6
L1H δ 2	2.149	0.071	3.515	0	5	0.6
L2H δ 2	2.686	-1.677	3.486	0	5	0.6
L3H δ 2	0.981	-1.236	2.988	0	5	0.6

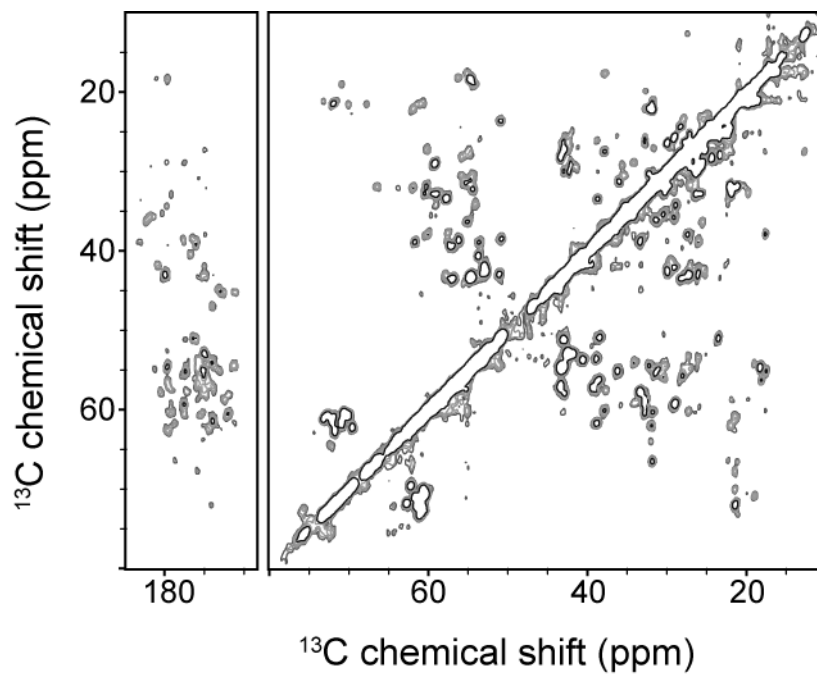


Figure 10-7 2D ^{13}C - ^{13}C PAR correlation spectra on $[\text{U-}^{13}\text{C},^{15}\text{N}]$ -GB1 obtained at $\omega_r/2 = 65$ kHz and $\omega_{\text{OH}}/2 = 500$ MHz. The PAR mixing time was 2.5 ms and used ~ 19.5 kHz ^{13}C and ~ 72.8 kHz ^1H irradiation. 16.5 kHz low power TPPM decoupling was employed during the acquisition and t_1 evolution.

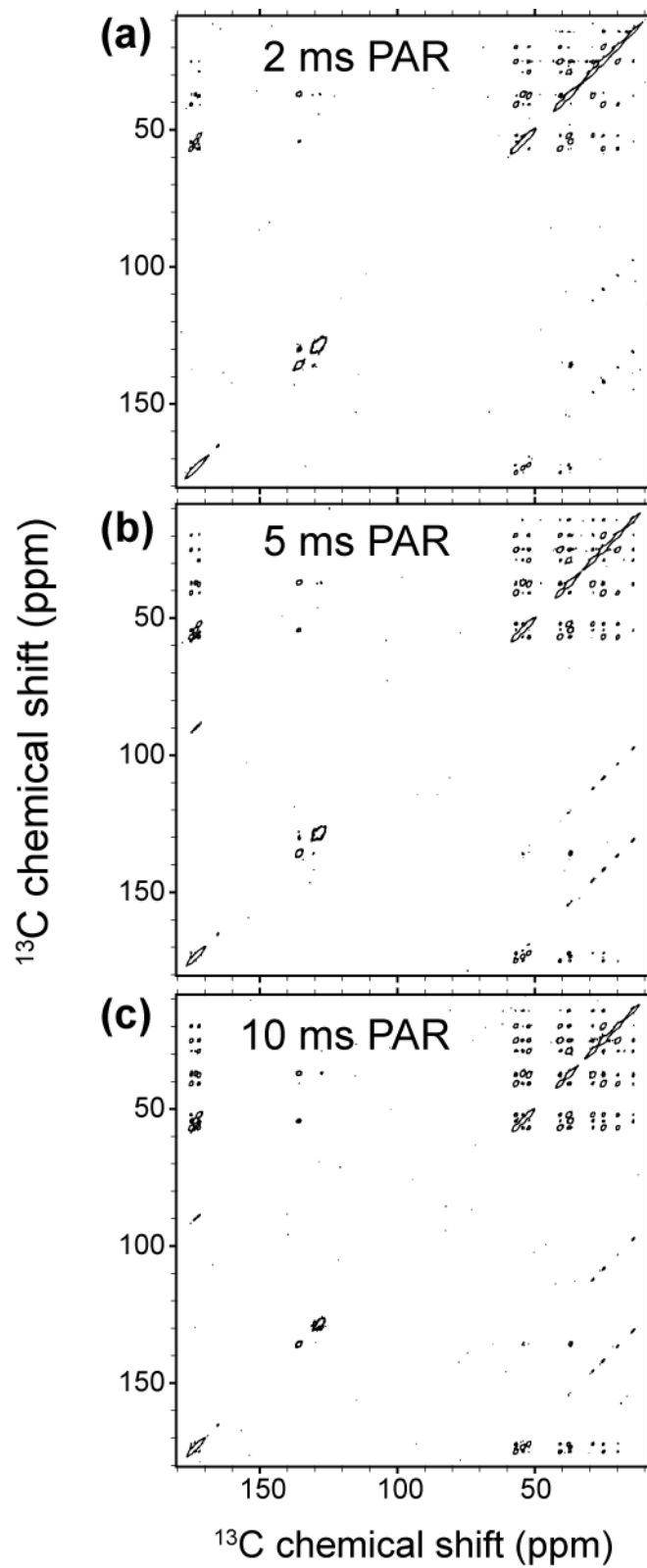


Figure 10-8 2D ^{13}C - ^{13}C PAR correlation spectra on $[\text{U-}^{13}\text{C},^{15}\text{N}]$ -f-MLF-OH obtained at $\omega_{\text{F}}/2 = 65$ kHz and $\omega_{\text{OH}}/2 = 500$ MHz. The PAR mixing time was (a) 2 ms, (b) 5 ms, (c) 10 ms and

used ~ 110 kHz ^{13}C and ~ 85 kHz ^1H irradiation. 230 kHz XiX decoupling (the XiX pulse was 60.2 μs i.e. $3.91 \tau_r$) was employed during the acquisition and t_1 evolution.

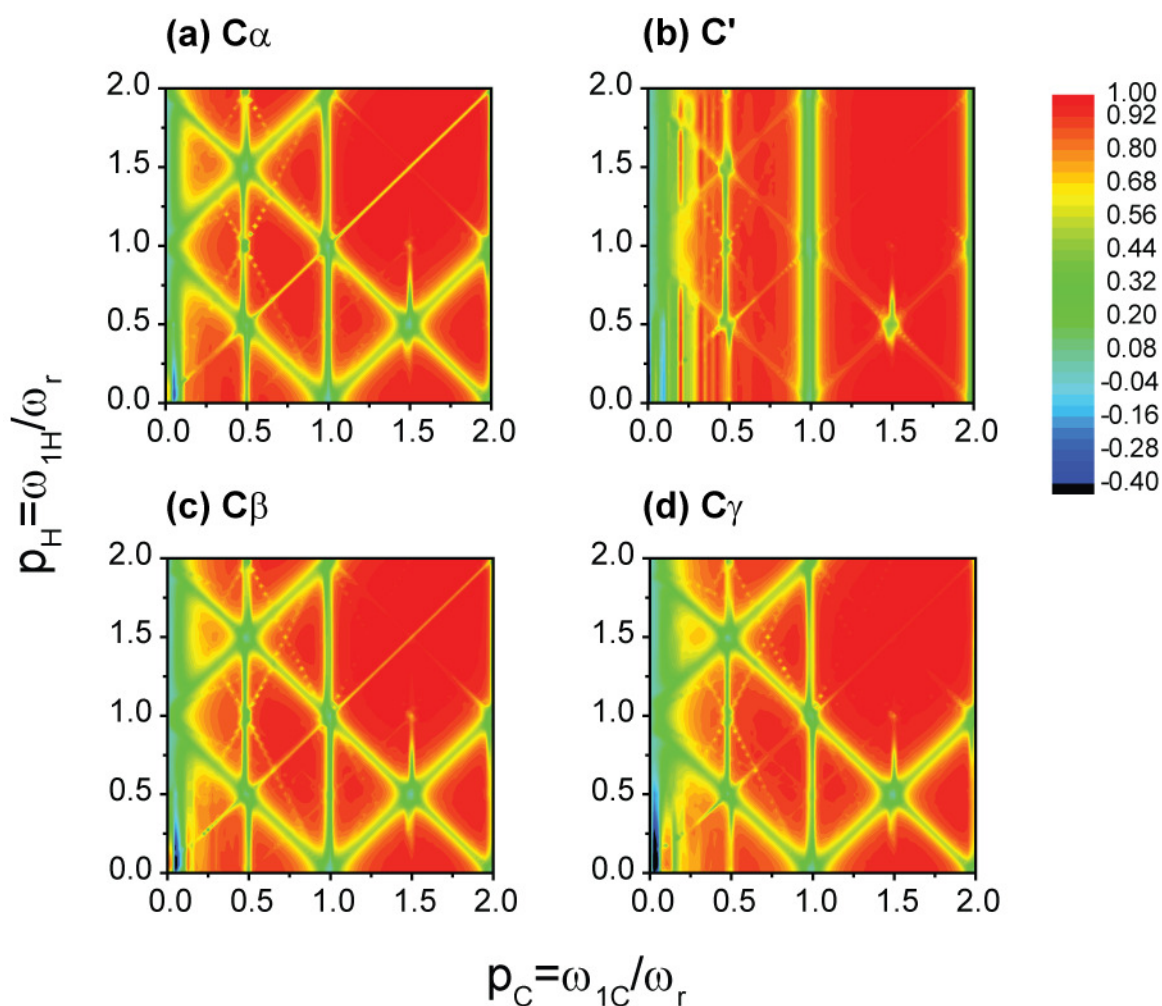


Figure 10-9 Numerically simulated “interference” map on the spin system in Table 10-1. In the interference map the decay of the magnetization on the carbons after the PAR mixing is monitored as a function of carbon (p_C) and proton (p_H) irradiation in units of spinning frequency. The initial magnetization is prepared on the x-axis on all the carbons. The settings for the simulation are identical to the settings used in Fig. 10-5. The comparison between the interference maps and the polarization transfer map shown in Fig. 10-2 and Fig. 10-5 allows one to choose the appropriate rf settings for performing PAR experiment.

10.6 References

- (1) Hartmann, S. R.; Hahn, E. L. *Phys. Rev.* **1962**, *128*, 2042-2053.
- (2) Andrew, E. R.; Bradbury, A.; Eades, R. G.; Jenks, G. J. *Nature* **1960**, *188*, 1096-1097.
- (3) Andrew, E. R.; Clough, S.; Farnell, L. F.; Gledhill, T. D.; Roberts, I. *Physics Letters* **1966**, *21*, 505.
- (4) Haeberlen, U.; Waugh, J. S. *Physical Review* **1968**, *175*, 453.
- (5) Pines, A.; Rhim, W.; Waugh, J. S. *Journal of Magnetic Resonance* **1972**, *6*, 457-&.
- (6) Pines, A.; Waugh, J. S.; Gibby, M. G. *Journal of Chemical Physics* **1972**, *56*, 1776-&.
- (7) Pines, A.; Gibby, M. G.; Waugh, J. S. *Journal of Chemical Physics* **1973**, *59*, 569-590.
- (8) Schaefer, J.; McKay, R. A.; Stejskal, E. O. *J. Magn. Reson.* **1979**, *34*, 443-447.
- (9) Aue, W. P.; Ruben, D. J.; Griffin, R. G. *Journal of Magnetic Resonance* **1981**, *43*, 472-477.
- (10) Munowitz, M. G.; Griffin, R. G.; Bodenhausen, G.; Huang, T. H. *Journal of the American Chemical Society* **1981**, *103*, 2529-2533.
- (11) Caravatti, P.; Bodenhausen, G.; Ernst, R. R. *Chemical Physics Letters* **1982**, *89*, 363-367.
- (12) Munowitz, M.; Aue, W. P.; Griffin, R. G. *Journal of Chemical Physics* **1982**, *77*, 1686-1689.
- (13) Munowitz, M. G.; Griffin, R. G. *Journal of Chemical Physics* **1982**, *76*, 2848-2858.
- (14) States, D. J.; Haberkorn, R. A.; Ruben, D. J. *Journal of Magnetic Resonance* **1982**, *48*, 286-292.
- (15) Szeverenyi, N. M.; Sullivan, M. J.; Maciel, G. E. *Journal of Magnetic Resonance* **1982**, *47*, 462-475.
- (16) Oas, T. G.; Griffin, R. G.; Levitt, M. H. *Journal of Chemical Physics* **1988**, *89*, 692-695.

- (17) Raleigh, D. P.; Levitt, M. H.; Griffin, R. G. *Chemical Physics Letters* **1988**, *146*, 71-76.
- (18) Gullion, T.; Schaefer, J. *Journal of Magnetic Resonance* **1989**, *81*, 196-200.
- (19) Raleigh, D. P.; Creuzet, F.; Gupta, S. K. D.; Levitt, M. H.; Griffin, R. G. *Journal of the American Chemical Society* **1989**, *111*, 4502-4503.
- (20) Creuzet, F.; McDermott, A.; Gebhard, R.; Vanderhoef, K.; Spijkerassink, M. B.; Herzfeld, J.; Lugtenburg, J.; Levitt, M. H.; Griffin, R. G. *Science* **1991**, *251*, 783-786.
- (21) Bennett, A. E.; Ok, J. H.; Griffin, R. G.; Vega, S. *Journal of Chemical Physics* **1992**, *96*, 8624-8627.
- (22) Nielsen, N. C.; Bildsoe, H.; Jakobsen, H. J.; Levitt, M. H. *Journal of Chemical Physics* **1994**, *101*, 1805-1812.
- (23) Bennett, A. E.; Rienstra, C. M.; Auger, M.; Lakshmi, K. V.; Griffin, R. G. *Journal of Chemical Physics* **1995**, *103*, 6951-6958.
- (24) Bennett, A. E.; Rienstra, C. M.; Griffiths, J. M.; Zhen, W. G.; Lansbury, P. T.; Griffin, R. G. *Journal of Chemical Physics* **1998**, *108*, 9463-9479.
- (25) Carravetta, M.; Eden, M.; Zhao, X.; Brinkmann, A.; Levitt, M. H. *Chemical Physics Letters* **2000**, *321*, 205-215.
- (26) Brinkmann, A.; Eden, M.; Levitt, M. H. *Journal of Chemical Physics* **2000**, *112*, 8539-8554.
- (27) Jaroniec, C. P.; Tounge, B. A.; Rienstra, C. M.; Herzfeld, J.; Griffin, R. G. *Journal of Magnetic Resonance* **2000**, *146*, 132-139.
- (28) Brinkmann, A.; Levitt, M. H. *Journal of Chemical Physics* **2001**, *115*, 357-384.
- (29) Takegoshi, K.; Nakamura, S.; Terao, T. *Chemical Physics Letters* **2001**, *344*, 631-637.
- (30) Detken, A.; Hardy, E. H.; Ernst, M.; Meier, B. H. *Chemical Physics Letters* **2002**, *356*, 298-304.
- (31) Lange, A.; Seidel, K.; Verdier, L.; Luca, S.; Baldus, M. *Journal of the American Chemical Society* **2003**, *125*, 12640-12648.

- (32) Takegoshi, K.; Nakamura, S.; Terao, T. *Journal of Chemical Physics* **2003**, *118*, 2325-2341.
- (33) De Paepe, G.; Elena, B.; Emsley, L. *Journal of Chemical Physics* **2004**, *121*, 3165-3180.
- (34) De Paepe, G.; Bayro, M. J.; Lewandowski, J.; Griffin, R. G. *J Am Chem Soc* **2006**, *128*, 1776-7.
- (35) Lewandowski, J. R.; De Paepe, G.; Griffin, R. G. *J Am Chem Soc* **2007**, *129*, 728-9.
- (36) De Paepe, G.; Lewandowski, J. R.; Griffin, R. G. *J Chem Phys* **2008**, *128*, 124503.
- (37) De Paepe, G.; Lewandowski, J.; Locquet, A.; Bockmann, A.; Griffin, R. G. *Submitted* **2008**.
- (38) Andrew, E. R.; Bradbury, A.; Eades, R. G. *Nature* **1958**, *182*, 1659-1659.
- (39) Andrew, E. R.; Bradbury, A.; Eades, R. G. *Nature* **1959**, *183*, 1802-1803.
- (40) Rienstra, C. M.; Tucker-Kellogg, L.; Jaroniec, C. P.; Hohwy, M.; Reif, B.; McMahon, M. T.; Tidor, B.; Lozano-Perez, T.; Griffin, R. G. *Proceedings of the National Academy of Sciences of the United States of America* **2002**, *99*, 10260-10265.
- (41) Jaroniec, C. P.; MacPhee, C. E.; Bajaj, V. S.; McMahon, M. T.; Dobson, C. M.; Griffin, R. G. *Proceedings of the National Academy of Sciences of the United States of America* **2004**, *101*, 711-716.
- (42) Castellani, F.; van Rossum, B.; Diehl, A.; Schubert, M.; Rehbein, K.; Oschkinat, H. *Nature* **2002**, *420*, 98-102.
- (43) Samoson, A.; Tuherm, T.; Gan, Z. *Solid State Nuclear Magnetic Resonance* **2001**, *20*, 130-136.
- (44) Samoson, A.; Tuherm, T.; Past, J. *Journal of Magnetic Resonance* **2001**, *149*, 264-267.
- (45) Samoson, A.; Tuherm, T.; Past, J.; Reinhold, A.; Anupold, T.; Heinmaa, N. In *New Techniques in Solid-State Nmr* 2005; Vol. 246, p 15-31.
- (46) Zhou, D. H.; Shah, G.; Cormos, M.; Mullen, C.; Sandoz, D.; Rienstra, C. M. *Journal of the American Chemical Society* **2007**, *129*, 11791-11801.

- (47) Zhou, D. H.; Shea, J. J.; Nieuwkoop, A. J.; Franks, W. T.; Wylie, B. J.; Mullen, C.; Sandoz, D.; Rienstra, C. M. *Angewandte Chemie-International Edition* **2007**, *46*, 8380-8383.
- (48) Lewandowski, J. R.; De Paepe, G.; van der Wel, P. C. A.; Birkett, N. R.; Belenky, M.; Maly, T.; Bayro, M. J.; Sivertsen, A. C.; Dobson, C. M.; Herzfeld, J.; Griffin, R. G. **2008**, *in preparation*.
- (49) De Paepe, G.; Lewandowski, J.; Locquet, A.; Bockmann, A.; Griffin, R. G. *in preparation* **2008**.
- (50) Ernst, M.; Samoson, A.; Meier, B. H. *Chemical Physics Letters* **2001**, *348*, 293-302.
- (51) Ernst, M.; Detken, A.; Bockmann, A.; Meier, B. H. *Journal of the American Chemical Society* **2003**, *125*, 15807-15810.
- (52) Ernst, M.; Meier, M. A.; Tuhem, T.; Samoson, A.; Meier, B. H. *Journal of the American Chemical Society* **2004**, *126*, 4764-4765.
- (53) Verel, R.; Baldus, M.; Ernst, M.; Meier, B. H. *Chemical Physics Letters* **1998**, *287*, 421-428.
- (54) Verel, R.; Ernst, M.; Meier, B. H. *Journal of Magnetic Resonance* **2001**, *150*, 81-99.
- (55) Veshtort, M.; Griffin, R. G. *J. Magn. Reson.* **2006**, *178*, 248-82.
- (56) De Paepe, G. Doctoral, École Normale Supérieure de Lyon, 2004.
- (57) Kotecha, M.; Wickramasinghe, N. P.; Ishii, Y. *Magn Reson Chem* **2007**, *45*, S221-S230.
- (58) De Paepe, G.; Hodgkinson, P.; Emsley, L. *Chemical Physics Letters* **2003**, *376*, 259-267.
- (59) Franks, W. T.; Kloepper, K. D.; Wylie, B. J.; Rienstra, C. M. *J Biomol NMR* **2007**, *39*, 107-131.
- (60) Schmidt, H. L. F.; Sperling, L. J.; Gao, Y. G.; Wylie, B. J.; Boettcher, J. M.; Wilson, S. R.; Rienstra, C. A. *Journal of Physical Chemistry B* **2007**, *111*, 14362-14369.

(61) Franks, W. T.; Zhou, D. H.; Wylie, B. J.; Money, B. G.; Graesser, D. T.; Frericks, H. L.; Sahota, G.; Rienstra, C. M. *Journal of the American Chemical Society* **2005**, *127*, 12291-12305.

(62) Tekely, P.; Palmas, P.; Canet, D. *Journal of Magnetic Resonance Series A* **1994**, *107*, 129-133.

(63) Rienstra, C. M.; Tucker-Kellogg, L.; Jaroniec, C. P.; Hohwy, M.; Reif, B.; McMahon, M. T.; Tidor, B.; Lozano-Perez, T.; Griffin, R. G. *Proceedings of the National Academy of Sciences of the United States of America* **2002**, *99*, 10260-10265.

11. Solid state NMR study of amyloid nanocrystals and fibrils formed by the peptide GNNQQNY from yeast prion protein Sup35p

Reproduced with permission from van der Wel PC, Lewandowski JR, Griffin RG." Solid-state NMR study of amyloid nanocrystals and fibrils formed by the peptide GNNQQNY from yeast prion protein Sup35p." J Am Chem Soc. (2007) 129(16):5117-30. Copyright © 2007 American Chemical Society.

11.1 Abstract

Sup35p is a prion protein found in yeast that contains a prion forming domain characterized by a repetitive sequence rich in Gln, Asn, Tyr and Gly amino acid residues. The peptide GNNQQNY₇₋₁₃ is one of the shortest segments of this domain found to form amyloid fibrils, in a fashion similar to the protein itself. Upon dissolution in water, GNNQQNY displays a concentration-dependent polymorphism, forming monoclinic and orthorhombic crystals at low concentrations, and amyloid fibrils at higher concentrations. We prepared nanocrystals of both space groups as well as fibril samples that reproducibly contain three (co-existing) structural forms, and examined the specimens with magic angle spinning (MAS) solid state nuclear magnetic resonance. ¹³C and ¹⁵N MAS spectra of both nanocrystals and fibrils reveal narrow resonances indicative of a high level of microscopic sample homogeneity that permitted resonance assignments of all five species. We observed variations in chemical shift among the three dominant forms of the fibrils which were indicated by the presence of three distinct, self-consistent sets of correlated NMR signals. Similarly, the monoclinic and orthorhombic crystals exhibit chemical shifts that differ from one another, and from the fibrils. Collectively, the chemical shift data suggests that the peptide assumes five conformations in the crystals and fibrils that differ from one another in subtle but distinct ways. This includes variations in the mobility of the aromatic Tyr ring. The data also suggest that various structures assumed by the peptide may be correlated to the "steric zipper" observed in the monoclinic crystals.

11.2 Introduction

Amyloidosis, or the class of disorders associated with amyloid-formation, continues to attract the attention of researchers from a wide variety of scientific disciplines. These studies are of great medical importance as a key to understanding human diseases¹, and are also of considerable scientific interest, potentially providing broader insights into fundamental biological processes such as protein (mis)folding. Unfortunately, the molecular structures of the proteinaceous aggregates, from which the name of the group is derived, remain elusive despite substantial ongoing efforts. The essential biophysical characteristics of amyloid fibrils complicate their structural characterization via conventional methods of structural biology, x-ray crystallography and solution NMR, since these techniques require either crystallization or dissolution of the material of interest.

For this reason, various complementary techniques are being applied to obtain insights into the mechanism behind the formation and structure of fibrillar aggregates^{2,3}. These studies often involve truncated fragments of amyloidogenic proteins, and are aimed at developing convenient model systems that yield detailed structural data. One such system is the yeast protein Sup35p which normally functions as a translation termination factor⁴⁻⁶. However, an aggregated form has been found to be the causative agent in the transmission of a phenotype [PSI(+)]⁷⁻⁹. The protein is the factor leading to an inheritable phenotype, that could also be induced by the introduction of preformed aggregates⁸. This is analogous to the role of the prion component in human prion disorders, a class of diseases characterized by the self-propagation of pathogenic amyloid aggregates¹⁰. The protein's prion-forming domain is characterized by a high percentage of glutamine and asparagine residues, similar to a class of amyloid-forming proteins implicated in various human diseases including Huntington's disease and spinal and bulbar muscular atrophy¹¹. Due to the relative convenience of the yeast organism, the Sup35p protein provides an easily accessible model system for the study of this class of disorders specifically and amyloid-forming proteins in general¹².

Since its identification as a prion-protein⁸, this 685-residue protein has been studied extensively¹³⁻²⁰, and it was generally established that the N-terminal segment of 123 amino acids is the prion-forming domain (PrD)⁸. The PrD displays a high level of amino acid degeneracy in its primary sequence, with just four residues -- Gln, Asn, Tyr and Gly -- accounting for 78% of its length^{3,8}. Various subsections of the PrD segment have been studied in a search for domains that are the cause, or at least share the features of, the fibril formation displayed by the larger protein²¹⁻²⁴. Eisenberg and co-workers identified a short section from the PrD domain, residues 7-13 (GNNQQNY), as one of the shortest segments that forms fibrils exhibiting physicochemical properties similar to those found for the protein's fibrils²⁵. They reported that the fibrils formed from this peptide resembled the protein fibrils in their fibrillization behavior, x-ray diffraction, and binding of Congo red. In addition, the same peptide is also able to form microcrystals that share some of the characteristics of the fibrils, and, using a newly developed microcrystal diffractometer, the x-ray structure of the monoclinic crystals was determined²⁶. Interestingly, the peptide also forms orthorhombic crystals that were the focus of earlier reports^{25,27}. Various features of the monoclinic crystal structure were proposed to be common to both the crystals and the fibrils, and even proposed to reflect general features of prion fibril formation and structure.

The x-ray structure reveals parallel β -strands that are stacked in register into β -sheets, along the longest dimension of the elongated crystals. The parallel stacked arrangement allows for strong interactions between the identical residues in neighboring strands involving 11 hydrogen bonds: backbone-backbone H-bonding, as well as Asn-Asn and Gln-Gln side chain H-bonding. This arrangement is reminiscent of a parallel version of the polyglutamine polar zipper^{28,29}, and the asparagine ladders found in parallel β -helix proteins^{30,31}. Another feature in common with parallel β -helix proteins³² is the stacking of Tyr side chains, in a manner allowing favorable π - π stacking interactions leading to β -sheet stabilization^{33,34}. Two β -sheets are tied together by strong steric interactions with one another, due to tightly packed Asn and Gln side chains on one face of the sheets, forming a *dry interface*. This closely packed interface featuring interdigitated, structurally complementary side chains was referred to as a *steric zipper*. It was suggested to be a key feature in the formation of the peptide fibrils and a general

mechanism in various other amyloid systems^{26,35,36}. Its formation would require a complementary structural motif in the two ‘mating’ surfaces. In contrast, the so-called *wet interface* features only a few direct contacts between the β -sheets, which are separated from one another by multiple water molecules, except for direct tyrosine side-chain interactions. The proximity and alignment of these Tyr rings seems to allow π - π stacking interactions between the β -sheets, in addition to the Tyr-Tyr stacking within each sheet. The potential implications of these crystals’ characteristics for prion fibril characterization have led to a number of experimental and theoretical studies into this peptide’s characteristics³⁷⁻⁴¹.

The reported formation of multiple crystallographic and fibrillar forms of GNNQQNY reflects a common observation in studies on amyloidogenic systems. Like many other amyloid fibrils, the Sup35p fibrils display a certain level of structural polymorphism, which appears to correlate to the existence of different strains of amyloid-related disorders *in vivo*⁴²⁻⁴⁴. The fact that the inter-stack assembly relies on a steric zipper, which does not necessarily require a high sequence specificity and could result in slightly different arrangements given the same primary sequence, has been proposed as a potential explanation for the polymorphism²⁶. While Nelson et al. did not discuss the potential for polymorphism due to variations in the so-called wet interface, it seems likely that even similarly assembled steric zippers (consisting of two β -sheets), can assemble in different ways as a result of rearrangements in the interactions on that face.

An obvious first step in the examination of these proposed generalizations would be to determine the extent to which the structure found in these crystals does or does not represent the fold in the fibrils formed by the same peptide, in order to eventually compare it to larger sections of the PrD domain of Sup35p. The crystals display a number of physicochemical amyloid-like characteristics, for instance the cross- β x-ray scattering pattern, and the binding of specific chromophores. Here we present a more detailed comparison of the structural features of the crystals and fibrils formed by these peptides, through investigations utilizing solid state nuclear magnetic resonance (SSNMR). Specifically, magic angle spinning (MAS) spectra have been employed in studies of other peptide-based fibrils derived from the amyloids transthyretin, A β and

various other systems⁴⁵⁻⁶². This technique is applicable to a wide variety of solid samples and in principle permits structural determinations of both crystalline and fibrillar aggregates. It does not require preparation of large crystals, and a reasonable level of microscopic structural homogeneity is sufficient to obtain high quality structural information.

Here, we use solid state MAS NMR methods to compare nanocrystals and fibrils formed by the peptide fragment GNNQQNY₇₋₁₃. At this initial stage, we focus on the determination of the assignments of the isotropic ¹³C and ¹⁵N chemical shifts of the peptide since differences in the shifts can be used to localize and identify differences in the structural features between the aggregated forms. Structural changes affecting the chemical shifts are typically dominated by the (local) structure of the monomer (i.e. its conformation), but can also include effects due to the proximity of other peptides involved in different packing arrangements. Therefore, a comparison of these parameters provides information on the localized similarities and differences between the crystalline and fibrillar forms of the peptide. In addition, structural features such as sample homogeneity and dynamics or motional flexibility can easily be evaluated with such measurements.

Samples prepared using segmentally ¹³C, ¹⁵N-labeled peptides yielded both crystalline forms and fibrillar samples in accordance with the documented polymorphic behavior of GNNQQNY²⁷. Subsequently, we employed a variety of multidimensional solid state MAS dipolar recoupling NMR techniques to compare different polymorphs of the peptide. Specifically, we deconvolved the spectra of three distinct structural forms within the fibrils and compared these to one another and to the two crystalline forms. The results provide a perspective on this array of five aggregates, allow direct comparisons among the polymorphs, and elucidate several proposed features of amyloids and their formative process.

11.3 Experimental Methods

11.3.1 Sample Preparation

GNNQQNY was obtained by solid phase peptide synthesis from CS Bio Inc. (Menlo Park, CA). The peptide was prepared both without isotopic enrichment, and with U-¹³C, ¹⁵N labeled amino acids from Cambridge Isotope Laboratories (Andover, MA) according to a segmental labeling scheme. The two isotopically labeled variants have labeled residues in either the first four positions ([U-¹³C, ¹⁵N-GNNQ]QNY) or in the final four positions (GNN[U-¹³C, ¹⁵N-QQNY]), allowing complete sequential chemical shift assignments. The peptide fragment GNNQQNY is known to form either crystals or fibrils, depending on the exact protocol used²⁵⁻²⁷. The general protocol involves rapid dissolution of the lyophilized peptide in water, resulting in an acidic peptide solution (pH 2-3), at a concentration of 1-25 mg/ml. Depending on concentration and treatment of the solution, the peptides form either monoclinic or orthorhombic crystals and/or fibrils. A brief description of some of the different samples prepared is contained in Table 11-1 with further details in the Results section.

11.3.2 Transmission electron microscopy

Both the fibrils and the nanocrystals were examined by transmission electron microscopy using a Philips EM410 electron microscope, as described previously⁶³. The peptide crystals and fibrils were negatively stained using aqueous uranyl acetate prior to measurement. The resulting micrographs were compared to reference grid samples (Electron Microscope Sciences, Hatfield PA) to ensure accurate measurements of the peptide aggregate dimensions.

Table 11-1 Description of the isotopically enriched samples used in this study. Samples were prepared using segmentally labeled peptides where either the N-terminus (GNNQ) or the C-terminus (QQNY) was U-¹³C,¹⁵N labeled. The samples are indicated as monoclinic (M), orthorhombic (O), or fibrillar (F), prepared at 4°C starting from an aqueous solution at peptide concentrations as marked.

[U-¹³C,¹⁵N-GNNQ]QNY			GNN[U-¹³C,¹⁵N-QQNY]		
ID	isotopic labeling	sample preparation	ID	isotopic labeling	sample preparation
M1	100%	monoclinic nanocrystal, 10 mg/ml	M3	100%	monoclinic nanocrystal, 10 mg/ml
M2	25%	monoclinic nanocrystal, 10 mg/ml	M4	20%	monoclinic nanocrystal, 10 mg/ml
O1	30%	orthorhombic nanocrystal, 2 mg/ml	O2	~20%	orthorhombic nanocrystal, 2 mg/ml
F1	100%	fibrils, 20 mg/ml	F4	30%	fibrils, 25 mg/ml
F2	30%	fibrils, 25 mg/ml			
F3	25%	fibrils + monoclinic crystal, 12 mg/ml			

11.4 NMR methods

11.4.1 Nanocrystal and fibril assignments

NMR spectra were recorded on Cambridge Instruments spectrometers (designed by D. J. Ruben, Francis Bitter Magnet Laboratory, MIT) operating at 500, 700 or 750 MHz ^1H frequencies, or on a Bruker Avance spectrometer operating at 900 MHz ^1H frequency. ^{13}C chemical shifts were referenced to aqueous DSS using external referencing via the published ^{13}C chemical shifts of adamantane⁶⁴. ^{15}N chemical shifts were referenced to liquid ammonia, via indirect referencing using the suggested IUPAC frequency ratios ($^{13}\text{C}/^1\text{H}$) of aqueous DSS and liquid NH_3 ($^{15}\text{N}/^1\text{H}$)^{65,66}. Experiments at 500 MHz utilized Varian triple-resonance probes equipped with 4-mm stators (Revolution NMR, Fort Collins, CO), spinning at 10-12 kHz regulated to ± 2 Hz with a Bruker spinning frequency controller (Bruker BioSpin, Billerica MA). At 700 and 750 MHz Varian and custom designed probes were used, respectively, using 3.2 mm rotors (Varian, Inc., and Revolution NMR, Fort Collins, CO) and MAS spinning rates of 15-20 kHz. Experiments at 900 MHz used a Bruker triple resonance probe equipped with 2.5 mm spinner module, and a spinning rate of ~ 20 kHz. The sample temperature was maintained by using a stream of cooled, 1°C nitrogen gas.

1D ^{13}C MAS spectra were recorded with ramped cross-polarization (CP), using a 2 ms contact time, and 100 kHz TPPM ^1H decoupling⁶⁷ during acquisition. The 2D ^{13}C - ^{13}C spin diffusion experiments used a 10-12 ms mixing time, during which a ^1H r.f. field matching the $n=1$ rotary resonance condition⁶⁸ was used to facilitate efficient ^{13}C - ^{13}C magnetization transfer (DARR/RAD mixing)⁶⁹⁻⁷². ^{13}C - ^{13}C correlation experiments using SPC5 mixing⁷³ were performed at 10 kHz MAS using a 1.5 ms mixing time with $\omega_{1\text{C}}/2\pi=50$ kHz and $\omega_{1\text{H}}/2\pi=100$ kHz in the form of CW decoupling. ^{13}C - ^{13}C recoupling experiments at 900 MHz and $\omega_r/2\pi = 20$ kHz utilized cosine modulation rotary resonance⁷⁴, CM₄RR, with a mixing period of 796 μs , $(\omega_1/2\pi)_{13\text{C}} = 84.6$ kHz and no ^1H irradiation during mixing.

^{15}N - ^{13}C correlations were obtained through a series of double CP-based measurements^{75,76}. NCA and NCO spectra⁷⁷⁻⁷⁹ were recorded using ^1H - ^{15}N CP followed by ^{15}N chemical shift evolution, and band-selective specific CP resulting in selective

transfer of the ^{15}N magnetization to directly bonded ^{13}CO or $^{13}\text{C}_\alpha$ by placing the ^{13}C carrier frequency in the middle of the CO (for NCO transfer) and C_α (for NCA transfer) regions. The ^{15}N radio frequency field strength was 5-20 kHz, the ^{13}C field was ramped linearly through the $n=1$ Hartmann–Hahn matching condition, and the DCP contact time was 3 ms. 2D ^{15}N - ^{13}C - ^{13}C spectra were recorded by using the NCOCX and NCACX⁸⁰ pulse sequences that included a 10 to 20 ms DARR/RAD period to establish the intra-residue ^{13}C - ^{13}C correlations. Unless otherwise noted, the NMR spectra of the fibrils were acquired in essentially the same manner as the crystals.

11.4.2 NMR data analysis

NMR data processing and assignment were done with the aid of the NMRPipe⁸¹ and Sparky⁸² software packages. Analysis of the peptide backbone (and C_β) chemical shifts was performed using the TALOS software (version 2003.027.13.05)⁸³, using the default database of 78 proteins. The N-terminal nitrogen and C-terminal carbonyl atoms were excluded from this analysis. Secondary shift calculations^{84,85} were performed by subtracting the random coil shifts listed by Zhang *et al.*⁸⁶.

11.5 Results

11.5.1 Peptide aggregate preparation

The type of aggregates formed by GNNQQNY can be controlled by seeding with pre-formed aggregates and other variations in the sample preparation protocol, with the most notable differentiation dependent on the peptide concentration²⁷. To illustrate the appearance of our samples, we show in Figure 1 photographs of the different aggregated forms. The formation of fibrils was predominantly observed at higher peptide concentrations, when dissolving the peptide at 10-25 mg/ml, followed by fibrillization for 2-3 days at 4°C or room temperature. This yielded a highly viscous gel-like sample, as illustrated in Figure 11-1a. In contrast, near 10 mg/ml the peptide has a tendency to form the monoclinic nanocrystals previously studied by x-ray diffraction²⁶. These monoclinic crystals form typical snowball-like clusters as seen in Figure 11-1b and c. At this concentration, the sample often contains both the snowball-like crystals and gel-

like fibrils (Figure 11-1c), unless one uses rapid filtration using 0.2 μm filters to remove initial fibrillization sources (Figure 11-1b). The fibril formation at higher peptide concentrations is unaffected by filtration of the solution. In our experiments, at low concentrations (1-2 mg/ml) the formation of fibrils is suppressed, but after several days at 4°C the formation of monoclinic crystals was observed even in the absence of filtration. If these low concentration peptide solutions are swirled during crystallization, the formation of crystals is accelerated, but the spherical clusters are not observed. Rather, one obtains white suspensions (Figure 11-1d) that, under seemingly identical conditions, comprise either the monoclinic crystals²⁶ or the orthorhombic crystal form reported in earlier literature^{25,27}. In general, we note that there was some level of variability in the result of the different protocols, especially in the size of the crystals and the relative amounts of fibrils and crystals.

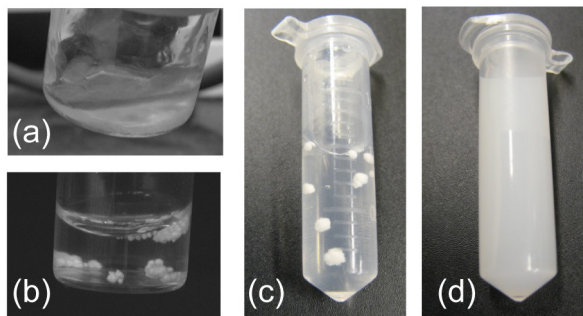


Figure 11-1 Photographs of various GNNQQNY aggregates: (a) fibrils prepared at 25 mg/ml, (b) clusters of monoclinic crystals at 10 mg/ml after filtration, (c) monoclinic crystals imbedded in fibril gel at 10 mg/ml (no filtration), and (d) a suspension of orthorhombic crystals obtained after swirling a 2 mg/ml solution.

11.5.2 Monoclinic nanocrystal characterization

We first focus our attention on the monoclinic crystals for which an x-ray structure exists²⁶. Figure 11-2(a) shows a transmission electron micrograph of typical crystallites making up the spherical aggregates shown in Figure 11-1(b) and (c).

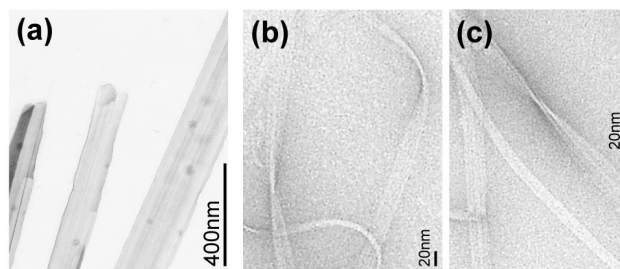


Figure 11-2 Transmission electron micrograph images of GNNQQNY monoclinic nanocrystals obtained at (a) 10 mg/ml and (b,c) fibrillar aggregates formed at 25 mg/ml.

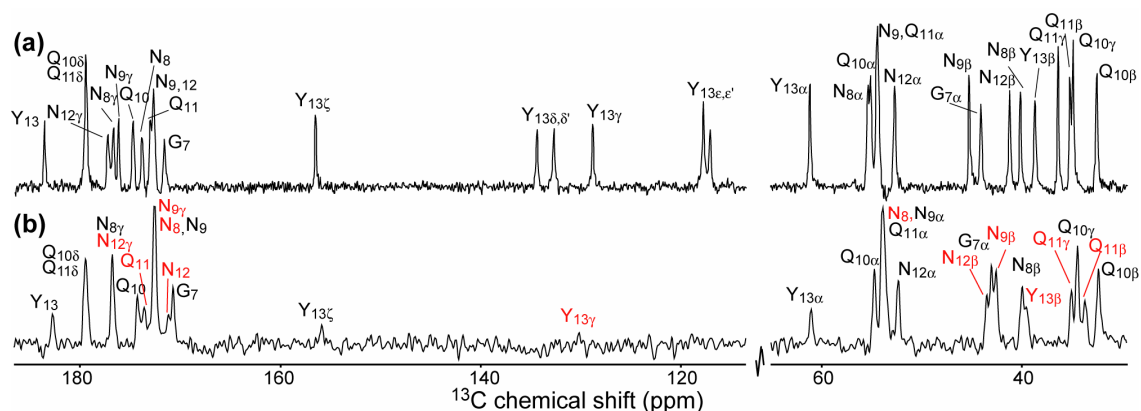


Figure 11-3 ^{13}C 1D spectra of natural abundance (a) monoclinic nanocrystals and (b) isotopically dilute ($\sim 3\%$ segmentally labeled in GNNQ₇₋₁₀) orthorhombic nanocrystals of GNNQQNY. Spectra were acquired at 750 and 700 MHz ^1H frequencies, respectively. Red labels indicate sites displaying the most significant change in chemical shift between the two forms.

TEM data acquired for crystals from a number of different samples revealed an average crystal width of $\sim 150\text{-}200$ nm, but with much longer lengths, of the order of micrometers. These dimensions are consistent with the monoclinic crystal size described in the literature²⁶. ^{13}C MAS spectra from natural abundance nanocrystals yielded spectra with very narrow line widths, indicative of a high level of homogeneity and uniformity (Figure 11-3 (a)). However, as judged by their line widths, the homogeneity of different monoclinic preparations varied slightly, but reproducibly yielded a single and identical set of chemical shifts. The 1D ^{13}C spectrum in Figure 3a was obtained at 750 MHz (^1H frequency), and illustrates the narrow line widths achievable with natural abundance samples (ranging from 31-52 Hz or 0.16-0.28 ppm).

Figure 11-3(a) also shows the assignments of the ^{13}C resonances obtained using two segmentally labeled peptides, prepared by solid phase peptide synthesis. The peptides were uniformly ^{13}C , ^{15}N labeled in the first four or last four residues of the heptapeptide: $[\text{U-}^{13}\text{C}, ^{15}\text{N-GNNQ}] \text{QNY}$ and $\text{GNN}[\text{U-}^{13}\text{C}, ^{15}\text{N-QQNY}]$. Each peptide was used to prepare both 100%-labeled and isotopically dilute (20-25% labeled) samples. One-dimensional ^{13}C and ^{15}N spectra for both peptides are shown in Figure 11-4 (panels (a) and (b)). The resonance frequencies are reproducible between samples and the ^{13}C frequencies match the earlier results from unlabeled peptide. The line widths are increased due to the presence of ^{13}C - ^{13}C J-couplings and variations in sample homogeneity.

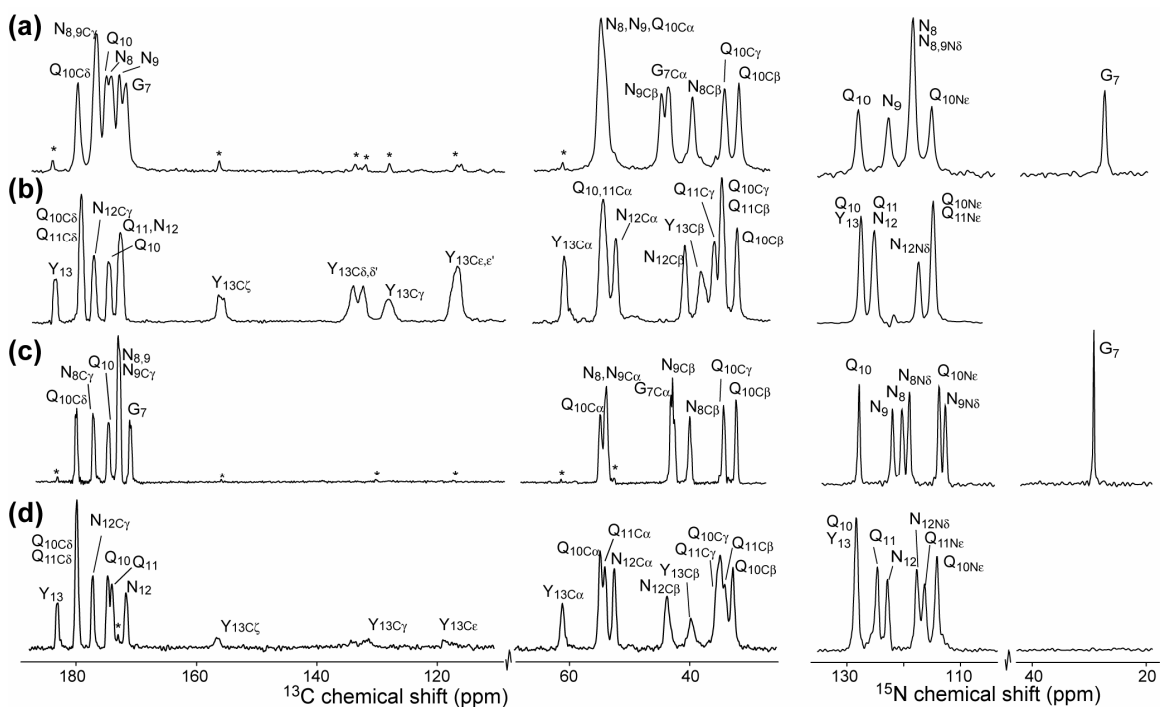


Figure 11-4 1D ^{13}C and ^{15}N spectra of (a,b) monoclinic and (c,d) orthorhombic GNNQQNY nanocrystals, obtained at 500 MHz and 700MHz ^1H fields, respectively. Rows (a) and (c) are for labeled $[\text{U-}^{13}\text{C}, ^{15}\text{N-GNNQ}] \text{QNY}$ samples M2 and M3, while (b) and (d) are labeled $\text{GNN}[\text{U-}^{13}\text{C}, ^{15}\text{N-QQNY}]$ O1 and O2.

A series of 2D experiments was performed on these samples in order to establish connectivity patterns and determine the specific resonance assignments. An overview of the results is included as Figure 11-5. The pulse sequences employed include standard

heteronuclear experiments such as NCA, NCO, NCOCX and homonuclear experiments relying on SPC5 and DARR/RAD mixing (see Methods).

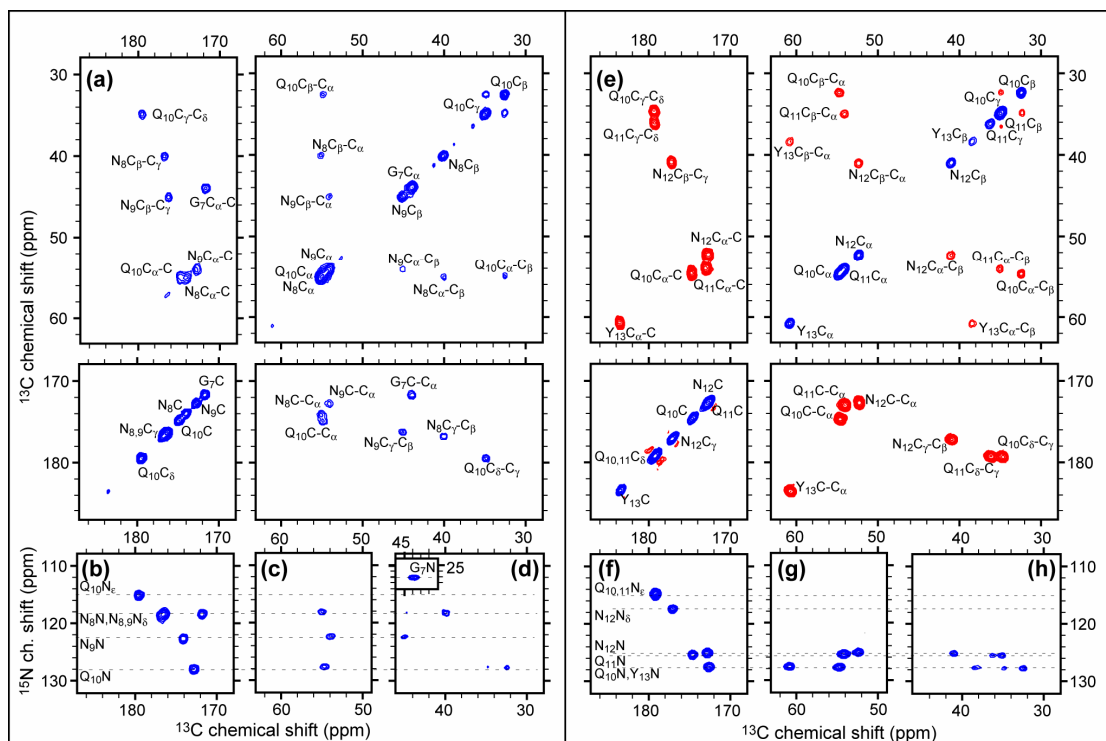


Figure 11-5 2D assignment data for monoclinic crystal samples of [U-¹³C,¹⁵N-GNNQ]QNY (sample M2, panels a-d), and GNN[U-¹³C,¹⁵N-QQNY] (M3, e-f). The data were obtained at 500 MHz ¹H frequency and 10 kHz MAS. ¹³C-¹³C correlations (a,e) were obtained via DARR/RAD and SPC5 mixing, respectively. ¹⁵N-¹³C correlations were obtained in N-CO (b,f), NCA (c,g) and NCACX experiments (d,h).

These 2D spectra were sufficient to unequivocally assign each of the observed resonances, and the shifts and the respective assignments are tabulated in Table 11-2. The ¹³C shifts are based on the natural abundance, high-field spectra, giving a typical standard deviation of 0.05-0.1 ppm, while the isotopically enriched samples were used to obtain the ¹⁵N resonances with a standard deviation of 0.1-0.2 ppm. As was apparent from the natural abundance spectra, the ¹³C resonances generally show good dispersion, but the overlap of the ¹⁵N chemical shifts is significant. This result is not unexpected given the degenerate nature of the peptide.

Table 11-2 Chemical shifts of the nuclei in monoclinic nanocrystals of GNNQQNY. The listed ^{13}C frequencies are based on natural abundance spectra, and have an uncertainty of 0.05-0.1ppm. The ^{15}N frequencies are based on ^{15}N enriched samples, and have an uncertainty of ~ 0.2 ppm. ^{13}C chemical shifts are referenced relative to DSS and ^{15}N chemical shifts are referenced relative to liquid NH_3 , according to IUPAC ^{65,66} using indirect referencing based on adamantane ⁶⁴.

Res	^{13}C chemical shift (ppm)									^{15}N chem. shift (ppm)			
	C'	C $_{\alpha}$	C $_{\beta}$	C $_{\gamma}$	C $_{\delta}$	C $_{\delta'}$	C $_{\epsilon}$	C $_{\epsilon'}$	C $_{\zeta}$	N	N $_{\delta}$	N $_{\epsilon}$	
Gly ₇	171.46	43.92									27.0		
Asn ₈	173.64	55.08	40.02	176.54							118.0	118.0	
Asn ₉	172.58	54.21	45.10	176.01							122.2	118.0	
Gln ₁₀	174.56	54.98	32.43	34.81	179.25						127.7		114.8
Gln ₁₁	172.68	54.21	35.10	36.25	179.25						125.4		114.8
Asn ₁₂	172.58	52.57	41.11	177.08							125.4	117.5	
Tyr ₁₃	183.35	60.93	38.58	128.94	134.50	132.81	117.99	117.32	156.46	127.7			

The chemical shifts obtained here can be indexed relative to averaged random coil shifts ^{86,87} to obtain a preliminary identification of the secondary structure. The results of such an analysis are shown in Figure 11-6, and indicate the expected β -sheet character typical of amyloid structures. Additionally, one can use the chemical shift analysis program TALOS ⁸³ to estimate the peptide backbone angles. The results of such an analysis are listed in 11.5.3 Orthorhombic crystals

Previous publications on crystals obtained for GNNQQNY have described two different crystal forms: earlier papers^{25,27} focused on an orthorhombic form, whereas more recent data²⁶ are for the monoclinic crystals described above. In our preparations, we typically encounter the monoclinic crystals, but also prepared some orthorhombic samples. Initial preparation involved a low concentration of peptide (2 mg/ml), which was swirled overnight. While seemingly identical conditions also yielded monoclinic crystals in other trials, we used seeding of the solution with existing crystals to control

the crystal form made. Figure 11-3(b) shows the ^{13}C 1D spectrum of this crystal form, in which it is clear that there are significant differences from the equivalent monoclinic sample in panel (a) (note that this is a weakly labeled sample containing about 3% [U- ^{13}C , ^{15}N -GNNQ]QNY peptide, as a result of seeding the crystallization). Again, the same segmentally ^{13}C and ^{15}N labeled peptides were used to obtain full assignments of the ^{13}C and ^{15}N resonances (1D ^{13}C and ^{15}N spectra in Figure 11-4). Note that the measurements for the orthorhombic crystals were done at higher field and higher spinning frequencies, explaining the apparent reduction in line width compared to the monoclinic crystals. The chemical shifts are largely similar to the monoclinic crystals, but do show significant changes in a number of positions. A more detailed description of the various changes follows in a later section. One of the more remarkable and obvious differences concerns the aromatic resonances of the Tyr side chain. These are all clearly distinguishable in the monoclinic form, suggesting a rigid, immobile arrangement of the aromatic ring. However, as can be seen for the unlabeled Tyr signals visible in Figure 11-3 and Figure 11-4(c), the aromatic intensities in the orthorhombic crystals are significantly reduced, with the C α /C β and C γ /C δ pairs now each degenerate in their chemical shift. Both features suggest that the aromatic ring is undergoing a twofold flipping motion at an intermediate exchange rate, resulting in an averaging of chemical shifts as well as interference with efficient cross polarization and proton decoupling^{88,89}. Another observation to make is that the initial measurements of this GNN[U- ^{13}C , ^{15}N -QQNY] ^{13}C sample showed signals due to a trace amount of monoclinic crystal that formed despite seeding with orthorhombic material. This could be the result of an inherent favorability of the monoclinic crystal form under the sample conditions employed, resulting in a competition between the formation of the two forms. Interestingly, successive measurements (not shown) of the same sample indicated a reduction of the amount of monoclinic crystals, which apparently spontaneously converted to orthorhombic form.

Table 11-3, which includes the same torsion angles obtained from the crystal structure²⁶. As expected, the chemical shifts are found to be consistent with the β -sheet structure. The accuracy of the TALOS backbone angles relative to the reported crystal

data, as seen in the table, is quite reasonable. Small deviations could be explained by the effect of intermolecular (non-local) contacts on the chemical shift in a tightly packed system. Note that some of torsion angles obtained for the orthorhombic crystals differ significantly from those observed for the monoclinic form of the crystals.

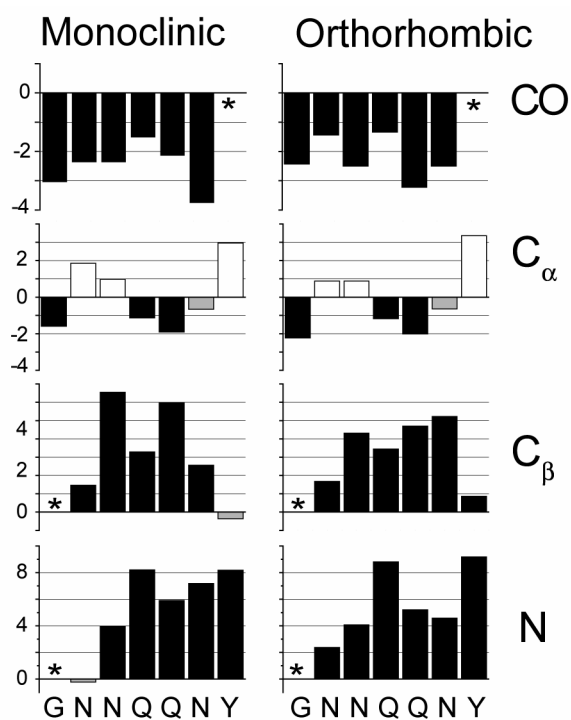


Figure 11-6 Secondary chemical shift for the monoclinic and orthorhombic nanocrystals. Color coding: black = β -sheet, white = α -helical, grey = indeterminate.

11.5.3 Orthorhombic crystals

Previous publications on crystals obtained for GNNQQNY have described two different crystal forms: earlier papers^{25,27} focused on an orthorhombic form, whereas more recent data²⁶ are for the monoclinic crystals described above. In our preparations, we typically encounter the monoclinic crystals, but also prepared some orthorhombic samples. Initial preparation involved a low concentration of peptide (2 mg/ml), which was swirled overnight. While seemingly identical conditions also yielded monoclinic crystals in other trials, we used seeding of the solution with existing crystals to control

the crystal form made. Figure 11-3(b) shows the ^{13}C 1D spectrum of this crystal form, in which it is clear that there are significant differences from the equivalent monoclinic sample in panel (a) (note that this is a weakly labeled sample containing about 3% [^{13}C , ^{15}N -GNNQ]QNY peptide, as a result of seeding the crystallization). Again, the same segmentally ^{13}C and ^{15}N labeled peptides were used to obtain full assignments of the ^{13}C and ^{15}N resonances (1D ^{13}C and ^{15}N spectra in Figure 11-4). Note that the measurements for the orthorhombic crystals were done at higher field and higher spinning frequencies, explaining the apparent reduction in line width compared to the monoclinic crystals. The chemical shifts are largely similar to the monoclinic crystals, but do show significant changes in a number of positions. A more detailed description of the various changes follows in a later section. One of the more remarkable and obvious differences concerns the aromatic resonances of the Tyr side chain. These are all clearly distinguishable in the monoclinic form, suggesting a rigid, immobile arrangement of the aromatic ring. However, as can be seen for the unlabeled Tyr signals visible in Figure 11-3 and Figure 11-4(c), the aromatic intensities in the orthorhombic crystals are significantly reduced, with the $\text{C}_{\delta 1}/\text{C}_{\delta 2}$ and $\text{C}_{\epsilon 1}/\text{C}_{\epsilon 2}$ pairs now each degenerate in their chemical shift. Both features suggest that the aromatic ring is undergoing a twofold flipping motion at an intermediate exchange rate, resulting in an averaging of chemical shifts as well as interference with efficient cross polarization and proton decoupling^{88,89}. Another observation to make is that the initial measurements of this GNN[^{13}C , ^{15}N -QQNY] ^{13}C sample showed signals due to a trace amount of monoclinic crystal that formed despite seeding with orthorhombic material. This could be the result of an inherent favorability of the monoclinic crystal form under the sample conditions employed, resulting in a competition between the formation of the two forms. Interestingly, successive measurements (not shown) of the same sample indicated a reduction of the amount of monoclinic crystals, which apparently spontaneously converted to orthorhombic form.

Table 11-3 Torsion angle data for the peptide backbone of crystalline GNNQQNY. The predicted torsion angles are based on analysis of the isotropic chemical shift values using the TALOS program⁸³. The table also lists the equivalent torsion angles found in the x-ray crystal structure of the monoclinic crystals²⁶.

	monoclinic crystals		orthorhombic crystals		monoclinic crystals	
	(NMR / TALOS)		(NMR / TALOS)		(x-ray)	
Residue	ϕ	ψ	ϕ	ψ	ϕ	ψ
Asn-8	-89 ±17	131 ±10	-120 ±23	130 ±10	-60.6	141.2
Asn-9	-139 ±13	136 ± 9	-129 ±19	128 ± 8	-119.2	125.2
Gln-10	-106 ±17	126 ±14	-128 ±16	134 ±20	-126.2	112.8
Gln-11	-134 ±18	142 ±15	-136 ±15	143 ±19	-115.0	126.8
Asn-12	-104 ±19	119 ±13	-135 ±14	132 ±16	-116.4	97.7

The results of the assignment experiments are included in the supporting information to this manuscript, with selected sections shown in figures in the paragraphs below. The assignments and chemical shifts are listed in Table 11-4. We also show the secondary chemical shifts in Figure 11-6, illustrating that the differences in the backbone chemical shifts between the two crystalline forms are small. This is also reflected in the results of a TALOS analysis included in Table 11-3. The only significant changes are toward the ends of the peptide, with basically no significant changes in the central residues. As will be discussed in more detail below, larger chemical shift differences are found in the side chains, and are not limited to the Tyr ring dynamics mentioned earlier.

Table 11-4 Chemical shifts of the nuclei in orthorhombic nanocrystals of GNNQQNY. The resonances are based on a combination of natural abundance and labeled data. * Tyr side chain resonances (in italics) are partially averaged indicating dynamics of the aromatic ring.

Residue	¹³ C chemical shift (ppm)									¹⁵ N chem. shift (ppm)		
	C'	C _α	C _β	C _γ	C _δ	C _{δ'}	C _ε	C _{ε'}	C _ζ	N	N _δ	N _ε
Gly ₇	170.86	43.28								29.2		
Asn ₈	172.73	54.11	40.23	176.97						120.6	119.4	
Asn ₉	172.73	54.11	42.86	172.73						122.3	113.0	
Gln ₁₀	174.40	54.94	32.59	34.67	179.67					128.3		114.1
Gln ₁₁	173.77	54.11	33.84	35.30	179.67					124.7		116.3
Asn ₁₂	171.34	52.58	43.77	176.97						122.8	117.9	
Tyr ₁₃ [*]	182.94	61.33	39.81	130.7	133.1	133.1	117.7	117.7	156.0	128.7		

11.5.4 GNNQQNY peptide fibril characterization

As reported previously by Diaz-Avalos et al.²⁷, we find that at higher concentrations (>10 mg/ml), the GNNQQNY peptides tend to form fibrils. TEM micrographs (Figure 11-2b and c) of these samples show extended fibrils that are both significantly longer and narrower than the nanocrystals depicted in Figure 11-2a. The narrow fibrils have a typical width of 10-20 nm width, but there are also wider fibril aggregates of widths up to ~50 nm. The thin strip-like fibrils are tens of micrometers in length, and display lengthwise striations spaced at ~5 nm of each other. Attempts at preparing fibrils at lower concentrations, as described by Eisenberg et al.^{25,26}, have as yet been unsuccessful, as also indicated by Diaz-Avalos et al.²⁷.

We used segmentally labeled [U-¹³C,¹⁵N-GNNQ]QNY peptide to prepare a number of fibril samples, under several different conditions, with the aim of evaluating the structural heterogeneity of these samples and allowing a qualitative comparison with the crystalline forms. Using this peptide, a fully (100%, F1) and several isotopically dilute (25-30%, F2-F3) labeled samples were prepared for solid state NMR analysis, as listed in Table 11-2. Figure 11-7 shows 1D ¹³C and ¹⁵N spectra for several of the samples, obtained with 700 MHz or 900 MHz spectrometers. The one-dimensional spectra are generally very similar, with some variations in their resolution, which is likely due to

heterogeneous broadening correlated to the extent of sample hydration. For example, we observed broadened signals from a sample that had been lyophilized, even after subsequent rehydration (data not shown). Secondly, the spectrum that displays the highest resolution (sample F3) was recorded at 900 MHz and $\omega_r/2\pi=20.161$ kHz, while the other spectra were observed at 700 MHz and $\omega_r/2\pi=12-15$ kHz MAS. Note that some of the narrower lines in that spectrum are due to co-existing monoclinic crystal signals, but also that the fibril line widths are actually not much larger than those observed for the nanocrystals. This suggests that these kinds of samples are quite amenable to SSNMR study. However, when one compares these spectra to the crystalline data shown in Figure 11-4(a) and (c), each of the fibril spectra displays multiple peaks for each resonance, thus limiting the amount of analysis that can be performed with 1D data. Nevertheless, one can establish that there are clear differences in chemical shifts when compared to the GNNQQNY crystals.

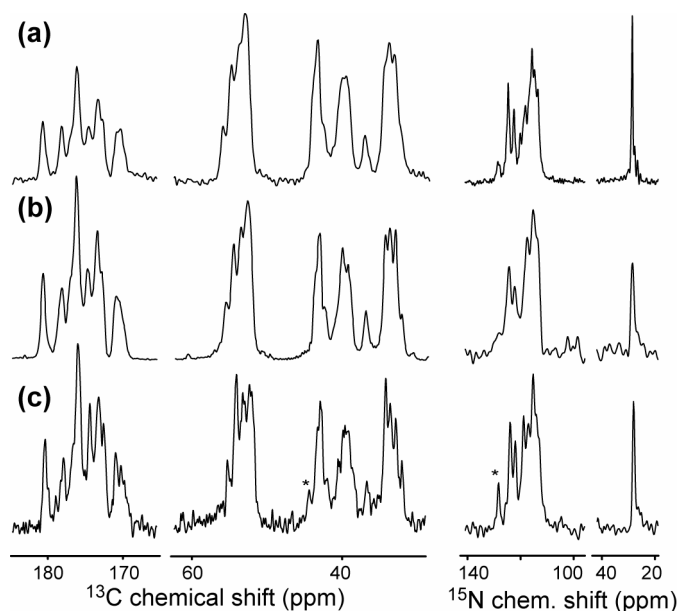


Figure 11-7 1D ^{13}C and ^{15}N spectra of fibrils formed using $[\text{U-}^{13}\text{C},^{15}\text{N}\text{-GNNQ}]\text{QNY}$: (a) 100%-labeled sample F1 (20 mg/ml) at 700 MHz, (b) 25%-labeled sample F2 (25 mg/ml) at 700 MHz, (c) sample F3 (12 mg/ml) at 900 MHz (contains monoclinic crystals as well (*)).

Two of the fibril samples (100% labeled F1 and 25% labeled F2) were used for complete resonance assignment experiments, which were performed at 700 MHz, using a number of two- and three-dimensional ^{13}C - ^{13}C and ^{15}N - ^{13}C correlation experiments. These experiments confirmed the presence of at least three conformations, present in unequal intensities. Thus, in both samples, the spectra are dominated by three distinct sets of cross peaks, each of which can be traced throughout the spectra. The chemical shifts for each of these fibril forms are listed in Table 11-5. The three different polymorphs are referred to as fibril forms 1-3, in order of the decreasing relative intensities of their spectral lines. The relative intensities varied slightly between samples, resulting in fibril 2 to be dominant in other samples. Cross peaks due to a fourth form could sometimes be distinguished, but its concentration was too low to allow extensive study.

As mentioned previously, the fact that we observe three sets of distinct chemical shifts tells us immediately that there are three distinct structures present in the form of fibrils. In Figure 11-8 we show the calculated secondary shifts for the labeled segment within the three different fibril forms. Interestingly, one of them (fibril 2) is not entirely consistent with a pure β -sheet secondary structure, since it exhibits various secondary shifts that are more consistent with a local α -helical structure (colored white in the figure). The other two fibril forms (1 and 3) have chemical shifts that are generally consistent with the presence of a β -sheet (compared to the crystal data in Figure 11-6, the C_α shifts are actually more strongly β -sheet-like in fibril 1 and 3). A TALOS analysis of the available chemical shifts allows one to estimate the backbone angles of Asn-8 and -9. For fibril 2 we find (ϕ, ψ) angles of $(54 \pm 6, 40 \pm 13)$ for Asn-8 (normally seen in left-handed α -helices) and ambiguous results for Asn-9. The other two forms do conform to a β -sheet structure, with (ϕ, ψ) angles for the Asn-8 and Asn-9 in fibril 1 of $(-108 \pm 20, 127 \pm 10)$ and $(-101 \pm 19, 131 \pm 8)$, and for fibril 3 of $(-119 \pm 18, 131 \pm 12)$ and $(-116 \pm 19, 128 \pm 8)$. Consistent with the CSI analyses, these backbone angles suggest a β -sheet structure, for both fibril forms 1 and 3, and an unspecified non- β -sheet structure for fibril 2. Note that the suggestion of ' α -helical' structure in a single residue is insufficient to expect an actual α -helix to be present.

Table 11-5 Assignment of fibril form resonances for the three predominant forms found in 100% [U-¹³C,¹⁵N-GNNQ]QNY fibril sample F1, prepared at 20 mg/ml. The sets of resonance labeled as 1-3 are listed alongside their estimated relative intensities in the spectra.²

	residue	¹³ C chemical shift (ppm)					¹⁵ N chem. shift (ppm)		
		C'	C _α	C _β	C _γ	C _δ	N	N _δ	N _ε
Fibril 1 (39%)	Gly₇	171.2	43.5				27.6		
	Asn₈	172.8	53.0	39.7	177.3		121.1	114.0	
	Asn₉	173.5	52.7	40.4	176.4		123.0	114.5	
	Gln₁₀	176.5	55.0	34.0	34.7	180.8	123.3		114.3
Fibril 2 (35%)	Gly₇	170.6	44.1				27.4		
	Asn₈	173.8	56.0	37.3	178.5		113.2	112.0	
	Asn₉	176.0	53.3	39.2	176.2		116.8	113.5	
	Gln₁₀	174.8	54.0	33.4	33.3	178.2	117.5		112.0
Fibril 3 (27%)	Gly₇	170.1	43.4				27.5		
	Asn₈	174.2	52.6	40.1	177.0		118.6	115.2	
	Asn₉	173.3	53.7	42.6	176.2		121.3	115.5	
	Gln₁₀	174.8	54.7	32.5	34.2	180.8	127.1		114.5

There are several reasons why it is of particular interest to examine the signals of the Tyr ring in the fibril samples. One of the major differences between the monoclinic and orthorhombic crystalline forms was found to be the dynamic behavior of the Tyr ring. Also, it has been suggested that aromatic residues may have a special role to play in the formation and/or stabilization of amyloid-like fibrils^{33,37,90}. Finally, Tyr is the second-most common amino acid in the PrD domain of Sup35p. Figure 11-9 shows both the background natural abundance signals observed in an isotopically dilute [U-¹³C,¹⁵N-GNNQ]QNY sample (panel a) and the same signals as determined in the isotopically labeled residue (panel b). Similar to the orthorhombic crystals, the Tyr signals in these

² Due to the low signal-to-noise of our labeled GNN[U-¹³C,¹⁵N-QQNY] fibril sample we have thus-far been unable to obtain a complete assignment for most resonances of the second half of the peptide.

spectra are attenuated and lack distinct peaks for each position along the aromatic ring. This shows that in the fibrils the Tyr residue is undergoing twofold flips and therefore must not experience the same steric restrictions that prevent it from flipping in the monoclinic crystal form.

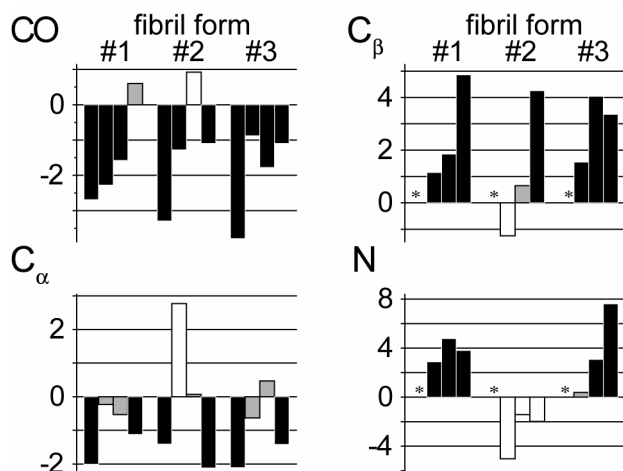


Figure 11-8 Secondary chemical shift analysis of GNNQ₇₋₁₀ in GNNQQNY fibril forms 1-3. Color coding: black = β-sheet, white = α-helical, grey = indeterminate.

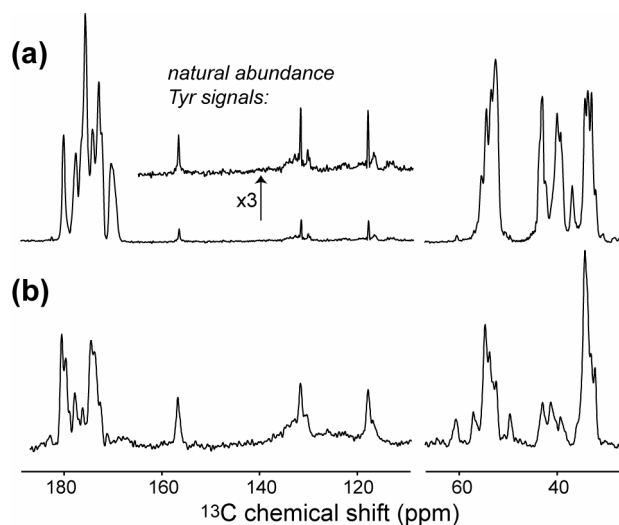


Figure 11-9 Tyrosine-13 in fibril samples consisting of (a) diluted [U-¹³C, ¹⁵N-GNNQ]QNY (F2) and (b) diluted GNN[U-¹³C, ¹⁵N-QQNY] (F4).

11.5.5 Comparison of the GNNQQNY aggregates

We can use the observed chemical shifts to compare the different aggregated forms observed for GNNQQNY. First, we determined the overall root-mean-square-deviation (RMSD) between the observed chemical shifts of the different forms.

Figure 11-11 highlights the aliphatic ^{13}C - ^{13}C cross-peaks for a number of [U- ^{13}C , ^{15}N -GNNQ]QNY samples. The two crystalline forms show subtle differences in chemical shift, mostly located in the Asn side chain resonances (panels (a) and (b)). From panel (c) it is clear that the three predominant fibril forms are particularly easy to distinguish in the Gln-10 side chain resonances, with ^{13}C chemical shift differences up to 1.5 ppm. However, the other resonances also show significant differences between the forms, with the largest differences in the Asn-C α resonances (e.g., a 3.4 ppm difference between Asn-9-C α in fibrils 2 and 3). In these spectra we also observe a varying degree of difference with respect to the (monoclinic) crystalline peptide, with none of the fibrils matching the crystals exactly. The latter is clearly illustrated in panel (d), which displays the same region for an isotopically dilute sample prepared at a peptide concentration of 12 mg/ml (F3). In this sample we observe the formation of monoclinic crystals (for which the resonances are connected by dashed lines) as well as the three fibril forms.

compares the chemical shifts of the five GNNQQNY aggregates – the two crystalline forms and the three forms in the fibril samples – that we examined with one another. These data show that the differences between the two crystalline forms are relatively small but far from insignificant. The data also show that the three different fibril forms display a range of chemical shift deviations. When comparing the fibrils to the crystal data, it is the fibril 3 that shows the smallest deviation relative to the monoclinic crystals, while fibrils 2 and 3 more strongly resemble each other rather than either crystalline polymorph.

This overall-RMSD comparison is inherently very approximate, and we can delineate the differences in more detail by examining a few selected regions of the spectra for the different crystal and fibril forms. For example, we can compare the ^{15}N and $^{13}\text{C}=\text{O}$ chemical shifts, by examining the N-CO spectra of the different polymorphs. Some typical spectra are shown in Figure 11-10, with color coding of the various assignments.

In the case of the two crystalline forms, the largest change is seen in the Asn-9 side chain resonances (*i.e.*, 5 ppm change for N_δ and 3.3 ppm for C_γ of Asn-9), although several of the other cross-peaks also shift by 1-1.5 ppm. Generally larger chemical shift differences are apparent between the various fibril forms. As mentioned above, we find the largest similarities between the monoclinic crystals and the fibril 3, which corresponds to the least intense signal in the different fibril samples. By far the largest changes are seen in the fibril 2, with for instance a large shift in the Gln-10 N/Asn-9 C' cross peak which is due to a change of 10 ppm for the Gln-10 backbone nitrogen and 3.4 ppm for the Asn-9 backbone carbonyl resonance. Also, its Asn-8 and -9 display large changes in their ¹⁵N chemical shifts (4.5-6 ppm) relative to the crystal forms. In general, we see that in particular the ¹⁵N chemical shift is a very sensitive indicator of the polymorph type.

Table 11-6 Overall chemical shift deviations between the different aggregate forms. Deviations are shown as the RMSD (in ppm) between any two polymorphs, based on all ¹³C or ¹⁵N assignments common to both forms (but excluding the mobile Tyr positions). The most similar pair in each row is indicated in bold.

	Monoclinic		Orthorhombic		Fibril 1		Fibril 2		Fibril 3	
	¹³ C	¹⁵ N	¹³ C	¹⁵ N	¹³ C	¹⁵ N	¹³ C	¹⁵ N	¹³ C	¹⁵ N
Monoclinic			1.1	2.0	1.6	2.9	2.1	5.6	1.1	1.5
Orthorhombic	1.1	2.0			1.4	2.9	2.0	6.1	1.1	2.2
Fibril 1	1.6	2.9	1.4	2.9			1.0	1.9	1.6	4.6
Fibril 2	2.1	5.6	2.0	6.1	1.0	1.9			1.8	4.8
Fibril 3	1.1	1.5	1.1	2.2	1.6	4.6	1.8	4.8		

Figure 11-11 highlights the aliphatic ¹³C-¹³C cross-peaks for a number of [U-¹³C, ¹⁵N-GNNQ]QNY samples. The two crystalline forms show subtle differences in chemical shift, mostly located in the Asn side chain resonances (panels (a) and (b)). From panel (c) it is clear that the three predominant fibril forms are particularly easy to distinguish in the Gln-10 side chain resonances, with ¹³C chemical shift differences up to 1.5 ppm.

However, the other resonances also show significant differences between the forms, with the largest differences in the Asn-C β resonances (*e.g.*, a 3.4 ppm difference between Asn-9-C β in fibrils 2 and 3). In these spectra we also observe a varying degree of difference with respect to the (monoclinic) crystalline peptide, with none of the fibrils matching the crystals exactly. The latter is clearly illustrated in panel (d), which displays the same region for an isotopically dilute sample prepared at a peptide concentration of 12 mg/ml (F3). In this sample we observe the formation of monoclinic crystals (for which the resonances are connected by dashed lines) as well as the three fibril forms.

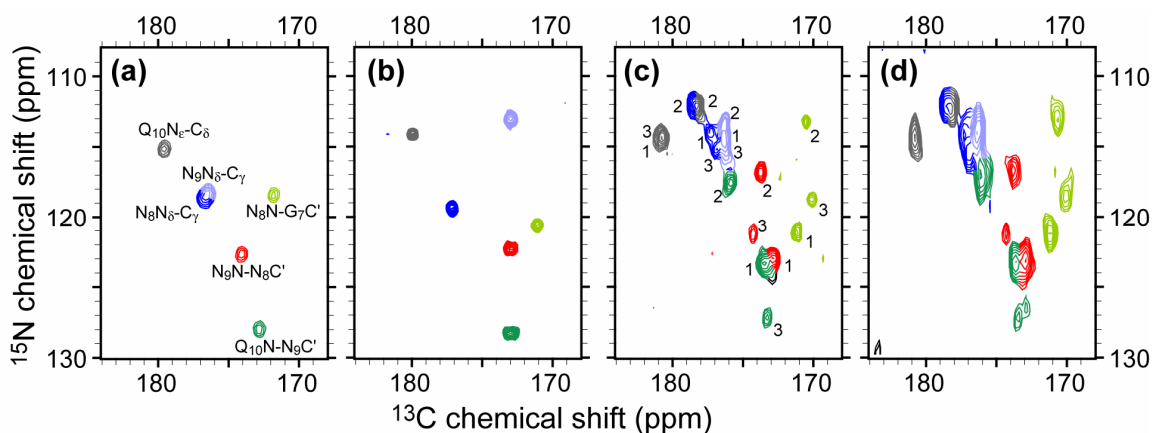


Figure 11-10 Comparison of the 2D ^{15}N - ^{13}C O correlation spectra of [U- ^{13}C , ^{15}N]-GNNQIQNY for the two nanocrystalline forms: (a) monoclinic and (b) orthorhombic. Panels (c) and (d) show spectra obtained from the two independent fibril samples F1 and F2. The assignments of the color-coded peaks are indicated in panel (a). Panel (c) includes the fibril form designations for the color-coded peaks. Data were acquired at 500 MHz (a) and 700 MHz ^1H field (b-d), respectively.

To facilitate a more detailed discussion, we have used the published monoclinic structure as a framework for examining the distribution and extent of the chemical shift variations within the peptide (Figure 11-12). The different extents of chemical shift deviation are color coded from black (no change) through green/yellow, to red (largest change), while non-determined or missing resonances (*e.g.* for the flipping Tyr ring of the orthorhombic form, or as yet unlabeled/unassigned positions) are colored grey.

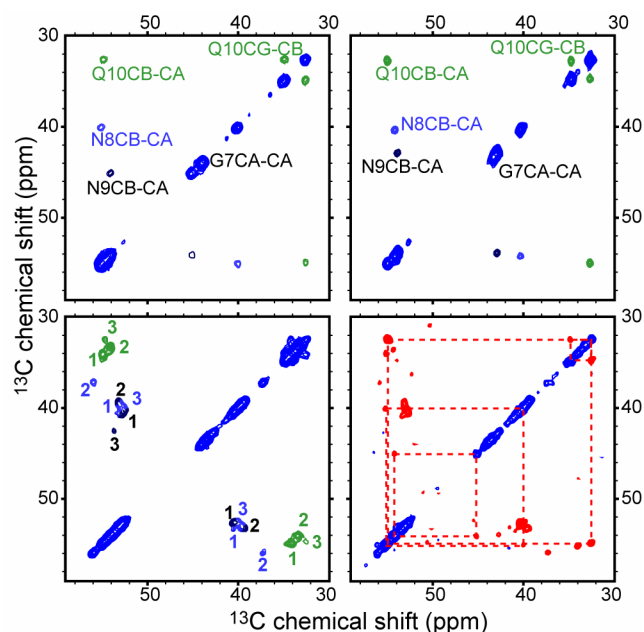


Figure 11-11 Comparison of the aliphatic ^{13}C - ^{13}C correlations of monoclinic and orthorhombic crystalline (a,b) and fibril (c,d) forms of $[\text{U-}^{13}\text{C},^{15}\text{N-GNNQ}]\text{QNY}$ (samples F1,F3). Cross-peaks in panels (a)-(c) are color coded by residue, with the fibril forms marked by number in panel (c). Panel (d) shows the co-existence of monoclinic crystals (dashed lines) and fibrils in a sample prepared at 12 mg/ml.

From these figures one can arrive at the following interesting observations. Comparison of the orthorhombic and monoclinic crystals (Figure 11-12a) shows that the smallest chemical shift changes are clustered around the Gln-10 residues and the directly surrounding nuclei (black/blue color). In the monoclinic crystals, the Gln-10 side chains of the two monomers were found to be the core of the so-called ‘dry interface’ within the unit cell. The lack of change in chemical shift might indicate that a similar interaction is maintained in the orthorhombic crystal form. The larger differences are in the positions facing the larger water-clusters between the monomers, and include a change in the dynamic behavior of the Tyr ring that now appears able to undergo a twofold flipping motion.

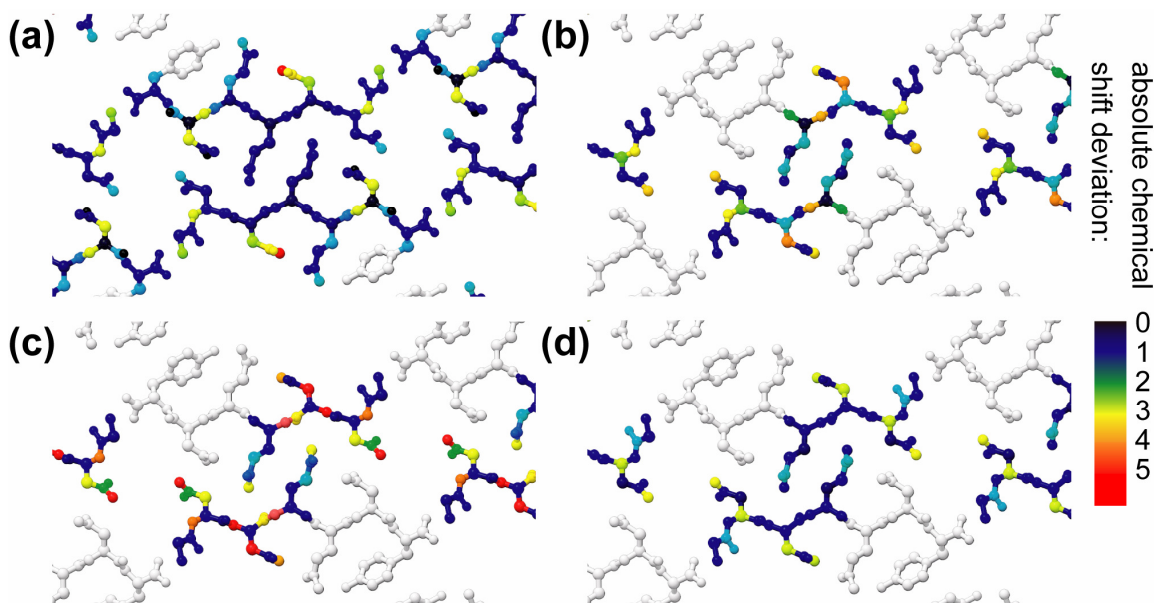


Figure 11-12 Illustration of chemical shift deviations between aggregate forms, projected onto the monoclinic crystal structure. We show the absolute chemical shift deviation (in ppm) relative to the monoclinic nanocrystals for the orthorhombic crystals (a), or each of the three dominant fibril forms 1-3 (panels b-d). The graphics were generated using UCSF Chimera ⁹¹.

As discussed above, the smallest changes among the fibril forms, in comparison to the monoclinic crystals, are found for fibril 3 which is the least abundant fibril species. As can be seen in panel (d), again the smallest changes are clustered around Gln-10 with larger deviations towards the ends of the amino acid side chains. This could be indicative of this fibril having a similar core arrangement, but a different packing scheme compared to the monoclinic crystals.

The two more dominant fibril forms display significantly larger deviations from the monoclinic crystals (or orthorhombic crystals). However, these two forms are also rather distinct from each other. As mentioned earlier, the intermediate intensity cross-peaks from fibril 2 actually indicate a number of resonances that are more consistent with a (local) α -helical structure rather than the expected β -sheet character typical of amyloid structures (ref. Figure 11-8). Panel (c), showing this form, also indicates that the chemical shift deviations are distributed throughout the peptide, consistent with an overall change in the structural fold. The fibril 1 appears to more closely follow the

predicted β -sheet character, but the significant chemical shift differences and their distribution make it unclear to what extent the structure resembles either of the crystalline forms. Still, it is interesting to point out that, analogous to the situation with fibril 3, the smallest differences are localized in the side chain of Gln-10.

11.6 Discussion

11.6.1 Polymorphism in GNNQQNY aggregation

Using isotopically labeled and unlabeled peptides, we have generally reproduced the polymorphic aggregation behavior that previous publications²⁵⁻²⁷ reported for the GNNQQNY peptide. At high peptide concentrations, >10 mg/ml, we observed formation of GNNQQNY fibrils that, based on TEM data, resemble those previously reported²⁷. As we reduce the concentration to around 10 mg/ml, the formation of nanocrystals becomes favorable. Under our particular conditions, and in the absence of seeding, we consistently obtained monoclinic rather than orthorhombic crystals. Lowering the concentration further reduces the propensity for, and rate of, crystal formation, unless the sample was agitated (swirling). This appears to match the observations by Diaz-Avalos et al.²⁷, who report a complete absence of aggregation below 5 mg/ml. Note that this is in contrast to experiments described by Eisenberg et al.^{25,26} who observed the formation of fibrils under these conditions. Despite several attempts under a variety of conditions, we have as yet been unable to reproduce the formation of fibrils in the peptide concentration regime 1 mg/ml and below. We observed mostly a large decrease in the rate of the crystallization process that at times took many days rather than the few hours or less near 10 mg/ml. Agitation resulted in accelerated crystallization, something that was not previously reported. While the crystals resulting from this procedure might be of smaller size, making this approach less interesting for the preparation of x-ray diffraction samples, they are more than suitable for SSNMR experiments because they maintain a higher level of overall sample homogeneity. In our hands, the formation of orthorhombic crystals was less common than the monoclinic form and appeared most frequently under lower concentration conditions and with agitation of the sample container.

Our TEM results are consistent with descriptions of crystals and fibrils previously reported²⁵⁻²⁷, with the main difference being that we require and used crystals of substantially smaller size than the μm -sized crystals used in the x-ray experiments. TEM of the fibrils shows extended ribbon-like fibers that have lengthwise striations, at 5 nm distances. This closely resembles observations by Diaz-Avalos et al.²⁷, who identify these as indications of protofibrils within the larger fibrils. We observe the presence of a variety of widths for these fibers, reflecting different multiples of the protofibrils (as indicated by the striations), but see no obvious indication of other polymorphism in the TEM results. Powder X-ray scattering data on the crystalline samples also matched the predicted or published reflections for the monoclinic and orthorhombic forms (data not shown).

In summary, the variety of GNNQQNY aggregates described here represent a number of forms that have been discussed in the existing literature. The salient feature of the solid state NMR spectra is that we can resolve the spectra of the individual species and each of these forms – crystals and fibrils -- under identical experimental conditions and compare them directly. Here, we report the observed resonances for the different atomic positions in the peptide, allowing us to perform an initial qualitative comparison. Both crystalline forms display narrow lines that suggest a high level of microscopic sample homogeneity and no indication of structural polymorphism *within* either crystal form. During the sample preparation procedures we do observe the co-formation of different aggregate forms. This mostly involves the coexistence of monoclinic crystals and fibril material (see Figure 11-11d), rather than of both crystal polymorphs. However, in one predominantly orthorhombic sample, we did observe the initial coexistence of a small amount of monoclinic crystals (data not shown). Interestingly, the NMR spectra indicated that over time the monoclinic signal decreased, and eventually disappeared after several days, suggesting a structural conversion between the two forms. Similar interconversion of crystal forms has been observed in x-ray diffraction experiments (D. Caspar, personal communication).

The NMR spectra of the fibrils clearly show the coexistence of three distinct, but self-consistent sets of resonances with chemical shifts that are remarkably reproducible between different sample preparations. This holds true when the preparation method is

varied – i.e., with changes in peptide concentration between 12-25 mg/ml, at different fibrillization temperatures in the range 4-30 °C, and upon lyophilization and subsequent re-hydration of the sample. Despite variations in the fibrillization conditions, we have observed only small variations in the relative intensities of the NMR signals for each of the different fibril forms. The three forms are close to equal in intensity; therefore, the dominant form is dominant by only a small margin. Intensity variations in the spectra can shift the identity of the dominant form among the three fibril forms. While it cannot be excluded entirely that two or more of the observed NMR forms are part of a single macroscopic aggregate, it seems most likely that each form represents an independent aggregate with a different peptide structure. Specifically, we have as yet not observed any polarization exchange between the different forms in the various spin-diffusion and other recoupling experiments.

11.6.2 Spectroscopic differences – crystal forms

The NMR data allowed us to precisely determine the ^{13}C and ^{15}N chemical shifts in both crystalline forms, and for over half of the residues in the fibril forms. While the absence of a complete assignment in the latter is forthcoming, the assigned resonances combined with the more qualitative data presented for the latter half do allow an initial comparison of structural features. While it is hard to establish precisely the origin of the differences, they are likely due to changes in the local conformation. Until more quantitative experiments have been completed, we will discuss the observed differences and similarities.

For this analysis, the obvious reference point is the published x-ray structure of the monoclinic crystalline form, with particular consideration for the various features that are proposed to be general for amyloid fibril formation. The ‘steric zipper’ thought to form the core of the peptide-peptide interactions, involves the even-numbered residues – N₈, Q₁₀, and N₁₂. When we compare the two crystalline forms to each other, we note that the chemical shifts and torsion angles are not that different from each other (especially compared to some of the fibril forms). The largest similarities are centered around Gln-10, which is at the center of the monoclinic crystal’s ‘dry interface’. The NMR data do show a significant difference in the dynamic behavior of the Tyr-13

aromatic side chain. The aromatic region of the monoclinic crystalline form shows the presence of distinct ϵ, ϵ' and δ, δ' ^{13}C 's indicating that the Tyr sidechain is completely rigid. In the orthorhombic peptide these same resonances are highly attenuated, due to the twofold motion of the Tyr aromatic ring. This distinction would suggest that the steric Tyr-Tyr interactions that immobilize the ring in the monoclinic crystals (and constitute the main direct peptide-peptide interactions across the 'wet interface' as illustrated in Figure 11-13) are absent in the orthorhombic crystals. Overall, the distribution of the similarities and differences throughout the peptide might be consistent with a structure that has a similar, close pairwise peptide-peptide interaction not unlike the monoclinic crystal, but could have a different packing arrangement of such units within the unit cell. Note that previous x-ray analyses already indicate that the orthorhombic unit cell should contain four rather than two peptides, in contrast to the monoclinic unit cell²⁷.

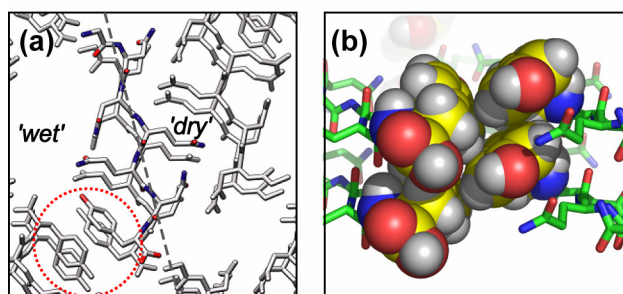


Figure 11-13 Illustration of the Tyr-Tyr contacts in the monoclinic crystals. Panel (a) contains a view along the fibril axis, highlighting the interactions of stacked Tyr across the 'wet interface' between peptide monomers. The side-ways view in panel (b), with space-filling Tyr residues, illustrates the steric interactions limiting the ring dynamics in the monoclinic crystals. The graphics were generated using UCSF Chimera and Pymol^{91,92}.

11.6.3 Spectroscopic differences - fibrils

Of more interest than the comparison of the two crystal forms, is the structural study of the fibrils formed by the peptides. Previous studies have shown that fibrils formed by GNNQQNY display features similar to that seen for amyloid formation in general, and the behavior of the Sup35p system in particular. In the MAS NMR spectra we have observed three distinct sets of resonances in all of the fibril preparations. In at least two

of these sets (forms 1 and 3), we see that they conform to the general features expected for amyloid fibrils, in that their NMR chemical shifts are consistent with an entirely β -strand type structure. Beyond that, these two also appear to share some features in common with the crystal forms, in that the highest level of similarity to the monoclinic data is observed for the resonances of the Gln-10 residue, at the core of the ‘steric zipper’. However, other regions of the peptide show significant deviations from the monoclinic resonances. Again, one notable difference between the monoclinic crystals and any of the other forms is correlated to the Tyr side chain.

More unusual (and unexpected) for a supposed amyloid-like fibril is that one of the aggregated forms in the fibril samples (‘form 2’) shows a significant number of chemical shifts that deviate from the values expected for β -strand secondary structure. As a result, this form also has the largest deviations from both crystalline forms. Due to the mixed nature of the samples, it is not clear which of the fibers seen in the TEM data correspond to a particular NMR spectrum. It is therefore unclear what the macroscopic nature of this particular ‘fibril form’ is. The relatively narrow line widths of the associated resonances and highly reproducible preparation under a variety of conditions would suggest that it is unlikely to be an inhomogeneous and non-specific aggregation of peptide. On the other hand, the observation of the signals via a CP mechanism indicates that they can not correspond to a (residual) soluble fraction. One perhaps intriguing observation that others have made is that there are some indications of α -helical (non-beta) structure in the pre-aggregates formed by the Sup35p protein²⁴.

11.7 Implications

In this section, we focus on the fibrillar forms that appear β -sheet in nature, and examine the various aspects of the proposed core-fold and other features of the monoclinic crystal structure. The data we have are consistent with a certain level of similarity that is centered around the core residue of the ‘steric zipper’ (Gln-10), which forms a self-complementary interaction across the dry interface of the monoclinic crystal assembly. Other residues show more significant deviations. One remarkable difference involves the Tyr side chain. As illustrated in Figure 11-13, the aromatic side

chain forms an extensive close interaction in the monoclinic crystal structure, seemingly stabilizing it via aromatic π - π interactions both within each β -sheet and between the sheets. And indeed, aromatic residues are thought to play an important role in the stabilization and formation of amyloid-like structures including GNNQQNY aggregates^{34,90}. In our NMR spectra, the extensive Tyr-Tyr interactions in the monoclinic crystals are reflected in its absence of spectral averaging, characteristic of a largely immobile ring. In contrast, this residue is found to be mobile in the orthorhombic crystals and in the fibrils. This could indicate a significant structural difference in the packing of the peptide within these structures, with potential implications for the energetics of stabilization. This should also have a drastic effect on the nature of the ‘wet interface’ which could display a more significant role in construction of these other forms. In this context, we note that the unit cell of the orthorhombic crystals is twice as large as the cell of the monoclinic crystals, and is thought to contain four peptide monomers rather than two.

11.8 Conclusion

¹³C and ¹⁵N MAS NMR spectra provide detailed information on a variety of solid materials, and have permitted us to examine the range of aggregates that the GNNQQNY peptide adopts. The GNNQQNY nanocrystals provide very narrow line widths despite the extremely small size of the crystals, an observation consistent with experiments on protein microcrystals. The fibrils themselves are yet another illustration of the fact that the line widths of amyloid fibrils can be relatively narrow indicating that the samples are microscopically well ordered despite being macroscopically disordered. The GNNQQNY crystals and fibrils are therefore very suitable for these types of experiments. The crystal and fibril data do suggest some (localized) commonalities between the conformations of the various GNNQQNY species, in particular near the center of the ‘steric zipper’. However, the data also show quite significant deviations from the monoclinic crystals, both in chemical shifts and in terms of mobility of the Tyr ring. Aside from the possible presence of a steric zipper-like core, questions remain on the nature of other interactions and how any core regions might be able to arrange themselves into the well-known fibril forms typical of amyloidogenic systems. The core

formation seen in the monoclinic crystals does not obviate how such packing arrangements and interactions would occur. The presence of seemingly substantial non- β type structure in one of the fibril forms raises other intriguing questions, to which few answers exist at this point.

One of the advantages of SSNMR is that it allows for numerous approaches to obtain detailed and quantitative structural information, in the form of distance and angular measurements. We are working on the application of such measurements to the GNNQQNY system to provide quantitative answers to the various questions raised by the current results. The preparation of more uniform fibril samples is part of the effort towards optimal application of these experiments. The study of the GNNQQNY peptide is instructive, not only in terms of the discussion of the basic structural features of amyloid fibers and their formation, but also in providing a platform for the development and demonstration of techniques applicable for larger protein domains with similar characteristics.

11.9 Acknowledgments

We want to thank David Eisenberg, Ruben Diaz-Avalos and Don Caspar for their suggestions and helpful discussions. Molecular graphics images were produced using the UCSF Chimera package from the Resource for Biocomputing, Visualization, and Informatics at the University of California, San Francisco (supported by NIH P41 RR-01081). This research was supported by the National Institutes of Health through grants EB-003151 and EB-002026.

11.10 Supporting Information

11.10.1 2D assignment data for orthorhombic GNNQQNY nanocrystals

Figure 11-14 shows a subset of the 2D data used to assign the GNNQQNY orthorhombic nanocrystal resonances. The measurements were performed at 700 MHz ^1H frequency using isotopically dilute samples consisting of $[\text{U-}^{13}\text{C},^{15}\text{N-GNNQ}] \text{QNY}$

11.10.2 Fibril assignment data

The figures below show representative segments from our 2D assignment data on 100% labeled [U- ^{13}C , ^{15}N -GNNQ]QNY fibrils, obtained at 700 MHz. The assignments for each fibril form are indicated and traced out (solid lines indicate backbone correlations, dashed lines are side-chain correlations), with color-coding according to residue number. The top four panels are part of a ^{13}C - ^{13}C correlation using 12 ms DARR/RAD mixing at 15 kHz MAS. The NCOCX and NCACX experiments were performed using 10ms ^{13}C - ^{13}C DARR/RAD mixing, following the DCP N-C transfer, at 15 kHz MAS. Solid lines indicate backbone-backbone correlations, whereas dashed lines involve side chain-side chain, or backbone-side chain correlations. Very similar data were obtained for a number of other samples, which were prepared using isotopically dilute peptide material. Each of the fibril forms displays a self-consistent correlation pattern, while no cross-peaks are seen connecting the different forms to each other (even with longer DARR/RAD mixing times).

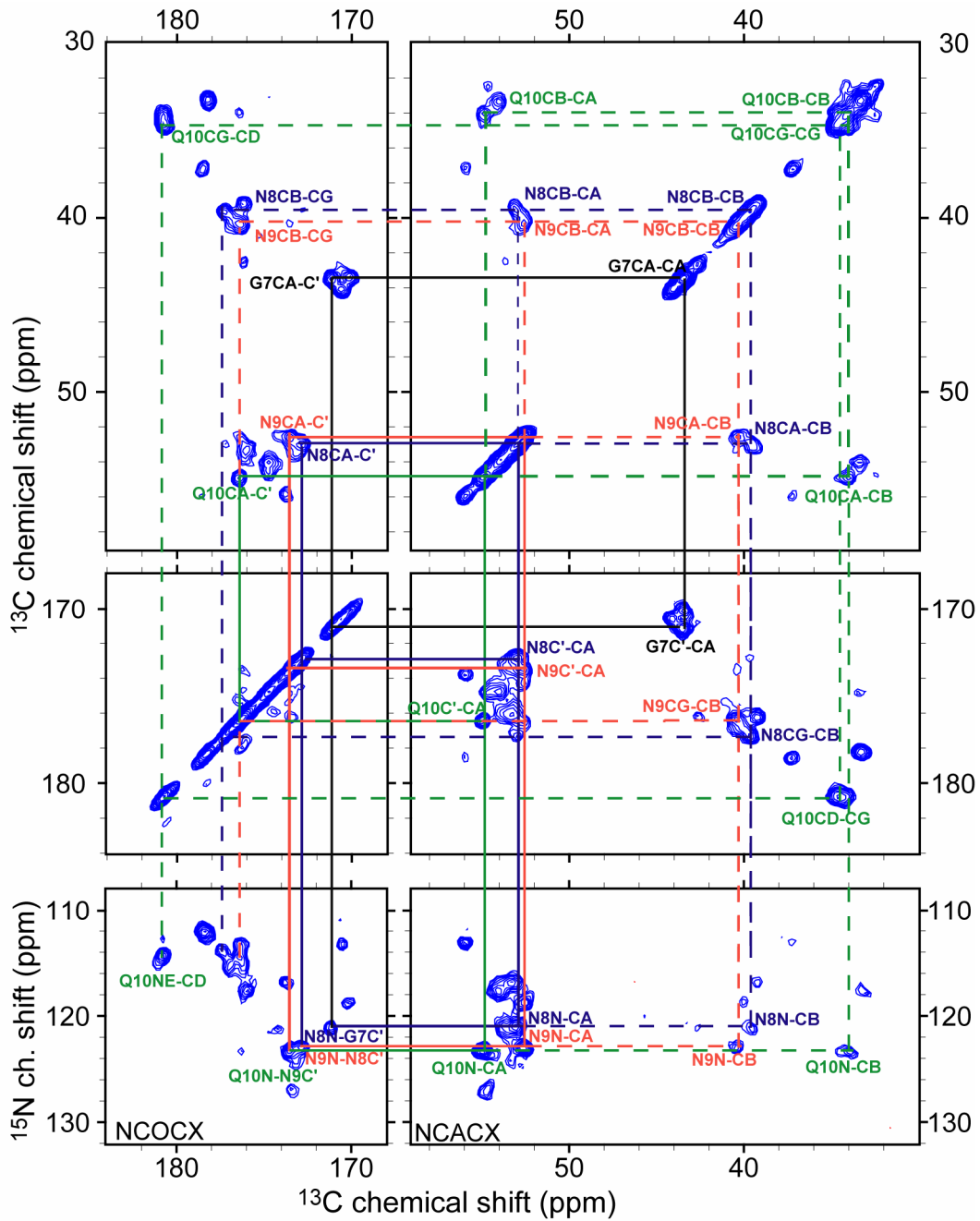


Figure 11-15 Correlation traces of fibril form 1 in 100%-labeled [U-¹³C,¹⁵N-GNNQ]QNY fibrils.

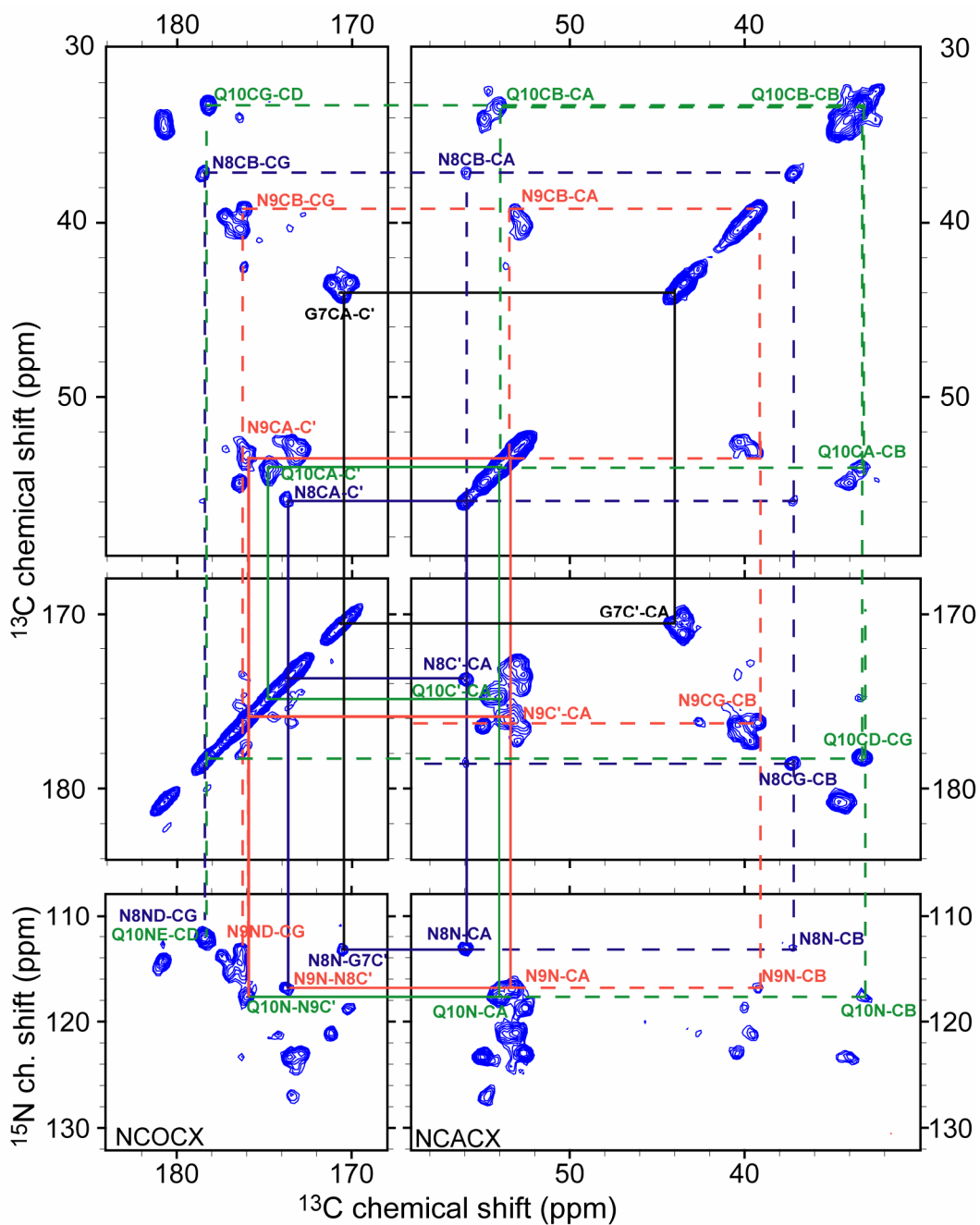


Figure 11-16 Correlation traces of fibril form 2 in 100%-labeled [U-¹³C,¹⁵N-GNNQ]QNY fibrils.

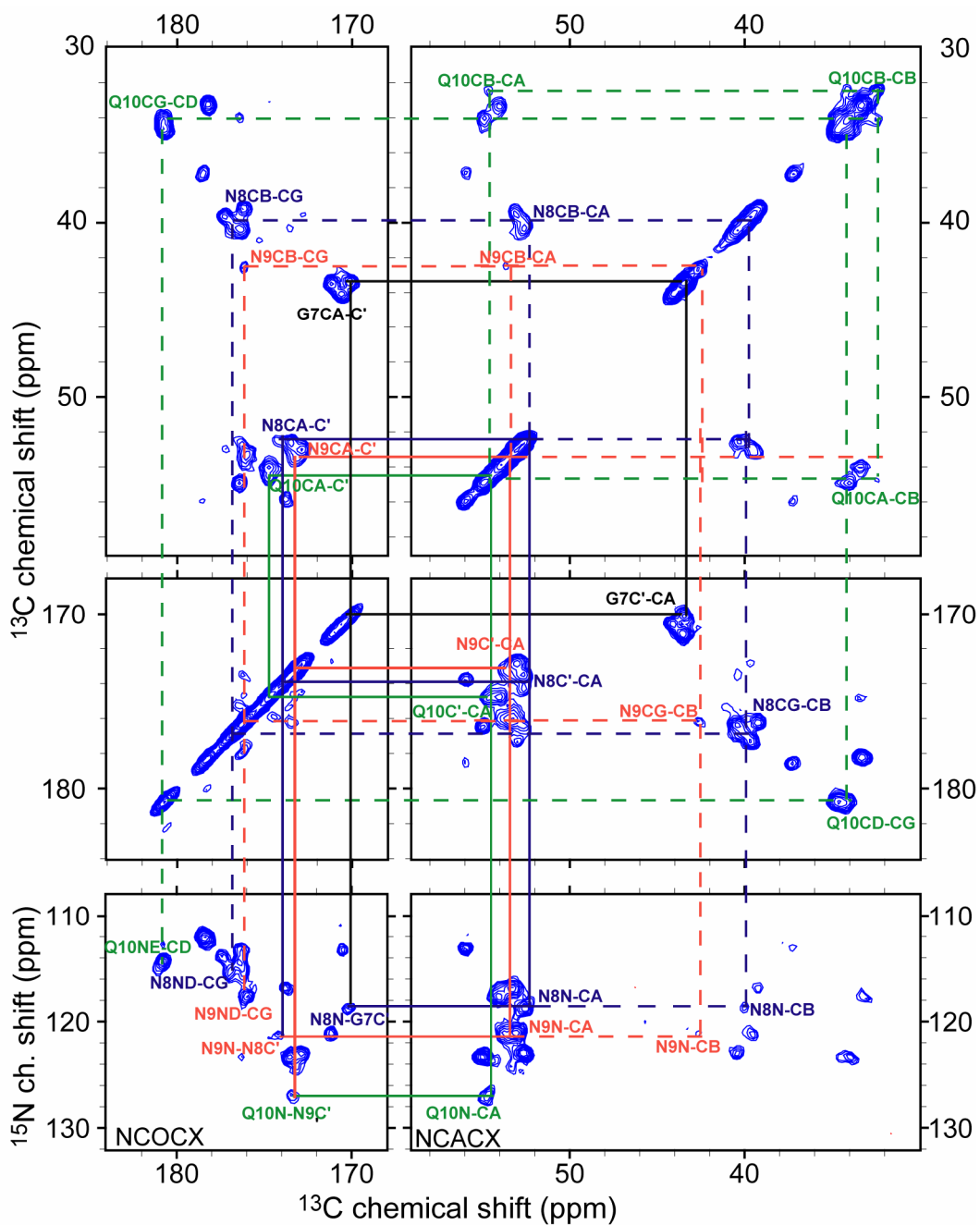


Figure 11-17 Correlation traces of fibril form 3 in 100%-labeled $[U-^{13}C,^{15}N\text{-GNNQ}]QNY$ fibrils.

11.11 References

- (1) Westermark, P. *FEBS Journal* **2005**, 272, 5942-5949.
- (2) Makin, O. S.; Serpell, L. C. *FEBS Journal* **2005**, 272, 5950-5961.
- (3) Tuite, M. F. *Cell* **2000**, 100, 289-292.
- (4) Hawthorne, D. C.; Mortimer, R. K. *Genetics* **1968**, 60, 735-742.
- (5) Inge-Vechtomov, S. G.; Andrianova, V. M. *Genetika* **1970**, 6, 103-115.
- (6) Stansfield, I.; Jones, K. M.; Kushnirov, V. V.; Dagkesamanskaya, A. R.; Poznyakovski, A. I.; Paushkin, S. V.; Nierras, C. R.; Cox, B. S.; Teravanesyan, M. D.; Tuite, M. F. *EMBO J.* **1995**, 14, 4365-4373.
- (7) Wickner, R. B. *Science* **1994**, 264, 566-569.
- (8) Patino, M. M.; Liu, J. J.; Glover, J. R.; Lindquist, S. *Science* **1996**, 273, 622-626.
- (9) Sparrer, H. E.; Santoso, A.; Szoka, F. C., Jr.; Weissman, J. S. *Science* **2000**, 289, 595-9.
- (10) Prusiner, S. B. *Science* **1997**, 278, 245-251.
- (11) Yamada, M.; Shimohata, M.; Sato, T.; Tsuji, S.; Takahashi, H. *Neuropathology* **2006**, 26, 346-351.
- (12) King, C.; Diaz-Avalos, R.; Caspar, D. L. D. *Biophys. J.* **2000**, 78, 289A-289A.
- (13) Baxa, U.; Taylor, K. L.; Steven, A. C.; Wickner, R. B. *Contrib Microbiol* **2004**, 11, 50-71.
- (14) Dobson, C. M. *Nature* **2005**, 435, 747-9.
- (15) Fernandez-Bellot, E.; Cullin, C. *Cellular and Molecular Life Sciences* **2001**, 58, 1857-1878.
- (16) Serio, T. R.; Lindquist, S. L. *Adv Protein Chem* **2001**, 59, 391-412.
- (17) Shorter, J.; Lindquist, S. *Nature Reviews Genetics* **2005**, 6, 435-450.
- (18) True, H. L. *Trends in Genetics* **2006**, 22, 110-117.
- (19) Bousset, L.; Melki, R. *Microbes and Infection* **2002**, 4, 461-469.
- (20) Ross, E. D.; Minton, A.; Wickner, R. B. *Nat Cell Biol* **2005**, 7, 1039-44.

- (21) Parham, S. N.; Resende, C. G.; Tuite, M. F. *EMBO J.* **2001**, *20*, 2111-9.
- (22) Shkundina, I. S.; Kushnirov, V. V.; Tuite, M. F.; Ter-Avanesyan, M. D. *Genetics* **2006**, *172*, 827-35.
- (23) Osherovich, L. Z.; Cox, B. S.; Tuite, M. F.; Weissman, J. S. *PLoS Biol* **2004**, *2*, E86.
- (24) Narayanan, S.; Walter, S.; Reif, B. *Chembiochem* **2006**, *7*, 757-765.
- (25) Balbirnie, M.; Grothe, R.; Eisenberg, D. S. *Proc. Natl. Acad. Sci. USA* **2001**, *98*, 2375-80.
- (26) Nelson, R.; Sawaya, M. R.; Balbirnie, M.; Madsen, A. O.; Riek, C.; Grothe, R.; Eisenberg, D. *Nature* **2005**, *435*, 773-778.
- (27) Diaz-Avalos, R.; Long, C.; Fontano, E.; Balbirnie, M.; Grothe, R.; Eisenberg, D.; Caspar, D. L. D. *J. Mol. Biol.* **2003**, *330*, 1165-1175.
- (28) Perutz, M. F.; Staden, R.; Moens, L.; De Baere, I. *Current Biology* **1993**, *3*, 249.
- (29) Perutz, M. *Protein Science* **1994**, *3*, 1629-1637.
- (30) Yoder, M. D.; Keen, N. T.; Journak, F. *Science* **1993**, *260*, 1503.
- (31) Steinbacher, S.; Seckler, R.; Miller, S.; Steipe, B.; Huber, R.; Reinemer, P. *Science* **1994**, *265*, 383.
- (32) Jenkins, J.; Mayans, O.; Pickersgill, R. *J. Struct. Biol.* **1998**, *122*, 236.
- (33) Tsai, H.-H.; Reches, M.; Tsai, C.-J.; Gunasekaran, K.; Gazit, E.; Nussinov, R. *PNAS* **2005**, *102*, 8174-8179.
- (34) Zheng, J.; Ma, B.; Tsai, C. J.; Nussinov, R. *Biophys J* **2006**.
- (35) Nelson, R.; Eisenberg, D. *Curr. Opin. Struct. Biol.* **2006**, *16*, 260-265.
- (36) Thompson, M. J.; Sievers, S. A.; Karanicolas, J.; Ivanova, M. I.; Baker, D.; Eisenberg, D. *Proc Natl Acad Sci U S A* **2006**, *103*, 4074-8.
- (37) Gsponer, J.; Haberthur, U.; Caflisch, A. *Proc. Natl. Acad. Sci. USA* **2003**, *100*, 5154-5159.
- (38) Chae, Y. K.; Lee, K.; Kim, Y. *Protein Pept Lett* **2004**, *11*, 23-8.
- (39) Kim, Y.; Kim, Y.; Park, J. J.; Hwang, J. H.; Park, T. J. *On the Convergence of Bio-Information-, Environmental-, Energy-, Space- and Nano-Technologies, Pts 1 and 2* **2005**, 277-279, 67-71.

- (40) Lipfert, J.; Franklin, J.; Wu, F.; Doniach, S. *Journal of Molecular Biology* **2005**, *349*, 648-658.
- (41) Esposito, L.; Pedone, C.; Vitagliano, L. *Proc Natl Acad Sci U S A* **2006**, *103*, 11533-8.
- (42) King, C. Y.; Diaz-Avalos, R. *Nature* **2004**, *428*, 319-323.
- (43) Diaz-Avalos, R.; King, C. Y.; Wall, J.; Simon, M.; Caspar, D. L. D. *Proc. Natl. Acad. Sci. USA* **2005**, *102*, 10165-10170.
- (44) Krishnan, R.; Lindquist, S. L. *Nature* **2005**, *435*, 765-72.
- (45) Spencer, R. G. S.; Halverson, K. J.; Auger, M.; McDermott, A. E.; Griffin, R. G.; Lansbury, P. T. *Biochemistry* **1991**, *30*, 10382-10387.
- (46) Jarrett, J. T.; Costa, P. R.; Griffin, R. G.; Lansbury, P. T., Jr. *J. Am. Chem. Soc.* **1994**, *116*, 9741-9742.
- (47) Griffiths, J. M.; Ashburn, T. T.; Auger, M.; Costa, P. R.; Griffin, R. G.; Lansbury, P. T., Jr. *J. Am. Chem. Soc.* **1995**, *117*, 3539-3546.
- (48) Lansbury, P. T.; Costa, P. R.; Griffiths, J. M.; Simon, E. J.; Auger, M.; Halverson, K. J.; Kocisko, D. A.; Hendsch, Z. S.; Ashburn, T. T.; Spencer, R. G. S.; Tidor, B.; Griffin, R. G. *Nature Struct. Biol.* **1995**, *2*, 990-998.
- (49) Costa, P. R.; Kocisko, D. A.; Sun, B. Q.; Lansbury, P. T.; Griffin, R. G. *J. Am. Chem. Soc.* **1997**, *119*, 10487-10493.
- (50) Tycko, R. *Protein Pept Lett* **2006**, *13*, 229-34.
- (51) Tycko, R. *Q Rev Biophys* **2006**, 1-55.
- (52) Antzutkin, O. N.; Balbach, J. J.; Leapman, R. D.; Rizzo, N. W.; Reed, J.; Tycko, R. *Proc. Natl. Acad. Sci. USA* **2000**, *97*, 13045-13050.
- (53) Antzutkin, O. N.; Balbach, J. J.; Tycko, R. *Biophys. J.* **2003**, *84*, 3326-3335.
- (54) Antzutkin, O. N.; Leapman, R. D.; Balbach, J. J.; Tycko, R. *Biochemistry* **2002**, *41*, 15436-15450.
- (55) Balbach, J. J.; Ishii, Y.; Antzutkin, O. N.; Leapman, R. D.; Rizzo, N. W.; Dyda, F.; Reed, J.; Tycko, R. *Biochemistry* **2000**, *39*, 13748-13759.
- (56) Balbach, J. J.; Petkova, A. T.; Oyler, N. A.; Antzutkin, O. N.; Gordon, D. J.; Meredith, S. C.; Tycko, R. *Biophys. J.* **2002**, *83*, 1205-1216.

- (57) Petkova, A. T.; Ishii, Y.; Balbach, J. J.; Antzutkin, O. N.; Leapman, R. D.; Delaglio, F.; Tycko, R. *Proc. Natl. Acad. Sci. U.S.A.* **2002**, *99*, 16742-16747.
- (58) Jaroniec, C. P.; MacPhee, C. E.; Astrof, N. S.; Dobson, C. M.; Griffin, R. G. *Proc. Natl. Acad. Sci. USA* **2002**, *99*, 16748-16753.
- (59) Jaroniec, C. P.; MacPhee, C. E.; Bajaj, V. S.; McMahon, M. T.; Dobson, C. M.; Griffin, R. G. *Proc. Natl. Acad. Sci. U.S.A.* **2004**, *101*, 711-716.
- (60) Chan, J. C. C.; Oyler, N. A.; Yau, W. M.; Tycko, R. *Biochemistry* **2005**, *44*, 10669-10680.
- (61) Siemer, A. B.; Ritter, C.; Steinmetz, M. O.; Ernst, M.; Riek, R.; Meier, B. H. *J Biomol NMR* **2006**, *34*, 75-87.
- (62) Ritter, C.; Maddelein, M. L.; Siemer, A. B.; Luhrs, T.; Ernst, M.; Meier, B. H.; Saupe, S. J.; Riek, R. *Nature* **2005**, *435*, 844-8.
- (63) van der Wel, P. C. A.; Hu, K. N.; Lewandowski, J.; Griffin, R. G. *J. Am. Chem. Soc.* **2006**, *128*, 10840-10846.
- (64) Morcombe, C. R.; Zilm, K. W. *J. Mag. Reson.* **2003**, *162*, 479-486.
- (65) Markley, J. L.; Bax, A.; Arata, Y.; Hilbers, C. W.; Kaptein, R.; Sykes, B. D.; Wright, P. E.; Wüthrich, K. *Pure & Appl. Chem.* **1998**, *70*, 117-142.
- (66) Harris, R. K.; Becker, E. D.; Cabral de Menezes, S. M.; Goodfellow, R.; Granger, P. *Solid State Nuc. Mag. Reson.* **2002**, *22*, 458-483.
- (67) Bennett, A. E.; Rienstra, C. M.; Auger, M.; Lakshmi, K. V.; Griffin, R. G. *J. Chem. Phys.* **1995**, *103*, 6951-6957.
- (68) Oas, T. G.; Griffin, R. G.; Levitt, M. H. *J. Chem. Phys.* **1988**, *89*, 692-695.
- (69) Takegoshi, K.; Nakamura, S.; Terao, T. *Chem. Phys. Lett.* **2001**, *344*, 631-637.
- (70) Takegoshi, K.; Nakamura, S.; Terao, T. *J. Chem. Phys.* **2003**, *118*, 2325-2341.
- (71) Morcombe, C. R.; Gaponenko, V.; Byrd, R. A.; Zilm, K. W. *J. Am. Chem. Soc.* **2004**, *126*, 7196-7197.
- (72) Costa, P. R.; Veshtort, M.; Griffin, R. G. *ENC Conference Abstracts* **1998**, Poster#156.

- (73) Hohwy, M.; Rienstra, C. M.; Jaroniec, C. P.; Griffin, R. G. *J. Chem. Phys.* **1999**, *110*, 7983-7992.
- (74) De Paepe, G.; Bayro, M. J.; Lewandowski, J.; Griffin, R. G. *J. Am. Chem. Soc.* **2006**, *128*, 1776-1777.
- (75) Schaefer, J.; McKay, R. A.; Stejskal, E. O. *J. Magn. Reson.* **1979**, *34*, 443-447.
- (76) Stejskal, E. O.; Schaefer, J.; McKay, R. A. *J. Magn. Reson.* **1984**, *57*, 471-485.
- (77) Baldus, M.; Petkova, A. T.; Herzfeld, J.; Griffin, R. G. *Mol. Phys.* **1998**, *95*, 1197-1207.
- (78) Petkova, A. T.; Baldus, M.; Belenky, M.; Hong, M.; Griffin, R. G.; Herzfeld, J. *Journal of Magnetic Resonance* **2003**, *160*, 1-12.
- (79) Egorova-Zachernyuk, T. A.; Hollander, J.; Fraser, N.; Gast, P.; Hoff, A. J.; Cogdell, J.; de Groot, H. J. M.; Baldus, M. *J. Biomol. NMR* **2001**, *19*, 243-253.
- (80) Pauli, J.; Baldus, M.; van Rossum, B.-J.; de Groot, H. J. M.; Oschkinat, H. *CHEMBIOCHEM.* **2001**, *2*, 272-281.
- (81) Delaglio, F.; Grzesiek, S.; Vuister, G. W.; Zhu, G.; Pfeifer, J.; Bax, A. *J. Biomol. NMR* **1995**, *6*, 277-293.
- (82) Goddard, T. D.; Kneller, D. G.; SPARKY 3 ed.; University of California, San Francisco.
- (83) Cornilescu, G.; Delaglio, F.; Bax, A. *J. Biomol. NMR* **1999**, *13*, 289-302.
- (84) Wishart, D. S.; Sykes, B. D.; Richards, F. M. *J Mol Biol* **1991**, *222*, 311-33.
- (85) Wishart, D. S.; Nip, A. M. *Biochem Cell Biol* **1998**, *76*, 153-63.
- (86) Zhang, H.; Neal, S.; Wishart, D. S. *J. Biomol. NMR* **2003**, *25*, 173.
- (87) Wishart, D. S.; Sykes, B. D. *J Biomol NMR* **1994**, *4*, 171-80.
- (88) Long, J. R.; Sun, B. Q.; Bowen, A.; Griffin, R. G. *J. Am. Chem. Soc.* **1994**, *116*, 11950-11956.
- (89) Maus, D. C.; Copié, V.; Sun, B.; Griffiths, J. M.; Griffin, R. G.; Luo, S.; Schrock, R. R.; Liu, A. H.; Seidel, S.; Davis, W. M.; Grohmann, A. *J Am. Chem. Soc.* **1996**, *118*, 5665-5671.

- (90) Azriel, R.; Gazit, E. *J. Biol. Chem.* **2001**, *276*, 34156-34161.
- (91) Pettersen, E. F.; Goddard, T. D.; Huang, C. C.; Couch, G. S.; Greenblatt, D. M.; Meng, E. C.; Ferrin, T. E. *J. Comput. Chem.* **2004**, *25*, 1605-1612.
- (92) DeLano, W. L.; DeLano Scientific: San Carlos, CA, USA, 2002.

12. Efficient high resolution structure determination of a protein by solid-state NMR

12.1 Abstract

De novo structure determination by solid-state NMR complements X-ray and solution NMR techniques to study biomolecular systems, among which membrane proteins and amyloid fibrils are of primary importance. Despite this promising high-impact, SSNMR is still lacking robust/efficient methods to undertake *de novo* structural studies on such complex systems. We present a method that allows one to efficiently detect structurally relevant medium to long range/distance intra-, as well as inter-molecular contacts and thus addresses one of the essential key problems in solid-state biomolecular NMR. The method relies on a Third Spin Assisted Recoupling (TSAR) process that allows transferring magnetization through space between $^{13}\text{C}/^{15}\text{N}$ nuclei using surrounding protons as assisting spins. It results in a highly efficient method for *de novo* high resolution solid-state protein structure determination.

The reference model system chosen to demonstrate the relevance and potential of the method is a uniformly labeled protein dimer Crh (2×10.4 kDa). The data were collected on a 900 and 750 MHz ^1H Larmor frequency system under magic angle spinning ($\omega_r/2\pi = 20$ kHz) using few milligrams of a single uniformly labeled sample. The distance restraints were extracted from ^{13}C - ^{13}C PAR and ^{15}N - ^{13}C PAIN-CP spectra using the Ambiguous Restraints Iterative Assignment program (ARIA) originally designed for solution-state NMR and recently modified for solid-state data. Combined with dihedral angle restraints predicted from chemical shifts and previously measured proton restraints, these restraints yielded a refined 3D structure of the fully labeled Crh dimer at a root mean square deviation of 0.65 Å and an accuracy of 2 Å with respect to the x-ray structure.

De novo atomic structure determination of biomolecules was one of the major breakthroughs in molecular biology during the last fifty years. X-ray diffraction was used to solve over 40000 crystal structures of proteins, nucleic acids and other biological molecules. The end of the 20th century also witnessed the establishment of a second technique -- solution NMR -- yielding atomic structures and dynamics of soluble proteins in the liquid state. The size limit of proteins amenable to structural determination with the later technique has nowadays reached 80 kDa enabling to solve so far over 6000 protein structures.¹⁻¹⁹ These techniques, together with electron microscopy and bioinformatics,²⁰⁻²⁷ have profoundly changed our understanding of the cell's operation thanks to an improved knowledge of the basis for protein stability, activity, folding and misfolding.²⁸⁻³¹ This knowledge is not only behind the heyday of the molecular biology but also important for the bionanotechnology that aims at designing and using the "tiny machines" first speculated about by Feynman in the mid-20th century³². A great deal of hope is placed on such biomimetic nanomechanical devices³³ for applications in areas ranging from enhanced energy production³⁴ to molecular memories^{35,36}, molecular electronics³⁷⁻³⁹, quantum computing or nanobiosensors.

Membrane proteins (playing a central role in cellular transport, intercellular signaling, and growth regulation) and amyloid fibrils (a primer of self-assembling systems; involved in many degenerative diseases), even though extremely important from both molecular biology and nanobiotechnology point of view, are underrepresented in the structural databases due to challenges associated with solving their structures with X-ray diffraction and solution NMR. An alternative technique, solid-state NMR (SSNMR), is currently emerging as a solution for studying such systems. Indeed, SSNMR comes closer to overcoming the two of its major challenges, i.e. sensitivity and resolution, and starts fully exploiting its intrinsic advantages, i.e. absence of molecular size limitation (present in solution NMR) and no necessity for long-range order (required for X-ray diffraction).

To date SSNMR was very successful in solving a variety of specific structural, mechanistic and dynamical problems in proteins.⁴⁰⁻⁴⁵ However, SSNMR in the context of proteomics and *de novo* protein structure determination is still a developing

field.^{40,41,43-49} In this report, we introduce a new approach for efficient detection of structurally relevant medium to long distance restraints and thus address one of the key problems in biomolecular SSNMR for 3D structure determination. The method relies on a Third Spin Assisted Recoupling (TSAR)⁵⁰ process that allows transferring magnetization through space between ¹³C/¹⁵N nuclei using surrounding protons as assisting spins. Since the approach is applicable to uniformly ¹³C and ¹⁵N systems it provides a venue for efficient high resolution protein structure determination in solid state. We use these methods in conjunction with the Ambiguous Restraints Iterative Assignment program (ARIA)⁵¹ to solve the structure of a Crh protein dimer⁵² (2 x 10.4 kDa). The obtained restraints, in combination with previously measured proton restraints from a heterogeneously ¹⁵N and ¹³C labeled sample⁵³ yield a structure with a backbone rmsd of 0.65 Å and an accuracy of 2 Å. This high resolution structure, obtained from data recorded within ~15 days, highlights the potential of TSAR based methods for structure determination of large biomolecules in the solid state.

Most of the biomolecular SSNMR studies are currently done under high resolution conditions provided by fast sample spinning at the magic angle (MAS)^{54,55} and the use of line-narrowing techniques.⁵⁶⁻⁵⁸ Access to higher magnetic fields and advanced nuclear hyper-polarization methods prior to conventional NMR experiments⁵⁹⁻⁶¹ in conjunction with adequate sample preparation⁶² are rapidly revolutionizing the scope of the technique. One of the main tools of high resolution SSNMR -- dipolar recoupling methods⁶³⁻⁶⁹ compatible with high spinning frequencies and high magnetic fields⁷⁰ -- have now matured to a point where assignment^{71,72} and structural studies of tens of kDa size biomolecules are currently under investigation.

The role of the protons is of central importance for understanding of the differences between biomolecular solution and solid-state NMR. In solution dipolar couplings involving protons are averaged out by isotropic tumbling but they remain present and lead to broadening in solids. Despite tremendous advances in MAS line-narrowing techniques^{73,74} the proton dimension alone is still not sufficiently resolved to mimic solution NMR where protein structure up to 20 kDa are solved routinely only based on ¹H-¹H NOE restraints. As a consequence, MAS SSNMR studies of biomolecules mainly rely on low gamma nuclei (¹³C, ¹⁵N) spectra obtained using cross polarization⁶⁸ and

high ^1H power decoupling conditions.^{56,75} Moreover, because of the low natural abundance of the ^{13}C and ^{15}N nuclei, and therefore the poor sensitivity of the NMR experiment, isotopic labeling is generally employed for protein structure determination by SSNMR (as in solution NMR for proteins larger than 20 kDa).

Access to structurally relevant restraints is currently one of the major challenges in biomolecular SSNMR with the promises for atomic 3D *de novo* structure determination of systems such as amyloid fibrils and membrane proteins. Looking at the methods for obtaining long distance contacts in solution and solid-state NMR we run into a seeming paradox. To transfer polarization over 4-5 Å ^1H - ^1H distance it requires ~250 ms NOESY mixing in solution and ~1 ms mixing in solids (or ~30-50 ms for 4-5 Å ^{13}C - ^{13}C distance). At first sight, it might appear that it should be easier to detect long distance transfer in solids than in liquids. However, multi-spin dynamics in solids induces a dipolar truncation effect with the largest couplings (shortest distance) quenching the polarization transfer over the smaller couplings (often encoding long-range information) that makes such measurements challenging in solids. In ^{13}C uniformly labeled system, the spin dynamics is often dominated by one-bond couplings leading to relayed transfer mechanisms, which is useful for assignment but cannot provide long distance restraints.^{72,76}

Attempts to reduce dipolar truncation and provide solid-state NMR alternative to the NOESY experiments have already been reported. The first class of approaches is based on a spin diffusion mechanism,⁷⁷⁻⁸¹ which for ^{13}C or ^{15}N detected MAS SSNMR experiments is nowadays referred as Proton Driven Spin Diffusion (PDS).^{80,82} The mechanism involved can be extended to higher MAS frequencies by the application of a Dipolar Assisted Rotational Resonance (DARR) irradiation on the ^1H channel.⁸³⁻⁸⁵ The second class is somewhat analogous to solution NMR and relies in probing ^1H - ^1H contacts with indirect detection on the rare spins.⁸⁶ A new class of recoupling sequences, Proton Assisted Insensitive Nuclei (PAIN-CP) and homonuclear Proton Assisted Recoupling (PAR), has been introduced by the same authors as an efficient way to reduce dipolar truncation in biomolecular solids yielding highly resolved and sensitive spectra.⁸⁷ The underlying mechanism is referred as TSAR (Third Spin Assisted Recoupling)⁵⁰ and relies on a (second order) three spin mechanism that can

provide efficient ^{15}N - ^{13}C , ^{13}C - ^{13}C and ^{15}N - ^{15}N polarization transfer using protons as assisting spins.

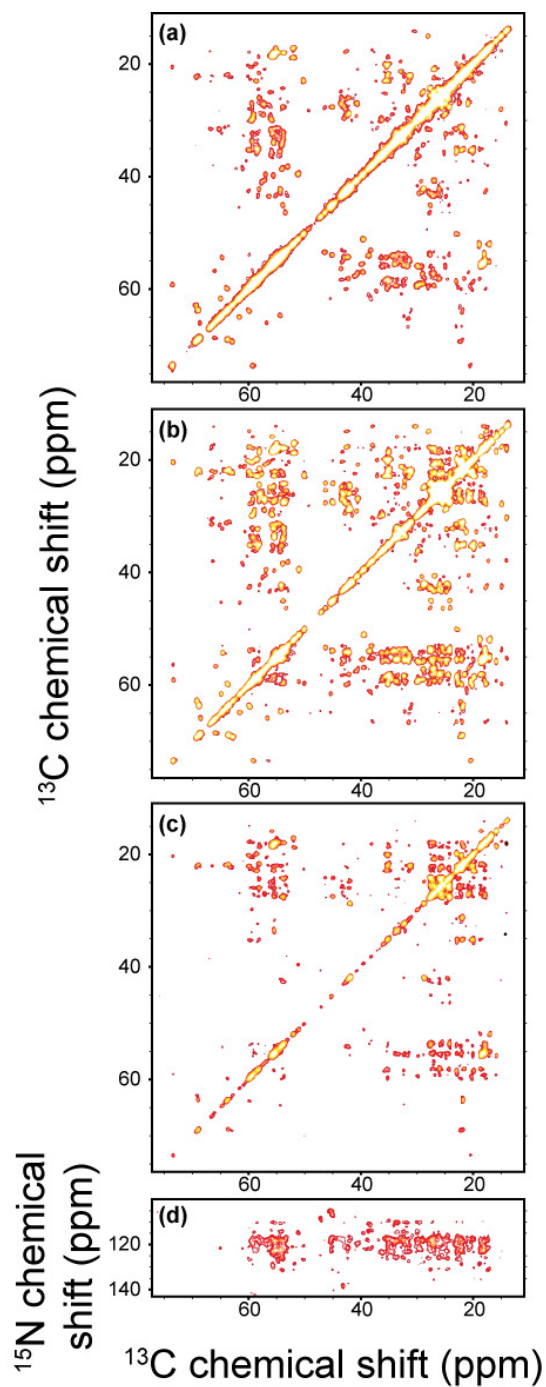


Figure 12-1 2D correlation spectra used for the de novo $[\text{U-}^{13}\text{C},^{15}\text{N}]$ -Crh protein dimer structure calculation : (a) 2 ms ^{13}C - ^{13}C PAR spectrum, (b) combined 5 ms, 10 ms and 15 ms ^{13}C - ^{13}C PAR spectra (c) 20 ms ^{13}C - ^{13}C PAR spectrum, (d) 15 ms ^{15}N - ^{13}C PAIN-CP spectrum. All spectra

were obtained at $\omega_r/2\pi = 20$ kHz. Spectra (a)-(c) were obtained at $\omega_{0H}/2\pi = 900$ MHz and spectrum (d) at $\omega_{0H}/2\pi = 750$ MHz.

We have used ^{13}C - ^{13}C PAR and ^{15}N - ^{13}C PAIN-CP as a source of distance restraints for protein structure calculations. The SSNMR experimental data used for *de novo* structure determination of the [U- ^{13}C , ^{15}N]-Crh dimer consisted of three TSAR-based experiments. ^{13}C - ^{13}C PAR spectra were recorded with 2, 5, 10, 15 and 20 ms mixing times using $\omega_r/2\pi = 20$ kHz at $\omega_{0H}/2\pi = 900$ MHz and ^{15}N - ^{13}C PAIN-CP spectra were collected with 1 and 15 ms mixing time using $\omega_r/2\pi = 20$ kHz at $\omega_{0H}/2\pi = 900$ MHz and $\omega_{0H}/2\pi = 750$ MHz respectively (see Fig. 12-1). The combination of high magnetic field and the highly efficient TSAR polarization transfer lead to extremely well resolved spectra with a large number of structurally valuable distance restraints. The data were collected on a single ~6 mg protein sample packed in a 2.5 mm rotor.

In order to assign the highly ambiguous cross-peaks (restraints) from SSNMR spectra of the [U- ^{13}C , ^{15}N] Crh dimer, we have used a dedicated SSNMR version of the program ARIA 2.2.²⁵ The protocol consists in three consecutive steps, comprising a total of 6 ARIA runs. The input of the ARIA calculation consisted in the amino-acid sequence of the Crh protein, the solid-state NMR chemical shift assignment,⁵² the TALOS⁸⁹ dihedral angle restraints predicted from the solid-state NMR chemical shifts, and peak lists extracted from two-dimensional ^{13}C - ^{13}C PAR (2 ms mixing time with target distance 4 Å, combined 5+10+15 ms mixing time with target distance 5 Å and 20 ms mixing time with target distance 6 Å), ^{13}C - ^{15}N PAIN-CP (15 ms mixing time with target distance 6 Å), and previously reported⁵³ NHHC correlation spectra from a heterogeneously ^{15}N and ^{13}C labeled Crh sample. Manual peak picking was realized using the program Sparky 3.1 (T. D. Goddard & D. G. Kneller, University of California).

The iterative assignment by the ARIA program proceeded through 3 steps. First (Step I), the signals from the PAR spectra were searched for intramolecular assignments. 5 ARIA runs were used to determine a list of unambiguous distance restraints sufficient to provide a good precision structure of the monomeric part, as shown in Fig. 12-2a, where the structure bundles are shown resulting from the first five runs (residues 12-82 are shown). In Step II we used NHHC data from the heterogeneously labeled Crh sample,⁵³

that contains exclusively intermonomeric restraints, in order to obtain the initial dimer fold. In Step III, we have focused on the intermolecular restraint search, by adding the possibility during the assignment for each cross-peak to be intra- and/or intermonomeric. The distribution and number of unambiguously assigned restraints after a single run of Step III are presented in Fig. 12-2.

The selected lowest energy conformers were aligned on the backbone atoms using MOLMOL 2K.2.²⁴ The quality of the SSNMR ensembles was analyzed by calculating the rmsd between the conformers (which we refer to as precision) superimposed on one of 2 hypothetical monomers (a short monomer from residue 12 to 82 and a long monomer from residue 2 to 82) or on the complete dimer (residues 2-82 from chains A and B), as well as the rmsd between the average structure of the NMR ensemble and the x-ray crystal structure (which we refer to as accuracy).

Figure 12 illustrates the convergence of the 3D protein structure after each step. Figure 12-3a shows resulting monomer structures after 5 iterations of Step I. Figure 12-3b shows the resulting structure bundles from the Step II. Finally, the result of Step III is shown in Fig. 12-3c. For comparison Fig. 12-3d depicts the x-ray structure of the Crh dimer.

The last run of the Step III yielded a refined 3D structure of the fully labeled Crh dimer at a root mean square deviation of 0.65 Å and an accuracy of 2 Å (rmsd with respect to the x-ray structure). Note that addition of the restraints from previously recorded CHHC and NHHC spectra on [U-¹³C,¹⁵N]-Crh⁸⁸ improved the precision to 0.45 Å but had not affected the rmsd with respect to the x-ray structure.

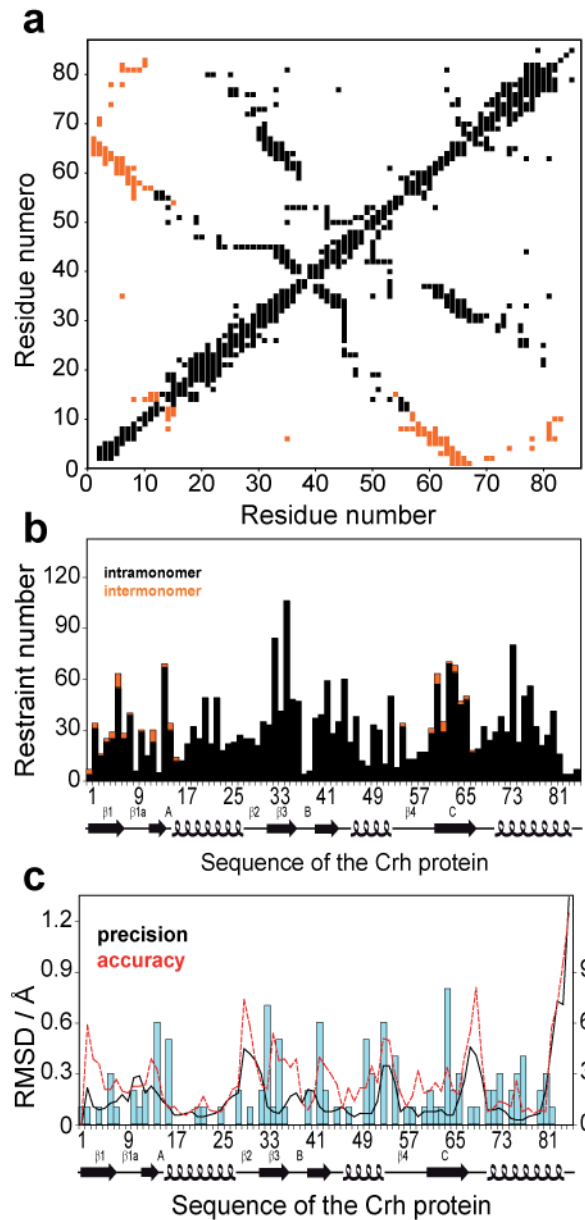


Figure 12-2 Contact plot of distance restraints unambiguously assigned at the end of Step III. (b) Number of distance restraints as a function of the primary sequence of the protein. The intramonomer restraints in panels (a) and (b) are indicated in black and the intermonomer restraints are indicated in orange. (c) Local rmsd of the 10 lowest energy conformers after Step III. The number of restraints corresponding to distances $> 7 \text{ \AA}$ in x-ray structure is indicated in blue (see right hand axis).

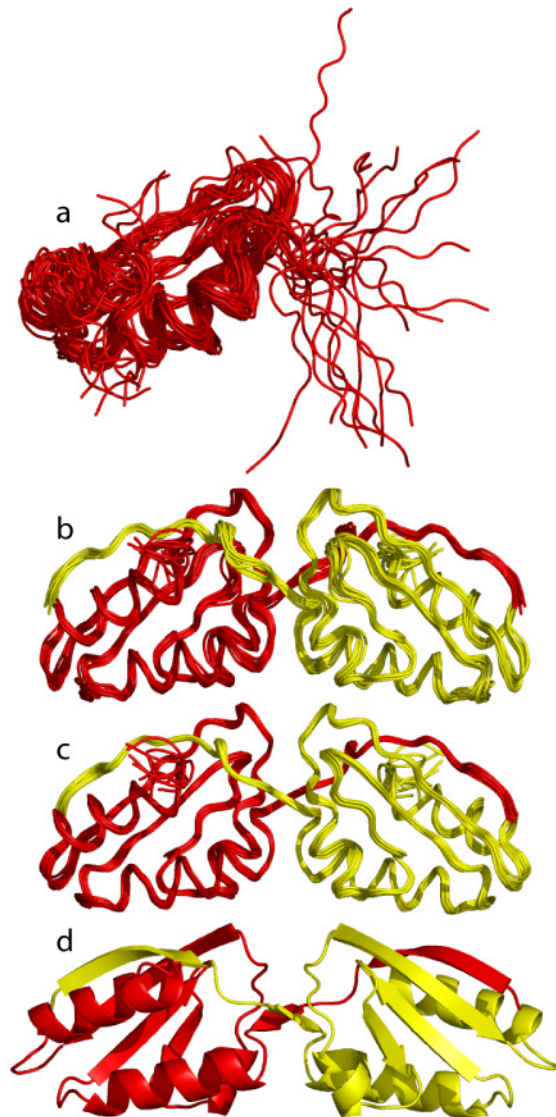


Figure 12-3 Lowest energy Crh structures from ARIA calculations: (a) 20 lowest energy conformers after the end of monomer calculations using PAR data, (b) 10 lowest energy dimer conformers after the calculations with PAR and intermonomer NHHC data, (c) 10 lowest energy dimer conformers after calculation with PAR, PAIN-CP and intermonomer NHHC data, (d) x-ray structure.

12.2 Conclusion

We have introduced a new approach relying on TSAR based techniques for efficient *de novo* high resolution structure determination of proteins. We show that ^{13}C - ^{13}C PAR and ^{15}N - ^{13}C PAIN-CP spectra on 2 x 10.4 kDa [U- ^{13}C , ^{15}N]-Crh protein dimer provide numerous long range and long distance restraints that in analogy to NOE based methods in solution NMR constrain tightly the fold of the protein – here with precision of 0.65 Å and accuracy of 2 Å. The TSAR based techniques are applicable over almost the entire range of currently available spinning frequencies ($\omega_r/2\pi \sim 10$ -70 kHz) and thus open-up a number of new exciting venues for structure determination of biomolecules and can be coupled with proton detection in solid-state as well low power NMR spectroscopy. The high sensitivity of the PAR and PAIN-CP spectra combined with reduced crowding compared to DARR and PDSM spectra should substantially increase the size of systems accessible for *de novo* structure determination in the solid state (a study on a 17.6 kDa protein MMP-12 analogous to the one presented here is currently in progress).

12.3 Acknowledgements

The work in this chapter is a result of collaboration with G. De Paëpe from Griffin Group, and Anja Böckmann and Antoine Loquet from IBCP, Lyon, France.

12.4 References

- (1) Adler, M.; Lazarus, R. A.; Dennis, M. S.; Wagner, G. *Science* **1991**, 253, 445-448.
- (2) Baleja, J. D.; Marmorstein, R.; Harrison, S. C.; Wagner, G. *Nature* **1992**, 356, 450-453.
- (3) Battiste, J. L.; Mao, H. Y.; Rao, N. S.; Tan, R. Y.; Muhandiram, D. R.; Kay, L. E.; Frankel, A. D.; Williamson, J. R. *Science* **1996**, 273, 1547-1551.
- (4) Clore, G. M.; Omichinski, J. G.; Sakaguchi, K.; Zambrano, N.; Sakamoto, H.; Appella, E.; Gronenborn, A. M. *Science* **1994**, 265, 386-391.

- (5) Brunger, A. T.; Clore, G. M.; Gronenborn, A. M.; Saffrich, R.; Nilges, M. *Science* **1993**, *261*, 328-331.
- (6) Gronenborn, A. M.; Filpula, D. R.; Essig, N. Z.; Achari, A.; Whitlow, M.; Wingfield, P. T.; Clore, G. M. *Science* **1991**, *253*, 657-661.
- (7) Ikura, M.; Clore, G. M.; Gronenborn, A. M.; Zhu, G.; Klee, C. B.; Bax, A. *Science* **1992**, *256*, 632-638.
- (8) Kay, L. E.; Clore, G. M.; Bax, A.; Gronenborn, A. M. *Science* **1990**, *249*, 411-414.
- (9) Ketchum, R. R.; Hu, W.; Cross, T. A. *Science* **1993**, *261*, 1457-1460.
- (10) Mittermaier, A.; Kay, L. E. *Science* **2006**, *312*, 224-228.
- (11) Neri, D.; Billeter, M.; Wider, G.; Wuthrich, K. *Science* **1992**, *257*, 1559-1563.
- (12) Omichinski, J. G.; Clore, G. M.; Schaad, O.; Felsenfeld, G.; Trainor, C.; Appella, E.; Stahl, S. J.; Gronenborn, A. M. *Science* **1993**, *261*, 438-446.
- (13) Otting, G.; Liepinsh, E.; Wuthrich, K. *Science* **1991**, *254*, 974-980.
- (14) Riek, R.; Hornemann, S.; Wider, G.; Billeter, M.; Glockshuber, R.; Wuthrich, K. *Nature* **1996**, *382*, 180-182.
- (15) Sprangers, R.; Kay, L. E. *Nature* **2007**, *445*, 618-622.
- (16) Tjandra, N.; Bax, A. *Science* **1997**, *278*, 1111-1114.
- (17) Wagner, G.; Wuthrich, K. *Nature* **1978**, *275*, 247-248.
- (18) Wuthrich, K. *Science* **1989**, *243*, 45-50.
- (19) Zahn, R.; Spitzfaden, C.; Ottiger, M.; Wuthrich, K.; Pluckthun, A. *Nature* **1994**, *368*, 261-265.
- (20) Brunger, A. T.; Adams, P. D.; Clore, G. M.; DeLano, W. L.; Gros, P.; Grosse-Kunstleve, R. W.; Jiang, J. S.; Kuszewski, J.; Nilges, M.; Pannu, N. S.; Read, R. J.; Rice, L. M.; Simonson, T.; Warren, G. L. *Acta Crystallographica Section D-Biological Crystallography* **1998**, *54*, 905-921.
- (21) Brunger, A. T.; Adams, P. D.; Rice, L. M. *Current Opinion in Structural Biology* **1998**, *8*, 606-611.
- (22) Herrmann, T.; Guntert, P.; Wuthrich, K. *Journal of Biomolecular Nmr* **2002**, *24*, 171-189.

- (23) Herrmann, T.; Guntert, P.; Wuthrich, K. *Journal of Molecular Biology* **2002**, *319*, 209-227.
- (24) Koradi, R.; Billeter, M.; Wuthrich, K. *Journal of Molecular Graphics* **1996**, *14*, 51-&.
- (25) Linge, J. P.; Habeck, M.; Rieping, W.; Nilges, M. *Bioinformatics* **2003**, *19*, 315-316.
- (26) Linge, J. P.; Williams, M. A.; Spronk, C.; Bonvin, A.; Nilges, M. *Proteins-Structure Function and Genetics* **2003**, *50*, 496-506.
- (27) Schwieters, C. D.; Kuszewski, J. J.; Tjandra, N.; Clore, G. M. *Journal of Magnetic Resonance* **2003**, *160*, 65-73.
- (28) Balbach, J.; Forge, V.; Lau, W. S.; vanNuland, N. A. J.; Brew, K.; Dobson, C. M. *Science* **1996**, *274*, 1161-1163.
- (29) Klein-Seetharaman, J.; Oikawa, M.; Grimshaw, S. B.; Wirmer, J.; Duchardt, E.; Ueda, T.; Imoto, T.; Smith, L. J.; Dobson, C. M.; Schwalbe, H. *Science* **2002**, *295*, 1719-1722.
- (30) Korzhnev, D. M.; Salvatella, X.; Vendruscolo, M.; Di Nardo, A. A.; Davidson, A. R.; Dobson, C. M.; Kay, L. E. *Nature* **2004**, *430*, 586-590.
- (31) Varley, P.; Gronenborn, A. M.; Christensen, H.; Wingfield, P. T.; Pain, R. H.; Clore, G. M. *Science* **1993**, *260*, 1110-1113.
- (32) Feynman, R. P.; Leighton, R. B.; Sands, M. *The Feynman Lectures on Physics* Reading, MA, 1963.
- (33) Mao, C. D.; Sun, W. Q.; Shen, Z. Y.; Seeman, N. C. *Nature* **1999**, *397*, 144-146.
- (34) Atsumi, S.; Hanai, T.; Liao, J. C. *Nature* **2008**, *451*, 86-U13.
- (35) Klibanov, A. M. *Nature* **2001**, *409*, 241-246.
- (36) Liu, Z. M.; Yasseri, A. A.; Lindsey, J. S.; Bocian, D. F. *Science* **2003**, *302*, 1543-1545.
- (37) Keren, K.; Berman, R. S.; Buchstab, E.; Sivan, U.; Braun, E. *Science* **2003**, *302*, 1380-1382.
- (38) Shen, Y.; Safinya, C. R.; Liang, K. S.; Ruppert, A. F.; Rothschild, K. J. *Nature* **1993**, *366*, 48-50.

- (39) Tang, X. P.; Kleinhammes, A.; Shimoda, H.; Fleming, L.; Bennoune, K. Y.; Sinha, S.; Bower, C.; Zhou, O.; Wu, Y. *Science* **2000**, *288*, 492-494.
- (40) Castellani, F.; van Rossum, B.; Diehl, A.; Schubert, M.; Rehbein, K.; Oschkinat, H. *Nature* **2002**, *420*, 98-102.
- (41) Creuzet, F.; McDermott, A.; Gebhard, R.; Vanderhoef, K.; Spijkerassink, M. B.; Herzfeld, J.; Lugtenburg, J.; Levitt, M. H.; Griffin, R. G. *Science* **1991**, *251*, 783-786.
- (42) Heise, H.; Seidel, K.; Etzkorn, M.; Becker, S.; Baldus, M. *Journal of Magnetic Resonance* **2005**, *173*, 64-74.
- (43) Zech, S. G.; Wand, A. J.; McDermott, A. E. *Journal of the American Chemical Society* **2005**, *127*, 8618-8626.
- (44) Lange, A.; Becker, S.; Seidel, K.; Giller, K.; Pongs, O.; Baldus, M. *Angewandte Chemie-International Edition* **2005**, *44*, 2089-2092.
- (45) Castellani, F.; van Rossum, B. J.; Diehl, A.; Rehbein, K.; Oschkinat, H. *Biochemistry* **2003**, *42*, 11476-11483.
- (46) Jaroniec, C. P.; MacPhee, C. E.; Bajaj, V. S.; McMahan, M. T.; Dobson, C. M.; Griffin, R. G. *Proceedings of the National Academy of Sciences of the United States of America* **2004**, *101*, 711-716.
- (47) Rienstra, C. M.; Tucker-Kellogg, L.; Jaroniec, C. P.; Hohwy, M.; Reif, B.; McMahan, M. T.; Tidor, B.; Lozano-Perez, T.; Griffin, R. G. *Proceedings of the National Academy of Sciences of the United States of America* **2002**, *99*, 10260-10265.
- (48) Seidel, K.; Etzkorn, M.; Heise, H.; Becker, S.; Baldus, M. *Chembiochem* **2005**, *6*, 1638-1647.
- (49) Zhou, D. H.; Shea, J. J.; Nieuwkoop, A. J.; Franks, W. T.; Wylie, B. J.; Mullen, C.; Sandoz, D.; Rienstra, C. M. *Angew Chem Int Ed Engl* **2007**, *46*, 8380-3.
- (50) Lewandowski, J. R.; De Paepe, G.; Griffin, R. G. *Journal of the American Chemical Society* **2007**, *129*, 728-729.
- (51) Nilges, M.; Macias, M. J.; ODonoghue, S. I.; Oschkinat, H. *Journal of Molecular Biology* **1997**, *269*, 408-422.

- (52) Bockmann, A.; Lange, A.; Galinier, A.; Luca, S.; Giraud, N.; Juy, M.; Heise, H.; Montserret, R.; Penin, F.; Baldus, M. *Journal of Biomolecular Nmr* **2003**, *27*, 323-339.
- (53) Etzkorn, M.; Bockmann, A.; Lange, A.; Baldus, M. *Journal of the American Chemical Society* **2004**, *126*, 14746-14751.
- (54) Andrew, E. R.; Bradbury, A.; Eades, R. G. *Nature* **1958**, *182*, 1659-1659.
- (55) Andrew, E. R.; Bradbury, A.; Eades, R. G. *Nature* **1959**, *183*, 1802-1803.
- (56) Bennett, A. E.; Rienstra, C. M.; Auger, M.; Lakshmi, K. V.; Griffin, R. G. *Journal of Chemical Physics* **1995**, *103*, 6951-6958.
- (57) Hodgkinson, P. *Progress in Nuclear Magnetic Resonance Spectroscopy* **2005**, *46*, 197-222.
- (58) Mehring, M.; Pines, A.; Rhim, W. K.; Waugh, J. S. *Journal of Chemical Physics* **1971**, *54*, 3239-&.
- (59) Abragam, A. *The Principles of Nuclear Magnetism*; Oxford University Press: London, 1961.
- (60) Barnes, A. B.; De Paepe, G.; van der Wel, P. C. A.; Hu, K.; Joo, C.; Bajaj, V. S.; Mak-Jurkauskas, M. L.; Sirigiri, J. R.; Herzfeld, J.; Temkin, R. J.; Griffin, R. G. *Applied Magnetic Resonance* **2008**.
- (61) Hall, D. A.; Maus, D. C.; Gerfen, G. J.; Inati, S. J.; Becerra, L. R.; Dahlquist, F. W.; Griffin, R. G. *Science* **1997**, *276*, 930-932.
- (62) Martin, R. W.; Zilm, K. W. *Journal of Magnetic Resonance* **2003**, *165*, 162-174.
- (63) Andrew, E. R.; Clough, S.; Farnell, L. F.; Gledhill, T. D.; Roberts, I. *Physics Letters* **1966**, *21*, 505-&.
- (64) Bennett, A. E.; Ok, J. H.; Griffin, R. G.; Vega, S. *Journal of Chemical Physics* **1992**, *96*, 8624-8627.
- (65) Griffin, R. G. *Nature Structural Biology* **1998**, *5*, 508-512.
- (66) Hartmann, S. R.; Hahn, E. L. *Phys. Rev.* **1962**, *128*, 2042-2053.
- (67) Oas, T. G.; Griffin, R. G.; Levitt, M. H. *Journal of Chemical Physics* **1988**, *89*, 692-695.

- (68) Pines, A.; Gibby, M. G.; Waugh, J. S. *Journal of Chemical Physics* **1973**, *59*, 569-590.
- (69) Raleigh, D. P.; Levitt, M. H.; Griffin, R. G. *Chemical Physics Letters* **1988**, *146*, 71-76.
- (70) De Paepe, G.; Bayro, M. J.; Lewandowski, J.; Griffin, R. G. *Journal of the American Chemical Society* **2006**, *128*, 1776-1777.
- (71) Baldus, M. *Progress in Nuclear Magnetic Resonance Spectroscopy* **2002**, *41*, 1-47.
- (72) Lewandowski, J.; De Paepe, G.; van der Wel, P.; Birkett, N. R.; Belenky, M.; Maly, T.; Bayro, M. J.; Sivertsen, A. C.; Dobson, C. M.; Herzfeld, J.; Griffin, R. G. *Submitted* **2008**.
- (73) Elena, B.; de Paepe, G.; Emsley, L. **2004**, *398*, 532-538.
- (74) Zhou, D. H.; Shea, J. J.; Nieuwkoop, A. J.; Franks, W. T.; Wylie, B. J.; Mullen, C.; Sandoz, D.; Rienstra, C. M. *Angewandte Chemie-International Edition* **2007**, *46*, 8380-8383.
- (75) Detken, A.; Hardy, E. H.; Ernst, M.; Meier, B. H. *Chemical Physics Letters* **2002**, *356*, 298-304.
- (76) De Paepe, G.; Lewandowski, J. R.; Griffin, R. G. *Journal of Chemical Physics* **2008**, *In Press*.
- (77) Suter, D.; Ernst, R. R. *Physical Review B* **1985**, *32*, 5608-5627.
- (78) Caravatti, P.; Neuenschwander, P.; Ernst, R. R. *Macromolecules* **1985**, *18*, 119-122.
- (79) Caravatti, P.; Deli, J. A.; Bodenhausen, G.; Ernst, R. R. *Journal of the American Chemical Society* **1982**, *104*, 5506-5507.
- (80) Szeverenyi, N. M.; Sullivan, M. J.; Maciel, G. E. *Journal of Magnetic Resonance* **1982**, *47*, 462-475.
- (81) Douglass, D. C.; McBrierty, V. J. *Macromolecules* **1978**, *11*, 766-773.
- (82) Grommek, A.; Meier, B. H.; Ernst, M. *Chemical Physics Letters* **2006**, *427*, 404-409.
- (83) Takegoshi, K.; Nakamura, S.; Terao, T. *Chemical Physics Letters* **2001**, *344*, 631-637.

(84) Takegoshi, K.; Nakamura, S.; Terao, T. *Journal of Chemical Physics* **2003**, *118*, 2325-2341.

(85) Morcombe, C. R.; Gaponenko, V.; Byrd, R. A.; Zilm, K. W. *Journal of the American Chemical Society* **2004**, *126*, 7196-7197.

(86) Lange, A.; Luca, S.; Baldus, M. *Journal of the American Chemical Society* **2002**, *124*, 9704-9705.

(87) De Paepe, G.; Lewandowski, J.; Locquet, A.; Bockmann, A.; Griffin, R. G. *Submitted* **2008**.

(88) Loquet, A.; Bardiaux, B.; Gardiennet, C.; Blanchet, C.; Baldus, M.; Nilges, M.; Malliavin, T.; Boeckmann, A. *Journal of the American Chemical Society* **2008**, *130*, 3579-3589.

(89) Cornilescu, G.; Delaglio, F.; Bax, A. *Journal of Biomolecular Nmr* **1999**, *13*, 289-302.

c

Curriculum Vitae

EDUCATION

Warsaw University, MISMaP	1997-1998. 1999-2000
Amherst College, B.A., Chemistry and Theater/Dance, <i>magna cum laude</i>	1998-2002
Massachusetts Institute of Technology, Ph.D. Physical Chemistry	2002-2008

HONORS AND AWARDS

Belevetz Prize	2001
Phi Betta Kappa	2002
Moore Graduate Fellowship	2002-2005
Marie Curie International Reintegration Grant	2008-2010

PUBLICATIONS

1. Pecul, M., Lewandowski J., Sadlej, J. (2001) "Benchmark calculations of the shielding constants in the water dimer" *Chem. Phys. Lett.* 333(1-2): 139-145.
2. van der Wel, P. C. A., K. N. Hu, Lewandowski, J., Griffin, R.G. (2006). "Dynamic nuclear polarization of amyloidogenic peptide nanocrystals: GNNQQNY, a core segment of the yeast prion protein Sup35p." *J. Am. Chem. Soc.* 128(33): 10840-10846.
3. De Paëpe, G., M. J. Bayro, Lewandowski, J. R., Griffin, R.G. (2006). "Broadband homonuclear correlation spectroscopy at high magnetic fields and MAS frequencies." *J. Am. Chem. Soc.* 128(6): 1776-1777.
4. Ramachandran, R., Lewandowski, J.R., van der Wel, P. C. A., Griffin, R. G. (2006). "Multipole-multimode Floquet theory of rotational resonance width experiments: ^{13}C - ^{13}C distance measurements in uniformly labeled-solids." *J. Chem. Phys.* 124(21) 214107-13.
5. Lewandowski, J.R., De Paëpe, G., Griffin, R.G. (2007) "Proton assisted insensitive nuclei cross polarization." *J. Am. Chem. Soc.* 129(4): 728-729.
6. van der Wel, P. C. A., Lewandowski, J. R., Griffin, R.G. (2007). "Solid-state NMR study of amyloid nanocrystals and fibrils formed by the peptide GNNQQNY from yeast prion protein Sup35p." *J. Am. Chem. Soc.* 129(16): 5117-5130.
7. De Paëpe, G., Lewandowski, J.R., Griffin, R.G. (2008) "Spin dynamics in the modulation frame: Application to homonuclear recoupling in magic angle spinning solid-state NMR" *J. Chem. Phys.* 128(12) 124503-26.
8. Lewandowski, J.R., De Paëpe, G., van der Wel, P. C. A., Birkett, N.R., Belenky, M., Maly, T., Bayro, M.J., Sivertsen, A.C., Dobson, C.M., Herzfeld, J., Griffin, R.G. (2008) "Double-quantum carbon-carbon relayed magnetization transfer for solid-state NMR biomolecular studies at high magnetic fields" *submitted*.
9. De Paëpe, G., Lewandowski, J.R., Loquet, A., Böckmann, A., Griffin, R.G. (2008) "Proton Assisted Homonuclear Recoupling" *submitted*.
10. Lewandowski, J.R., De Paëpe, G., Eddy, M., Griffin, R.G. (2008) " ^{15}N - ^{15}N Proton Assisted Homonuclear Recoupling for Structure Determination of Proteins" *submitted*.
11. Lewandowski, J.R., De Paëpe, G., Eddy, Struppe, J., M., Griffin, R.G. (2008) "Applications of PAR for 2D ^{13}C - ^{13}C Correlations Spectra of Protein GB1 at 65 kHz Magic Angle Spinning" *submitted*.
12. De Paëpe, G., Lewandowski, J.R., Loquet, A., Böckmann, A., Griffin, R.G. (2008) "Efficient determination of high-resolution protein structures by solid-state NMR" *in preparation*.